STRONG MICROWAVES IN PLASMAS

Volume 1

Institute of Applied Physics
Nizhny Novgorod 1991

Academy of Science of the USSR
Institute of Applied Physics

STRONG MICROWAVES IN PLASMAS

PROCEEDINGS OF THE
INTERNATIONAL WORKSHOP
Suzdal, 18 - 23 September 1990

Edited by
A.G. Litvak

In two volumes
Volume 1

Nizhny Novgorod 1991

Printed in the USSR
at Gorkovskaya Pravda,
32 Figner Street, 603006 Nizhny Novgorod

Editor's Preface

Recent advance in the development of powerful sources of microwave radiation introduced into plasma experiments new microwave devices, such as gyrotron and generators of the BWO-, CARM- and FEL-type operating at high-current beams. It also contributed to extensive investigation of powerful microwave interaction with plasma, rich in new physical effects. For example, one of the first experiments on the interaction of powerful electromagnetic waves with extended plasma was performed in, 1970 in Gorky (now Nizhny Novgorod), hardly had the first gyrotron been invented and produced. This experiment, in which the effect of wave beam self-focusing in plasma was first observed, manifested, at the same time, true potentialities of the gyrotron as a powerful source of millimeter wavelength radiation. It also initiated proposals on using gyrotrons for ECR heating of toroidal plasma at the Ioffe Institute in Leningrad and Kurchatov Institute in Moscow. A few years later the concept of plasma ECR heating with quasi-optical beams of electromagnetic waves in large-scale tokamaks was developed. Similar ideas are widely used also for lower-hybrid heating and current drive. For these purposes gyrotrons operating at centimeter wavelengths are also produced. Thus, ECRH and LH heating are not only close conceptually, but use similar equipment.

LH heating experiments are principally connected with nonlinear effects, while for ECRH it is usually possible to eliminate them. The situation is essentially different when short-pulse FELs are used for ECR heating. In the planned experiments within the MTX project (Livermore), where nanosecond pulses with gygawatt powers are employed, even relativistic dependence of the electron mass on its vibrational energy gains significance, and changes the character of ECR absorption drastically.

Development of powerful microwave sources gave rise also to extended study of the so-called freely-localized gas discharge in focused wave beams. It is of great interest as a new peculiar object of nonlinear physics; certainly, it has a lot of various applications as well. In the recent ten years these investigations have formed an independent and rather broad field of plasma physics.

Thus, now there are several lines of research within plasma physics, which are closely interrelated and highly dependent on the present situation with powerful microwave sources. It was only natural to organize a special meeting for researchers in these fields. The Institute of Applied Physics in Nizhny Novgorod is involved in studying all the said problems, so we pioneered this international endeavour.

The present book is a collection of review papers and some interesting contributions of the International Workshop on Strong Microwaves in Plasma held in Suzdal on September 19-23, 1990. In the participants' opinion, it proved to be exceedingly fruitful. We hope that the published materials giving the state-of-art overview of research in this field, will be useful also for a Reader interested in the problems of developing powerful sources of coherent microwaves and interaction of powerful electromagnetic radiation with plasma.

A.G. Litvak

CONTENTS OF VOLUME 1

Production and heating of plasma by microwaves in fusion devices

RF discharge processes in wave fields

Production and heating of plasma by microwaves in fusion devices

CONCEPTUAL DESIGN OF AN ELECTRON CYCLOTRON WAVE SYSTEM FOR ITER

L.Rebuffi for the ITER Team
ITER Team, Max-Planck-Institut für Plasmaphysik
D-8046 Garching, FRG

With contribution from:

EURATOM:

W.Henle, A.Jacobs, W.Kasparek, H.Kumric, G.A.Müller, P.G.Schüller (IPF - Stuttgart), M.Thumm (IPF - Stuttgart / KfK - Karlsruhe), M.Q.Tran (CRPP-Lausanne), G.Faillon, P.Garin, G.Mourier (Thomson T.E.), B.Jödicke (ABB), A.Dellis (UKAEA-Culham), R.Magne (CEA-Cadarache)

JAPAN:

K.Maki, T.Nagashima, K.Sakamoto, M.Tsuneoka, T.Yamamoto (JEARI), T.Kariya, Y.Itoh, Y.Mitsunaka, T.Ohno, T.Okamoto, Y.Saito (Toshiba)

SOVIET UNION:

V.V.Alikaev, V.I.Belousov, G.G.Denisov, A.S.Fix, V.A.Flyagin, V.N.Glazman, A.L.Goldenberg, V.I.Hizhnyak, S.Yu.Kornishin, V.I.Kurbatov, A.N.Kuftin, V.I.Malygin, G.S.Musinovich, L.V.Nikolaev, V.V.Parshin, .B.Pavaljev, N.Yu.Peskov, M.I.Petelin, A.V.Pylin, M.Yu.Shmelyov, P.B.Sushilin, I.N.Treskin, V.G.Usov, N.P.Venediktov, D.V.Vinogradov, V.E.Zapelatov (IAP - Nizhny Novgorod / Kurchatov - Moscow), B.V.Cheremuhov, L.B.Dinaburg, K.I. Finkelshtein, A.I. Fomichev, V.A.Geltov, G.A.Grad, E.V.Seredenko (Efremov Inst.-Leningrad) , V.E. Myasnikov (Toryi)

USA:

T.Luce, R.Prater (General Atomics), R.Temkin (MIT - Boston), H.Huey, H.Jory (Varian)

ITER Current Drive and Heating Group:

V.Parail, N.Fujisawa, H.Hopman, W.Lindquist, H.Kimura, W.Nevins, L.Rebuffi, M.Sironi, D.Swain, J.-G.Wégrowe.

The activity of the International Thermonuclear Experimental Reactor (ITER) is conduced under the auspices of the International Atomic Energy Agency (IAEA) by Euratom, Japan, The Union of the Soviet Socialist Republics and the United States of America.

1. Introduction

The conceptual design of the International Thermonuclear Experimental Reactor (ITER) has been carried out at the technical site of Garching (FRG) between 1988 to 1990, considering advanced physics and technological requirements.

The goal of ITER is to demonstrate the scientific and technological feasibility of fusion power i.e. plasma ignition and extended burn, with steady-state operation as an ultimate goal.

Auxiliaries systems contribute to create and heat the plasma to thermonuclear temperatures and to sustain and control the plasma current. In the reference scenario, the use of 75 MW / 1.3 MeV Neutral Beam, 50 MW / 5 GHz Lower Hybrid waves, 20 MW / 120 GHz Electron Cyclotron Waves (ECW) is considered [1].

World wide specialists participated at the conceptual design of the ECW system for ITER. The main problems for high power - high frequency (CW) generation, transmission and coupling in a nuclear fusion reactor have been identified. Solutions have been proposed and, considering present requirements, a reference design of the system has been retained [2], (Fig.1). This work was only the first step for the project of the ITER ECW system. In the next ITER Engineering Design Activity (EDA) a more detailed project is expected, following possible new requirements and new technological results.

The choice of the most suited frequency depends on the value of the magnetic field of the machine. Possible future variations of this parameter should not influence the design of the ECW system. In the same way, the size, the arrangement and in general all the interfaces with the machine and other systems have been defined in order to accommodate future technological improvements and/or alternatives without main changes of the design.

The general philosophy adopted for the design of the ECW system was to place the most critical components as far as possible from the machine. Furthermore the design has been realized in order to offer the high degree of flexibility demanded from the wide range of possible uses of ECW in ITER.

The ECW system should satisfy physics requirements, advanced requirements of reliability and availability, and will have to be compatible with a fusion environment (which requires radiation resistance and the possibility of remote maintenance of the transmission line and antenna system).

A sensitive technological effort should be done in the next years to develop and/or improve the main components of the ECW system responding to ITER requirements. The source and window development as well as the antenna design are probably the main issues for future R&D. Before finalizing the design, an experimental confirmation of the physics modelling for the current profile control is also required.

2. Physics requirements

ECW are considered in the ITER reference scenario to assist gas breakdown, plasma formation and pre-heating, and for local current profile control near the q=2 magnetic surface (to avoid disruption) using non-inductive current drive in the "up-shifted" mode ($\omega \simeq 1.3\ \omega_{ce}\ (r_{q=2})$) [3].

With the present ITER central magnetic field value of 4.85 T and minor radius of 2.15 m, a frequency of about 120 GHz appears appropriate for these functions.

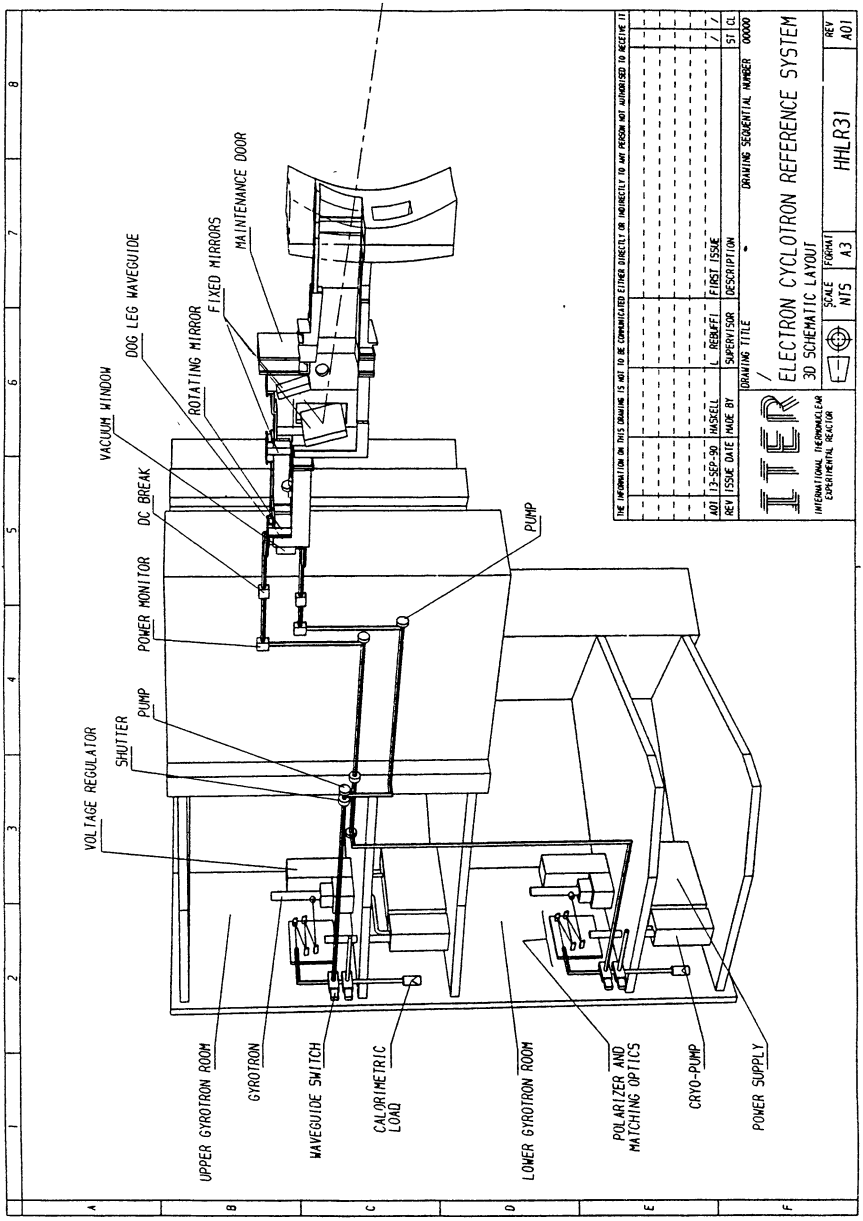

Fig.1 - Reference ITER Electron Cyclotron wave system, general 3D schematic layout.

Injection would be in a quasi-ordinary mode from the outboard side around the equatorial plane at about 20^0 with respect to the major radius direction (in the opposite direction with respect to the current).

The maximum power needed for these functions should be about 10 MW, in pulses of the order of 1 s for plasma formation and pre-heating and about 20 MW, CW for current profile control around q = 2.

For this latter function, the absorption profile of the waves should be controlled over a (minimum) radial distance of about 0.34 m in one second to follow a maximum variation of the current of about 7 MA and a radial distance of about 0.16 m to follow a maximum variation of the temperature at the q = 2 surface from 10 to 2 keV. This could be achieved by controlling the direction of wave injection, using a rotatable mirror (with an angle variation of about 10^0 in steps of about 2^0, each step in 0.2 s) and a fixed frequency, or using a fixed angle of injection and a fast frequency variation (about 5 GHz overall in 1 s, in steps of 1 GHz).

Based on theoretical predictions, a frequency of about 140 - 160 GHz and a power of 20 MW, CW, is required for heating of the plasma core and burn control (proposed ECW supplementary system, not yet approved). Injection of waves should be in a left-handed elliptical polarized quasi-ordinary mode from the outboard side around the equatorial plane as close as possible to the major radius direction. In this case the injected beam would have a fixed angle of injection.

A trade-off between proposed technological solutions and physics requirements has been made to design a system which accomplish the desired physics tasks and is technologically feasible.

The physics requirements which will be considered for the design of the reference ECW system are:

Injected power : 20 MW

Pulse length : CW (maximum two weeks of 100% availability: 336 hours).

Frequency : fixed at 120 GHz (depending on the value of the magnetic field of the tokamak).

Injection : in an (almost) horizontal plane as close as possible to the equatorial plane of the machine. Possibility of scanning in this plane between 15^0 and 25^0 with respect to the normal to the magnetic field at the plasma edge. The scan speed should be about 10^0 in 1.0 s (centered at the port).

Beam parameters at q=2 : Gaussian beam (composed of superimposed independent beamlets) with horizontal width = 50 cm (at 1/e of the central maximum); horizontal divergence: $\leq 1^0$ (at the beam half width), vertical divergence $\leq 3^0$.

The physics requirements for the supplementary ECW system are:

Injected power : 20 MW

Power variation : 10 MW in 1 s

Pulse length: CW

Frequency : fixed at about 140 GHz

Injection : in an horizontal plane close the equatorial one and as close as possible with the normal at the magnetic field.

Beam parameters : width = 1 m (diameter of a circular Gaussian beam); divergence $\leq 5^0$ (at the beam half width)

3. Power supply and auxiliaries

In the design, power supply units (one for each gyrotron) fed by a 80-100 kV/DC line from the main AC to DC (remote) power supply have been considered. Each power supply unit is composed of a series regulator (one for each MW of RF power, considering triode gyrotrons) having the following characteristics: about 3 MW power; voltage 80-100 kV (ripple $\pm 0.5\%$); turn off time $\simeq 10\mu s$ (20 J dissipated for 1 MW RF tube); current $\simeq 38$ A (for 1 MW/tube at $\eta \simeq 35\%$ and 80 kV), efficiency $\geq 90\%$, reliability $\approx 95\%$, lifetime about 10000 h.

A new kind of power supply based on DC-DC converters which would be capable of an efficiency superior to 95% could be considered in the future. It consists of a low voltage DC converter, high frequency inverters with Giant Transistor modules , step-up transformers and high voltage DC converters. The windings of the tranformer core (amorphos steel) need some R&D.

The size of the considered 3 MW power supply is quite reduced. The power supplies necessary to control the tubes (series regulator), will be placed in the auxiliary rooms below the source rooms. Aside these power supplies, there will be the pumps for water cooling, for cryo-cooling and for control of the vacuum in the transmission line. A load for each tube will be also installed in these rooms (Fig.2). The auxiliary rooms will be insulated from the source rooms against fire, radioactivity and water.

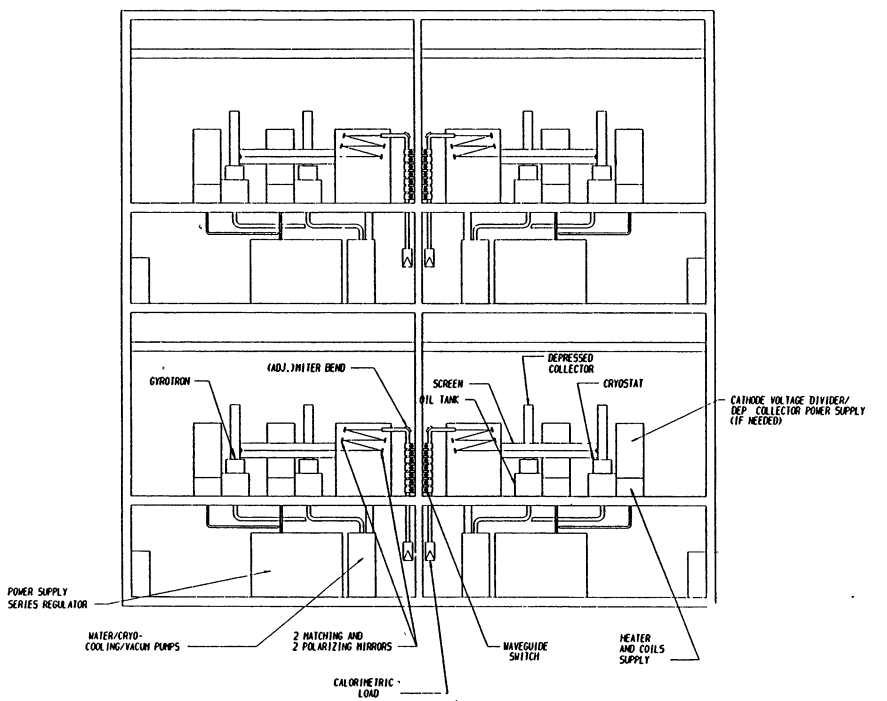

Fig.2 - EC source and auxiliary rooms, schematic side view

Close to each gyrotron in the source rooms, are located a crowbar, the heater and coil supplies (very well stabilized) and if necessary, the gun voltage divider and the power supply for the depressed collector. In case of step frequency tuning of the source a fast cavity magnetic field control will be installed (and hence the respective power supply).

The ECW control system should be fully managed by computers. The informations collected by specialized sensors should be transmitted to the main computer in a way to avoid environmental interferences.

The use of a depressed collector would allow an energy recovery of the spent electron beam, increasing the source efficiency by several tens percent (up to 70% overall efficiency). Beside, it could reduce the need for high precision voltage stabilization at high power level. An analysis for the optimization between the advantages and the disadvantages of increasing the complexity of the system (without reducing the reliability) should be carried out.

4. Microwave sources

A source assessment has been conducted to determine the best concept among the CARM, FEL, gyrotrons and other novel ideas. In the evaluation, consideration was given to the time scale presently considered for ITER. The result of the assessment is that only the cylindrical cavity gyrotron has gained an extensive on-the-field experience during ECW experiments and could provide in the given time schedule a relevant technical demonstration.

For the cylindrical cavity gyrotron, the use of volume modes (and possibly of an internal mode converter) are considered to give the potentiality to meet ITER power, frequency and pulse requirements.

Open key issues are: a) mode selectivity; b) cavity; and collector wall losses; c) electron beam quality (gun); d) reliability e) tunability at high average power (if needed).

Source developments have been conducted in the frame of the ITER R&D [4].

The 100 GHz quasi-optical Quasi Optical gyrotron at CRPP-Lausanne has reached a power of 90 kW in 10 ms pulses ($\eta = 12\%$); sheet beam gun tests seems to demonstrate the expected increase in efficiency; potential for continuous tunability has been demonstrated; positive cold tests of a grating mirror for gaussian output coupling in a 10 GHz range have been effectued.

In USA a BWO development study for the FEL on MTX at LLNL has been carried out.

In Soviet Union a 140 GHz gyrotron in the $TE_{22,6}$ mode, has been developed (industrial tube by Toryi) and tested at Kurchatov-Moscow. The main results are (Gaussian beam output with linear polarization) : regime1 P = 970 kW, 1 ms, efficiency 34%; regime2 P = 550 kW, 0.55 s, efficiency 32%; regime3 P = 940 kW, 0.3 s. Demonstration of the possibility of frequency step tunability on the same radial index (from $TE_{20,6}$ to $TE_{23,6}$:about 8 GHz in steps of about 2.5%) with a degradation of the output power of only 20%.

The availability of a fast tunable source would allow to reduce the dimensions of the antenna and increase the flexibility of the system. The transmission system, and above all the windows, should be in this case broadband.

Step frequency tuning of a tube on the same radial mode is possible only within the time scale of the magnetic field variation in the cavity (minutes). Therefore it does not seem possible to tune the same tube in the short time (about 100 ms) required to control

instabilities. A possible way to perform a fast frequency variation can be obtained adding a small coil to change the field of the main cryogenic magnet only in the cavity region. In this process about 30J are absorbed irreversibly by the magnets. A strong magnet cooling would be necessary but the problem of hystereris would remain. This proposal has been considered as an alternative option and proposed for a parallel R&D activity.

As a reference source for the design of the system we have considered 1 MW, CW 120 GHz (fixed frequency) cylindrical cavity gyrotrons having a triode electron gun for higher stability at high power CW operation, an efficient built-in quasi-optical converter (conversion efficiency from cavity mode to $HE_{11} \geq 95\%$) which permits also the separation between the RF and the electron beam, a lateral output in a Gaussian beam of the RF. power, (possibly) a depressed collector, with an RF window (first choice: cryogenically cooled window), an optimized cooling (gun, cavity, collector). All the tubes should have a frequency within ± 0.2 GHz. This gyrotron should have a minimum of 90% reliability (2000 h warranty) and a lifetime (mean time before failure) of about 10000 h. The expected efficiency (including the efficiency of the built-in quasi-optical converter and of the gyrotron mode purity) measured in the HE_{11} mode, after the coupling in the corrugated waveguide, should be between 30-35% and 50% (optimization of the cathode of the tube and development of a depressed collector, at present are envisaged as supplementary options).

28 gyrotrons, 1 MW, CW each will be installed in the source rooms (on two floors to reduce the horizontal size of the plant) to guarantee the injection of 20 MW in the plasma. 24 tubes will be running and 4 will be in hot stand-by or in maintenance.

A distance of about 3 m between the tubes is considered to avoid parasitic interferences of the magnetic field (staggered disposition to reduce the room size).

The RF source rooms are considered, even in case of an accident like the break of a tokamak RF window, as a non contaminated area (fast shutters are inserted in the transmission line close to the source rooms to avoid large contamination in case of major accident).

5. Transmission line

The RF power produced in the gyrotron cavity in a high order mode (volume or whispering gallery) will be converted within the source by a quasi-optical converter into a Gaussian beam for low loss propagation. Among the different concepts of quasi-optical converter proposed, the Quasi-Optical Adiabatic Periodical converter developed at IAP Nizhny Novgorod seems the most promising (efficiency ≥ 0.97) [5].

The RF Gaussian beam emitted by the gyrotron must be matched to the Gaussian TEM_{00} free space fundamental mode which is optimized for coupling to the HE_{11} mode of a low loss corrugated waveguide. The filtering of higher modes should be done out of the tube by two matching mirrors for each source. Large losses (several percent) could be produced by a non sufficiently precise alignment of the gyrotron output beam. If these losses are avoided, a good coupling efficiency (about 98%) to the HE_{11} mode can be obtained.

The correct coupling of the power to the plasma calls for a control of the injected elliptical polarization with the machine parameters and the injection angle. This can be accomplished by a special polarizer which transforms an input linear polarization into any desired elliptical polarization. No variation of the polarization is expected between the polarizer device and the plasma. The polarizer proposed in the design is composed of two

rotatable reflectors with rectangular corrugations respectively $\lambda/4$ (polarization rotation) and $\lambda/8$ (to create a circular polarization) deep. This device, like all the transmission line, will be under vacuum: no problems of power handling at the corrugated surface are expected.

The matching optics, the polarizer as well as all the beam between the gyrotron output and the waveguide entrance are contained in a box for RF shielding and evacuation (a pumping station is foreseen close to this location).

After the polarizer, the TEM_{00} beam is coupled into the HE_{11} mode of the corrugated waveguide. The first adjustable mitre bend of the waveguide line allows a correct matching/alignment between the guide and the beam.

The general requirements for the transmission system are to transport with the minimum losses the RF power from the source rooms to the tokamak, providing tritium containment and possibility for decontamination (baking and evacuation).

The chosen ECW transmission system combines the advantages of HE_{11} circular waveguides and of TEM_{00} quasi-optical waveguides [6] (Fig.3,4).

The transmission system will be evacuated (10^{-2} to 10^{-5} bar) to increase the power capability, avoid the problem of condensation on the external face of the cryo-windows and reduce the stresses in the window induced by atmospheric forces. Each line will have its pumping systems of reduced dimension.

All the transmission line components (waveguides and reflectors) will be water cooled. The water cooling system could also be used to provide a simple waveguide decontamination (by baking them, using steam or hot gas) in case of accidental exposure to tritium.

28 closed waveguide transmission lines will be installed (one for each installed source). 24 lines will be used and 4 are spare ones.

The average length of the transmission line is about 45 m with about 11 to 13 mitre bends and 4 reflectors (matching optics and polarizer). Only 90^0 bends are foreseen to simplify the installation and the alignment. Closed evacuated corrugated waveguides are capable of carrying 1 MW, CW in the HE_{11} mode with negligible ohmic losses and with very broadband features. First option is to use a largely oversized waveguide of a diameter of about 88.9 mm. Where possible, a smaller diameter of $\approx$ 32 mm could be used to reduce the sensitivity to alignment errors, the conductance to tritium gas flow in case of window failure and the neutron streaming.

Copper corrugated waveguides carrying the HE_{11} mode have at 120 GHz with a diameter of 88.9 mm and a rectangular slot depth of about 0.6 $\lambda/4$ an ohmic attenuation (including a factor of 2) of 0.3% for 100 m, and 2% / 100 m for SS or Ni-P coating (lower conductivity materials could be used to select higher spurious modes). Special tools to build 2m sections of corrugated waveguides with thick wall to support the atmospheric pressure are under development.

Use of corrugated waveguides permits the introduction of slots (for DC break, pumping - gas purging, insertion of valves, compensation of axial movements), and of compact mitre bends.

90^0 mitre bends have very low total losses (at 120 GHz, 0.5-0.7 % per bend in the 88.9 mm diameter and only 0.2-0.4 % for an improved phase corrected mitre bend) and allow an optical alignment of the transmission system.

The installation of a mode and polarization analyzer, as well as of forward and reflected power detectors are possible in a mitre bend close to the tokamak. Beside, a waveguide

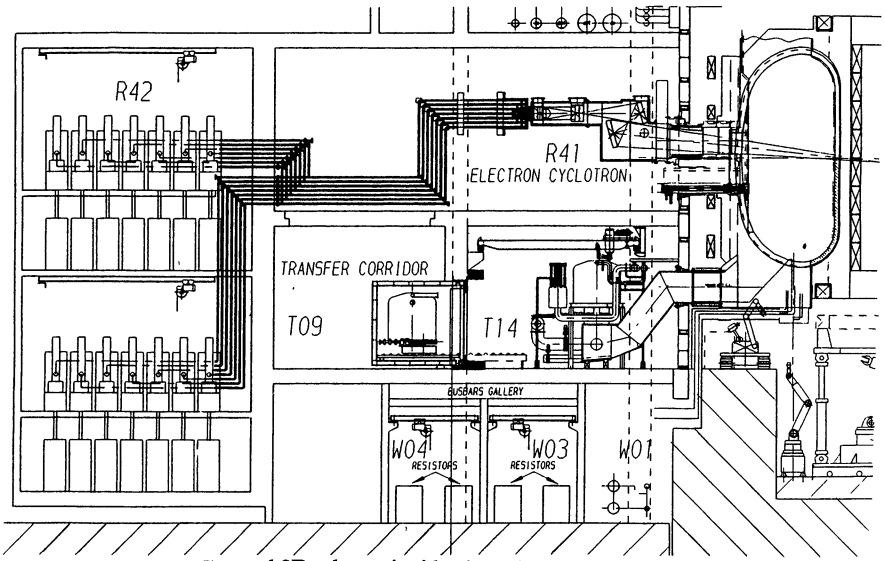

Fig.3 - General 2D schematic side view of the EC system

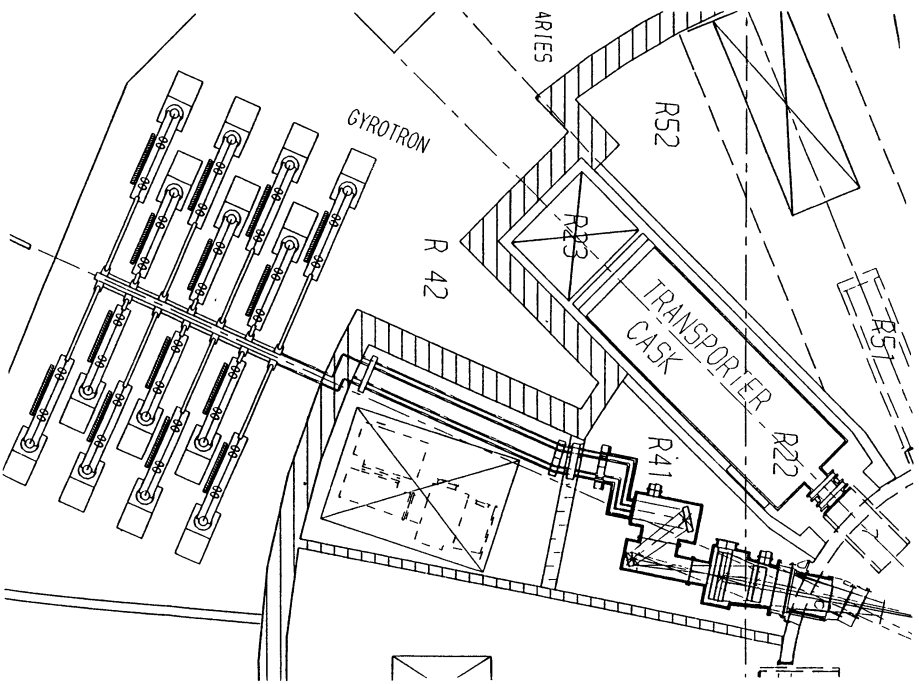

Fig.4 - General 2D schematic top view of EC system

switch can be inserted at the place of a mitre bend close to the gyrotron in order to direct the power to calorimetric loads (for gyrotron test and conditioning) or to the machine. A "circular" disposition of these switches will allow to increase the availability of the whole system, switching the RF power from one line to another when necessary (Fig.5).

For this kind of large diameter corrugated waveguides, tilts (0.1-0.2 % loss each) and above all unintentional curvatures (sags: 1.2% loss each) are dangerous imperfections. Therefore it will be necessary to provide a first optical (laser) alignment of the line and have very good supports to maintain this alignment. Further random imperfections could give additional losses (about 1% / 50 m).

Studies of a quasi-optical transmission system has been carried out in the frame of the ITER R&D with interesting results (e.g. beam splitter, multiplexer, optical coupling). This option has been considered as alternative, and could be implemented in the design, if necessary, without major modifications.

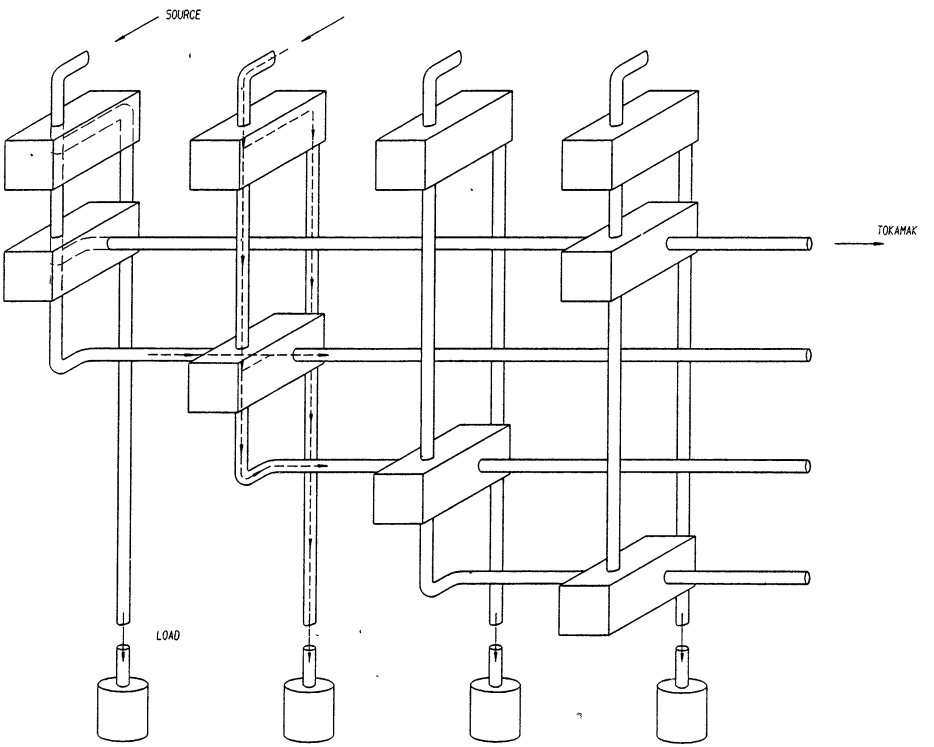

Fig.5 - Schematic of the "circular" disposition of the switches to increase the system availability

The transmission line efficiency for the proposed system is:

Gaussian beam coupling from the gyrotron into the waveguide (including matching optics and polarizer ohmic losses)	0.96
Corrugated waveguide propagation (88.9 mm diameter, 50 m long, with ohmic and unintentional curvature losses)	0.98
12 optimized 90^0 mitre bends (ohmic losses) and 5 slots (mode conversion and radiation losses)	0.95
Tokamak window (dielectric losses 0.1%, reflections 0.4%)	0.995
Coupling HE_{11} to TEM_{00} in the antenna	0.98
Launching antenna	0.98
Total efficiency	0.85

The total efficiency of the reference transmission system at 120-140 GHz is about 85% (the efficiency of the quasi-optical converter is considered within the gyrotron efficiency).

6. Windows

Reliable vacuum windows are supposed to be placed at the gyrotron exit and at the tokamak entrance. While the gyrotron windows should support 1 MW, CW at about 120 GHz, further requirements for the tokamak windows are: provide tritium and dust containment; act safely as a first containment barrier; be placed in a screened position with respect to neutrons; have an average lifetime of about six years (a substitution every 2 years of all the windows is foreseen); easy maintenance by remote handling; support (if possible) 2 bar overpressure in case of Loss Of Coolant Accident (LOCA). An integrated window set (4 modules of 7 windows) has been proposed to reduce the number of connections and hence easy the maintenance (Fig.6). For safety reasons, two barriers are required with tritium monitoring in-between. Therefore there will be at least two ceramic barriers in a window assembly. Only one gate valve (at the tokamak side of the window block), is considered at the moment for window maintenance.

A cryogenically edge cooled window made of sapphire, with an internal diameter of about 90 mm, should be able to support 1 MW, CW at 120 GHz with a safe margin to avoid thermal instabilities. The optimum coolant temperature should still be defined. This concept has been retained as first option for the design of the system.A good level of vacuum should be assured close to the ceramic disks cryogenically cooled to avoid any possibility of frost, above all at the tokamak side (Hydrogen from the plasma).

If a fast frequency tuning is demanded the window should be intrinsically broadband. A possible solution is the motheye concept.

Experiments indicate that gamma rays do not influence the required ceramic properties.

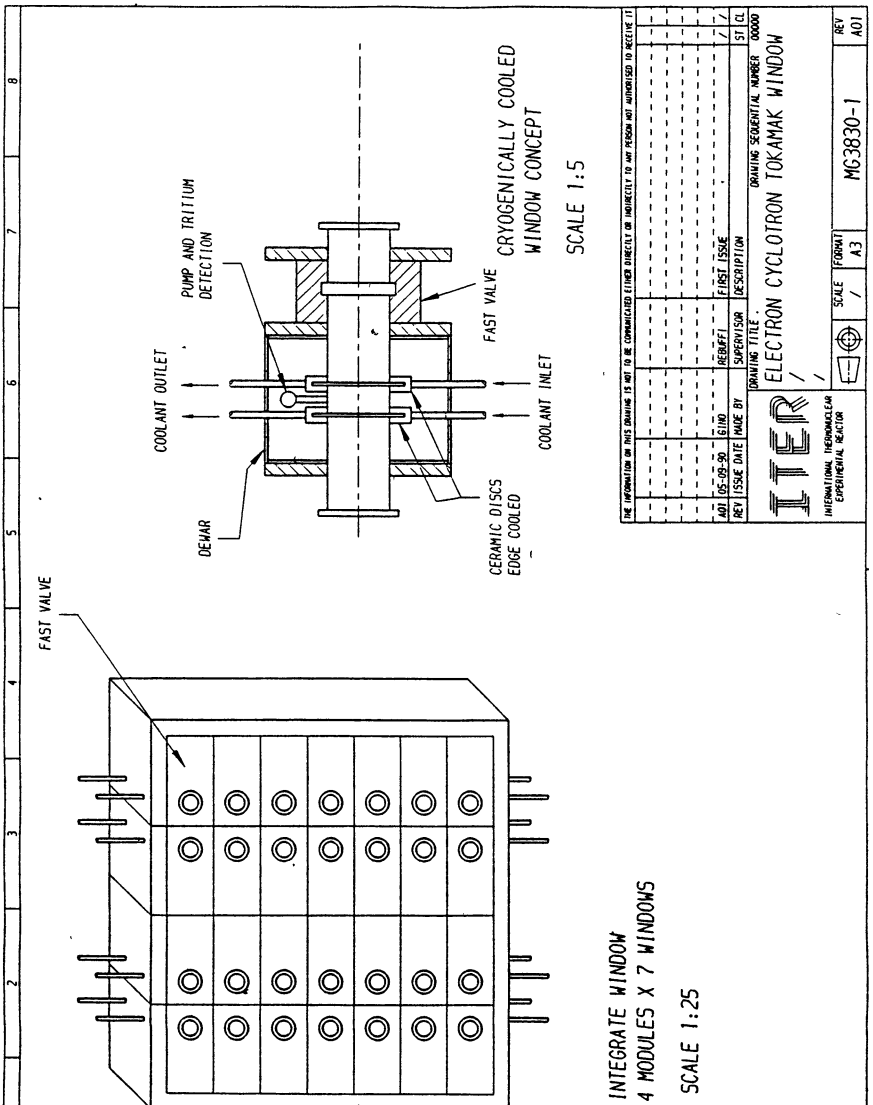

Fig.6 - Schematic of the cryogenically cooled window concept and of the integrated window system

A degradation of the mechanical properties of window ceramics is not expected for the considered fluence (lower than 10^{16} n/cm^2 at the window position). At this fluence, for neutron energies superior at 0.1 MeV, electrical permittivity and loss tangent, are not affected. Also the degradation in the thermal conductivity (critical driving factor for the position of the windows) is practically avoided.

Interesting alternative windows geometries have been proposed. In the "distributed window" concept two evacuated waveguides are placed in parallel (side by side or coaxial) and connected by a large number of small coupling holes or slots (phase velocity coupling) filled with ceramic. Such a window would be highly robust and resistant to thermal and mechanical shock. The expected losses, in the dielectric and in the waveguide, are comparatively high (some percent). The solution of electrodynamics problem to optimize the phase velocity coupling will demand a R&D effort.

7. Antenna generalities

The antenna is the most critical part of the system because it has to satisfy physics (beam sweeping, beam size and divergence), thermomechanical (sputtering, swelling, cooling), nuclear (neutrons, gamma, tritium, activated dust), maintenability, safety and reliability requirements and it has a non negligible impact on the machine (blanket, port, cryostat).

The design of the antenna is the result of an optical optimization and trade-off with respect to integration and maintenance requirements, where all the reflectors are installed outside the cryostat (Fig.7).

The antenna containing the reflectors has been divided in modules which should allow an easier maintenance. A rectangular shape of the modules has been retained for integration reasons. A set of windows (integrated window system), connects the transmission line outside the antenna with a waveguide run inside. At the end of these waveguides the RF beams are launched towards the first reflector. The internal waveguide run presents two bends to optimize the launched pattern. The space between the guides could be filled by a suited material to reduce the neutron energy or to absorb them. Each bend is also intended to provide a reduction by about one order of magnitude of the neutron streeming inside the pipes.

Two pumping ducts are foreseen in the two main modules.

At the module extremities some valves (real valves, maintenance door or fast shutters) are foreseen for maintenance and safety.

All the components in the antenna should be bakeable at a temperature of about 180^0.

The antenna boxes are connected to the machine via a duct where large bellows are foreseen.

The material preferred for the antenna boxes and for the duct is SS-316.

Two pumping apertures are foreseen in the two main antenna modules.

The supports for the reflectors and for the antenna boxes as well as the services in the antenna (cooling, mirror drive, diagnostics, electrical connections, etc...) should be studied in the future detailed design phase.

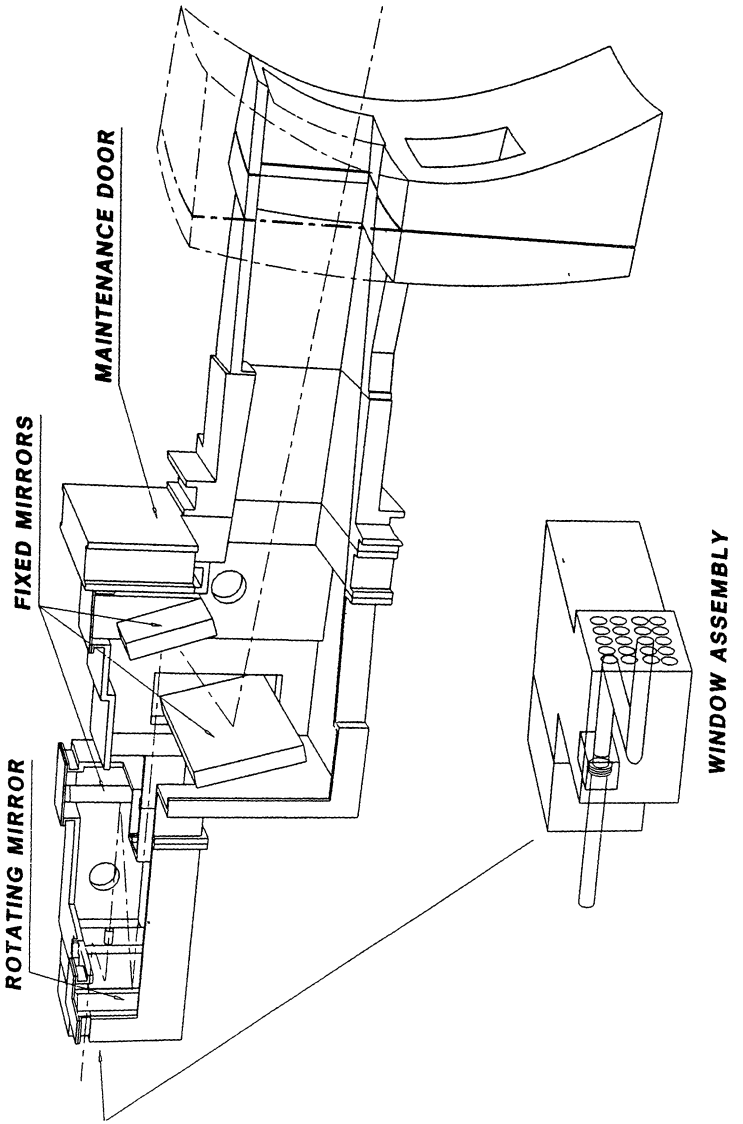

Fig.7 - Reference ITER Electron Cyclotron wave system, 3D schematic layout of the antenna

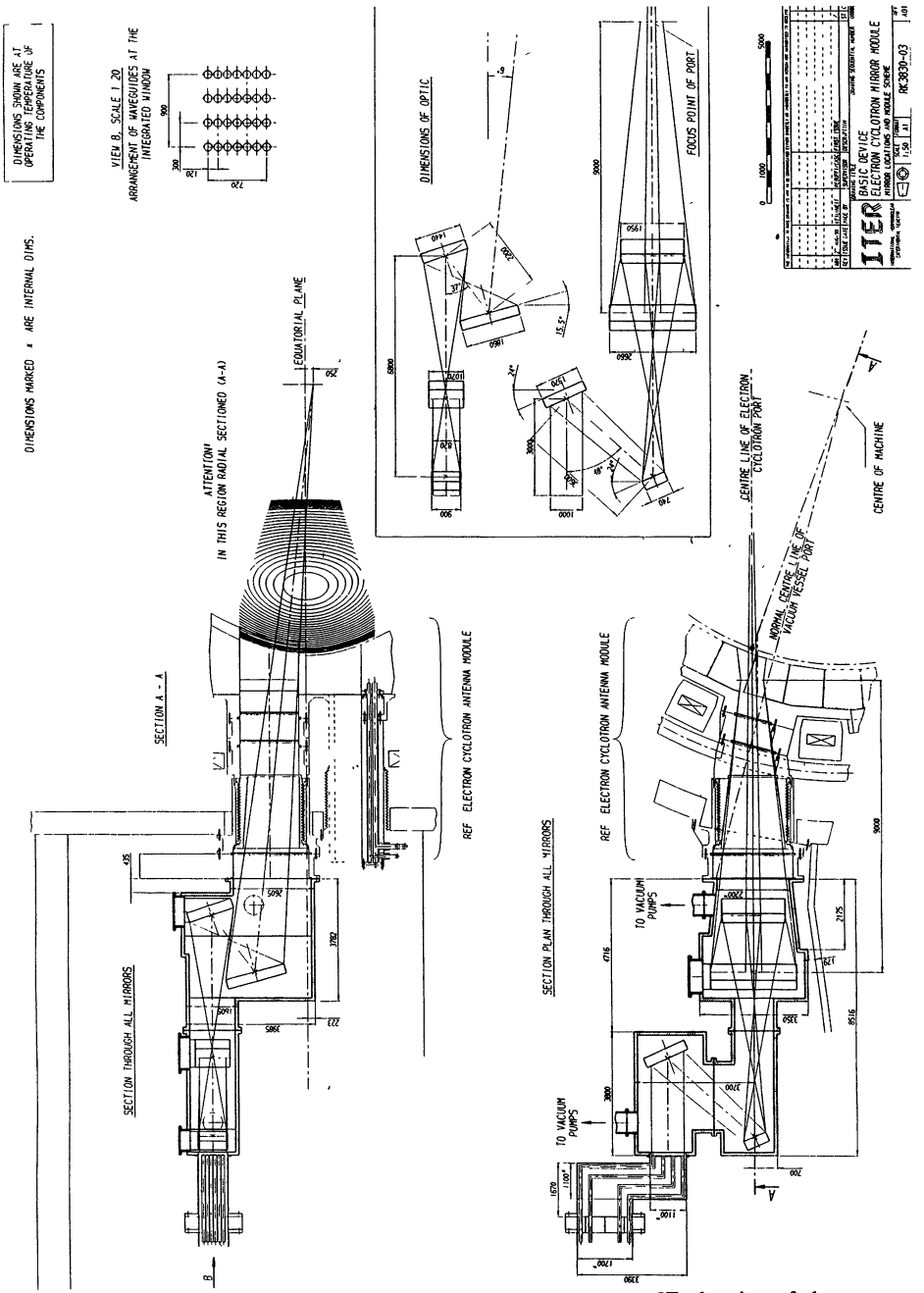

Fig.8 - Reference ITER Electron Cyclotron wave system, 2D drawing of the antenna module: side view, top view and antenna optics

8. Antenna reflectors

The launching system has been optimized from the optical point of view in order to meet the physics requirements for beam size, divergence and scanning angle, and for protection of the components from nuclear and thermomechanical damages. Other requirements for the optical system design of the antenna are: last mirror placed out of the cryostat; rotatable mirror placed as far as possible from the plasma and in a screened position; rotatable mirror small and flat; simplicity of the system for maintenance; avoid aberrations (beam characteristics modifications) during the sweeping; launched beam slightly convergent (perpendicular to flux surfaces) to get smaller dimensions at the resonant layer; necessity of concentrating all the beams radiated from the waveguide ends in one multiple beam.

From the point of view of optics, the antenna works as follows (Fig.8). 28 beams are radiated by an open-ended (HE_{11} carrying) waveguide array with the natural divergence of the individual beams (in the considered oversized waveguide the divergence is minimized). The beamlets are collected by a mirror array composed of four ellipsoidal mirrors. This mirror array combines the beamlets in a way to have on the rotatable (flat) reflector the same image (geometrical - optical imaging) as desired at the rotating point close to the plasma (narrowest point of the port). Its geometrical-optical image is such that the beams cross in a plane containing the axis of the torus, therefore each beamlet will not contribute to the total horizontal beam divergence (the multi-beam divergence is equal to the divergence of a single beamlet). The third reflector (flat and wide) is needed to fold the beam in the proper way on the last mirror. The last reflector is an ellipsoidal mirror (with foci at the rotatable mirror and at the narrowest part of the duct) which produces the desired beam characteristics without aberrations during the sweeping. The relatively large size of the two last mirrors is due to the fact that they should present a large surface in order to intercept the scanning beam. The size of the beam bundle at the plasma edge is of about 40 cm in the horizontal and 50 cm in the vertical direction, but the effective beamsize is about 10 cm, the effective horizontal and vertical divergence are about 1^{0} and 3^{0} respectively.

No problems are expected to drive the rotatable mirror at the required speed. To enable fast acceleration a stepper motor and a gear with a small transmission ratio has to be considered for the drive.

The reflector supports should be designed to avoid vibrations of the optics, keep the correct alignment and facilitate the maintenance of the components.

To avoid breakdown at the degassing surface of the reflectors and reduce the mirror variation in dimension due to dilatation, the temperature of the reflectors should be maintained constant during operation by an electric or a water system.

A partial conceptual design has been conducted for the supplementary system antenna (20 MW, CW at 140 GHz) which can be placed in the lower part of the reference system ECW port. In the supplementary antenna a compact bundle of 28 waveguides radiate on a first flat folding reflector and then on a second elliptical mirror which focuses the beams in the plasma center. Due to integration problem the injection angle is about 20^{0} (Fig.9).

9. Reflector materials

The materials for the last four reflectors should satisfy the following requirements: low erosion rate and rather low atomic number, resistance against radiation damage, low

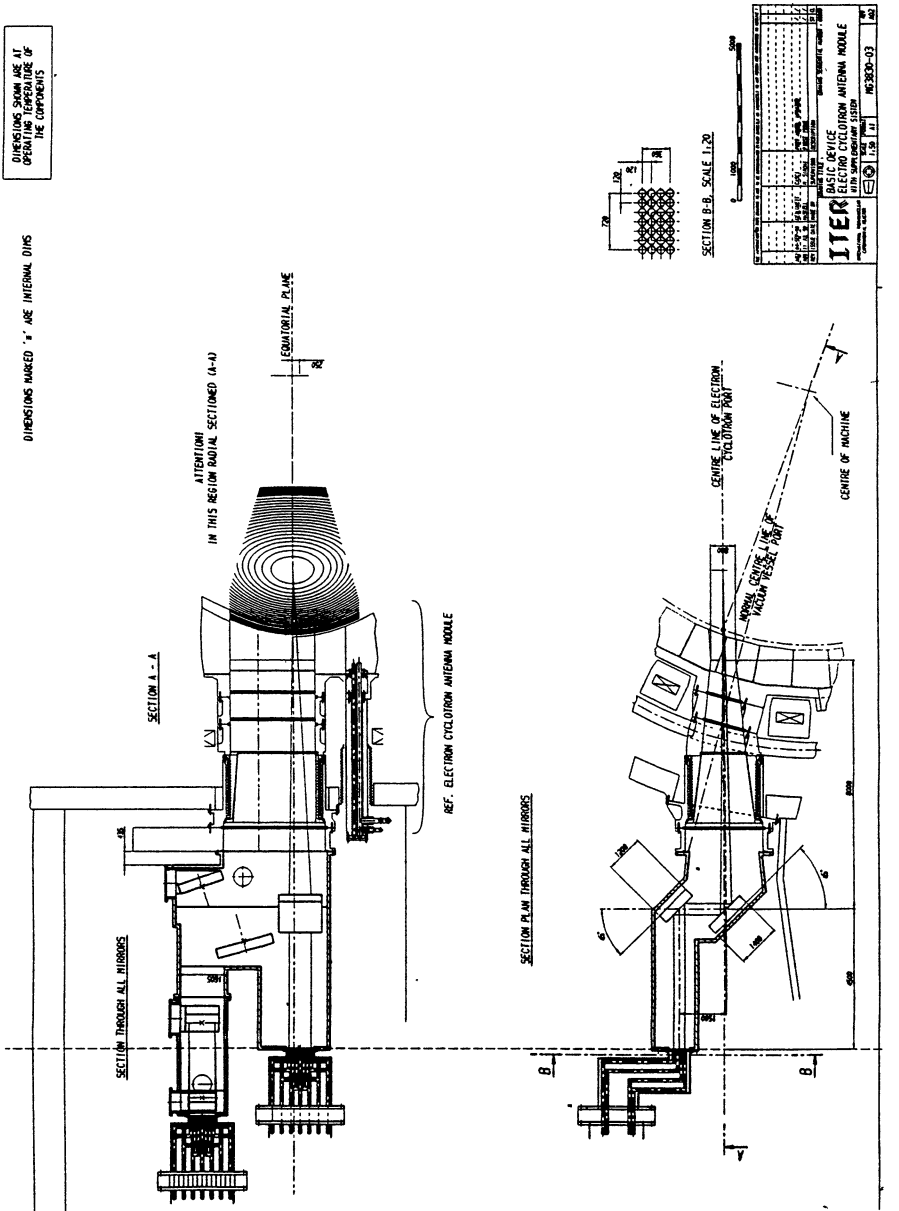

Fig.9 - Draft drawing of the supplementary EC system integrated in the reference antenna, top and side views

tritium permeation and retention, good thermo-mechanical properties, light weight and good machinability.

The possible damages created at the mirror materials by the fusion environment are sputtering (erosion) and swelling.

The neutrals, produced by charge exchange reactions, are responsible of the sputtering.

The geometry of the duct gives a strong contribute at the reduction of the neutral flux dangerous for the last mirror. At its position (more than 10 m from the plasma) a sputtering of the order of 0.002 to 0.02 mm/year is expected for SS and Cu.

Given the long distance between the source of neutrals and the reflectors, we should expect an uniform erosion. The maximum surface roughness tolerated at these wavelengths is about 0.15-0.2 mm, which is very big compared to the characteristic length of the macrostructure in the material. The (expected) homogeneous sputtering should not be a problem if the erosion is not too large (in that case it should be necessary to proceed at a new surface coating).

The neutrons create damage on the volume of the material (change in the microstructure, production of vacancies, bubbles: swelling), change in thermomechanical properties and in the electrical conductivity, increase of the activation.

At the first wall a dose of 12 dpa in 8000 hours of burn (reactor lifetime) is expected. A figure valid for Cu materials is about $4x10^{-7}$ dpa/s of burn. At 400^0C and 30 dpa, the swelling becomes a danger for these materials.

As the dose on the last mirror should be 100 times less than the first wall (hence = 0.1 dpa), swelling problems are not expected.

Nuclear grade, oxigen free dispersion strengthened copper (Cu with alumina particles) is a promising material. It keeps good strength at high temperatures. Its macrostructure is stable. Its thermal and electrical conductivity are about 90% of the copper ones at room and at high temperatures. It is quite stable under irradiation. It is relatively easy to machine but brazing is necessary. The erosion and the activation, similar at copper, should not give problems.

Only certain allowed materials should be used for the antenna design ito reduce the production of activated dust from antenna components.

10. Valves and pumps

At the duct, a metal door will be used for maintenance. Placed in a cask containing special tools it will be lowered, when necessary, and bolted at the mirror box flange. This door is supposed to be used also for safety in case of accident.

Close to each window, on the tokamak side, it is considered the use elastometer seal valves. A 10 cm diameter valve could close in about 1 s.

Fast shutters are required in each transmission line close to the source room to avoid (or reduce) the propagation of radioactivity in this room. These fast shutters should close in about 30 ms. Fast shutters could also be introduced in the waveguide run within the antenna to prevent accidental window coolant leakage inside the machine.

The transmission line will be evacuated in normal operation to about 10^{-2} bar to increase power handling, and to 10^{-5} bar for decontamination operations. Each line will have at least two pumping stations, one at the beginning of the line, in the matching optic box, and the other in the antenna room, probably connected to a mitre bend or to a waveguide gap.

For the antenna, a vacuum lower than 10^{-2} Torr is necessary, and this is provided by the tokamak main pumps and by the plasma itself (there should be 10^{-4} Torr in the last box).

Cryogenic and/or turbomolecular pumps have been foreseen for the antenna in case of need of a lower pressure to avoid breakdown at the reflectors due to degassing, for maintenance cleaning and to avoid condensation at the window surface due to gases from the machine.

11.Integration and maintenance

For the integration of the antenna in the machine the common general requirements should be followed (double sealing between the primary and the secondary vacuum or the atmospheric pressure environment with tritium monitoring, single barrier between the secondary vacuum and the environment, shielding around the toroidal field coils, accommodation for an horizontal and a vertical displacement of the antenna of about 2 to 3 cm).

The ECW antenna will be supported by the cryostat (it is disconnected mechanically from the movements of the vacuum vessel) to limit the problems of alignment and vibration of the waveguides and of the optics. An external support will connect the antenna with the floor of the antenna room.

The reference antenna is placed in the upper part of the port (about 0.85m over the equatorial plane). The lower part of the port will be occupied by the supplementary ECW system (integrated in the reference one) or by a plasma diagnostic.

An internal duct has been placed to avoid stray radiations on the bellow. The double bellow is of reasonable size and its length is provisional. The casing of the mirror modules is a single envelope, 100 mm (provisional, to be optimized) thick SS. It is not expected to have failures in the reactor lifetime. The maximum angle of injection allowed for integration of the antenna, is about 25^0, limited by the conflict with the neighbouring lower hybrid system. If a higher angle would be necessary because of optimization of physics requirements, new solutions for the layout should be studied.

The size, the weigth and the rugged design of the mirror boxes practically exclude a removal of these modules and their transfert to hot cells for repair. Only an unscheduled maintenance of these boxes (once or twice in the reactor life) could be accepted. For this reason the number of valves is reduced. If one module should be removed, the valve (or the door) will be closed and maintenance of these modules can take place. The ECW antenna room, is filled by inert gas and insulated from other rooms. If necessary it can be decontaminated.

A remote maintenance of all the reflectors and the components inside the antenna should be foreseen. This maintenance should be effectued via flanges on the top or on the side (for the largest mirror) of the antenna modules. The mirrors and their services (cooling pipes, diagnostics, etc) should be supported by these flanges. In this way the maintenance will be easier (modular maintenance of each reflector, without intervention on other part of the system) and the positioning of the reflectors will be effectuated with the required precision.

Personal access around the cryostat 24 h after shut-down is not necessary for maintenance of the ECW system. Anyway provision to allow access in the antenna room few time after shut-down should be taken. A removable shielding composed of hard concrete blocks

around the antenna (position still to be clearly defined) should be sufficient to guarantee human access to this area in case of necessity.

Remote maintenance of valves as well as of the final part of the transmission line should also be foreseen.

The maintenance of the windows has been simplified, grouping the window assemblies in four blocks to limit connection and disconnection procedures.

Provision for detritiation of the antenna and of the transmission line could be foreseen in the design in order to allow an easier maintenance (hands-on maintenance where the components are not activated).

Remote maintenance of valves as well as of the final part of the transmission line should also be foreseen.

12. Neutron doses

At the first wall there should be a dose of 2.2×10^{13} mRem/h (1.4×10^{14} n/cm^{2}s). 3D Montecarlo computations for the ECW antenna foresee at the last mirror a dose of about 1×10^{11} mRem/h (about 1×10^{12} n/cm^{2}s). One day after shut-down there is still a dose in the antenna of 1 to 5×10^4 mRem/h (about seven order less than during operation). For personal access in the rooms outside the ECW antenna room at least 1m of hard concrete would be necessary (limit dose for professionals = 2.5 mRem/h).

The neutron streaming in the pipes could create some damages at the window ceramics. The insertion of the waveguide run and of two bends before the windows should reduce the dose at the expected level of 10^{16} n/cm^2 at the window location. Some care should be taken for the neutron streaming in the transmission line down to the source room. At least 4 bends should be inserted considering the reduction of one order of magnitude for each bend, also with the help of absorbing materials around the guide and the bends.

13. System efficiency and cost

The reference efficiencies are reported in the following table. Note that the systems used at present are at lower frequency and CW or long pulse operation with respect to the ITER system.

	Present	ITER min expected	ITER desirable
Power supply	0.90	0.90	0.95
Sources	0.30-0.35	0.30 - 0.35	0.50
Transm. line	0.75-0.85	0.85	0.85
Total sys. effic.	0.25	0.25	0.40

The minimum values are expected for 1995.

With an efficiency of about 25% the requested electrical power (continuous during operation) is of 80 MW. The cooling power is 60 MW.

A tentative estimation of the cost of the ITER ECW system is about 4.0 $/W (RF) installed, assuming 1 MW/unit gyrotrons.

14. Reliability / Availability

The ECW system in all its components is requested to satisfy (for control of m=2 instabilities) the required availability of 2 weeks of continuous operation every 6 weeks. Therefore the minimum mean time before failure of the main components should be > 336h. A higher lifetime is requested to reduce the costs of the system.

The outage risk is the product of the failure rate (in 1/h) per component times the mean down time (in h). The minimum objective for the ECW system is one outage in about 2000 h of calender time (4 times per year). The main critical components are the windows, the gyrotrons and probably some reflectors. The reliability of gyrotrons and windows should be improved with respect to present performances. Anyway the high availability requirement will be met by installing excess capacity (15% spare) thereby maintaining the required power level after sustaining failures. Therefore the system will be comprised of 28 gyrotrons of 1 MW each, 28 transmission lines, 28 vacuum windows and one antenna. At present it is foreseen to operate 24 channels while 4 are in maintenance or hot spare.

15. Safety

In the design of the machine the priorities for safety are: first people, than operation and at last maintenance.

Three barriers (including the building) are required, to satisfy safety criterias, between the vacuum vessel (inventory) and the public (environment non professional). Only the antenna module should be considered as highly contaminated. The part of the system in the same room of the antenna could also be contaminated (neutrons, and gamma rays, tritium and radioactive dust during maintenance operations). The gyrotron room should not be contaminated, but the access could be regulated. During a LOCA (Loss Of Coolant Accident) in the machine, a large quantity of steam is produced (slow dynamic process). The consequent thermal shock on the windows could break them. A passive shutter (as close as possible to the plasma, possibly in the waveguide run in the antenna) could be a good safety back-up of active devices (valves) to avoid contamination spread in case of accident with lost of electrical power.

16. Critical Issues and Long Term Technology R&D

In the next ITER Engineering Design Activity, a detailed design of the system will be carried out. The critical issues recognized in this first phase will be studied and the realization of the planned technology R&D, will support the design. A total budget of about 30 M$ has been proposed for the development of a prototypical channel by 1995 [7].

Starting from ongoing developments, which should give a concrete technological experience for future activities, the proposed budget comprises the development of the following items. Gyrotron and tokamak windows (cryogenically cooled and advanced concepts); 1 MW, CW gyrotron at 120 GHz; 1 MW, CW gyrotron at 140 GHz; transmission line components specific for the ITER environment; improved mode converter; integrated system tests and lifetime tests (to destruction); support to advanced solution/improvements

(gyrotron efficiency enhancement, power supply improvement, gyrotron tunability, quas optical gyrotron).

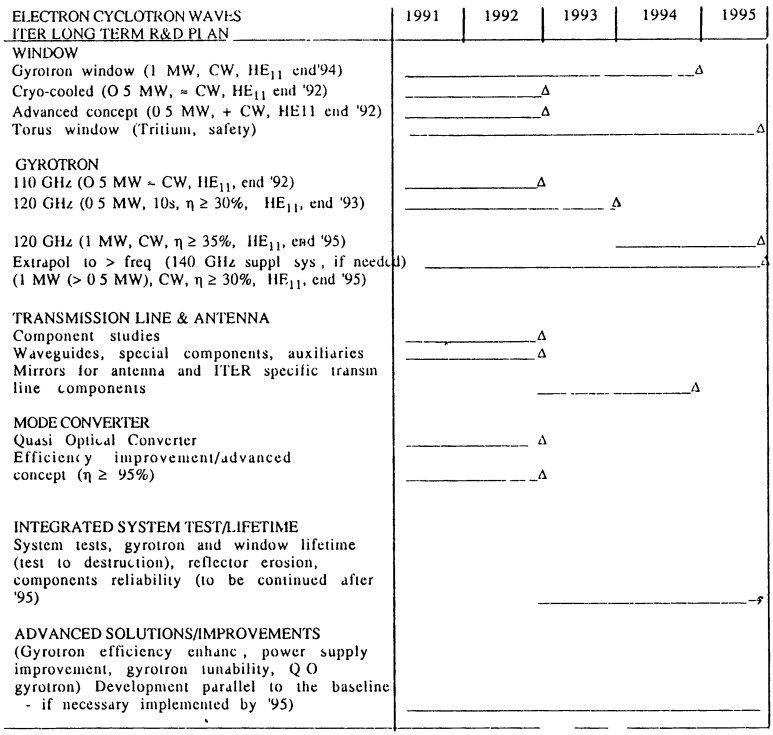

Physics studies to support the ECW system design are needed in the following areas: a) demonstration of noninductive current drive with the theoretically predicted efficiency in the upshifted mode; b) experimental investigation of local current profile control; c) optimization of the modelling to define final requirements for the range of variation of the angle of injection and related frequency, following ITER reference parameters.

17. Conclusion

The Conceptual Design of the ITER ECW system has been carried out. The main problems for the installation of an ECW system in ITER have been recognized and different solutions have been proposed. Among these, a reference solution has been retained for the Conceptual Design, the others are possible alternatives which could be reconsidered in future.

The designed system of 28 MW (installed), CW at about 120 GHz satisfies the requirements of continuous injection of 20 MW of Electron Cyclotron waves for assist in plasma formation and disruption control (m=2 mode) in ITER. As microwave sources, 1 MW/unit gyrotrons are foreseen to be used. An optimized optical device will convert

the gyrotron mode to a Gaussian beam for optimum coupling in a low loss corrugated waveguide to transport the microwave power over about 50 m to the tokamak. Special components will assure power and mode monitoring as well as polarization control. An antenna composed of four mirrors will inject the beam satisfying stringent requirements on its size, divergence and launching angle. The beam can be swept by about 10^0 to adjust the absorption profile to the q=2 magnetic surface in about 1s. The system has been designed (materials and remote maintenance issues) considering ITER requirements with respect to nuclear and thermo-mechanical loads and to assure a high degree of safety and reliability. More details can be found in the final report of the Conceptual Design Activity.

The overall efficiency of an ECW system (power supply, RF source, transmission line and antenna) should be about 25%. Possible technological improvements within the ITER time-scale (if sufficiently supported) could lead to an increase of the overall system efficiency up to 40%.

An optimisation of the physics modelling is necessary as well as the experimental confirmation of theoretical models.

Critical issues for the final detailed engineering design of the system have been recognized and a long term technology R&D for the system has been proposed as a support of the future EDA activity. It has been recognized as necessary to develop by 1995 a complete channel rated at 1 MW, CW in the 120 - 140 GHz range.

Acknowledgement

The author is indebted with the participants at the ITER ECW meetings for their active collaboration at the definition of the design. A particular thank to G.G.Denisov, V.A.Flyagin, W.Kasparek, M.I.Petelin, R.Prater, K.Sakamoto, R.Temkin, M.Thumm, M.Q.Tran, M.Tsuneoka.

References

[1] W.Lindquist et al. "ITER Current Drive and Heating Systems" Proc 13th Int. Conf. Plasma Physics IAEA Washington 1990.IAEA-CN-53/F-3-5.

[2] L.Rebuffi "ITER Electron Cyclotron Wave System Common Conceptual Design, Final Report" ITER-IL-HD-6-0-30

[3] W.M.Nevins et al. "ITER Current Drive and Heating Physics" Proc 13th Int. Conf. Plasma Physics IAEA Washington 1990.IAEA-CN-53/F-3-4.

[4] L.Rebuffi "Summary of the ITER Technology R&D Tasks on ECW" ITER-IL-HD-6-0-31.

[5] A.V.Gaponov, M.I.Petelin "High-power, high-frequency classical electronics: status, trends and problems" This conference.

[6] M.Thumm "Electrodynamic Systems for Mode Conversion, Transmission and Diagnostics of High-Power Millimeter-Wave Radiation" This conference. [7] L.Rebuffi "ITER Technology Long Range R&D. HCD-2: Electron Cyclotron Wave System" ITER-IL-HD-6-0-29

CRITICAL ISSUES IN THE APPLICATION OF LOWER HYBRID WAVES TO THE NEXT STEP DEVICE

J.-G. Wégrowe

The NET Team, c/o Max-Planck-Institut fur Plasmaphysik, D-8046 Garching bei München, Federal Republic of Germany

1 - INTRODUCTION

A number of functions have to be fulfilled in NET or ITER by non-inductive power.

In order of occurrence in a discharge, these are:

i) Plasma preionization and ii) current start-up (to reduce the maximum loop voltage required from the transformer)

iii) Current ramp-up assist (to save inductive flux consumption in view of extending the burn duration)

iv) Plasma heating to burn

v) Current drive during burn (to allow control of the current profile and as a means of extending the burn duration).

Finally, non-inductive power will also be required for

vi) burn control and

vii) during ramp-down of the current to avoid disruption due to exceeding the density limit.

The rationale for selecting LHW to fulfill some of these functions in ITER and NET are based on the present experimental database, on the degree of understanding, and on the technical status.

1.1 Experimental database

Lower hybrid waves (LHW) have already demonstrated their ability to fulfill most of these functions in present-day devices[1]. The current drive efficiencies are the highest ever obtained by a current drive method and have reached 0.34 $\left[10^{20} m^{-2} MA/MW\right]$ (in JT-60[2] and, more recently, in JET[3]), the level adequate for ITER applications. (Fig. 1[4] shows the present status of current drive efficiency experimentally achieved by various methods.) Other important recent results include the achievement of H-mode discharges with LH (JT-60), flexible current profile control (e.g by using tailored wave spectra in ASDEX[5]). Very long discharges have been sustained by LHW alone (TRIAM-1M[6]: 1hr, low density; TORE-SUPRA[7]: 22s, 2 10^{19} m^{-3}).

Suppression of sawteeth with moderate LHW power levels is obtained in all experiments, high electron temperatures with peaked profiles are reached by stabilization of the m=1 MHD mode (ASDEX: see Fig. 2[5]). Efficient current ramp-up has been investigated and found to be in good agreement with theory in a number of experiments (PLT, ALC-C, PETULA, JT-60, WT3).

1.2 Degree of understanding

Agreement between theory and experiment is good in most areas, including current drive efficiency in the presence of a toroidal electric field. A few questions - for which theories have

\been offered - still require effort at experimental verification: they concern mainly the origin of the spectral broadening during wave propagation and the enhanced current penetration observed in today's experiments.

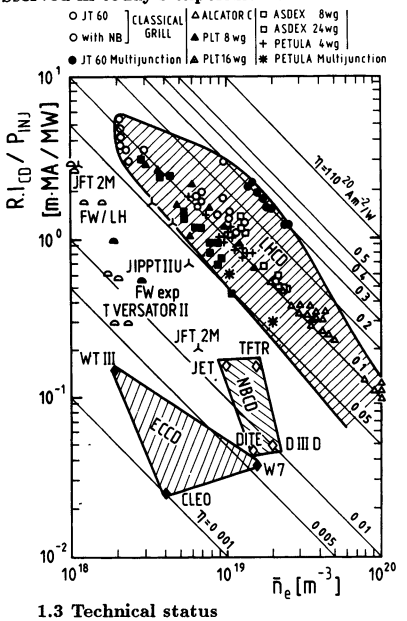

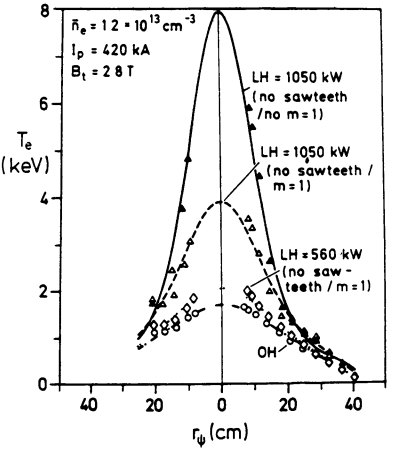

Fig. 1 (left) Experimental Current Drive Efficiency for various methods (accordg. to [4]): LHW, NBI(Neutral Beam Injection), ECW (electron Cyclotron Waves) and FW (Fast waves) experiments

Fig 2 (right): Electron Heating in ASDEX [5]

1.3 Technical status

The present stage of development of technical components, ranging from the antennas to the RF generators provides a solid basis for the design of a LHW system to be used in the Next Step Device which does not require large extrapolations beyond the present-day technology[8].

The on-going programme includes large-scale (JET, Tore-Supra, FT-U, JT-60, PBX) and medium-scale experiments and should provide, together with an adequate Research and Development programme based on the present state of the art[9], the complementary information - in physics as well in technology - still required for the next step.

1.4 Functions of LHW in the Next Step Device

Extrapolating the present results to reactor conditions, it appears, however, that penetration of the LHW into the high-β core can only be achieved in a restricted range of parameters, inedequate for ITER (low density or about one half of the standard β). For standard ITER scenarios, LHW are predicted to penetrate during the burn phase to $r/a \simeq 0.6$. The situation is more favourable for NET owing to its larger magnetic field. During the high β phases of the discharge, LHW will thus be used to provide heating, current drive and current profile control in the outer regions of the plasma.

Restricted penetration also limits the total current which can be driven by LHW due to the requirement of having a monotonic safety factor profile.

Conversely, LHW appear as the method of choice to assist the ohmic current ramp-up which shall be performed in a range of plasma parameters close to those of present experiments.

1.5 Objectives of this presentation

The objective of this paper is to discuss the physics issues of importance for the main applications of LHW to the next step (functions iii to vii above), especially their role in the selection of the design and operation parameters, the relevant data base and the areas requiring further effort. (A discussion of the technical and design issues may be found in [8]).

We shall first consider the issues of importance for the high-β phases of the discharges, including the problems of wave penetration (§2), the considerations leading to the selection of the operating frequency (in particular the necessity of avoiding interaction of the waves with α-particles : §3) and the current drive efficiency (§4). §5 deals briefly whith problems and prospects relating to the antenna concept.

The questions connected with the current ramp-up assist are presented §6.

2 - Penetration of LHW towards the plasma core

The penetration of LHW into the core of hot and dense plasmas is restricted by two effects. On the one hand, strong wave damping already occurs at moderate values of the local β . While this is a reason for the good performance of LHW in the experiments performed up to now, this will handicap their penetration to the centre of a high-β reactor plasma.
Furthermore, waves trajectories - as computed by ray-tracing - do not reach the plasma centre in toroidal geometry but rather encircle it at a distance, the 'whispering gallery radius', which is shown to be comparable to the damping penetration radius in the next step device plasmas.

2.1 Penetration limit due to wave damping

Strong Landau damping causes total single-pass absorption of LHW already in moderate temperature and density plasmas. A very rough evaluation of the maximum attainable electron temperature $T_{e,max}$ is obtained with the often used criterion:
$N^2_{/\!/,max} T_{e,max} \leq 50$ (where $N_{/\!/,max}$ is the highest wave parallel refractive index in the local LHW spectrum). A better estimate results[10] when writing that the absorption length $\rho = \frac{P_{LHW}}{dP_{abs}/dr}$ is a small fraction λ of the minor plasma radius, the locally absorbed power P_{abs} being roughly estimated by simple quasi-linear formulae[11,12,13] (P_{LHW} being the impinging LHW power). This yields

$$N^2_{/\!/,max} T_{e,max} = m_e c^2 \Big/ 2\ Ln\Big[\frac{n_e^2 e^4 Ln(\Lambda)}{(2\pi)^{3/2}\epsilon_0^2 \sqrt{m_e\ kT_{e,max}}} \frac{5+Z_{eff}}{4} \frac{\Delta N_{/\!/}}{N_{/\!/}} \frac{V_{pl}}{P_{inj}} 2\lambda \frac{r_{pen}}{a}\Big], \qquad (1)$$

where $\Delta N_{/\!/}$ is the total spectral width, P_{inj} is the injected LHW power, V_{pl} the total plasma volume and r_{pen} and a are the deepest penetration radius and the plasma minor radius.

This formula is found to be in good agreement with detailed simulations for ITER (using λ of the order of 0.25 and $r_{pen}/a \simeq 0.6$).

According to Equ.(1) , the product $N^2_{/\!/,max}\ T_{e,max}$ varies between 90 and 60 keV when $\frac{n_e^2}{\sqrt{T_e}} \frac{V_{pl}}{Pinj} \frac{\Delta N_{/\!/}}{N_{/\!/}}$ varies from 0.1 to 0.3 $[10^{40} m^{-6}\ keV^{-1/2}\ m^3/MW]$.

In order to maximize the temperature, one has to choose the smallest possible parallel refractive index. This is given by the "accessibility limit"
$N_{/\!/,acc} = \omega_{pe}/\omega_{ce} + \sqrt{1 + \omega_p e^2/\omega_{ce}^2 - \sum_{ions} \omega_{pi}^2/\omega^2}$
which is the value of $N_{/\!/}$ below which the slow LHW converts to a fast wave conveying energy in the outward direction (ω_{pe}, ω_{ce} and ω being the electron and ion plasma frequencies, the electron gyrofrequency and the LHW frequency, respectively).

In the range of parameters considered for the next step device, this index depends mainly on the ratio n_e/B^2.

Consequently, when $N_{/\!/,max}$ is chosen close to the accessibility limit, $N_{/\!/,max} = N_{/\!/,acc} + \Delta N_{/\!/}$, Equ.(1) gives a β limit rather than a temperature limit, as illustrated Fig. 3.

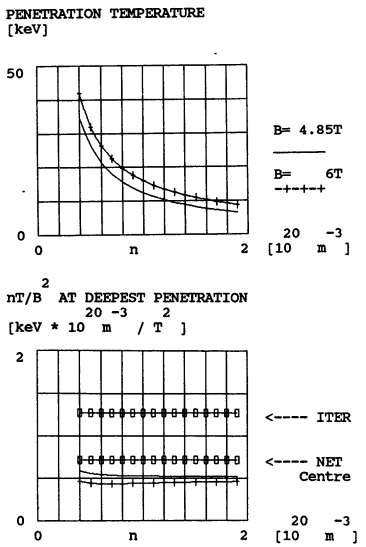

Fig. 3: Damping Penetration Limit of LHW

Equ.(1) shows further that this β limit decreases rapidly with increasing spectral width $\Delta N_{//}$: ($\frac{d\beta}{\beta} \simeq 0.1 \frac{d\Delta N_{//}}{\Delta N_{//}}$).

The spectral width of the launched spectrum is inversely proportional to the number N_{wg} of waveguides stacked in the toroidal direction in a grill, which can be of the order of one hundred in ITER or NET, leading to $\Delta N_{//} / N_{//} \leq 0.1$. An attempt to conceive a launcher providing a thinner spectrum, apart from being technically demanding, would be illusory since a number of mechanisms can broaden the spectrum during wave propagation as will be discussed below.

For an injected power of 100 MW and a spectral width of 0.1, Fig. 3 shows that the approximate β-limit found in this way is more than twice as low as the reference values at the plasma centre for the ITER reference scenarios. (This product $n_e(0)T_e(0)$ is about 30 10^{20} m^{-3} keV for the scenarios A1,B1 and B6[14].) This means that for conventional ITER profiles ($T_e(r) = T_e(0)\,(1-r^2/a^2)$; $(n_e(r) = n_e(0)\,(1-r^2/a^2)^{1/2})$, *the LHW during flat-top will be totally absorbed when reaching* $r/a \simeq 0.6$. As also shown by this figure, a much better penetration can be expected for a NET long pulse scenario[15]. (This shows a way for optimizing a device for LHW heating and current drive by selecting large aspect ratio and magnetic field.)

Conversely, wave absorption will not limit penetration to the plasma core during the current ramp-up phase (see Fig. 6).

Increasing the launched power level also improves the penetration, though less strongly: ($\frac{d\beta}{\beta} \simeq 0.1 \frac{dP_{inj}}{P_{inj}}$) and very large power levels would thus be required to ensure complete penetration under standard ITER conditions. A LHW system using pulsed - high peak and low average power - generators[16] has not been considered in the present conceptual design, since the physics is not yet proven and the technology would be more demanding.

2.2 Penetration limit due to propagation effects in toroidal geometry

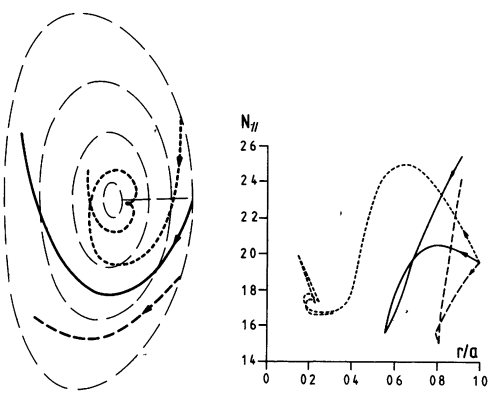

Fig. 4: Ray trajectories in ITER [23] for various poloidal location of the launcher

Ray-tracing techniques can be used to describe the propagation of waves in inhomogeneous media independently of the absorption process.

In toroidal geometry, they predict sizeable variations of the components of the LH wave vector along the trajectory. This results from spatial variations of the toroidal and poloidal magnetic fields, as well as from coupling between poloidal and parallel components of the wave vector.

Two consequences are: oscillations of $N_{//}$ (down and/or upshift) and the existence of the 'whispering gallery': a point of minimum approach to the plasma centre.

However, single-pass ray-tracing is usually insufficient to explain the $N_{//}$ upshift required to account for the magnitude of the power absorption in the experiments.

Ray-tracing techniques give a consistent picture of the experiments only if the spectral broadening (see §2.3) is attributed to multiple bouncing of the rays at the plasma edge[17], though often requiring many passes through the plasma.

Ray-tracing would have to be considered as merely indicative if the spectral broadening mechanism was not due to this effect.

Furthermore, diffraction effects - neglected in the ray-tracing procedure - are likely to alter significantly the picture it gives[18].

Another way to treat the problem in general is to use a full wave description[19,20]. Such

descriptions need extensive numerical computations, which are still in a preliminary stage and need to be pursued.

There are no simple analytical predictions of the whispering gallery radius (except in special cases - circular geometry, far from the accessibility limit[22] - not relevant to the next step device). For ITER, ray-tracing analyses show that propagation effects impose a limit on the wave penetration comparable to that due to absorption.

The major parameters influencing the penetration are the poloidal position of the launcher, $N_{//}$, and the peak density. Fig. 4 is an example of such calculations performed for one value of $N_{//}$ and three different poloidal positions of the launcher[23].

Fig. 5[21] gives similar plots for top and bottom launch in the case of a plasma with circular cross-section (plasma current anti-parallel to the toroidal magnetic field). Though this configuration is not relevant to ITER or NET, it illustrates the drastically different behaviour of the rays in the two cases. Excellent penetration is predicted for bottom launch, though at the cost of a strong $N_{//}$ upshift.

Since the rays will not penetrate beyond the absorption limit, the ultimate penetration will be determined by the intersection of the diagrams $N_{//}$ (r/a) with a curve representing Equ.(1) , as done in Fig. 5.

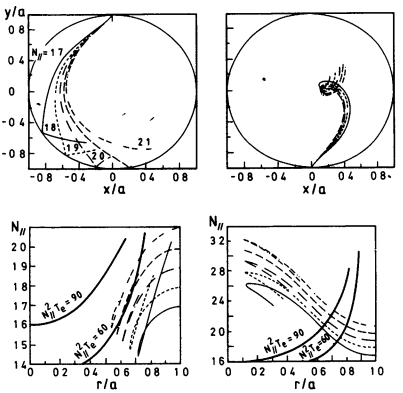

Fig. 5: Ray trajectories in a circular plasma [21]

It is clear from these curves that only the case with upshift allows control of the location of the power deposition zone. A LHW launcher designed for coupling the total power through a single port would fill it up completely in the poloidal direction, causing a spread of the trajectories comparable to that of the extreme cases of Fig. 4.

These considerations constitute one of the reasons for the choice of the *location of the LHW launchers in the bottom half of two main ports* (the requirements of the current ramp-up phase and maintenance and reliability considerations being two further reasons).

Note that this choice dictates the relative directions of the plasma current and the toroidal field

The whispering gallery radius is found[21] to vary between r/a = 0.75 and r/a = 0.4 when $N_{//}$ varies from 1.7 to 2.1 (equatorial launch, circular cross-section). It improves very slightly with frequency at 'large' $N_{//}$ [21,24] (e.g[21] between 5 and 8GHz from 0.4 to 0.35 at $N_{//}$ =2.1).

Toroidal propagation effects do not impede central wave penetration at somewhat lower density than during burn[25,23](see Fig. 6)

2.3 The spectral broadening issue

As discussed above, spectral broadening occurring during propagation influences the LHW penetration. To explain the magnitude of the absorbed power and driven currents observed in many experiments, it is necessary[26,27] to invoke an 'upshift' of the wave power spectrum $P(N_{//})$, i.e. to assume the presence of some wave power at considerably lower phase velocity than expected from the launched spectrum (by a factor of typically 2 to 3). It has been shown that just a small amount of power added to the launched spectrum in the low-phase velocity region may account for a much larger absorption[28,29].

A number of possible explanations for the occurrence of the upshift have been proposed: edge bouncing of the the rays[17], strong edge density fluctuations[30], non-linear effects in caustics[31], effect of Parail-Pogutse instability[32], ponderomotive effects[33], diffraction effects[18], ray stochasticity[34], wave scattering from toroidal inhomogeneities like the magnetic ripple[35,36], effects of parametric decay instability[37], and radiative resonant interaction[38].

Some of the mechanisms invoked would not affect the propagation in the high-β phases of

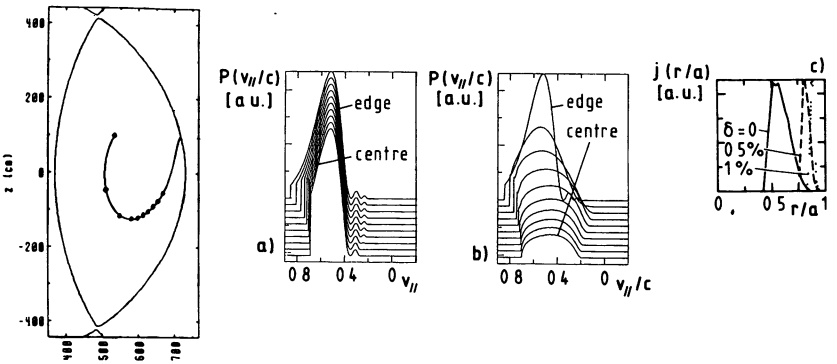

Fig. 6 (left): Ray trajectory in ITER at reduced density [64](end of ramp-up phase: $n_e(0)$= 0 8 10^{20} m^{-3} , T(0)= 33 keV, $N_{//}$ =1 6,P_{inj} = 100 MW)- each dot represents 10% incremental absorption

Fig. 7 (right): Effect of Ripple Broadening on LHW Penetration [36]

a) simulation of an ASDEX shot. Wave power spectrum during propagation towards centre without ripple broadening,(note the absence of wave absorption)

b) the same with a 2% ripple at edge, (this values yields ther actually driven current)

c) effect of ripple δ (at edge) on LHW penetration in NET

next step device plasmas: this is the case for the 'edge-bouncing' scheme since it will not act on the first wave pass during which full absorption of the LHW occurs. Others, occurring in single pass could be deleterious like ripple broadening (as examplified in Fig. 7) or density fluctuations, or diffraction broadening. There are even cases where the broadening could be beneficial (if occurring close to the plasma centre, as a result of, for instance, scattering from magnetic islands[35]).

As yet, no experimental evidence exists for supporting one or the other specific mechanism. As seen above, it is mandatory to understand the nature and factors acting upon the spectral broadening, in order to predict the penetration of the LHW in the next step device, and *experimental effort is recommended in this direction*

2.4 Consequences of restricted penetration: restricted total power and current (*monotonic q(r)*)

Restricted penetration also limits the total current which can be driven by LHW since the local current density should never exceed the average current density in the inner shells to comply with the (perhaps stringent[39]) requirement of having a monotonic safety factor profile for MHD stability.

When used in conjunction with neutral beams as the central current driver, *this limits the LHW current to about 2 5 - 3 MA and the injected LHW power to 30-40 MW in standard discharges* **with a safety factor at centre of q(0) $\simeq$ 1. A typical example is shown in Fig. 8.** *Further theoretical studies are needed to assess the MHD stability of slightly non-monotonic q-profiles.*

However, if central values of q of the order of 1.7 to 2 can be tolerated, MHD equilibria with a *large fraction of bootstrap current (e g $\geq$ 70%) can be obtained*[40] **by using a narrow central seed current (by neutral beams or fast waves injection). In this case, the LHW power deposited in the outer zones controls the total current, and acceptable equilibria are found even for ratios of LHW to central (fast-wave) current drive powers of 69MW/8MW to 85MW/55MW, as illustrated Fig. 9.Two critical points have to be elucidated before adopting this type of operation:** *1) is operation at q(0) $\geq$ 1 acceptable (absence of control on mild sawteeth, useful to expel*

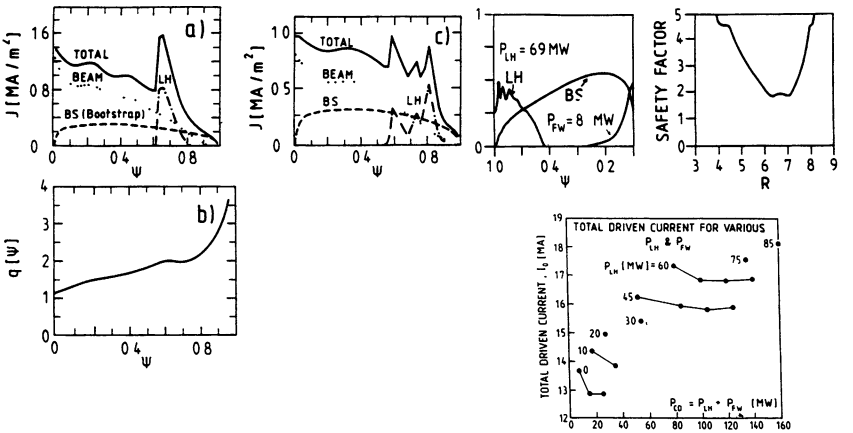

Fig. 8 (left): Combined use of NBI and LHW in ITER [24] ,

a) & c) current density ; b) q profile versus flux function Ψ.

a) and b) ITER (version 88) ; f=5.5GHz, equatorial launch

P_{NBI} = 84 MW I_{NBI} = 10.8 MA; P_{LHW} = 25 MW I_{LHW} = 2 MA; $I_{Bootstr}$ = 5.3 MA

c) ITER (version 90) ; f=8GHz, staged, off-plane launch

P_{NBI} = 84 MW I_{NBI} = 9.3 MA; P_{LHW} = 30 MW I_{LHW} = 2 3 MA, I_{BS} = 5.3MA

Fig. 9 (right): MHD Steady-State Equilibria with large bootstrap fraction in ITER (NBI + FW) [40]

top. driven current (weighted) density and q profile for 69 MW of LHW and 8 MW of FW

bottom Total driven current with various P_{LHW} and P_{FW}

impurities from the centre), and 2) can high bootstrap current persist in stationary states ?

2.5 Current diffusion

The diagnostics used to localize the presence of the fast electron tails created by LHW in present-day experiments (e.g X-ray bolometry), usually show a deeper penetration of these electrons than predicted by modelling (e.g. Fig. 10).

The commonly accepted explanation for this is that the slowing-down time $\tau_s \simeq 1s/(90 n_{20} N_{//}^3)$ of the fast electrons is large as compared with their confinement time τ_e. The resulting delocalization of the RF current is predicted to occur[41] even when the inequality is slightly reversed (as is the case in JT-60, where roughly $\tau_s \simeq 5 - 15ms$ and $\tau_n \geq 100ms$). These estimates are, however, very uncertain owing to the uncertainties on τ_e, and *more experimental and modelling data are required to establish the validity of this or another explanation* (since other phenomena - such as an anomalously deep power deposition, could also be suspected).

For high-β phases of the next step device, no enhanced penetration of the current is expected **owing to the strong inequality $\tau_s << \tau_e$.**

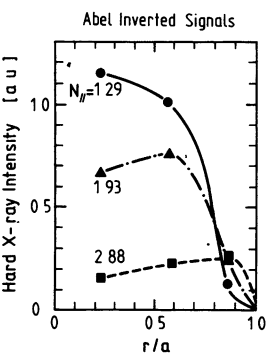

Fig. 10: Hard X-ray signals during LHW Current Drive in JT-60 [43]

3 - SELECTION OF OPERATING FREQUENCY

The operating frequency of the LHW system for ITER or NET has been selected to be 5 GHz; a number of physical and technical criteria had to considered to make this choice.

A major physical constraint is the necessity to avoid absorption by energetic ions, in particular α-paricles; which would decrease the current drive efficiency, worsen the penetration and might increase fast α losses. This imposes a lower bound on the frequency for the envisaged operating conditions of ITER, as will be shown in §3.1

Most of the technical constraints[8]are the more readily fulfilled the lower the frequency is (availability of well developed RF generators, robustness of the plasma-facing components, RF power losses etc.). The same is true of the problems connected with the matching of the antenna to the edge plasma as discussed in §3.2

3.1 Lowest frequency for avoiding interaction with α-particles

The physics underlying the onset of interaction of LHW with thermal[42] and fast ions is well understood; the interaction of LHW with injected neutral beams has been investigated in a number of tokomaks, a recent experiment in JT-60[43,44] confirming the dependence of its onset on the parameters involved(Fig. 11).

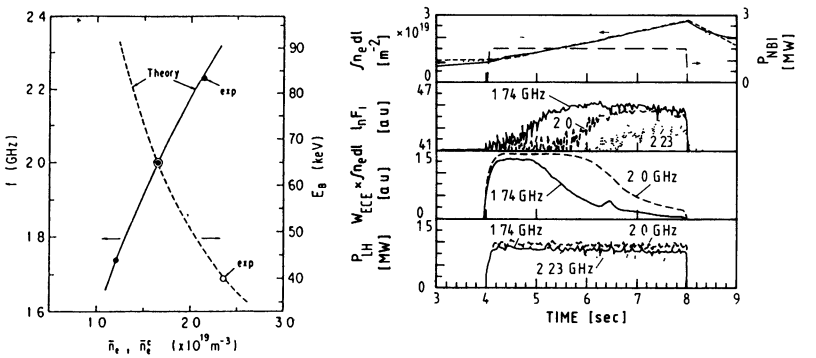

Fig. 11: Onset of interaction of LHW with Beam Ions in JT-60 [44]

left: Onset of ion absorption theoretical curves and experimental points for various beam energy and LHW frequency.

right: plasma density, NBI power, fast ion signals, ECE signals and LHW power as a function of time, for various frequencies

LHW can only interact with α-particles when the perpendicular phase velocity of the wave $v_{\Phi\perp} = c/N_\perp$ is smaller than the birth velocity $v_{b\alpha} = \sqrt{2E_b/M_\alpha}$ of the α-particles (i.e for $N_\perp > 23.1$). $N_\perp$ is given by the dispersion relation as a function of $N_{//}$ and the plasma parameters; it increases roughly as $N_{//}\sqrt{n_e}/\omega$, and thus for a given maximum operating density and maximum $N_{//}$ a minimum frequency is required to avoid the interaction strictly. (To evaluate $N_\perp$ correctly, the so-called 'electrostatic' approximations of the dispersion relation are not sufficient, owing to the proximity of the launched spectrum to the fast wave conversion layer.)

This result is confirmed by several modelling works performed for ITER[45,46,47] in which the amount of LHW power absorbed by α-particles is evaluated when the strict condition $v_{\Phi\perp} < v_{b\alpha}$ is not obeyed in the plasma. Fig. 12 shows a summary of these results: the onset of the absorption at low frequencies is less dramatic than could have been surmised even when taking into account an extension of the α distribution beyond the birth velocity, due to quasi-linear interaction.

Table I [48] shows that *any interaction with α-particles is avoided by choosing a frequency of 5 GHz*, for a wave spectrum extending up to $\Delta N_{//} = 0.2$ above the (central) accessibility limit and

for densities of up to 1. 10^{20} m^{-3} (which is more than the density at the deepest penetration radius).

TABLE I:
MAXIMUM ALLOWABLE DENSITY AND SPECTRAL WIDTH TO AVOID ABSORPTION BY ALPHA-PARTICLES

FREQUENCY	$\Delta N_{//}$	n_e [10^{20} m^{-3}] B = 4.85 T	n_e [10^{20} m^{-3}] B = 6 T
5 GHz	0.1	1.36	1.46
	0.2	1.09	1.16
	0.3	0.91	0.97
8 GHz	0.1	3.08	3.25
	0.2	2.52	2.62
	0.3	2.13	2.21

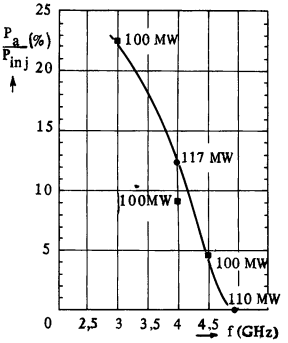

Fig. 12: Power Absorption by α-particles below the critical frequency [4]

Note that when the strict condition is obeyed, interaction with beam deuterons or tritons injected at 1.3MeV is also avoided.

3.2 Coupling density

Coupling of a grill launcher to the plasma is well described by the theory[49]. To minimize the reflection coefficient, a plasma density at the surface of the launchers of the order of $n_g \simeq N_{//}^2\ \omega^2\ m_e\epsilon_0/e^2$ is required. The optimal density in front of the grills for tolerably low RF power reflection is of the order of 2. 10^{18} m^{-3} at 5 GHz. (Note that this value increases roughly with the square of the RF frequency.) Since the multijunction type of launcher[50] - used in most of the present large LHW systems and in the present ITER design - is a self-matching system, the range of good matching (power reflection $\leq$ 5% at any phasing) is found to extend from 5. 10^{17} m^{-3} to 4.5 10^{18} m^{-3} at 5 GHz[51] (see Fig. 13) (versus about 1.3 10^{18} m^{-3} to 8 10^{18} m^{-3} at 8 GHz[52]).

The expected wall density as presently evaluated[14] falls into the required range for 5 GHz so that *the LHW launcher can be positionned flush to the first wall* in this case. However, still large uncertainties persist in these evaluations and *provision for radial motion of the grill is included in the launcher design*[8]. The power loading on the side limiters of the launchers - including the α-particle loading - appears to be still within the present technical possibilities - though demanding - if the launcher has to protrude into the scrape-off layer till the required density is matched. (Conversely, maintaining the plasma by position control close enough to the launchers is a preferred solution.)

3.3 Selection of the frequency for the ITER LHW system, summary

5 GHz is a sufficiently high frequency to avoid interaction of LHW with α-particles and beam ions in all considered operation scenarios of ITER.

The possible occurrence of parametric decay instabilities at the plasma edge, which would possibly prevent wave penetration has also been theoretically investigated[53] and found unlikely both at 5 GHz and at 8 GHZ.

A very slight improvement of the penetration features in the upper frequency range (8 GHz) has been predicted.

However, two main penalties would have to be paid if the higher frequency range was selected. On the one hand, the plasma density required at the launcher mouth for good grill matching would increase by a factor of about 2.5. This would narrow - or even suppress - the range of possible operation with the launchers flush to the first wall or, conversely, increase by about 4 the the heat flux on the guard limiters if the launcher had to protrude. On the other hand, RF power losses increase with frequency.

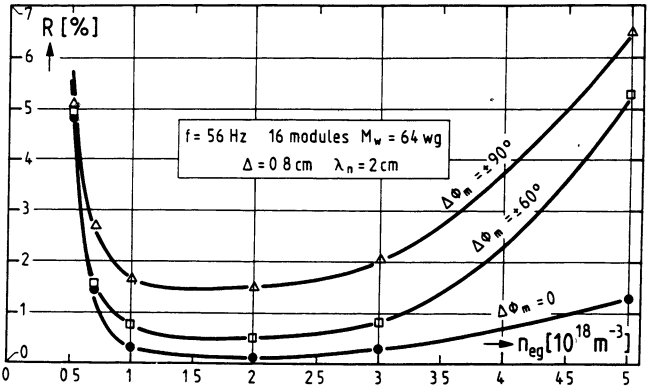

Fig. 13: Reflection coefficient of a multijunction [4] as a function of the edge density and for various intermodule phasings

In both frequency ranges the development of dedicated RF power tubes would be required, though not considered problematic. However, the klystrons (usable in the lower range up to about 6 GHz), benefit from a wide experience, while in the upper frequency range gyratrons with sufficient efficiency and phase controllability would have to be developed. (A clear demonstration of the latter feature has been recently obtained[54].

The selected frequency of 5 GHz appears convenient for all functions of LHW system on ITER

4 - CURRENT DRIVE EFFICIENCY

The local current drive efficiency (in the absence of an electric field) is well represented by the theoretical formula[57,55,56]

$$\gamma \equiv \frac{n_e R I_{driven}}{P_{abs}} = \gamma_0 \; F(x, Z_{eff}) \; G(x, \epsilon) \tag{2}$$

where: γ_0 is the 'Fisch-Boozer' efficiency,

$$\gamma_0 = \frac{2 m_e \epsilon_0^2 c^2}{e^3 ln(\Lambda)} \; \frac{1}{< N_{//} >^2} \; \frac{4}{5 + Z_{eff}} \tag{3}$$

and $\frac{1}{<N_{//}>^2} = \left[\frac{1}{N^2_{//,Min}} - \frac{1}{N^2_{//,Max}}\right] \frac{1}{ln(N^2_{//,Max}/N^2_{//,Min})}$ is an average over the wave spectrum extending from $N_{//,Min}$ to $N_{//,Max}$; $N_{//,Min}$ is taken as the refractive index at the accessibility limit: $N_{//,acc} = \omega_{pe}/\omega_{ce} + \sqrt{1 + (\omega_{pe}/\omega_{ce})^2 - \sum_i (\omega_{pi}/\omega)^2}$ (using volume-averaged density and magnetic field on axis); $x = v_\Phi / v_{e,th} = c/(< N_{//} > v_{e,th})$ is the ratio of phase velocity to electron thermal velocity $v_{e,th} = \sqrt{T_e/m_e}$

The term $\mathbf{F}(x, Z_{eff})$ is a temperature correction:

$$F \equiv 1 + \frac{1}{x^2} \left[\frac{5 + Z_{eff}}{4} + \frac{3(6 + Z_{eff})}{2(3 + Z_{eff})}\right] + \frac{1}{x^3} \; \frac{3\sqrt{2\pi}(5 + Z_{eff})}{8 Z_{eff}}$$

and $G(x, \epsilon)$ is a correction accounting for trapped electrons[58] (ϵ being the local inverse aspect ratio r/R), which reads for slow LHW[57]

$$G(x, \epsilon) = 1 - \frac{\epsilon^{0\,77} \sqrt{12.25 + x^2}}{3\,5 \epsilon^{0\,77} + x}$$

(These expressions are strictly valid only for narrow wave spectra, and should apply for ITER).

For ITER technology phase conditions, $N_{//,acc} \simeq 1.85$. Using $N_{//} = 2$ yields $\gamma_0 = 0.3 \left[10^{20} m^{-2} MA/MW\right]$;
The temperature at the deepest penetration point is such as $N_{//}^2 T_e \simeq$ 60keV to 90keV. Evaluating
$F(x, Z_{eff}) = 1.55$ for $N_{//}^2 T_e = 60keV$, $Z_{eff} = 2$ and $F(x, Z_{eff}) = 1.85$ for $N_{//}^2 T_e = 60keV$, $Z_{eff} = 2$;
and assuming very poor penetration during burn ($\epsilon = 0.25$),
$G(x, \epsilon) = 0.69$, for $N_{//}^2 T_e =$ 60 to 90keV,
efficiencies of the order of $\gamma =$ 0.32 - 0.38 $\left[10^{20} m^{-2} MA/MW\right]$ result from the above formulae.
They are also consistent with the value $0.34 \left[10^{20} m^{-2} MA/MW\right]$ obtained in JT-60.

5 - ADVANCED LAUNCHER CONCEPTS

The Grill-type launcher has been used in the quasi-totality of modern LHW experiments and benefits from a wide experience on which the design of an antenna for the next step device could reasonably be based[8]. Nevertheless, the proximity to the plasma of the relatively delicate waveguide structure constitutes a difficult technical problem to be solved in order to operate a system in a reactor. For this reason, *the search for advanced launcher concepts should be strongly encouraged.*

The principle of such a launcher has recently been proposed[59]. In this device, the slow wave is produced by an array of thick rods, recessed from the scrape-off plasma. The main potential advantages is the replacement of the thin-walled waveguides by the thick, easily cooled rods and their distance from the plasma; a potential inconvenience is the larger electric field strength arising in this (resonant) structure. Preliminary calculations show that the required wave spectrum should be achievable. *Further modelling, conceptual design studies and tests are required.*

6 - CURRENT RAMP-UP ASSIST WITH LHW

Lower hybrid waves (LHW) benefit from an extensive experimental database for this type of application[1]; recent results[43,60] such as those shown Fig. 14 (2 Vs saving with 1.6 MW of injected LHW power in JT-60[43]) give further support to the selection of LHW as the method of choice to assist ohmic current ramp-up (since it is to be performed in a range of plasma parameters close to those of present experiments, the main difference being the time scales involved: ramp-up duration and skin time).

The physical constraints to be respected in a LHW-assisted current ramp-up scenario include:

i) achievement of a transformer flux saving significant as compared with the flux consumption during the reference inductive burn phase - in order to provide an extension of the inductive burn duration (note that a saving of the order of 30 Vs would extend the burn duration by 190 s and 460 s in the reference ITER technology phase scenarios B1 and B6);

ii) avoidance of non-monotonic q-profiles - deleterious for MHD stability - which can arise if the ratio of the skin time to the ramp-up time is too large, this resulting in turn from the large plasma dimensions and the additional LHW heating;

iii) evolution of the representative point of the discharge in a prescribed domain of the q-l_i diagram to ensure the stability of the discharge;

iv) achievement of a ramp-up duration compatible with the operation scenarios: in particular, the duty cycle with LHW assist should improve over the purely inductive one.

Technical constraints must also be considered, the main ones being:

i) Power exhaust considerations: to minimize the additional power requirements, the current ramp-up is to be performed at sufficiently low density. However, the total power acceptable in the divertor decreases rapidly with the density. During the early phases of ramp-up, the plasma must be close to the launchers and will thus lean on an outboard limiter. The power handling capacity of such a device will impose a severe restriction

on the total power conducted to the limiter[61]. The low-density power handling limits of both divertor and limiter operation have still to be assessed.

ii) Stress in the poloidal field system also limits the maximum flux swing saving obtained by non-inductive means. Present estimates[62] show that a flux saving of up to 50 Vs is tolerable from this point of view.

iii) Finally, the technical requirements imposed by LHW-assisted current ramp-up system - especially the required wave spectrum flexibility and the geometry of the launchers - is to be made compatible with the design of the LHW system developed for burn phase current drive.

Modelling studies[63,64,65,66] have consistently shown that of the order of 20-40 Vs can be saved by ramping up the injected LHW power to 20 to 35 MW, when operating at a low density: $\bar{n}_e \simeq 2\ 10^{19}\ m^{-3}$, or correspondingly, about 20 Vs using up to 45 MW of current drive power when operating at $\bar{n}_e \simeq 4\ 10^{19}\ m^{-3}$, the current ramp-up being performed at a rate comparable with the purely ohmic one (0.35MA/s). The physical constraints mentioned above can be respected, partly owing to the fact that account is taken of the evolving plasma geometry.

'Slow' ramp-up scenarios have also been studied (ramp-up time several 100 s, at zero surface voltage)[67], aiming at large flux savings to minimize the number of shots for a given fluence.

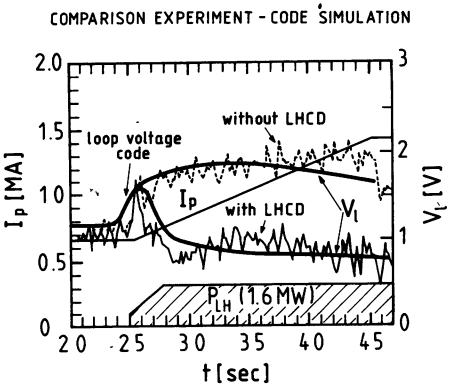

Fig. 14: LHW-Assisted Ramp-up in JT - 60

According to this work, it appears possible to decrease the number of shots in the technology phase by a factor of up to 6, with savings of 100 to 130 Vs (which might be beyond the limit imposed by the poloidal field system), still using up to 40 MW power.

The LHW spectrum required at the beginning of the ramp-up phase is broader - and at a larger $N_{//}$ than that required during the high-β phase. Launching the former type of spectrum, however, is not needed in present-day experiments owing to spectral broadening (these experiments are performed in the same range of plasma parameters as those envisaged in the next-step ramp-up phase). One may thus rely upon the same broadening - or upshift - and use the high-β phase design for all applications. As a back-up provision for a possibly different broadening on the ITER/NET scale, and to ensure spectral flexibility during operation, it is envisaged to use 'composite spectra' (i.e. to launch a small fraction of the power at higher $N_{//}$, a scheme which proved very efficient in ASDEX[5] and appears compatible with the high-β design[8]).

LHW-assisted current ramp-up appears attractive and the physical constraints can be respected. The main point of concern is the ability of the power exhaust system to withstand the additional power in the low-density range.

7 - CONCLUDING REMARKS

The present database, degree of understanding and the status of the technology permits to envisage the use of LHW for a number of functions in the Next Step Device. The most important of them, for which LHW present specific advantages over other methods, are to assist the ohmic drive during the current ramp-up phase and to drive current and perform current profile control in the outer regions of the burning plasma.

Already achieved performance at large power level and/or in long discharges include operation in H-mode, high current-drive efficiency, plasma heating, current profile control and

assisted current ramp-up.

The physics of wave coupling and current drive can be considered as sufficiently well understood to permit a reliable design. Wave propagation behaves in many respects as theoretically expected, but its full understanding requires, however, a further experimental effort concerning mainly the origin of the spectral broadening. This phenomenon, for which many possible explanations have been offered, must be clarified to permit reliable estimates of the penetration of LHW in high-β plasmas.

Further theoretical or experimental work to be performed in the next future should include, besides detailed modelling of the various phases and scenarios of a discharge in the Next Step Device; studies on the localization of the LHW power and current deposition; on the MHD stability of combinations of inductive, non-inductive and bootstrap currents; on fast electron diffusion and on prospects for advanced launchers.

Aknowledgements A large part of the material presented in this paper was contributed and discussed by experts on the occasion of eight ITER physics and design workshops and three NET meetings held between 1988 and 1990. The author would like to thank all participants in this activity and his colleagues from the ITER Current Drive and Heating Group and from the Physics Group of NET for their fruitfull participation

[1] N. Fujisawa et al , INTOR Phase IIA, Part III, Vol. I, Ch V, IAEA Vienna, 1988
[2] M Nagami and JT-60 Team, Plasma Phys and Controlled Fusion, 31,10,(1989),p.1597
[3] C Gormezano at al., APS, 1990
[4] G Tonon et al,"Technical constraints and Design of a LHCD system for NET/ITER, ITER-IL-HD-5-0-E-1, March 1990
[5] F X. Söldner et al, 'Review of Lowe-Hybrid Experiments in ASDEX', Proc. 13th Int Conf. on Plasma Physics and Controlled Fusion Research, Whashington, USA, 1990
[6] S. Itoh et al., 'Experiments on Steady-State Tokomak Discharges by LHCD in TRIAM-1M', Proc 13th Int Conf. on Plasma Physics and Controlled Fusion Research, Whashington, USA, 1990
[7] Equipe TORE-SUPRA, F. Parlange, Progress to Long Pulse Operation in TORE-SUPRA', Proc 13th Int Conf on Plasma Physics and Controlled Fusion Research, Whashington, USA, 1990
[8] J.-G. Wégrowe LHW System for ITER, in ITER Current Drive and Heating Systems, ITER Documentations series No. 32, IAEA, Vienna, to be published, 1991
[9] ITER Physics and Technology R&D needs for ITER, ITER Documentations series No. 20, IAEA, Vienna, to be published, 1991
[10] R.W. Harvey et al, 'Limitation on Lower-Hybrid Heating of dense hot Plamas', Proc. 3rd Topical Conf. on RF Heating of Plasmas, Pasadena, USA, (1978)
[11] N.J FISCH, 'Confining a Tokomak Plasma with RF driven Currents', Phys Rev. Lett. 41, 13, (1978)
[12] C.F.F. KARNEY and N.J FISCH, Numerical Studies of Current Generation by RF travelling Waves', Phys. Fluids, 22,9 (1979)
[13] N. J Fisch, and A.H. Boozer, 'Creating an asymmetric Plasma Resistivity with Waves', Phys Rev Lett. 45,9 (1980)
[14] ITER PHYSICS, ITER Documentations series No 21, IAEA, Vienna, to be published, 1991
[15] The NET Team,R. Toschi, 'The NET Project, an Overview', 12th. Int Conf on Plasma Phys. and Controlled Nuclear Fusion, Nice, France, (1988), IAEA-CN-50/G-1-1
[16] M. Porkolab et al., Proc. 13th. Int Conf. on Plasma Physics and Controlled Fusion Research, Whashington, USA, 1990
[17] P Bonoli and R C. Englade Phys Fluids, 29, 2937 (1986)
[18] G V Pereverzev, 'Effect of diffraction on absorption of lower hybrid waves in a Tokamak',JETP Lett.,44,9,(1986), 549
[19] D. Moreau et al, 16th EPS Conf, Venice 1989
[20] A. Fukuyama, ITER-IL-Ph-6-9-J-5
[21] E. Barbato & F. Santini, ITER IL-Ph-6-9-E-15
[22] A. Cardinali, F. Romanelli et al , A. Cardinalli and M Brambilla, Rpt EUR-CEA-FC-1092, Grenoble, F , (1981)
[23] Y. Baranov & A.R. Esterkin, ITER-IL-Ph-6-9-S-16
[24] R S. Devoto et al. ITER-IL-Ph-6-0-U-6
[25] P. Bonoli, ITER-IL-Ph-6-0-U-4, (July 1990)
[26] IAEA Workshop on Non-Inductive Current Drive, Garching, 1987
[27] J.-G. Wégrowe and G. Zambotti, 16th Eur Conf on CFPP, Venezia, (1989),IV-1247
[28] S. Succi et al., Proc. of the 4th Int. Symp on Heating in toroidal Plasmas, Roma, It, (1984)

[29] J -G Wégrowe, Course and Workshop on Applications of RF Waves to toroidal Plasmas, Varenna, It, Sept 1985
[30] P Bonoli, E Ott, Phys Fluids, 25(2), 359, Feb 1982
[31] E Barbato, A Cardinali, F Santini, Proc of the 4th Int Symp on Heating in toroidal Plasmas, Rome Italy, (1984)
[32] see e g J Vacklavik et al Plasma Physics 25, 1283, (1983)
[33] R Croci and E Canobbio, Z für Naturf A-42,10, (1987), 1067
[34] D Moreau et al , 15th Eur Conf on CFPP, Dubrovnik (1988),III-995 and , 16th Eur Conf on CFPP, Venezia, (1989),III-1169
[35] J -G Wégrowe , "Broadening of the Lower Hybrid Wave Spectrum due to Departure from Axisymmetry", Proc 14th Eur CCPP, Madrid 1987 III, 911
[36] J -G Wégrowe , G Zambotti, 8th Topical Conference on application of RF power to plasmas, Irvine, Calif May 1-3rd , 1989
[37] A M Rubenchik, 'Electron and Ion Acceleration Associated with Lower-Hybrid Plasma Heating', Plasma Phys and Controlled Fusion, 31,8,(1989)
[38] S I Popel and V N Tsytovitch, this conference
[39] B B Kadomtsev Sov J Plasma Phys , 1,5, (1975); V V. Parail & G.V Pereverzev, Sov J. Plasma Phys 6(1), (1980)
[40] D Ehst "Generation of high-bootstrap stable equilibria", July 1990
[41] J M Ráx and D Moreau, Nucl Fusion 29,10,(1989)
[42] J -G Wégrowe and G Tonon, IAEA Tech. Meetg. on non-inductive current drive in Tokamaks, Culham, 1983, J -G Wégrowe , Comments in Pl Phys. 8,6,(1984); J -G Wégrowe , F Engelmann, G Tonon, 4th Int Symp Heating of Tor Plasmas, Rome, It (1984)
[43] K Ushigusa, 17th CFPP - EPS Conf., Amsterdam, 1990, to be publ in Plasma Physics & Controlled Fusion, 1990
[44] M Nemoto et al , 'Acceleration of Beam Ions in simultaneous Injection of NB and LHW in JT-60, Vol III, p 1183, Proc. 17th CFPP - EPS Conf , Amsterdam, 1990
[45] Yu Baranov & A R Esterkin, 'LH Current Drive and Optimization of Power Spectrum, ITER-IL-Ph-6-9S-16
[46] E Barbato, F Santini,'Quasi-Linear Effects on α Absorption of LH Waves', ITER-IL-Ph-6-9E-13 , NET Report No , 1990, and Nuclear Fusion, to be published, 1991
[47] P Pavlo, L Krlin, Z. Tluchor, 'Influence of α Particles on the LH Current Drive in a fully Quasi-linear Approach', ITER-IL-Ph-6-9S-23
[48] J -G Wégrowe ITER-IL-Ph-6-0E-1
[49] M Brambilla, Nucl Fusion 16,1(1976)
[50] T.K. Nguyen and D Moreau, Proc 12th Symp on Fusion Technology, Vol II, p 1381, Jülich, FRG, (1982)
[51] G Tonon et al. ITER-IL-HD-5-0-E-2, (1990)
[52] J J Yugo et al ITER Current Drive and Heating Meeting, July 1988, Contrib No 13
[53] A Cardinali et al , NET Report to be published, 1990
[54] I Antakov and V E Myasznikov, this conference
[55] C F.F KARNEY and N.J. FISCH, 'Numerical Studies of Current Generation Waves', Phys. Fluids, 22,9,(1970)
[56] N J FISCH and A H. BOOZER, 'Creating an Asymetric Plasma Resistivity with Waves', Phys. Rev Lett 45,9,(1980)
[57] D A Ehst & C F F Karney, "Neoclassical effects on RF current drive", ANL/FPP/TM-247, Apr 1990
[58] G Giruzzi, Nucl Fusion, 27, (1987), 1934
[59] M I Petelin, E V Suvorov, 'Quasi-optical grill for excitation of lower-hybrid waves in plasmas' Letter to Journ Techn Phys (Pisma v JTF, 15, (1989), p 23; N.F Kovalyov et al , this conference
[60] K Ogura et al., Nuclear Fusion, 30, 4, 1990
[61] H D Pacher, G W Pacher, M F A Harrison ITER-IL-Ph-13-0-E-6
[62] Int Rept ITER IL-PF-1-9-27
[63] Summary of ITER modelling workshop on LHW assisted ramp-up
[64] P Bonoli, '1 1/2 D Transport study of LH assisted ramp-up in the ITER Device', ITER-IL-Ph-6-0-U-1 and U-3 (1990)
[65] G. Pereverzev, Ohmic and LH assisted Current Ramp-up in ITER', ITER-IL-Ph-6-0-S-5, Feb 1990
[66] J -G Wégrowe and G. Zambotti, 17th EPS Conf Contr Fusion and Plasma Heating, Amsterdam, 1990 , III, 1235
[67] G. Pereverzev, Optimization of Operational Cycle with LH Ramp-up Assist in ITER, ITER-IL-Ph-6-9-S-5, Feb 1990

PECULIARITIES AND PROBLEMS ASSOCIATED WITH THE ELECTRON-CYCLORTON HEATING (ECH) OF PLASMA IN STELLARATORS.

G.M. Batanov
General Physics Institute, Moscow

It is known that the experiments on a current-free stellarator plasma production and heating by microwaves in the gyroresonance regime were first carried out in the Liven´-1 stellarator [1]. Table 1 shows the results achieved in recent years. We can see that two-turn stellarators are widely adopted. As a rule, there are used high-power gyrotrons in the 28-75 GHZ range and quasi-optical systems producting Gaussian beams with a linear polarization (an ordinary mode at the fundamental harmonic of a cyclotron frequency and an extraordinary mode at the second one). The attention is also drawn to the high density of the

Stellarator	W-7A	W 7AS	L-2	ATF	H-E	CHS
B_0 (T)	3,5	3,0	1,4	2,0	2,0	1,5
R (cm)	200	200	100	210	220	100
$\bar{a}$ (cm)	10	20	11,5	27	20	18
ℓ / M	2/5	2	2/14	2/12	2/19	2/16
$\iota(0) / \iota(\bar{a})$	0,1/0,1 0,6/0,6	0,39/0,39	0,2/0,8	0,3/1,0	0,5/2,2	0,3/1,0
q (W/cm^3)	1,5	8÷16	2÷40	–	0,4	–
τ_E (ms)	1,8÷3,3	~10	3÷5	10	15	–
W (kj)	0,2÷1,0	4,5	0,45	4	~1,0	–
F (GHz)	28, 70	70	37,5, 75	53	53,2	28
Mode	O/X, O/X	O, X	O, X	O, X	TE_{02}	TE_{01}, X
P_0 (kW)	170	400	200, 300	200	720	200
$T_e(0)$ (keV)	1,2 2,3	1,9 1,24	0,9 0,8	0,6÷1,1	1,5	0,3÷0,9
$\bar{n}_e$ ($10^{13} cm^{-3}$)	0,5 2,4	1,25	0,75 1,8	2,5	2,0	0,2÷0,6

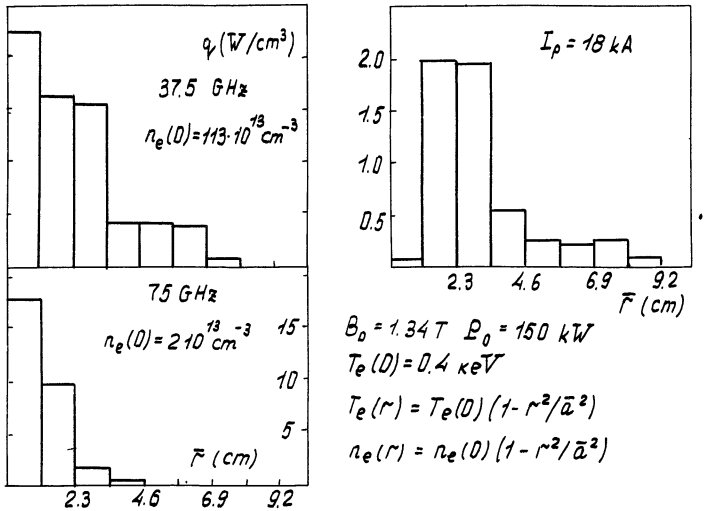

Fig.1 Distribution of power deposition density

energy deposition, which exceeds that in tokamaks. Now we consider the scheme of our report.

1. At present all the stellarator teams have developed the numerical codes for the calculation of the ray trajectories in the geometrical optics approximation and the codes for the calculation of the cyclotron wave damping in a hot plasmas. The codes allow us to calculate a distribution of absorbed power in separate parts of a Gaussian beam and, consequently, the total absorption coefficient. We shall give the typical results of calculations from the paper [2] carried out for the L-2 stellarator. In the case of a resonant magnetic field, when ECR is at the center of the magnetic surfaces, the density of deposited power has a sharp peak (Fig.1). The change in the plasma density causes the broadening of the power deposition region in comparison with to the optimum density regime due to the strong effect of refraction (because of an oblique incidence of the wave at the plasma column). The longitudinal current in a stellarator changes the shape of the magnetic surfaces (the center of the plasma is displaced outwards). This results in the change of ray trajectories due to the change in the density distribution and in the change of the distribution and magnitude of the density of absorbed power. Hence, the total absorption coefficient turns out to be close to 100%, the electron

temperature in the center of the column being Te(0)=0.5-1 KeV, that is quite acceptable for the stellarators of the present and next generations.

One of the most urgent theory problems is the developing of codes for calculations of the electron distribution function at high microwave power densities when quasi-linear effects play an important role.

As for the thermal conductivity theory, a self-consistent program have been now developed, which takes into account the power deposition during ECRH and Te (electron temperature) distribution due to the neoclassical transport processes, and also the particle sources [3]. Te distributions for the given density profile and distribution of the deposited power are obtained with earlier calculations [4]. It has been, in particular, shown that in the case of the narrowing of the energy deposition region, the central temperature Te(0) noticlable changes, whereas the total energy W and the energy confinement time change slightly.

2. One of the main questions, to which the experiments should give answer, is, first of all, the problem of agreement between theoretical predictions and results of measurements. Another problem is the effect of the auxiliary heating on the transport processes.

All previous experiences shown that it is necessary to use the Gaussian beams. This allows us to choose directly the region and the density of power deposition and also to produce the longitudinal current. At the same time, this approach permits to avoid quite a number of uncertainties in the interpretation of the experimental results.

The comparison of the heating for the case of a wavequide and a quasi-optical system used for power launching has been already made in the W-7A stellarator (Fig.2) [5]. One can see that, in the case of a quasi-optical launching of a Gaussian beam, the central temperature doubles its value, so that the absorption coefficient reaches 80% and the plasma energy is 2 times higher. Nevertheless the use of a beam with a linear polarization causes some energy losses due to the Faradey rotation in those cases when there is a strong radial component o the magnetic field at the periphery of the column. For example, these losses may have amounted to 20 % at the second harmonic in the L-2.

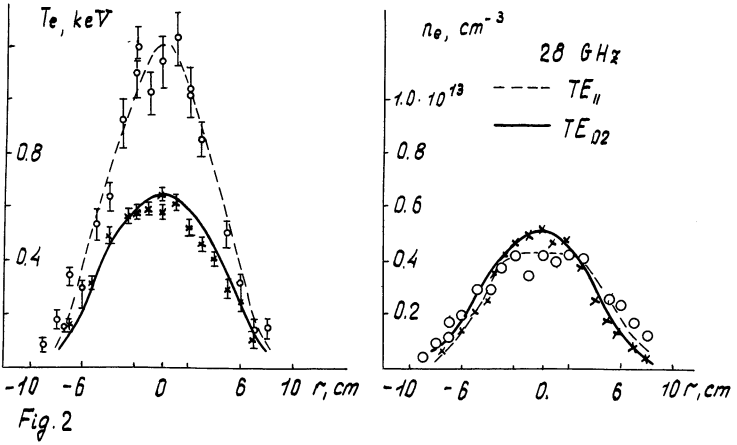

Fig. 2

The absorbed microwave powers obtained from a diamagnetic signal disagree with the calculations of absorption for both the fundamental and the second harmonics [6,7]. Fig.3 shows that in the W-7A the absorption coefficients experimentally observed in the region of low plasma densities were less than the calculated ones. In the L-2 (Fig.4) the measured absorption coefficient turned out to be 1.5 or 2 times less than the calculated one and did not depend on Te, that qualitatively contradicts the theory. It is a paradox, that in this case a complete wave damping was observed at the distance about 0.1 of the torus perimeter from the cross-section of launching. This effect would be attributed to the wave absorption at the plasma periphery in multiple passes

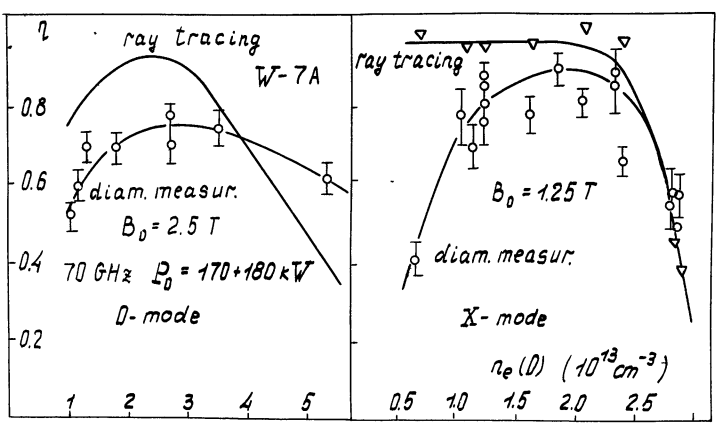

Fig. 3

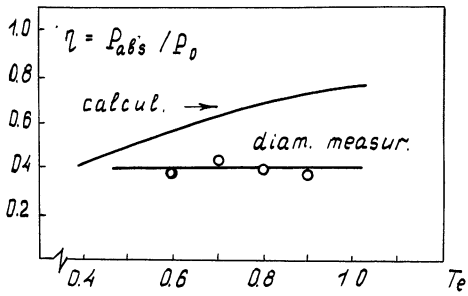

Fig. 4 O- wave, 37.5 GHz, $B_0 = 1.34$ T, $n_e(0) = 1.12 \cdot 10^{13}$ cm^{-3}

through the column and to a short confinement time of this fraction of energy. That's why this part of energy was not observed in diamagnetic measurements due to the screening effect of the vacuum chamber. Hence, direct measurements of the wave damping during a single pass through the plasma column are important. The results of such measurements with four antennae in L-2 stellarator plasma with a current [8] showed almost a complete absorption of the radiation (Fig.5). The variation of the average density from $0.92*10^{13}$ up to $1.82*10^{13}$ cm^{-3} does not lead, as it followed from the calculations, to the change in the absorption. The experimental and calculated absorption dependencies on the magnetic field are close, the only discrepancy concerning the region of a low magnetic field.(Recently the direct measurements of single-pass absorption efficiency during ECRH in W7-AS stellarator have been made [21]).In our experiments it was also measured the central beam splitting due to the Faradey rotation. The agreement with the estimation was found.

Let us now consider in detail the disagreement between

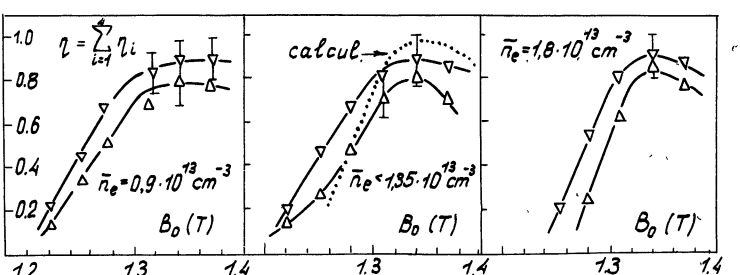

Fig. 5 75 GHz, $P_0 = 220$ kW, $I_0 = 16$ kA, $T_e(0) = 350$ eV, Δ - 1 ms
$T_e(0) = 650$ eV, ∇ - 5 ms

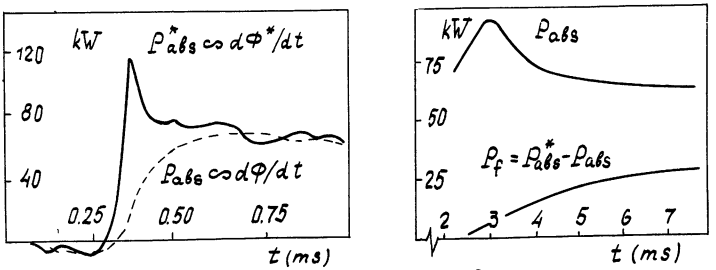

Fig. 6

microwave measurements and the measurements of the derivative of the diamagnetic signal. In the paper [9] an account was taken of the skin-effect of both the chamber and magnetic field coils on the diamagnetic measurement. As a result it was found a fast change in the derivative of the magnetic flux (Fig.6), hence, a real existence of a short-life component of the plasma energy was proved. It is established that these losses fall with the increase in the plasma density and grow with the increase in the radiation power. However, even the account for these fast losses does not give the agreement between the calculations and both microwave and diamagnetic measurement (Fig.7). This may be associated with the localization of these losses near the cross-section of the microwave power launching, whereas the technique is aimed to observe the parameters averaged over the axis of the torus. If may be supposed that these losses are caused by the producing of electrons with high transverse energies in the region of absorption. These electrons were actually observed from

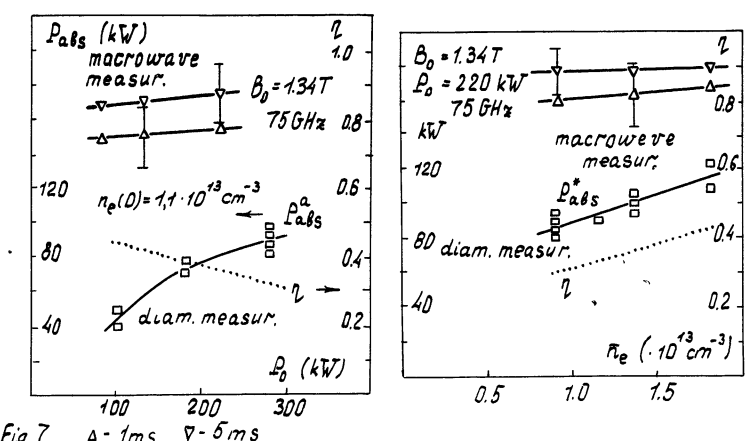

Fig.7 Δ - 1ms, ∇ - 5ms

the radiation at the second harmonic of the gyrofrequency in the W-7A [6], and in the L-2 [10] during the plasma heating by an ordinary wave at the fundamental harmonic of the gyrofrequency.

3. Let us now dwell on the problem of localization of the power deposition. We have considered above the experimental results from W-7A at the field 2,5 T (70 GHz) with an extraordinary mode, the resonance being located at the axis of the chamber.We have seen that the beam narrowing in the case of HE_{11} mode, compared to TE_{02} mode, results not only in the increase in the heating efficiency but also in the narrowing of the electron temperature profile.In the W-7A, the temperature and density distributions were measured at the frequencies 28 and 70 GHz, ECR being both located on the axis of the chamber and displaced for 4 cm from the axis (Fig.8). Whereas the density distribution does not practically vary, the temperature distribution noticeably broadens. In the L-2 experiments the broadening of the power deposition region was reached by varying the magnetic field. The calculation show that the broadening of the power deposition profile does not practically change neither the energy content not the energy confinement time, but decreases the central temperature. The measurements of the electron

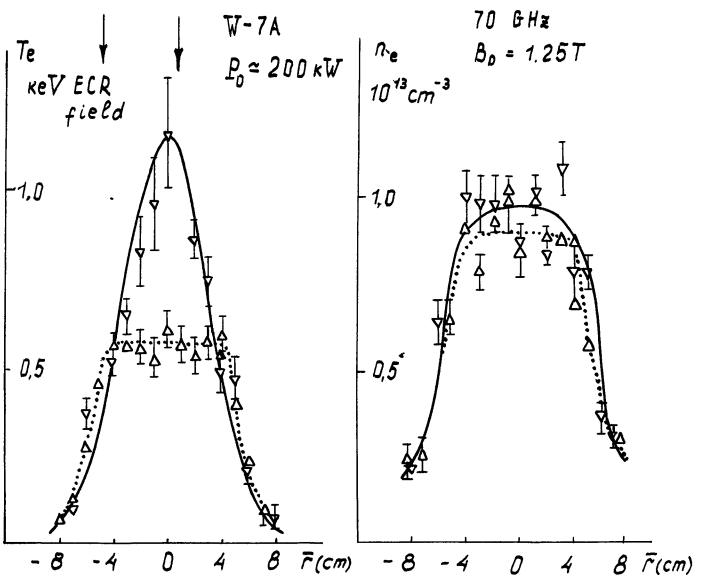

Fig. 8 Radial Te profiles

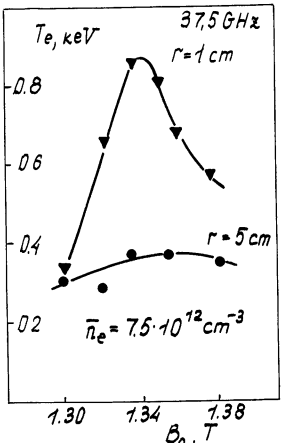

Fig. 9

L-2 $n_e = n_e(0)(1-r^2/a^2)$ $T_e = T_e(0)(1-r^2/a^2)$

$n_e(0) = 1.125 \cdot 10^{13} cm^{-3}$

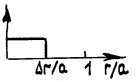

Δr/a	0,2	0,5	0,75
$T_e(0)$, keV	1,19	0.85	0.65
W, kJ	0.2	0.17	0.16
τ_E, ms	2.8	2.6	2.3

temperature from the soft X-ray radiation was carried out in the center of the column and in moving away from the center at the distance of 4 cm. Dependence of this temperature on the magnetic field confirmed the theoretical predictions (Fig.9).[1] Hence, there is indirect experimental evidence for the theoretically predicted localization of the power deposition region.

The increase in the heating power in recent experiments led to the observation of a new effect: density and temperature decrease in the central plasma regions compared to the peripheral regions (hollow profiles). Such profiles are most distinctly observed in the W-7AS [12]. Figure 10 shows that, in the case of a resonance in the center of the column and at a power of 90 kW, the ordinary peaked density and temperature profiles are observed.At a power of 200 kW, the flattening of the temperature profile is seen and density profile becomes hollow. At the power of 400 kW the hollow in the density profile reaches 30%. The shift of the resonance region for 6 cm from the center (Z=13 cm) leads to the hollow temperature profile.

In the recent L-2 experiments [13], it has been reached the highest density of the deposited power - 40 W/cm^3 or about 10 eV per electron during the time between pair collisions (in the W-7AS the power deposition density was 8-16 W/cm^3). It is established that the density distribution changed with time and

[1] the data were presented by I.S.Sbitnikova and K.S.Dyabilin

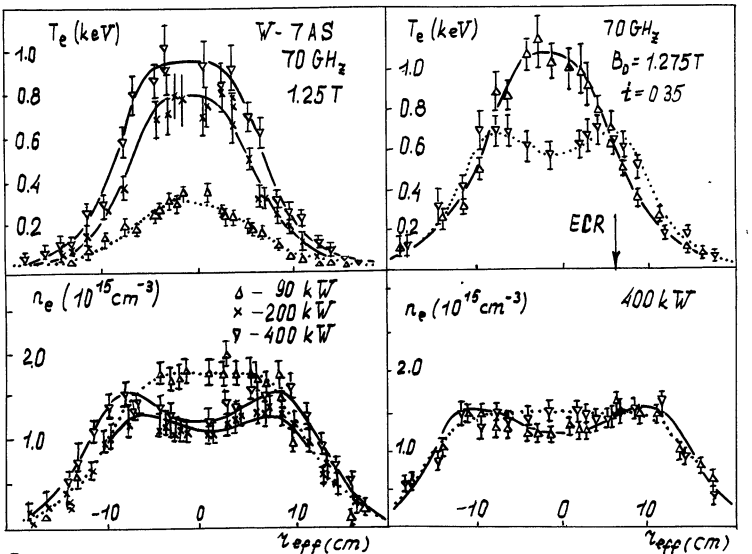

Fig. 10

the temperature distribution changed with the increase in the radiation power and plasma density. First of the attention is drawn to the density profile flattening with time, the more strong, the higher is the radiation power and the lower is the plasma density (Fig.11). The electron temperature was determined from the soft X-ray radiation measured along four chords (Fig.12).

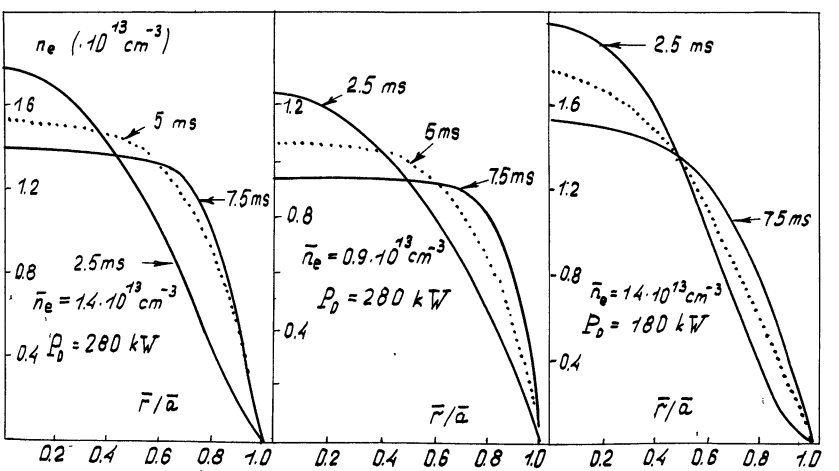

Fig. 11 Time evolution of the density profile in the L-2

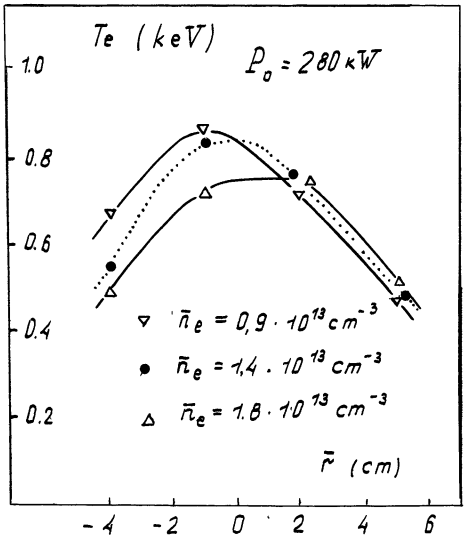

Fig. 12

It is well seen that the distribution broadens with the density increase and that it is displaced out of the center of the chamber.

The latter effect may be explained by the displacement of the magnetic surfaces disturbed by the plasma pressure. Really by the end of heating $\beta(0)=8\pi*n_e(0)*Te(0)/Bo^2=5*10^{-3}$, that corresponds to the outward shift of the magnetic axis for 2.5 cm. Since the resonance region in this case is not displaced, the power deposition changes from the peaked in the center of the magnetic surfaces to the ring-like. The formation of hollow profiles has been recently explained qualitatively by L.M. Kovrizhnykh [14] on the basis of neoclassical transport theory. Such a peculiar plasma density and temperature distribution is a typical plasma phenomenon caused by the processes of thermal diffusion, particle diffusion and the diffusion in the electric field, so that the total flux is always directed out of the center whereas separate components of the flux in the central regions of the column may be oppositely directed. Unfortunately, it remains still unclear what are the consequences of the formation of such peculiar profiles for the energy confinement time.

4. The problem of the ECH effect on the processes of thermal conductivity and diffusion is likely to be the least investigated for the present. The draw conclusion that transport processes

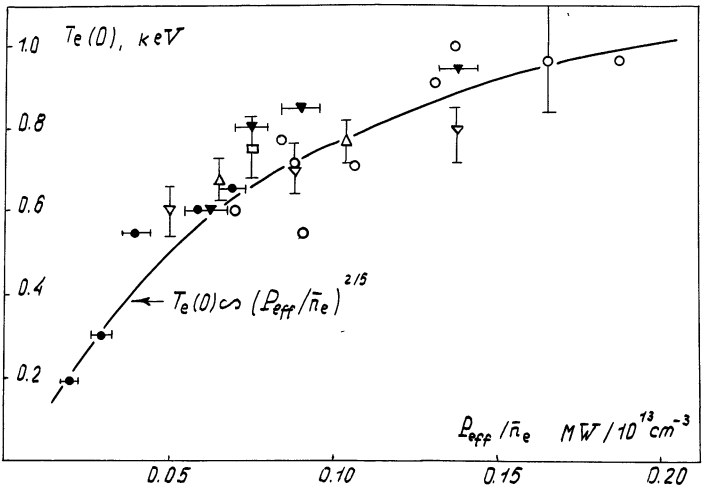

Fig.13 H-E (0), W 7A $\bar{n}_e = 1.1 \cdot 10^{13}\,cm^{-3}$ (●), $\bar{n}_e = 2.4\text{-}2.8 \cdot 10^{13}\,cm^{-3}$ (▼)
L-2 $\bar{n}_e = 0.9 \cdot 10^{13}\,cm^{-3}$ (▽), $1.35 \cdot 10^{13}\,cm^{-3}$ (△), $1.8 \cdot 10^{13}\,cm^{-3}$ (□)

agree with the neoclassical model [4,6,13,15]. However, it was necessary to incorporate the anomalous losses at the periphery of the plasma column which in the case of W-7A, include up to 1/3 of the plasma radius. The calculations of the energy content and central temperature dependencies on the absorbed power, made for the L-2 [15], agree satisfactorily with the measurement results if only we accept the power absorbed by the plasma to be the power measured from the derivative of the diamagnetic signal, that is not to incorporate the fast losses. However, if we study the dependence on the incident power, it turns out that the growth of the central temperature is abruptly slowed down with the power increase (Fig. 13). When the average plasma density is constant, the increase in the energy content is also slow. At the same time, it the power increases with the plasma density, the energy content follow the density increase, the central plasma temperature being almost constant (Fig. 14). Such a slowing-down in the temperature growth indicates the existence of some process which slow down the energy storage by the electrons. The energy losses via trapped particles could be such a process. However, according to the calculations for maxwellian plasma these losses should play their role at higher powers corresponding to higher temperatures. Hence, again the question arises concerning the additional source of the losses, whose power increases with the

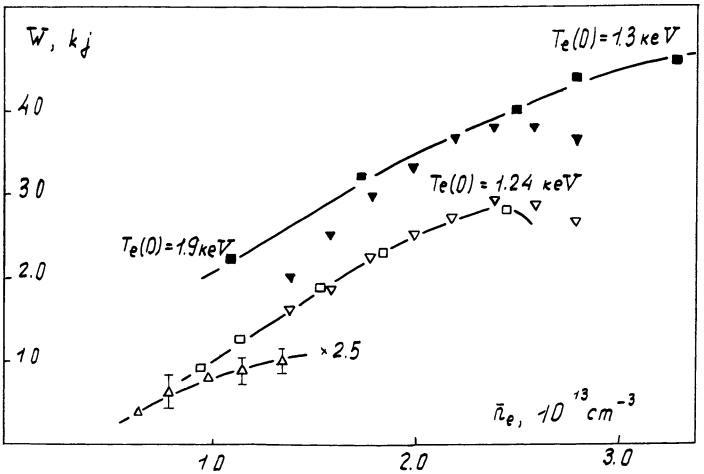

Fig 14. W 7AS $B_0 = 2.5$ T, $P_0 = 400$ kW (■), 200 kW (□)
$B_0 = 1.25$ T, $P_0 = 400$ kW (▼), 200 kW (▽)
L-2 $B_0 = 1.34$ T $P_0 = 280$ kW (△)

heating power, decreases with the increase in the plasma density, and is close in the order of magnitude to the neoclassical losses. However, all the calculations do not take account of the change in the density and temperature distributions, and also the shape of the magnetic surfaces (for example, their shift) caused by the proper plasma pressure. Meanwhile the theory predicts the increase in the trapped-particle losses and the increase in the MHD safety factor at the displacement of the center of the magnetic surfaces out of the axis (I.S.Danilkin draw our attention to this fact). In this connection, it is of interest to compare the heating of the plasma without and with a current when the magnetic axis is displaced outwards. If in the L-2 during the heating at the fundamental harmonic the different in temperatures at the center of the column reaches 200-300 eV ($\Delta Te/Te=0.2-0.3$), while during the heating at the second harmonic there is not practically and difference (no change in the density distribution is observed in this case). Since in the first case the plasma pressure in a current-free regime is insufficient to displace the column and in the second case it is almost the same in both regimes then it is likely that the shift of the magnetic surfaces affects the transport. In this connection, an convincing data was obtained in the Heliotron-E experiments [16], where the shift of the magnetic surfaces was reached due to the auxiliary transverse

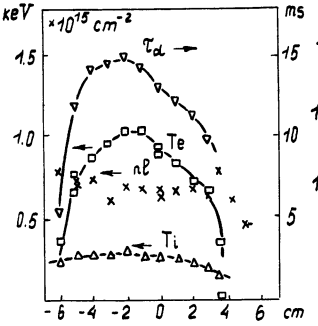

Fig.15 Magnetic axis shift

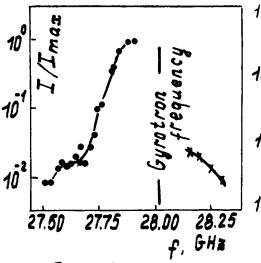

Fig 16

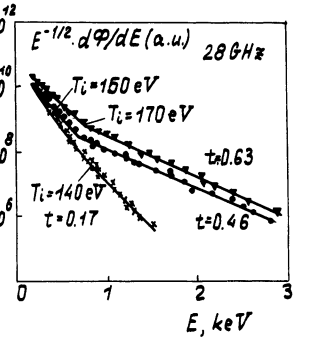

field (Fig.15). The presented curves show that the inward shift of the column leads to a noticeable increase in the confinement time and temperature in the center of the column. The similar results were obtained with the CHS [17].

Hence, in quite a number of cases there is a qualitative agreement with neoclassucal calculations. However the question concerning fast losses and their nature remains still open.

5.The most curious was always the problem of the effect of the heating on the growth of turbulent oscillations and their effect on thermal conductivity. In the first L-2 experiments on plasma heating by an extraordinary mode at the fundamental harmonic it was already established the onset of decay process, formation of fast electrons and ions [18]. In the case of heating by an ordinary wave, the similar results were obtained at the initial stage of plasma production and heating. Then, 2 or 3 msec after the beginning of the discharge, i.e. at Te(0)>400eV, the intensity of decay spectra fell in an order of magnitude [7,19]. Also the fast particles were not practically observed at this moment. Somewhat different results were obtained in the W-7A during plasma heating by an ordinary wave [5]. The power unabsorbed during the first pass (about 30%) was converted into an extraordinary wave by a convertor (twister) and then again was focused into the plasma.No any noticeable increase in the plasma energy was observed, but decay spectra and tails of fast ions were registerated (see Fig.16). In the experiments at the second harmonic no decay processes were yet found. Hence, it has not been established up to now a noticeable effect of a high-frequency turbulence on heating and confinement.

A fairly extensive data on a low frequency turbulence during electron cyclotron heating was obtained in the L-2 by microwave

scattering technique [20]. A scattered waves (wavelength 2.5 mm) was observed from the column region with r/a=0.63, for three scattering angles: 15°,30°,45°. In plasmas with and without current, a wide spectrum of turbulent oscillations was observed in the range of 10-100 kHz. The study of the dependencies allows us to attributed them either to the collisionless drift mode or to the mode excited by the trapped particles.

The results of ECH measurements for the fundamental and second harmonics slightly differ from each other, apparently due to difference in densities of power deposition by an order of magnitude. As for the measurements at the fundamental harmonic, an attention is drawn to the correlation between the values of density fluctuations and central temperature (Fig.17). Higher level of density fluctuations corresponds to the lower temperatures at the center of the plasma. It is remarkable that such a dependence takes place at a practically constant heating power. This allows us to think that the noise level and peripheral turbulent transport are, to a certain extent associated with the density and temperature distribution at the periphery of the column which are determined by the flux of neutral particles from the chamber walls. It is of interest to note, that the data for the plasma with a current also correspond to the mentioned dependence (Fig.17). Meanwhile, as it is clear

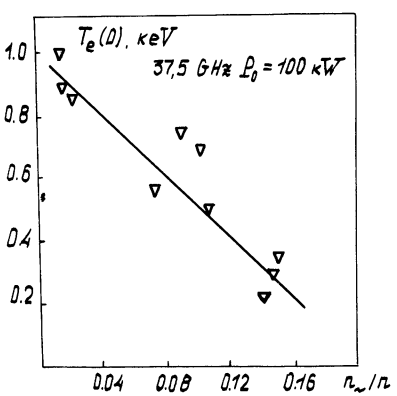

Fig.17

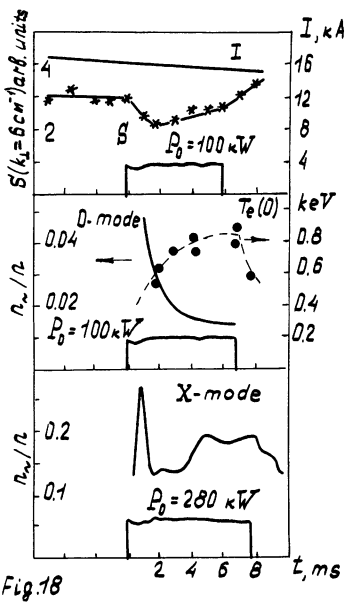

Fig.18

from the Fig.18, when a microwave pulse is switched on, the noise level in a plasma with a current falls, and the central plasma temperature increases by 20 -30% (from 300-400 eV up to 600-650 eV). At the same time the loop voltage is such that the radiation power is enough only to compensate the decrease in the ohmic losses, that is the total heating power remains the same.

The time evolution of the noise level also correlates with the mentioned dependence (Fig.18): the central temperature increases with the fall in the noise level, while the absorption coefficient determined from diamagnetic measurements, remains constant. In the heating at the second harmonic the increase in the radiation power leads to the increase in fluctuations (Fig.19), the central temperature varies,however, only slightly during the power change from 150 to 270 kW, since density fluctuations become 3 times larger.

Despite of the discrepancies in temperature dependencies on the drift noise level in the case of heating at the fundamental and at the second harmonics, a general dependence of the value n_e*Te(0)/P_{abs}., proportional to the energy confinement, on the value of fluctuations (Fig.20). Here the power absorbed in the ECR region is taken as the absorbed power P_{abs}. It is evidently seen that the energy confinement time tends to decrease with the increase in the amplitude of density fluctuations. In this connection, the calculations were made to estimate the value of the turbulent flux of particles and heat in the quasilinear approximation for collisionless drift-waves, using experimentally

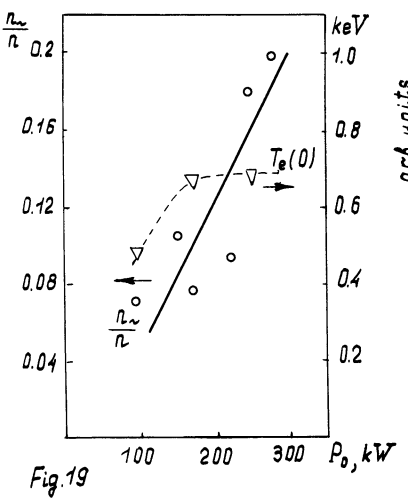

Fig.19

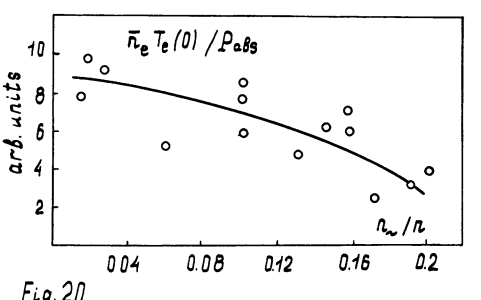

Fig.20

measured plasma parameters and density fluctuations. It turns out that the turbulent coefficient of thermal conductivity is of order 10^3-10^4 $cm^2/sec.$, that is comparable with the neoclassical conductivity coefficient and close the result of measurements. Hence, a conclusion may be, apparently, drawn that heat flux due to the drift turbulence play an essential role in the plasma energy balance.

Some data, however, indicate that the relationship between fluctuations and plasma heating and confinement is more complex, than it follows from simple estimations. Really, if we take the heating power obtained from diamagnetic measurements as the absorbed power for the parameter $n_e*Te(0)/P_{abs.}$, then the mentioned parameter becomes constant over the entire range of the oscillation-amplitude. The independence of the confinement time, determined by such a procedure, on oscillations permits to draw a conclusion about the connection of density fluctuations with the fast losses, which, as we have seen, grow with power, the same as the amplitude of fluctuations. An attention is also drawn to the correlation between the time evolution of the amplitude of fluctuations (Fig.18) and fast losses (Fig.6). Three millisecond after the beginning of the discharge we see the minimum amplitude of oscillations, which corresponds to the minimum value of fast losses. Then the noise level grows and also the fast losses grow. Note that at the same time the plasma density profiles flatten. The correlation between these three measurements is striking.

6.Hence the stellarator studies made during peculiarities of ECR in toroidal confinement systems of this type.

It is established that the diamagnetic measurements give lower values of the absorption coefficient than those predicted by theory which does not incorporate quasi-linear effects, despite the agreement between the calculations and microwave measurements of the wave damping. These discrepancies amount to (1.5-2) times, the deposited power density rise being higher than (1-3) KeV/msec per electron. At the same time, fast energy losses from the plasma column were observed, for which the confinement time is (1.5-2) orders less than for the main plasma energy.

The theoretically predicted localization of the power deposition region during ECH was qualitatively proved. It is established that at high densities of energy deposition the density and temperature profiles are deformed and hollow profiles appear that is qualitatively explained by the theory.

It was observed that the temperature rise at the center of the plasma is limited while radiation power grows. At the same time no limitation in the energy (content) rise with heating power was found, if the increase in plasma density is provided.

A qualitative agreement is established between plasma parameters and results of calculation in terms of neoclassical theory of transport processes. At the same time, a correlation is observed between plasma parameters and the turbulent drift noise level. The value of turbulent heat flux is shown to be comparable in the order of magnitude with the neoclassical flux. A correlation is also observed between the noise level and fast energy loses.

In conclusion I would like to thank my colleagues from the L-2 team who presented me the results of their studies and a number of new papers. Without their skilled discussions of the stellarator problems this review would hardly appear.

References

1.D.K.Akulina,S.E.Grebenshchikov,Yu.I.Nechaev,I.S.Sbitnikova, I.S.Shpigel.Sov.J. ZhETF,v.56,3,1969,pp.721-729.

2.K.M.Likin,B.D.Ochirov,N.N.Skvortsova.15th Eur.conf.on contr. fusion and pl.heating.Dubrovnik,May 16-20, 1988. V.12B, P.II, pp.451-454

K.M.Likin,B.D.Ochirov.17th EPS conf.on contr.fusion and pl. heating. Amsterdam.25-29 June,1990.,v.14B,P.II,pp.467-468.

3.I.S.Danilkin.7th Inter.workshop on stellarators.Oak Ridge, Tennessee.April 10-14,1989.

4.K.S.Dyabilin,L.M.Kovrizhnykh.Sov.J. Fizika plazmy.1987,v.13,6, pp.515-527.

5.V.Erkmann,G.Janzen,W.Kasparek et.al.Fusion Technology. March 1985.,v.7,pp.275-282.

6.V.Erkmann and W-VIIA Team,ECRH Group. Plasma Phys.and Contr. Fusion.1986,v.28,9A,pp.1277-1290.

7.E.D.Andryukhina,D.K.Akulina,G.M.Batanov et.al.15th Eur.conf. on contr.fusion and pl.heating.May 16-20,1988,v.12B,P.II, pp.447 - 450.

8.K.M.Likin,G.M.Batanov,L.M.Kolik et.al.17th EPS conf.on contr. fusion and pl.heating.Amsterdam,25-29 June,1990,v.14B,P.II, pp.469-470.

9.E.D.Andryukhina,K.S.Dyabilin,O.I.Fedyanin.17th EPS conf.on contr. fusion and pl.heating.Amsterdam,25-29 June,1990,v.14B, P.II, pp.463-466.
10.D.K.Akulina,A.N.Nakladov,O.I.Fedyanin,V.I.Chepizhko.16th Eur.conf.on contr.fusion and pl.phys.Venice,March 13-17,1989, v.13B,P.II.
11.D.K.Akulina,E.D.Andryukhina,G.M.Batanov et.al.Proc. of 12th conf. on pl.phys. and contr. nuclear fus.research.Nice, 12-19 October,1988,v.2,pp.359-368.
12.H.Renner,W-7AS Team,NBI Group,ICF Group,ECRH Group. Max Plank Institut fur Plasmaphysik. Euratom Association. D-8046. Garching,FRG.
13.D.K.Akulina,E.D.Andrukhina,G.M.Batanov et.al.13th Int. conf. on plasma phys. and contr.fusion.Vashington,1-6 October,1990.
S.E.Grebenshchikov.Proceeding of IOFAN (in Russian).V.31,1990, Moskva,Nauka.
14.L.M.Kovrizhnykh.Comments on pl.phys. and contr.fusion.V.13, 1990,6,p.267.13th Int.conf.on pl.phys. and contr.fusion. Vashington. 1-6 October,1990. IAEA-DIII-2.
15.E.D.Andryukhina,K.S.Dyabilin,O.I.Fedyanin.15th Eur.conf. on contr.fusion and pl.heating.Dubrovnik,May 16-20,1988.V.12B, P.II, pp.459-462.
16.O.Motojema,T.Mutoh,M.Sato et.al.12th Int.conf.on pl.phys. and contr.fus.research.Nice,France,12-19 October,1988.V.1, pp.551-561.
17.S.Okamora,M.Fuzewara,M.Hosokawa et.al. 16th Eur.conf.on contr.fusion and pl.physics.Venice,March 13-17,1989.V.13B,P.II, pp.571-574.
18.G.M.Batanov,L.V.Kolik,A.V.Sapozhnikov et.al.Sov.J. Fizika plazmy.V.12,9,1986,pp.1027-1032.
19.G.M.Batanov,L.V.Kolik,K.M.Likin et.al.Sov.J. Fizika plazmy. V.15,2,1989,pp.151-154.
20.G.M.Batanov,L.V.Kolik,A.V.Sapozhnikov,K.A.Sarksyan,M.G.Shats. Sov.J. Fizika plazmy.V.15,5,1989,pp.527-533.
Proceeding of IOFAN (in Russian).V.31,1990.Moskva,Nauka.
21.V.Erckmann,U.Gasparino,H.Maaβberg et.al. 13th Int.conf.on pl. physics and contr.nucl.fus.research.October1-6,1990. Washington. IAEA-CN-53/C-3-1.

COMPARISON BETWEEN THE ELECTRON CYCLOTRON CURRENT DRIVE EXPERIMENTS ON DIII–D AND PREDICTIONS FOR T–10*

John Lohr, R.A. James,† G. Giruzzi,‡ Y. Gorelov,¶ J. DeHaas,§
R.W. Harvey, T.C. Luce, Kyoko Matsuda, C.P. Moeller, C.C. Petty, and R. Prater
General Atomics, P.O. Box 85608, San Diego, California 92186-9784, USA

ABSTRACT

Electron cyclotron current drive has been demonstrated on the DIII–D tokamak in an experiment in which ~1 MW of microwave power generated ~50 kA of non-inductive current. The rf-generated portion was about 15% of the total current. On the T-10 tokamak, more than 3 MW of microwave power will be available for current generation, providing the possibility that all the plasma current could be maintained by this method.

Fokker-Planck calculations using the code CQL3D and ray tracing calculations using TORAY have been performed to model both experiments. For DIII–D the agreement between the calculations and measurements is good, producing confidence in the validity of the computational models. The same calculations using the T-10 geometry predict that for $n_e(0) \sim 1.8 \times 10^{13}$ cm^{-3}, and $T_e(0) \sim 7$ keV, 1.2 MW, that is, the power available from only three gyrotrons, could generate as much as 150 kA of non-inductive current. Parameter space scans in which temperature, density and resonance location were varied have been performed to indicate the current drive expected under different experimental conditions.

The residual dc electric field was considered in the DIII–D analysis because of its nonlinear effect on the electron distribution, which complicates the interpretation of the results.

---

*Work supported by the U.S. Department of Energy under Contract Nos. DE-AC03-89ER51114 and W-7405-ENG-48.

†Lawrence Livermore National Laboratory.
‡Association Euratom-CEA, Tore Supra Cadarache, France.
¶Kurchatov Institute for Atomic Energy, Moscow.
§Joint European Torus.

A 110 GHz ECH system is being installed on DIII–D. Initial operations, planned for late 1991, will use four gyrotrons with 500 kW each and 10 second output pulses. Injection will be from the low field side from launchers which can be steered to heat at the desired location. These launchers, two of which are presently installed, are set at 20 degrees to the radial and rf current drive studies are planned for the initial operation.

I. INTRODUCTION

Within the past few years encouraging progress has been made in tokamak fusion research which has indicated that the path to a successful demonstration experiment, though rocky perhaps, is at least clear of major obstacles. This optimistic forecast has heightened interest in experiments relevant to a tokamak fusion reactor operating continuously, such as non-inductive current generation.

One candidate for non-inductive current drive is the asymmetric interaction in velocity space between the plasma electrons and injected electromagnetic waves at the electron cyclotron resonance frequencies. First demonstrated on the CLEO tokamak [1], EC current drive is the subject of ambitious programs on both the DIII–D and T–10 devices.

Although the theory of electron cyclotron damping is well understood, details of the experiments, such as localized pumpout of portions of the velocity distribution, interaction with relativistically downshifted resonances, refraction and so on leave considerable room for creative prognostication and interpretation of the results. In this paper we discuss the application of two fundamental analysis tools, Fokker-Planck calculations and ray tracing, to the experiments on these two tokamaks both to understand previous experiments and thereby benchmark the analysis and to predict the results of work planned for the near future.

II. THE ELECTRON CYCLOTRON CURRENT DRIVE INSTALLATIONS

A. DIII–D

The DIII–D ECH installation consists of ten gyrotrons each of which generates approximately 200 kW at 60 GHz in pulses 0.5 sec in duration. The transmission lines propagate the TE_{01} mode with approximately 85% efficiency. The waves were launched in the X–mode fundamental from the high field side of the tokamak at an angle of 17 degrees to the radial. The technical details of the installation have been described previously [2].

B. T–10

On T–10, 11 gyrotrons, each producing up to 400 kW in pulses up to one second long will be available. Nine of the tubes operate at 81 GHz and inject with a tangential component so that the microwaves cross the magnetic axis at an angle of 30 degrees to the radial. Two tubes are at 75 GHz with radial injection for heating only. A schematic of the installation and representative TORAY output indicating the model geometry for the midplane launcher is shown in Fig. 1. The power is launched in the O–mode at the fundamental from four toroidal locations, each of which has a slightly different geometry. For simplicity, these modelling calculations all use the "sector B" arrangement, which has three beamlines at 81 GHz, one of which is at the midplane with two others arranged symmetrically above and below it. The three lines are aimed so that the launched waves intersect at the geometric center of the tokamak.

III. THE ANALYSIS CODES

A. Ray Tracing

The General Atomics version of the code TORAY [3] was used for all the ray tracing studies reported here. The dispersion relation is calculated for the superposition of a relativistic Maxwellian distribution function and a superthermal tail characterized by forward, backward, and perpendicular temperatures

$$f = \underbrace{n_e(1-\alpha)\, f_0(T_e)}_{\text{Maxwellian}} + \underbrace{\alpha\, n_e\, f_1(T_{\parallel f}, T_{\parallel b}, T_\perp)}_{\text{tail}} \quad . \tag{1}$$

All quantities are functions of ρ, the normalized flux coordinate. Damping of an electromagnetic wave is calculated from the dispersion relation and the driven current is estimated from Cohen's theory [4].

TORAY is interfaced to General Atomics' transport code ONETWO [5] so that kinetic and Z_{eff} profiles can be input directly to a self-consistent calculation of the loop voltage.

For the T–10 calculations, a half power half width of 3 degrees was used and 18 rays were followed for each launcher from a point at the approximate location of the ceramic vacuum window. The plane mirror was not included in the model. The DIII–D calculations used 30 rays and a half power half width of about 7 degrees.

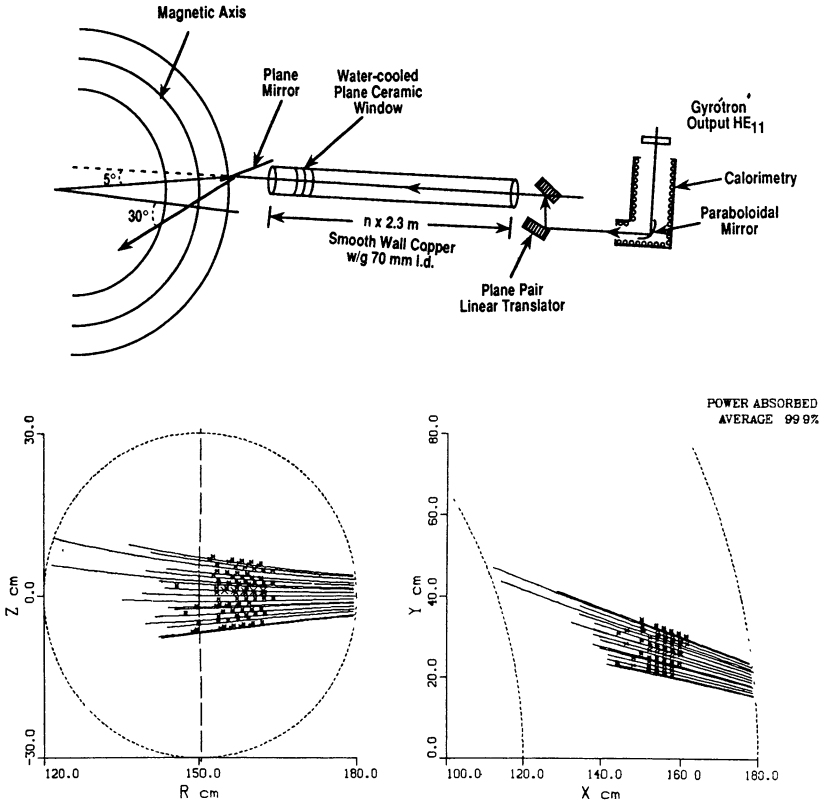

Fig. 1. Schematic representation of the waveguide installation on T–10. Also shown is a typical TORAY plot of the launch geometry and power deposition for the ECH resonance at the geometric center of the machine. For clarity, only the midplane bundle is shown. Parameters were $T_e(0) = 5$ keV, $n_e(0) = 3 \times 10^{13}$ cm^{-3}, $B_T(0) = 2.89$ T.

B. Fokker Planck

The Fokker-Planck calculations were done either with the code CQL3D [6], which calculates the two-dimensional bounce-averaged relativistic electron velocity distribution function at each point in a radial array or with the code of Giruzzi [7]. The ECH energy deposition model in CQL3D includes quasi-linear damping along a single ray but models the spread of the beam by a spectrum in $k_\parallel$. This model is sharper in k-space than the actual experiment.

The code solves

$$\frac{\partial f_0}{\partial t}\,(\bar{v}_{\parallel 0}, v_{\perp 0}, r, t) = C(f_0) + Q(f_0) \quad ,$$

at each radial location and the rf energy transport equation

$$\cdot\, \nabla \cdot (v_g\, \epsilon) = -P_{\rm ABS}(r, \theta_{\rm pol}) = -\int d\bar{v}\; 2mv^2 Q(f) \quad ,$$

where C and Q are the collisional and quasi-linear operators respectively, f_0 is the midplane electron distribution function, ϵ is the rf energy density and v_g is the group velocity.

IV. RESULTS

The two codes described above have been used to model the electron cyclotron current drive experiments on DIII–D and T–10. For DIII–D, calculations for high field launch X–mode fundamental current drive are compared with the experimental data. Predictions for low field X–mode second harmonic and low field O–mode fundamental current drive on DIII–D have also been made. For T–10, the expected fundamental low field O–mode current drive was calculated. Variation of the parameters indicates the sensitivity to launch angle, resonance location, density and temperature.

A. DIII–D High Field X–Mode Fundamental Current Drive

TORAY, CQL3D, and Giruzzi's Fokker-Planck code have been applied to the analysis of the electron cyclotron current drive experiment on DIII–D. Using 30 rays to represent the Gaussian beam, TORAY predicted current drive efficiencies of 0.04 $\rightarrow$ 0.12 amperes/watt. The TORAY predictions assuming zero residual dc electric field in the plasma (i.e., full current drive) are plotted in Fig. 2 for a representative equilibrium and different scaled temperatures and densities. For these discharges the inductive electric field was not decreased to zero during the rf pulse and this complicates the analysis.

Electrons heated or accelerated by the rf move into the tail of the distribution function where they are less collisional. If subjected to an accelerating dc electric field, they then move to still higher energies under the influence of the field. This apparently rf-induced current is not strictly speaking "rf-driven" because should the inductive electric field decrease to zero this portion of the driven current, for fields well below the critical runaway field, also disappears.

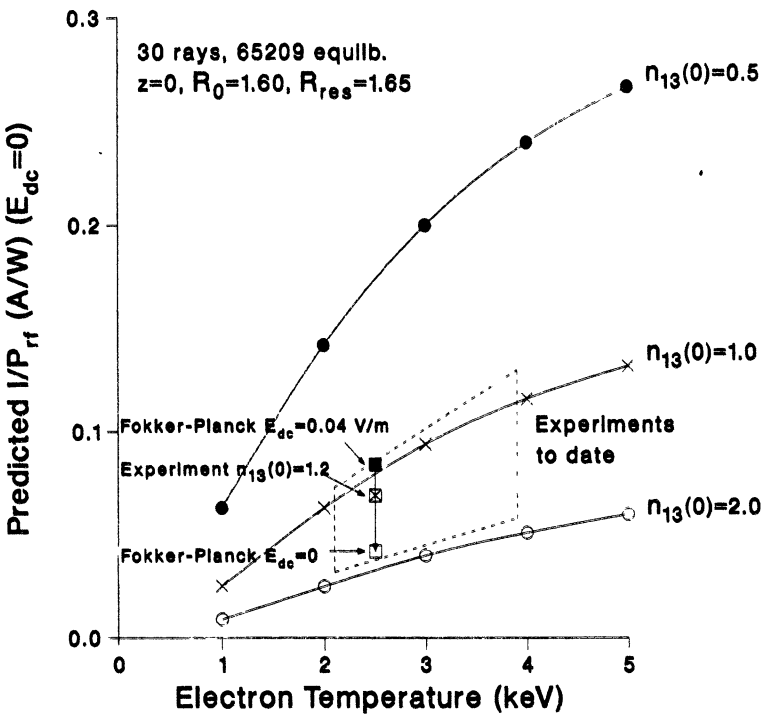

Fig. 2. TORAY calculations of rf current drive for the DIII-D high field launch X-mode fundamental experiment. The predicted 50 kA non-inductive current is in reasonable agreement with the measurements.

An estimate of the importance of this "inductively driven, rf augmented" current is indicated by three points in Fig. 2. The upper point is the current predicted by Fokker Planck calculation assuming $E_{dc} = 0.04$ V/m, the experimentally measured value. The middle point is the total current inferred from the measured kinetic profiles and the measured Z_{eff} profile assuming neoclassical resistivity. Finally, the lowest point is a Fokker-Planck calculation in which the residual dc electric field was arbitrarily set to zero. This lowest point should be compared with the field-free TORAY calculations. The analyses span a factor of two in inferred current drive efficiency. Although the agreement between the Fokker Planck for $E_{dc} = 0$ and TORAY for the experimentally measured $n_{13}(0) = 1.2$ and $T_e(0) = 2.5$ keV is not extremely good, the experimental and calculational uncertainties are fairly large and could be accounted for by uncertainties in the kinetic profiles, for example. The ECE spectrum calculated by

the Fokker-Planck code is in good agreement with the experimental measurements. Figure 3 summarizes the TORAY output, showing ray tracing, power deposition, and the ECE data from CQL3D.

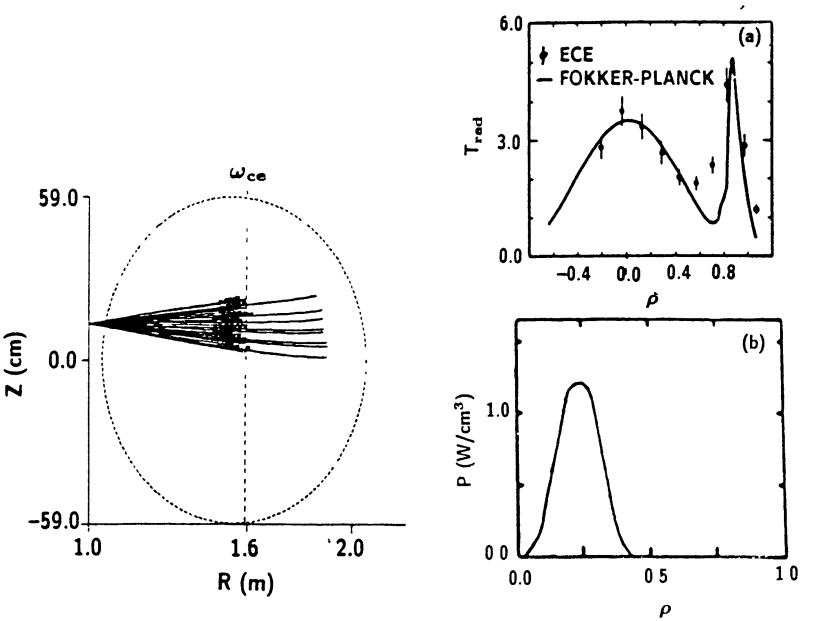

Fig. 3. TORAY output and the ECE spectrum calculated by CQL3D for the DIII–D experiment. The resonance was at the magnetic axis and $\bar{n}_e \sim 1.2 \times 10^{13}$ cm^{-3}.

The non-linear interaction between electrons accelerated into the superthermal tail and the residual field was considered by Giruzzi, who found in an independent Fokker-Planck calculation that such a residual dc electric field could increase the current which appeared to be rf-driven by as much as a factor of two. These results are summarized in Fig. 4. Here the ratio of the current observed with no dc electric field to that with electric field is plotted as a function of the electric field normalized to the critical (Dreicer) field. Considering the T_e dependence of the critical field, both 2 and 4 keV temperatures give the same enhancement. The additional current can be equal to the rf-driven current, and when the DIII–D measurement is

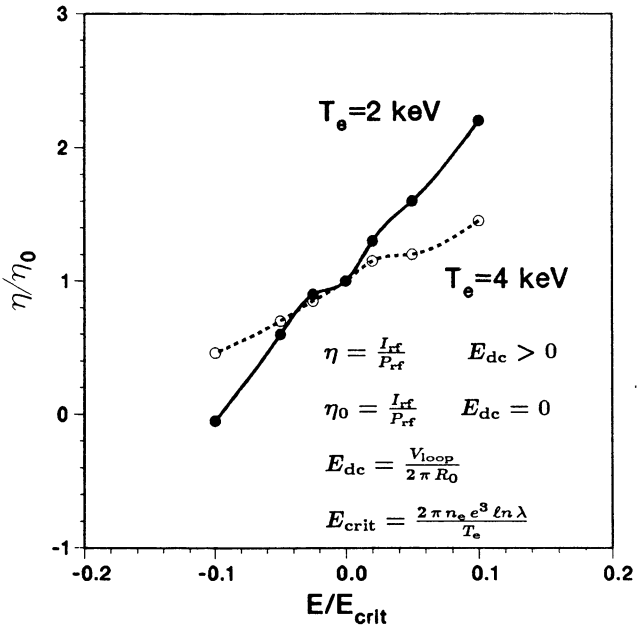

Fig. 4. The effect of a residual dc electric field is shown by the enhanced current in the co-direction as a function of the electric field normalized to the critical (Dreicer) field for electron runaway. The factor of two enhancement at fields present in the experiment is consistent with the loop voltage measurement for co versus counter rf current generation and with the correction required to obtain agreement between the measurement and field-free TORAY.

corrected for this phenomenon, the rf-driven current at $E_{dc} = 0$ is recovered for comparison with TORAY.

To address this issue experimentally, the direction of the inductive current, and therefore the dc electric field, was reversed and the current drive experiment was repeated with the rf-driven current opposing the inductive current. In this case the measured loop voltage was greater than that calculated from the profiles, indicating an rf-driven component opposing the inductive current. Approximately a factor of two difference between the co- and counter-rf current cases was found, suggesting that this analysis is qualitatively correct. TORAY calculations agree with the corrected experimental data.

B. T–10 Low Field O–Mode Current Drive

The relatively good agreement between theory and experiment in the DIII–D case suggests that the T–10 experiment can be described reasonably well by TORAY and CQL3D. A series of calculations was performed with TORAY in which the density, temperature, and resonance radius were varied for the T–10 geometry as described above. The results are shown in Fig. 5.

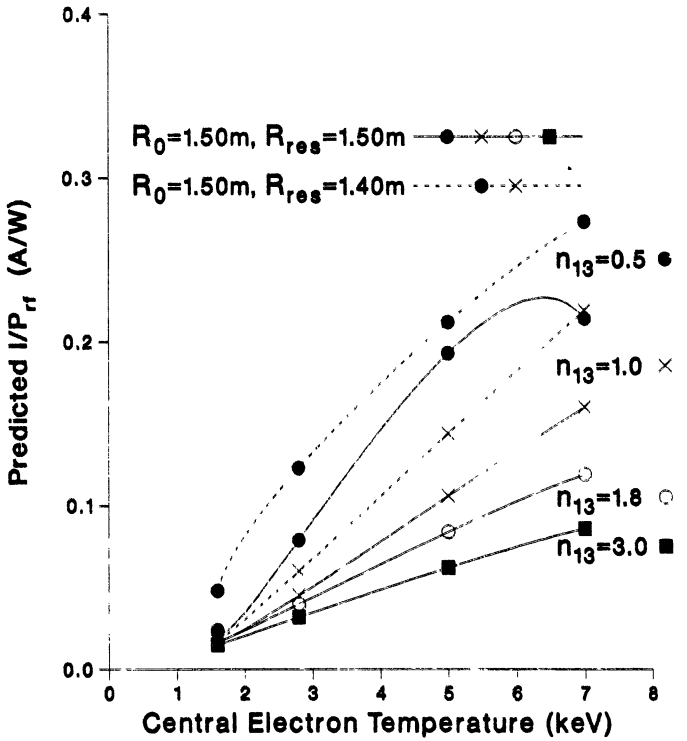

Fig. 5. TORAY calculations of the current drive expected for T–10 from the "Sector B" geometry shown in Fig. 1. Highest current drive requires low density, high temperature and a resonance at $R \sim 140$ cm. From these calculations, T–10 could achieve rf driven currents greater than 400 kA.

Calculations were performed for four values of central electron temperature and four values of central density. The *ad hoc* profiles were approximately

$$T_e(r) = T_e(0)(1 - r^2/a^2)^{1.5} \quad ,$$

and

$$n_e(r) = n_e(0)(1 - r^2/a^2)^{0.5} \quad .$$

For most of the calculations the ECH resonance was placed at the geometric center of the machine, but for central densities of $1.0 \times 10^{13}/\text{cm}^3$ and $0.5 \times 10^{13}/\text{cm}^3$ the resonance was also located at $r = -10$ cm.

In general, current drive efficiency increases approximately linearly with electron temperature and decreases linearly with density. There is a very large increase in current drive efficiency when the density is reduced below $1 \times 10^{13}/\text{cm}^3$.

For achievable values of T_e and n_e on T–10, efficiencies as high as $0.10 \rightarrow 0.20$ A/W should be realized. This is approximately three times the efficiency measured in the DIII–D experiment owing primarily to better localization of the absorption at the hottest region of the discharge with low field launch. Because of the relativistic mass shift of the superthermal population the resonance should be located inside the magnetic axis so that resonant damping will actually occur near the center of the discharge where T_e is highest. This also reduces trapped particle effects. At a central density of $1 \times 10^{13}/\text{cm}^3$ the efficiency is approximately 40% greater with the resonance at $r = -10$ cm compared with the resonance at $r = 0$.

The Fokker-Planck code CQL3D was exercised for a hypothetical DIII–D experiment employing low field launch of the O–mode and the current drive efficiency as a function of launch angle was calculated. Although done for DIII–D, the calculation is for circular cross section and is generally applicable to T–10. The results, plotted in Fig. 6 along with TORAY calculations for the same cases show a broad maximum in efficiency for launch angles between 15 degrees and 25 degrees from perpendicular.

The Fokker-Planck calculations agree fairly well with the ray tracing at low power, however exhibit up to a factor of two enhancement in efficiency over the TORAY estimate at higher power. This enhancement over the linear regime efficiency is due to a quasi-linear increase

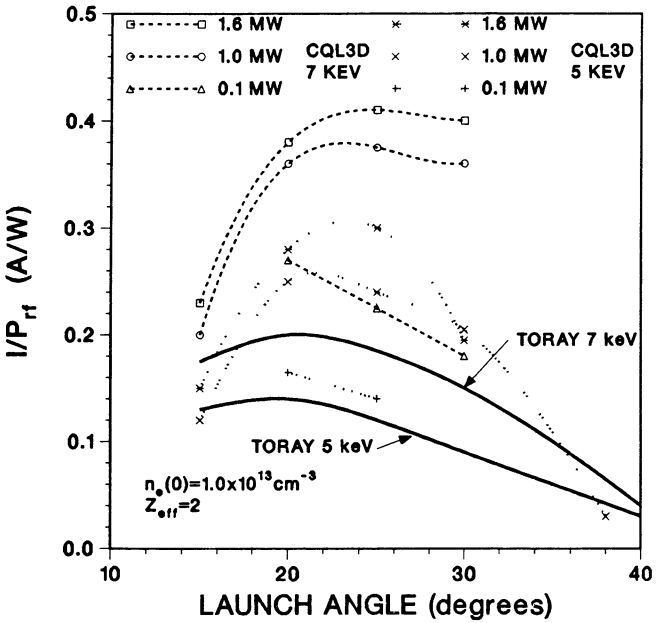

Fig. 6. Fokker-Planck and TORAY calculations for 60 GHz low field launch O–mode fundamental heating on DIII–D showing a substantial enhancement in current drive at high power. These results are relevant for the T–10 experiment as well.

in the tail electron population and to a decrease in the trapping of heated electrons owing to relativistic effects. Neither of these phenomena is modeled by TORAY. The result is encouraging for the T–10 experiment because of the very large rf powers, possibly greater than 3 MW, which could be available.

The distribution function of Eq. (1) was used in TORAY to model the effect of a superthermal tail on the spatial distribution of both the absorption and driven current. The results are plotted in Fig. 7 for the parameters listed in Table I.

It is seen that the superthermal tail leads to a substantial increase in the current drive efficiency over that for the Maxwellian. The calculations also illustrate the excellent localization of the driven current, which may mean that current generation, for example, in the vicinity of the $q = 2$ surface could be employed to stabilize tearing modes and prevent disruptions.

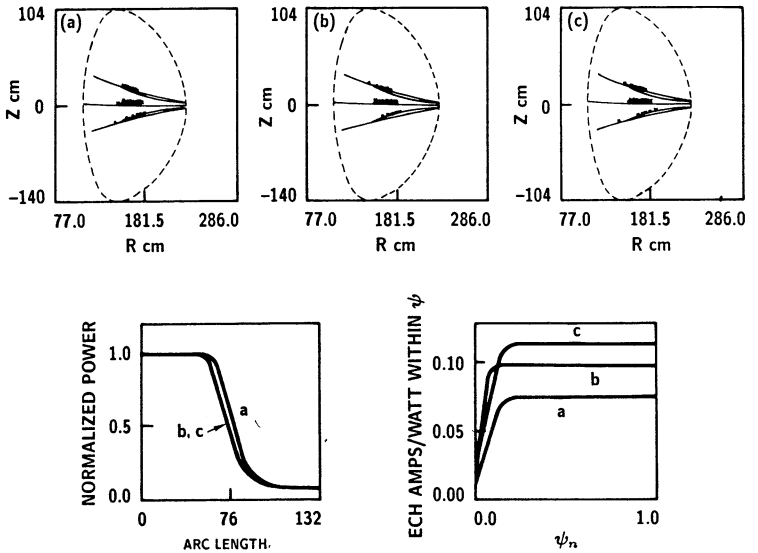

Fig. 7. With the addition of a suprathermal tail, TORAY predicts a substantial increase in current drive efficiency compared with a Maxwellian.

TABLE I

Curves	Tail Density (%)	$T_e(0)$ (keV)	$T_{\parallel f}$ (keV)	$T_{\parallel b}$ (keV)	$T_\perp$ (keV)	ρ
a	0	5	–	–	–	
b	5	5	15	7	10	0
	5		5	3	5	1
c	5	5	20	10	13	0
	5		7	5	6	1

Additional work must be done to examine the deleterious effects of trapping and possibly unstable $j(r)$ profiles.

V. FUTURE PLANS FOR DIII–D

On the DIII–D tokamak, installation of a low field spatially scannable launcher system for 110 GHz has begun. The present plan calls for operation of a four 500 kW gyrotrons capable of 10 second pulses in late 1991 in addition to the existing 2 MW, 60 GHz system. The

waveguide transmission line will propagate the HE_{11} mode and be evacuated, thus eliminating the machine vacuum window. The transmission system [8] is shown schematically in Fig. 8, and a photograph of the first steerable launcher assembly currently installed on DIII–D is shown in Fig. 9. The launched waves will be X–mode at 20 degrees to the radial.

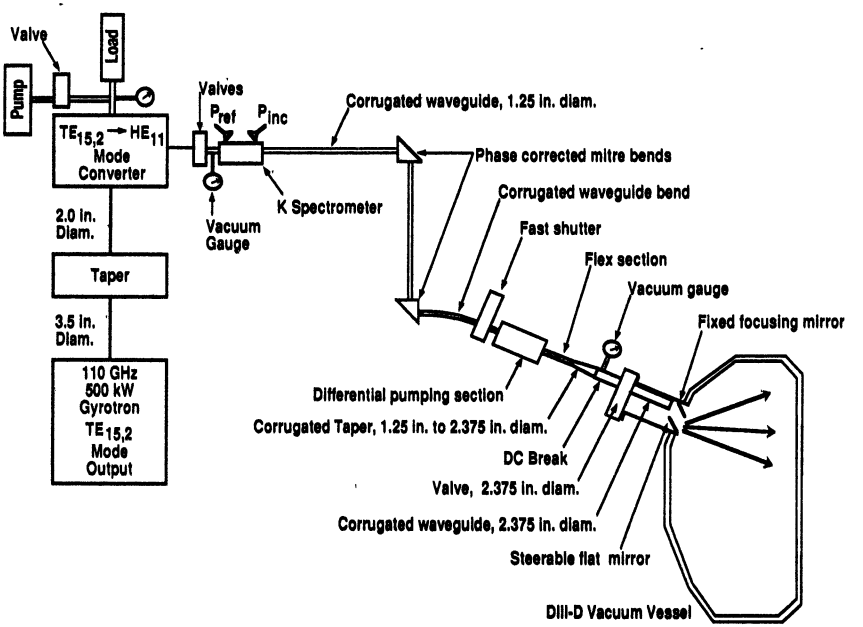

Fig. 8. Schematic of the evacuated 110 GHz transmission line for DIII–D. The rf power can be scanned across the plasma by moving a mirror.

Preliminary TORAY calculations for second harmonic X–mode low field launch, done for the parameters of Table I, show that the current drive efficiency may be ~30% greater than the low field O–mode fundamental efficiency and that the efficiency is only weakly dependent on the presence of a superthermal tail. These calculations are summarized in Fig. 10.

VI. CONCLUSIONS

Model calculations have been performed for both the DIII–D and T–10 electron cyclotron current drive experiments. Agreement between the calculations and measured non-inductive current on DIII–D is good, increasing the confidence in the predictions of 0.1–0.2 amperes/watt

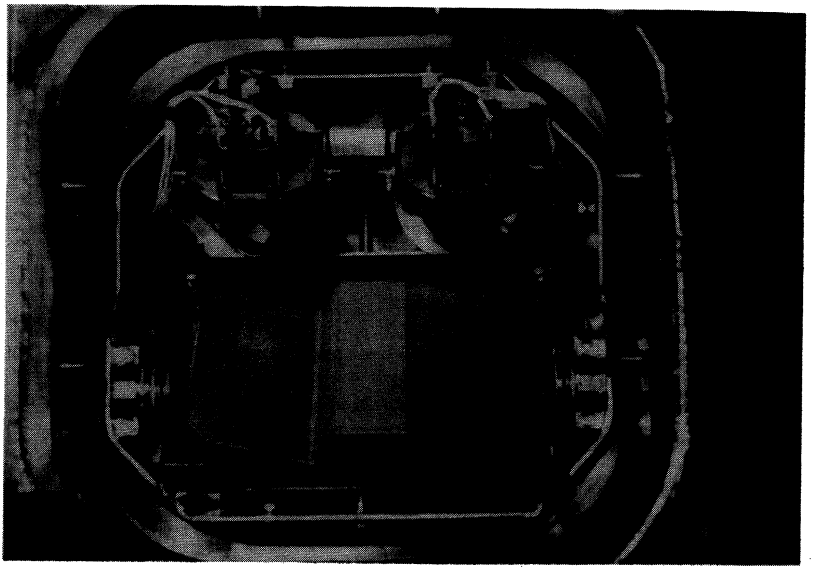

Fig. 9. Photograph of the first steerable launcher installed on DIII-D. This assembly accommodates two rf beams and injects into the torus at an angle of approximately 20 degrees to the radial for current drive experiments. The assembly is approximately 30 cm across.

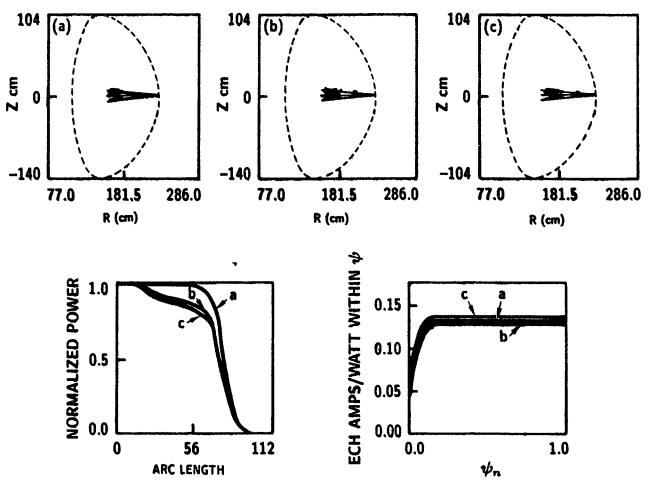

Fig. 10. Preliminary TORAY calculations for the DIII-D 110 GHz low field launch second harmonic X-mode experiment. Damping is excellent and is not extremely sensitive to the presence of a suprathermal distribution function.

for T–10. Fokker-Planck calculations indicate that non-linear effects at high power may further enhance the current drive efficiency on T–10. The location of the ECH resonance should be inside the magnetic axis to realize the best efficiency. Installation of the DIII–D 110 GHz system has begun.

REFERENCES

[1] Lloyd, B., Edlington, T., O'Brien, M.R., *et al.*, Nucl. Fusion **28**, (1988) 1013.

[2] Moeller, C.P., Prater, R., Riviere, A.C., *et al.*, Proceedings of 6th Joint Workshop on Electron Cyclotron Emission and Electron Cyclotron Resonance Heating. Oxford (1987), Culham Report CLM-ECR, 355 (1987).

[3] Matsuda, Kyoko, IEEE Transactions on Plasma Science **17**, (1989) 6; Kritz, A.H., Hsuan, H., Goldfinger, R.C., and Batchelor, D.B., in Proceedings of 3rd Joint Varenna-Grenoble International Symposium on Heating in Toroidal Plasmas, Brussels, (1982) Vol. 2, p. 707.

[4] Cohen, R.H., Phys. Fluids **30**, (1987) 2442.

[5] Pfeiffer, W.W., Davidson, R.H., Miller, R.L., and Waltz, R.E., General Atomics report GA–A16178 (1980).

[6] Harvey, R.W., McCoy, M.G., and Kerbel, G.D., in Applications of Radio Frequency Power to Plasmas, American Institute of Physics Conference Proceedings **159**, Kissimmee, (1987) p. 49.

[7] Giruzzi, G., this conference.

[8] Moeller, C.P., Prater, R., Callis, R.W., *et al.*, Proceedings of the 16th Symposium on Fusion Technology, London (1990).

ELECTRON CYCLOTRON CURRENT DRIVE AND HEATING IN WT-3 TOKAMAK

Shigetoshi TANAKA*)
Department of Physics, Faculty of Science
Kyoto University, Kyoto 606, Japan

Electron cyclotron current drive at the second harmonic (ECCD) has been studied on the WT-3 tokamak. When microwave power P_{EC} is injected into the plasma after ohmic heating (OH) power is shut down, the plasma current I_p up to 70 kA is sustained with zero loop voltage, as long as P_{EC} is applied. Here, the current I_p is produced by ECCD and the current carrying electrons are composed of high energy tail electrons up to 500 keV. The velocity distribution function of these tail electrons is estimated by measuring the x-ray emission spectra from these tail electrons. The $2\Omega_e$ ECCD efficiency is $\eta=5\times10^{-2}$ [10^{19}A/Wm^2], which is one order smaller than that for the lower hybrid (LH) current drive on WT-3.

Sawtooth oscillations (STO) are observed to be modified significantly by a sharply localized electron cyclotron resonance heating (ECH) at the safety factor q=1 flux surface. The effct is much stronger when the ECH is applied on the high field side of q=1 surface than the low field side. The complete stabilization of STO was obtained in the former configuration with ECH above the threshold, for low density plasmas, where the high energy electrons are generated by ECH. A modified current density profile, which reduces shear in the q=1 region, and a high energy electrons are attributed to the STO stabilization mechanism.

[A] ELECTRON CYCLOTRON CURRENT DRIVE

§1. INTRODUCTION

Non-inductive current drive (CD) is one of the most

important issue to realize the steady-state operation of tokamak reactors [1]. Experiments have shown that the plasma currnt is started up, ramped up, and sustained by the lower hybrid (LH) wave in many tokamaks. Here we present the experimental results on the electron cyclotron current drive (ECCD). Few reports on these experiments have been published, though ECCD is important for future tokamak reactor and is interesting from the physical point of view. When ECCD is applied to tokamaks, however, difficult problems such as cancelling and neoclassical effects occur [2]. In order to avoid this cancelling effect in our small tokamak WT-3, EC driven current is produced by injecting EC wave into the slideaway discharge [3,4]. Here EC wave can resonant-interact with the uni-directionally drifting electrons, since there are no electrons drifting in the reverse direction.

The experiments were carried out in WT-3 tokamak [4], wich has an iron core, major and minor radii R=65 and a=20.6cm, respectively, the toroidal field $B_t \leq 1.75$T, and the plasma current $I_p \leq 150$kA. The mm waves from a gyrotron ($\omega/2\pi=56.16$GHz, $P_{EC} \leq 200$kW, $\tau \leq 100$ms, and TE_{02} mode) were transferred through circular waveguides to the Vlasov-Nakajima antenna with a parabolic or elliptic reflector placed along the major radius and injected from the low-field side. This sharply focused wave, propagating as the X-mode with an angle of 60 degree to the field B_T without meeting the cyclotron cut off is absorbed at the second harmonic EC resonance layer ($\omega = 2\Omega_e$), if $\omega_p/\omega^e < 1/2$ (ω_p : plasma frequency).

§2. EXPERIMENTAL RESULTS

(1) Flat Top Discharge: In Figs.1 (a)-(i), the temporal evolution of plasma parameters with and without P_{EC} is shown. Here the $2\Omega_e$ ECR layer $R_{2\Omega_e}$ ($\omega=2\Omega_e$) is located at $r_{2\Omega_e}=R_{2\Omega_e}-R_0=8.9$ cm. The initial plasma with bulk electron density $n_e=(5-6)\times10^{12}$cm^{-3} is produced by OH discharge. After the OH power is turned off at t=30ms, plasma current I_p decreases and disappears at t=75 ms (dotted curve). The positive V_L ($\sim$0.5V) of t<75 ms is caused by the change of I_p ($V_L \propto -dI_p/dt$). Weak SXR and HXR emissions, I_{SX} (2.5 keV) and I_{HX} (35 keV), are observed during OH

discharge, showing the presence of suprathermal electrons accelerated by the positive V_L. When the $2\Omega_e$ EC wave power P_{EC} (144 kW, 100 ms) is applied at the time of 10ms after the OH power is turned off, a constant plasma current I_p=70 kA continues to flow for 70 ms with loop voltage V_L=0 (solid curves) as long as P_{EC} is applied. The total plasma current is sustained by the $2\Omega_e$ EC wave, since no OH current flows for V_L =0 ($2\Omega_e$ ECCD plasma). The line-averaged bulk electron density n_e decreases to 2×10^{12} cm^{-3} in the first 20ms of P_{EC} injection, but is kept at the constant during the $2\Omega_e$ ECCD plasma. The waveform of I_{SX}(0.2 keV) emitted from the bulk electrons is similar to that of n_e. The emission I_{SX}(0.9 keV) decreases with the decreasing n_e in the early phase, but increases gradually during the latter phase of the $2\Omega_e$ ECCD plasma. Both I_{SX}(2.5 keV) and I_{HX}(35 keV) increase at the instant of P_{EC} injection in spite of decrease of n_e, suggesting the build-up of the high energy tail electrons. Non-thermal ECE I_μ(70GHz) also increases strongly when P_{EC} is injected, implying enhancement of the tail electron's energy. These data suggest that the slide-away electrons pre-existing in the OH plasma are strongly EC heated, form a strong energetic tail and carry the EC-driven current.

The energy spectra of HXR emitted from the plasmas are shown in Fig.2. X-ray temperature T_x obtained from the slope of spectrum is T_H=45 keV just before P_{EC} injection.(Curve 1) When P_{EC} is applied, T_H increases (2,3) and attains 110 keV(4) and the maximum photon energy extends to 400 keV. At the same time, the photon count with energy E_H > 80 keV increases strongly and becomes saturated during P_{EC} injection. Measurements of Thomson scattering shows that the bulk electron temperature at the plasma center is T_e=510±30 eV at t=40 ms just before P_{EC} injection and T_e=490±30 eV at t=100 ms in the $2\Omega_e$ ECCD, and does not change during the $2\Omega_e$ ECCD. These data imply that in the $2\Omega_e$ ECCD plasma the electrons are composed of bulk electrons with T_e= 500eV, n_e =2×10^{12} cm^{-3}, and energetic tail electrons with T_t=100 keV, n_t =4×10^{10} cm^{-3}.Here the n_t of the tail is estimated by assuming that the current I_p=70kA is carried by them.

Filling-gas pressure affects strongly on formation of the high energy tail electrons and the $2\Omega_e$ ECCD plasma. For low filling-gas pressure, $p=(0.5\text{-}1.2)\times10^{-2}$ Pa, non-thermal emissions I_μ (70 GHz) and I_{HX} (35keV) appear in OH plasma and the flat-top or ramp-up discharge is formed when P_{EC} is injected after OH power being turned off. For $p>1.4\times10^{-2}$ Pa, these emissions are weak and I_p decreases with time and the $2\Omega_e$ ECCD plasma is never obtained when P_{EC} is injected. These results show that the presence of the high energy tail electrons in the initial OH plasma is necessary for formation of the $2\Omega_e$ ECCD plasma. In the slide-away discharge in the low pressure regime, high energy tail electrons moving only in the one toroidal direction are produced and they can resonant-interact with the $2\Omega_e$ EC wave, resulting in EC-driven current. On the contrary, these uni-directional tail electrons is not created in the initial OH plasma in high pressure regime and the $2\Omega_e$ ECCD is not achieved.

(2) Ramp-up Discharge: In Fig.3 (a), the temporal evolution of I_p is shown for three different P_{EC} in the case of $n_e=1.0\times10^{12}\,cm^{-3}$ As P_{EC} increases, the $2\Omega_e$ EC-driven current I_p changes from ramp-down to flat-top, and ramp-up discharges can be obtained above the power level of 70kW. Correspondingly, the voltage V_L changes from a positive to a negative value ($V_L \propto -dIp/dt$) (Fig.3(b)).The ramp-up discharges clearly demonstrate that the current I_p is driven by the $2\Omega_e$ EC wave, since the direction of the electric field due to V_L is opposite to that of the electron drift.At the same time, I_{SX}(1.7keV) emitted from the tail electrons increases, while I_{SX}(0.2 keV) emitted from the bulk electrons does not change as P_{EC} increases(Fig.3(c)). This result shows that the $2\Omega_e$ EC wave mainly heats the tail electrons, which are carrying the plasma current. Further, experiments show that duration of the flat-top discharge increases corresponding to the pulse length of P_{EC}. Similarly, as the bulk electron density increases, the $2\Omega_e$ EC-driven current I_p changes from ramp-up to flat-top, then to ramp-down, keeping P_{EC} at constant. Correspondingly, V_L changes from a negative to a positive value and I_{SX}(0.2keV) increases,

I_{SX}(1.7keV) decreases.

(3) ECCD vs. Toroidal Field B_T : The $2\Omega_e$ ECCD is examined by changing B_{t0} for various wave injection methods. As B_{t0} increases,the ramp-up rate $\Delta I_p/\Delta t$ during P_{EC} injection approaches zero,becomes positive, and then negative, while it is negative in the case of no P_{EC}. Correspondingly, V_L varies from positive to negative, then to positive. Non-thermal emission I_{SX}(1.7keV) and I_μ(70GHz) also become intense near the range of $\Delta I_p/\Delta t \geq 0$, though thermal emission I_{SX}(0.2keV) does not change with B_{t0}. Thus the flat-top or ramp-up discharge ($\Delta I_p/\Delta t \geq 0$) is obtained only when B_{t0}=1-1.15T, i.e., $r_{2\Omega_e}$=0-10cm.
There is no remarkable difference when the wave is injected in the opposite direction.For the perpendicular propagation of the O-mode,the effect of the $2\Omega_e$ EC wave is smaller than that of X-mode,but the flat-top discharge can be obtained. These results may be interpreted that as the single-pass absorption is low, the wave is reflected at the chamber wall and mode-converted, finally absorbed by the resonant electrons moving in the one toroidal direction in the slide-away discharge.

(4) ECCD Efficiency : The $2\Omega_e$ ECCD flat-top discharges of I_p=20-73kA were obtained in $n_e=(1.0\text{-}2.4)\times10^{12}cm^{-3}$ for P_{EC}=30-144 kW(Fig.4).With use of these data, the figure of merit for the $2\Omega_e$ ECCD is obtained as, $\eta = n_e I_p R / P_{EC} = (3.2 - 6.4)\times10^{-2}$ ($10^{19}A/Wm^2$).This is the same order as $\eta = 10^{-2}$ for the Ω_e ECCD, but one order smaller than $\eta_{LH}=(3\text{-}6)\times10^{-1}$ for LHCD in WT-3 . On the other hand, the theoretical figure of merit is given by η=1.22 T_e(keV)$(\ln\Lambda)^{-1}$ j/p_d ($10^{19}A/Wm^2$), where $\ln\Lambda$ is the Coulomb logarism and the uniform distribution is assumed. According to Fisch-Boozer [1], the normalized efficiency for Z_{eff}=1 is given by, j/p_d=uw/2 ,where $u=v/v_{Te}$, $w=v_{//}/v_{Te}$ and $v_T{}^2{}_e = 2T_e/m_e$, respectively. If we assume $\ln\Lambda$=16 and that u=w=20 (corresponding energy is 80keV for T_e=200 eV), we obtain the theoretical η =3.2. This value is 50-100 times large compared with experimental one. Further, according to the quasilinear theory on ECCD given by Cordey et al.[2], we can obtain that η_{EC} = 0.82, 1.2 and 1.4 for n=1,2 and 3, respectively. These values

are nearly the same as that predicted by Fisch-Boozer. The experimental low value of efficiency is explained by the rapid loss of current-carrying fast electrons, as described later.

(5) HXR Spectrum and Velocity Distribution Function of High Energy Tail Electrons : HXR spectra are measured at the various angle with respect to B_T (θ=0-180°). In Fig.5 are shown the angular dependence of normalized HXR photon count for various energy range for ECCD plasmas. The tail electron's velocity distribution function f(p) can be estimated by comparing these measured HXR spectra as function of emission angle θ with the emission spectra calculated from the model distribution function of electrons, f(p). We assume that the distribution function is uniform in real space and the model distribution function is given by the so-called 'three-temperature model', where f(p) has a Gaussian shape characterized by the three temperatures and forward, backward density. The best fitting calculated curves to the experimental ones are obtained for the plasma parameters with $T_{//F}$ =100, $T_{//B}$=50, T = 75keV and n_{tF}=6.6 × 10^{10}, n_{tB}=6.6 ×10^{9} cm^{-3}. The ratio of the total tail electron density to the total bulk electron is 1.5%.

(6) $2\Omega_e$ EC Absorption and Energy Confinement Time : Numerical calculation on the $2\Omega_e$ EC absorption have been made by using a code which includes the Doppler and the relativistic effects of the tail electrons. The power deposition due to bulk electrons is localized near the $2\Omega_e$ ECR layer, while that due to tail electrons is distributed broadly by the Doppler and the relativistic effects. The total single-pass absorption is ~0.24 and the ratio of the power absorption by the bulk electrons and the tail electrons is 2:3. By using the stored energy of plasma, where the absorbed EC wave energy flow from the tail electrons to the bulk electrons, the energy confineent time is estimated as τ_{Et}=6.47ms and τ_{Eb}=0.56ms, for tail and bulk electrons, respectively. Since τ_{Et} of tail electrons is much smaller than the slowing down time τ_{coll} (~152ms) with the bulk electrons, most of the tail electrons are lost directly to the wall. Luckhard [5] have calculated the current-drive efficiency,

$(j/p_d)_L$, including this effect. Using the above estimated values, the efficiency decreases by factor of 0.05, which is nearly the same as the experimental one.

(7) RF tokamak : By injecting the lower hybrid wave (LHW) into the ECR plasma, produced by injecting mm wave (f=56GHz, P_{EC} =100kW, τ_{EC}=15ms) from a gyrotron, the plasma current I_p is generated, started up and sustained (I_p=25kA) by RF (EC and LH) power only without the OH power (so-called RF tokamak). The plasma parameters such as the density, the temperature of high energy tail electrons as well as bulk electrons are similiar to those of LHCD plasmas.

§3. CONCLUSION

Electron cyclotron current drive at the second harmonic without inductive electric field is demonstrated. Flat-top and ramp-up discharges are obtained when $2\Omega_{ce}/\omega$=1-1.15. The $2\Omega_{ce}$ ECCD plasma has two components of electrons, bulk electrons and the current-carrying, high energy tail electrons. Analysis of HXR data shows that the tail electron's distribution function is asymmetric along the toroidal direction and possesses the tail electrons with high perpendicular energy due to $2\Omega_{ce}$ EC heating. The uni-directional high energy tail electrons are neccessary in the initial, target plasma in order to achieve ECCD. The experimentally obtained $2\Omega_{ce}$ ECCD efficiency is η_{EC}=(3.2 - 6.4)x10^{-8}(10^{19}A/Wm^2),which is one order smaller than that of LHCD. This low η_{EC} is attributed to low confinement time of high energy tail electrons. Further, the formation of plasma current of the RF tokamak is described.

[B] SAWTOOTH STABILIZATION BY ECH

§1. INTRODUCTION

The sawtooth instability is one of the relaxation phenomena observed in tokamaks. Recent experiments on strong additional heating in the large tokamaks showed that sawtooth amplitude becomes very large (T_e(max)/ T_e(min) ~ 2) and the sawtooth instability plays an important role on determining heating and confinement in the plasma center. Hence, understanding of the

instability mechanism and search for possible stabilization techniques have become major issues in tokamak research. When the lower hybrid driven current was superposed in the Ohmic heating discharge, sawtooth oscillations (STO) were suppressed in various tokamaks. Although this stabilization mechanism was not clear, it was explained in Asdex by the flattering of global current profile with raising central safety factor above unity [6]. During period of ICRF or ICRF plus NBI heating in JET, the sawtooth instability was suppressed for period up to 3.2 s, where the fast-ion population could have contributed to the stabilization of the m=1 mode [7]. The effect of the electron cyclotron heating (ECH) on STO is sensitive to the toroidal field and STO were strongly modified by ECH [8,9]. In this paper we present significant findings that the ECH stabilization effect on STO is strong when ECH resonance layer r_{ECR} is at the safety factor q=1 surface $r_{q=1}$ on the high field side (HFS).

§2. EXPERIMENTAL RESULTS

The experiments were carried out in the WT-3 tokamak. STO are observed in the OH plasma when the safety factor at the limiter is set as $q_L = 2.2 \sim 6.0$. The period τ_S as well as the amplitude of STO increase when the ECH power P_{EC} is applied.These modifications of STO are very sensitive to the field B_T , as shown in Figs.6(b)~(d), where the changes of soft X-ray (SXR) detected signal I_{SX} ($h\nu \gtrsim 0.7$ keV) by application of ECH with a constant P_{EC} are shown for the various field B_T. When the ECR layer r_{ECR} is placed at the q=1 surface $r_{q=1}$ on the HFS, STO are stabilized completely during the application of ECH (b). On the other hand, when $r_{ECR} = r_{q=1}$ on the LFS, the period of STO, τ_S, increases enormously (τ_S = 3ms >> τ_E = 1 ms, energy confinement time) and the amplitude becomes saturated (d). Further, when r_{ECR} is placed on the plasma center (on-axis heating), I_{SX} increases rapidly in the ramp-up phase and drops deeply in the crash phase. Here ECH with sharp beam is applied on the minor axis and not on the q=1 surface (c). The geometrical configuration for $r_{ECR} = r_{q=1}$ in the two cases,(b),(d) and (c) is shown in Fig. 6(a). Thus, it is concluded that the

effect of ECH on STO is much strong when $r_{ECR}=r_{q=1}$ on HFS, compared with other two cases, since the change of B_T is small ($B_T(0)$ = 0.91 - 1.08T) and the OH plasmas without P_{EC} are nearly the same. With ECH at $r_{q=1}$ on HFS the electron density n_e decreases slightly (n_e =(7 → 6) x $10^{12}cm^{-3}$) and the temperature $T_e(0)$ measured by Thomson scattering increases ($T_e(0)$ = 510 → 670 eV), resulting in the decrease of loop voltage (V_L =1.5→0.8V), while the plasma current is kept constant at I_P =80kA(q_L =4.3). There is no change of the OV impurity line emission.

In Fig.7(a) the period τ_s is plotted as a function of the field B_T with the same value of q_L =3.4 in both cases of with and without the ECH. The period τ_s increases sharply at $r_{ECR}=r_{q=1}$ and τ_s becomes extremely large on the low B_T side, compared to that in the high B_T side and complete stabilization of STO is possible only in the former case ($r_{ECR}=r_{q=1}$ on HFS). As shown in Fig.7(b) the amplitude for the on-axis heating is larger than those for $r_{ECR}=r_{q=1}$,in which the sawtooth becomes saturated. In Fig.7(c), twice the inversion radius r_{inv} of STO for ECH and OH plasmas are plotted as functions of safety factor q_L . Both radii r_{inv} decrease with the increasing q_L and r_{inv} of OH plasma increases when ECH is applied. The radii $r_{q=1}$ are obtained by computer tomographic reconstructed images of SXR emissivity at the crash phase and, also, by $T_e(r)$ profile measured by Thomson scattering and plotted here. The radius $r_{q=1}$ is usually larger than r_{inv}, since the latter is determined by the spatial variation of SXR signal integrated along the line-of-sight. It is noted that $r_{q=1}$ is just coincident with r_{ECR}, where the effect of ECH on STO is the strongest and complete stabilization of STO is attained.

As shown in the insets of Fig.8 the sawtooth period as well as the amplitude increase with ECH power and STO is stabilized completely for intense P_{EC} in the case of $r_{ECR}= r_{q=1}$ on HFS. The conditions of complete stabilization depend on plasma parameters such as B_T , n_e , q_L and P_{EC} . In Fig.8 the period τ_s is plotted as functions of the EC power P_{EC} /P_{OH} for the three ECH cases and

the increment of τ_s becomes larger in the order, on-axis heating, heating at $r_{ECR}=r_{q=1}$ on the LFS and on the HFS. It is noticeable that τ_s increases non-linearly and STO are completely stabilized in the case of $r_{ECR}=r_{q=1}$ on HFS, for P_{EC} above the threshold value $P_{EC}^{three}/P_{OH} \sim 3$. This threshold decreases with the increasing q_L and $P_{EC}/P_{OH} \sim 1$ in the case of $q_L = 4.7$. In these high q_L region, the complete stabilization of STO occurs even when $r_{ECR}=r_{q=1}$ on LFS with P_{EC}^{three} 1.7 times larger than that of HFS.

The effect of ECH on STO is strongly dependent on the electron density n_e for $r_{ECR}=r_{q=1}$ on HFS in Fig. 9(a), where the period τ_s increases abruptly with the decreasing n_e below $n_e = 6\times10^{12}cm^{-3}$ and the complete stabilization of STO is obtained in $n_e = 5\times10^{12}cm^{-3}$. In contrast, τ_s increases slightly with the decreasing n_e for the other two cases, (b) on axis heating and (c) LFS. Measurements of X-ray energy spectra show that the high energy tail elecrons with T_{eh} = 60keV extending up to 300keV are generated by ECH in the low density plasmas, which has no such electrons in OH plasma with T_e = 0.5keV. The X-ray emission in the various energy range emitted from the ECH and OH plasmas are measured as functions of the density n_e. In Fig. 9 (d) I_{SX}(2.5keV) emitted from these high energy electrons increases enormously with ECH in the low n_e region ($n_e \lesssim 0.8 \times 10^{13}cm^{-3}$). Further, I_{HX} (35keV) is observed only for these low n_e region in ECH plasma. On the contray, I_{SX} (0.9)keV emitted from the thermal electrons with and without ECH, repectively, increases with the density n_e. These results suggest that the high energy tail electrons are generated by ECH in these low n_e region and might be responsible to the strong effect, such as the complete stabilization of STO. It is noted, however, that presence of such electrons is not sufficient for complete stabilization of STO, since the tail electrons are generated also when ECH is applied at $r_{ECR}=r_{q=1}$ on LFS or at the center (on-axis).

§3 THEORETICAL CONSIDERATION

Here we propose that the STO stabilization by ECH is due a modification of the current profile [10] in such a manner as to

lower the shear at the q=1 surface, thus stabilizing the resistive m/n =1/1 mode. Specifically we suggest that when ECH is applied, $T_{e\perp}$ increases , $(\delta T_{e\perp}/T_{e\perp} \simeq 0.3)$, and the electron collisionality and hence the plasma resistivity is reduced, driving more current in this region. This incremental change of the current density would result in a local reduction of the shear,

$$s = \frac{2}{q}\frac{dq}{d\psi}\frac{V}{dV/d\psi} ,$$

where ψ refers to the poloidal flux, and V refers to the plasma volume enclosed by the surface. We note that this is the toroidal equivalent of s = r/qdq/dr. This reduction in s will stabilize the resistive mode which plays an important role in STO. We have modelled this, using the PEST code. We start with a current profile that smoothly vanishes at the plasma edge with q_{axis} = 0.83, and q_L=3.37, and has the q=1 surface at an average radius of 0.35 of the plasma minor radius, a parabolic pressure profile is chosen. We determine the stability of this model equilibrium to the ideal and resistive m/n = 1/1 modes. The q-profile is modified locally near the q=1 surface in a manner which reduces the shear at that surface, and a new equilibrium is computed. The stability limits of such a sequence of equilibria at different values of β_{pol} are obtained. In the initial OH phase the plasma is unstable to the resistive mode, and as the ECH is applied the shear is reduced and the plasma is at marginal stability, further heating reduces the shear further and stabilizes the mode completely. The current profile at this point shows a local peak near the q=1 surface, which is more substantial on the HFS than the LFS. This difference in the current profile serves to explain the differences when heating on the HFS and LFS. When ECH is applied on the HFS, the high energy electrons can traverse most of the surface enhancing a locally peaked current profile on the entire surface. In contrast, when the ECH is applied on the LFS, many of the high energy electrons are easily trapped in the banana region and localized to the LFS and will not influence the shear to the

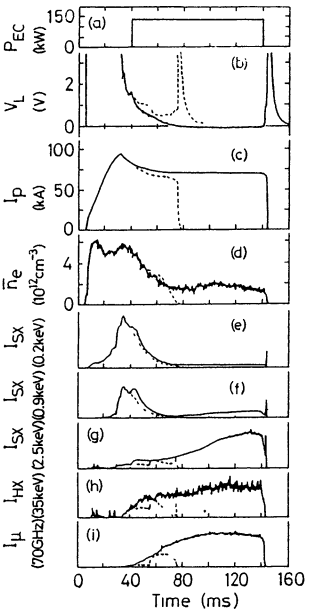

Fig. 1

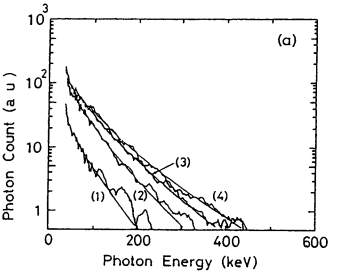

Fig. 2

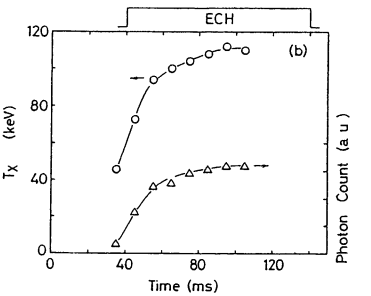

Fig. 3

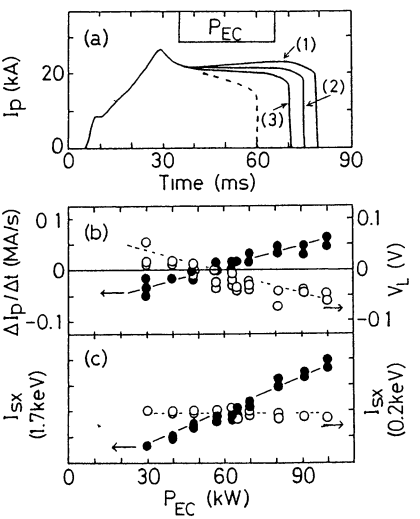

Fig. 4

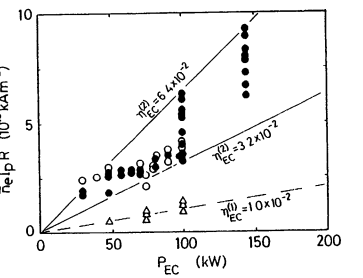

Fig. 5

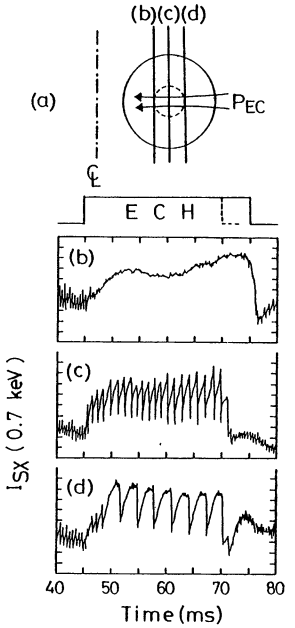

Fig. 6

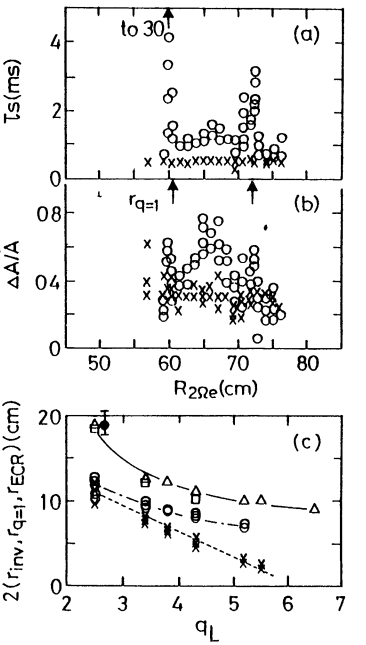

Fig. 7

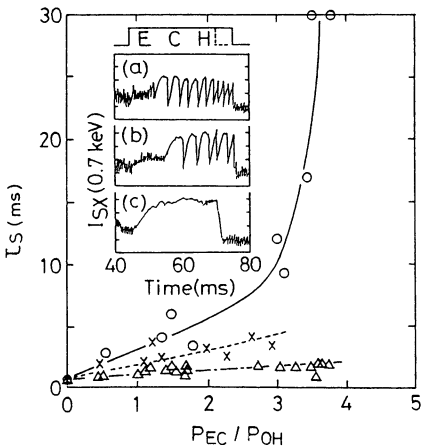

Fig. 8

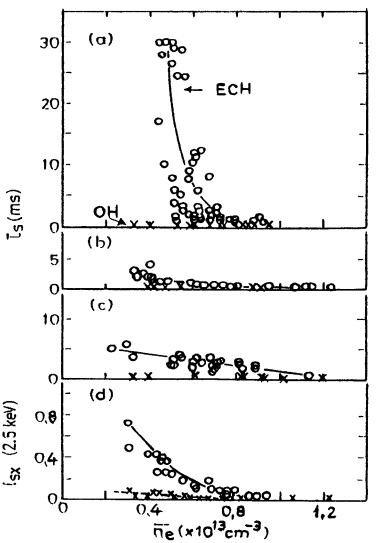

Fig. 9

same extent. As indicated earlier, in addition to the effects of the high energy electrons on the shear through the current profile, we might expect an energetic particle stabilization effect as discussed in White et. al.[11] Although the stability window discussed in Ref.11 does not exist in the present experiment, since $\beta_p \ll 1$ and $\omega_A > \omega_e{}^*$,one might still expect some stabilizing effect from the high energy electrons, which are precessing much faster than the background diamagnetic velocity. Hence $\omega_{de} > \omega_e{}^*/2$, where $\omega_{de} = W_\perp/erRB_T$ and $\omega_e{}^* = (k_\theta/eB_T)\nabla p/n_e$. This criterion can be written as $W_\perp > R\nabla p/n_e \sim T_e R/a \sim 1.5\mathrm{keV}(T_e = 0.5\mathrm{keV})$ and is well fulfilled, since the measured HXR temperature is $T_{eh} \sim 60\mathrm{keV}$. At present , however, it is difficult to quantitatively estimate the stabilization due to this effect.

§4 CONCLUSION

In conclusion we have found a clear stabilization of STO due to ECH when it is applied near the q=1 surface. This effect is much stronger when the ECH is applied on the high field side. There is a power threshold above which complete stabilizatiion is obtained, below that the sawtooth period increases linearly. Similarly there is a density threshold below which only the stabilization occurs. The stabilization is attributable to a local reduction of the shear near the q=1 surface with some contribution due to energetic particle effects. This latter effect may be similar to that observed with ICRF heating in JET [11]. These results also suggest that STO may be controlled effectively with ECH at the q=1 surface, especially by application on the high field side.

This work was supported by a Grant-in-Aid of Scientific Research from the Ministry of Education in Japan and U. S. Department of Energy, under Contract No. DE-AC02-76CH03073.

*)in collaboration with WT-group in Kyoto University and M. Yamada, J. Manickam. and R. White in PPPL, USA.

References

1. N.J. Fisch, Rev. Mod. Phys.59(1987) 175.
2. J.G. Cordey et al.,Plasma Phys. 24(1982) 73.

3. A. Ando et al., Phys. Rev.Lett. 56(1986) 2180.
4. H. Tanaka et al., Phys. Rev. Lett. 60(1988) 1033.
5. S.C. Luckhardt, Nucl. Fusion 27(1987) 1914.
6. F.X. Soldmer et el., Phy. Rev. Lett. 57(1986) 1137.
7. D.J. Campbell et al., Phys. Rev. Lett. 60(1988) 2148
8. G.A. Bobrovskii et al., Sov, J, Plasma Phys. 13 (1987) 665.
9. Y. Terumichi et al., 13th Intern. Conf. Plasma Phys. and Control. Fusion Res. Washington, (1990) E-3-5.
10. H. Soltwisch et al.,Proc. 10th Intern. Conf. on Plasma Phys. and Contr. Nucl. Fusion Res., Kyoto, 1986 (IAEA, Vienna, 1987) Vol. 1, p. 263.
11. R. B. White et al., Phys. Rev. Lett. 62,(1989) 539.

Figure Captions

Fig. 1 Temporal evolution of plasma parameters for ECCD plasma.

Fig. 2 Energy spectra of hard X-ray radiation from plasma.

Fig. 3 Ramp-up, flat-top, and ramp-down discharges for various P_{EC}

Fig. 4 $n_e I_p R$ vs. P_{EC}

Fig. 5 Angular dependence of normalized photon count for various energy range.

Fig. 6 Temporal evolution of I_{SX} (0.7 keV) for ECH at $r_{q=1}$ on (b) HSF, (d) LFS and (c) on minor axis.

Fig. 7 (a) Period τ_S and (b) amplitude $\Delta A/A$ of sawtooth oscillation vs the position of ECH layer (or B_T). (c) r_{inv}, $r_{q=1}$ and r_{ECR} vs q_L.

Fig. 8 Period τ_S vs EC power P_{EC}/P_{OH}.

Fig. 9 Period τ_S vs n_e for ECH at q=1 surface on (a) high field side, (b) I_{SX} on axis heating and (c) low field side. (d) soft X-ray ($h\nu$>2.5keV) vs n_e.

ABSORPTION OF A STRONG EC WAVE IN A PLASMA

R. Pozzoli, D. Farina*, A. Mennella [+], D. Ronzio

Dipartimento di Fisica, Università di Milano,
via Celoria 16, I-20133 Milano, Italy.

**Istituto di Fisica del Plasma, Consiglio Nazionale delle Ricerche,*
EURATOM-ENEA-CNR Association, via Bassini 15, I-20133 Milano, Italy

[+] ENIRICERCHE S.p.A., I-20097 San Donato, Milano, Italy

Introduction

The recent use of powerful radio frequency (RF) sources, as gyrotrons and FEL's, for plasma heating and current drive, gives rise to conditions where the nonlinearity in the electron motion plays a dominant role [1]. Similar conditions also occur, at lower electromagnetic (EM) power density, in the RF plasma pre-ionization [2], and in the interaction of EM waves with the ionospheric plasma [3]

Our aim is to characterize the process of EM power absorption in the different nonlinear regimes. Theoretical investigations on this subject have been performed e.g. in Refs. 1 - 11. Referring to the electron cyclotron (EC) range of frequency, we observe that the power injected into the plasma is spatially localized, entailing a finite duration (the flight time τ_f) of the interaction between the single electron and the EM field, and assume, for definiteness, that the amplitude of the perturbation has a characteristic width $2L$ in the direction of the static magnetic field $\mathbf{B}_0 = B_0\mathbf{e}_z$, and is described by the function

$$\varepsilon(z) = eE(z)/mc\omega = \varepsilon_M \exp(-z^2/L^2), \tag{1}$$

where ω is the wave frequency, and $\varepsilon_M < 1$.

A rough distinction between the linear and the nonlinear regime can then be made introducing the characteristic time of the nonlinear motion τ_l , which can be estimated as the period of the electron trapping in the wave field. In the linear regime $\tau_l \ll \tau_f$, while the nonlinear motion is characterized by the opposite condition $\tau_l \ll \tau_f$. In this last case we shall consider the adiabatic regime, in which the trapping time is shorter

than the time scale of variation of the field amplitude τ_F (more precisely the time scale of the evolution of the singular points in phase space). A regular nonlinear regime, and a globally stochastic regime can be identified, depending on the field amplitude ε_M, respectively lower or higher than a threshold value ε_R characterizing the overlapping of resonant islands in the phase space [12]. A strongly and weakly regular nonlinear regime can be also identified, characterized by the conditions $\varepsilon_M > \varepsilon_c$, $\varepsilon_M \ll \varepsilon_c$, respectively, where ε_c is a threshold for a topological variation of singular trajectories in phase space.

In the following sections we perform a quantitative investigation of the above regimes, considering, for definiteness, the case of propagation perpendicular to the magnetic field $\mathbf{B}_0$.

Formulation of the problem

To determine the connection between the initial and final electron states, which correspond to unperturbed motions, we look for a formulation of the problem in terms of a time independent Hamiltonian.

In a gauge with zero scalar potential, the electron Hamiltonian can be written $H(\mathbf{x}, \mathbf{P}, t) = \gamma = (1 + (\mathbf{P} + \mathbf{A})^2)^{1/2}$, where $\mathbf{P}$ is the canonical momentum, conjugate to the position $\mathbf{x}$, $\mathbf{A}$ is the vector potential, and adimensional quantities have been used. Time, length, momentum, energy, and vector potential are normalized over Ω^{-1}, $c\Omega^{-1}$, mc, mc^2, and mc^2/e, respectively, where $\Omega = eB_0/mc$ is the classical electron gyrofrequency. For the case under consideration, we specify the vector potential as $\mathbf{A} = \mathbf{A}_0 + \mathbf{A}_1$, where $\mathbf{A}_0 = -y\mathbf{e}_x$ and

$$\mathbf{A}_1 = -\varepsilon(z)[\eta_x \cos \chi \mathbf{e}_x + \eta_y \sin \chi \mathbf{e}_y + \eta_z \cos \chi \mathbf{e}_z],$$

where η_x, η_y, and η_z, are the component of the polarization vector, $\chi = \nu(Nx - t)$ is the wave phase, $N = kc/\omega$ is the refractive index, and $\nu = \omega/\Omega$. From the above Hamiltonian, by means of canonical transformations, the following time independent Hamiltonian can be obtained

$$H(z, \theta_1, \theta_2, P_z, I_1, I_2) = \gamma - \nu I_2 = \left[1 + (\sqrt{2I_1} \sin \theta_1 + A_{1y})^2 + (\sqrt{2I_1} \cos \theta_1 + A_{1x})^2 + (P_z + A_{1z})^2\right]^{1/2} - \nu I_2, \tag{2}$$

where θ_1, θ_2, I_1, I_2, are angle action variables. They are related to $\mathbf{x}$, and to the kinetic momentum $\mathbf{p}$, by the relations $\theta_1 = \tan^{-1}(p_y - A_{1y})/(p_x - A_{1x})$; $\theta_2 = -\nu t + C_x$, being $C_x = \nu N(x - p_y + A_{1y})$ a constant of motion; $I_1 = 1/2\,[(p_x - A_{1x})^2 + (p_y - A_{1y})^2]$;

$I_2 = (y + p_x - A_{1x})/(\nu N)$. The phase of the wave is expressed as $\chi = \theta_2 + N\nu\sqrt{2I_1}\sin\theta_1$. For the unperturbed system ($\varepsilon = 0$), θ_1 represents the phase of the electron momentum gyration, I_1 the perpendicular energy $p_\perp^2/2$, and I_2 is proportional to the y coordinate of the guiding centre. Note that the electron energy change at any time $\delta\gamma$ is proportional to the change of I_2 : $\delta\gamma = \nu\delta I_2$.

The phase space trajectory, corresponding to the electron motion, lies on the 5D surface $H = const$. When the perturbation vanishes ($\varepsilon = 0$), this H –surface becomes the unperturbed Hamiltonian surface $H_0(P_z, I_1, I_2) = \Gamma(P_z, I_1) - \nu I_2 = const$ (with $\Gamma(P_z, I_1) = (1 + 2I_1 + P_z^2)^{1/2}$). Since before and after the crossing of the radiation beam the condition $H_0 = const$ has to be satisfied, the initial and final electron momenta lie on the same H_0 –surface, and the crossing of the beam can be viewed as a jump of a point on this surface.

Expressing the $\cos\chi$ and $\sin\chi$ terms in Eq.(2) by means of the relation $\exp(i\chi) = \sum_n J_n(b)\exp(i(\theta_2 + n\theta_1))$, with $b = \nu N\sqrt{2I_1}$, the Hamiltonian H to first order in ε reads

$$H = \Gamma(P_z, I_1) - \nu I_2 - \frac{\varepsilon}{\Gamma}\sum_n \Theta_n(P_z, I_1)\cos(\theta_2 + n\theta_1), \tag{3}$$

where

$$\Theta_n = \sqrt{2I_1}\left[\eta_- J_{n-1}(b) + \eta_+ J_{n+1}(b)\right] + P_z\eta_z J_n(b),$$

being $\eta^\pm = (\eta_x \pm \eta_y)/2$ the right and left components of the polarization vector.

When the frequency ω is close to a harmonic of the gyration frequency $m\Omega/\gamma$, i.e., the condition $|\nu - m/\gamma| \ll |1/\gamma|$, is satisfied during the motion, averaging over θ_2 [13], leads to the relation $mI_2 - I_1 = const$, and the Hamiltonian (3) reduces to the following Hamiltonian with two degrees of freedom

$$H(z, \theta, P_z, I) = \gamma - \nu_m I = \Gamma - \nu_m I - \varepsilon\frac{\Theta_m}{\Gamma}\cos(m\theta), \tag{4}$$

with $\nu_m = \nu/m$, $\theta = \theta_1 + \theta_2/m$, and $I = I_1$. Note that at any time $\delta\gamma = \nu_m\delta I$. The level curves of the relevant unperturbed Hamiltonian $H_0(P_z, I) = \Gamma - \nu_m I$ are shown in Fig. 1, in the $P_z^2, 2I$ plane. The electron crossing of the beam corresponds to a jump on the same level curve, characterizing an energy transition.

The condition $H_0 = const$ can be also written in terms of the initial energy γ, and the variations due to the crossing of the radiation beam, ΔP_z^2, and $\Delta\gamma$, as

$$\Delta P_z^2 = (\Delta\gamma)\,[\Delta\gamma - 2(1/v_m - \gamma)] \tag{5}$$

An approximate estimate of $\Delta\gamma$ can be given for the case where the variation of P_z^2 can be neglected, i.e., assuming $\Delta P_z^2 \ll (\Delta\gamma)^2$. In this case we obtain, for $P_z^2 \leq 1/v_m^2 - 1$,

$$\Delta\gamma = 0, \quad \text{or} \quad \Delta\gamma = \overline{\Delta\gamma} = 2(1/v_m - \gamma), \tag{6}$$

and the only solution $\Delta\gamma = 0$ when $P_z^2 \geq 1/v_m^2 - 1$.

Note that, in this approximation, $\Delta\gamma$ is independent of the field amplitude, provided that the energy transition takes place.

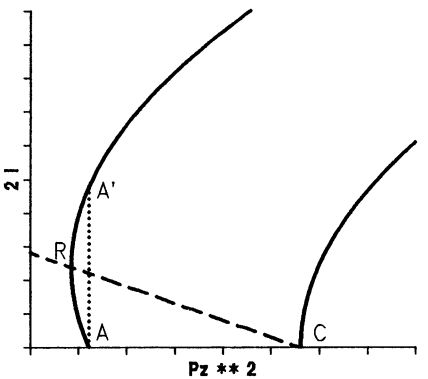

Fig. 1 Level curves of the unperturbed Hamiltonian $H_0(P_z, I)$ relevant to a given m, in the $(P_z^2, 2I)$ plane. The dashed line contains the resonant points R, satisfying the resonant condition $v_m = 1/\gamma$. The points A, A′ correspond each other in a net energy transition with $\Delta P_z = 0$. Such transition is possible only if $P_z^2 < 1/v_m^2 - 1$, this value corresponding to the abscissa of point C.

Regular motion

We begin the investigation of the power absorption process in the case of regular motion, described by the Hamiltonian (4), by analyzing the electron energy variation due to the crossing of the radiation beam $\Delta\gamma(\mathbf{p})$ (as a function of the initial electron momentum $\mathbf{p}$) and its average value over the initial phase of the electron motion $<\Delta\gamma>$. From this last quantity, the power absorbed by the plasma is then computed.

In the linear case, where trapping cannot occur owing to the short duration of the interaction, the dynamics is determined linearizing each canonical variable X, entering the Hamiltonian (4), around its unperturbed state $X^{(0)}(t)$. The quantity $<\Delta\gamma>$ is pro-

portional to ε_M^2 and is nonzero when P_z, and I belong to a tight region around the resonant curve $\nu_m = 1/\Gamma(P_z, I)$ (the broadening being due the finite duration of the interaction). Its explicit expression reads

$$<\Delta\gamma> = \frac{\pi}{2} m^2 \nu_m \frac{\gamma}{P_z} \frac{\partial}{\partial I} \left[\frac{\Theta_m^2}{\gamma P_z} F^2\left(\varepsilon, m \frac{1 - \nu_m \gamma}{P_z}\right)\right], \tag{7}$$

being $F(f,p)$ the cosine transform of the function f.

The behaviour of $<\Delta\gamma>$ as a function of I for a fixed P_z is shown in Fig. 2, for the ordinary mode (OM) at the first harmonic. Note that, when the width of the radiation beam increases, the curve tends to a function proportional to $\delta'(\gamma - 1/\nu_m)$, reproducing the familiar uniform amplitude case.

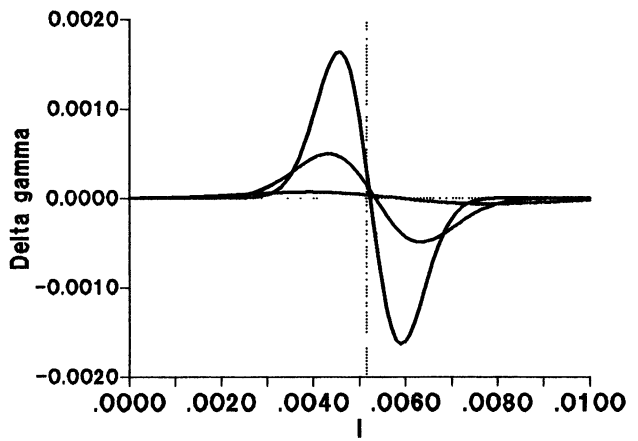

Fig. 2 Behaviour of the average energy change $<\Delta\gamma>$ of an electron with a fixed P_z, as a function of the initial I, in the linear regime, for the OM with $m = 1$. The curves refer to different z – widths of the radiation beam: $L = 50$, 100, 150, respectively. The injected power is the same in the three cases. The vertical dotted line indicates the resonant I.

For the case of nonlinear regular motion, the behaviour of $\Delta\gamma(\mathbf{p})$ is nontrivial: it can be well interpreted physically and described analytically when the adiabatic conditions are satisfied. Under these costraints, $\varepsilon(z)$ and P_z are slowly varying in time and the integral $J = m/(2\pi)\int I\, d\theta$ performed along a phase space trajectory at fixed ε is an adiabatic invariant. It experiences jumps whenever a separatrix in the (θ, I) space is

crossed, providing the mechanism for the electron energy change. A net electron energy variation in the transition between two unperturbed states is made possible by the existence of a range of H_0 values (for $P_z^2 < 1/v_m^2 - 1$), where $I(H_0)$, at fixed P_z, is double valued (Fig.3). The two values of I, corresponding to different energies, characterize the upper and the lower branch of the H_0 -curve in the (θ, I) plane, with I values larger and lower than the resonant value I_m, respectively (see Fig.4).

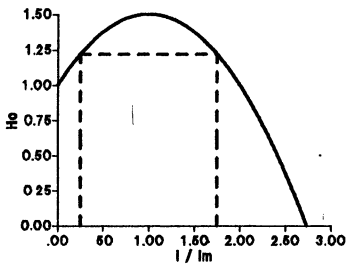

Fig. 3 Profile of the unperturbed Hamiltonian H_0 versus I, for a fixed P_z, satisfying the condition $P_z^2 < (1/v_m^2 - 1)$. Two action values corresponding to the same value of H_0 are shown. I_0 represents the resonant I.

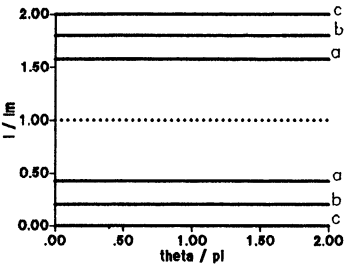

Fig. 4 Level curves of H_0 in the (θ, I) plane for $P_z^2 < (1/v_m^2 - 1)$. A same letter indicates the two branches of the same level curve. The dotted line corresponds to the resonant I value.

Let the trajectory of an electron with initial I_0 and P_{z0}, belonging to a given branch of H, cross firstly the separatrix at a given value $\varepsilon = \varepsilon_s$, while ε is increasing. The particle will change its energy only if its trajectory will end on the other branch of the Hamiltonian, after having crossed the separatrix, again at $\varepsilon = \varepsilon_s$, while ε is decreasing. Since the motion is adiabatic in each different stage, excluding the separatrix crossing, the variation in the action ΔI will be equal to the jump of the adiabatic integral at the separatrix $\overline{\Delta I}(\varepsilon_s, P_{zs})$. By the constancy of H, the corresponding energy variation is then $\overline{\Delta \gamma} = v_m \overline{\Delta I}$.

To determine $\overline{\Delta I}$, the values of ε_s and of P_{zs} are required. They can be computed in terms of the initial I_0, P_{z0} by means of the constancy of the adiabatic invariant J and of the Hamiltonian during the first stage of the motion

$$\begin{aligned} I_0 &= |J(\varepsilon_s, P_{zs})| \\ H_0(I_0, P_{z0}) &= H_s(\varepsilon_s, P_{zs}) \end{aligned} \tag{8}$$

being H_s the Hamiltonian on the separatrix. The condition for the occurence of the energy variation is $\varepsilon_s < \varepsilon_M$. Eqs.(8) then determine the nonlinear interaction region, i.e., the region in the space of initial momenta characterizing the electrons experiencing the energy transition. Outside this region $\Delta\gamma = 0$. The solution of Eqs.(8) requires the knowledge of the function $H_s(\varepsilon_s, P_{zs})$ and of the adiabatic invariant at the separatrix $J(\varepsilon_s, P_{zs})$. These two functions can be determined by the analysis of the trajectories in the (θ, I) plane, and, in particular, from the behaviour of the separatrix as ε varies. The explicit computation of $\overline{\Delta\gamma}$, the interaction region, and the absorbed power density can be easily performed in terms of a few parameters in the weakly relativistic limit, which applies to most cases of interest for plasma heating [7].

A net energy change can occur if the separatrix splits the (θ, I) plane in at least three regions with nonzero areas, at the moment of the crossing. The analysis of the singular points for the case of the first and second harmonic shows that this requirement is no more satisfied when ε exceeds a critical value $\varepsilon_c(P_z)$. In that case, during the stage of the motion with $\varepsilon > \varepsilon_c$, no further contribution to $\Delta\gamma$ is possible: this leads to the saturation of the interaction region in momentum space as ε_M is increased. A different behaviour occurs for $m \geq 3$ where the saturation process does not take place.

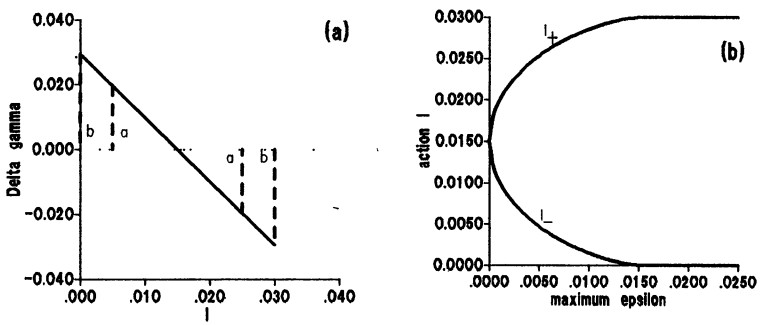

Fig. 5 (a) Net energy variation $\overline{\Delta\gamma}$ vs. initial I for different ε_M, for the XM with $m = 2$. The curve is symmetric with respect to $I = I_m$, $\overline{\Delta\gamma} = 0$, and coincides with the estimate (6). The curve b corresponds to $\varepsilon_M = \varepsilon_c$, curve a to a value $\varepsilon_M < \varepsilon_c$.
(b) Extrema of $\overline{\Delta\gamma}(I)$ as a function of ε_M at fixed P_z. $\overline{\Delta\gamma}$ is zero for $I < I_-$, $I > I_+$.

Note that $\overline{\Delta\gamma}$ at given P_z, I is a step function of ε_M, i.e., it is zero for $\varepsilon_M < \varepsilon_s(P_z, I)$, and assumes a value independent of ε_M for $\varepsilon_M > \varepsilon_s$. The behaviour of $\overline{\Delta\gamma}$ as a function of I, for fixed P_z, at different ε_M's, is shown in Fig.5a for the case of the extraordinary mode (XM) at the second harmonic. In this case, $\Delta P_z^2 \ll (\overline{\Delta\gamma})^2$, and the

curve is very well approximated by the expression (6) derived from the constancy of H_0 where ΔP_z^2 is neglected. In this approximation, $\overline{\Delta\gamma}$ is simply proportional to the difference $I_m - I$, and is truncated at $|I_m - I| = \delta I(\varepsilon_M, P_z)$, this last quantity saturating at I_m when $\varepsilon_M = \varepsilon_c(P_z)$. The saturation process can be visualized in Fig.5b, where the truncation values I_-, I_+ are represented as a function of ε_M.

By comparison with the previous case, $\overline{\Delta\gamma}(I)$ is represented in Fig.6a for the XM at the third harmonic. In this case, ΔP_z^2 is non negligible when I is far from I_m' : the approximation (6) is not valid at high ε_M , where the truncation values I_- , I_+ are no more symmetric with respect to I_m (Fig.6b).

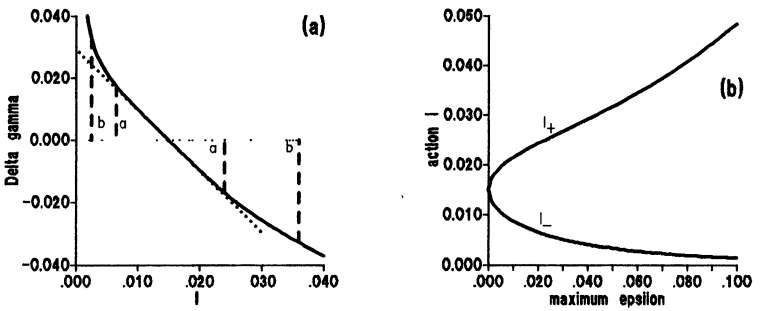

Fig. 6 Same as in Fig. 5 for the XM at the third harmonic. The dotted line represents the estimate (6).

When the conditions for a transition are satisfied, the energy variation can be either 0 or $\overline{\Delta\gamma}$, according to the final H_0 branch. The averaged energy variation $<\Delta\gamma>$ can be expressed as $<\Delta\gamma> = q\overline{\Delta\gamma}$, where q represents the probability for the energy transition. The transition probability to the upper (lower) branch with respect to the separatrix can be estimated, under the condition of an uniform phase distribution, in terms of the variations of the area enclosed by the separatrix S, and of the area of the upper (lower) region $S_{u(l)}$, when crossing occurs [14]

$$q_{u(l)} = \left| \frac{\dot{S}_{u(l)}}{\dot{S}_s} \right| . \tag{9}$$

The explicit computation can be performed analytically in the weakly relativistic approximation, giving 1/2 for $m = 1$, 2, and exhibiting a non trivial dependence on the

parameters for $m > 2$, and in the weakly nonlinear case, where it reduces to 1/2, for any m [7].

An example of nonlinear interaction region in momentum space is shown in Fig. 7 , for different ε_M 's for the XM with $m = 2$. For vanishing ε_M it corresponds to a very small region around the resonant curve. For increasing ε_M it covers an increasing area, which tends to saturate, according to the previous discussion.

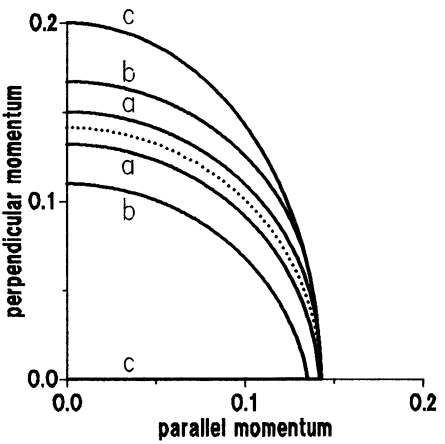

Fig. 7 Nonlinear interaction region in momentum space, in case of the extraordinary mode at the second harmonic for three different values of ε_M: $\varepsilon_a < \varepsilon_b < \varepsilon_c$. The dotted line represents the resonant condition.

We are able now to compute the absorbed power per unit area in the plane (x, y), which can be written in the following form [5 – 7]

$$W = mc^2 \int d\mathbf{p}\, f_0(p_z, p_\perp)\, \frac{|p_z|}{\gamma} < \Delta\gamma > \tag{10}$$

where f_0 the unperturbed electron distribution function, and the integration is performed over the interaction region.

In the linear case, taking into account Eq.(7), the Eq.(10) reduces to

$$W = -\, \nu_m m^2\, \frac{\pi}{2} \int d\mathbf{p}\, \frac{\partial f_0}{\partial I}\, \frac{\Theta_m^2}{\gamma |p_z|}\, F^2. \tag{11}$$

The absorption profile $W(v)$ for a Maxwellian f_0 is plotted in Fig. 8 for the OM at the first harmonic, for different beam widths L. It is proportional to ε_M^2, exhibits the broadening due to the non uniform field amplitude, and tends to the well-known uniform amplitude profile, when $L \to \infty$.

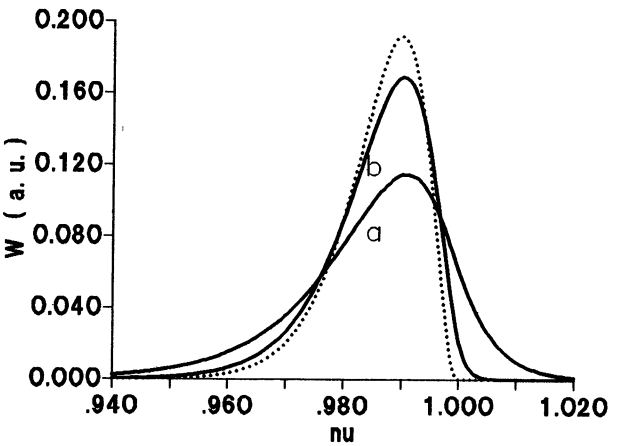

Fig. 8 Absorbed power density versus the normalized frequency v_1 for the OM at the first harmonic, in the linear regime, for a Maxwellian plasma. Curves a and b refer to increasing width L of the beam. The dotted curve corresponds to $L \to \infty$. The injected power is kept constant. A 2 *keV* electron temperature has been chosen.

Concerning the nonlinear case, we present here the results for the absorbed power density W obtained for a Maxwellian distribution function f_0 of temperature T_e. To check the validity of the theory, these results have been compared with those obtained by a numerical simulation code which integrates the equations of motion for a representative set of particles. The comparison for the case of XM at the second harmonic is shown in Fig. 9. The agreement between numerical simulations and analytical computations is excellent. We note that the nonlinear absorption profile is generally broader than the linear, with a maximum shifted at a lower frequency v_m, exhibiting, as expected, much lower values. A simple expression for the behavior of W with ε_M and v_m cannot be found in the general case since these quantities are contained in the integration limit in Eq. (10) in a non trivial way.

The behavior of the absorption profile, for XM with $m = 2$, as ε_M varies, is shown in Fig. 10. Its main features are valid for $m = 1, 2$, independently of the polarization.

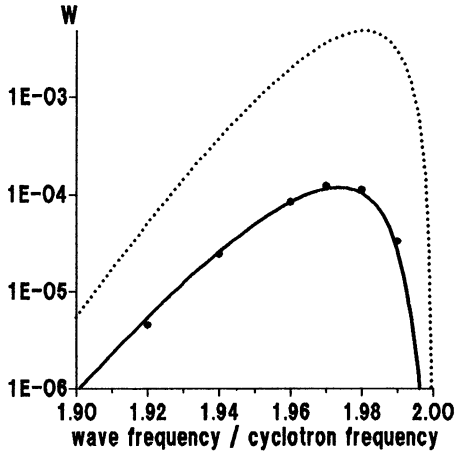

Fig. 9 Profile of the normalized absorbed power W as a function of ω/Ω, for XM with $m = 2$, and $N\varepsilon_M\eta_- = 5 \times 10^{-3}$. A Maxwellian unperturbed function f_0 has been chosen, with $T_e = 2\,keV$. The solid line is obtained from Eq. (10). The points represent the results obtained by means of a numerical simulation code which solves the equations of motion for a particle ensemble. The linear profile is represented by the dotted line.

A peculiarity of the family of curves is the existence of a limit profile W_l as ε_M is increased. This can be viewed in two different ways: (i) at a fixed frequency ν_m, a maximum value of the absorbed power density is reached when ε_M reaches the critical value, mentioned previously, which corresponds to the saturation of the nonlinear interaction region; if the field amplitude is furtherly increased the absorbed power density maintains itself constant; (ii) at a fixed ε_M there exists always a ν_m interval with upper limit 1 where the absorption assumes the limit value W_l; this interval, which depends on the mode under consideration, enlarges toward lower ν_m values when ε_M is increased. The limit profile W_l depends only on ν_m and the electron temperature, and is independent of the polarization. It can be computed evaluating the integral (10) over the saturation region (i.e. in the formal limit $\varepsilon_M \to \infty$), and reads

$$W_l = \frac{2^{1/2}}{\pi^{1/2}\mu^{3/2}}\left[s_m - 3 + \frac{1}{\nu_m} - \frac{3}{\mu} + \frac{4}{\nu_m}e^{-s_m} + \left(s_m - 3 + \frac{1}{\nu_m} + \frac{3}{\mu}\right)e^{-2s_m}\right], \quad (12)$$

where $\mu = mc^2/T_e$, and $s_m = \mu(1/\nu_m - 1)$.

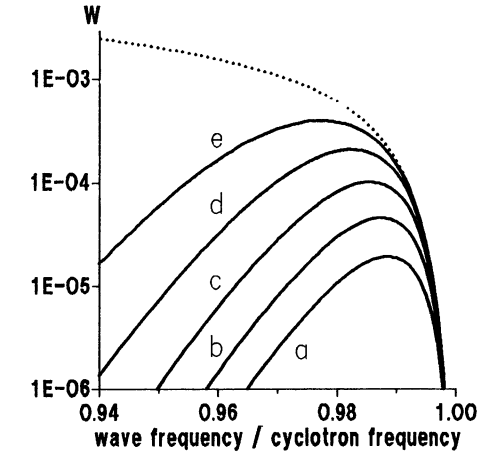

Fig. 10 Absorbed power density profile for different values of ε_M, for the XM with $m = 2$ Curves a to e refer to increasing ε_M. The dotted curve represents the saturation.

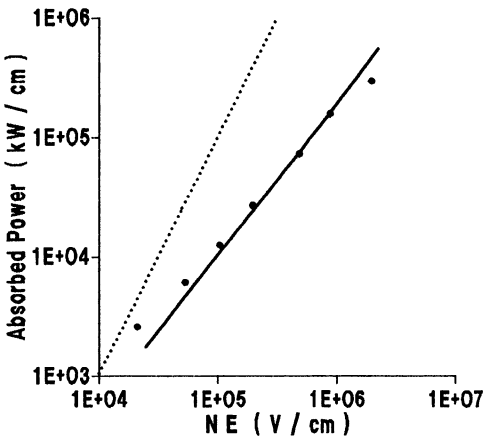

Fig. 11 Comparison between the integrated values of W over the propagation direction x for different $N E$ values, resulting from our model (solid line) and from the numerical simulation performed in Ref. 1 (points). The ordinary mode at the first harmonic has been considered. The dotted curve represents the linear result. The reference parameters are $B_0 = 5\ T$, $n = 10^{14}\ cm^{-3}$, $T_e = 1\ keV$.

Referring now to the total absorbed power (proportional to $\int W\,dv$ in the case of a nonuniform magnetic field), the comparison between the integrated values of W over the propagation direction x, for the ordinary mode at the first harmonic, resulting from our theory and from the simulation performed in Ref. 1 is shown in Fig. 11. The agreement is quite good in the central region of the plot, where our analysis is valid, since it corresponds to adiabatic motion. The behaviour in the strongly nonlinear regime is found to be very close to a $\varepsilon_M^{4/3}$ scaling [1, 4, 5]. We stress the fact that in our model there are no free parameters, so that the curve has not been adjusted for a better fit of the numerical results.

Stochastic regime

When the regions in the (θ, I) plane relevant to the regular motion around two adjacent resonances overlap, a trajectory can pass from one region to the other. In this condition the reduction to the Hamiltonians (4) is no longer possible, and the motion is described by the complete Hamiltonian (2). We compare here two possible interaction scheme, the OM with $m = 1$, and the XM with $m = 2$. The investigation has been performed at constant ε. An extension of the Chirikov criterium of resonance overlapping [12], taking into account the actual shape of the separatrix, has been used to determine the threshold value of the perturbation ε_R for the transition to stochasticity. In Fig. 12 the widths of the separatrices relevant to the two cases are plotted versus ε, showing no overlapping at reasonable ε for the OM and overlapping for the XM for $\varepsilon > 0.12$.

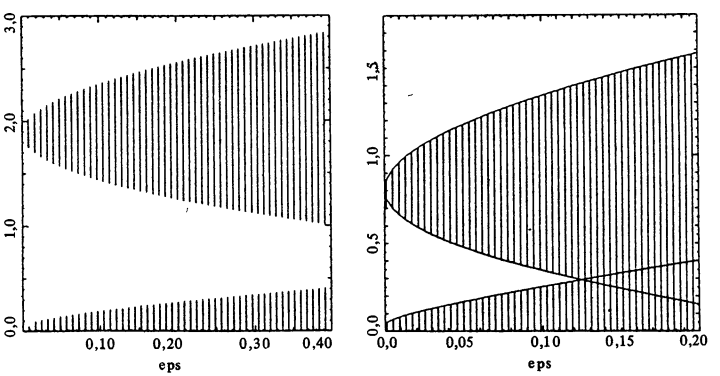

Fig. 12 I – width of the resonance versus ε for the OM with $m = 1$ (left), and the XM with $m = 2$ (right), at $P_z = 0.4$, and $v_m = 0.9$.

The transition to the stochastic regime has been investigated by means of the Poincaré surfaces of section, at fixed θ_2, obtained by a mapping derived analytically from the equations of motion. An example of such surfaces for the XM is shown in Fig. 13 , for different values of ε. In the case under consideration overlapping occurs, above the threshold, for all $m \geq 2$.

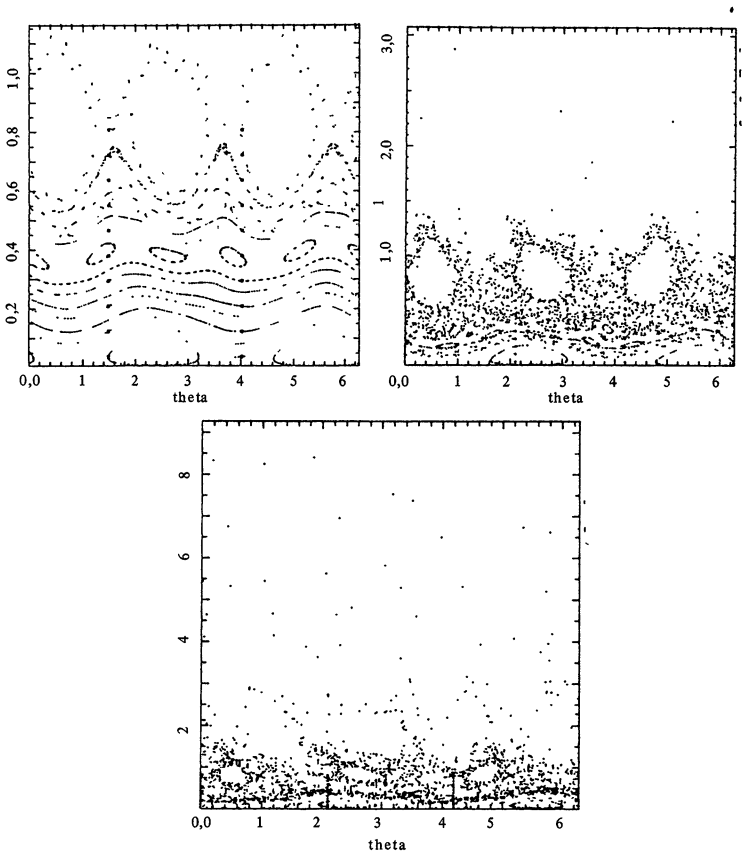

Fig. 13 Poincaré surfaces of section ($\theta_2 = \pi$) for the extraordinary mode, for ε values 0.03, 0.07, 0.1 and $\nu = 1.8$. Λ mapping for the Hamiltonian system (2) has been used.

When the global stochastic regime is established the diffusion process in phase space can be described by a Fokker-Planck-Kolmogoroy (FPK) approach, which allows the computation of the diffusion coefficient in the variable I [9,10]:

$$\frac{\partial f}{\partial I} = \frac{\partial}{\partial I}\left[D(I) \frac{\partial f}{\partial I} \right] \tag{13}$$

with

$$D(I) = \frac{\pi}{2} \frac{\varepsilon^2}{\gamma^2 \nu^3} \sum m^4 \Theta_m^2(I)\, \delta(I - I_m) \tag{14}$$

An average diffusion coefficient can be defined as

$$d = \frac{1}{\Delta I} \int dI\, D(I) \tag{15}$$

where the integration is performed over the resonant diffusion region ΔI [10].

The integration of the equation of motion has been performed for a representative set of particles (N_p), with initially the same actions and an uniform distribution in the angle variables. The numerical average energy gain, defined as

$$\Delta\gamma(t) = \frac{1}{N_p} \sum_{i=1}^{N_p} \nu(I_2(t) - I_{20}), \tag{16}$$

and the numerical average diffusion coefficient

$$d_c(t) = \frac{1}{N_p} \sum_{i=1}^{N_p} \frac{(I_i(t) - I_0)^2}{t}, \tag{17}$$

are represented in Fig. 14.

We have verified the consistency between the average diffusion coefficient (15) and the numerically computed value (17). It is generally found that, in addition to a diffusion process of most electrons, groups of very few particles acquire energies largely exceeding those foreseen by a FPK diffusion.

By the same simulation, the process of redistribution of the action I among the different harmonics, starting from a peaked distribution, has been described, as shown in Fig. 15.

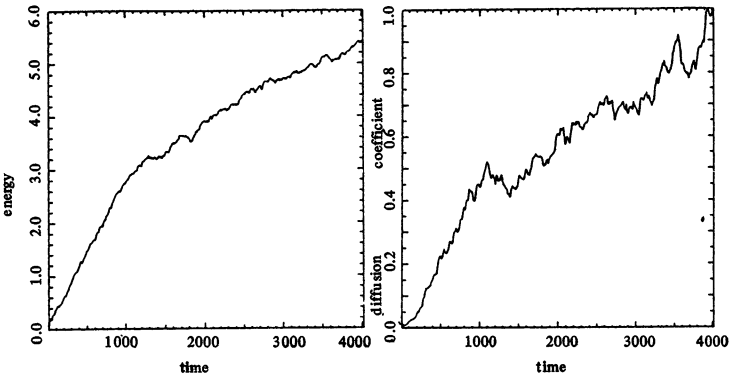

Fig. 14 Time evolution of the average electron energy (left) and of the average diffusion coefficient of the action I (right). The parameters are $\nu = 1.8$, $P_z = 0.1$, $\varepsilon = 0.13$, $N_p = 100$, and the value of the diffusion coefficient is normalized over its maximum value 0.28.

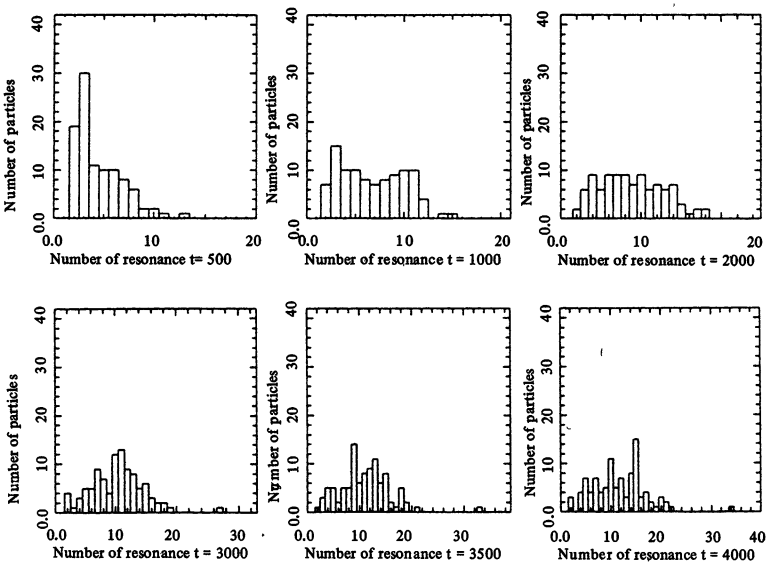

Fig. 15 Time evolution of the distribution of the action I among the different harmonics. The particles start with the same I close to the resonant value at the 2nd harmonic. Extraordinary mode is considered, $\nu = 1.8$, $\varepsilon = 0.1$.

Conclusions

For the case of regular motion, we have performed a theoretical investigation of the process of the linear and of the adiabatic nonlinear power absorption of an electron cyclotron wave with space dependent amplitude in perpendicular propagation. This analysis provides the computation of the absorbed power density at any cyclotron harmonics. The theoretical model is based on the analysis of a constant Hamiltonian, and, in the nonlinear case, on the adiabatic invariance of the action integral.

Concerning the linear regime, we have pointed out the modifications of the absorption profile due to the localization of the field. We note that this analysis applies also to the case of intense, strongly localized fields, provided that the condition $\tau_F < \tau_T$ be verified.

In the nonlinear regime, the obtained results have been shown to agree with those obtained by a numerical simulation code which integrates the motion equations. The computation of W is reduced to the quadrature. The main features of the results have been interpreted by means of the investigation of the nonlinear interaction region in momentum space. For $m = 1, 2$, it has been shown that for a fixed frequency the nonlinear absorption attains a saturation value which depends only on ν_m and T_e, reflecting the saturation of the nonlinear interaction region. For $m \geq 3$, this process does not occur. The absorbed power depends only on the maximum value ε_M of the field amplitude and not on its profile, provided that adiabatic conditions be satisfied. The value of ε_M controls the extension of the interaction region, while it is inefficient in varying the change in electron energy, once the minimum condition for the occurence of the transition is reached.

Finally, we observe that, when adiabaticity conditions are not met, the energy gain process can differ considerably from the adiabatic case. To illustrate this point we compare in the two cases the evolution of the action I and of the phase θ for a set of initial conditions characterized by the same I value and uniformly distributed phases. Under adiabatic conditions, the two different final energy states are approximately equally reached by the particles (Fig. 16), and the phases remain uniformly distributed during the whole motion.

In a nonadiabatic case the probability for the transition to one of the final states differs from the theorical value computed assuming adiabaticity, and can even be 1, as in the case shown in Fig. 17, where all particles pass to the higher energy state, gaining the energy $\overline{\Delta\gamma}$. At the same time, a bunching of the phases occurs.

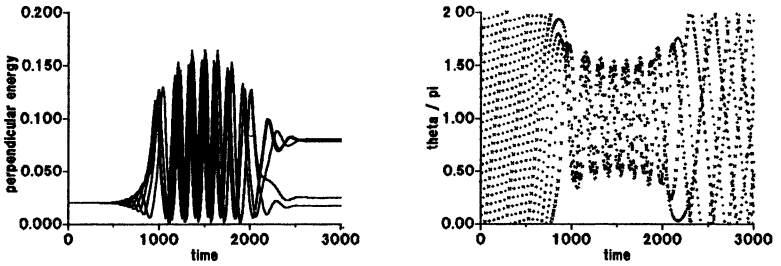

Fig. 16 Time evolution of the perpendicular energy $2I$ and of the phase θ (normalized over π (mod 2)) of a set of particle with the same initial I, P_z, and with uniformly distributed initial phases θ. The $\varepsilon(z)$ profile has been chosen in order that adiabatic conditions be satisfied.

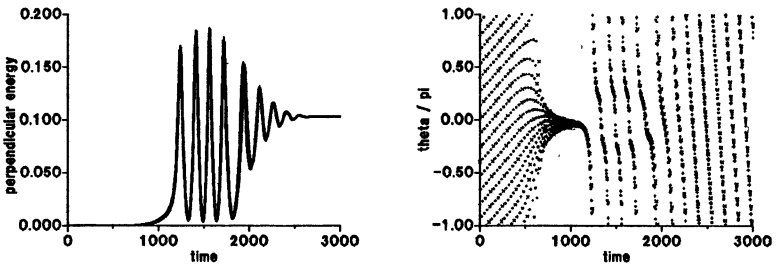

Fig. 17 Time evolution of the perpendicular energy and of the phase θ in a non adiabatic case. All particles experience the same energy transition. The process of phase bunching is apparent.

Referring to the stochastic regime, we have in particular investigated the XM at the second harmonic. We have found that in perpendicular propagation the energy diffusion of most electrons is in agreement with the picture derived by the FPK approach. No saturation of the diffusion coefficient is observed.

References

[1] W. M. Nevins, T. D. Rognlien and B. I. Cohen, Phys. Rev. Lett. **59**, 60 (1987).

[2] E. V. Suvorov and M. D. Tokman, Sov. J. Plasma Phys. **14**, 557 (1988).

[3] C. R. Menyuk, A. T. Drobot and K. Papadopoulos, Phys. Rev. Lett. **58**, 2071 (1987).

[4] I. A. Kotel'nikov and G. V. Stupakov, Phys. Fluids B, **2**, 881 (1990).

[5] D. Farina, R. Pozzoli, D. Ronzio, Internal Report FP 89/12, Istituto di Fisica del Plasma, C.N.R., Milano, Italy (1989).

[6] I. A. Kotel'nikov and G. V. Stupakov, Preprint 89-100, Institute of Nuclear Physics,Novosibirsk (1989).

[7] D. Farina, R. Pozzoli, Internal Report FP 90/4, Istituto di Fisica del Plasma, C.N.R., Milano, Italy (1990). D. Farina and R. Pozzoli, Proc. 17th EPS Conference on Controlled Fusion and Plasma Heating, Amsterdam 1990, III, 1088 (1990);

[8] C. R. Menyuk, A. T. Drobot and K. Papadopoulos, H. Karimabadi, Phys. Fluids **31**, 3768 (1988).

[9] R. Z. Sagdeev, D. A. Usikov, G. M. Zaslavsky, *Nonlinear Physics from the Pendulum to Turbulence and Chaos*, (Harwood Academic, 1988), and references therein.

[10] K. Hizanidis, L. Vlahos, C. Polymilis, Phys. Fluids B **3** , 682 (1989)

[11] A. Mennella, R. Pozzoli and D. Ronzio, Proc. 17th EPS Conference on Controlled Fusion and Plasma Heating, Amsterdam 1990, III, 1104 (1990).

[12] B.V. Chirikov, Phys. Rep. **52**, 263 (1979).

[13] A. J. Lichtenberg, M. A. Lieberman, *Regular and Stochastic Motion*, (Springer-Verlag, New York, 1983).

[14] A.I. Neishtad, Sov. J. Plasma Physics, **12**, 568 (1986).

FOKKER-PLANCK MODELLING OF RF HEATING AND CURRENT DRIVE

G. Giruzzi

ASSOCIATION EURATOM-CEA SUR LA FUSION
Département de Recherches sur la Fusion Contrôlée
Centre d'Etudes Nucléaires de Cadarache
13108 - Saint-Paul-lez-Durance (FRANCE)

Abstract. Present-day RF heating and current drive experiments in tokamaks are very often characterized by strong distortions of the electron or ion velocity distribution functions. This is due to the RF-induced diffusion in velocity space, which, for high wave power, can easily be dominant over Coulomb collisions and lead to the generation of high energy tails. These distorted distribution functions can be described by simple analytical models in special cases only. A unified approach to describe the plasma behaviour in these regimes consists in solving the appropriate quasilinear / Fokker-Planck equation for the phase-space distribution function. The main physical effects to be included in this equation and the numerical methods used to solve it are discussed. In order to illustrate the method, some applications to electron-cyclotron and lower-hybrid waves interacting with superthermal electrons are presented.

1. Introduction

The importance of non-Maxwellian electron distributions in plasma physics has greatly increased in the last years. Ten years ago, the only relevant non-Maxwellian electron distribution in tokamaks was the runaway distribution, generated by the action of the dc electric field in low-density discharges, consisting of a long flat tail in the velocity direction parallel to the toroidal magnetic field [1]. In the early 80's, a new class of non-thermal distributions was observed during the first lower hybrid current drive (LHCD) experiments [2]. Those experiments were performed in conditions (low density, parallel refractive index $n_{\parallel} \rightarrow 1$) such that the electron distribution was characterized by a long flat parallel tail as well. However, this tail is generated by a physical process of quite different nature, i.e., not by a steady parallel force (as in the case of the dc electric field),

but rather by parallel diffusion in velocity space. The structure of the distribution turns out to be different, especially in the perpendicular direction, in which a tail is also generated due to collisional pitch-angle scattering. Since then, the parameter range of LHCD experiments has been considerably extended, particularly to higher densities (which changes the structure of the tail via the extension of the accessible $n_{\parallel}$ range) and higher powers [3]. The possibility of a spatial tayloring of the LH-driven tails has been demonstrated [4], which poses the problem of spatial diffusion of the fast electrons. An important addition to this wide data base will be given by the forthcoming JET experiment, aiming at localized LHCD [5].

At the same time, electron cyclotron current drive (ECCD) was experimentally demonstrated as well [6,7]. Since this CD method relies on wave-induced perpendicular diffusion and subsequent transfer of energy into the parallel direction by collisions, the structure of the electron distribution is quite different from that of a LH-sustained tail. Moreover, relativistic and toroidal effects lead to a further splitting of the ECCD regime into two different regimes, depending on whether the wave frequency ω is larger or smaller than the EC frequency ω_{ce}. These two regimes are characterized by a substantially different behaviour of the trapped electron populations and therefore by tails of different structure [8]. Interplay with the dc field [9], often important in ECCD experiments, or with LH waves in combined experiments [10] generate additional new features. Fast wave current drive (FWCD) experiments are expected to start very soon [11]. They will be characterized by the simultaneous presence of two different wave-particle interaction mechanisms, namely, Landau damping and transit-time magnetic pumping (TTMP), which should lead to a new class of non-thermal distributions [12]. If, in addition, we also consider the distorted distributions generated during high-power ion cyclotron [13] or EC heating, we come to the conclusion that in the last ten years an abundant and varied fauna of non-Maxwellian distributions has developed in tokamak experiments, as a result of the different RF heating and CD methods.

The growing number and variety of these non-Maxwellian populations poses two main problems, i.e., i) how to detect and measure the salient

features of these distributions; ii) how to model them theoretically. The two questions are strongly connected to each other, since a very refined theoretical modelling calls for adequate diagnostics of the modelled features and viceversa. Now, the runaway distribution results from a relatively simple physical process, involving a steady, nearly uniform electric field and Coulomb collisions only. For this reason, excellent analytical theories exist, describing the structure of the runaway distribution [1]. On the other hand, modelling the effects of the RF diffusive process is much more difficult, since the diffusion coefficient generally has a complicated structure in phase space. Some analytical modelling of the LH tail is possible in the saturation regime, i.e., when the effect of the RF is dominant over the collisions, but this does not hold uniformly in phase space. Simple analytical models for the ECCD and FWCD distribution functions do not exist. Another possible approach consists in representing the distribution function by a model form, with a number of adjustable parameters, which can in principle be determined by appropriate diagnostics, such as EC or X-ray emission. Unfortunately, this method has proved ambiguous in most attempts of determining the structure of non-thermal distributions, the constraint represented by the chosen analytical model being usually too strong.

For these reasons, it seems important to look for a unified approach to the problem. An approach of this type, which is gaining more and more credit in plasma physics, is now made possible by the use of large, vector-processing computers, and consists in solving the appropriate Fokker-Planck equation for the phase-space distribution function numerically. This equation contains a diffusion term describing the effect of the RF power on the electron distribution, derived in the framework of the quasilinear theory. In this paper, a review is given of the theoretical basis of this method and of the physical effects which can be described in this approach. The plan of the paper is the following. In Sec. 2, the theoretical framework of the method is presented. In Sec. 3, some numerical methods used to implement the Fokker-Planck equation on a computer are shortly reviewed. Some examples of physical effects which were fully investigated by use of Fokker-Planck

codes are discussed in Sec. 4, focussing on EC and LH current drive and on comparisons between Fokker-Planck simulations and tokamak diagnostics. The conclusions are drawn in Sec. 5.

2. The quasilinear/Fokker-Planck equation

The goal of this method is, given the plasma and RF parameters as an input, to solve for the phase-space distribution function (of the electrons and/or of the ions), then to use this result to compute the measurable quantities which are the output of the plasma diagnostics. Thus, the first important point in the discussion of the theoretical framework of the method is: what is the appropriate phase space in which the problem has to be solved. We are mainly interested in the investigation of an RF-driven steady-state, established by the competing effects of RF wave absorption and collisions, thus we are interested in phenomena characterized by a time scale longer than a collision time. In a magnetic confinement machine, typically a tokamak, particles are subject to much faster motions, i.e., gyration around the magnetic field lines and drift along the magnetic flux surfaces. Thus, the equation for the distribution function can be averaged over these two fast particle motions. As a result of this averaging and of the geometrical symmetries of the magnetic configuration (e.g., in a tokamak the axial symmetry around the torus axis), the problem to be solved is 2-dimensional in velocity space (parallel and perpendicular velocities with respect to the magnetic field) and 1-dimensional in ordinary space (in a tokamak, the flux or radial coordinate). Further reductions in dimensions are generally motivated by drastic approximations and will not be considered in the following. The basic ingredients of the model discussed here are:

a) RF-field propagation and absorption
b) Quasilinear approach to the Vlasov equation
c) Fokker-Planck theory of Coulomb collisions
d) Bounce-averaging along the flux surfaces
e) Radial transport.

2.a RF-field propagation and absorption

The input of the calculation is the spatial structure of the RF field in the plasma, given its structure at the launching antenna. That structure is determined by the following effects:

i) coupling antenna/plasma (diffraction)

ii) wave propagation (refraction)

iii) wave absorption.

For most applications a geometrical optics description of the wave propagation [14] is sufficient, at least outside the diffraction region close to the antenna. Note that the resulting ray trajectories depend on the gross plasma parameters only (density, current, magnetic field) and not on the actual distribution function. On the other hand, wave absorption critically depends on the shape of the distribution function. Thus, the wave beam has to be split into several rays. For each of these rays the trajectory and the refractive index have to be computed by means of a ray-tracing code, starting from appropriate boundary conditions at the antenna mouth. This allows the computation of the initial wave damping, thus of the initial distribution of the wave power spectrum inside the plasma. As the distribution function evolves, the wave damping must be re-evaluated self-consistently. Since the absorption coefficient is generally given in terms of integrals of the distribution function in velocity space, the problem is integro-differential and non-linear, thus it generally calls for a time-dependent solution, computed in very short time steps.

2.b Quasilinear equation

The derivation of the familiar quasilinear equation for waves absorbed by a magnetized plasma [15] is here only sketched. The starting point is the Boltzmann equation for the distribution function $F(\vec{x};\vec{v};t)$ of particles of charge q and mass m, subject to static electric ($\vec{E}_o$) and magnetic ($\vec{B}_o$) fields as well as to the wave field $\vec{E}$, $\vec{B}$:

$$\frac{\partial F}{\partial t} + \vec{v}\cdot\frac{\partial F}{\partial \vec{x}} + \frac{q}{m}\left[(\vec{E}_o + \vec{E}) + \frac{\vec{v}}{c} \times (\vec{B}_o + \vec{B})\right]\cdot\frac{\partial F}{\partial \vec{v}} = C(F) \qquad (1)$$

where C(F) is the collision term. The distribution function F is split into the sum of a rapidly oscillating part $\tilde{f}$ and a slowly varying part f. By time-averaging Eq.(1) and neglecting mode-coupling terms [15] the following equation for the slowly varying part $f(v_{\parallel}, v_{\perp}; r; t)$ can be obtained

$$\frac{\partial f}{\partial t} = \frac{\partial}{\partial \vec{v}} \cdot \vec{\vec{D}} \cdot \frac{\partial f}{\partial \vec{v}} - \frac{q}{m} \vec{E}_0 \cdot \frac{\partial f}{\partial \vec{v}} + C(f) \quad . \tag{2}$$

Equation (2) contains a collision term, to be specified later, a convective term, describing the effect of the dc electric field, and a diffusion term due to the RF. This diffusion is essentially parallel to $\vec{B}_0$ for Landau and TTMP effects (i.e., for LH waves and FW), and essentially perpendicular (with a small parallel component for $N_{\parallel} \neq 0$) for EC waves. Detailed expressions of the diffusion coefficient, specific to different waves, can be found, for instance, in Ref. 16 (LH), Ref. 17 (FW) and Ref. 18 (EC). The general structure of the diffusion coefficient is

$$\vec{\vec{D}}(r) = \int \delta\vec{k}\, \vec{\vec{A}}\,(\vec{k},\omega)\, \frac{P_{rf}(\vec{k},r)}{S(r)}\, \delta(\omega - n\omega_c/\gamma - k_{\parallel} v_{\parallel}) \quad , \tag{3}$$

where $\vec{k}$ is the wave vector, S(r) the area of the flux surface of radius r, the tensor $\vec{\vec{A}}$ describes the wave polarization, n is the harmonic number (n = 0 for Landau damping or TTMP), and γ is the relativistic mass variation factor, an essential ingredient of the equation for EC waves. Note that the resonance condition contained in the δ-function gives $\vec{\vec{D}}$ a well defined structure in velocity space. P_{rf} is the local RF power spectrum at the location r. It is essentially determined by the damping the wave beam has suffered before attaining the flux surface S(r), i.e.,

$$P_{rf}(r) = P_{in} \exp\left[-\int_0^{\ell(r)} d\ell'\, \alpha(k_{\parallel},\omega)\right] ,$$

where P_{in} is the injected wave power, ℓ is the arc length along the ray trajectory, and α is the wave absorption coefficient, depending on f, as discussed in Sec. 2a.

2.c Fokker-Planck collision operator

The Coulomb collision term in the Fokker-Planck form writes [19]

$$C(f) = \sum_{\alpha} \frac{\partial}{\partial \vec{v}} \cdot \left[\vec{\vec{D}}_{coll}(f_{\alpha}) \cdot \frac{\partial f}{\partial \vec{v}} - \vec{F}_{coll}(f_{\alpha})\, f \right] \qquad (4)$$

where the sum is over different ion species and electrons. The term in Eq. (4) contains both collisional diffusion and friction, and, in general, it is an integro-differential term. For RF heating and CD problems, much simpler forms of this term are usually appropriate [20]. Expansion of the coefficients in Eq. (4) in Legendre harmonics, truncated at the 1st order, is generally sufficient to obtain a correct estimate of the current drive efficiency. CD problems typically involve tail electrons, for which $v >> v_{thermal}$, which allows a useful asymptotic expansion of Eq. (4). This reduces the problem to a differential one (instead of integro-differential). However, it has been shown that at reactor-relevant temperatures some important current drive effects are due to the full integro-differential structure of the collision operator [21].

2.d Bounce-averaging

Because of the fast electron and ion motion along the flux surfaces, Eq. (2) has to be averaged along those surfaces and, as a consequence of this average, the distribution function turns out to be a function of r, $v_{\parallel}$, $v_{\perp}$ only. In this averaging, the adiabatic invariant $v_{\perp}^2/B$ has to be conserved. This means that a given particle will have two different perpendicular (and parallel) velocities while interacting with the RF on the high or low B-field side of a given flux surface. This has to be properly taken into account in the averaging procedure [22]. Moreover, high $v_{\perp}$, low $v_{\parallel}$ particles may be trapped at the low-field side of the flux surfaces, thus they cannot interact at all with the RF on the high field side. This well-known effect, due to the toroidal structure of the tokamak geometry, has an important impact on off-axis current drive (the number of trapped particles increases with r). In fact, trapped electrons do not circulate toroidally, thus they do not contribute to the plasma current and therefore the RF power absorbed by them is lost

for current drive. The methods for implementing these effects in a Fokker-Planck code are exhaustively described in Refs. [13, 23]; examples of toroidal effects on the quasilinear evolution of the electron distribution function will be shown in the following.

2.e Radial transport

Although radial transport takes place on long time scales, it can have important effects on the overall physical process. In fact, it determines a sort of slow non-local response of the plasma to the RF interaction. Since radial transport is determined by several complicated macroscopic and microscopic processes, and in particular the effect of those mechanisms on fast electrons is largely unknown, at the present state of the art radial transport can be included in the quasilinear / Fokker-Planck equation via model terms only. Typically, this can be done by adding to Eq. (2) the term [24]

$$\left(\frac{\partial f}{\partial t}\right)_{tr} = \frac{1}{r}\frac{\partial}{\partial r}\left[r D_{tr}(\vec{v},r)\frac{\partial f}{\partial r} + V_{tr}(\vec{v},r)\, f\right] \qquad (5)$$

where the radial transport is described by a diffusion coefficient D_{tr} and by a pinch velocity V_{tr}. However, the functional dependences of these two transport coefficients on $\vec{v}$ and on r are unknown and only ad hoc forms can be used. For this reason, including radial transport in the quasilinear / Fokker-Planck equation, although of great importance and physical interest, changes the nature of the model, introducing ad hoc terms together with quasilinear and collision terms which are derived in well-established theoretical frameworks. Without any doubt, this is the area in which Fokker-Planck modelling needs most theoretical effort and in which the most challenging problems can be formulated.

3. Numerical methods

The quasilinear/Fokker-Planck equation can be solved by standard numerical methods used in partial differential equations. The specific way in which these methods can be applied to solve Eq. (2) are extensively discussed in Refs. [20, 25], which contain exhaustive and detailed lists

of the typical problems encountered and of the special tricks needed to solve them. A commercially available subroutine exists in the IMSL library, which has been succesfully applied to solve the Fokker-Planck equation in typical current drive problems [26]. Here, the numerical methods used to solve Eq. (2) are only rapidly sketched.

The solution of the quasilinear/Fokker-Planck equation is a mixed initial condition / boundary value problem. Usually, the initial condition is the thermodynamic equilibrium in the presence of Coulomb collisions only, i.e., a Maxwellian distribution. The natural boundary of the problem is a surface at velocity high enough that the number of electrons excluded from the computation is negligible and that no appreciable interaction with the external RF or dc fields takes place. In this case, the distribution function at the high-velocity boundary can be assumed to be unchanged from the initial Maxwellian. An important and well-known exception to this assumption is the runaway problem, in which the interaction with the dc electric field is not only non-negligible, but maximum at very high velocities. However, in this case the asymptotic solution for high velocities (i.e., negligible collisions) is known, and can be employed as a boundary condition instead of the Maxwellian [27]. Other boundary conditions (internal boundaries) depend on the coordinate system used. Both polar coordinates (v,θ) and cylindrical ones $(v_{\parallel},v_{\perp})$ can be used, but generally polar coordinates are more adequate to treat the collision operator. For instance, in polar coordinates, the internal boundary conditions are

$$f(v=0,\ \theta) \text{ independent of } \theta$$

$$\partial f/\partial\theta(v,\ \theta=0) = \partial f/\partial\theta(v,\ \theta=\pi) = 0$$

$$\partial f/\partial v(v=0,\ \theta=\pi/2) = 0 \quad .$$

To these boundary conditions a symmetry condition must be added, imposing $v_{\parallel}$-symmetry of the distribution function in the trapping region [25]. The equation can be discretized either by using finite differences [20, 25] or finite elements [28, 26]. In both methods the solution is advanced in time, until a kinetic steady-state is attained. Using sufficiently short time steps allows to include the self-consistent evaluation of the wave damping. A steady-state solution can also be obtained directly, by using the appropriate differencing scheme [29, 30], and assuming that

the RF power deposition profile in space does not change from the initial one. This assumption, as it will be shown in the following, has important exceptions, and should be used cautiously. If it is valid, the steady-state solution can be obtained in a much shorter computer time than by computing the full time evolution. This method is particularly appropriate for coupling with long time-scale phenomena, such as radial transport [24]. In any case, the numerical solution of the Fokker-Planck equation can be made considerably faster by using vectorization techniques [20]. Simulating a RF-sustained plasma typically requires several minutes (or tens of minutes) CPU on Cray-like computers. The main problem comes from the fact that the coefficients of the equation are generally very awkward, being numerically computed themselves or non-linear, which makes the convergence of the equation difficult and to be established case by case.

4. Physical effects

The main interest of the method described in Secs. 2-3 is that it allows a thorough study of effects which otherwise could be the subject of qualitative investigations only. Some examples of kinetic effects of this kind are discussed in this section. One important point is to show that this method is a powerful tool for predicting the output of several tokamak diagnostics, thus for studying the potential of different diagnostic methods on a simulated distribution function, possessing the most important properties of the real ones. This is now routinely used to optimize the diagnostic systems and even to project new kinds of diagnostics.

4.a Saturation and enhancement of EC wave damping

Since the quasilinear term for EC waves is essentially a perpendicular diffusion term, the main effect of high-power EC heating is a perpendicular flattening of the electron distribution function, accompanied by an enhancement of the high-$v_\perp$ population. An example of this perpendicular stretching of the distribution function is given by Fig. 1, for the case of a 4 MW wave beam, injected perpendicularly

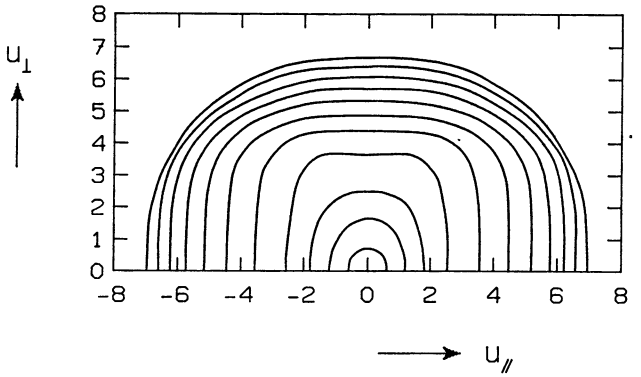

Figure 1. *Level curves of the steady-state electron distribution function at the plasma center, for R = 1.5 m, a = 0.4 m, frequency = 84 GHz, B = 3 Tesla. A Maxwellian distribution would be represented by equally spaced half-circles.*

to the magnetic field and absorbed close to the plasma center. Plasma density is 2×10^{13} cm^{-3}, the electron temperature is 2 keV; $u_{\parallel}$ and $u_\perp$ are the parallel and perpendicular electron momenta normalized to $mv_{thermal}$. The distribution function is computed by the code described in Ref. 31. The local absorption coefficient is an integral in velocity space, substantially proportional to the number of resonant electron and to the perpendicular derivative of the electron distribution function at the resonant velocity. Thus, two effects are generally present at the same time: the wave absorption decreases because of the perpendicular flattening [32] and it increases because of the enhancement in the superthermal population [33], the latter effect being dominant if the resonant velocity lies in the superthermal tail. Since ω_c varies in space, the resonant velocity also varies along the wave trajectory, thus the quasilinear stretching of the distribution function results in a spatial redistribution of the wave damping. This is shown

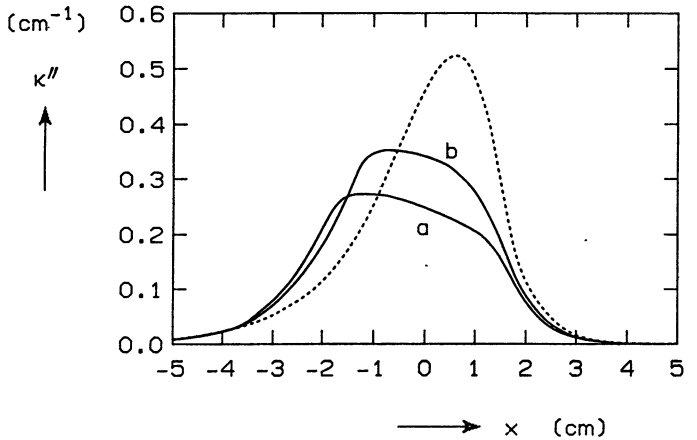

Figure 2. *Imaginary part of the wave vector (averaged over a wave beam with a 5 degrees angular spread) vs the radial position in the equatorial plane x, for the Maxwellian distribution (dashed line) and for the condition of Fig. 1, at 4MW (a) and 2 MW (b).*

in Fig. 2, for the conditions of Fig. 1, two values of the injected wave power, i.e., 4 MW (a) and 2 MW (b), and for the initial Maxwellian distribution (dashed line). The imaginary part of the wave vector is plotted as a function of the coordinate x along the radial direction in the equatorial plane, x = 0 being the plasma center. Since ω_c increases for decreasing x, the resonant velocity also increases and for $x < 0$ lies in the superthermal tail driven by the wave absorption itself, whereas for higher x values it lies in the flat region (see Fig. 1). It appears from Fig. 2 that both effects can be quite significant, causing variations in the local absorption coefficient as large as a factor of 2, for reasonable amounts of the injected wave power. This shows the importance of the self-consistent computation of the wave damping. For obliquely injected extraordinary modes (which is important for CD), the effect of damping enhancement is usually dominant [33].

4.b Toroidal effects on ECCD and ECE

A well-known example of important physical effect which has been quantitatively investigated by means of 3-D Fokker-Planck codes is the impact of electron trapping on ECCD [8,23,34,35]. The EC waves tend to increase the perpendicular velocity of the resonant electron, which can more easily become trapped; this is a negative effect for CD, since trapped electrons carry no toroidal current. A full relativistic Fokker-Planck analysis has been able to elucidate this effect, which is important for the choice of the best current drive scenario for next step devices (ITER). However, since a convincing experimental proof of these effects has not yet been found, it would be interesting to develop a diagnostic sensitive enough to detect such subtle kinetic effects. It has been suggested (and the suggestion supported by Fokker-Planck studies) [36] that vertical EC emission (ECE) could be quite useful to this end. This can be illustrated by the following example.

Let us consider an extraordinary wave beam, obliquely injected from the high field side, for the same tokamak parameters of Figs. 1-2. The space location where the beam is absorbed depends on the value of the magnetic field; in particular, two values can be chosen in such a way that the beam is absorbed off-axis at $r \simeq a/2$, but on the low-field side (case a) or on the high-field side (case b). Since on the high-field side there are no trapped electrons, the resulting steady-state distribution functions have quite different structures in the two cases, as shown in Fig. 3, for $P_{rf} = 2$ MW. Note the difference in the shape and extension of the distorted region and especially the different structure in the trapping region, i.e., the region between the two straight lines.

The corresponding differences in the vertically observed non-thermal radiation, evaluated from the computed distribution functions, are shown in Fig. 4. It appears that the trapped electrons, having large perpendicular energies emit quite intensely and their contribution dominates the non-thermal spectrum in case a). On the other hand, the emitted spectrum in case b) is very similar to the Maxwellian one (dashed line). Such large differences are easily detectable and should yield useful information on the role of electron trapping in the kinetic

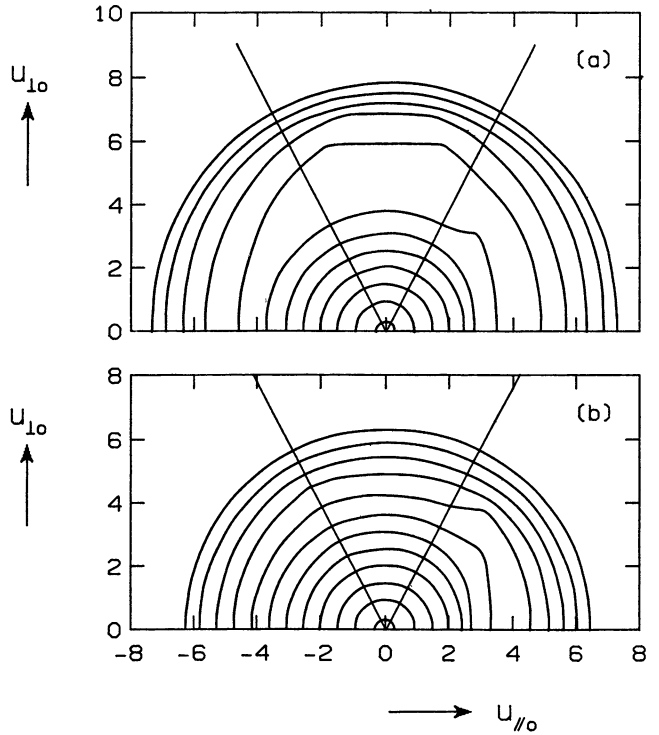

Figure 3. *Level curves of the computed steady-state distribution functions at r = a/2 = 20 cm; low-field side (a) and high-field side (b) absorption*

evolution during high-power EC heating and current drive. This is an example of how the Fokker-Planck modelling can help in projecting ideal experiments which can be used as diagnostics of specific physical effects.

4.c Tail electron relaxation

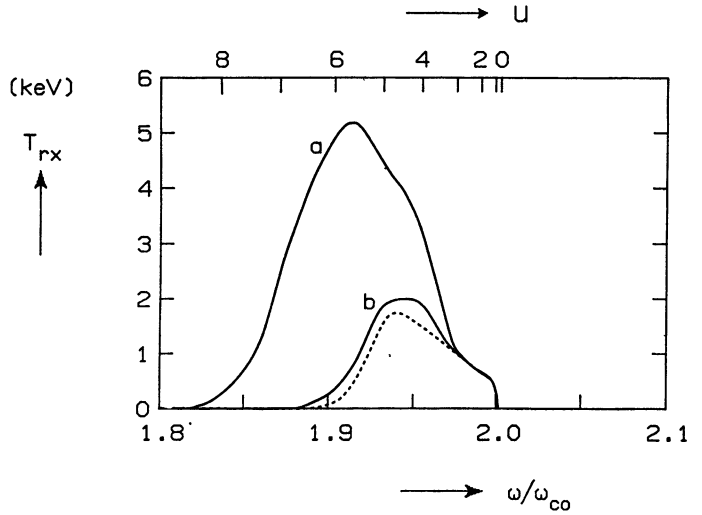

Figure 4. *Radiative temperature observed from a top location in the vertical direction, for the 2nd harmonic extraordinary mode. On the lower scale, frequency normalized to the central gyrofrequency. On the upper scale, the normalized resonant momentum.*

Fokker-Planck codes can be used to investigate not only the establishment of a non-Maxwellian equilibrium sustained by the RF, but also, of course, the transient phase after the end of the RF pulse, characterized by the relaxation of the electron tail back to the previous equilibrium state. This phase is extremely interesting, since in the absence of the RF perturbation the study of the dissipative processes is, in principle, much easier. The physics of these relaxation phenomena is particularly rich in the presence of runaway electrons [37]. Fig. 5a shows a typical runaway distribution in the plasma center, computed for medium size tokamak parameters ($n_e = 2 \times 10^{13}$ cm^{-3}, $T_e = 1.5$ keV, $E_{dc} = 2.7 \times 10^{-3}$ V/cm, R = 1 m, a = 0.2 m, B = 2.5 Tesla). This flat parallel tail is a good absorber of electron cyclotron radiation and can be used as a target for EC heating. After application of a long

pulse of EC wave power (70 kW), obliquely injected in the extraordinary mode at frequency 60 GHz, a new steady-state is set up, shown in Fig. 5b. If now the RF power is switched off, the distribution function

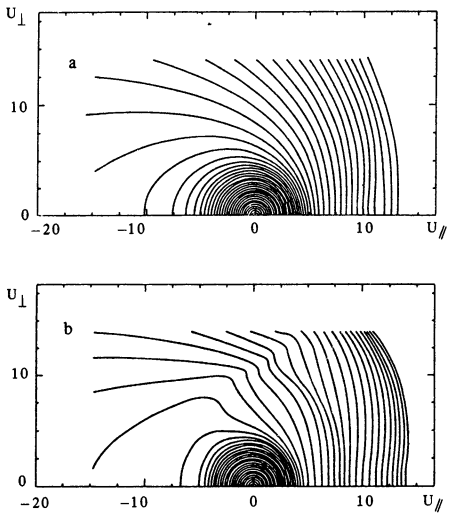

Figure 5. *Steady-state runaway distribution without (a) and in the presence (b) of 70 kW of EC wave power*

decays back to that shown in Fig. 5a, in a time of the order of 200 collision times. However, this process is not a trivial one, since it involves, for instance, the formation of positive slopes in the parallel distribution, accompanied by Cherenkov plasma wave emission and subsequent flattening of the tail on a lower level. As discussed in Ref. 37, during this transient phase the perpendicular energy of the tail electrons is redistributed, which yields peculiar ECE spectra, as those computed and shown in Fig. 6. Here τ is the time normalized to the collision time; the first spectrum (τ = 400) is related to the first (and last) steady-state, i.e., the runaway distribution of Fig. 5a. This spectrum is characterized by a radiation temperature much higher than the bulk temperature, as expected. The second steady-state is

obtained at the end of the RF pulse (τ = 700). Note the strong increase in the radiation temperature in the high-frequency part of the spectrum, associated to the part of the electron tail which was actually resonant with the EC wave. Finally, τ = 870 is an intermediate time during the relaxation phase, before the system returns to the initial state. Note that the radiation temperature has increased in a large part of the spectrum, indicating a significant amount of conversion of parallel into perpendicular energy during the relaxation. This result is not surprising, since an increase in the ECE signal after the RF pulse was observed in several experiments (see references in [37]). This example illustrates the interest of experiments in which an RF pulse is selectively coupled to a part of a pre-existing tail, in order to study its properties, and the essential role of a Fokker-Planck code in the interpretation of such experiments. Similar considerations hold for the LH tail [38].

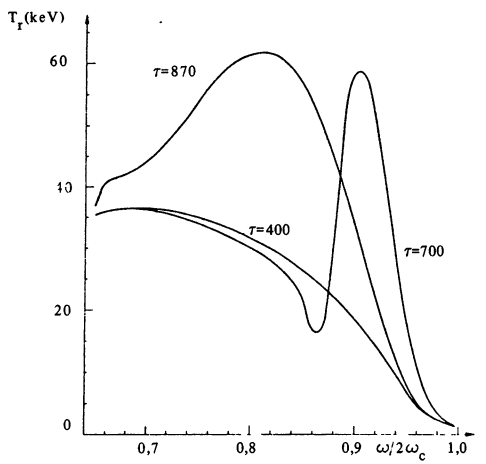

Figure 6. *Radiative temperature observed from a top location in the vertical direction, before, during and after the RF pulse*

5. Conclusions

Several examples could be added to those given in Sec. 4. For instance, current drive by the combined effects of two or more different RF waves is a typical problem which can be correctly addressed only by numerical methods. In fact, Fokker-Planck calculations have shown [39] that the ECCD efficiency may be strongly enhanced in the presence of LH waves, due to a favourable kinetic cross-effect: EC wave generates high $v_\perp$, low $v_\parallel$ electrons, which are then pushed to much higher parallel velocities by the LH waves, which increases the efficiency. Similar synergistic effects are expected in combined EC and FW current drive experiments [12]. On the other hand, Fokker-Planck simulations [24, 40] have shown that radial transport is expected to decrease the CD efficiency in present-day tokamaks, whereas the effect should be much less significant in a reactor.

Fokker-Planck codes can also be applied to the simulation of tokamak discharges, or, at least if they do not include transport, to the steady-state phases. Since the output of the code is the distribution function, the comparison with several diagnostics is relatively easy. Successful examples of this technique are found, for instance, in Refs. [23,24,41]. Because of the many parameters involved in a tokamak discharge, success in obtaining the right value for a macroscopic quantity, such as, for instance, the RF-driven current, may, of course, be accidental. Simulation of more detailed outputs, such as an ECE non-thermal spectrum with the right intensity level and shape, is, of course, a much more interesting result. Reproducing several detailed diagnostics by a unique distribution function is the most ambitious and challenging goal of this kind of simulations.

In conclusion, the advent of fast vector-processing computers has now made possible a routine use of Fokker-Planck codes in theoretical investigation and simulation of RF-driven plasmas. This method has two main merits, i.e., i) it is a unified approach for all RF heating and CD experiments; ii) it needs, as input, physical and measurable parameters only, such as density and temperature profiles, wave power spectrum at the antenna, etc. It has been demonstrated that including radial transport is technically possible, but, at the present state of

the art, only introducing ad hoc models for the transport coefficients, and much theoretical effort is needed in this subject. In order to develop and refine the model, extensive comparison is now required with relevant and detailed diagnostics, i.e., diagnostics as sensitive as possible to the 3-D shape of the RF driven distribution functions.

Acknowledgements

I wish to thank Dr. I. Fidone for introducing and guiding me in the labyrinth of kinetic theory, and Prof. R.L. Meyer for initiating me in Fokker-Planck codes.

References

[1] H. KNOEPFEL, D.A. SPONG, Nucl. Fusion **9** (1979) 785.
[2] S. BERNABEI et al., Phys. Rev. Lett. **49** (1982) 1255; M. PORKOLAB et al., Phys. Rev. Lett. **53** (1984) 450.
[3] T. IMAI et al., Nucl. Fusion **28** (1988) 1341.
[4] F. SOLDNER et al., Contr. Fusion and Plasma Heating (EPS, Amsterdam, 1990) **14B**, III, 1323.
[5] C. GORMEZANO et al., Fusion Technology (Pergamon Press, Oxford, 1987) **15**, 287.
[6] H. TANAKA et al., Phys. Rev. Lett. **60** (1988) 1033.
[7] B. LLOYD et al., Nucl. Fusion **28** (1988) 1013.
[8] K. YOSHIOKA, T. M. ANTONSEN, Nucl. Fusion **26** (1986) 839.
[9] R.L. MEYER et al., Phys. Fluids **28** (1985) 127.
[10] A. ANDO et al., Nucl. Fusion **26** (1986) 107.
[11] M.J. MAYBERRY et al., RF Power in Plasmas (AIP, New York, 1989), 298.
[12] G. GIRUZZI, I. FIDONE, Contr. Fusion and Plasma Heating (EPS, Amsterdam, 1990) **14B**, III, 1279.
[13] G.D. KERBEL, M.G. McCOY, Phys. Fluids **28** (1985) 3629.
[14] S. WEINBERG, Phys. Rev. **126** (1962) 1899.
[15] C.F. KENNEL, F. ENGELMANN, Phys. Fluids **9** (1966) 2377; J. ROWLANDS et al., Sov. Phys. JETP **23** (1966) 661.
[16] I. FIDONE et al., Phys. Fluids **27** (1984) 2468.
[17] S.C. CHIU et al., Nucl. Fusion **29** (1989) 2175.
[18] I. FIDONE et al., Phys. Fluids **25** (1982) 2249.
[19] B. TRUBNIKOV, Rev. Plasma Physics (Cons. Bureau, New York, 1965), **1**, 105.
[20] C.F.F. KARNEY, Comp. Phys. Rep. **4** (1986) 183.
[21] C.F.F. KARNEY, N.J. FISCH, Phys. Fluids **28** (1985) 116.
[22] A.N. KAUFMAN, Phys. Fluids **15** (1972) 1063.
[23] M.R. O BRIEN et al., Nucl. Fusion **26** (1986) 1625.

[24] M. COX et al., Contr. Fusion and Plasma Heating (EPS, Amsterdam, 1990) **14B**, III, 1219.
[25] J. KILLEEN, et al., Computational Methods for Kinetic Models of Magnetically Confined Plasmas (Springer-Verlag, New York, 1986).
[26] M. SHOUCRI et al., Comp. Phys. Comm. **55** (1989) 253.
[27] G. GIRUZZI et al., Plasma Phys. **27** (1985) 1151.
[28] K. APPERT et al., Contr. Fusion and Plasma Physics (EPS, Aachen, 1983) **7D**, I, 329.
[29] M.R. O'BRIEN et al., Comp. Phys. Comm. **40** (1986) 123.
[30] M.G. McCOY et al., Comp. Phys. Comm. **40** (1986) 115.
[31] R.L. MEYER et al., Comp. Phys. Comm. **40** (1986) 153.
[32] I. FIDONE et al., Phys. Fluids **26** (1983) 3292; V. ALIKAEV, V. VDOVIN, Sov. J. Plasma Phys. **9** (1983) 538.
[33] V. KRIVENSKI et al., Phys. Fluids **30** (1987) 438.
[34] G. GIRUZZI, Phys. Fluids **31** (1988) 3305.
[35] R. HARVEY et al., Phys. Rev. Lett. **62** (1989) 426.
[36] G. GIRUZZI, Nucl. Fusion **28** (1988) 1413.
[37] G. GIRUZZI et al., Nucl. Fusion **26** (1986) 662.
[38] I. FIDONE, G. GIRUZZI, Nucl. Fusion **30** (1990) 803.
[39] I. FIDONE et al., Nucl. Fusion **27** (1987) 579.
[40] A. FUKUYAMA, T. UEEDA, Contr. Fusion and Plasma Heating (EPS, Amsterdam, 1990) **14B**, III, 1251.
[41] R.A. JAMES et al., Contr. Fusion and Plasma Heating (EPS, Amsterdam, 1990) **14B**, III, 1259.

ECR BREAK-DOWN IN MAGNETIC TRAPS

E.V.Suvorov, M.D.Tokman
Institute of Applied Physics,
Academy of Sciences of the USSR, Nizhny Novgorod, USSR

I. Introduction

Applying ECR power to a small pressure neutral gas seems to be promising and reliable way of plasma production in all types of magnetic traps. Due to simplicity of experimental technique for ECRH such experiments are performed in a great deal of fusion facilities and in many of them experiments on pre-ionization are tried on. In a tokamak, ECR pre-ionization and pre-heating save volt-seconds of a transformer and reduce peak loop voltage thus eliminating the run-away electron production[1-8]. In stellarator-like devices this gives a unique opportunity to create and study hot currentless plasma testing in this way the confinement properties of installation[9-11]. Some experiments on ECR plasma production were also performed on mirror machines (see refs.[12,13]). There is a great deal of small-scale experiments on mirror machines in which ECR-produced plasma is used for various applications (see e.g. Proc. of this Conf., Sect.D).

For the ITER 20 MW ECR system in project at present, among other applications there is also a task of plasma start-up and pre-heating[14].

The main feature of an ECR discharge which distinguishes it from a conventional r.f.discharge is the fact that electrons gain their energy from r.f.field in a collisionless manner. That is why, usually, an ECR discharge is accompanied with substantial (≅1KeV) pre-heating. This also gives difference in the localization of these two types of discharge. A conventional r.f.discharge is localized in a region where the r.f.field amplitude exceeds some threshold value. In the case of an ECR discharge, the region of electron-r.f.field interaction in the gradB direction is attributed to a thin resonant layer with a dimension $\Delta a \cong$

RV_T/c for oblique launch of r.f.power or $\Delta a \cong W_\perp/mc^2$ for transverse launch (R is the major radius of a torus, V_T is the longitudinal thermal velocity, $W_\perp$ is the characteristic transverse energy of accelerated particles). Due to the fast motion along magnetic field lines, energetic electrons become almost instantly uniformly distributed in the toroidal direction. The shape of the discharge in a small cross-section of a torus depends on the poloidal magnetic field distribution. Three typical structures in this cross-section are shown in fig.1: a) vertical component of poloidal magnetic field is imposed, b) randomly distributed poloidal component,* c) closed magnetic surfaces.

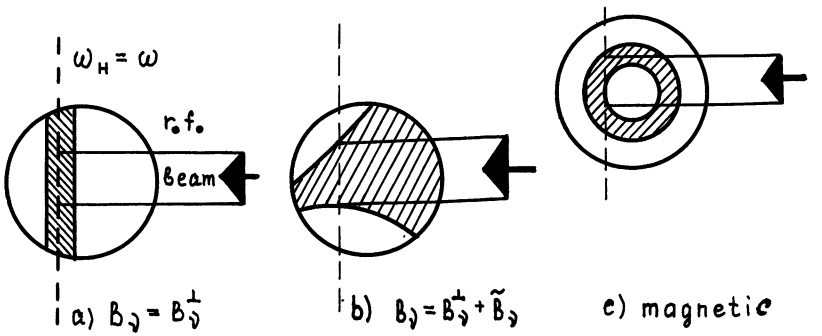

Fig.1

There are three main schemes of ECR plasma production which are based on the same idea of using the x-mode that is most effective for resonant acceleration of electrons. In order to avoid a cut-off layer, the x-mode must be launched from the high-field side of a torus. These three schemes are the following:

a) HFS injection of the x-mode or a mixture of the x- and 0-modes - a very popular scheme at an early stage of experiment on ECRH and for small installations;

b) LFS launch of the o-mode with the subsequent reflection and transformation to the x-mode by the mode-converting mirror at a HFS chamber wall (W VII-A ideology);

c) The scheme in which an arbitrary mixture of the x- and

---

* *With plasma density increase the discharge structure may vary due to arising ambipolar electric fields[15,16].

o-modes is launched from the low-field side is rather popular nowadays; the break-down in this case takes place due to mode conversion at reflections by chamber walls and multipass absorption of the x-mode. This idea is also proposed to be used in ITER. Successful use of the latter scheme shows that ECR break-down is a rather simple and reliable technique which gives one the opportunity to achieve the final goal even without any specific design of a launch system.

d) One more scheme of ECR plasma production should be mentioned: ECR pre-ionization with LFS launch of the x-mode at the second cyclotron harmonic[17,18]. Within this scheme the production of an energetic tail at the electron distribution function should be expected.

Two main mechanisms of a HFS launched x-mode absorption in a plasma may be of importance: resonant cyclotron absorption and absorption in an upper-hybrid resonance layer. Much attention was paid to the second mechanism at the early stages of experiments on ECRH at small tokamaks [1,3,7]. However at present it has lost its importance because in large tokamaks all the r.f.power is absorbed in a resonant layer either in the form of the o-mode or in the form of the x-mode.

In the investigation of ECR break-down two different problems are to be considered: the r.f.field - electron interaction and particle and energy confinement at the start-up stage. In our presentation we shall mainly deal with the first problem. As for confinement mechanisms, we should mention the following considerations:

a) at the initial stage of break-down in a tokamak, the confinement time is determined by toroidal drift and by plasma expansion along the magnetic field lines when $B_v \neq 0$[15]. As the plasma density increases, ambipolar effects come into action [15,16]; for a large tokamak of ITER scale, plasma confinement time is mainly defined by plasma expansion along the open magnetic field lines ($B_v \neq 0$) with ion-sound velocity;

b) in stellarators, a closed system of magnetic surfaces formed by external windings provides nearly absolute confinement of plasma during start-up stage[20], with the only exception for electrons deeply trapped into magnetic ripples, which may be lost due to toroidal drift;

c) for mirror traps electron scattering into the loss-cone

due to quasilinear diffusion in the r.f.field may be the main mechanism of accelerated electron losses in ECR discharge [21].

II. Electron-R.F.Field Interaction Under ECR Condition

Usually ECRH in contemporary installations may be described within the quasi-linear approximation[22]. For the extraordinary wave at the first cyclotron harmonic, the interaction is weak due to the depression of the resonant component of r.f.field, E_+, in a dense plasma[22]:

$$E_+/E_o \cong (\omega_B^2/\omega_p^2)\ \max\{n_\parallel \beta_T, \beta_T^2\} \tag{1a}$$

Here $n_\parallel$ is the longitudinal (with respect to the magnetic field direction) refractive index, $\beta_T = V_T/c$ is the ratio of electron thermal velocity to light velocity, ω_p and ω_B are plasma and gyro- frequencies respectively and E_o is the r.f.field amplitude. In a rarefied plasma with [23]

$$\omega_p^2/\omega_B^2 \leq \max\{n_\parallel \beta_T, \beta_T^2\} \tag{1b}$$

there is no depression of E_+ component ($E_+ \cong E_o$). In this case, for present day levels of r.f.power the electron-r.f.field interaction may be essentially nonlinear[26]. Great interest in this problem was also stimulated by the proposal to use a powerful free electron laser in a fusion experiment[24]. In recent years there was a splash of theoretical activity on this subject[25-32] based on the idea of utilizing the Hamiltonian technique for averaged equations of electron motion in r.f.field under ECR condition. We present here the main ideas and results of these investigations.

Consider first the averaged equations of electron motion in the r.f.field under condition of ECR at the first harmonic. Let the guiding center of an electron move along the magnetic field line (l-coordinate is the characteristic of this motion) and the r.f.field be distributed along l as follows:

$$\vec{E}_{r.f.} = \vec{E}_o(l, \vec{r}_\perp)\ \exp(-i\omega t + i\int k_\parallel dl + i\int \vec{k}_\perp d\vec{r}_\perp) \tag{2}$$

Here $k_\parallel$ and $\vec{k}_\perp$ are longitudinal and transverse (with respect to magnetic field) components of the wave vector $\vec{k}$ and $\vec{r}_\perp$ is perpendicular to the external magnetic field. The quantities $\vec{E}_o$, $\vec{k}$ and

$\vec{B}_o$ are assumed to be slowly varying in the scale on the order of wavelength, and the wavelength is assumed to be large compared with the gyroradius (dipole approximation). In the vicinity of the gyrofrequency ($|\omega_B-\omega| \ll \omega$) the electron motion is governed by the following set of averaged equations:

$$d\mu/d\tau = \dot{\mu} = -(2\mu)^{1/2}\lambda\cos\Psi \tag{3}$$

$$\dot{\Psi} = \Omega - 1 - \beta^2/2 + n_\parallel\beta_\parallel + (2\mu)^{-1/2}\lambda\sin\Psi \tag{4}$$

$$\dot{\beta}_\parallel = -n_\parallel\dot{\mu} - \mu\, d\Omega/d\xi - (2\mu)^{1/2}\sin(\Psi+\phi)\, d/d\xi\, |\lambda_+| - (1/4)\, d/d\xi\, (|\lambda_\parallel|^2 + |\lambda_-|^2) \tag{5}$$

$$\dot{\xi} = \beta_\parallel \tag{6}$$

In (3)-(6) the following dimensionless variables are used: $\tau=\omega t$, $\xi=\omega l/c$, $\Omega=\omega_B/\omega$, $\beta_{\parallel,\perp}=V_{\parallel,\perp}/c$, $\beta=V/c$, and $\mu=\beta_\perp^2/2\Omega$; Ψ is the phase of electron gyration with respect to the r.f.field phase; the dimensionless r.f.field amplitude components are defined as

$$\lambda_{+,-} = (E_{ox} \mp iE_{oy})/2B_o, \quad \lambda_\parallel = E_{oz}/B_o,$$
$$\lambda = |\lambda_+ + \beta_\parallel n_\perp \lambda_\parallel/2|, \quad \phi = \arg\,(1+\beta_\parallel n_\perp\lambda_\parallel/2\lambda_+) \tag{7}$$

The r.f.field components in (7) are determined with respect to the local co-ordinate system x,y,z with $\vec{z}_o \parallel \vec{B}_o$, the wave vector $\vec{k}$ being in the (x,z)-plane.

The averaged eqs.(3)-(6) together with (7) have a rather clear physical meaning. The variation of the transverse energy μ takes into account two mechanisms of the electron-r.f.field resonant interaction: interaction with the E_+ component typical of longitudinal and transverse propagation of the x-mode and with the $E_\parallel$ component typical of transverse propagation of the o-mode [33]. Phase variation is defined by the frequency shift with respect to precise resonant condition taking into account the Doppler shift and relativistic variation of gyrofrequency as well as by the so called "forced phasing" which is proportional to the r.f.field amplitude. The longitudinal motion is defined by adiabatic invariant conservation in a nonuniform magnetic field and by various constituents of ponderomotive force, one of which (proportional to $d|\lambda_+|/d\xi$) depends not only on the $|E_+|^2$ distribution but also on the gyration phase. Under usual ECR conditions, the rate of the longitudinal electron energy ($\beta_\parallel^2/2$) variation is small compared with that of the transverse energy. So we

shall consider averaged electron motion assuming $\beta_{\parallel}$ to be a slowly varying value and for simplicity confine ourselves to the case of quasitransverse propagation ($n_{\parallel}^2 \ll 1$)*†.

We begin the investigation of eqs. (3),(4) with slowly varying parameters (λ, $n_{\parallel}$, $\beta_{\parallel}$) assuming all of them to be constant. In this case we obtain a Hamiltonian system:

$$\dot{\mu} = -\partial H/\partial \Psi, \qquad \dot{\Psi} = \partial H/\partial \mu \tag{8}$$

with $H = (2\mu)^{1/2}\lambda\sin\Psi - \mu^2/2 + \Delta\Omega\mu$ depending on two parameters λ and $\Delta\Omega = \Omega - 1 - \beta_{\parallel}^2/2 + n_{\parallel}\beta_{\parallel}$, which are varying along the electron trajectory in a nonuniform electromagnetic field.

Figure 2 shows different variants of the phase plane corresponding to this dynamic system *‡ with fixed parameters λ and $\Delta\Omega$. In the case $\Delta\Omega \gg \lambda^{2/3}$, the characteristic frequency of the bounce oscillations of resonant particles trapped by the r.f. field is $\Omega_b = \omega\,\lambda^{1/2}\,(\Delta\Omega)^{1/4}$ and the characteristic scale of their energy variation is $\Delta\mathcal{E} \cong mc^2\,\lambda^{1/2}\,(\Delta\Omega)^{1/4}$ (the quantity $\Delta\mathcal{E}$ is defined as a width of the region of trapping in the phase plane). Under the condition $\Delta\Omega \leq \lambda^{2/3}$, we have $\Omega_b \cong \omega\,\lambda^{2/3}$ and $\Delta\mathcal{E} \cong mc^2\,\lambda^{2/3}$. Other characteristic values depending on the values of λ and $\Delta\Omega$ can be found in fig.2.

Consider now various regimes of the electron - r.f. field resonant interaction which takes place in the homogeneous dc magnetic field when electron passes through the region occupied by the wave beam with the characteristic transverse scale L. (The peculiarities of resonant interaction of electrons with a strong r.f. field in an essentially inhomogeneous magnetic field are discussed in [25,26,28]). Usual linear absorption of the wave beam takes place if two conditions are held[34]:

a) the variation of the energy of resonant particles is small enough: $\Delta\mathcal{E} \ll \beta_T^2$, that is

---

† * Effect of finite value of $n_{\parallel}$ and taking into account $\beta_{\parallel}$ variation are considered in[26,28].

‡ *Due to the presence of a singular point μ=0 it is more covinient to use polar co-ordinates ($\rho = (2\mu)^{1/2}$, Ψ) for the phase plane.

$$\lambda^{2/3} \ll \beta_T^2 \qquad (9a)$$

b) the transient time of an electron through the r.f. field

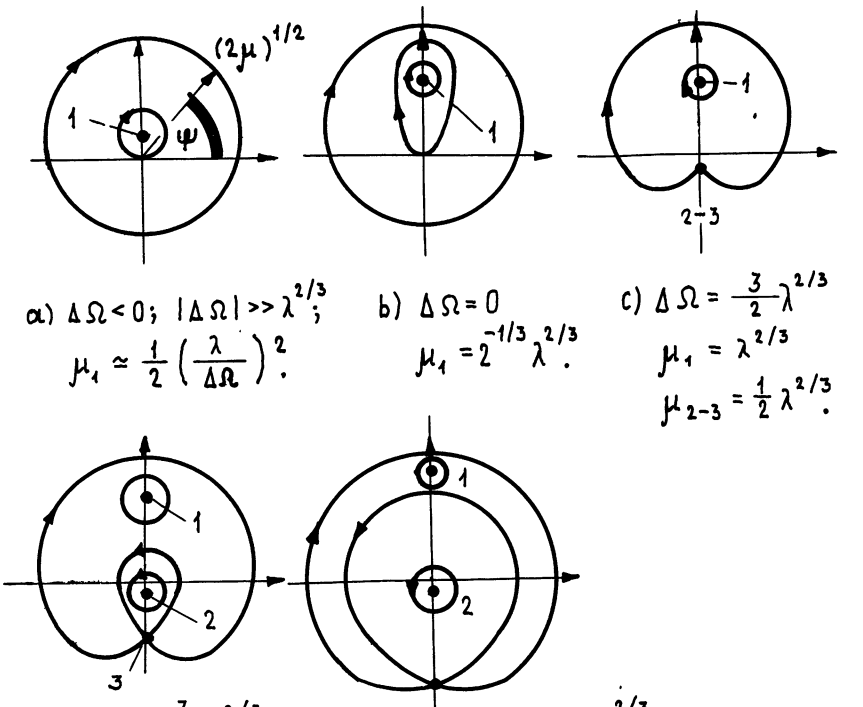

Fig. 2

region is small compared with the period of nonlinear bounce oscillations of resonant electrons: $\Omega_b(L/V_T) \ll 1$, that is

$$(\omega L/c\beta_T^{1/2})\cdot\lambda^{1/2} \ll 1 \qquad (9b)$$

(in the estimates given above we consider that $\Delta\Omega \cong \beta_T^2$).

When the condition (9b) is violated and (9a) holds we have a

so-called "weakly nonlinear" regime of cyclotron interaction (see [30-32]); this regime is not typical of break-down stage. So we shall consider in more detail a strongly nonlinear regime in which the variation of the resonant particle energy is much greater than their initial energy:

$$\lambda^{2/3} \gg \beta_T^2 \tag{10a}$$

and the time of the electron transition through the resonant region is much greater than bounce-period $\omega^{-1}\lambda^{-2/3}$:

$$(\omega L/c\beta_T)\lambda^{2/3} \gg 1 \tag{10b}$$

Within the condition (10b), the variation of the parameters of the dynamic system (8) is slow and the electron motion is characterized by the conservation of the adiabatic invariant - the area bounded by the phase trajectory in the phase plane (see fig.3). However, if the maximum value of λ on the particle trajectory satisfies the condition $(3/2)\lambda^{2/3} > \Delta\Omega > 0$, the phase trajectory inevitably approaches the separatrix region of the dynamic system (8) and crosses it. In this case, a swift (in the time-scale $L/c\beta_T$) "jump" of adiabatic invariant takes place.* In the course of electron interaction with the r.f.field (the electron enters and then escapes the region occupied by the r.f.field) the magnitude of λ varies nonmonotonously along the trajectory of the guiding center: when λ varies from λ_{max} to zero, the phase trajectory crosses the separatrix the second time. In this case with equal probability the electron either loses all the energy gained in the first crossing of the separatrix or escapes the r.f.field region with substantial energy gain. Both these opportunities of the electron crossing the r.f.field region in a strongly nonlinear regime are shown schematically by a diagram in fig.3.

Therefore for the frequency shift $\Delta\Omega$ in the range $0 < \Delta\Omega < (3/2)\lambda_m^{2/3}$, 50% of the electrons passing through the r.f.field region gain the energy $\mathcal{E} \cong 2mc^2\Delta\Omega \leq (3/2)\lambda_m^{2/3}mc^2$. In the appro-

---

*This effect is similar to well known sharp variation of nonlinear oscillator amplitude with slow variation of external force frequency.

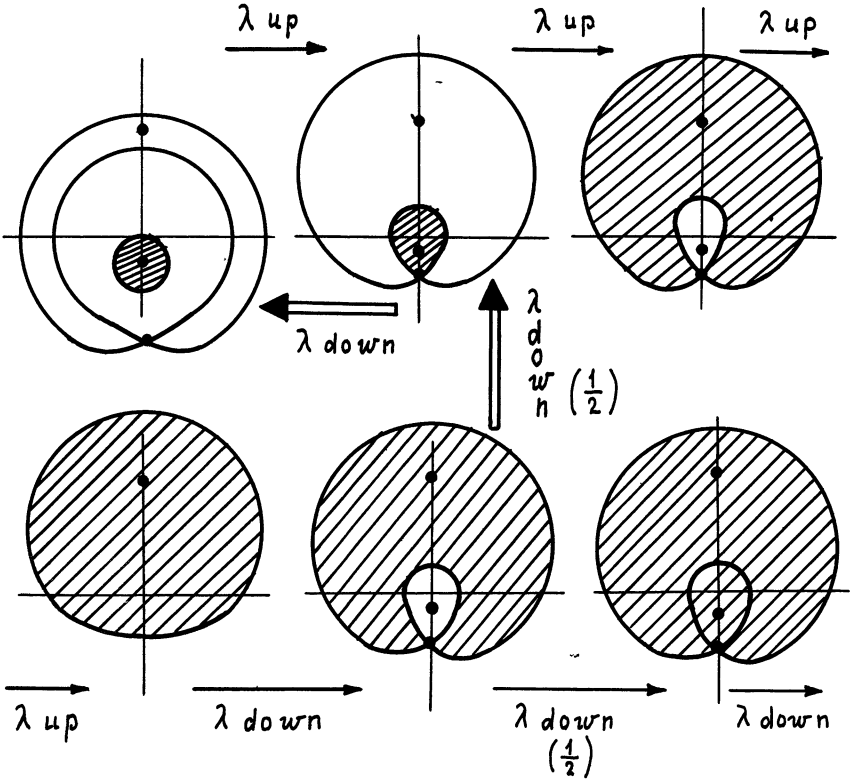

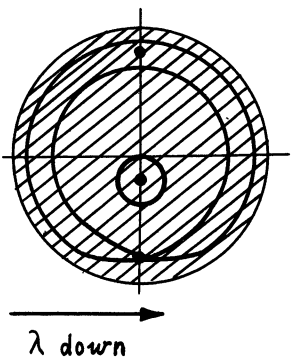

Fig. 3

ximation of a fixed distribution of the r.f.field amplitude, independent of x, the nonlinear optical depth may be obtained in the case of transverse propagation in the grad B_t direction (this procedure may be easily understood from fig.4):

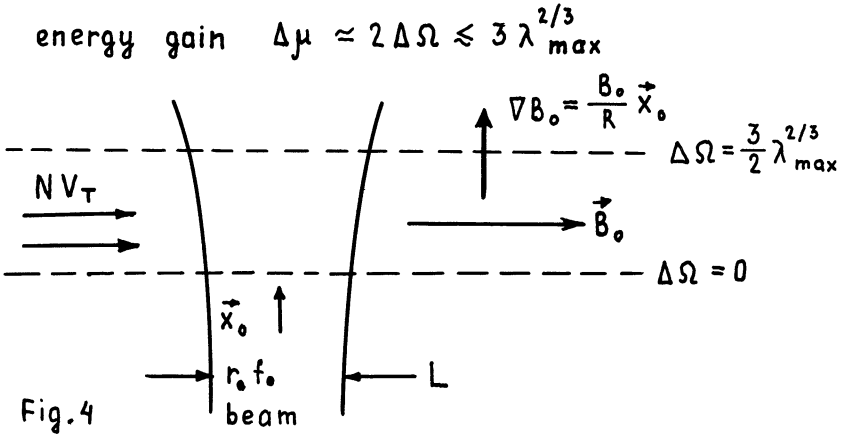

Fig.4

$$\tau_{NL} \cong (\omega_p^2/\omega^2)\beta_T(R/L)(B_o^2/E_o^2)\ \lambda_{o,x}^{4/3} \qquad (11)$$

Here ω_p is the plasma frequency, ω is the r.f.field frequency, R is the major radius of a torus defining the scale of toroidal magnetic field inhomogeneity, B_o is the toroidal magnetic field in the resonant region, E_o is the maximum value of the r.f.field amplitude and the values $\lambda_{o,x}$ are defined by (7) taking into account the polarization of the o- and x- modes.

Equation (11) may be presented in a similar fashion for the o-mode and x-mode in the regime without the suppression of the E_+ component:

$$\tau_{NLo,x} = \tau_{Lo,x}(\beta_T/k_oL\ \lambda_{o,x}^{2/3}) \qquad (12)$$

with $\lambda_o = \beta_T n_\perp (E_o/B_o)$ and $\lambda_x = E_o/B_o$. Linear optical depths are defined by[22]:

$$\tau_{Lo} \cong (\omega_p^2/\omega^2)\ \beta_T^2\ k_o n_\perp R, \quad \tau_{Lx} \cong (\omega_p^2/\omega^2)\ k_o R \qquad (13)$$

with $k_o = \omega/c$.

The nonlinear optical depth is less than a linear one since in the nonlinear regime according to (10b) $k_oL\ \lambda^{2/3}\ \beta_T \gg 1$.

A similar Hamiltonian description may be applied to the electron motion in the r.f.field under resonance condition at the second cyclotron harmonic. The averaged equations of electron motion in this case take the form:

$$\dot{\mu} = -\lambda\mu\cos\Psi, \qquad \dot{\Psi} = \Delta\Omega - \mu + \lambda\sin\Psi \tag{14}$$

with $\lambda = n_{\perp}E_{+}/B_{o}$ and $\Delta\Omega = 2\omega_{B}/\omega - 1 - \beta_{\parallel}^{2}/2 + n_{\parallel}\beta_{\parallel}$. The set of equations (14) is also characterized by the Hamiltonian $H \doteq \lambda\mu\sin\Psi + \Delta\Omega\mu - \mu^{2}/2$. The phase plane corresponding to (14) is shown in fig.5 (a rectangular co-ordinate system μ,Ψ is more suitable in this case). Under the condition $\Delta\Omega \gg \lambda$, the bounce-frequency of trapped particles is $\Omega_{b} \cong \omega\,(\lambda\Delta\Omega)^{1/2}$ and the width of

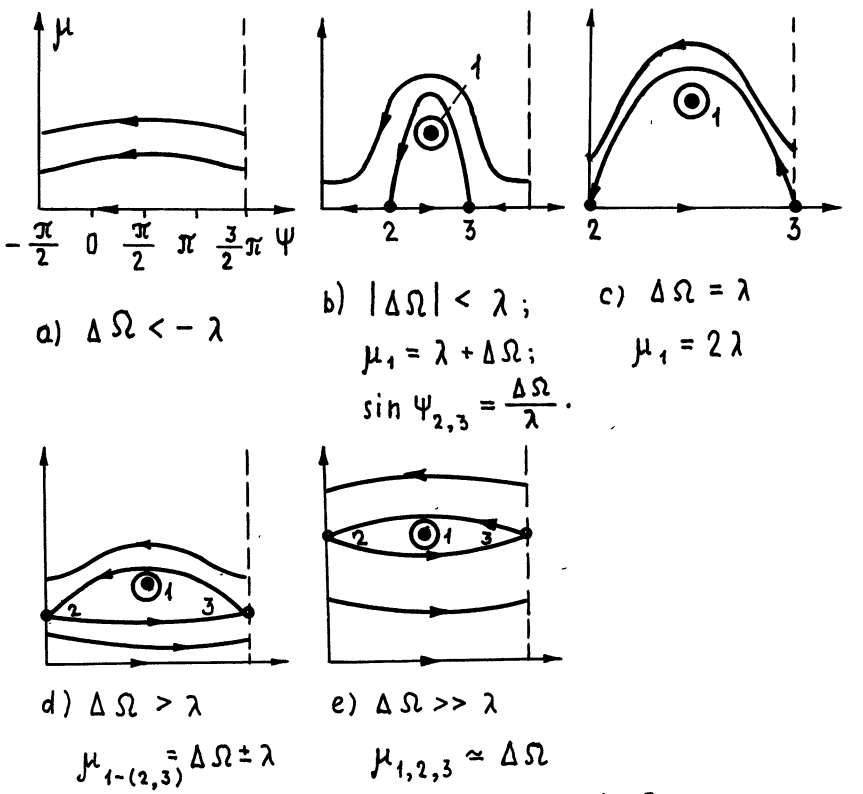

Fig. 5

the trapping region (over electron energy) is $\Delta\mathcal{E} \cong mc^{2}(\lambda\Delta\Omega)^{1/2}$.

In the case $\Delta\Omega \leq \lambda$, we have $\Omega_b \cong \omega\lambda$ and $\Delta\mathcal{E} \cong mc^2\lambda$. Assuming $\Delta\Omega \cong \beta_T^2$ one can obtain conditions of the linear absorption of the r.f. beam with the diameter of the cross-section L:

$$\Delta\Omega \ll \beta_T^2 \quad \rightarrow \quad \lambda \ll \beta_T^2 \tag{15a}$$

$$(L/V_{th})\Omega_b \ll 1 \quad \rightarrow \quad k_o L\lambda \ll 1 \tag{15b}$$

Like in the case of the ECR at the first harmonic, we shall pay no attention to the weakly nonlinear regime ($\lambda \ll \beta_T^2$, $k_o L\lambda^{1/2} \gg 1$)* .

A strongly nonlinear regime is realized under the following conditions:

$$\Delta\mathcal{E} \gg \beta_T^2 \quad \rightarrow \quad \lambda \gg \beta_T^2 \tag{16a}$$

$$(L/V_{th})\Omega_b \gg 1 \quad \rightarrow \quad (k_o L/\beta_T)\lambda \gg 1 \tag{16b}$$

The mechanism of nonlinear energy gain is quite similar to that at the first cyclotron harmonic and is shown schematically by a diagram in fig.6. The energy gain after the particle transit through the r.f. field region is $\Delta\mathcal{E} \cong mc^2\Delta\Omega$, when $\Delta\Omega$ is within the range $0 < \Delta\Omega < \lambda_{max}$; in this case also 50% of particles pass through the r.f.field region without change in their energy. The nonlinear optical depth, estimated for this case is independent of the r.f.field amplitude** :

$$\tau^{(2)}_{NLx} = \tau^{(2)}_{Lx}(1/k_o L\beta_T), \tag{17}$$

where the linear optical depth for the extraordinary mode at the second harmonic is $\tau^{(2)}_{Lx} = (\omega_p^2/\omega^2)\beta_T^2 k_o n_\perp R$. It should be noted that within the conditions (16a, 16b) of a strongly nonlinear regime, the nonlinear optical depth may either exceed or be smaller

---

*Detailed description of this regime as well as others with taking into account distribution function of electrons over adiabatic invariants is presented in invited talk by prof.R.Pozzoly at R.F.Heating session.

**This is due to the fact that characteristic energy gain multiplied by the dimension of resonant region in grad B direction is proportional to r.f.field amplitude squared.

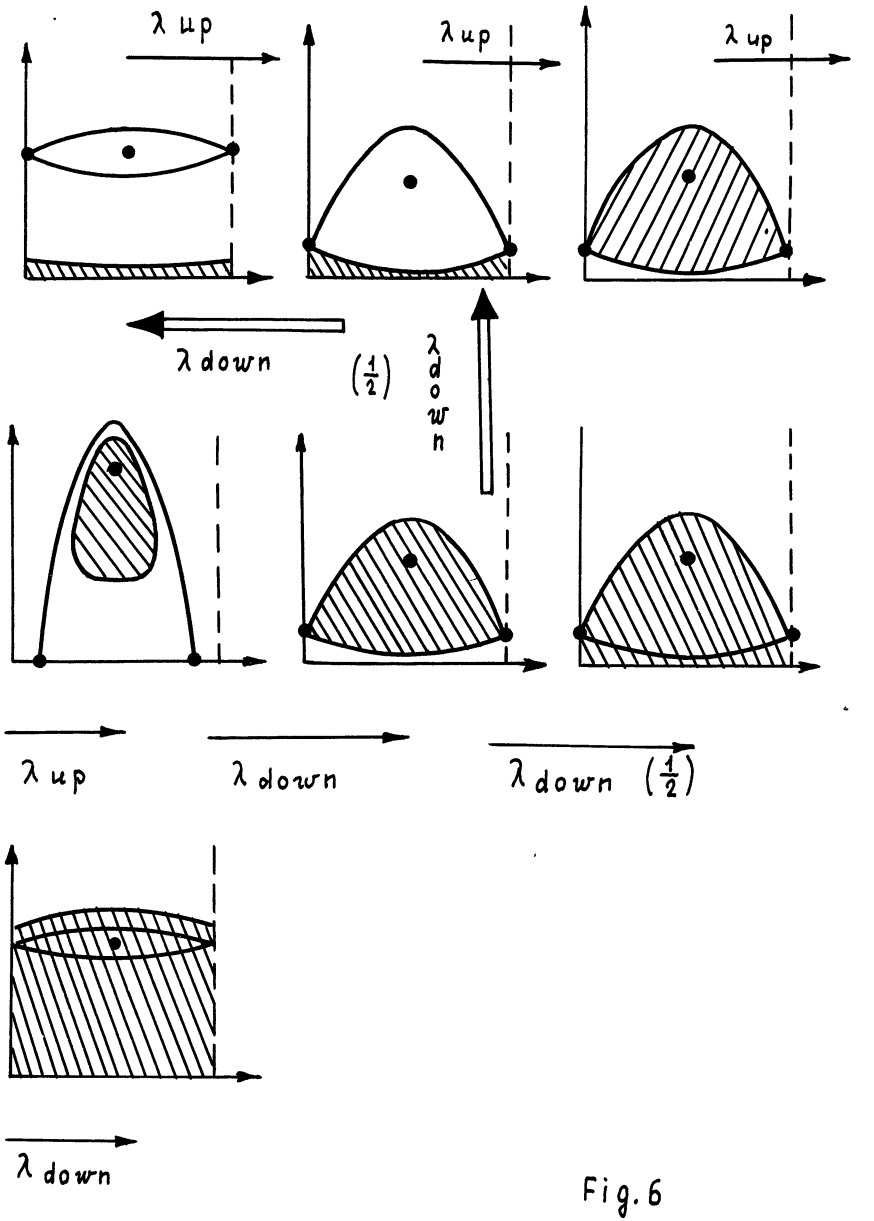

Fig. 6

than its linear value.

Here we present some estimates referring to the experimental conditions of ECRH at L-2 stellarator[9] and to planned parameters of an ECR system for ITER[14] -

a) L-2: $B_o \cong 1T$, $R \cong 1m$, $P_{rf} \cong 0.2MW$, $L \cong 5cm$;

b) ITER: $B_o \cong 6T$, $R \cong 6m$, $P_{rf} \cong 2.5MW$, $L \cong 0.5m$.

For L-2 stellarator with the electron temperature $T_e \cong 10eV$ typical of a break-down stage, there is no depression of the resonant component E_+ of the r.f.field in the extraordinary mode at the first harmonic for plasma density $n_e < 10^{11} cm^{-3}$. In this, case we have a rather strongly nonlinear regime ($k_o L (E_o/B_o)^{2/3}/\beta_T \cong 30$); the characteristic energy of accelerated electrons is $W_\perp \cong mc^2 (E_o/B_o)^{2/3} \cong 5$ KeV. For the second harmonic with the same parameters, the regime is still nonlinear: $k_o L E_o/B_o \beta_T \cong 3$, the energy of accelerated particles is $W_\perp \cong mc^2 (E_o/B_o) \cong 0.5$ KeV. The optical depth for plasma density $n_e < 10^{11} cm^{-3}$ is small compared with unity both at the first and at the second harmonics in linear and nonlinear regimes.

For ITER parameters, the depression of the resonant component E_+ is negligible for plasma densities $n_e \leq 10^{12}$ cm^{-3}. With the electron temperature $T_e \cong 10eV$ strongly nonlinear regime of electron - x-mode interaction takes place both at the first ($k_o L (E_o/B_o)^{2/3}/\beta_T \cong 100$) and at the second ($k_o L E_o/\beta_T B_o \cong 10$) cyclotron harmonics. Characteristic energies of accelerated electrons are about 1KeV and 50 eV for the first and the second harmonics respectively. The nonlinear optical depth reaches the value 2 at the first harmonic with $n_e \cong 10^{12}$ cm^{-3} and is small compared with unity at the second harmonic.

So, at the break-down stage in contemporary fusion experiments, strongly nonlinear regimes of the electron-r.f.field ECR interaction are easily realized with the energy gain in a single pass of the electron through the r.f.field region greatly exceeding the ionization potential. In the case of an optically thin plasma column, it is necessary to take into account the interaction of electrons with the r.f.field scattered by the chamber wall[20]. Scattered radiation will most probably possess a "noise" angular spectrum in which electron heating may be adequately described within a quasilinear approximation[19] with the exception, perhaps of the deeply trapped electrons in magnetic ripples.

III. Pre-Ionization in a Tokamak-Reactor

The most simple scheme of ECR start-up seems to be as follows. Microwave radiation in the form of the o-mode is injected from LFS. At the initial stage of discharge, it passes through the plasma column almost unabsorbed and after reflection by the chamber wall a considerable content of the x-mode arises in it, which effectively accelerates electrons, thus providing the rise of the plasma density. With the plasma density increase, the absorption of o-mode in the first pass becomes significant and provides preliminary heating of a plasma created by the x-mode.

We shall briefly discuss the peculiarities of such a discharge in a tokamak of ITER scale assuming a diffusive character of radiation scattering by a chamber wall. This regime is investigated in more detail in [19] and presented to the Heating session by M.Tokman. Electron heating here may be described in the quasi-linear approximation. The E_+ component depression is insignificant for plasma densities $n_e < 10^{12}cm^{-3}$ and the optical depth for the extraordinary wave exceeds unity beginning with the density $10^{10}cm^{-3}$. The vertical and the random poloidal magnetic field components are on the order of 0.1% of toroidal magnetic field in ITER; this means that energetic electrons freely move along "open" magnetic field lines while losses of secondary electrons with $T_e \cong 10eV$ correspond to ion-sound velocities. With a few megawatts of r.f. power applied, electrons in a resonant region may be accelerated due to quasi-linear diffusion up to energies 3-5 KeV (see[19]). With a neutral gas density $n_n \cong 10^{12}cm^{-3}$, "hot" electrons lose their energy before reaching the chamber wall due to the motion along open magnetic field lines; energy losses due to the expansion of the "cold" component with ion-sound velocity are lower than the losses due to ionization and neutral atom excitation. Assuming that a "target" plasma is optically thick for the x-mode, the duration of the break-down stage may be estimated from simple energetic considerations: for the total volume $V \cong 10^9\ cm^3$, the neutral gas density $n_n \cong 10^{12}cm^{-3}$ and the energy 30-50 eV lost per one ionization act with a few megawatts of r.f.power, the duration of the break-down stage is a few milliseconds. The break-down threshold obtained in[19] from model balance equations is several hundreds of kilowatts; in this case,

ionization takes place approximately in 1/10 of the chamber volume.

Conclusions

Nonlinear effects (trap-detrap electron acceleration) may be easily achieved in a low-density low-temperature plasma during ECR start-up at moderate levels of the r.f.power flux density.

Assuming absolutely diffusive scattering of the o-mode by the inner chamber wall with its simultaneous transformation into the x-mode, a simple quasilinear model of ECR break-down can be constructed; it shows the possibility of plasma production ($n_e \cong 10^{12} cm^{-3}$, $T_e \cong$ 10eV) in ITER during few milliseconds with ECR power from several hundreds kilowatts up to several megawatts.

Possibly, the same r.f.power will be sufficient to produce a plasma with nonlinear trap-detrap heating but, really, it is the subject of future modeling.

References

1. Bulyginsky D.G., Larionov M.M., Levin L.S. et.al., Ioffe Phys.Inst.Rep. N 611, 1979.
2. Cho T., Kubo S., Ikeda M. et.al., In: Int.Conf.on Plasma Phys., Nagoya, paper 9P-11-06, 1980.
3. Tanaka S. et.al., Nucl.Fusion, 26, N3, p.349, 1986.
4. Holly D.F. et.al., Prepr. Univ. of Wisconsin COO-2387-120, 1980.
5. Holly D.F. et.al., In: Joint Workshop on ECE and ECRH, Contr.Papers, Oxford, July 1980.
6. Tanaka S. et.al., In: 14-th Europ.Conf on Contr.Fusion and Plasma Phys., Contr.Papers, Pt.III, p.886, Madrid, 1987.
7. Gilgenbach R.M., Read M.E., Hackett K.E. et.al., Nucl.Fusion, 21, N3, p.319, 1981.
8. Alikaev V.V., Bagdasarov A.A., Borshegovskii A.A., In: 17-th Europ.Conf. on Contr.Fusion and Plasma Heating, Contr.Papers, Pt.III, p.1084, Amsterdam, 1990.
9. Andryukhina E.D., Batanov G.M., Berezhetskii M.S., Plasma Phys. and Contr.Nucl.Phys.Res, London, 1984; Nucl.Phys.Suppl., vol.2, p.409, 1985.
10. Wilhelm R. et.al., Plasma Phys. and Contr.Fusion, v.26, N12, p.1433, 1984.
11. Uo K., Iioshi A., Obiki T., Proc. of the 3rd Joint Varenna-Grenoble Int.Symp. on Heating in Toroidal Plasmas,

March 1982, v.2, p.667.
12. Mauel M.E., Phys.Fluids, 27, N12, p.2889, 1984.
13. Bocharov V.N. et.al., Voprosy Atomnoi Nauki i Tekhniki (Term.Sintez), N3, p.64, 1985.
14. Basic Design Engineering Meeting on the Electron Cyclotron System for ITER, Summary Report, ITER - IL - HD - 6 - 9 - 1, Garshing, 1989.
15. Peng Y-K.M., Borowski S.K., Kammash T., Nucl.Fusion, 18, p.1489, 1978.
16. Pereverzev G.V., Zakharov L.E., Fizika Plazmy, 14, p.214, 1988.
17. Sano F., Obiki T., Motojima O., Nucl.Fusion, 26, p.473, 1986.
18. Erckmann V., and W VII - A Team, NI Team, ECRH Group, Plasma Phys. and Contr. Fusion, 28, p.1277, 1986.
19. Tokman M.D., ITER-IL-Ph-6-9-S-13, Garshing, 1989.
20. Carter M.D., Batchelor D.B., England A.C., Nucl.Fusion, 27, p.985, 1985.
21. Suvorov E.V., Tokman M.D., Fizika Plazmy, 15, 934, 1989.
22. Alikaev V.V. et.al., Electron cyclotron plasma heating in toroidal systems. - In: High-Frequency Plasma Heating (ed. A.G.Litvak), Amer.Inst. of Phys., New York, 1990.
23. Zheleznyakov V.V., Radio Emission from the Sun and Planets, Pergamon Press, New York, 1970.
24. Free-Electron Laser Experiments in Alcator-C, ed. Thomassen K.I., VS GPO, Washington, D.C., 1986.
25. Neishtadt A.I., Timofeev A.V., Sov.Phys.-JETP, 66, p.973, 1987.
26. Sergeev A.S., Suvorov E.V., Tokman M.D., Preprint N172, Inst. of Applied Phys., Gorky, 1986.
27. Newins W.M., Rognlien T.O., Cohen B.I., Phys.Rev.Lett., 59, p.60, 1987.
28. Suvorov E.V., Tokman M.D., Sov.J.Plasma Phys., 14, p.557, 1988.
29. Kotelnikov I.A., Stupakov G.V., Internal Peport IC 1881426, International Centre for Theor. Phys., Trieste, Italy, 1988.
30. Kotelnikov I.A., Stupakov G.V., Preprint N 89 - 100, Inst. of Nucl.Phys., Novosibirsk, 1989.
31. Farina D., Pozzoli R., Ronzio D., Internal Report FP90/12, Inst. Phys. Plas., Milano, 1989.

32. Farina D., Pozzoli R., Internal Report FP90/4, Inst. Phys. Plas., Milano, 1990.
33. Litvak A.G. et.al., Nucl.Fusion, 17, p.659, 1979.
34. Suvorov E.V., Tokman M.D., Plasma Phys., 25, p.723, 1982.
35. Tokman M.D., Fizika Plazmy, 15, p.377, 1989.

THE DESIGN OF AN ECRH EXPERIMENT AT 140 GHZ, 1.6 MW, ON FTU TOKAMAK

L. Argenti, A. Bruschi, S. Cirant, °F. De Luca, G. Gorini, G.Granucci, A. Jacchia, *L. Mania , P. Mantica, S. Nowak, A. Simonetto, G. Solari

Istituto di Fisica del Plasma, CNR, Milano
°Universita degli studi di Milano
*Dip. Elettronica, Universita di Trieste

1 - Main features and physical objectives.

Plasma heating with Electron Cyclotron electromagnetic waves in the frequency band above 30 GHz has the attractive feature that a good matching of the load to the generators can be achieved without any particular tuning device in a wide range of operating parameters. In toroidal machines, where the most convenient launch is from the low toroidal field side, full absorption occurs for high temperature plasmas provided that the wave is given the right polarization to pass the extra-ordinary mode cut-off when entering the plasma volume. Full absorption, or negligible reflection, has also been observed in moderate-temperature plasmas with low optical thickness /1, 2, 3,4/. In these cases the low attenuation per pass through the plasma is still stronger than wall losses, so that at the end most of the e.m. power is damped into the plasma volume.

With increasing temperatures, the power deposition becomes more and more localized within the plasma, the ultimate dimension of the directly heated spot being the size of the microwave beam. A high electron density, beneficial to the optical thickness, limits the absorption efficiency only if it is too close to the cut-off density, which in turn is proportional to the square of the toroidal magnetic field (B_{tor}). High temperature, high field machines are therefore the best suited to exploit all the potentials of ECRH. In this respect FTU and the newly developed high power 140 GHz generators (2 mm free-space wavelength) represent an ideal combination to perform a heating experiment /5/ with distinctive features.

In the 140 GHz ECRH experiment on FTU, almost central ECRH of Ohmic plasmas ($B_{tor} \approx 5$ T) can be done at peak densities up to 2.3×10^{20}

m^{-3}. This is an important feature of the experiment, since at these high densities the electron-ion energy transfer time is much lower than the energy confinement time, resulting in the simultaneous heating of both electron and ion populations. The size of the directly heated spot is only a small fraction of the minor radius ($\approx a/10$). Both strong absorption and small size of the high-gain launching antennas provide a sharp localization of the power deposition.

The electromagnetic energy is launched from the low toroidal field side, in the form of microwave beams steerable in the vertical plane. The polarization provides efficient coupling to the O-mode in the magnetized plasma, and the position of the heated volume can be changed at a fixed toroidal field. To emphasize these features, a precise localization of the power deposition profile has been given priority with respect to global heating efficiency. This is crucial for a clear interpretation of the energy transport properties both in steady-state and transient plasma conditions.

Combined EC and LH heating can be performed in FTU at full toroidal field ($B_{tor} > 7$ T). In this case the cold resonance is outside the plasma region. Good absorption can be provided by the energetic tail during LHH at a down-shifted EC resonance, and current can be driven up to 90 kA/MW with an oblique launch (20° from normal to B_{tor}) /6/.

Localized heating close to magnetic islands can lead to the suppression of MHD modes /5/. The possibility of moving along the minor radius the position of the heated volume by tilting the beams allows the analysis of the mode stabilization (or de-stabilization) at a given toroidal field and q-value at the limiter.

An important feature of the ECRH experiment on FTU is the advanced microwave system design, based on concepts and technical solutions presently under consideration for next-step fusion devices /7,8/. In particular, the power density in the transmission line is at the level foreseen for reactor-grade systems.

The EC power deposition profile in the plasma is determined by ray tracing methods, using the warm plasma absorption coefficient /9/ to calculate the wave damping along the ray trajectory /10/, as given by the cold plasma dispersion relation and the density profile. The target plasma has a peak electron temperature of 1.5 keV, which ensures strong and localized absorption over a very broad range of operating conditions.
In Figs.1, 2 the ray-tracing and the power deposition profile for a low (4×10^{19} m^{-3}) and a high (2.3×10^{20} m^{-3}) density case are shown respectively. Multiple wall reflections spread absorption inside the plasma column, so that a minimum value of the density is required to get localized

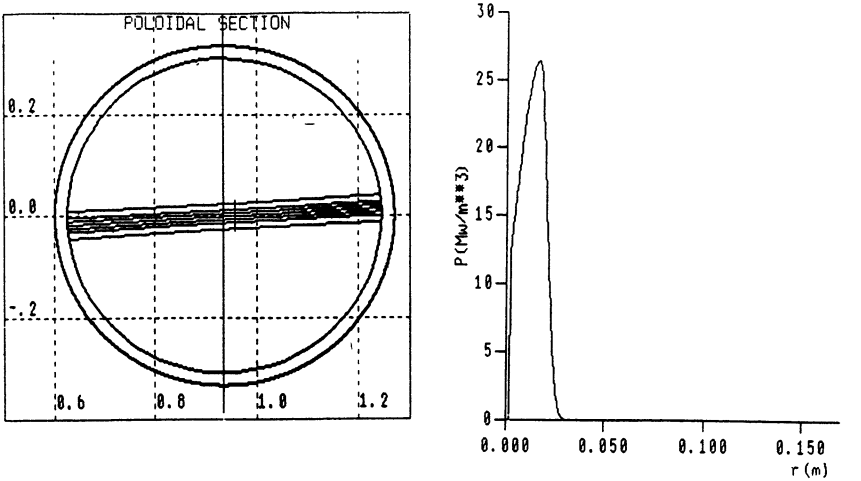

Fig.1 - Ray tracing and power deposition profile for central heating at low density (4 x 10^{19} m^{-3}). Absorption is 83.4% after the first and 95% after the second pass. $T_{e,peak}$= 1.5 keV.

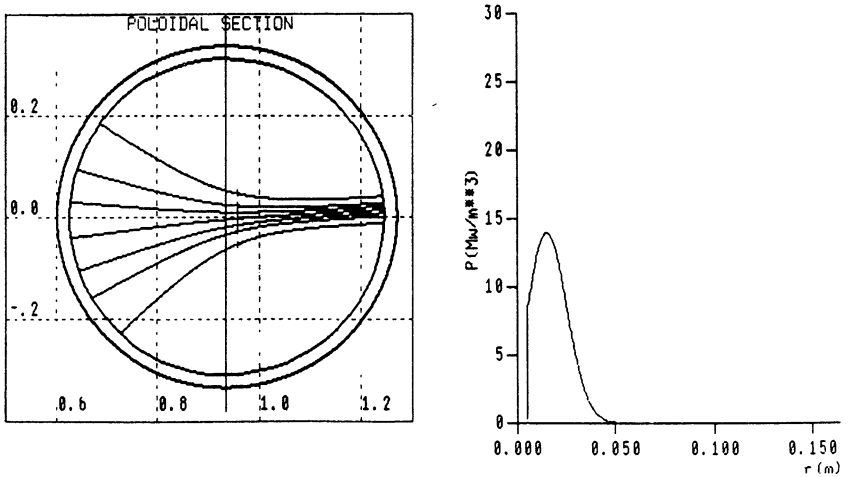

Fig.2 - Ray tracing and power deposition profile for central heating at high density (2.3 x 10^{20} m^{-3}). Absorption is 81.7% after the first and 95% after the second pass. $T_{e,peak}$= 1.5 keV.

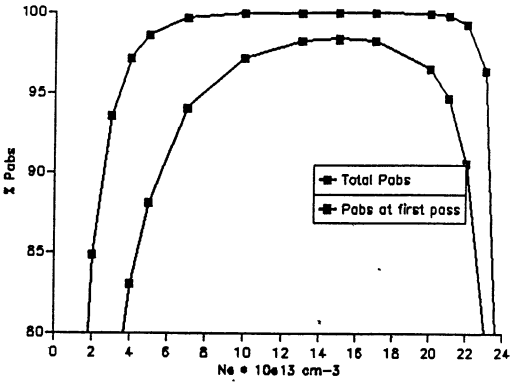

Fig.3 - Total absorbed power for central heating as a function of the peak density. The two curves are for one and two passes respectively. $T_{e,peak}$*= 1.5 keV.*

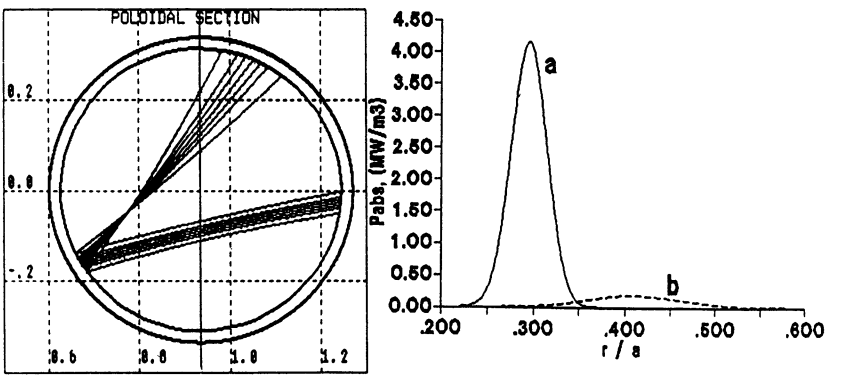

Fig.4 - Ray tracing and power deposition profile for off-axis ECRH by tilting the microwave beam. In the case of modest single-pass absorption, heating at the following passes would occur on different magnetic surfaces than the first one. The power deposition profile would be uncertain.

heating. If the inner wall of the vacuum vessel can be regarded as a cilindrical reflector, also the second pass can be taken reasonably into account in determining the power deposition profile /11/. In Fig.3 the fractional absorbed power in the first two passes is shown. The use of an inner mirror considerably extends the range of densities over which the absorption can be assumed localized (95% absorption within 10% of the minor radius). Provided that the resonance is slightly out-shifted from the centre, full absorption and central heating are obtained even for peak densities very close to cut-off.

Localized off-axis heating can be achieved either by steering the beam in the vertical plane (e.g. in Fig.4) or by changing the toroidal field (Fig.5a,b).

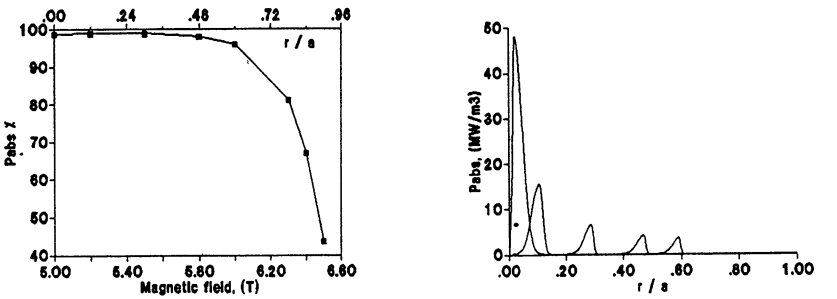

a *b*

Fig. 5 - a) Single pass fractional absorption as a function of the toroidal field. b) power deposition profiles for a few different values of the toroidal field. $n_{e,peak} = 1.5 \times 10^{20}\ m^{-3}$.

2 - Heat-wave generation by RF power modulation.

Two types of experiments can be performed for the purpose of studying energy transport using additional heating. The first is based on determining the electron energy balance in steady-state, the second on determining the propagation properties of the heat wave generated by a modulated power source.

The plasma electron energy balance equation can be written as

(1) $$n\frac{\partial T}{\partial t} - \partial_r[n\chi\partial_r(T) + nUT] = S + D$$

where T(r,t) and n(r,t) are the measured electron temperature increase and density profiles, and $\chi(r)$ is the electron thermal diffusivity. S(r,t) is the additional heating term due to ECRH, and D(**r**,t) represents all other sources and sinks of energy (including the power transfer to the ions, the power loss due to radiation and the Ohmic power due to the plasma current). The term nUT represents a non-diffusive heat transport process. This additional term, if present, complicates the transport analysis considerably. In fact, for steady-state conditions, it is not possible to separate the $\chi(r)$ and U(r) terms unambiguously. Besides, D must be accurately known in this case. To overcome these difficulties, a second type of experiment based on the temporal modulation of the EC power source is receiving increasing consideration.

If a periodic source term S is applied to the plasma, then also the temperature variation is periodic and its dependence on space and time can be described as the superposition of harmonic heat waves. Considering a single harmonic heat wave, the temperature perturbation $T_\omega(r)$ can be measured in its amplitude, A_ω, and phase, ϕ_ω. These are defined by $T_\omega = A_\omega e^{i\phi_\omega}$. T_ω will satisfy the equation

(2) $$\frac{3}{2}i\omega T_\omega - \partial_r(\chi_{eff}\partial_r T_\omega + U_{eff} T_\omega) = S_\omega + D_\omega$$

where we have neglected the density perturbation. S_ω is now the modulated heat source and D_ω represents the perturbed energy sinks and sources which can be modelled by a damping term proportional to T_ω:

(3) $$D_\omega = -\alpha T_\omega$$

Note that χ_{eff} and U_{eff}, as determined by a perturbative experiment, are related to the steady-state χ and U but are not necessarily the same, as discussed in /13/. Below we drop the subscript *eff* for simplicity.

ECRH is an ideal technique to generate the heat wave, particularly in the millimeter-wave band in high density maxwellian plasmas, because it heats the electron population in a well known region of the plasma volume. In order to define the modulation frequency and amplitude required for the high power microwave system in FTU, we analyze the heat wave propagation problem in more detail.

In a finite slab with constant diffusivity χ the steady periodic temperature distribution outside the heated volume is given by:

$$T(x,t) = \left\{ C_1 e^{-\gamma(\omega,\chi,\ldots)x} e^{-i\beta(\omega,\chi,\ldots)x} + C_2 e^{\gamma(\omega,\chi,\ldots)x} e^{i\beta(\omega,\chi,\ldots)x} \right\} e^{i\omega t}$$

where C_1 and C_2 are determined by the boundary conditions.

In the case of pure diffusion $\gamma = \beta = k = \sqrt{(3\omega/4\chi)}$. The heat wave propagates with the phase velocity $v_\phi = \sqrt{4\omega\chi/3}$.

To the lowest order damping can be described by $D = -\alpha T$. It affects both the attenuation coefficient and the phase velocity to the same extent; $\gamma \approx k\ \{1 - \alpha/(3\omega)\}$; $\beta \approx k\ \{1 + \alpha/(3\omega)\}$. In the presence of convection, to the lowest order only the wave damping is affected, i.e., $\gamma \approx k\ \{1 - 5u/(3v_\phi)\}$; $\beta \approx k$.

The modulation frequency should be chosen in a way to minimize uncertainties in determining χ. A first simplification occurs if the edge (x=a) can be assumed to be a perfect thermal sink, so that C_2=0. In fact, for $\gamma a >> 1$ the wave is damped well before reaching the edge, and the heat wave propagation is insensitive to the boundary conditions.

We require that $\gamma a \approx 10 \div 15$. For a=0.33 m, χ=1 m^2/s, it must be $\omega/2\pi \approx 100 \div 200$ Hz. At these high frequencies, the effect of damping is small as shown in Fig.6 for typical FTU plasmas. The condition $\alpha/\omega < 0.15$ (satisfied over most of the FTU plasma radius) corresponds to a maximum phase error of ±5%. Also the effect of a non-diffusive term, which scales as U/v_ϕ, is reduced at high frequencies. Thus, it can be seen that a modulability of the EC wave generators up to at least 100÷200 Hz is necessary.

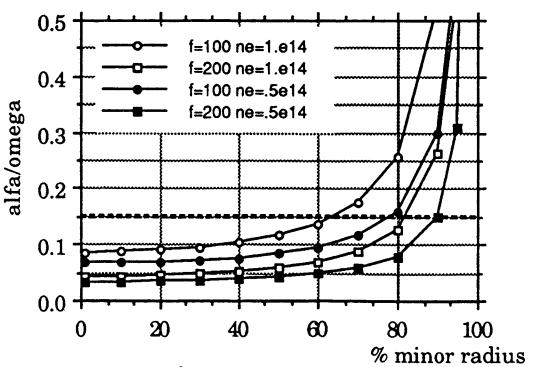

Fig.6 - Ratio between the modulation period and the characteristic time for the 'effective' energy damping (electron-ion energy transfer and OH input power reduction).

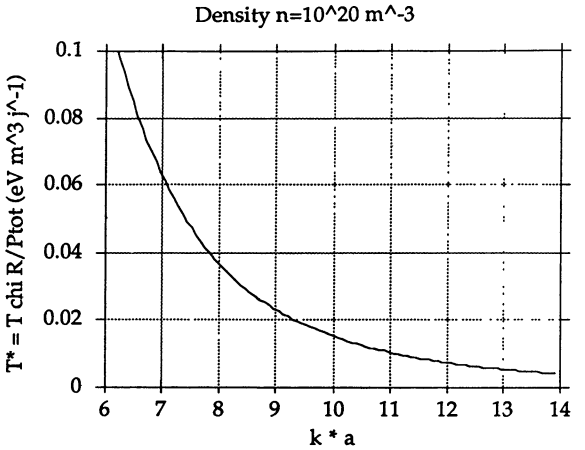

Fig.7 - Normalized fluctuating temperature at half radius in the case of central heating.

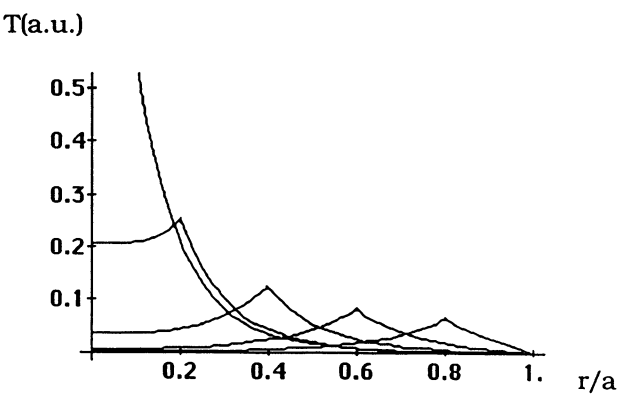

Fig.8 - Fluctuating temperature distribution for heating at different radii, with the same total absorbed power (γa = 10).

In order to estimate the amplitude of the modulated heating power, the fluctuating temperature can be calculated by solving eq.2 with the appropriate source term.
The normalized amplitude of the modulated temperature at half radius for central heating (i.e., $A_\omega \chi R/P_{tot}$) is shown in Fig.7 as a function of the product ka. With χ=1 m^2/s, R=.932 m, it follows that at 100 Hz $A_\omega/P_{tot} \approx 16$ eV/MW. Thus, an absorbed power of ≈200÷300 kW is adequate to provide a fluctuating temperature of ≈5 eV, well within the sensitivity of the ECE diagnostic capability taking into account the large signal-to-noise ratio obtainable by the use of synchronous detection.

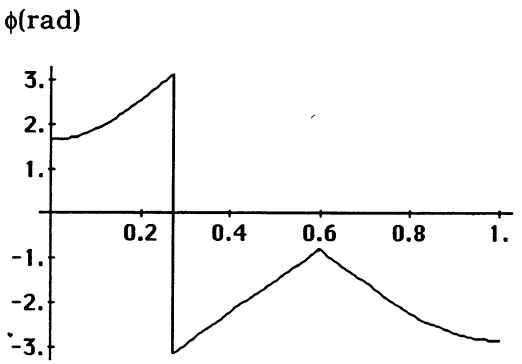

Fig.9 - Phase shift (with respect to the modulated rf power) vs. normalized radial position in the case of off-axis heating (r/a = 0.6) (γa = 10).

It should be noted that the good localization of the absorbing volume allows in principle to move the measuring point closer to the directly heated volume, with some benefit for the amplitude of the fluctuating temperature. This localization is high also for off-axis heating (see Fig.4-5). In that case also inward propagation of the heat wave can be in principle be detected (Fig.8,9), and the technique applied to study transport in the plasma centre.

3 - Millimeter-wave system.

The high power microwave complex is a hybrid system using a circular, oversized, corrugated waveguide to transfer the e.m. waves from the gyrotrons to the tokamak with low attenuation and mode conversion losses. Quasi-optical components match the line both to the gyrotron and to the plasma.

The present design is based on the assumption that the output mode of the gyrotron is a whispering gallery $TE_{15,2}$. The total power of 1.6 MW is provided by 4 tubes, delivering 400 kW each, with an estimated dominant-mode efficiency of 95%. The output mode is converted into a Gaussian beam by a quasi-optical Vlasov-type antenna and beam-matching mirrors. The estimated whispering gallery-to-Gaussian beam conversion efficiency is at least 80%.

Full control of the polarization can be achieved by reflecting surfaces arranged to form a quasi-optical polarizer /14/. The Gaussian beam is then efficiently coupled to the $HE_{1,1}$ mode in a circular corrugated waveguide with an i.d. of 88.9 mm. Within the approximately 30 m length of the transmission line, 5 90° mitre bends accomplish for the necessary changes in the direction and cope with the site constraints. The line is truncated at the tokamak end, and radiates a Gaussian beam with an estimated overall Gaussian beam-to-Gaussian beam efficiency of 85%. It follows that the estimated overall gyrotron output-to-end beam efficiency is ≈ 65%.

Each output beam is matched to one of a set of 4 ellipsoidal tiltable mirrors, to launch into the plasma converging Gaussian beams movable in the poloidal cross-section. A few details of this antenna system will be given in a following section.

The quasi-optical converter at the output of a $TE_{15,2}$ gyrotron oscillating at 140 GHz, with an output diameter of 3.5" (88.9 mm) is uncomfortably long (≈ 1.4 m). An antenna with two diametrically opposed longitudinal cuts would be half in length, and two coherent beams would be generated (Fig.10). The two beams can be coaxially combined and their polarization and phase controlled to provide a single beam with any desired polarization (Fig.11). The same arrangement, based on the use of wire-grid reflectors sensitive to the polarization, could be used either as a directional coupler or a microwave switch.

The transmission line together with the launching system is fully compatible with gyrotrons delivering directly a Gaussian beam. Only an appropriate matching mirror would be required in this case.

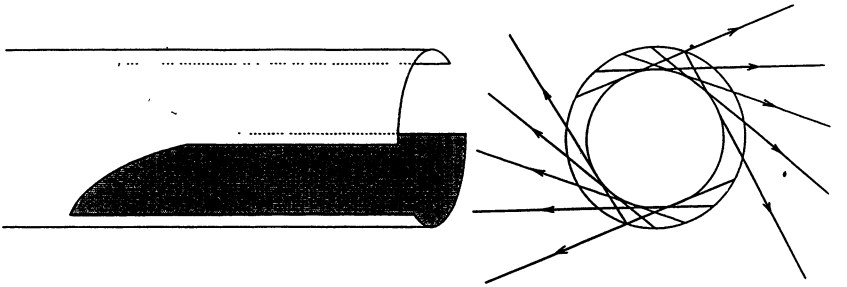

Fig.10 - Scheme of a dual-cut quast-optical radiator.

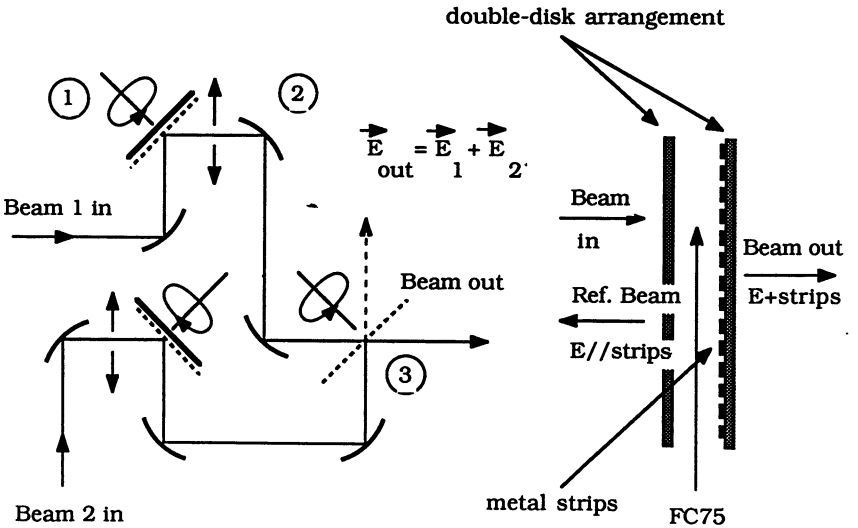

1 - Polarization-twisting reflector
2 - Ellipsoidal mirror
3 - Polarization-sensitive reflector

Scheme of the polarization-sensitive reflector

Fig.11 - Scheme of a dual-beam polarizer

4 - Quasi-optical components at the gyrotron output.

The design of the proper truncation of oversized waveguides to radiate polarized TEM waves /15,16,17,18,19,20,21/ can be based on the description of the guided propagation in terms of rays periodically bouncing at the walls of the waveguide /22/. This description finds its mathematical basis in the approximate solution of the Helmoltz equation for the electromagnetic field in regions bounded by conducting walls /23/. We want to obtain here the same result by finding an asymptotic approximation of the exact solution for the e.m. fields of rotating $TE_{m,n}$ modes in the waveguide. By posing:

$$\chi_{m,n} = n - \text{th root of } J'_m \; ; \; k_c = \frac{\chi_{m,n}}{a}$$

'a' being the waveguide radius, it follows that if m>>1 and $k_c r > m$ the Bessel function of integer order $J_m(k_c r)$ and its derivative can be approximated as (Debye approximation):

$$J_m(k_c r) = J_m(m \sec\beta) \cong \sqrt{\frac{2}{\pi m \tan\beta}} \cos\left[m(\tan\beta - \beta) - \frac{\pi}{4}\right]$$

$$J_m'(k_c r) = J_m'(m \sec\beta) \cong -\sqrt{\frac{\sin 2\beta}{\pi m}} \sin\left[m(\tan\beta - \beta) - \frac{\pi}{4}\right]$$

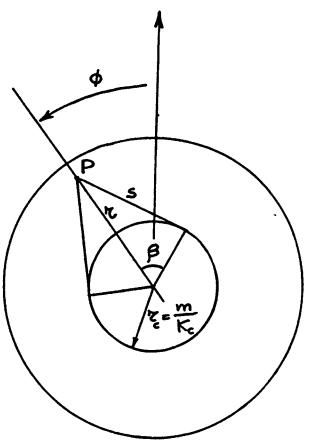

Fig.12 - Geometry of the waveguide rays.

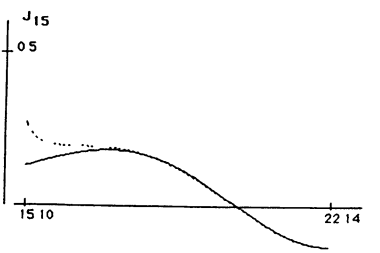

Fig.13 - Exact and approximate plot of $J_{15}(x)$.

where:

$$\sec\beta = \frac{k_c}{m} r \quad ; \quad \beta = \cos^{-1}\left(\frac{r_c}{r}\right) \quad ; \quad r_c = \frac{m}{k_c} = \frac{m}{\chi_{m,n}} a$$

The geometrical meaning of the angle β and of the radius r_c can be seen in Fig. 12. The exact radial dependence of $J_{15}(x)$ between $x \approx 15$ and $x = \chi_{15,2} = 22.14$ is shown together with the approximating expression in Fig.13. By introducing the length $S = \sqrt{(r^2 - r_c^2)}$, it is obtained:

$$m(\tan\beta - \beta) = k_c[S - r_c\beta]$$

The whispering gallery modes in oversized waveguides satisfy the conditions to apply the Debye expansion. By writing the trigonometric functions in their exponential form and taking into account the term $e^{im\phi}$, the electric field components of rotating modes in a circular waveguide set along the z-axis can therefore be given by the following approximate expressions:

$$E_r = -i\frac{m}{r}\sqrt{\frac{2}{\pi S k_c}}\left\{\frac{e^{-i\Psi_1}}{2} + \frac{e^{-i\Psi_2}}{2}\right\}e^{-ik_z z}$$

$$E_\phi = -ik_c\sqrt{\frac{2Sr_c}{\pi m}}\left\{\frac{e^{-i\Psi_1}}{2} - \frac{e^{-i\Psi_2}}{2}\right\}e^{-ik_z z}$$

Taking into account the modulus $2m\pi$, the phases Ψ_1 and Ψ_2 can be written as:

$$\Psi_1 = k_c[S - r_c\beta - r_c\phi] - \frac{\pi}{4} + k_c r_c \cdot 2\pi = k_c l_1$$

$$\Psi_2 = k_c[S - r_c\beta + r_c\phi] - \frac{\pi}{4} + k_c r_c \cdot 2\pi = k_c l_2$$

both the radial and the azimuthal components of the electric field are therefore given by the superposition of two waves propagating along rays as shown in Fig.14. In fact, let us consider the total electric field of one of the two waves at any point $r_c < r < a$:

$$\mathbf{E}_i = E_r^i \hat{r} + E_\phi^i \hat{\phi} = i\frac{1}{r}\frac{e^{-i\Psi_1}}{2}\left\{-\sqrt{\frac{2m}{\pi}}\sqrt{\frac{r_c}{S}}\hat{r} - k_c\sqrt{\frac{2}{\pi m}}\sqrt{Sr_c}\hat{\phi}\right\}$$

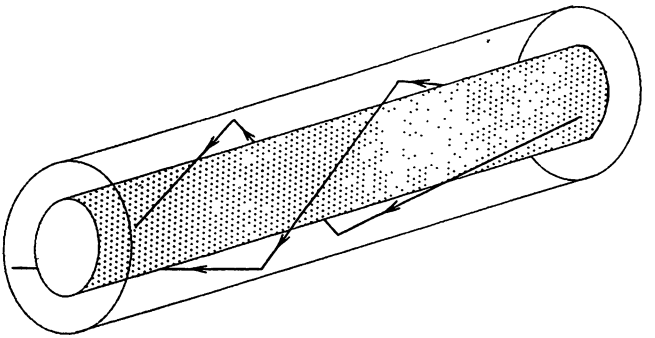

Fig. 14 - Scheme of the rays bouncing in the waveguide.

Since (Fig.15):

$$\tan\beta = \frac{S}{r_c} \quad ; \quad \frac{E_\phi}{E_r} = \frac{S}{r_c}$$

then it follows that the electric field $\mathbf{E}_i$ and the ray $\mathbf{S}_i$ are perpendicular, as in free TEM waves. At the wall (r=a) E_ϕ=0, and one of the two families of rays can be obtained from the first one by reflection at the wall (Fig.16).
At the point B in Fig.16 the ray 1 has a phase given by $\Psi_1^i = -k_c r_c[\beta-\phi-2\pi]-\pi/4$, while the ray 2 has the phase $\Psi_2^i = -k_c r_c[\beta-\phi]-\pi/4$. The two rays can be considered correspondent, but with a phase jump of $\pi/2$, as normally occurs in optics on crossing a caustic.
In conclusion, the description of the guided propagation of whispering gallery modes in oversized circular waveguides in terms of rays tangent to a caustic and periodically reflected at the walls is fully consistent with the requirements of the Geometrical Optics Theory.
The field radiated from a truncated waveguide can therefore be obtained to the lowest order by continuing the propagation along the 'incident' rays in the guide. The approximating assumptions are in this case that the structure of the rays in the ideal homogeneous waveguide remains unaffected by the cut in the wall, and that diffraction phenomena are negligible.

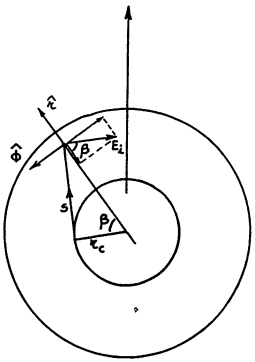

Fig. 15 - Electric field components of the 'incident' ray.

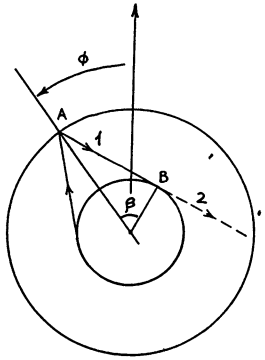

Fig.16 - Rays at wall reflection and caustic crossing.

The primary radiated field is therefore given by:

$$\mathbf{E}_{rad}(r,\phi,z) = i\frac{\sqrt{k_c}}{r}\left\{-\frac{r_c}{\sqrt{S}}\hat{r} - \sqrt{S}\hat{\phi}\right\} e^{-i\Psi} e^{-ik_z z}$$

$$\Psi = k_c[S - r_c\beta - r_c\phi] \quad ; \quad S = \sqrt{r^2 - r_c^2}$$

The rays emerge inclined with respect to the waveguide axis by an angle:

$$\theta_v = \arctan\frac{k_c}{\sqrt{k_0^2 - k_c^2}}$$

and are uniformly distributed to form a fan of amplitude (Fig.17)

$$2\alpha = 2\ \arccos\left(\frac{m}{k_c a}\right)$$

Mirrors can be used to modify the shape of the phase-front. In order to obtain a plane wave, a cylindrical mirror with proper cross section is necessary. The exact profile for a mirror reflecting rays parallel to the x-axis of Fig.18 is given in parametric form by:

$$\begin{cases} x(\delta) = r_c\cos\delta - S(\delta)\sin\delta \\ y(\delta) = r_c\sin\delta + S(\delta)\cos\delta \end{cases}$$

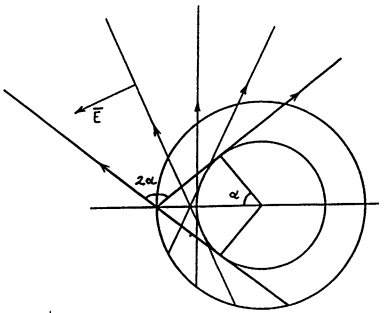

Fig.17 - Radiated field and rays.

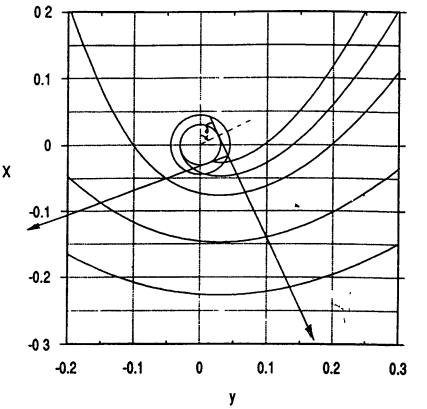

Fig.18 - Family of mirrors for reflection parallel to x-axis.

where:

$$S(\delta) = \frac{2F + r_c\left(\cos\delta - \delta + \frac{\pi}{2}\right)}{1 + \sin\delta}$$

A family of mirrors is obtained by changing the free parameter F. The position of the radiating cut can be changed by rotating the waveguide around its axis. Different portions of the mirror are in this case illuminated and the power density profile in a plane perpendicular to the reflected rays is also changed. Two free parameters are therefore available to obtain a reflected beam with the highest $TEM_{0,0}$ Gaussian mode content. In particular, F is adjusted in order to radiate a beam with equal widths in the E-plane and in the H-plane. The position of the radiating cut is chosen in order to obtain a symmetric power distribution profile.

The normalized field distribution of a Gaussian beam propagating along a z-axis is given by:

$$u_{0,0}(x,y,0) = \frac{1}{\sqrt{\frac{\pi}{2} w_x w_y}} e^{-\left[\left(\frac{x}{w_x}\right)^2 + \left(\frac{y}{w_y}\right)^2\right]}$$

The power in the Gaussian mode of the output beam if therefore given by:

$$P_{0,0} = \frac{1}{2}\sqrt{\frac{\varepsilon_0}{\mu_0}}\, C_{0,0}^2$$

$$C_{0,0} = \frac{1}{\sqrt{\frac{\pi}{2} w_{0,x} w_{0,y}}} \int_{Y_1}^{Y_2} E_y(y) e^{-\left(\frac{y-y_0}{w_{0,y}}\right)^2} \left(\int_{G_1(y)}^{G_2(y)} e^{-\left(\frac{x'-x_0}{w_{0,x}}\right)^2} dx' \right) dy$$

where Y_1, Y_2, G_1, G_2 define respectively the contour of the beam cross-section A in a plane perpendicular to the beam axis (Fig.19). The total power in the beam is:

$$P_A = \frac{1}{2}\sqrt{\frac{\varepsilon_0}{\mu_0}} \iint_A E_y(y)^2 dxdy$$

and the Gaussian mode coupling efficiency is therefore given by:

$$\eta = \frac{P_{0,0}}{P_A} = \frac{C_{0,0}^2}{\iint_A E_y^2(y) dxdy}$$

In the specific case of a $TE_{15,2}$ mode at 140 GHz, radiated from a waveguide with an inner diameter of 88.9 mm, a maximum efficiency of 80.2% has been obtained with F=147 mm and δ=(66.5)°. The Gaussian mode with the best coupling coefficient to the reflected beam (Fig.20) has a waist radius $w_{0x}=w_{0y}$=123 mm.

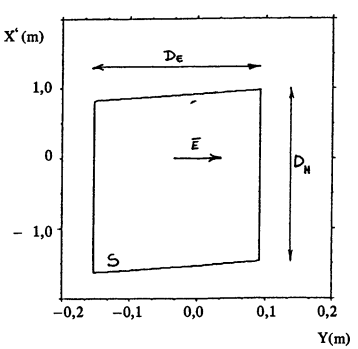

Fig.19 - Beam cross-section after reflection

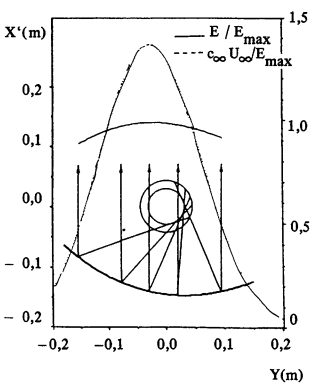

Fig.20 - Electric field after reflection compared with Gaussian distribution.

5 - Quasi-optical antennas for plasma irradiation.

A primary requirement posed to the waveguide-to-plasma coupler is to provide for the best localization of the absorbed power. Furthermore, the position of the heated volume should be movable in the poloidal cross section. A quasi-optical solution has been chosen, based on a set of 4 tiltable ellipsoidal mirrors launching 4 Gaussian beams with the waist close to the centre of the vacuum vessel (Fig.21). Other ellipsoidal and flat mirrors match the final beams and mirrors to the HE1,1 mode in the transmission line (Fig.22).

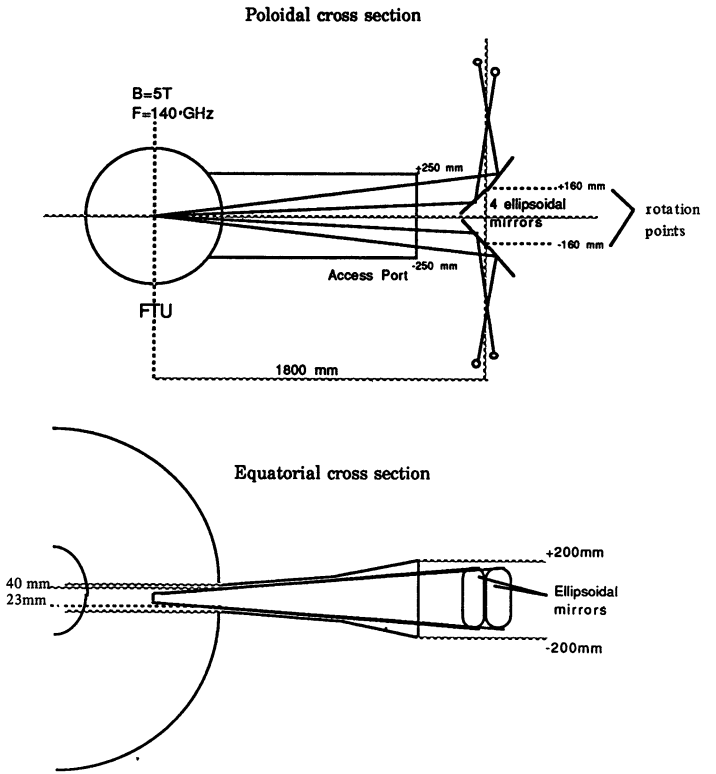

Fig.21 - Scheme of the final mirrors and Gaussian beams for plasma irradiation.

The waist w_1 in the vacuum, close to vertical mid-plane, varies between 16 and 20 mm depending on tilt angle (±2.5°). The input beam has a waist radius w_2 of 8 mm and is matched by an ellipsoidal mirror to the Gaussian beam (w_0 = 29.3 mm) excited by the $HE_{1,1}$ propagating in the 88.9 mm i.d. corrugated waveguide.

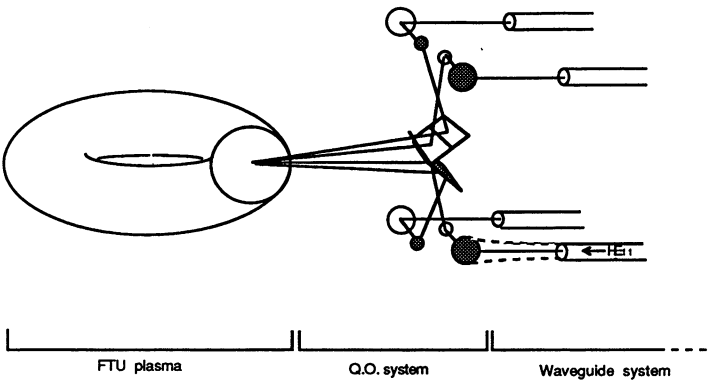

Fig.22 - Scheme of the quasi-optical arrangement for the plasma-to-waveguide coupling system.

References

/1/ Airoldi A. et al., Plasma Phys. **30**, 681 (1988)

/2/ Robinson D.C. et al., Proc. 3rd Joint Varenna-Grenoble Int. Symposium on Heating in Toroidal Plasmas, Grenoble (Euratom Report EUR7979 EN, 1982) v. II, p. 647.

/3/ Alikaev V.V. et al., Sov. J. Plasma Phys. **2**, 212 (1976)

/4/ Bulyginski D.G. et al., Proc. 10th Int. Conf. Plasma Physics and Controlled Nuclear Fusion, London, 1984 (IAEA-CN-44/Vienna, 1985) v. I, p. 491

/5/ Airoldi A. et al., Proc. 14th EPS Conf. Controlled Fusion and Plasma Physics, Madrid, 1987, v. III, p. 976

/6/ Farina D., Pozzoli R., Phys. Fluids B, **1**, 815 (1989)

/7/ Rebuffi L., this conference

/8/ Thumm M., this conference

/9/ Krivenski V., Orefice A., J. Plasma Physics, **30**, 125 (1982)

/10/ A.Airoldi et al., Lettere al Nuovo Cimento, **43**, 340 (1985)

/11/ S.Cirant et al., Proc. 17th EPS Conf. Controlled Fusion and Plasma Heating, Amsterdam, 1990, v. III, p. 1108
/12/ De Luca F. et al., Proc. Joint Varenna-Lausanne Int. Workshop on Theory of Fusion Plasmas, Varenna, 1990
/13/ Gentle K.,
/14/ Thumm M. et al., Conf. Digest 13th Int. Conf. on Infrared and Millimeter Waves, Honolulu, 1988, p.111.
/15/ Vlasov S.N., Orlova J.M., Radiofizika, **17**, 115 (1974)
/16/ Vlasov S.N., Zagryadskaya, Petelin M.I., Radio Eng. **20**, 14 (1975)
/17/ Möbius A., Kreischer K., Temkin R., Conf. Digest 13th Int. Conf. on Infrared and Millimeter Waves, Honolulu, 1988, p.121
/18/ Vlasov S.N., Shapiro M.A., Sheinina, Radio Phys. **31**, 1482 (1988)
/19/ Möbius A., Thumm M., Conf. Digest 14th Int. Conf. on Infrared and Millimeter Waves, Würzburg, 1989
/20/ Iima M. et al., Conf. Digest 14th Int. Conf. on Infrared and Millimeter Waves, Würzburg, 1989
/21/ Gaponov A.V., Petelin M.I., this Conference
/22/ Plonsey, Collin, "Principles and applications of EM fields", McGraw-Hill, 1961
/23/ Keller, Rubinow, Annals of Physics, **9**, 24 (1960)

ECR HEATING EFFECT ON PLASMA CONFINEMENT IN GAMMA 10

T. Saito, Y. Kiwamoto, K. Kurihara, T. Honda, A. Kasugai,
T. Cho, K. Ishii, I. Katanuma, A. Mase,
N. Yamaguchi and S. Miyoshi

Plasma Research Center, University of Tsukuba
Tsukuba City, Ibaraki 305, Japan

ABSTRACT This paper describes results of electron cyclotron resonance heating (ECRH) experiments from the view point of its effets on plasma confinement in the GAMMA 10 tandem mirror. On application of the fundamental ECRH, large amount of differences are formed in the distribution of the plasma potentials and the end loss ion flux is drastically reduced while an enhanced axial electron flux is observed. From the measurement of the energy spectrum of the end loss electrons a physical concept is developed that electrons are strongly diffused along heating characteristics associated with ECRH and then driven into the loss cone of a mirror field, which consequently results in high plasma potentials. A model calculation of potential profile between the outer mirror throat and the floating end plates is presented with the effect of the magnetic field profile taken into account. Recent experiment of hot electron production in an Min-B anchor cell is also given.

1. INTRODUCTION

Use of electron cyclotron resonance heating (ECRH) has been one of the main subjects in studies of magnetic confinement fusion and the study of ECRH has a long history [1]. However, frequencies and output powers of available microwave sources were limited in the initial stage of ECRH study. Development of a high power

gyrotron has broken through these limits [2] and full-scale applications of ECRH have since been carried out in tokamaks and stellarators[3]. The current tandem mirror with a thermal barrier also relies extensively on gyrotrons for ECRH [4,5].

While use of ECRH in a tandem mirror is based on results of basic ECRH experiments in mirror fields, it should be studied from the view point of new physics issues to meet its specific roles in a tandem mirror. One of the major roles of ECRH is the formation of an axial potential profile as shown in Fig. 1. A tandem mirror basically consists of a center cell in which the bulk of ions are confined and end cells which are located on both sides of the center cell. Ions are confined magnetically and electrostatically. The potential peak at the position p in Fig. 1 is an ion confining plug potential. The height of the plug potential is raised by the fundamental (ω_{ce}) ECRH via local heating of warm electrons in the plug region. The depression of the potential at position labeled b is a thermal barrier and isolates warmer electrons in the plug region from colder electrons in the central region. For the formation of the thermal barrier the second harmonic ($2\omega_{ce}$) ECRH is supposed to create mirror confined hot electrons near the midplane of the end cell. Thus each ECRH applied to different positions in a tandem mirror has a specific purpose. High power microwave is injected into a restricted area and it should be absorbed locally. Electrons interact with localized strong wave fields, which characterizes the ECRH in a tandem mirror.

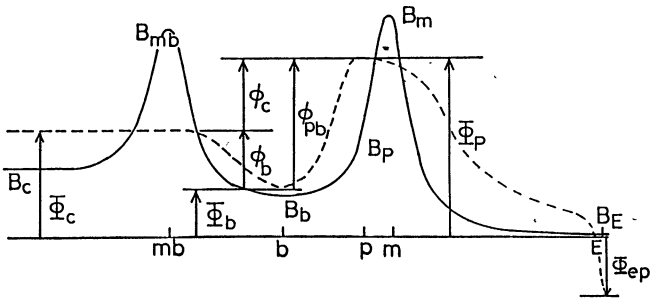

Fig. 1 Profiles of the magnetic field and the potential in the region extending from the end cell to the end plate. The solid and dashed lines denote the magnetic field and the potential, respectively. The center cell is located to the left.

Experimental results of $2\omega_{ce}$ ECRH has been reported elsewhere [6,7,8]. Thus in this paper we put emphasis on ω_{ce} ECRH, which has been observed to be predominantly responsible for the potential formation and consequently to have strong effects on plasma confinement in the GAMMA 10 tandem mirror[9,10]. Moreover, the ω_{ce} ECRH is concerned with many physics issues. First, the heating configuration is that of the beach heating[11]. The microwave power is injected from the high field side of the fundamental resonance surface and a very high efficiency of one pass absorption is expected[12]. This feature is suitable for localized heating of warm electrons in the plug region.

Secondly, electrons are strongly accelerated by the ω_{ce} ECR wave and diffused along heating characteristics in velocity space [13,14]. A part of the heated electrons are driven into the loss cone, which results in high plasma potential. Thus measurement of end loss electrons has a particular significance to understanding of mechanisms of electron heating as well as of potential formation. We present measurement of end loss electrons and then discuss about the inseparable relation between the enhanced velocity diffusion and the potential formation. The potential profile of a thermal barrier tandem mirror is based on the existence of non Maxwellian electrons, which is brought about by the strong heating in rather a low density plasma.

The end loss electron measurement also provides a basis of a model for calculation of the potential profile in the end region between the outer mirror throat and the floating end plates. We extend a sheath model so that it includes the effect of secondary electrons emitted from the end plate materials and calculate the potential profile taking account of the fanning effect of magnetic field lines.

The compositon of the present paper is as follows. The GAMMA 10 device and the ECRH configuration is described in Sec. 2. Experimental results on confinement and measurement of the end loss electrons are given in Sec. 3 and the relation between electron diffusion in velocity space and the potenial formation is discussed in Sec. 4. Calculation of the potential profile is also described in Sec. 4. Preliminary results of hot electron production in an Min-B anchor cell is presented in Sec. 5. A summary is given in Sec. 6.

2. GAMMA 10 AND ECRH SYSTEM

2.1 GAMMA 10

The GAMMA 10 tandem mirror is an effectively axisymmetrized tandem mirror[15]. It has a center cell, two anchor cells and two axisymmtric end mirror cells. The anchor cells are MHD stabilizers with a Min-B configuration. The plug potential and the thermal barrier are formed in the axisymmtric end mirror cells, which we refer to merely as the end cells from now on. The mirror ratios of the center cell, the anchor cell and the end cell are 5, 3, and 6, respectively. Although the magnetic field strength of each cell is independently adjustable, the magnetic flux tube is circular in both the center cell and the end cells for particular combinations of the field strength. For a standard plasma shot the field strengths at the midplane of each cell are 0.405 T, 0.610 T and 0.497 T, respectively. Plasmas are radially bounded by a limiter of 36 cm in diameter located near the midplane of the center cell.

Ion cyclotron heating antennas are installed in the center cell. High energy neutral beams are injected into the anchor cells for MHD stabilization (Anchor NBI) and into the end cells for formation of a sloshing ion distribution (Sloshing NBI). Plasma shots are usually started with a stream plasma which is injected along the field line with plasma guns located on both end walls.

Electrically floating end plates are installed in front of both end walls. The role of the plates is to adjust the potential distribution so as to reduce the non ambipolar radial transport[9]. The plates are made of stainless steel and radially divided into five pieces. Each piece is connected to the machine ground with a resister of 1 MΩ which reads the floating potential of each plate.

2.2 ECRH system

ECRH has been carried out in both end cells for the formation of a combination of a thermal barrier and a plug potential. Microwave source for the ECRH is a 28 GHz TOSHIBA gyrotron(E3955). It delivers maximum power of 140 kW in TE_{02} mode and the pulse width is 75 ms. Four 28 GHz gyrotrons are used in both ends (two

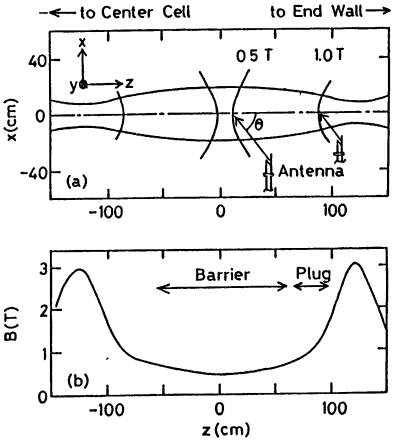

Fig. 2 Configuration of ECRH in the end cell. (a) Magnetic field lines and resonance surfaces. (b) Profile of the magnetic field strength.

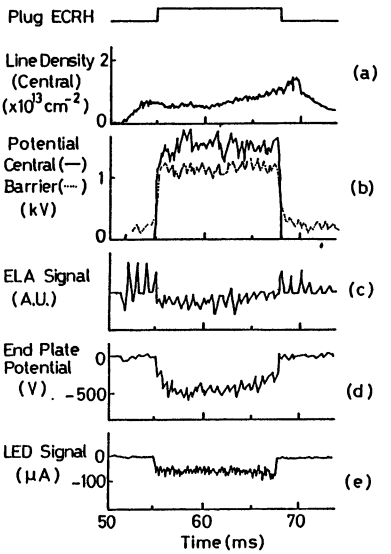

Fig. 3 Wave forms of densities and potentials. Electron and ion end loss fluxes are also shown.

per each cell). The microwave power is transmitted in TE_{02} mode in circular waveguides, the diameter of which are tapered down from 62.6 mm (the diameter of the gyrotron) to 37 mm, and then radiated from an antenna onto the resonance surfaces as shown in Fig. 2. The antenna is a Vlasov-Nakajima type which converts the TE_{02} mode into the linearly polarized TEM mode. The figure shows two antennas. One is used for ω_{ce} ECRH (plug ECRH) and the other is used for $2\omega_{ce}$ ECRH (barrier ECRH). The radiated microwave is linearly polized in the y-direction (extrordinary mode) and collimated in a pencil beam with FWHM≒11° in the H-plane and ≒7° in the E-plane. Thus the cross section of the microwave beam is slightly elliptic. It is launched upward at an angle of 50° to the z-axis. The resonance surfaces form hyperboloids and the central ray of each microwave beam intersects the on-axis vertex of the resonance surface. The microwave of plug ECRH is launced from the high field side and then it is expected to be absorbed very efficiently at the magnetic beach. The magnetic field scale length

L=1/B(dB/dz) is about 26 cm at the 1.0 T surface.

We have recently installed a 41 GHz gyrotron (TOSHIBA E3962). It delivers 200 kW in TE_{02} mode for 100 ms. This gryrotron is used for production of hot electrons in an anchor cell. The transmitted power is injected onto the midplane of the Min-B mirror field with a Vlasov-Nakajima antenna in the extraordinary mode.

3. EXPERIMENTAL RESULTS

3.1 ECRH effects on confinement and potential formation

On application of the ω_{ce} ECRH the ion confining plug potential is formed and consequently the endloss ion flux is strongly reduced as shown in Fig. 3. Plasma potentials measured at different positions go up simultaneously and the floating potential of the end plate goes down deeply from the machine ground. Contrary to the reduction of the ion flux, the end loss electron flux remarkably increases. The electron flux as measured with a multi-gridded energy analyzer (Loss Electron Diagnostic LED) installed behind the end plate is also shown in Fig. 3. The electron flux is measured through a small hole on the end plate. The equivalent radial position of LED mapped back to the plug position along the magnetic filed line is 2.8 cm off the magnetic axis. An end loss analyzer (ELA) placed in front of the end plate can also measure the electron flux. The ELA is usually used to measure the ion flux and the maximum potential in the plsma (plug potential). It is scannable along the x-direction.

As shown in Fig. 3 the ω_{ce} ECRH has a very strong effect on confinement as well as on plasma potential. The difference between the center cell potential Φ_C and the end plate potential Φ_{EP} works as the confining potential of the center cell electrons. Figure 4 plots $\Phi_C-\Phi_{EP}$ as a function of the ion confining potential $\phi_c=\Phi_P-\Phi_C$. Both values are normalized by the center cell electron temperature T_{ec} and the ion temperature T_i, respectively. It is seen that the normalized electron confining potential is very large (up to 20) during the turn-on time of the ω_{ce} ECRH. The solid and dashed lines in the figure represent the theoretical relation between the electron confining potential and the ion confining potential which is predicted from the ambipolar condition.

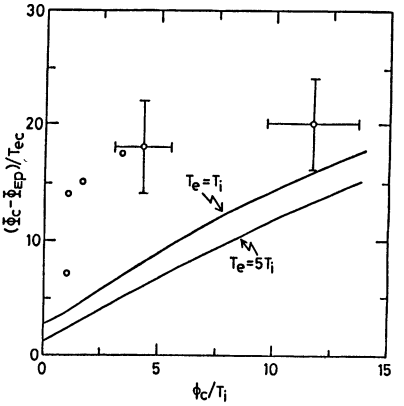

Fig. 4 Electron confining potential as a function of the ion confining potential. Solid lines stand for the prediction from the ambipolar condition.

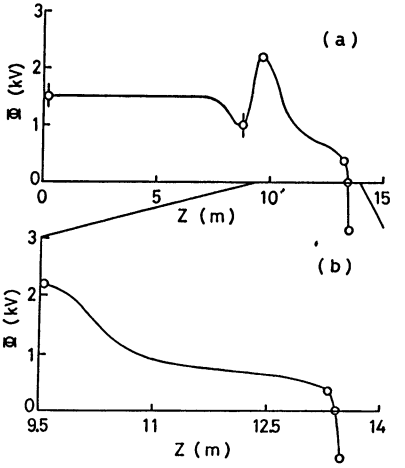

Fig. 5 Experimentaly obtained potential profile. The mid-plane of the center cell is located at z=0.

$$\tau_e = \tau_i \qquad (1)$$

where τ_e and τ_i are the electron and ion axial particle confinement times. They are evaluated with the Pastukhov formula [16]. The experimental points lie far away above the theoretical lines. Thus the center cell bulk electrons are considered to have little role on formation of the high plasma potentials.

Plasma potentials are measured at different positions along the axis. The center cell potential Φ_C and the barrier potential Φ_B are measured with gold neutral beam probes[17]. The plug potential Φ_P is measured with the ELA. The potential profile in front of the end plate is measured with a Langmuir probe. Figure 5 shows an example of the axial profile thus measured, which is considered to be typical one obtained in GAMMA 10 when the ω_{ce} ECRH is applied.

The radial profile of the plug potential is measured with ELA which is scannable along the x-direction. Figure 6 plots radial profiles of the plug potential, end loss electrons measured with ELA and the absorption profile of the microwave power[12].

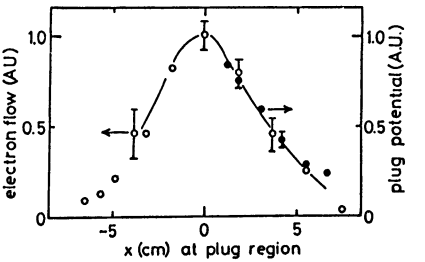

Fig. 6 Profiles of electron axial flow and plug potential. The solid line is absorption profile of microwave power.

Each profile is mapped back onto the fundamental resonance plane. They coincide with each other very well. Electrons are strongly heated with the plug ECRH and then a part of the heated electrons is driven into the loss cone along heating characteristics. These measurements indicate that the axial flow of electrons has a particular role on potential formation and plasma confinement.

3.2 Analysis of end loss electrons

We have analyzed the energy spectrum of the end loss electron flux [18]. Figure 7 (a) represents the electron current flowing into the collector of the LED as a function of the voltage V_{er} applied to the electron repeller grid. The end loss electrons

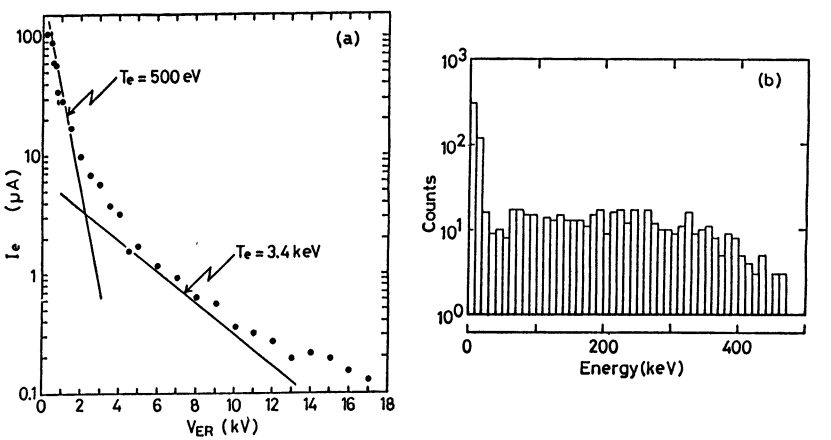

Fig. 7 Energy spectra of end loss electrons. (a) Enery spectrum measured with LED. (b) Spectrum of high energy electrons detected with SSB.

are apparently composed of multiple energy components. The spectrum can be principally divided into two components. The lower one has a mean energy of about 500 eV and the higher one has a mean energy of about 3.4 keV. The energies vary depending on experimental parameters such as the microwave power, the electron density, the radial position, etc.. However, the energy spectrum is mainly composed of the two components in usual shots. In high V_{or} region we can see another higher energy components, the mean energy of which is estimated to be about 15 keV. Its amount is very small; less than 0.5% of the total current. The spectrum of the end loss electrons extends continuously to much higher energies.

Figure 7 (b) shows an energy spectrum of end loss electrons measured with a silicon surface barrier diode[19]. The radial position of the detector is different from that of LED and the microwave power is not the same as that of Fig. 7 (a). However, we may essentially combine the two spectra. Both spectra were obtained during the ω_{ce} ECRH was turned on. The spectrum shown in Fig. 7 (b) has high counts at energies lower than 20 keV and continues to about 400 keV with an almost constant count rate.

The energy spectrum of the end loss electrons is thus obtained. Plasma potentials are determined to satisfy the charge neutrality. The electron confining potential is about four through six times the temperature of the low energy component. Thus these electrons are expected to have a major role in formation of high potentials. However, the mechanism is very complicated. The secondary electron emission from the end plate and the fanning of magnetic field lines in the end region also have significant effects. We shall present a model calculation of the potential profile in the end region in Sec. 4.

4. ELECTRON DIFFUSION AND POTENTIAL PROFILE

4.1 Diffusion of electrons in velocity space

Electrons are strongly diffused along heating characteristics in velocity space due to the interaction with cyclotron waves at the fundamental resonance. In the present experiment the electron density is rather low and hence the electron collision time is

much longer than the heating time. Then the diffusion process clearly appears to be observed in macroscopic quantities, e.g., the energy spectrum of end loss electrons.

It is worthwhile to compare the strengh of diffusion with that of the collisional process. The heating time τ_h associated with ω_{ce} ECRH and the drag time τ_d are appropriate figures for comparison. We use a formula for τ_h derived from the quasi-linear heating model[20].

$$\tau_h^{-1} = \frac{1}{T_{ew}} \frac{e^2|E_+|^2 L}{4m\Omega_0 l} \tan\theta , \qquad (2)$$

where E_+ is the electric field of the right-hand circularly polarized wave, Ω_0 is the cyclotron frequency at the midplane, $L=1/B(dB/dz)$ at the resonance position, l is the scale length of the magnetic field at the midplane and θ is the pitch angle of the resonant electron at the midplane. The drag time is estimated from the following equation[21]

$$\tau_d = 2.1\times10^4 (T_{ew}/n_e) \quad (\text{sec}) \qquad (3)$$
(T_{ew} in eV, n_e in cm^{-3}).

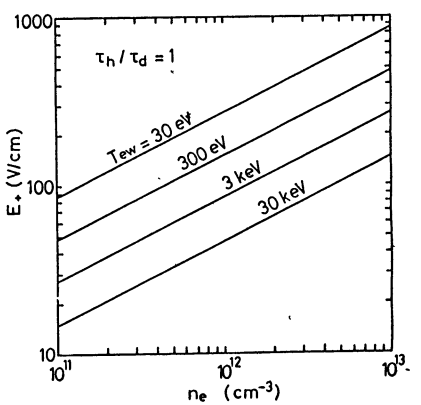

Fig. 8 $\tau_h/\tau_d=1$ curves for warm electrons with different temperatures. The pitch angle θ is assued to be 45 degree.

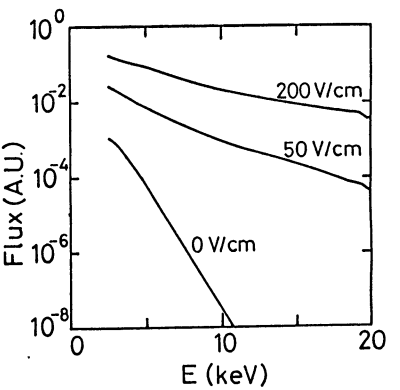

Fig. 9 Energy spectra of end loss electrons calculated wit the Fokker-Planck code for different wave fields.

Figure 8 plots curves of $\tau_h/\tau_d=1$ for various warm electron temperature T_{ew}. Because potentially confined electrons suffer from the drag effect due to cold electrons in the central region a factor, which is the ratio of the length of the end cell to that of the plasma region, is mutiplied in evaluation of τ_h/τ_d. In the upper side of the curves τ_h is smaller than τ_d. The electric field is 200 V/cm through 500 V/cm and the electron density is lower than (2 4)X10^{12} cm^{-3} in the present experiment. Therefore, non Maxwellian warm electron component may exist not to be thermalized with the background cold electrons.

A Fokker-Planck code has been developed to study the heating process of electrons by ECRH[22]. The code calculates the evolution of the electron distribution function taking account of quasi-linear diffusion by ECRH and Coulomb collisions. Then it yields energy distribution of the flux of electrons which pass the loss cone boundary. Figure 9 plots calculated energy distributions in the energy range lower than 20 keV. The calculation does not include the potential effect. However, we may compare the calculated distribution with experimentally obtained one in the range of the energy higher than electron confining potential (2 3 keV). Energy distributions in this range is similar to the high energy component of the end loss elecrons measured with the LED (see Fig 7(a)). The calculated flux is very small in the absence of the ω_{ce} ECRH. These features are consistent with observations and hence the quasi-linear diffusion model is considered to be essentially correct.

4.2 Velocity distribution of electrons at the plug region

Figure 10 shows the velocity space of electrons as referred to the plug position. Electrons in the elliptical curve is confined by the peak potential (see Fig. 1) and electrons above the line $v_\perp=v_{//}\tan\theta_{LC}$ are magnetically confined. Electrons in the shaded area (loss region) are not confined and reach the end plate. Heating characteristics are vertical lines in this space. Electrons are diffused very fast along the characteristics. Thus electrons are promptly lost when they transfer by a small pitch angl scattering to heating characteristics which reach the loss region [14]. The mechanism which causes the multi-component energy

spectrum of end loss electrons has not been fully revealed yet. The Fokker-Planck code calculation probably provides a partial explanation.

Recently x-ray measurement has indicated that a flat electron distribution function is formed in the ellipsoid in Fig. 10 by the ω_{ce} ECRH [23]. This observation also confirms the very strong diffusion of electrons in velocity space due to the ω_{ce} ECRH.

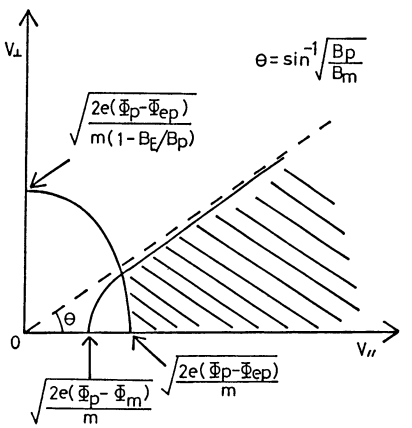

Fig. 10 Velocity space of electrons as referred to the plug position.

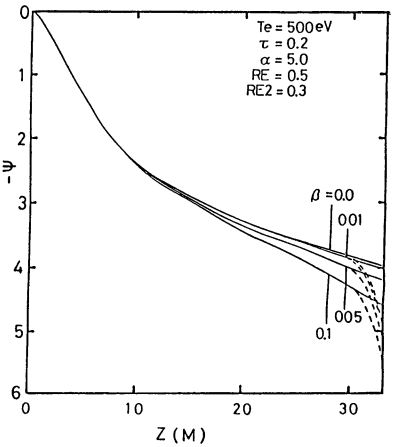

Fig. 11 Potential profile in the end region calculated with the model.

4.3 Calculation of potential profile in the end region

The distribution of the plasma potential varies so as to maintain the charge neutrality of the plasma. Therefore knowledge of loss flux (current density, enegy distribution, etc) is essential for examination of the process of the potential formation. We now have such knowledge even if not enough and try to reconstruct a potential distribution in the end region.

We have developed a model which is an extension of a model of the sheath potential[24]. Our model includes the fanning of magnetic field lines, secondary electron emission from the end plate, two component energy distribution of the end loss electrons. The distribution functions of end loss electrons and

ions are half Maxwellians at the outer mirror throat of the end cell. Then they become truncated Maxwellian on the way to the end plate. The flux of each species conserves. The density ratio between each species are determined from the condition that the total net current flowing into the end plate is zero.

An example of the calculated potential distribution between the outer mirror throat and the floating end plate is shown in Fig. 11. The potential plotted with the solid line is determined from the charge neutrality condition.

$$n_i(\Psi,B)-n_e(\Psi,B)-n_{se}(\Psi,B)=0, \qquad (4)$$

because the scale length of the potential variation is large compared with the Debye length. Here, Ψ is the normalized potential $e\phi/T_e$ with the temperature T_e of the low energy component, n_i, n_e and n_{se} are the ion, electron and secondary electron density, respectively. There is a sheath region just in front of the end plate where the charge neutrality is not satisfied. Thus the potential profile is determined from the Poisson's eq.

$$d^2\Psi/dz^2=-e^2\{n_i(\Psi,B)-n_e(\Psi,B)-n_{se}(\Psi,B)\}/\varepsilon_0 T_e \ . \qquad (5)$$

The potential falls by about four through five times T_e dué to the magentic field fanning and then further falls by about T_e in the sheath region. The calculation well reproduces the experimentally observed profile (see Fig. 3).

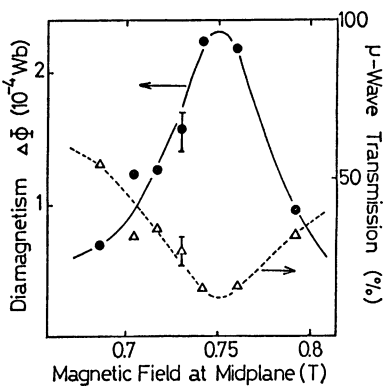

Fig. 12 Hot electron diamagnetism and microwave transmission as a function of the magnetic field at the midplane of the anchor cell.

5. HOT ELECTRON PRODUCTION IN ANCHOR CELL

Recently we have started an experiment to produce hot electrons in an Min-B anchor cell. Here we describe the preliminary results. The purposes of the experiment are 1) to obtain a high β plasma for an MHD stabilizer, 2) bulk electron heating in the central region and 3) potential control at the anchor cell.

Hot electrons are produced by $2\omega_{ce}$ ECRH. Figure 12 plots the hot electron diamagnetism as a function of the vacuum magnetic field strength at the anchor midplane. Hot electrons are produced most effectively near the field strength of the $2\omega_{ce}$ resonance (B_{rcs}=0.732 T). The hot electron diamagnetism continues to increase during the ECRH pulse. As the pulse width is increased, the maximum diamagetism is obtained at the field strength slightly higher than B_{rcs}. This is probably due to the diamagnetic effect of hot electrons. The maximum β value so far achieved is estimated to be 12% at the midplane.

6. SUMMARY

We have studied ECRH in the GAMMA 10 tandem mirror. Emphasis is put on the ω_{ce} ECRH and its effect on plasma confinement. Results are summarized as follows. 1) Application of the ω_{ce} ECRH is very effective for creation of the plug potential and axial particle confinement time of ions remakably increases. 2) The ω_{ce} ECRH is predominantly resonsible for high plasma potentials. It causes enhanced diffusion of electrons in velocity space and consequently produces a axial warm electron flux. Then the response of the plasma to maintain the charge neutrality results in the high plasma potentials. 3) A model has been developed which examine the potential profile of the end region and the model reproduces the experimentally obtained potential profile.

ACKNOWLEDGMENT

The authors would like to thank the members of the GAMMA 10 group for their collabolation and for stimulating discussions.

REFERENCES

[1] N.A.Uckan, Phys. Fluids 25 (1982) 2381.
[2] V.A.Flyagin et al., IEEE Trans. Microwave Theory and Tech. MTT-25 (1977) 514.
[3] A.C.England, IEEE Trans. Plasma Sci. PS-12 (1984) 124.
[4] D.E.Logan et al. Phys. Rev. Lett. 43 (1979) 1318.
[5] B.W.Stallard, IEEE Trans. Plasma Sci. PS-12 134.
[6] Y.Kiwamoto et al., Phys. Fluids 29 (1986) 2781.
[7] T.Cho, et al., Nucl. Fusion 27 (1987) 1421.
[8] T.Saito et al., Nucl. Fusion 30 (1990) 1533.
[9] M.Inutake et al., Phys. Rev. Lett. 55 (1985) 939.
[10] T.Cho et al., in Plasma Phys. and Cont. Nucl. Fusion Research 1988 (Proc. 12th Int. Conf. Nice, 1988), Vol.2, IAEA Vienna (1989) 501.
[11] T.H.Stix, The Theory of Plasma Waves (McGraw-Hill, NY 1962).
[12] T.Kariya et al. Phys. Fluids 31 (1988) 1815.
[13] T.D.Rognlien, Nucl. Fusion 23 (1983) 163.
[14] Y.Kiwamoto et al., J. Phys. Soc. Japan 58 (1989) 2619.
[15] T.Cho et al., in Plasma Phys. and Cont. Nucl. Fusion Research 1984 (Proc. 10th Int. Conf. Nice, 1984), Vol.2, IAEA Vienna (1985) 275.
[16] R.H.Cohen et al., Nucl. Fusion 18 (1978) 1229.
[17] K.Ishii et al., Nucl Fusion 30 (1990) 1051.
[18] K.Kurihara et al., J. Phys. Soc. Japan 58 (1989) 3453.
[19] T.Saito et al., Phys. Rev. Lett. 59 (1987) 2748.
[20] D.B.Batchelor, in Proc. of the Workshop of EBT Ring Phys. (Oak Ridge, Tennessee, 1979) 261.
[21] K.Miyamoto, in Plasma Physics for Nucl. Fusion (MIT Press, Cambridge, 1976).
[22] I.Katanuma et al., Phys. Fluids 30 (1987) 1142.
[23] T.Cho et al., Phys. Rev. Lett. 64 (1990) 1373.
[24] L.A.Schwager et al., Phys. Fluids B2 (1990) 1057.

PLASMA PRODUCTION AND HEATING EXPERIMENTS BY ECH IN CHS

S. Kubo, H. Idei, M. Hosokawa, Y. Takita and CHS group
National Institute for Fusion Science,
Nagoya 464-01, Japan

Introduction

Plasma production and heating by microwave in the frequency range of electron cyclotron resonance (ECH) is well established method in the stellarator/torsatron type device [1,2,3]. ECH have advantage of high efficiency, relatively simple heating mechanism, and feasibility of the steady state operation.

Plasma production and heating by fundamental and second harmonic ECH have been performed in Compact Helical System (CHS). CHS is heliotron/torsatron type device with major and averaged minor radius R=1 m and $\bar{a}$ = 0.2 m, respectively. One of the specific features of the CHS device is its low aspect ratio ($\approx$ 5) [4]. Main purpose of the CHS experiment is to clarify the confinement properties of such low aspect ratio heliotron/torsatron system. The magnetic field strength at the center of the vacuum vessel B_0 is up to 1.5 T. Microwave power from 28 and 53.2 GHz gyrotron are used for the fundamental and second harmonic ECH, respectively. In these experiments, total absorbed power and deposition profile are the key issue to the confinement analysis. Here, the efforts to clarify them in the fundamental and second harmonic heating experiment are described.

Fundamental (28 GHz) Heating

In the fundamental (28 GHz) ECH experiments, microwave power of up to 120 kW is injected from the high field side with straight cut waveguide antenna of circular TE_{01} mode. Electron temperature on the magnetic axis T_{e0} attained so far, only by the 28GHz ECH is up to 0.8 keV at the averaged electron density $\bar{n}_e \approx 2 \times 10^{18} m^{-3}$ In Fig. 1 are shown the electron temperature and density profile during the fundamental resonance heating discharge. The temperature profile is highly peaked but the density profile is flat or rather hollow. The hollowness of the density profile is left further investigation.

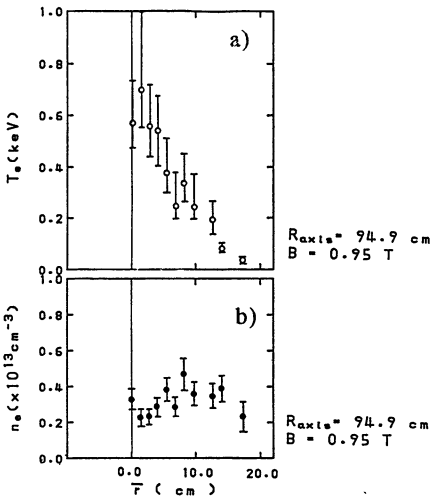

Fig. 1. a) Electron temperature and b) density profile during fundamental ECH with B_t= 0,94 T, R_{axis}= 94,9 cm. Injected power is 120 kW, at 28 GHz

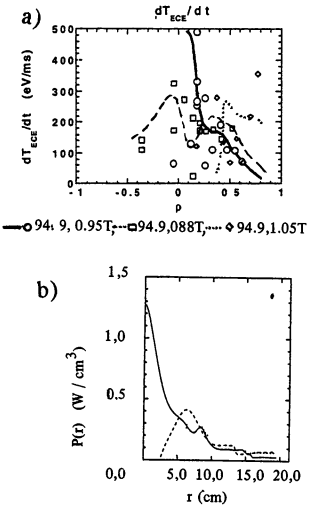

Fig 2 Power deposition profile a) deduced from ECE decay measurement, and b) estimated by the multi-reflection model

Power deposition profile and total absorbed power during the fundamental ECH experiment are estimated from the multi-reflection model [5]. Power deposition profile is estimated from resonance structure with the assumption that the injected microwave power is spread homogeneously inside the vacuum vessel which is justified by very low one path absorption rate and the method of injection (not focussing) in the experimental condition. Total absorbed power in the plasma is deduced to be about 80 % of the injected power by interpreting the parametric dependence of microwave leakage power distribution along the toroidal direction. Adequacy of these estimations are partially confirmed indirectly by the experimental result [5]. Using the power deposition profile estimated by this method, deduced electron thermal transport coefficient is 2-3 times higher than that estimated from neoclassical transport theory. Direct confirmation is deducing the experimental power deposition profile by the local electron temperature decay using electron cyclotron emission spectrum just after the turn off of the microwave power. In Fig. 2 are shown the comparison between the estimated power deposition profile and that measured by second harmonic ECE decay. Here, ECE system is calibrated by the noise source and in order to avoid the wall reflection effect, viewing damp is set on the other side of the receiving antenna. Deposition profile deduced from both method coincide with each other qualitatively.

Focussed Second Harmonic Heating

In order to elucidate the effect of the deposition profile control and also the mechanism of the density clamping phenomena, experiments of the localized heating by the focussed microwave beam are under way. The focussing system is shown in Fig. 3 a). Microwave power from 53.2 GHz gyrotron is transferred to the stair-cut Vlasov coupler by the circular waveguide with TE_{02} mode. The reason for the choice of this mode is that the propagation angle at the Vlasov coupler should be large by the limitation of the height above CHS. The power radiated from the stair-cut Vlasov coupler is collected and converted to the parallel beam by the mirror which can convert the power diffracted by the edge of the stair-cut waveguide as well as the main beam. The contour plot of this mirror surface is shown in Fig. 3 b). This beam have a linear polarization parallel to the toroidal field. As the required polarization is X-mode in the second harmonic heating, reflecting polarizer [5] is adopted for the rotation of the polarization. The beam with preferable polarization is finally focussed by the movable axis-symmetric parabola mirror with its axis along the major radius on the midplane of the CHS. Beam profile on the focal point taken at cold test is shown in Fig. 4. Focal point is just on the designed point. The elliptical beam profile is attributed to the finite size and shape of the axis-symmetric parabola mirror. In consequence, the beam dimensions are 20 mm and 60 mm at $1/e^2$ point of electric field along the toroidal and radial direction, respectively.

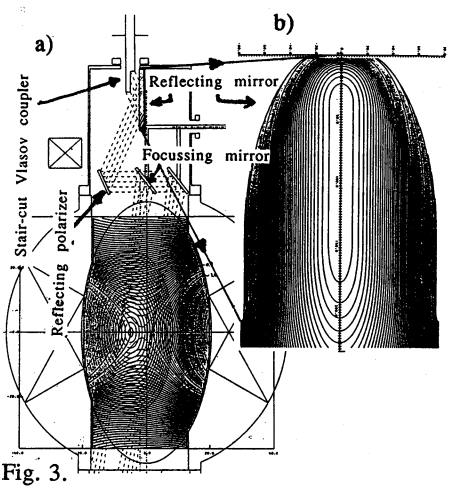

Fig. 3.

a) 53.2 GHz microwave focussing system and b) improved reflecting mirror surface contour.

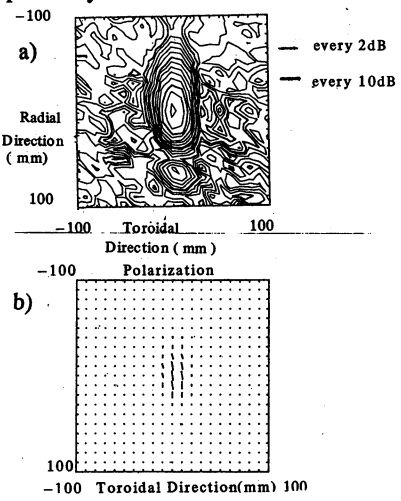

Fig. 4.

Focussed beam profile, a) intensity contour plot, here thin line indicates every 2 dB level, and thick line for every 10 dB level. b) polarization plot.

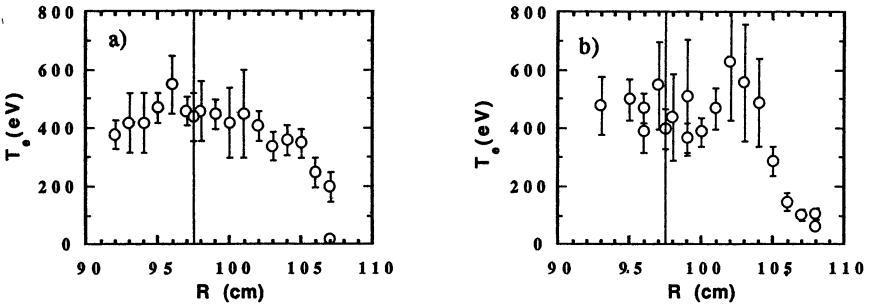

Fig. 5. Electron temperature profile for a) on-axis and b) off- axis heating.

The focussing beam heating experiment is performed as the superposition of focussed 53.2 GHz second harmonic and 28 GHz fundamental heating. The electron temperature profiles measured by the Thomson scattering for on- and off-axis heating are shown in Fig. 5 a) and b). It is clear that the at least some part of the 53.2 GHz microwave power is absorbed at near the focal point.

Fig. 6.

a) Multi–ray trace and b) resultant deposition profile for various setting magnetic field.

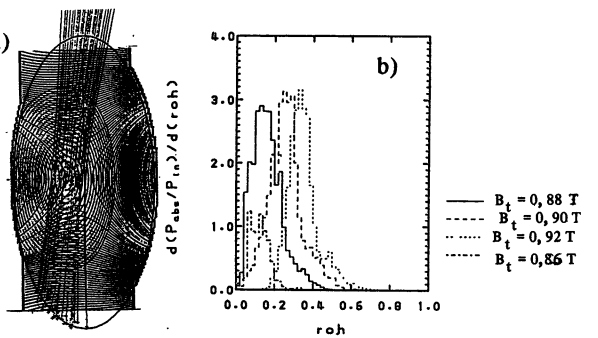

From the multi-ray trace calculation (as shown in Fig. 6 a)) which incorporate with the above mentioned input beam profile, deposition profiles become as shown in Fig. 6 b) and total one pass absorption is about 70 % at maximum. The small difference of the central electron temperature may be deduced to the microwave power which is transmitted through plasma without absorption and reflected back into the plasma by the wall. The poloidal cross section of mod-B surface and plasma at the injection point is shown in Fig. 6 a). Power deposition profile deduction from the second harmonic ECE is at present impossible because of the high stray power of heating microwave. Inserting the high pass filter, only the second harmonic ECE near the magnetic axis can be effective. For obtaining the electron temperature variation at the peripheral region the oxygen emission intensity ratio of OVI 2s-3p

and 2s-sp is used, for this ratio is approximately linear function of the electron temperature at the emitting region of about 100 eV, and weak function of the electron density. So, the correlation between intensity ratio and ECE signal indicates the localization of the deposition profile. In Fig. 7 is shown these correlation for on- and off-axis heating during the power modulation experiment. These result indicates the 53.2 GHz power is well focussed by above mentioned system, but there are also some evidence that some part of the injected microwave power is absorbed other than the focal point.

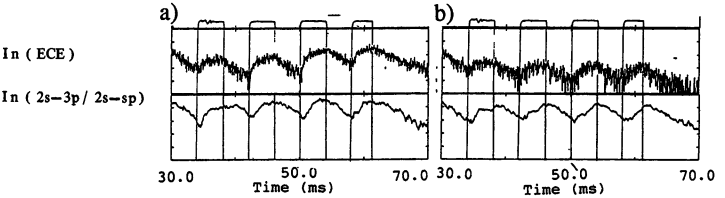

Fig. 7. Correlation of ECE and OVI intensity ration durig power modulation for a) on-axis and b) off-axis case.

Summary

In the low aspect ratio heliotron/torsatron CHS, electron cyclotron plasma production and heating at fundamental and second harmonic resonance is successfully performed. For the transport analysis precise power deposition profile is needed. In the fundamental heating, deposition profile and absorbed power could be modelled and its adequacy is examined by the experimental result. For the second harmonic heating, local heating became possible by the improved Vlasov coupler and focussing mirror attached recently. This will be the powerful tool for the plasma profile control and transport analysis. For the more precise experiment, installation of the beam dump and monitors for the transmitted power monitor is planned.

References

[1] V.Erckmann et al., Plasma Phys. and Contr. Fusion **28**, 1277 (1986).

[2] H. Zushi et al., Nuclear Fusion **28**, 1801 (1988).

[3] V. Erckmann et al., Fusion Technology

[4] S. Okamura, et al., Proc. 16th European Conf. on Contr. Fusion and Plasma Phys., Venice, Italy, 1989, EPS Vol. 13B, Part II, p.571.

[5] S. Kubo, et al., Porc. of the 1-st International Toki Conference on Plasma Phys. and Nucl. Fusion, Toki, Japan (1989) p. 240.

[6] J. D. Hanfling, G. Jerinic, L. R. Lewis; IEEE Trans. Antennas and Propagation, Vol. AP-29 (1981) 622.

ECRH HEATING OF HELIOTRON-E WITH 106 GHz GYROTRON

– An Approach to High Power ECRH System to Large Helical Device –

M.Sato[1], H.Zushi[1], S.Sudo[1], F.Sano[1], M.Iima[1], S.Kobayashi[1], T.Obiki[1], M.Nakajima[2], S.Kubo[3], M.Hosokawa[3], K.Ohkubo[3], T.Kuroda[3], O.Motojima[3], K.Sakamoto[4], T.Nagashima[4], W.Kasparek[5], M.Thumm[6],

1. *Plasma Physics Laboratory, Kyoto University, Gokasho, Uji 611, Japan*
2. *Department of Electronics, Kyoto University, Kyoto 601, Japan*
3. *National Institute for Fusion Science, Nagoya 464-01, Japan*
4. *Japan Atomic Energy Research Institute, Naka, Ibaragi, Japan*
5. *Institut für Plasmaforschung der Universität Stuttgart, 7. Stuttgart 80, F.R.G.*
6. *Institut für Technische Physik Kernforschungszentrum, Karlsruhe GmbH*

A 106 GHz half megawatt ECRH system has been developed at PPL Kyoto University since 1986. The high density ($\sim 7 \times 10^{19}$ m^{-3}) plasma will be produced and heated by the system. The engineering object of the project is a breakthrough in the present two hundreds kW system to one MW system with a tube at the frequency around hundred GHz.

Gyrotron Tube Development

The first 106 GHz and 400 kW minimum (500 kW objective) power tube was ordered to Varian in 1988. The design and testing of the tube were done simultaneously with the US-DOE's 140 GHz half megawatt project. It was delivered in 1988. The performance of the tube is good as a proto type tube. The output power exceeds 400 kW in the long pulse operation and 500 kW in the short pulse. The dynamic range for oscillation is 1.5~2 times wider than the existing 200 kW class tubes as shown in Fig.1~3.

The output mode from the window is a whispering gallery $TE_{12,2}$ mode. The mode purity was measured by a wave number spectrometer[1]. The solitary spectrum can be identified to be $TE_{12,2}$ within the resolution of the spectrometer. The waveguide arc happened frequently at the power higher than hundred kW. We could not measure spectrums at the higher power operation.

Quasi-Optical Mode Converter Development

The whispering gallery mode is a rotating transverse electric ($TE_{m,n}$) mode in a cylindrical waveguide with a high azimuthal (m) and a low radial (n) mode numbers. The improved efficiency quasi-optical (Vlasov) converter has been developed to get the simple Gaussian-like beam. The Vlasov converter is a kind of parabolic antenna which has a specially cut radiator to get the linearly polarized microwave. The conversion efficiency is less than 80% by the original Vlasov's design, since the radiation field has a flat power density profile which shall be eased to a Gaussian-like profile by the generation of side lobes during the propagation along the beam axis. The best way to reduce the side lobe is to obtain a Gaussian-like radiation field from the radiator directly. The new mirror, we call "Visor" is added to the output mouth of the radiator. The shaped of Visor is analyzed by the methods of geometrical optics. The methods also showed us that the propagating angle of the optical rays are very important to increase the efficiency. The rays are propagating in the waveguide at the angle $\theta_B = \sin^{-1}\left(\frac{k}{k_c}\right)$ to the axis, where $k_c = 2\pi/\lambda$, $k = \chi'_{m,n}/a$, $\chi'_{m,n}$ is the m'th root of Bessel-function and a is the radius of the waveguide. The trajectory of the reflecting point of rays on the waveguide wall draws a helical line with a pitch angle $\alpha = \tan^{-1}\left\{\frac{\theta_w}{\sin\theta_w}\tan\theta_B\right\}$. All the rays can be contained in the main lobe, if we cut the waveguide at the pitch angle of α.

The cold test has been done using one inch radiator[2]. $TE_{12,2}$, 120 GHz whispering mode generator was developed by I.P.F. Stuttgart for the experiments[3]. The measured radiation patterns are shown in Fig.4(a) and (b) for the comparison of the Vlasov's converter and improved Q-O converter. The side lobe level can be reduced from 20 % to less than 5 %.

The Gaussian-like beam is coupled to the HE_{11} corrugated wavegide. The phase correcting focal mirror is employed. The shape of the mirror will be determined to obtain a pure circular Gaussian-like profile at the waveguide mouth. The $1/e$ radius must be 0.455 D, where D is the HE_{11} wave diameter. The coupling efficiency will be measured by the cold and hot testing.

Waveguide Transmission Line

The microwave is transmitted in the HE_{11} corrugated waveguide line. It consists of straight ϕ63.5 m/m HE_{11} waveguides, miter bends, vacuum tight window and up and down tapers. The grooves of the HE_{11} waveguide is cut directly by a lathe by the help of specially made support tool. The errors in machining are $\pm$0.03 m/m, $\pm$0.015 m/m

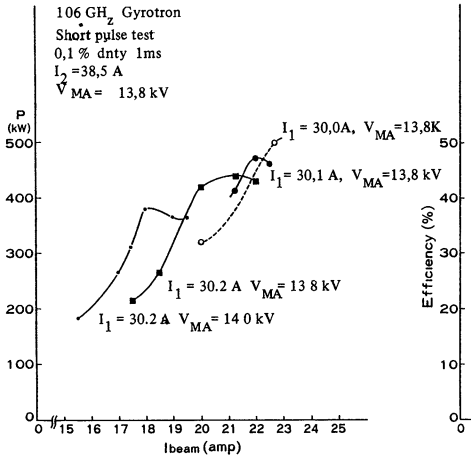

Fig.1

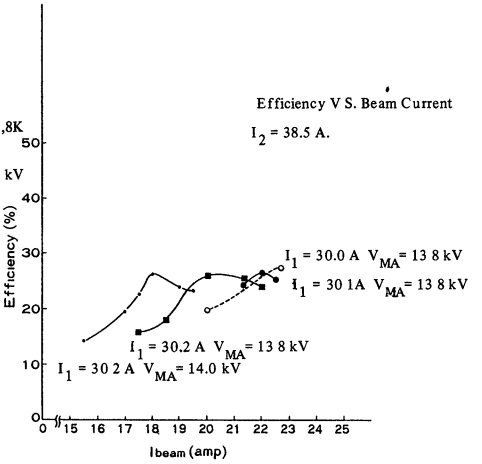

Fig.2

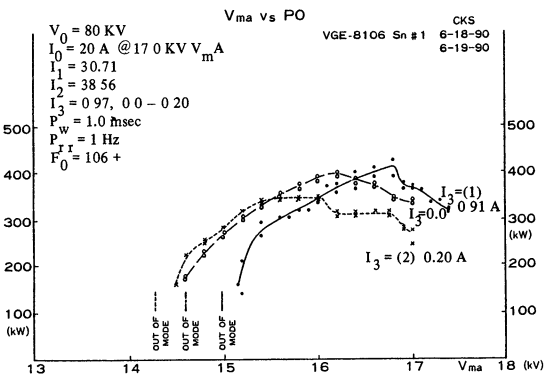

Fig.3

Fig.1~3

Dynamic range of 106 GHz Gyrotron

(Varian VGB8106A1)

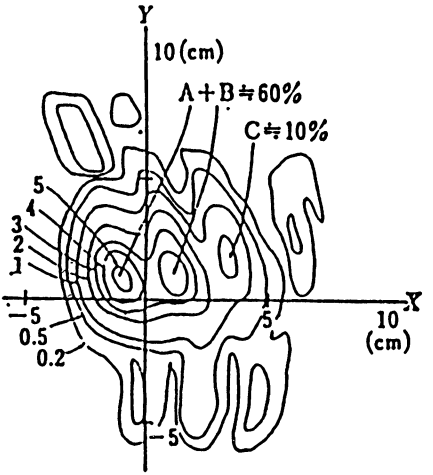

Fig.4(a)

Power counter levels for conventional converter.

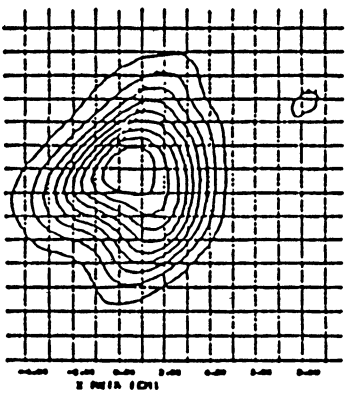

Fig.4(b)

Power counter levels for improved converter.

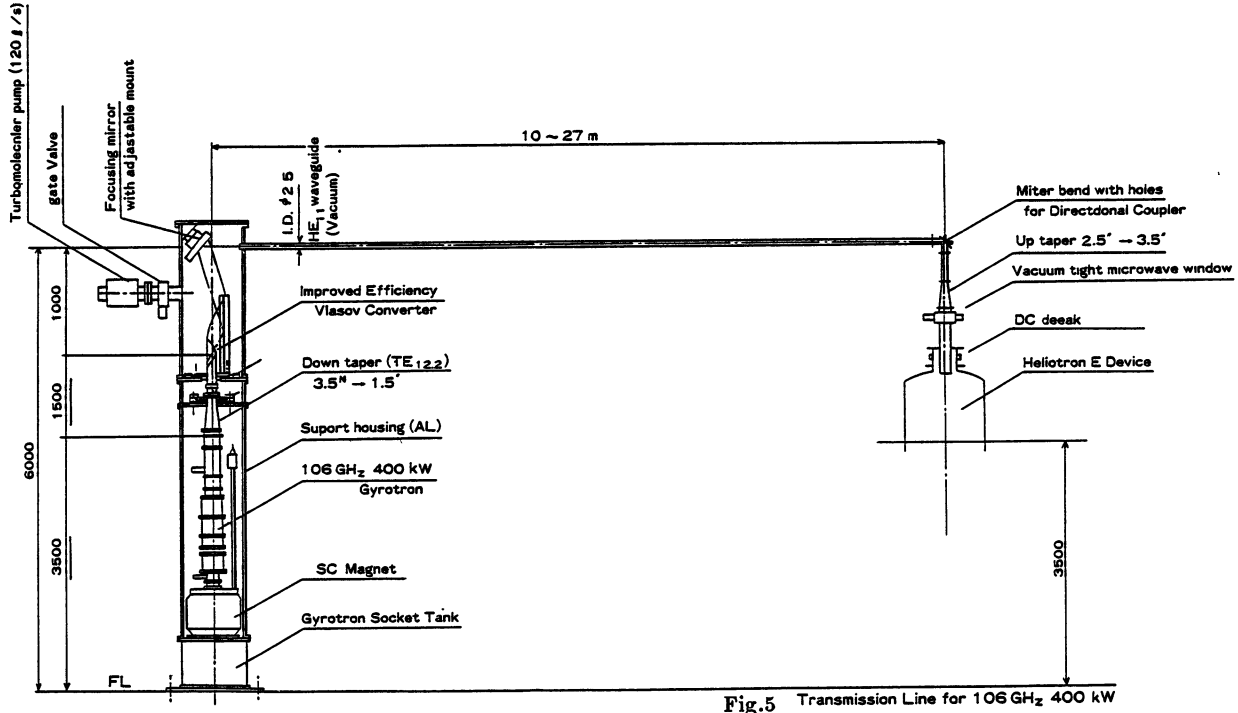

Fig.5 Transmission Line for 106 GHz 400 kW ECRH System

and ± 0.01 m/m to the diameter, pitch and depth respectively. The estimated attenuation and mode conversions are -47 dB and -22 dB, respectively. Three miter bend will be set in the line. The mode conversion at each bend is -26 dB. The total transmission loss is about -16 dB.

Reference

[1] W. Kasparek, G.A.Müller, Int. J. Electronics 64, 5(1988).

[2] M. Iima, M. Sato, et al.,; Measurement of radiation field from an improved efficiency Q-O converter for whispering Gallery mode, Proc. of 14th int. Conf. on Infrared and millimeter waves, Würgburg F.R.G. 1989.

[3] M. Thumm, A. Jacobs, "In-Waveguide TE_{01}– to – Whispering Gallery Mode Conversion Using Periodic Wall Perturbations", 13th International Conference on Infrared and Millimeter Waves at Hawaii, Conference Digest (1988), 465-466.

PLASMA-WAVE INTERACTION IN TOKAMAK TUMAN-3 AT THE SECOND ECR HARMONIC

Arbuzov A.N., Vinogradov N.I., Goncharov S.G., Its E.R., Lebedev S.V., Podushnikova K.A., Razdobarin G.T., Rozhdestvenskiy V.V., Sacharov N.V., Shakhovetz K.G., Fedorov O.V.

A.F.Ioffe Physico-Technical Institute, Leningrad, USSR

The high power microwave ,MW, - plasma interaction at the second electron cyclotron, EC, harmonic in the broad range of the plasma density change was studied in the tokamak TUMAN-3, [1]. It was of interest to clear what arises from the MW-pumping of the ohmically heated ,OH, plasma with and without an accelerated electron beam, in what conditions the electron cyclotron plasma heating ,ECH, is effective.

For this goal the MW-power was fed into the plasma with mean density $\bar{N} = (0.4 \div 2.0) \cdot 10^{13} cm^{-3}$ during the OH quasistationary stage of the discharge. The discharge current was $J_p = (60 \div 80)$ kA, the toroidal magnetic field - $B_t = (3 \div 7)$ kGs. The OH electron temperature at the discharge axis reached $T_e = (300 \div 500)$ eV.

A gyrotron was used for MW-pumping. Its power is $P_{MW} \approx 100$ kW, operating frequency - $f_o = 37.5$ GHz, pulse duration - $\tau_{MW} \approx 6$ ms.The ordinary mode was fed into the discharge chamber with the circle oversized, 55 mm - diameter, waveguide placed from the low magnetic field side along the major torus radius.

To determine Te(r) and N(r) radial profiles Thomson scattering and multichannel MW-interferometry were used. MHD-activity was observed with magnetic probes. Data on accelerated electrons one could obtain with a MW-radiometer and hard X-ray ,HXR, detector of quantum energy larger $\approx$ 100 keV. The radiometer operating in the frequency range (53÷78)GHz registered the synchrotron emission ,SE, at (3÷4) EC harmonics accumulated in the discharge chamber during multiple wall reflections.

The experimental results obtained at the central location of the electron cyclotron resonance ,ECR, plasma layer are presented in Fig's 1÷3.

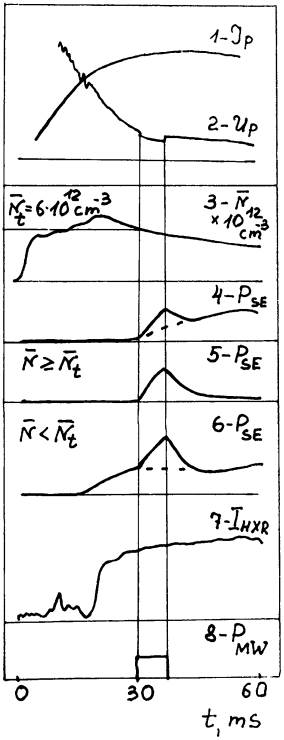

Fig.1

The Fig.1 shows, in OH, (1,2), with the falling slowly plasma density, (3), SE, (4), arises only at 30 mc of the discharge when $\bar{N} < \bar{N}_t^{OH} = 6 \cdot 10^{12}$ cm^{-3} and $T_e(0) \simeq 400$ eV. During MW-pumping the SE intensity, (4), increases sooner than under OH, but after the pumping - diminishes firstly with the time constant $\tau_{SE} \simeq 6$ ms and further it grows slowly again like in the OH case.

In OH of the constant high density plasma, $\bar{N} > \bar{N}_t^{OH}$, SE and HXR were not observed. During MW-pumping the SE intensity increases and after - falls with the previous time constant.

In OH of the constant low density plasma, $\bar{N} < \bar{N}_t^{OH}$, SE, (6), appears at 15÷20 ms simultaneously with HXR, (7). But their behavior is different. The SE intensity grows slowly and reaches at 30 mc the stationary level. The HXR intensity increases quickly, for $\simeq$ 3 ms, then it changes inconsiderable. Any relaxations of discharge and plasma parameters were not registered. During MW-pumping the SE intensity, (6), increases and after - falls down but with the time constant, $\tau_{SE} \simeq$ 3 ms, less than under OH. The HXR intensity does not change practically at this time. Under MW pumping the loop voltage, (2), diminishes from 2.5 V to 2.0 V. But in error limits changes of $T_e(r)$, N(r), MHD-activity, relaxations are not observed.

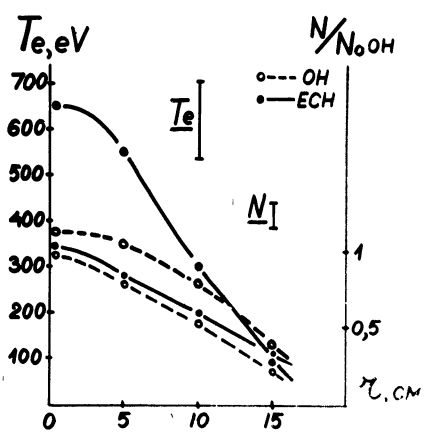

Fig.2.

The plasma ECH becomes more effective in discharges with $\bar{N} = (0.8 \div 1.0) \cdot 10^{13}$ cm^{-3}. At this time the loop voltage decrease is of $\simeq$ 0.5 V. SE and HXR are not arise. In Fig.2 $T_e(r)$ and the relative plasma density profiles before and at the pumping end are exhibited. One can see that the density profile is not changed, T_e increases in the region with radius equal ~ 12 cm, and near the discharge center - from 400 eV till 650 eV. The $T_e(r)$ profile becomes more narrow. In density increase the ECH efficiency diminishes quickly.

When the region with the density larger than the cut-off one of the pumping wave ordinary mode, $N^o_{cr} = 1.75 \cdot 10^{13}$ cm^{-3}, appears MW-pumping produces the MW-emission flash more intensive then the SE one. The Fig.3 shows that the emission intensity at frequencies $\simeq$ 65 GHz, (3), increases exponentially during the pumping and falls down more quickly in the end.

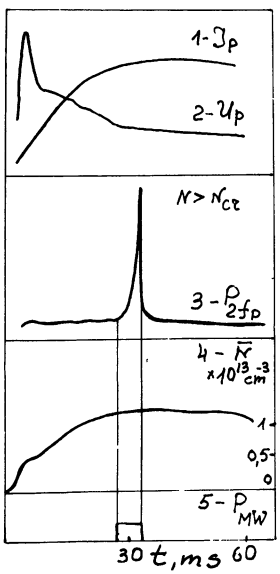

Fig.3

Analyses of the experimental data and estimations made with taking into account discharge and plasma parameters known accordingly [2,3], shows that in the plasma density range studied one can distinguish four regions. They differ in the plasma-wave interaction character.

1. $N < N^{OH}_t$. In OH the two component beam of accelerated electrons can exist in the plasma of $\bar{N} \simeq 5 \cdot 10^{12}$ cm^{-3}, $T_e(0) = 500$ eV, $Z_{ef} = 1.5$.

The more dense, $N_b/N \simeq 0.02$, but of less energy, $W_o \simeq 80$ keV, and life time, $\tau_b \simeq (3 \div 6)$ ms, component arises in the central plasma region with radius $r_b \simeq 10$ cm. Here the ratio of vortex electric field to Dreicer one is of $E/E_d \simeq 0.06$, the runaways birth velocity $\Gamma \simeq 3 \cdot 10^{-5}$. During continuous acceleration with the vortex field for the life time the electron energy may reach in order of some hundreds keV and transverse energy - of tense keV. When the longitudinal electron energy becomes larger than the threshold value $W > W^* \simeq 40$ keV, the beam excites inte-

nsive oblique Lengmuir plasma waves because of the anormal Doppler effect. In this case the beam is slowing down, its energy becomes isotropic, $W_{\parallel} \simeq W\perp \simeq 40$ keV. The energy anysotropy is $\frac{W_{\parallel} - W\perp}{W_{\parallel}} \simeq 2 \cdot 10^{-3}$. The full beam energy determined on the experimentally measured relativistic shift of EC harmonics equals to $W_o \simeq$ 80 keV. The accelerated electrons life time was estimated on the SE intensity drop, Fig.1.4÷6. Under the beam-limiter interaction HXR with the quantum energy less than ≈ 100 keV is produced. In the tokamak with a low magnetic field when EC and plasma frequencies are equal, $f_{ce} \simeq f_p$, the threshold value of fast electron energy anisotropy goes down. Therefore the soft excitation of the Lengmuir turbulence can occur. Relaxations of plasma parameters accompanying the hard excitation regime usually were not observed in our conditions.

The less dense, $N_b/N \simeq 2 \cdot 10^{-3} \div 2 \cdot 10^{-5}$, but more energetic component is born in the plasma layer with radius r_b= (10 ÷ 15) cm where $E/E_b \simeq (0{,}04 \div 0{,}02)$ and $\Gamma \simeq 8 \cdot 10^{-7} \div 2 \cdot 10^{-8}$ and is in the continuous acceleration regime. For the drift orbit displacement time, ≃ 40 ms, electrons can obtain energy of some MeV. In the experiment HXR with quantum mean energy equal ^ 300 keV was detected.

The beam and plasma energy contents are the same: $N_b \cdot T_b \simeq \bar{N} \cdot \bar{T}_e \simeq 2 \cdot 10^{15}$ eV/cm^3 The discharge current part carried by fast electrons is not higher than (3 ÷ 6) per cent.

In plasma density increase, $N > N_t^{OH}$, the runaways birth velocity falls down quickly. The beam goes in the continuous acceleration regime firstly and then disappears. This is confirmed by the essential SE and HXR intensities decrease.

Under MW - pumping the plasma with the beam a large part of the MW - power is absorbed by accelerated electrons, as optical thicknesses of the ECR region for thermal and fast electrons are approximately equal. At the same time not only energy but density grows due to the fast increase of the runaways transverse energy in the ECR - region. Therefore the SE - intensity goes up too . But the HXR - intensity experimentally registered is not changed, Fig 1.6,7.This means that the full beam energy is not higher than ≃ 100 keV. When $N_b \cdot T_b > N \cdot T_e$, the MW - power is basically absorbed by the beam. The plasma ECH is inconsiderable.

2. $N_t^{OH} < N < N_t^{MW}$. In this case the beam is born under MW - pumping only . The MW - power is firstly absorbed with thermal and nonthermal electrons. During beam formation the MW - power

absorption increases. But $W_o < 100$ keV, as the HXR intensity growth appropriating the SE amplification, Fig.1.6, was not observed. In these conditions the ECH efficiency goes down. The electron temperature growth is not apparently higher than ,measurement error limits , $\Delta T_e < 100$ ev.

3. $N_t^{MW} < N < N_{cr}^o$ The plasma ECH becomes effective in the narrow density change interval, $\bar{N} = (8 \div 10) \cdot 10^{12} cm^{-3}$. The upper limit is determined with the odinary mode cut - off dlasity for the pumping wave. The lower one - with the density in which the MW - pumping can not initiate the beam in the plasma. In this case the maximal growth, $\Delta T_e(o) \approx 250$ eV, was fixed.

4. $N > N_{tr}^o$ When the region with the density higher than N_{cr}^o arises in the plasma, at the cut off surface the parametric plasma waves excitation under the MW - pumping occurs in the frequency range $f \approx n \cdot f_p$. Because of the plasma wave transformation into electromagnetic one the intensive MW - emission at $f \approx 2f_p$ can be induced. Apparently the such MW - emission was registered in our experiment.

In conclusion it should be noticed the results obtained show that the plasma - pumping wave interaction character essentially depends on plasma density and in a large extent is determined with the energetic distribution of electrons, forming in the OH stage and under MF - pumping.

References

1 . Vorobiov G. M. , Golant V. E. Gornostaev S. V. et al Fizika Plasmi , 1983, v. 9, N 1, s. 105 - 120.

2 . Parail V. V. ,Poguze O. P. " Accelerated electrons in a tokamak ", red. M. A. Leontovitsh and B. B. Kadomtzev, m. , Energoizdat, 1982, N 11, s. 5 ÷ 55.

3 . Pickaar H. W. , Rutgers W. R. , " Cyclotron radiation from thermal and nonthermal electrons in the WEGA stellarator ", FOM Institute, Nederland, Rijnhuizen Report 80 - 128, November, 1980.

LOWER HYBRID EXPERIMENTS AT 2.45 GHZ IN ASDEX

F.Leuterer, F.Söldner, ASDEX-Team, LH-Team, NI-Team
Max Planck Institut für Plasmaphysik
EURATOM - IPP Association, D- 8046 Garching, FRG

R.Bartiromo, R.Cesario, R.DeAngelis, L.Gabellieri, V.Pericoli, A.Tuccillo
EURATOM - ENEA Association, I- 00044 Frascati, Rome, Italy

S.Bernabei, C.Forest
Princeton Plasma Physics Laboratory, Princeton, NJ 08543, USA

R.Harvey
General Atomics,San Diego, USA

1) Lower Hybrid System and Coupling

In ASDEX a lower hybrid system with 3 MW / 1 sec at 2.45 GHz has been installed,/1/. The power is launched through a grill antenna with two stacked arrays of 24 waveguides each. The phase can be set arbitrarily in each waveguide. Thus we are able to launch symmetric wave spectra, normal current drive spectra and opposite current drive spectra at different $N_{||}$ values. At a phasing of 180° between successive waveguides the peak value of the spectrum is located at $N_{||} = \pm 4.4$. The width of these spectra is $\Delta N_{||} = 0.8$. Our arrangement allows to launch simultaneously two different wave spectra at different power levels with the upper and the lower grill.
The antenna is usually set a few millimeters behind the protection limiter and the distance to the separatrix is normally set at 4.5 cm by means of the plasma position control. The coupling was found to be very sensitive to the plasma conditions immediately in front of the grill, /2/. The average reflection coefficient <R> improved by up to a factor of 3 when protective graphite tiles surrounding the grill, which originally protruded beyond the actual grill surface by only 3 mm, were cut back to be flush with the metal walls. An example is shown in fig. 1 for a current drive phasing of $\Delta\phi = 90°$. The variation of <R> with power is due to a change in the edge density because of the ponderomotive force /3/.

2) Current drive efficiency

a) Current drive efficiency at zero electric field

The experiments are performed with a feedback controlled plasma current I_p so that the sum of rf-driven current I_{rf} and inductively driven current $I_{ind} \sim U_{loop}$ is constant. From these shots where $U_{loop} = 0$ we can determine the current drive efficiency η_o at zero electric field:

$$\eta_{o,exp} = \bar{n}_e \, I_p \, R / P_{lho} \, , \quad (10^{13} cm^{-3} Am/W) \qquad (1)$$

where $\bar{n}_e$ is the line averaged density, R is the major radius of the plasma and P_{lho} is the net LH power. Fig. 2 shows experimental results at low density as a function of the grill phasing, respectively $N_{||}$. Fig. 3 shows the density dependence of η_o.

Assuming homogeneous current density and absorbed power density profiles, full absorption of the accessible power by the fast electrons, and a confinement time longer than their slowing down time, we can derive from theory,/4/, the zero electric field efficiency

$$\eta_{o,theor} = 1240/\{\ln\Lambda(5+Z_{eff}) \langle N_{||}^2 \rangle\} \qquad (2)$$

in the same units as in equ.(1), with /5/

$$\langle N_{||}^2 \rangle^{-1} = \frac{\int_{N_{||acc}}^{\infty} P(N_{||})/N_{||}^2 \, dN_{||} - \int_{-\infty}^{-N_{||acc}} P(N_{||})/N_{||}^2 \, dN_{||}}{\int_{-\infty}^{\infty} P(N_{||}) \, dN_{||}} \qquad (3)$$

$N_{||acc}$ is determined from the plane wave accessibility condition with the line averaged density $\bar{n}_e$ and the central magnetic field. We take the spectrum as launched from the antenna without any broadening or upshift. The results of this calculation are also shown in figs.2 and 3. In fig. 2 the dashed lines indicate the range in Z_{eff} encountered in these experiments due to different wall conditions. In fig. 2 all spectra, except those for $\Delta\phi < 75°$, satisfy the accessibility condition and the agreement with the experiment is quite good. In fig. 3 the spectrum with $\Delta\phi = 75°$ suffers from decreasing accessibility when $\bar{n}_e$ increases. The experimental values, however, decrease more then we expect on the basis of our assumptions. But also the 90° spectrum, which should be accessible in the whole density range shown, indicates a decreasing efficiency. One reason for this may be nonlinear effects,/6/.

b) Efficiency at nonzero electric field

If the power is not sufficiently high, the loop voltage does not drop to zero. The efficiency for current drive in the presence of an electric field has been calculated in a number of papers,/7/. We use for our comparison with theory an analytic approximation for η normalized to the efficiency η_o without E-field /8/

$$\eta/\eta_o = \ln\{(1-X_2)/(1-XX_2)\}/(XX_2-X_2), \qquad (4)$$

with $X_2 = \alpha u_2^2 E_N$, $X = (N_{||2}/N_{||1})^2$, $\alpha = 12/(Z_{eff}+7)$, $u_2 = v_{ph2}/v_{th}$ and $E_N = E/E_{Dreicer}$. The index 2 relates to the upper boundary of the phase velocity spectrum. With the same assumptions as before and with the circuit equations we obtain

$$P_{lh}/P_{lho} = (1-U_{lh}/U_{oh} \cdot T)/(\eta/\eta_o). \qquad (5)$$

U_{lh} and U_{oh} are the loop voltage during the lower hybrid and the ohmic phase, T describes the enhancement of the plasma conductivity due to bulk heating or a change in Z_{eff}, and P_{lho} is the power needed to reach zero loop voltage in these conditions. The term X_2 can be expressed as $X_2 = U_{lh}/U_{oh} \cdot A$, with

$A = 0.023(Z_{eff,oh}+0.72)/(Z_{eff,lh}+7) \cdot I_p/\bar{n}_e (N_{||2})^2 T_{e,oh}^{3/2}$.

I_p, $\bar{n}_e$, T_e are in units kA, 10^{13} cm^{-3}, keV. Except for $N_{||2}$ all these quantities can be determined experimentally.

In figs. 4 and 5 we compare experimental results at $B_t = 2.8$ T, $I_p = 420$ kA and two different densities with this theory. The curves have been calculated with an average value A determined experimentally and with a calculated $N_{||2}$, and for various values of T. At high density, fig. 4, the agreement is quite good and the variation of T can be explained by the observed electron heating with increasing power, ($T_e(0)$ rises from 1.4 keV to 3 keV). At low density, fig. 5 we find already at low power ($P_{lh}/P_{lho} \leq 0.25$) a strong drop in loop voltage which would require $T \approx 2$. This cannot be explained by bulk heating. In this range the loop voltage is not yet low enough and we observe runaway electrons which may carry part of the plasma current and which are not included in this simple theory. At high power where the electric field is near zero the high value of T can again be explained by the observed strong electron heating, ($T_e(0)$ rises from 2 keV to 7.5 keV). Comparisons at different current drive spectra and plasma currents yield the same result.

With a symmetric spectrum of waves we drive in principle currents in

both toroidal directions, however according to equ. 4 because of the nonzero electric field, with different efficiencies. Thus a net current drive results. Assuming that both these currents behave additively we can use the same model and obtain a similar agreement with the experimental results,/9/.
Current drive opposite to the inductively driven current can also be described with this model, but in the experiment much more runaway electrons are generated than in the normal current drive case, and the agreement is no longer as good.
We have also studied current drive during neutral beam injection in a L-mode plasma at a density of $\bar{n}_e = 2.4 \cdot 10^{13} cm^{-3}$. We found that the current drive efficiency is the same with and without neutral beam injection. The efficiency in this case is marked in fig.3 as a thick cross,/9/.

3) Power absorption

We determined the power absorption coefficient α experimentally by measuring the rate of change of the plasma energy on a time scale shorter than the energy confinement time upon sudden switch-on and switch-off of the heating pulse /10,11/. We use an effective $\beta_p = (2\beta_p^{equ} + \beta_p^{dia}) / 3$ because of the anisotropic distribution function. For a time interval shorter than the response time of the current feedback system (≈20 ms), the dc electric field is still constant leading to a fast rise in the plasma current. We therefore evaluated α from the rate of change in the plasma energy, as given by $\Delta\beta_p$, and in the magnetic energy, given by the total inductance of the plasma loop and I_p.
At low density, $\bar{n}_e \approx 1.3 \cdot 10^{13}$ cm^{-3}, we find that all power in the main peak of the spectrum is absorbed by the plasma core in current drive experiments. This is in agreement with the results on current drive efficiency, which are close to their maximum theoretical value given by total absorption. At this low density we find α higher for lower $N_{||}$.
In opposite current drive conditions, we observe a reduction of α by a factor of about 2. Intermediate results are obtained with symmetric spectra. The reason for this difference is not understood.
With increasing plasma density, we find a remarkable decrease of α for low $N_{||}$ current drive spectra, in particular at lower magnetic field, as expected from accessibility considerations and as already found earlier,/12/. In fig. 6 we compare the measured α with the fraction of power satisfying the accessibility condition determined from the line averaged density and the central magnetic field. The decrease of α correlates with the degradation of accessibility. However, for a

symmetric low $N_{||}$ spectrum α did not show such a density dependence,/13/. Absorption is also found in cases where no power should reach the plasma core.
The measured absorption coefficient does not show any appreciable dependence on the launched power. At intermediate density ($\bar{n_e} \approx 2.1 \cdot 10^{13}$ cm^{-3}) the value of α is only weakly dependent on $N_{||}$ and the width of the spectrum. No variation of α was found by changing q with the current.

4) Energy confinement

The total energy content W_p is calculated from the effective $\beta_p = (2\beta_p^{equ} + \beta_p^{dia}) / 3$. The energy content of the thermal electrons W_e is determined from the radial profiles of $n_e(r)$ and $T_e(r)$, as measured by YAG laser scattering. The scaling of both W_p and W_e with the total power $P_{tot} = P_{OH} + P_{LH}$ (assuming $\alpha = 1$) is shown in Fig. 7 for current drive at two different densities, $\bar{n_e} \approx 1.3 \cdot 10^{13}$ cm^{-3} and $\bar{n_e} \approx 3.5 \cdot 10^{13}$ cm^{-3}.
At the lower density highly suprathermal electron distributions with large anisotropy are produced by LH,/11/. The total energy content W_p in hybrid operation of OH+LH current drive is about 50% higher than with OH current drive alone with the same total power input. At lower LH power we find an operation regime with a total power input even smaller than required for the same discharge with pure OH current drive. In this regime, the total energy content still remains above the corresponding ohmic values, corresponding to improved global confinement. Up to the highest LH powers applied, the slope $\Delta W_p / \Delta P_{tot} = \tau_E^{inc}$ is constant. Its value is smaller than the ohmic confinement time. The global confinement time therefore degrades continuously with power, starting already at $P_{tot} < P_{OH}$,/13/. The thermal energy content of the electrons W_e is the same in hybrid operation, LH+OH current drive, with the same total power input as in ohmic discharges. The thermal ion energy content, as determined by CX analysis, also remains the same in both cases. The improvement in global confinement can therefore only be attributed to superior confinement of the suprathermal electrons.
At the higher density (Fig. 7, lower part) the electron distribution stays close to thermal and nearly isotropic, and the improvement of global energy confinement with LH disappears. At a density of $\bar{n_e} \approx 3.5 \cdot 10^{13}$ cm^{-3} the total power input always exceeds the input power of the OH phase and τ_E degrades with power.
With a combination of LH+NI, degradation of τ_E with P_{tot} is found consistently with Goldston scaling. For the same powers, the global

confinement time with LH is comparable with NI if the total injected LH power is rated.

5) Profile control

a) Control of MHD activity

The sawtooth repetition period τ_{st} increases with LH power, as seen in fig. 8,/14/. It correlates with the drop in ohmic power input. It is strongest for current drive with low $N_{||}$ ($\Delta\phi$ = 75°, $N_{||}$ = 1.8). No change is seen with symmetric LH spectra at high $N_{||}$ ($\Delta\phi$ = 180°, $N_{||}$ = ±4.4) and opposite current drive ($\Delta\phi$ = -90°, $N_{||}$ = -2.2). For symmetric spectra with $N_{||}$ = ±2.2, the sawtooth period saturates at about twice the ohmic value $\tau_{st}^{LH} = 2\,\tau_{st}^{OH}$ for P_{LH} > 300 kW. In this regime the reduction in P_{OH} also saturates. The variation of τ_{st} may be explained by the enhanced electrical conductivity in the presence of suprathermal electrons. Suppression of sawteeth occurs only when current drive spectra are applied and seems to be related to changes in the current profile. The threshold power $P_{LH} \approx$ 300 kW is nearly independent of phasing. Stabilization by kinetic effects due to the suprathermal electron population can be ruled out as a larger suprathermal electron population is produced with symmetric spectra with $N_{||}$ = ±2.2 than with the corresponding current drive spectrum. The reduction of the dc electric field also seems not to be decisive: sawteeth persist for symmetric wave spectra with $N_{||}$ = ±2.2 up to the highest LH powers where P_{OH} and thus the electric field is reduced below the values at which sawteeth are stabilized by LH-current drive. Stabilisation was observed up to densities of $\overline{n_e} = 5\ 10^{13} cm^{-3}$ with increasing threshold power.

The m=1 mode is still present after stabilization of sawteeth as also found on PLT /15/. A q=1 surface therefore continues to exist and the amplitude of the m=1 mode grows to a much higher steadystate level.
With even higher LH power also the m=1 mode is stabilized,/14/. As for sawtooth suppression, stabilization of the m=1 mode is obtained with LH in current drive operation only. This is shown in fig. 9 where the central electron temperature T_{eo}, its peaking factor $Q_{Te} = T_{eo} / \langle T_e \rangle$ and the increase in energy content ΔW_p^{dia} with power are compared for current drive and symmetric spectra, both with $N_{||}$ = 2.2. Up to a power level of $P_{tot} \approx$ 750 kW little difference is seen. For higher powers much stronger central heating, peaking of $T_e(r)$ and improved global confinement are achieved with LH current drive. The bifurcation occurs at the threshold

power for stabilization of the m=1 mode which is about twice the threshold for sawtooth suppression. While the electron temperature profile peaks strongly, the current profile j(r) flattens. Current and temperature profiles can therefore be completely decoupled with LH current drive.
Stabilization of the m=1 mode was also achieved with LH current drive during NBI, also with peaking of $T_e(r)$ and enhanced global confinement.

b) Control of the Current Profile

With low $N_{||}$ current drive spectra a reduction of l_i is observed in conditions where the m=1 mode is stabilized,/14/. Local current density profile measurements with the Li-beam show only small changes of j(r) with slight flattening in the central region The largest drop in l_i, as observed earlier /16/, is obtained with compound $N_{||}$ spectra, i.e. low $N_{||}$ current drive phasing applied to one grill and high $N_{||}$ phasing to the other one. This is documented in fig. 10 for a discharge where LH waves are launched first with 700 kW in current drive phasing ($\Delta\phi$ = 75°, $N_{||}$ = 1 8). Then in a second phase a symmetric spectrum ($\Delta\phi$ = 180°, $N_{||}$ = 4.4) with 300 kW is added. During the first phase both β_p^{dia} and $\beta_p^{equ} + l_i/2$ increase, the latter more strongly owing to the anisotropy $\beta_p^{||} > \beta_p^{\perp}$ produced with LH. In the second phase β_p^{dia} rises still slightly, while $\beta_p^{equ} + li/2$ decreases strongly. The long time constant indicates a reduction of l_i and therefore appreciable flattening of j(r) Li-beam measurements confirm a clear change in the current distribution in the cases of such low $N_{||}$ / high $N_{||}$ compound spectra The safety factor q rises above 1 over the whole plasma cross-section, consistent with the stabilization of the m=1 mode in these discharges
The results on current profile broadening with different LH spectra are summarized in fig 11. With low $N_{||}$ current drive spectra ($\Delta\phi$ = 90°) a slight drop of l_i is seen only at high power. With high $N_{||}$ symmetric spectra ($\Delta\phi$ = 180°), l_i starts decreasing already at the lowest power applied The latter may be explained by a broad profile of LH generated suprathermal electrons which carry then part of the inductively driven current With simultaneous injection of low and high $N_{||}$ spectra the drop of l_i is larger than the sum from both spectra separately The central electron heating from LH current drive diminishes when the high $N_{||}$ spectrum is added. We conclude that the absorption of the low $N_{||}$ current drive spectrum is shifted more toward the periphery where fast

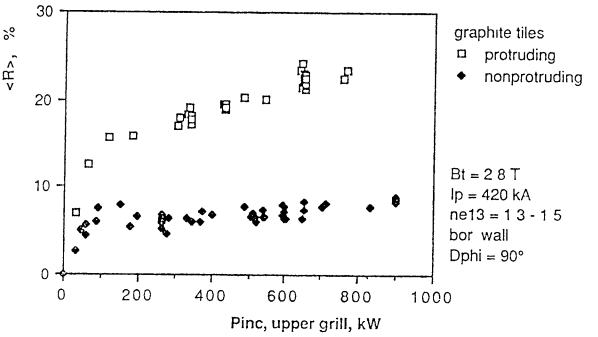

Fig. 1

$$\eta_{Exp} = \frac{\bar{n}_e I_p R}{P_{LH}} \quad (10^{13}\ cm^{-3}\ A\,m\,W)$$

$$\eta_{theor} = \frac{3.10}{\ln \Lambda} \; \frac{4}{5 + Z_{eff}} \; \frac{1}{\langle N_{//}^2 \rangle}$$

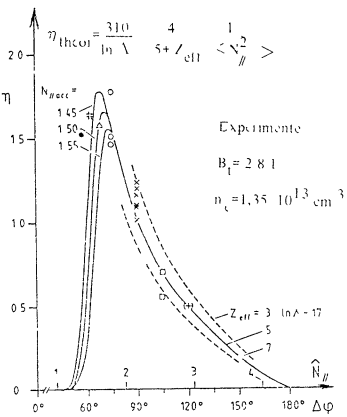

Fig. 2

$$\eta_{theor} = \frac{3.10}{\ln \Lambda} \; \frac{4}{5 + Z_{eff}} \; \frac{1}{\langle N_{//}^2 \rangle}$$

$$\eta_{Exp} = \frac{\bar{n}_e I_p R}{P_{LH}} \quad (10^{13}\ cm^{-3}\ A\,m\,W)$$

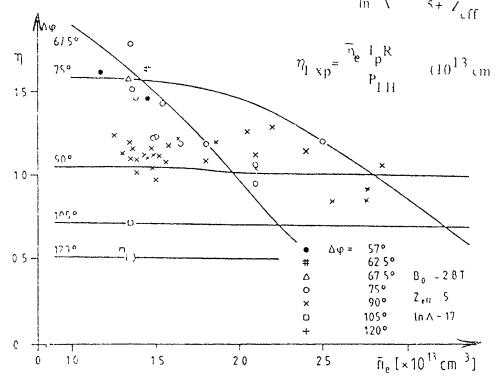

Fig. 3

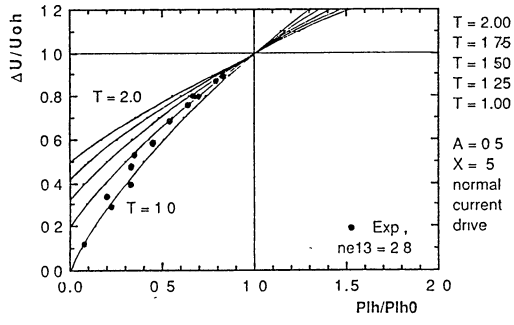

Fig. 4

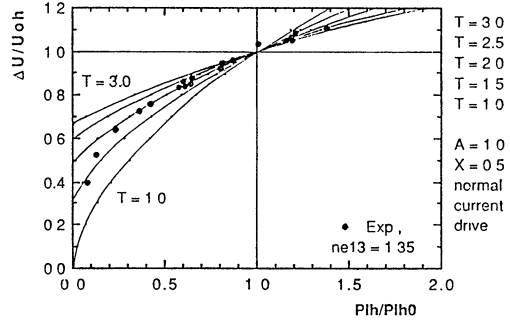

Fig. 5

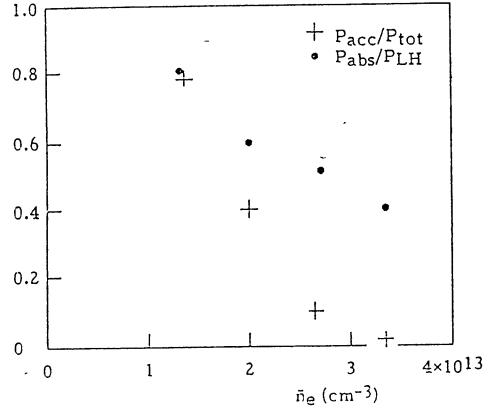

Fig. 6

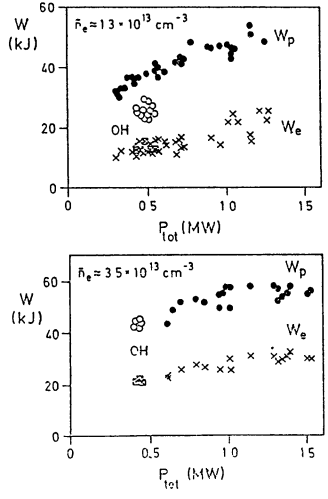

Fig. 7

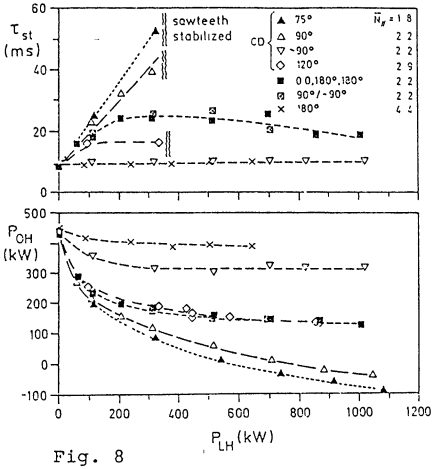

Fig. 8

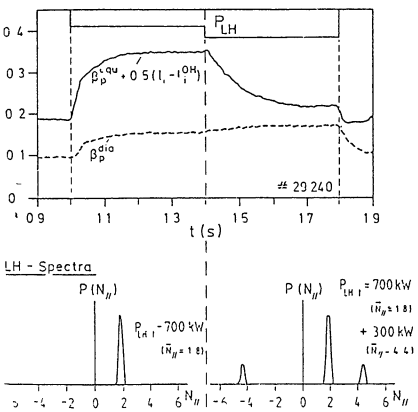

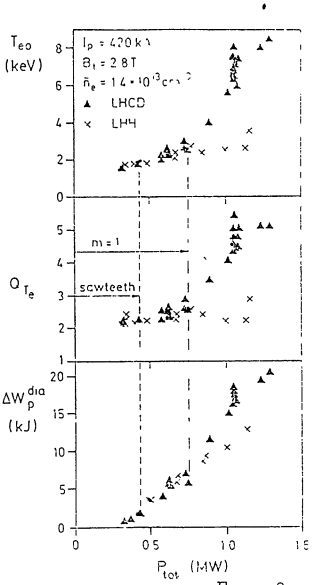

Fig. 9

Fig. 10

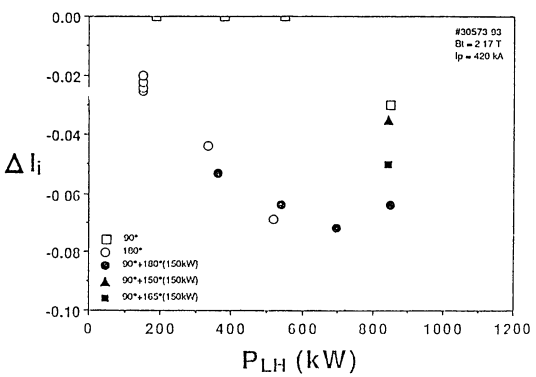

Fig. 11

Figures

Fig. 1: Average reflection coefficient <R> of the upper grill with and without protruding protection tiles as function of rf power

Fig. 2: Zero electric field current drive efficiency as function of $N_{||}$, $\overline{n_e} = 1.35\ 10^{13}cm^{-3}$, $B_t = 2.8$ T.

Fig. 3: Zero electric field current drive efficiency as function of density $B_t = 2.8$ T, different phasings

Fig. 4: Calculated and measured drop in loop voltage for partial current drive, $\overline{n_e} = 2.8\ 10^{13}cm^{-3}$, $B_t = 2.8$ T, $I_p = 420$ kA, $\Delta\phi = 90°$.

Fig. 5: Calculated and measured drop in loop voltage for partial current drive, $\overline{n_e} = 1.35\ 10^{13}cm^{-3}$, $B_t = 2.8$ T, $I_p = 420$ kA, $\Delta\phi = 90°$.

Fig. 6: Absorption coefficient α as function of density, compared with the fraction of accessible power. Bt = 2.8 T, $\Delta\phi = 75°$.

Fig. 7: Total energy content W_p and thermal electron energy content W_e as function of total input power for current drive at two different densities. $B_t = 2.8$ T, $I_p = 420$ kA, $\Delta\phi = 90°$.

Fig. 8: Variation of sawtooth period with LH power for different N|| spectra. $B_t = 2.8$ T, $I_p = 420$ kA, $\overline{n_e} = 1.4\ 10^{13}cm^{-3}$.

Fig. 9: Variation of central electron temperature T_{eo}, peaking factor $Q_{Te} = T_{eo} / \langle T_e \rangle$ and increment in energy content ΔW_p^{dia} with total power input $P_{tot} = P_{OH} + P_{LH}$ for LH current drive (LHCD) and symmetric LH spectra (LHH).

Fig.10: Temporal evolution of β_p^{dia} and $\beta_p^{equ} + l_i/2$, during injection of a narrow current drive spectrum and a compound spectrum, as plotted in the lower part of the figure.
$B_t = 2.8$ T, $I_p = 420$ kA, $\overline{n_e} = 1.4\ 10^{13}cm^{-3}$.

Fig.11: Variation of the drop of internal inductance Δl_i with LH power for wave spectra with different phasings and for compound spectra.
$B_t = 2.8$ T, $I_p = 420$ kA, $\overline{n_e} = 1.4\ 10^{13}cm^{-3}$.

electrons are generated by the high $N_{||}$ spectrum. This idea is supported by numerical modelling,/13/. At constant low $N_{||}$ power, the drop in l_i increases with the high $N_{||}$ power and also with increasing the value of the high $N_{||}$. The injection of combined $N_{||}$ spectra therefore provides a means to control the deposition profile of LH waves and the resulting current density profile.

This experiment has been performed in cooperation between IPP Garching, ENEA - Frascati and PPPL - Princeton.

References

/ 1/ Leuterer, F., et al., 16th Europ. Conf. on Contr. Fusion and Plasma Physics, Venice 1989, Vol. IV, 1287.
/ 2/ Leuterer, F., et al., 17th Europ. Conf. on Contr. Fusion and Plasma Physics, Amsterdam 1990, Vol. III, 1287.
/ 3/ Petrzilka V., Leuterer F., IPP-Garching Report IPP-4/243, (1990) to be published
/ 4/ C.F. Karney, N. Fisch, Phys. Fluids 28,116,(1985)
/ 5/ Stevens, J., et al., Nucl. Fusion 28 (1988) 217.
/ 6/ Cardinali A., Cesario R., Pericoli-Ridolfini V., 17th Europ. Conf. on Contr. Fusion and Plasma Physics, Amsterdam 1990, Vol. III,1203.
/ 7/ N. Fisch, Review of Modern Physics 59,175,(1987)
/ 8/ K. Yoshioka et al., Phys. Fluids 31,1224,(1988)
/ 9/ Leuterer, F., et al., 17th Europ. Conf. on Contr. Fusion and Plasma Physics, Amsterdam 1990, Vol. III, 1291.
/10/ Söldner, F.X., et al., 12th Europ. Conf. on Contr. Fusion and Plasma Physics, Budapest 1985, Vol. II, 244.
/11/ Bartiromo, R., et al., 17th Europ. Conf. on Contr. Fusion and Plasma Physics, Amsterdam 1990, Vol. III, 1092.
/12/ Söldner, F.X., et al., Proc. Workshop on Applications of RF waves to Tokamak plasmas, Varenna 1985, Vol. I, 740.
/13/ Söldner F.X., et al., 13th Int. Conf. on Plasma Physics and Contr. Nuclear Fusion Research, Washington Oct. 1990
/14/ Söldner, F.X., et al., 17th Europ. Conf. on Contr. Fusion and Plasma Physics, Amsterdam 1990, Vol. III, 1323.
/15/ Chu, T.K., et al., Nucl. Fusion 26 (1986) 666.
/16/ Leuterer, F., et al., 13th Europ. Conf. on Contr. Fusion and Plasma Physics, Schliersee 1986, Vol. II, 409.

PROPAGATION OF WEAKLY-DAMPED LOWER-HYBRID WAVES IN TOROIDAL PLASMAS

A.D. Piliya, A.R. Esterkin, Yu.F. Baranov
A.F. Ioffe Physical Technical Institute
Leningrad, USSR

Introduction

Analysis of the lower-hybrid wave propagation in toroidal plasmas is an interesting theoretical problem, which has been attracting considerable attention for some years. Many of the essential features of the wave behavior has been obtained using ray tracing techniques [1]. Because of the key role of $k_{\parallel}$ in the wave-particle interaction, the most significant of them are large variations of this parameter, first reported in [2]. Especially, the $k_{\parallel}$ evolution becomes important for the waves which are initially weakly damped and require considerable slowing down for their absorption. It should be noted, however, that the wave slowing-down due to toroidal effects has not been studied properly so far. Even such fundamental questions as whether the process is regular or stochastic and what are limitations on possible $k_{\parallel}$ growth, remain unanswered.

This paper attempts to fill this gap in the theory. Actually we investigate the dynamical system with two degrees of freedom which governs the ray trajectories in the poloidal cross-section of a tokamak (third coordinate, the toroidal angle φ, is an ignorable variable). Generally speaking, Hamiltonian systems with two degrees of freedom are very well studied, because they represent the simplest example of non-integrability [3]. In this particular case, however, motion demonstrates rather unusual features resulting mostly from the initial wave equation being hyperbolic in the greater part of the plasma volume. For example, there is a domain in the allowed phase space of this non-integrable system where chaotic behavior is forbidden. Instead, some phenomena associated rather with dissipative systems, like the frequency locking and attractors, are observed.

In the present paper, we study only general characteristics of long-term ray evolution. For this purpose the electrostatic approximation for the wave equation is quite sufficient. The case of the full electromagnetic equation as well as comparison with experimental data and practical conclusions will be published elsewhere. The problem under investigation has sense on condition that the electron Landau dumping is negligible. In practice it means that all thermal effects should be small and, therefore, the cold plasma approximation can be used.

1. Near-integrable form of ray equations.

For simplicity we assume that the wave frequency ω is much higher than the local lower-hybrid frequency anywhere inside the plasma volume. Then the electrostatic dispersion relation takes form:

$$H \equiv k_\perp^2 + \eta k_\parallel^2 = 0 \ , \qquad (1)$$

where $\eta=1-\omega_{pe}^2/\omega^2$ and ω_{pe} is the electron plasma frequency. Partly the $k_\parallel$ variations along the ray trajectory is a result of magnetic shear and appears also in a cylindrical plasma. In the lowest order in the inverse aspect ratio ε, cylindrical approximation to a tokamak $k_\parallel$ is given by

$$k_\parallel = \frac{1}{R}(n+m/q) \ , \qquad (2)$$

where m and n are the poloidal and toroidal mode numbers, respectively, and $q(r)=B_\varphi r/B_\theta R$ is the safety factor. At $\varepsilon=0$ both m and n are constants of motion, nevertheless $k_\parallel$ changes due to the r dependence of q. These variations can be quite large, but their magnitude is strictly limited. In contrast with these oscillations, slow change of $k_\parallel$ caused by the m non-conservation at $\varepsilon\neq0$ has no obvious limits and can eventually become the reason for the wave absorption by plasma electrons. Therefore the evolution of the poloidal momentum m due to toroidal effects is the main concern of this paper. As the first step, it seems reasonable to assume these effects to be small and take advantage of the assumption writing down the Hamiltonian function (1) explicitly. To this end, we suppose, in addition to the condition $\varepsilon<<1$, the shape of the poloidal cross-sections of magnetic surfaces to be close to circles centered on the magnetic axis. We formulate this assumption as follows: if $\rho(r,\theta)=\text{const}$ is the equation of a magnetic surface, then

$$\rho=\frac{r}{a}[1+\varepsilon f(r/a,\theta)] \qquad (3)$$

where $f(r/a,\theta)$ is of order unity, r,θ,φ are the usual toroidal

coordinates, and $\rho=a$ on the plasma edge. As a matter of convenience, we formally characterize all toroidal effects by the only small parameter ε. The function f depends periodically on θ and can be expressed as

$$f(r/a,\theta)=\sum_{p=1}^{\infty} f_p(r/a)\cos(p\theta) \qquad (4)$$

(first three terms in (3) are simply related to the parameters often used to describe the shape of a magnetic configuration: shift, ellipticity and triangularity).

The wave vectors perpendicular and parallel to the magnetic field are expressed in terms of k_α ($\alpha=\rho,\theta,\varphi$) as follows:

$$k_\perp^2=k_\rho^2+(k_\theta\cos\alpha-k_\rho\sin\alpha)^2 \ , \quad k_{||}=k_\varphi\cos\alpha+k_\theta\sin\alpha \ , \qquad (5)$$

where

$$\sin\alpha=B_\theta/B \qquad (6)$$

In turn, the physical components k_α should be substituted in the Hamiltonian function (1) by the corresponding canonical momenta p_α according to

$$k_\alpha=p_\alpha/h_\alpha \ , \qquad (7)$$

with h_α being the transformation coefficients. It is convenient to write down the coefficients h_α as

$$h_\rho=ah_1 \ , \quad h_\theta=\rho h_2 \quad \text{and} \quad h_\varphi=R_0h_3 \ , \qquad (8)$$

where R_0 is the major radius. In the first order in ε the functions h_i ($i=1,2,3$) can be easily found:

$$h_1=1-\varepsilon f_1(\rho,\theta) \ , \quad h_2=1-\varepsilon f_2(\rho,\theta) \ , \quad h_3=1+\varepsilon\rho\cos\theta \qquad (9)$$

with

$$f_1=\frac{\partial}{\partial\rho}(\rho f) \ , \qquad f_2=f+\int_\rho^1 \frac{\partial^2 f}{\partial\theta^2}\frac{d\rho'}{\rho'} \qquad (10)$$

To calculate $\sin\alpha$ we put $B=B\varphi$, use for B_φ its vacuum value and take advantage of the expression $B_\theta=\frac{1}{R}|\nabla\psi|$, where $\psi(\rho)$ is torcidal flux, for the poloidal field. Then,

$$\sin\alpha=\varepsilon\rho/qh_1 \ , \quad \frac{1}{q}=\frac{d\psi}{d\rho}\frac{1}{B_0\rho} \qquad (11)$$

Due to the specific form of the electrostatic Hamiltonian (1) the transformation $p'_\alpha=Cp_\alpha$, $H'=H/c^2$, $q'=q$, where C is an arbitrary constant, can be used to diminish the number of parameters in the equations. We take $C=p_\varphi q(0)$ and introduce $p=p_\rho/p_\varphi q(0)$ and $\mu=p_\theta/p_\varphi q(0)$. Then, substituting Eqs. (5)-(11) into (1) and keeping terms of zeroth and first order in ε, we obtain

$$H = H_0 + \varepsilon H_1 \ , \qquad (12)$$

where $H_0=p^2-F(\rho,\mu)$ with

$$F=\Phi(\rho)(\hat{q}+\mu)^2-\mu^2/\rho^2 \qquad \Phi=-\eta(\varepsilon/q)^2 \qquad \hat{q}=q/q(0) \qquad (13)$$

and

$$H_1=-2\Phi(q+\mu)[\mu f_2-\hat{q}(\rho\cos\theta+f_1)]+2(f_2-f_1)\mu^2/\rho^2 \qquad (14)$$

Taking into account the fact that only motion with H=0 is considered we multiplied H in (12) by the factor $h_1\neq 0$. The zero order term H_0 in (12) is integrable and the angle dependent term H_1 is small; therefore, Eq. (12) represents the ray equations in the near-integrable form.

According to (4) the non-integrable part of H can be written as

$$H_1 = \sum_{p=1}^{\infty} H_p(\rho,\mu)\cos p\theta \quad . \qquad (15)$$

We note that every term in (15) with p>1 is proportional to the corresponding form-factor $f_p(\rho)$ in (4). At p=1 there is also an additional contribution from toroidal modulation of k_φ. It is convenient sometimes to consider, instead of (12) a non-autonomous system for μ and θ, with ρ being an independent variable. To present the system in this form, one should find $p=P(\mu,\theta,\rho)$ from the equation H=0, then θ and μ satisfy the canonical equations

$$\frac{\partial\theta}{\partial\rho} = -\frac{\partial P}{\partial\mu} \quad , \qquad \frac{\partial\mu}{\partial\rho} = \frac{\partial P}{\partial\theta} \qquad (16)$$

$$\text{with } P = \pm\sqrt{F+\varepsilon H_1} \simeq \pm\left(\sqrt{F} + \frac{\varepsilon H_1}{2\sqrt{F}}\right) \qquad (17)$$

2. Preliminary analysis of the ray equations.

We begin the analysis of the system (17) with investigation of its accessible phase space to find the limits in which the normalized poloidal momentum μ is confined.

At $\mu\to\infty$ the Hamiltonian (17) takes the form $P=\pm\frac{\mu}{\rho}\sqrt{\rho^2\Phi-h_1}$ and motion is possible when there is a region in the plasma volume with $\Phi\rho^2>h_1$. The wave equation is hyperbolic inside this domain and elliptic outside. The function $\rho^2\Phi$ equals zero on the axis and near the plasma edge and typically has a single maximum. The maximum value of $\rho^2\Phi$ depends on ω and is rather large for $\omega\leqslant(2\div3)\omega_{LH}$, where ω_{LH} is the lower-hybrid frequency on the axis. In this case, the hyperbolic region has the form of a ring ($0\leqslant\theta\leqslant2\pi$) occupying the greater part of the poloidal cross-section. With ω increasing, the radial width of the hyperbolic ring diminishes and becomes more angle-dependent. At a frequency $\omega=\omega_1\simeq\omega_p r/q$ two elliptic areas, central and peripheral, touch each other. At higher frequencies the hyperbolic region is restricted in both radial and poloidal directions and consists of one or

several isolated domains, depending on the plasma shape. At $\omega=\omega_2$ the hyperbolic region disappears completely. In the frequency interval $\omega_1 \leqslant \omega \leqslant \omega_2$ the wave propagation is especially strong influenced by the poloidal inhomogeneity of the system. Interesting phenomena observed here shall be shortly discussed in the section 5. Formally the interval $\omega_2-\omega_1$ is small, of the order $\varepsilon\omega_1$, however in tokamaks with non-circular cross-section it may be quite large numerically. Thus, at $\omega<\omega_2$ the accessible phase space is unlimited in μ direction.

At $\mu<0$ the separation between two roots of P progressively decreases with $|\mu|$ and equals zero at a certain μ^*, depending on θ. The curve $\mu^*(\theta)$ $(0\leqslant\theta\leqslant 2\pi)$ in the (μ,θ)-plane is the lower limit of the accessible phase space.

Behavior of a near-integrable system is determined to a great extent by its unperturbed motion. For the system (12) the zero-order motion consists of radial oscillations with a period $T_1(\mu)$ and poloidal rotation, having a period $T_2(\mu)$. Radial motion is confined to a ring-wise region $b(\mu)\leqslant\rho\leqslant a(\mu)$, where a and b are the roots of P at $\varepsilon=0$. At $\omega<\omega_1$ $b\ll 1$ and $(1-a)\ll 1$ in the whole interval of $\mu>0$. An important parameter of the zero-order ray-trajectory $\theta(\rho)$ is its poloidal shift per one radial period which we denote as $2\pi\delta(\mu)$ (obviously, $\delta=T_1/T_2$). According to (16),

$$\delta=\frac{1}{\pi}\frac{\partial}{\partial\mu}\int_b^a \sqrt{F(\mu,\rho)}\,d\rho \qquad (18)$$

A striking feature of δ, having a dominating effect on the system behavior, is its rather weak dependence on μ at $\mu>0$. Fig. 1 shows an example, calculated for the model profiles of the plasma density $n(\rho)$ and $q(\rho)$:

$$n(\rho)=n_0(1-\rho^2) \quad , \quad q=q_0(1+\gamma\rho^2) \qquad (19)$$

Behavior of the function $\delta(\mu)$ can be easily understood from (18) for $\delta>1$. The function $\Phi(\rho)$ typically has a peaked profile, therefore, rather large values of $\Phi_0=\Phi(0)$ are needed to get $\delta\sim 1$. Assuming $\Phi_0\gg 1$, we see that the main contribution to the integral (18) is μ-independent[I].

[I] Actually, the second term in (20) should be $-\mathrm{sign}\mu/2$. However, the discontinuity of $\delta(\mu)$ at $\mu=0$ does not manifest in physical effects and is ignored.

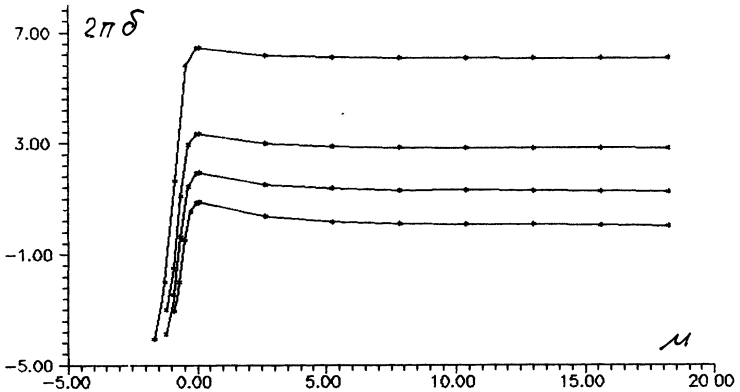

Fig. 1 Poloidal shift $2\pi\delta(\mu)$ for different frequencies.

$$\delta = \frac{1}{\pi}\int_b^a \sqrt{\Phi}\,d\rho - \frac{1}{2} + O(\Phi_0^{-1/2}) \qquad (20)$$

Numerically this result is valid even for $\delta<<1$. At δ irrational, the motion is quasiperiodic and a trajectory fills up the whole region $b<<\rho<<a$. If $\delta=r/s$ with r and s being integers, all trajectories are closed and consists of s radial transits and r poloidal circuits.

3. Discrete maping for ray trajectories.

At small $\varepsilon\neq 0$, a ray trajectory $\theta(r)$ still consists of repeating radial oscillations; however their parameters (a,b,δ) now slowly vary due to the μ evolution. The long-term behavior of this type can be most clearly described by presenting each radial period by a point μ_n of a discrete map in (θ,μ)plane (n denotes the period number [4,5]. For concreteness we assume that the n-th period begins in the n-th inner reflection point b_n and take initial values θ_n, μ_n of θ and μ for coordinates of μ_n. Now our purpose is to find a maping $\mu_n \to \mu_{n+1}$ giving (θ_{n+1},μ_{n+1}) when (θ_n,μ_n) are known.

Computation of this maping can be carried out, of course, using a numerical ray tracing code. This procedure, however, is, as a matter of fact, rather empirical and, in addition, a very time-consuming. Therefore, we define the maping by a system of two transcendental equations and determine their explicit form demanding the maping to be, first, area-preserving and, second,

correct in the first order in ε. A considerable simplification is achieved by introducing a new angular variable $\psi=\theta-\pi\delta(\mu)$ (transformation $\theta\to\psi$, $\mu\to\mu$ is canonical and does not change the form of Hamiltonian P). Now, to satisfy the first demand, we take the mapping in the form of a canonical transformation with a generating function $S(\mu_{n+1},\psi_n)$:

$$\psi_{n+1}=\psi_n+\frac{\partial S}{\partial\mu_{n+1}}+2\pi\delta(\mu_{n+1}) \qquad \mu_n=\mu_{n+1}+\frac{\partial S}{\partial\psi_n} \tag{21}$$

The function S depends periodically on ψ_n and can be presented in the form:

$$S=\sum_{p=0}^{\infty} S_p(\mu_{n+1})\cos[p\psi_n+\alpha_p(\mu_{n+1})] \tag{22}$$

To find the functions S_p and α_p, we compare the change of μ per a period, $\Delta\mu_n=\mu_{n+1}-\mu_n$ given by Eq. (21) with the result of direct integration of Eq. (16). With the needed accuracy, the integration should be carried out along the zero-order trajectory. Then, taking into account its symmetry, and using (15) we obtain:

$$S_p(\mu)=2\varepsilon\int\frac{H_p\cos p\phi\, d\rho'}{\sqrt{F}} \tag{23}$$

Elimination of μ-dependent phase shift α_p is the reason for introducing the variable ψ instead of θ. For $S_0(\mu)$ we simply have

$$S_0=2\pi\int^{\mu}\delta(\mu')d\mu' \tag{23'}$$

because $\Delta\theta=\theta_{n+1}-\theta_n$ does not include a contribution linear in ε and independent of θ_n. To get an idea of the μ-dependence of S_p, we can once more use the condition $\Phi(0)>>1$. Then

$$S_p=\alpha_p-\beta_p\mu \tag{24}$$

where α_p and β_p are positive constants. This approximation is actually rather good in the whole region $\mu>0$. At $\mu<0$ the functions S_p remain nearly constant up to the limit $\mu=\mu^*$. The maping (21) with (24) for S_p for $\mu>0$ and $S_p=\alpha_p$ at $\mu<0$ quite satisfactory describes the long-time behavior of the system (16). Nevertheless, in the results presented in this paper functions $S_p(\mu)$ obtained by the numerical integration of (16) or recovered from the ray tracing, are used. Accuracy of the mapping in this case is illustrated by Fig 2.

4. Results

The presentation of the phase trajectories given by Eqs. (21) reminds of the familiar maping of a toroidal magnetic field in the presence of the helical perturbations, with $\delta(\mu)$ playing the role of rotational transform. At small $\varepsilon\neq0$ we must anticipate formation of islands structures associated with rational surfaces

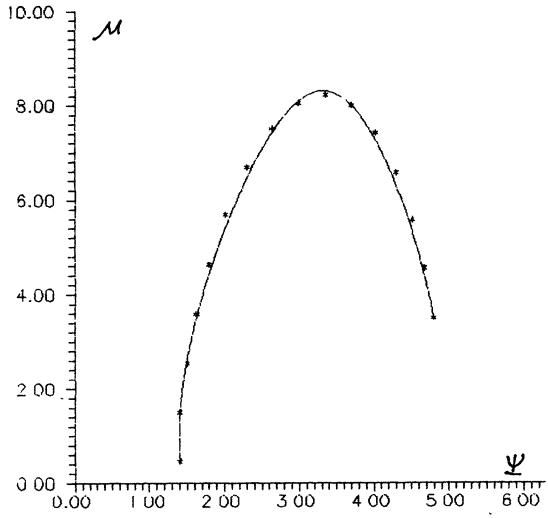

Fig. 2 Phase trajectory from the maping (dots) and ray tracing code (solid line).

$\delta=r/s$. With ε increasing the onset of stochasticity due to islands overlap should be expected. To select the part of perturbation, specifically responsible for destruction of the closed trajectories with a given $\delta=r/s$ we substitute into Eqs. (15) the zero-order solution for $\theta(t)$ and $\rho(t)$. Then Fourier decomposing the p-th term in H_1 we see that it consists of harmonics with the frequencies $\Omega_n = n\Omega_1 \pm p\Omega_2$ where n is the whole number. The major distortion is caused by the harmonics with $\Omega=0$ i. g. with $n/p=r/s$. Keeping in H_1 only the resonance part (with fixed n/p) we obtain an integrable system having a constant of motion independent of H. In this case, the points generated by the maping (21) should lie on smooth curves in the (μ,ψ)-plane. In particular, for resonances of the type n/p=k, k=0,1,2,... which we consider in more detail, the additional integral has the form $\bar{S}\equiv S(\mu,\psi)-2k\pi\mu=\text{const}$ (this result directly follows from Eqs. (21) at $|\delta-k|\leqslant\varepsilon$). Therefore, the orbits governed by Eqs. (21) must follow level curves of the function $\bar{S}(\mu,\psi)$. Fig. 3 and 4 show these curves for the circular and elliptic shape of the plasma cross-section respectively (in the first case the function f in (4) consists of the single term p=1, whereas in the

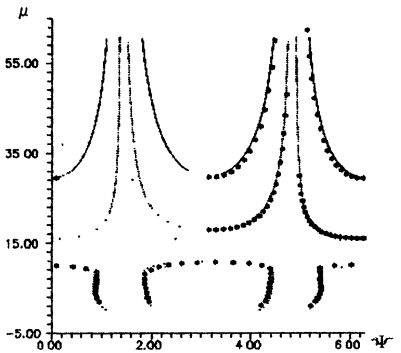

Fig 3. Level curves of $\bar{S}$ for the circular cross-section and phase trajectories from the maping; $\delta_\infty=1$, $\varepsilon=0.24$

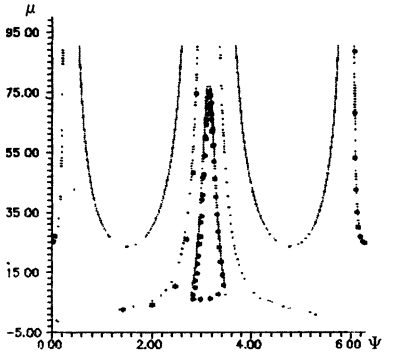

Fig.4 Level curves and phase trajectories for the elliptic cross-section; $\delta_\infty=0.957$, ellipticity $k=1.5$

second case harmonics p=1 and p=2 are included. The parameter $\delta_\infty=\lim_{\mu\to\infty}\delta(\mu)$ is chosen to be close to 1, then the resonance zone $|\delta(\mu)-1|\leqslant\varepsilon$ covers the greater part of the phaseplane. This fact is illustrated by behavior of the phase trajectories, which closly follow the level curves at $\mu>0$.

In the case of the circular cross-section the upper part of the μ-ψ plane is completely separated from its lower part. The separatrix is the line $\mu=\mu_0$ on which the only angle dependent term in S, $S_1(\mu)$ is equal to zero. The separatrix is obviously inpenetrable for trajectories launched in the lower part of the phase plane and thus put a limit to possible μ groth. On the other hand if the resonance condition $2\pi|\delta-1|<\varepsilon S_1$ is satisfied at $\mu\to\infty$ the level curves lying above the separatrix are opened and go to infinity. Accordingly, the phase trajectories, launched in this region experience unlimited μ growth. In the case of the elliptic cross-section the separatrix is absent and we anticipate unlimited slowing down of the waves, having initially $\mu=0$ at the resonance conditions. Fig. 5 and 6 give examples of trajectories generated by Eq. (21) for the circular cross-section and fig. 7 show the Kolmogorov entropy inside the stochastical domain for the both cases. It is seen, that the treshold for the onset of

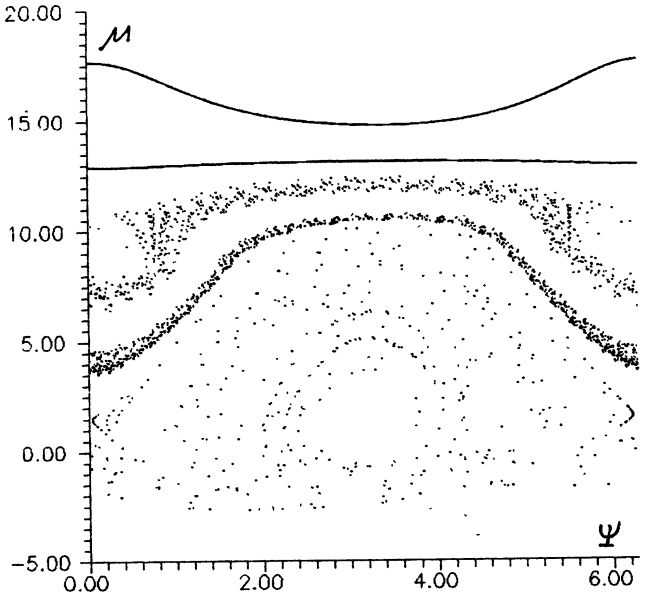

Fig. 5 Phase trajectories for the circular cross-section δ_0=0.95, ε=0.24. Five trajectories are shown, 1000 points each.

stochasticity is extremely low and for realistic values of ε the degree of randomnes of motion is rather high. Nevertheless, observing the trajectories in the dynamics we see, that the motion looks erratic and unpredictable only in the large shear region μ<0, which occupies, in the case of Fig 5 , only minor part of the whole stochastic domain. In its remaining part, the trajectories still lie on the smooth curves. This fact explains probably lesser value of the entropy in this case. The μ excursions in the well-behaved part of the motion are much larger then $\bar{\Delta}\mu$ in one step of the mapping. Therefore, the μ evolution cannot be described as diffusion in the phase space. Fig. 8 illustrates the character of motion in the case of the elliptic cross-section. The δ_0 value is chosen just outside the resonance zone to confine the points to the finite region in μ-ψ plane. The resonance zone is the interval of δ_0 in which all trajectories eventually go to infinity.

5. Motion in the large μ region

Observation of the phase trajectories shows that motion

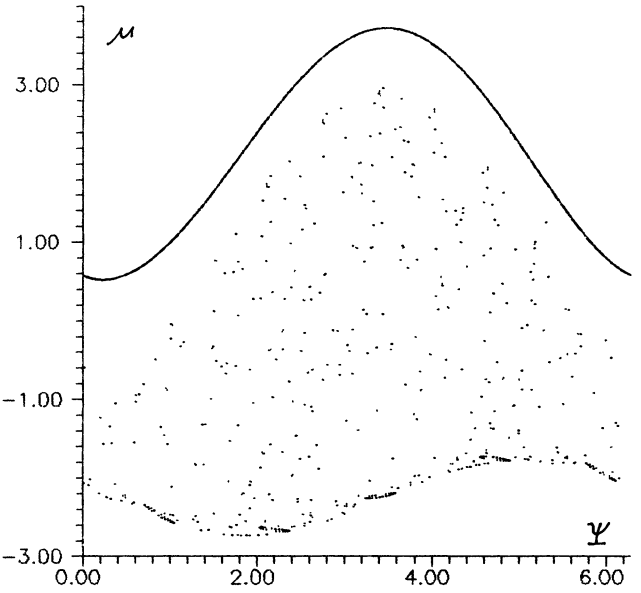

Fig. 6 Two trajectories for the circular cross-section δ_0=0.95, ε=0.24, 1000 points each

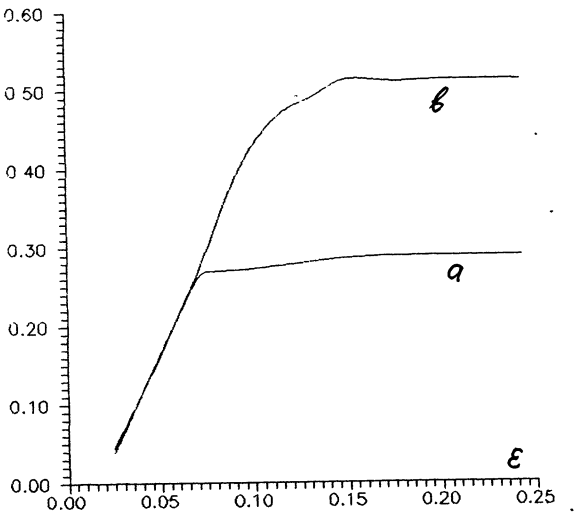

Fig.7 Kolmogorov entropy vs ε: (a)-the case of Fig. 5; (b)-the case of Fig. 6.

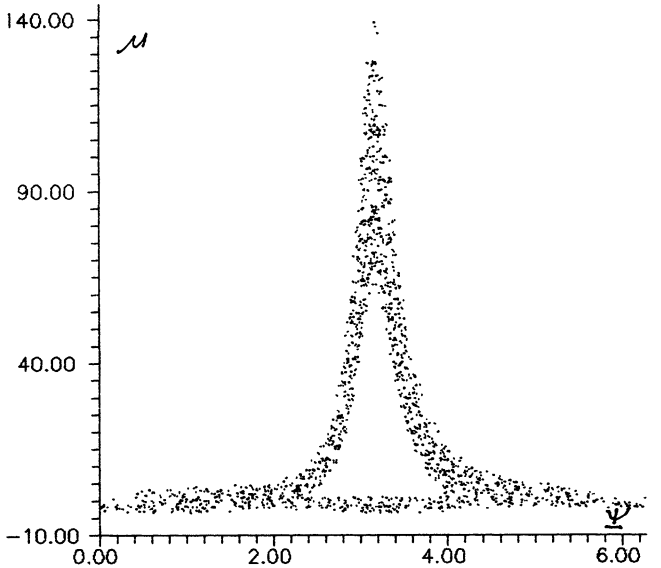

Fig. 8 A phase trajectory (2000 points) for the case of Fig. 4 with $\delta_\infty = 0.92$

becomes more regular with μ increasing and that stochastisity never occurs in the asymptotic region $\mu \gg 1$. To explain these facts consider the equations of motion (16) in the limit $\mu \to \infty$. Taking Eq.(17) for P, we see that $\theta(\rho)$ satisfied the equation

$$\frac{\partial \theta}{\partial \rho} = \pm \frac{1}{h_2} \sqrt{\Phi - h_1/\rho^2} \tag{25}$$

which is independent of μ. With $\theta(\rho)$known, the function $\mu(\rho)$ is given by the explicit expression

$$\mu = \mu_0 \exp\{\pm \int^{\rho} \frac{1}{h_2} \sqrt{\Phi - h_1/\rho^2} \tag{26}$$

The integral curves of Eq. (25) can be visualized as lying on the surface of a flat torus (or of a two-fold ring), two sides of which correspond to two signs in Eq. (25), such a curve cannot intersect itself or any other curve on the torus. This simple circumstance rules out complicated stochastic behavior of the trajectories and thus explains absence of stochastisity in the $\mu \to \infty$ region. Two possibilities remain open, depending on

parameters: there are no closed orbits on the torus or such orbits are present. In the first case a trajectory winds up the torus endlessly, while μ osscillates in certain limits. The second case is more interesting. Because the torus bearing the trajectories $\theta(\rho)$ are inhomogenious in θ direction, the closed orbits can only appeare as isolated curves. Now, considering the topology of the problem we easily conclude that any trajectory which is not closed can exist on the torus without self-intersections only approaching asymptotically a closed orbit, which, therefore is an attractor of these trajectories. Appearance of such an object is possible because the motion, described by Eq. (25) is not Hamiltonian by itself: the phase volume preservation is provided by corresponding change of μ. Therefore, $\mu \to \infty$ as a trajectory tends to an attractor, in accordance with behavior of level curves and phase trajectories shown above. A real ray-trajectory in the vicinity of a periodic attractor, calculated using a ray tracing code is shown in Fig.9.

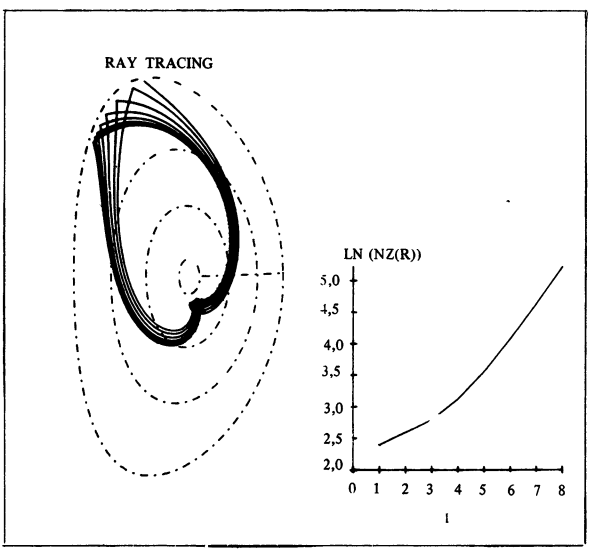

Fig. 9 A ray trajectory in the vicinity of the periodic attractor, and the wave slowing-down NZ.

The phenomenon just described represents an example of non-linear frequency-locking; the frequency of any radial oscillation, which depends on initial conditions eventually approaches the same limit $\Omega=\Omega_1$. The maping (21) also takes more simple form in the limit $\mu\to\infty$:

$$\psi_{n+1}=2\pi\delta_\infty+\psi_n+F(\theta_n) \cdot \qquad (27)$$

$$m_{n+1}=\frac{m_n}{1+F'(\theta_n)} \qquad (28)$$

where $\varepsilon F_n=\Sigma\ \beta_p \cos p\psi_n$ (see (24)) is a periodic function. Eq. (27) is an exact consequence of Eq. (25), independent of ε value, because it simply expresses the fact of periodical dependence of the solution on the initial conditions ψ_n. However, the restriction $|F'|<0$ arising from the non-intersection of trajectories appears when the maping is generated by the differential equation (25). The circular maping (27) has been investigated in considerable detail at a special forms of F [6], [7], and for $|F'|<1$ the results support the above consideration. At $|F'|>1$ Eq. (25) describes a very interesting chaotic motion

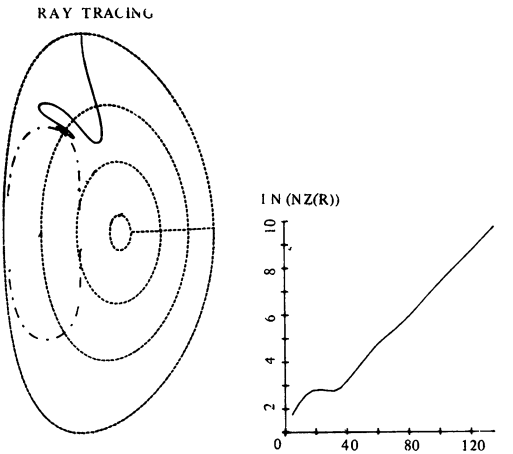

Fig. 10 Attracting point on the parabolic line. A ray trajectory (solid line), magnetic surfaces (dotted line) and parabolic line (broken) are shown.

including chaotic attractors. This regime, however, probably cannot be realized in the problem under consideration. Nevertheless, the periodic attractor described above are not the only one, appearing at $\mu \to \infty$. Attractor of a different type is observed in the frequency interval $\omega_1 < \omega < \omega_2$. In this case the line separating the hyperbolic and elliptic regions of the wave equation inevitably has a point where this line is perpendicular to a magnetic surface. According to [8,9] this point is an attractor of ray trajectories (see Fig. 10). In the case of the circular cross-section the resonance zone of this attractor lies above the separatrix. For the elliptic tokamak every trajectory is eventually attracted to the singular point.

References

1. V.L. Ginzburg. Propagation of Electromagnetic Waves in Plasma. Nauka, Moscow, 1970 (in Russian).
2. Ju.F. Baranov, V.I. Fedorov. In: Heating in Toroidal Plasmas. Como, 1980, Vol. 1, p. 313-316.
3. G.H. Walker, S. Ford. Phys. Rev. **188**, 416 (1969).
4. Yu.F. Baranov, E.Z. Gusakov, A.D. Piliya. In: Proc. of the Joint Varenna-Lausanne International Workshop, 1988, p. 707.
5. E. Barbato. In: Proc. of the Joint Varenna-Lausanne International Workshop, 1988, p. 577.
6. L. Glass, R. Perez. Phys. Rev. Lett. **48**, 1772 (1982).
7. M.H. Jensen, P. Bak, T. Bohr. Phys. Rev. Lett. **50**, 1637, (1983).
8. A.D. Piliya, V.I. Fedorov. In: High-frequency Plasma Heating. Gorky, IAP, USSR Academy of Science, 1983, p. 6-70.
9. Yu.F. Baranov, A.D. Piliya, A.R. Esterkin. Pis'ma Zh. Eksp. Teor. Fiz. **51**, 617 (1990).

Quasi-Optical Grill for Excitation of Lower-Hybrid Wave in a Plasma

N.F.Kovalyov, M.I.Petelin, E.V.Suvorov, S.E.Fil'chenkov
Institute of Applied Physics,
Academy of Sciences of the USSR, Nizhny Novgorod, USSR

We present here a new concept of launch system for the excitation of lower-hybrid waves in toroidal plasma. It is aquasi-optical concept, its main idea can be easily understood considering a simple model of a plane plasma layer irradiated by a plane electromagnetic waveincident from the vacuum . Of course these two waves cannot be coupled directly to each other since the LH wave is slow ($n_{\parallel}>1$) and the e.m.wave is fast ($n_{\parallel}<1$). Nevertheless coupling may be provided by placing in front of the plasma surface a periodical structure e.g., of metal rods - a quasi-optical grill (see fig.1) [1] An infinite series of spatial harmonics generated by a grill structure satisfy the condition :

$$k_{nx} = k \sin\alpha + nk_g \quad , \qquad (1)$$

where $k = \omega/c$, α is the incidence angle of electromagnetic wave in vacuum, $k_g = 2\pi/d$, with d being the period of grill structure, $n = 0, \pm1, \pm2, \ldots$ .The geometry, direction of axes and wave polarization are shown in fig.1. Adjusting properly k, α and d it is easy to provide a regime in which the only reflected wave corresponding to n=0 exists in a vacuum. All other harmonics except n=0 are not propagating in vacuum but, being slow ($ck_x/\omega > 1$) they can be coupled to the LH waves propagating in a plasma. The coupling efficiency from the incident electromagnetic wave via n-th harmonic to LH wave is proportional to the exponent $e^{-2\gamma_n D}$ where D is

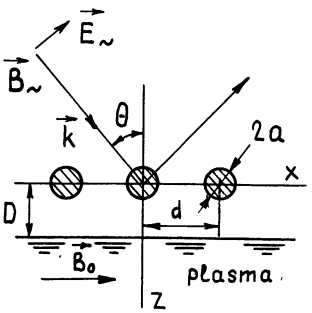

Fig.1. Single-layer QO grill.

the distance between the grill and plasma boundary, $\gamma_n^2 = k_{xn}^2 - k^2$ (γ_n is the decrement index of the n-th harmonic in the vacuum). Using the n=-1 harmonic it is possible to provide preferable excitation of an LH wave with necessary slowing-down

$$n_{\parallel} = \left| \sqrt{[(2\pi/kd - \sin\alpha)^{-2} - 1]} \right| \qquad (2)$$

while the excitation of other harmonics will be inessential. The selectivity condition takes the form:

$$\exp \{ 2(\gamma_1 - \gamma_{-1}) D \} \gg 1 \qquad (3)$$

From (2),(3) it follows that with a fixed radiation frequency, the slowing-down of the LH wave may be controlled by the variation of the incidence angle α and the selectivity may be controlled by the variation of the distance D from the grill to the plasma boundary.

To inject all the r.f.power into plasma, it is necessary to suppress the reflected wave. It can be done by placing an additional reflector in front of the launch system, e.g. the second grill structure (see fig.2). In this case a quasi-optical cavity is formed which may be matched with 100% efficiency to the incident electromagnetic wave. In order to diminish the Q-factor of the cavity the single-grill structure must provide the highest possible efficiency of LH wave excitation. Analytical calculation by the perturbation method using two small parameters ka and a/d (a is the radius of the grill rods of a circular cross-section) results in an expression for efficiency of LH wave excitation which is proportional to both of these two parameters squared[1]:

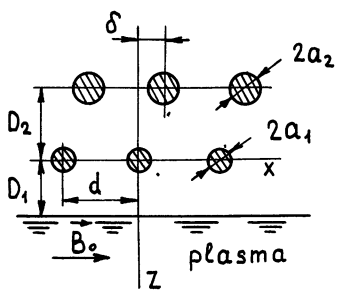

Fig.2. Double-layer QO grill

$$\frac{P_{-1}}{P_o} = \frac{2}{\cos\alpha} \frac{\gamma_{-1}}{k} |\alpha_{-1}|^2 \, \mathrm{Im}\, R_{-1} \qquad (4)$$

with

$$\alpha_{-1} = \pi \frac{k a^2}{d} \left[i(1-R_o)\cos\alpha - (1+R_o) \frac{2 k_{-1} \sin\alpha - k_o}{2 \gamma_{-1}} \right]$$

where reflection coefficient from the plasma R_n for the n-th spatial harmonic is defined by (see e.g.[2])

$$R_n = \exp\left(-2\gamma_n D\right) \frac{1 - Z_p}{1 + Z_p}$$

and Z_p depends on the plasma density profile:

$$Z_p = 1 \Big/ i \sqrt{n_o/n_c - 1} \quad \text{for the profile} \quad n = \begin{cases} 0 & \text{for } z < D \\ n_o > n_c & \text{for } z > D \end{cases} \qquad (A)$$

and $$Z_p = -(\gamma_n L)^{1/3} \frac{Bi\left[\varepsilon_o (\gamma_n L)^{1/3} \right] - i\, Ai \left[\ldots \right]}{Bi'\left[\ldots \right] - i\, Ai'\left[\ldots \right]}$$

for the profile $$n = \begin{cases} 0 & \text{for } z < D \\ n_o + n_c (z-D)/L & \text{for } z > D \end{cases} . \qquad (B)$$

where *Ai* and *Bi* are Airy functions of two types and ε_o in the argument of Airy functions is defined as $\varepsilon_o = 1 - n_o/n_c$, n_c being critical density.

Optimization of one-layer grill structure was performed by numerical calculation of its coupling efficiency based on the solution of an integral equation for magnetic current distribution over the surface of metal rods with a circular cross-section. Integral equation takes the form:

$$j_m^s(\phi) = \cos(\alpha+\phi) \exp\left[ika \cos(\alpha+\phi)\right] -$$
$$- R_o \cos(\alpha-\phi) \exp\left[-ika \cos(\alpha-\phi)\right] +$$

$$- \frac{a}{d} \sum_{n=-\infty}^{\infty} \int_{-\phi}^{\phi} d\phi' j_m^s(\phi') \exp\left[ika\ (\sin\phi - \sin\phi')\right] \cdot \qquad (5)$$

$$\cdot \left\{ \alpha_n^{(-)} \exp\left[ig_n a\ (\cos\phi' - \cos\phi)\right] + \alpha_n^{(+)} R_n \exp\left[ig_n a\ (\cos\phi' + \cos\phi)\right] \right\} -$$

$$- \frac{a}{d} \sum_{n=-\infty}^{\infty} \alpha_n^{(+)} \int_{\phi}^{2\pi-\phi} d\phi' j_m^s(\phi') \exp\left[ika\ (\sin\phi - \sin\phi')\right] \cdot$$

$$\cdot \left\{ \exp\left[ig_n a\ (\cos\phi' - \cos\phi)\right] + R_n \exp\left[ig_n a\ (\cos\phi' + \cos\phi)\right] \right\} ,$$

where $\alpha_n^{(\pm)} = \frac{h_n}{g_n} \sin\phi \pm \cos\phi$, $g_n^2 = k^2 - h_n^2$ $(= -\gamma_n^2$ for $h_n^2 > k^2)$.

The integral equation (3) includes the following dimensionless parameters: ka, kd, kD, α and values determining the plasma density profile (n_0/n_c and kL); some of them are related by eq.(2), in which the required slowing down of the LH wave is involved. The numerical optimization of the single-layer grill was mainly performed with fixed values α, kd and n_o/n_c for the density profile (A). Figures 3 and 4 show the efficiency of LH wave (n=-1 harmonic) excitation on the plane ka, kD. Maximum efficiency reaches 15% for $n_\parallel$ =1.5 and 10% for $n_\parallel$ = 1.7 with the incidence angle being 45° and n_o/n_c= 2. Some dependencies on the grill-plasma distance and on the edge plasma density may be understood from Tables I and II.

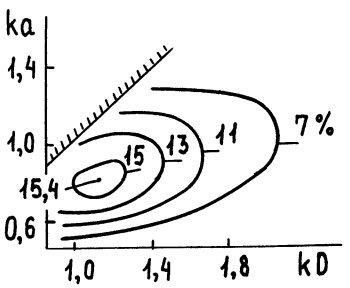

Fig.3: kd=2.9, $\theta=\pi/4$, $n=2n_c$, $n_\parallel$=1.5

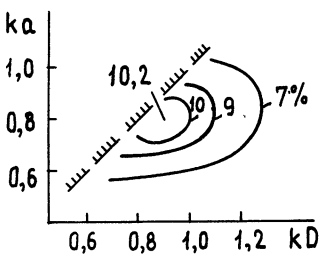

Fig.4: kd=2.6, $\theta=\pi/4$, $n=2n_c$, $n_\parallel$=1.71

Table I ($\theta = 45^{o}$, $n/n_c = 2$, $kd = 2.9$, $n_{\parallel} = 1.46$)

kD	1.2	1.3	1.4	1.5	1.6	1.8	2.0
P_{-1}/P_o	0.15	0.14	0.13	0.12	0.11	0.08	0.06
$P_{-1}/P_{n\max}$	9.1	16	27	46	75	210	580

Table II ($\theta = 45^{o}$, $kd = 2.9$, $kD = 1.2$, $n_{\parallel} = 1.46$)

n/n_c	2	3	4	5
P_{-1}/P_o	0.15	0.12	0.09	0.07
$P_{-1}/P_{n\max}$	7.7	5.8	4.2	3.2

For the illustration of the possibility of 100% coupling by means of two-layer grill, the dependence of reflection coefficient from a double-layer structure on the grill-plasma distance is shown in fig.5. It can be seen that when the reflection coefficient from the second grill in vacuum coincides with that from the first grill together with plasma (ka=1.34), the double grill parameters may be properly adjusted to provide 100% coupling efficiency. If these reflection coefficients do not coincide exactly, optimal coupling efficiency is lower but it is less sensitive to the variation of grill parameters.

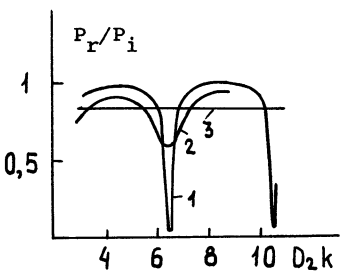

Fig.5: $ka_1=0.85$, $kd=2.9$, $kD_1=1.1$, $n_{\parallel}=1.5$, $\theta=\pi/4$, $\delta=0$;
$ka_2=$ 1.34 (1)
1.1 (2)
0 (3)

At present the numerical code for the calculation of r.f. field amplitude distribution around grill elements is under development.

Further investigations are needed when elaborating an optimal quasi-optical grill for any specific installation taking into account plasma parameters, dimensions of the port, the frequency to

be used etc.

The idea of testing a quasi-optical grill using the existing conventional grill structure is presented in fig.6, where an obliquely incident plane wave is formed by proper phasing of modes in adjacent waveguides. Possible scheme of quasi-optical grill irradiation by means of several oversized waveguides is shown in fig.7.

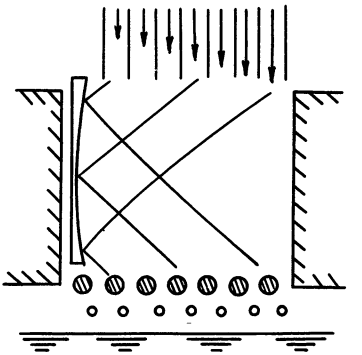

Fig.6.

In principle, quasi-optical grill seems to be rather attractive as compared with the conventional grill. For example, for ITER scale machine it is supposed to use about 10^3 waveguides of the conventional grill in a 1m x 3m port; a quasi-optical grill for 3-7 GHz will contain only 10-20 metal rods (or pipes) 2-3 cm in diameter. It may be irradiated with a system of independent quasi-optical waveguides. Its negligible mass makes it very convenient for fast feed-back reaction to the variation of plasma parameters. The shape and size of its elements make it suitable for cooling. On the other hand, it should be noted that testing of a quasi-optical grill is possible only on a large-scale machine and the frequency used must be high enough.

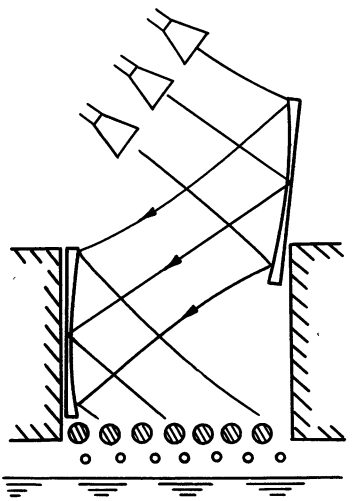

Fig.7.

Referencies

1. M.I.Petelin, E.V.Suvorov, Piz'ma v ZhTF, 1989, 15, p.23.
2. M.Brambilla, Nuclear Fusion, 1976, v.16, N 1, p.47.

SOME FEATURES OF THE ELECTRON CYCLOTRON HEATING IN INHOMOGENEOUS MAGNETIC FIELDS

BELAVIN M.I., ZIL'TSOV B.A., SKOVORODA A.A., SCHERBAKOV A.G.
I.V.KURCHATOV INSTITUTE OF ATOMIC ENERGY, MOSCOW, USSR

1. Introduction

High power ECRH is one of the basic methods to obtain high temperature thermonuclear plasmas. Numerous experimental and theoretical investigations on this topic are summarized in recent revues [1,2]. Great progress is amounted in practical implementation ECRH, but some principal questions have no answers up to now.

In this report, we collect some unclear problems, arising by the way of discussion on the results, obtained in two installations with the inhomogeneous magnetic fields and high power ECRH density.

2. Experiment

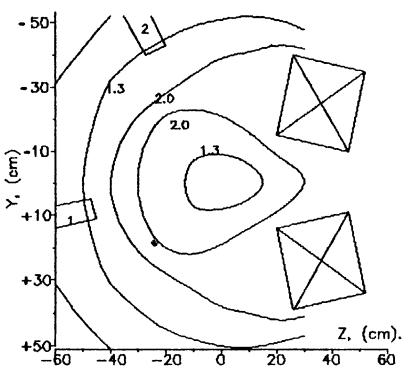

Fig. 1. OGRA–ECR const–B lines (T).
1 – throat 8 mm gyrotron,
2 – throat 4.8 mm gyrotron.

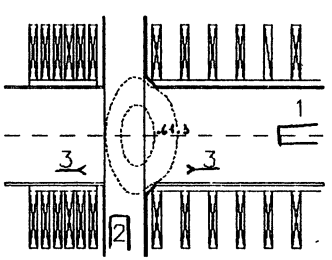

Fig.2. OGRA–4K const–B lines,
1 – throat 8 mm gyrotron,
2 – throat 10 mm gyrotron.

Two different super conducting magnetic systems are used to match resonance condition for 8 mm or 10 mm wavelength gyrotrons (first harmonic) and 4.8 mm wavelength gyrotron (second harmonic).

Const-B lines for baseball type min-B OGRA-ECR axially asymmetric machine [3] are shown on fig.1. Here two high power ECRH throat are pointed up (longitudinal - 1 connected with the 8 mm gyrotron and "transverse" - 2 with the gyrotron for second harmonic 4.8 mm).

Another axially symmetric OGRA-4K cusp machine [4] is sketched on fig. 2, where the so called "longitudinal" throat - 1 connected with the 8 mm gyrotron and "transverse" throat - 2 with the 10 mm gyrotron. Each gyrotron provide gauss-type microwave beam up to the 150 kWt during the 5-100 ms. Usually pulse gas puffing into the confinement region up to the 10^{-6}-10^{-5} torr pressure precede high power microwave pulse.

A detailed description of the installations, diagnostics and some results used here one may find in previous articles [3-7].

3. Electron distribution

Different diagnostic systems show complex electron spectrum. One may roughly point out three groups of the electrons: cold (0-100 eV), warm (0.1-10 keV) and hot (10-500 keV). First of them determine end loss flow, second - density in the confinement region and third - diamagnetic signal of the plasma. But in the cusp lust group is absent [4], and the second one determine plasma density and its diamagnetic pressure.

Some our results coincide with that obtained in other open traps [8,9] and bumpy-tori [10] under ECRH.

It is not clear what determine hot electron energy which don't vary during plasma heating with the significant increment of their density n_h.

Multi-frequency heating by means of two gyrotrons causes only significant increase of hot electron density n_h, without change of their energy. For example one can see on fig.3, that during simultaneous action of two gyrotrons diamagnetic pressure considerable enhancement take place and confinement time after the microwave pulse termination drop by the n_h increase.

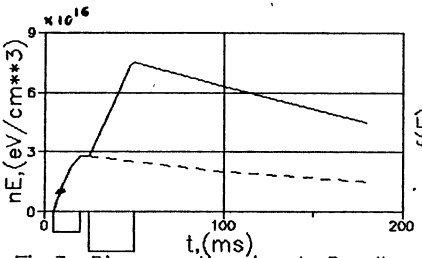

Fig.3. Diamagnetic signal. Small rectangular – one gyrotron pulse, (dashed line), big rectangular – common work of two gyrotrons (solid line).

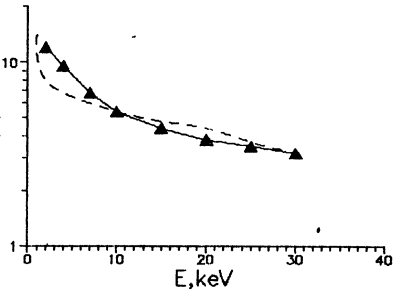

Fig. 4. Electron distribution. Solid line – experiment, dashed – theory [12].

We undertook some experiments with the end plate potential variation to investigate cold electron role in plasma build up. Negative of the one end plate reflect cold electron flow along the magnetic field toward the ECRH region. If we suppose longitudinal absorption coefficient equal 1, then each cold electron must obtain energy up to a half of a keV after overcoming ECR-zone. This circumstance must cause significant modification of the electron distribution, but the experiments show that negative potential only redistribute current along the magnetic field between two end plates and conserve full current without any significant change in plasma macro parameters (except plasma potential).

Timofeev and Haritonov [12] have explained this discrepancy by the supposition that the greater part of microwave power is absorbed by hot electrons due to the Doppler-effect before it can reach ECR zone to heat cold electrons.

Triangles in fig. 4 show electron spectrum measured by means of photo emission electron spectrometer (OGRA-ECR) and theoretical estimation followed previous supposition (solid line). Similar comparison is shown in fig. 5 for "hot" part of the electron distribution measured by the NaJ scintillator. This good consistence with the experimental results one may consider as a preliminary confirmation of the model, which it is necessary to complete by numerical evaluation of two-dimension Fokker-Planck equation.

It is interesting that this model allow to obtain maximal electron energy consistent with the experimental data for OGRA-ECR (500 keV). Space electron distribution was studied to obtain supplementary information about the electron velocity and angular distribution. For example, in OGRA-ECR warm electrons - the main plasma component are restricted inside the ECR-surface (where $B(x,y,z)=B_r$, B_r-quantity of the resonance magnetic field for the first harmonic), so that the plasma dimensions vary with the strength of the magnetic field. Outside the resonance surface we observe much stronger electron density decrease along the magnetic lines [6], then that predicted by the quasi linear diffusion theory in the presence of ECRH [2]. This model forecast elongation electron distribution along lines with $\mu=E/B_r$*const, where E,μ - energy and magnetic moment of the electron [2] so that the "sloshing electrons" distribution is formed with the maximum along the magnetic field lines under $B=B_r$. This discrepancy require supplement explanation.

. On the other hand high energy electron space distribution is approximately uniform everywhere in the plasma confinement region in OGRA-ECR [3,6]. It seems, that this fact is difficult to explain without any supposition about transverse high energy electron transport. Perhaps, resonance neoclassic transverse diffusion of these electrons due to the axial asymmetric magnetic field in baseball [11], when the frequency of the hot electron magnetic drift approach bounce frequency.

4. Microwave power absorption

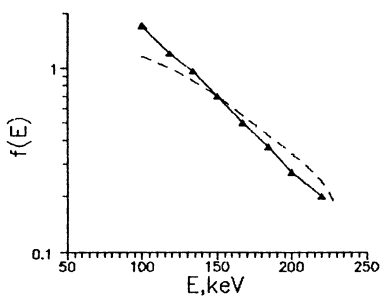

Fig. 5. Electron distribution. Solid line – experiment, dashed – theory [12].

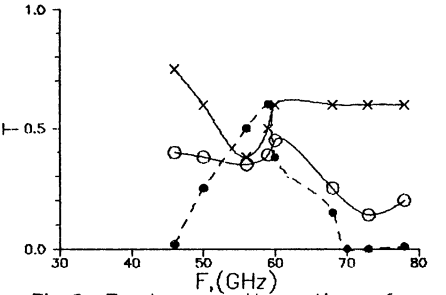

Fig.6. T–plasma attenuation of microwave signal, • –during gyrotron pulse, o–in 20 ms after it, x–relative fluctuations of the recieved signal.

We observe good plasma absorption of microwave power in both installation: usually from 30% up to the 100% of the power in beams are absorbed by the plasma by one pass.

Besides that we have measured absorption of the low power microwave beam by means of two horns, adjusted at the angle 45° to the plain of fig. 1 as a function of probing frequency for OGRA-ECR. These averaged data obtained during gyrotron pulse and in 20 ms after it are shown in fig.6.

It's interesting that the amplitude of the microwave passed through the plasma is modulated by noise. Fig. 6 shows the relative level of this fluctuations. The same measurement were carried out in the cusp plasma, by means of two horns - 3, shown on fig 2. Remarkable fact, that the fluctuations were observed at the frequency 41 GHz (far from the gyrotron frequency 37.6 GHz) and in some cases amplification of the wave was indicated.

All these may be manifestation of the instability related to the electron distribution anisotropy. Now we may only suppose that the formation of the electron distribution, microwave power absorption and plasma instability are self consistent and it is necessary to investigate them further together.

It is interesting to mention two another phenomena observed in OGRA-ECR. First, the longitudinal launch of the microwave power cause small current along the magnetic field. Second, intense microwave radiation escapes plasma during the simultaneous work of two gyrotrons, while it is absent when any one of them is working.

5. Conclusion

Experimental results presented here show that there are many vague questions in physics of ECRH in inhomogeneous magnetic fields. The purpose of our report is to formulate these questions with the aid of real examples and to stimulate their resolving.

The most part of results were obtained in OGRA-ECR baseball-type axial-asymmetric trap and some less in symmetric trap - cusp (OGRA-4K).

Further we are going to work with the cusp and to investigate some questions on non adiabatic motion of the particles and the symmetry of the magnetic field and their

influenoe on the ECRH.

REFERENCES

1. Vysokochastonyj nagrev plasmy. Materialy Vsesouznogo soveschanija. Gorkiy, 1983.

2. Timofeev A.V.// Voprosy teorii plasmy. V. 14. M. Energoatomizdat,1985, p.56.

3. Belavin M.I., Zhiltsov V.A., Kosarev P.M. et al.//Voprpsy Atomnoi Nauki i Tekh. Ser. Termojad. Sintez. 1988, v. 1,p.51.

4. Belavin M.I., Goljvin I.N., Zhiltsov V.A., et al // 12-th Int. Conf. in Pl. Phys. and Contr. Nucl. Fus. Res. Nice. France. Nucl. Fusion Supplement, 1989, v.2, p.691.

5. Tarabrin Yu.A.//Voprosy Atomnoi Nauki i Tekh. Ser. Termojad. Sintez. 1987, v. 2,p.38.

6. Zhiltsov V.A., Skovoroda A.A., Scherbakov A.G. //Preprint IAE-4855/7,CNIIAtominform, M., 1989.

7. Belavin M.I., Zhiltsov V.A., Kucheriaev Yu.A. et al.//Sov. J. Plasma Physics, 1990, v.16 to be published.

8. Ard W.B., Blanken R.J., Colchin J.L. et al // 4-th Conf. in Pl. Phys. and Contr. Nucl. Fus. Res. Madison, IAEA, 1971, v.2,p.619.

9. Smaltlak D.L., Chen X., Garner R.c. et. al.// MIT PL. Fus. Center report PFC/RR-86-15,1986.

10. Uckan N.A. and EBT Group // Oak Ridge Nat. Lab. report ORNL/TM-8430,1982.

11. Rutov D.D., Stypakov G.B. // Voprosy teorii plasmy. V. 13. M. Atomizdat,1983.

12. Timofeev A.V., Kharitonov K.Yu. //Preprint IAE-5084/6,CNIIAtominform, M., 1990.

EFFICIENCY OF ECR WAVE ABSORPTION IN THE L-2 STELLARATOR.

Eh. D. Andryukhina, K.S. Dyabilin, O.I. Fedyanin
General Physics Institute, Moscow, USSR

Introduction

The study of ECR heating of a currentless plasma in the L-2 stellarator has shown that this method allows us to produce plasma with the following parameters : $T_e(0)$=1 keV, $n_e < 2 \cdot 10^{13} cm^{-3}$, $T_i(0)$=0.1 keV [1]. The energy confinement time of plasma in this regime is τ_E= 3 ms.

According to theoretical calculations the absorption coefficient of a microwave in plasma with such parameters should be about 90 %, but actually this value measured from the jump of the energy derivative at the moment when the heating power is switched off, does not exceed 50-60%. The low absorption coefficient of microwave power determined from diamagnetic measurements was observed at different types of UHF waves : ordinary wave at the fundamental harmonic ($\Omega_0 = \Omega_{ce}$), extraordinary wave at the second harmonic ($\Omega_0 = 2 \cdot \Omega_{ce}$).

In the present paper a study is made of some peculiar features of the method of measuring the absorption power from the plasma diamagnetism. The measurements of both longitudinal magnetic flux and transverse flux due to the equilibrium plasma currents were used.

Experimental results

The method of determining the absorbed power P_{ab} is based on the plasma energy balance equation:

$$dW/dt = P_{ab} - P_s - P_v \qquad (1)$$

where W is the total plasma energy, P_s and P_v are the powers of energy losses through the plasma boundary (thermal conductivity) and the volume losses, respectively (radiation, charge-exchange) at the moment of termination being invariable constant, the change in the plasma energy derivative is equal to P_{ab}. In our case, the invariability of the volume losses follows from the "direct" measurements, while the constancy of the heat flux through the boundary follows from the direct measurements of the plasma parameters at the periphery.

To measure correctly the change in the magnetic flux it is necessary to incorporate the influence of the conducting vacuum chamber. In our case it is easy to make correction for the influence of the chamber using the expression :

$$(d\Phi /dt)_{true} = (1 + \tau_{chamber} \cdot d /dt) \cdot (d\Phi/dt)_{measured}, \qquad (2)$$

where $(d\Phi /dt)_{true}$ is the real change of the magnetic flux $(d\Phi/dt)_{measured}$ is the measured value, obtained from the diamagnetic loop voltage measurements, $\tau_{chamber}$ is the time constant of the chamber. The value of $\tau_{chamber}$ amounts 110 μs in the measurements of the longitudinal flux and 150 μs in the measurements of the transverse magnetic flux.

Apparently, the term in expression (2) associated with the incorporation of the chamber effect, may make an essential contribution only in the case when there exists a fast phase of the energy decay , whose scale is comparable with $\tau_{chamber}$. The study of experimental data has shown that in particular conditions such a phase really exists.

The importance of incorporation of an additional term

$$\tau_{chamber} \cdot \frac{d}{dt} (d\Phi/dt)_{measured} \qquad (3)$$

for determining the absolute value of the jump of the energy derivative we are going to illustrate using the experiments on plasma heating at the second harmonic (f=75 GHz, B_0=1.34 T) as example. The value of the input microwave power in these regimes could reach 200 kW , the pulse time was 8 ms. Fig. 1 shows the typical time dependencies of the average density n_e, electron temperature in the central region $T_e(0)$, plasma energy W and

absorption power P_{ab} determined from the jump of derivative W without the account the chamber effects. Here the magnitude P_{ab} characterizes. apparently , the power absorbed by the main plasma component whose energy life time is τ_e = 3 ms.

The figure shows that at the beginning of the discharge P_{ab} is noticeable higher than in the stationary phase. Such a peculiar behavior of P_{ab} in time is typical for almost all the heating regimes which differ from each other in the values of plasma density, levels of input power, types of the wave employed for the heating.

Fig. 2 presents the behavior of the time derivatives of longitudinal and transverse fluxes at the time of termination of the microwave power in the regime with P_0 =180 kW and mean density $n_e=0.9\cdot10^{13}cm^{-3}$ (the time of termination of microwave power is 50-70 μs). The figures show the measured signals (solid curves) and real values obtained with account for the correction for the chamber effects (dotted curves). A note should be made here of two peculiarities which are important in our view point.

First, there is a fast phase of decay i.e. a certain fraction of energy with the small life time exists in the plasma. It is natural to connect this fraction with the short-life component of the plasma. The fast phase of decay, which is not recorded due to the integrating effect of the chamber, corresponds just to this component. The energy entrained from the plasma during the fast phase of decay does not, as a rule, exceed 5 % of the thermal plasma energy, however, the increment of the absorbed power with account for this phase is in some cases fairly essential (sometimes up to 100%). The other peculiarity is that the relative amplitudes of the fast phase turn to be different in the signals of time derivatives of longitudinal and transverse fluxes. The most simple explanation of this fact is, in our case, the following. Let us assume that the plasma energy (and, consequently, the gasokinetic pressure, causing the corresponding equilibrium currents and the change in the magnetic fluxes associated with them),in the case of short-life plasma component, may be distributed nonuiformly along the torus. For example the maximum of the plasma pressure may exist near the port of the microwave power input. In this case also the values of magnetic fluxes (both transverse and longitudinal) should be

correspondingly distributed. The change in the longitudinal magnetic flux is recorded by the loops covering the vacuum chamber (diamagnetic winding). The turns lie in separate sections along the torus perimeter, while near the microwave power input pot there are no recording windings. On the other hand, in our experiments the changes in the transverse flux are recorded by a loop covering all the torus including the region of the increased pressure. Hence, the larger relative amplitude of the phase in the case of measuring the transverse flux, may be explained by the peculiarities of recording, if the assumption of nonuniform distribution of the short-life component pressure is true.

As a rule, the fast phase of decay is mostly manifested in the quasistationary phase of the discharge. Fig. 3 shows the time evolution of the magnitudes P^*_{ab}, P_f and P_{ab} during the heating pulse. The value $P_{ab}= P^*_{ab}+ P_f$ is the total absorbed power obtained with the corrections of the signal incorporating the chamber effect. P_{ab} and P_f are the powers absorbed by the main and short-life components respectively. The dependencies are obtained in the regime with $n_e =10^{13}cm^{-3}$, P_0=180 kW. It is seen that the microwave power absorbed by a short-life component can reach 20-50 kW at the end of the heating pulse. It is of interest to note that the total absorbed power P^*_{ab} remains practically constant during all the heating pulse, i.e. the processes of power absorption by a thermal component and a short-life one are competing processes. The fraction of the fast phase in the total energy balance is the higher, the higher is the value of the introduced microwave power and the lower is the plasma density. Fig. 4 shows the dependence of P_{ab}, P^*_{ab} and P_f on P_0 at $n_e=10^{13}cm^{-3}$, and Fig. 5 shows their dependence on the density at P_0=180 kW. As it is seen the dependence of full absorbed power on the density is rather weak. Also, the value of absorption coefficient defined as $\eta = P^*_{ab}/P_0$ vary slowly depends on input power P_0.

Conclusion

The analysis of the results of diamagnetic measurements during UHF plasma heating in the L-2 stellarator allowed us

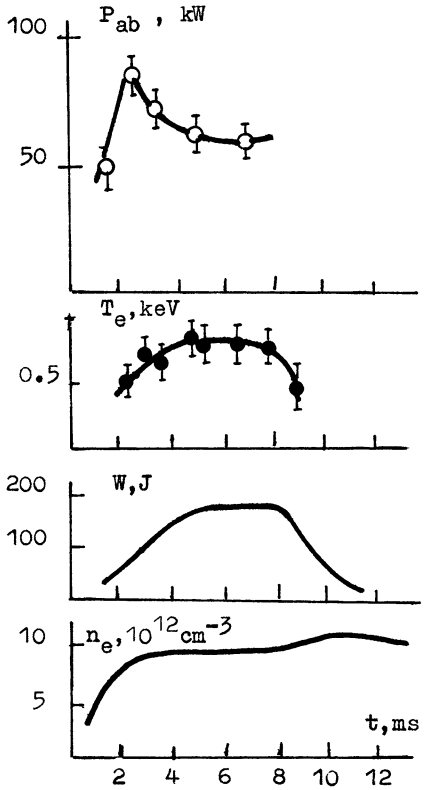

Fig. 1

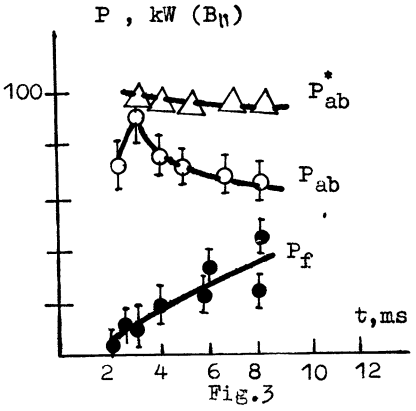

Fig.3

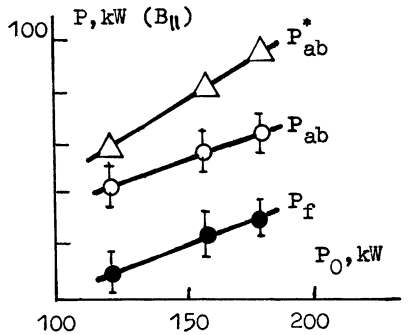

Fig.4

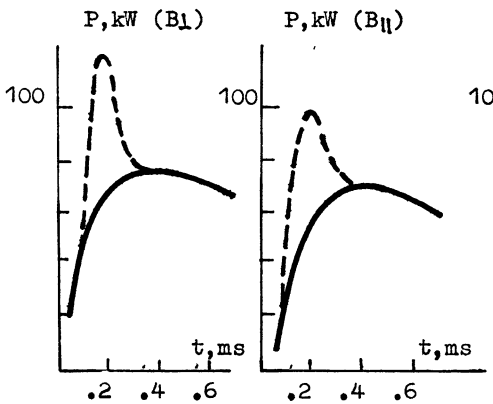

Fig.2

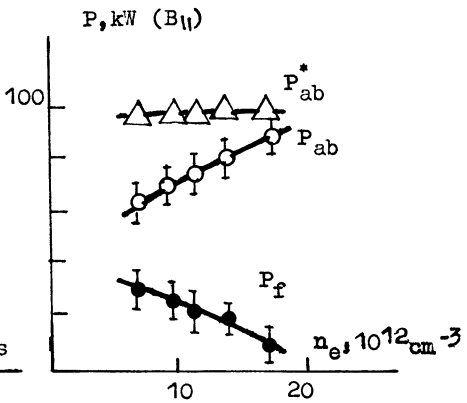

Fig.5

discover the existence of a short-life plasma component which may absorb a significant fraction of the power introduced in the plasma , the energy stored in this component being very low. The question what are the particles in the short-life component remains open. These particles may supposed to be trapped in the stellarator field ripples, localized in the region of the microwave power input.

References

1. D.K. Akulina et al., IAEA-CN-/C-I-3, IAEA Conference (Nice), 1988.

ON ELECTRON-CYCLOTRON START-UP IN A TOKAMAK

M.D.Tokman
Institute of Applied Physics
Academy of Sciences of the USSR; Gorky, USSR

I. Introduction

The goal of our communication is to investigate the pre-ionization for a tokamak with ITER parameters. We are dealing with a modern scheme for microwave complex: microwave power is injected from the toroidal chamber exterior in the form of the o-mode while the x-mode needed for the pre-ionization is produced by the partial depolarization of initial radiation when reflected from the internal wall of the chamber*) (Fig. 1).

Bearing in mind that the microwave beam reflection from the vessel wall is quasi-diffusional we shall assume for simplicity that the radiation is uniformly scattered into a cone with an apical angle $\theta_s \sim 1$ (Fig. 1). We shall restrict ourselves to the case of moderately dense plasma and neglect the depression effect of the right-polarized component of the r.f. field. Also, we shall mainly take interest in the case of not so small x-mode optical depth τ_x, where $\tau_x \gtrsim 1$. For characteristic electrons energies of the order of the ionization potential $T_e \sim \mathcal{E}_i \sim 10$ eV and for ITER parameters this corresponds to plasma density $10^{10} \lesssim N_e\ (cm^{-3}) \lesssim 10^{12}$.

II. Interaction of particles with microwave field. Quasi-linear equation

The regime of cyclotron acceleration of particles depends appreciably on the relation between the characteristic frequency of nonlinear oscillations of particle energy under the action of a resonance r.f. field Ω_N and the transit time through the interaction region [1]. In the case of EC heating

*) At the initial stage the o-wave absorption is small and the radiation injected into the tokamak reaches the vessel wall almost without losses.

in the scattered radiation field the nonlinear oscillation period must be compared with the transit time through the field coherency region $t_c = L_c / V_\parallel$ ($V_\parallel$ is the particle velocity along the magnetic field $\vec{B}_0$, L_c is the correlation length). Under the condition

$$\Omega_N t_c < 1 \tag{1}$$

the EC heating regime will be linear or quasi-linear [1]. The quantity L_c is determined by the angular spectrum width θ_c of waves reaching the observation point:

$$L_c \sim k_0 \theta_c^{-1} \tag{2}$$

where $k_0 = \omega/c$, $\theta_c \sim D_s/a$, a is the minor radius of the torus and D_s is the diameter of the microwave beam on the scattering wall. The quantity Ω_N is given by [1]:

$$\Omega_N \simeq \omega \left(E_{(+)} / B_0 \right)^{2/3} \tag{3}$$

where B_0 is the toroidal magnetic field, $E_{(+)}$ is the amplitude of the resonant (right-polarized) circular component of the r.f.field.

Assuming that the scattering radiation forms a "spot" with a diameter $L_s \sim a$ (Fig.1) and that half of the radiation power P transforms, when reflected, into the x-mode we find:

$$\Omega_N t_c \simeq \left(\frac{4P}{c a^2 B_0^2} \right)^{1/3} \cdot \frac{a c}{D_s V_\parallel} . \tag{4}$$

For ITER parameters ($B_0 \simeq 5.3$ T, $a \simeq 2$ m, $D_s \simeq 0.5$ m) and for $V_\parallel \simeq (2\mathcal{E}_i / m)^{1/2}$ it follows from (4):

$$\Omega_N t_c \simeq 0.1 \left(P(\mathrm{MW}) \right)^{1/3} . \tag{5}$$

This relation ship permits one to neglect the influence of nonlinear effects on the EC acceleration of particles for radiation powers not more than hundreds of megawatts.

If condition (1) is met, the particle heating in the ECR region can be described by the quasilinear equation [1]:

$$\frac{\partial}{\partial t} f = \frac{\partial}{\partial W_\perp} \left(W_\perp D \frac{\partial}{\partial W_\perp} f \right) , \tag{6}$$

where $W_\perp$ is the transverse kinetic energy. For the diffusion coefficient D we shall use a model expression, which, of course, can be obtained by rigorous averaging over the major toroidal ring but is readily found euristically. Note that microwave radiation with a wide angular spectrum in the reference frame accompanying the particle has a frequency spectrum as wide as $\Delta\omega_{eff} = \Delta k_\parallel v_\parallel \sim \omega v_\parallel / c$ and that the radiation power is distributed over an area $S = 2\pi R L_s$ (Fig. 1), where R is the major radius of the torus. For a homogeneous distribution of radiation intensity in the frequency range $\Delta\omega_{eff}$ we have:

$$D = \begin{cases} \frac{\pi e^2}{m}\left(\frac{P}{cS}\right)\frac{1}{\Delta\omega_{eff}}\,; & \left|\frac{\omega_H^0}{\gamma}-\omega\right| < \frac{1}{2}\Delta\omega_{eff}\,; \\ 0 \qquad\qquad\qquad\quad ; & \left|\frac{\omega_H^0}{\gamma}-\omega\right| > \frac{1}{2}\Delta\omega_{eff}\,; \end{cases} \tag{7}$$

where $\omega_H^0 = eB_0/mc$ and γ is the relativistic gamma factor. From Eqs.(6)-(7) it follows that the energy of "hot" electrons is restricted to

$$T^* = mc^2 \left|\frac{\Delta\omega_{eff}}{\omega}\right| \simeq mc^2 \frac{v_T}{c}\,, \tag{8}$$

and the acceleration time to T^* is

$$t^* = \frac{T^*}{D} \simeq \omega^{-1} \frac{(v_T/c)^2}{\pi^2 (P_c S B_0^2)}\,. \tag{9}$$

In Eqs.(8)-(9) we have taken for estimates $\Delta\omega \simeq \omega v_T / c$, where v_T is the thermal velocity of particles along the field lines.

The efficiency of quasilinear EC heating is determined by the relationship between the times t^* and t_{eR}, where t_{eR} is the "life time" of the particle in the resonance region, determined by the particle motion in the minor toroidal cross-section plane. The characteristic energy picked up by electrons in the resonance region T_{hR} tends to T^* under the condition $t_{eR} \geq t^*$, while for $t_{eR} < t^*$ we have [1]:

$$T_{hR} \simeq T^* (t_{eR}/t^*)\,. \tag{10}$$

III. The model of particle escape from toroidal chamber.

Balance equations.

Gas ionization by "hot" electrons provides "cold"electrons with energies T_c of the order of the ionization potential $\mathcal{E}_i$ [2] .Such electrons escape along the magnetic field lines with the ion-sound velocity V_s . In the ECR region the particles are accelerated assuming a characteristic transverse energy $T_{hR} = \langle W_\perp \rangle \gg T_c$ (the spreading velocity along the field lines corresponds to the initial energy $T_c \sim \mathcal{E}_i$). For estimates, the ratio of the transverse $B_\perp$ to the toroidal B_0 magnetic field is taken to be 10^{-3} [3, 4] ; the scattered magnetic fields are also about 0.1 per cent of B_0 .

Within the framework of such a model the following equations describing the gas ionization and the plasma spreading are valid:

$$\left(\frac{\partial}{\partial t} + \tau_c^{-1}\right) N_c = \nu_i N_h \left(\rho_h / a\right)^2; \qquad (11)$$

$$\left(\frac{\partial}{\partial t} + \tau_h^{-1}\right) N_h = \frac{P}{T_{hR}} \cdot V_T^{-1} ; \qquad (12)$$

$$\rho_h = V_T \frac{B_\perp}{B_0} \left(T_{hR} / 5 \nu_i \mathcal{E}_i\right); \qquad (13)$$

where $N_{c,h}$ are averaging densities of "cold" and "hot" particles, $\tau_h = a B_0 / V_T B_\perp$; $\tau_c = a B_0 / V_s B_\perp$; $V_T \simeq (2\mathcal{E}_i / m)^{1/2}$; $V_s = (2\mathcal{E}_i / M)^{1/2}$; M is the ion mass, ρ_h is the distance at which "hot"electrons lose energy, ν_i is the ionization frequency, V_T is the chamber volume. Energy T_{hR} is given by (10), where $T_{eR} = (R V_T / C) / (V_T B_\perp / B_0) \simeq B_0 R / B_\perp C$.

From Eqs.(11)-(13) we obtain that for several MW power the gas with density $N_a = 10^{12} cm^{-3}$ will be ionized in a few milliseconds. In this regime: $T_{hR} \simeq$ 3-5 KeV; $\rho_h \simeq a$; $N_h \simeq 10^{10}$ cm^{-3}; $N_c \simeq N_a + \nu_i N_h t$. The threshold power is several hundreds of kilowatts.

Note that we neglected Coulomb collisions and the electron

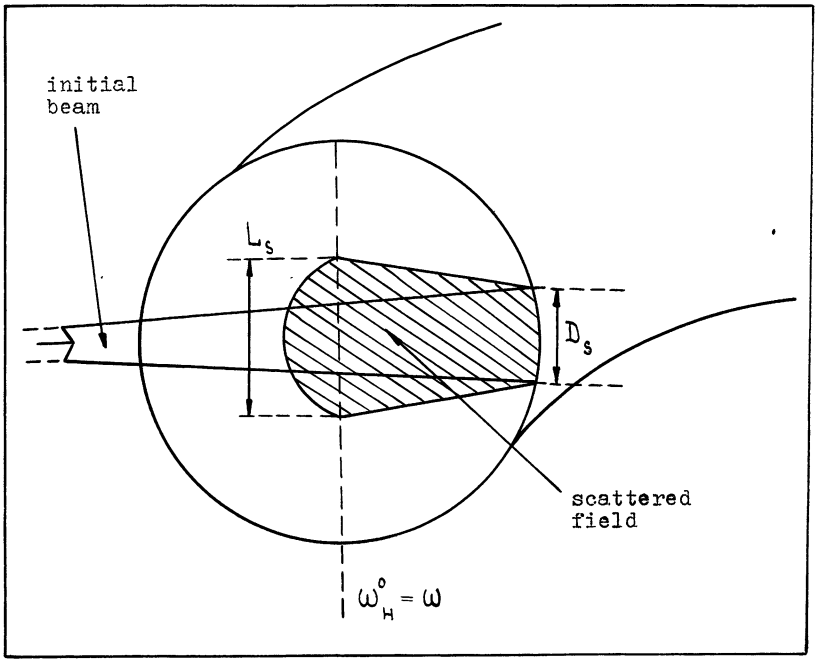

Fig.1

scattering influence on the characteristic velocity of "hot" particle escape along the field lines. Such a simplification is probably allowed for rough estimates:the transport frequency of collisions with neutral ν_{tr} for the energies 1-10 keV is very close to the energy loss frequency $\sim 5\nu_i \delta_i / T_{hR}$ [5] ,and the Coulomb collision frequency ν_e is commensurable with $5\nu_i \delta_i / T_{hR}$ at $N_e \sim N_a$.

References

1. V.V.Alikaev et al. Electron-cyclotron plasma heating in toroidal systems. - In: High-Frequency Plasma Heating (ed. A.G.Litvak), Amer.Inst.of Physics.(to be published).
2. N.F.Mott, H.S.W.Messey. The Theory of Atomic Collisions.Oxford. Clarendon Press, 1965.
3. G.V.Pereverzev, L.E.Zakharov.Fiz.Plazmy, 1988, v.14, p.214.
4. G.V.Pereverzev. Inductiveless start-up and current ramp-up scenario optimization for a tokamak-reactor.(pres.at Meeting of ITER experts on CD/H, 17-18 June, 1988, Garching.
5. H.Jick et al. Phys.Fluids, 1986, v.29, N4, p.1238.

NUMERICAL SIMULATION OF CURRENT DRIVE BY EC-WAVES IN THE TOKAMAKS T-10, T-15, ITER

Kuznetsova L.K.
I.V.Kurchatov IAE, Moscow, USSR

An opportunity to use ordinary EC-waves for a steady-state current drive in tokamaks T-10, T-15,ITER and for the tearing mode stabilization in ITER is numerically studied in the paper.

The technique for finding the current drive efficiency, $\eta=\bar{n}_e I_0 R_0/P_0$, includes the calculations of EC-wave propagation and absorption, determinations of the current profile and the total current driven in the plasmas . The propagation EC-waves is represented in the geometrical optics approximation, i.e. by the ray tracing technique [1]. The dispersion equation necessary for this is considered in the cold plasma approximation.

The expressions (2.2.23), (2.2.24), (2.2.30) [2] which include the dependence on dispersive properties of a medium and on polarizational characteristics, on the distribution function, on the relationship between the longitudinal and transversal momenta in the explicit form and take account of an effect of various harmonics on the absorption process, have been used for calculation of the absorption coefficients.

Dispersive and polarizational characteristics in the absorption coefficient are also taken into account in the cold plasma approximation. It is connected with that the total relativistic calculation of the dielectric tensor components, ε_{ij} , and that of the quantities related to them is rather expensive because of large computer time consumption. Some estimates have shown that the relativism is more manifested in the form of a distribution function and in the relativistic modification of a resonance condition (not in the dispersive and polarizational characteristics).The conclusions are true in case of an oblique incidence, when the wave is absorbed, not reaching the center of a line. Moreover,the local efficiency of current drive in the zone beyond the cyclotron resonance in large toka-

maks is rather low and has a weak effect on the magnitude of a driven current.

After corresponding transformations the absorption coefficient acquires the form as represented in [3].(See.[3],p.6).

The power absorbed in the plasma, P_i, when the l_i-point is reached at the ray,is related to the wave absorption coefficient, α^* by the following relationship:

$$P_i=P_0\left(1 - \exp\left(-\int_0^{l_i} \alpha^* dl\right)\right) . \qquad (1)$$

The power absorbed upon a given magnetic surface is assumed to be uniformly distributed across the whole surface.

A matrix of magnitudes $(J/P)_{\varepsilon,u_0,s}$, for local current drive efficiencies, calculated by A.P.Smirnov and A.G.Shishkin in [4], taking account of relativistic and toroidal effects,is used for determination of the current profiles and η . The total current I_0, is determined by integration over the plasmas cross-section.

The calculations are done for the parameters given in Table I:

T A B L E I

	T-10	T-15	ITER
R_0	1.50	2.40	6.00
a_0(m)	0.35	0.70	2.15
B_0(T)	3.00	3.00	4.85
$n_{e0}10^{20}(m^{-3})$	0.08-0.30	0.30-0.70	1.00
T_{e0}(keV)	5.-10.	2.-10.	10.-30.
Z_{eff}	3.	3.	2.16
λ	1.	1.	1.7+0.3s
∇(m)	0.	0.	0.4
P_0(MW)	0.1	4.	100.
f(GHz)	86.	86.	110-120;170-210
n_e/n_{e0}	$(1-s^2)$	$(1-s^2)$	$(1-s^2)^{1/2}$
T_e/T_{e0}	$(1-s^2)$	$(1-s^2)$	$(1-s^2)$

In this Table λ is an ellongation, ∇ - Shafranovs' shift, s is a magnetic flux coordinate.The triangularity δ and poloidal magnetic field are equal to zero in our calculations.

Some results of numerical simulations are given in Figs. Wave trajectories (a,b), wave damping characteristics (c,d) and the current profile (e) for T-10 tokamak are given in Fig.1 as an example. These dependences for T-15 are similar. The dependence of a driven current on the temperature and plasma density for T-15 is given in Figs.2 and 3. The current is proportional to the temperature and inversely proportional to the plasma density. The dependence of the current I_0 on the angle of the EC-wave launch, ξ_0, on the equatorial plane for T-15 is given in Fig. 4. The calculations, which are represented in Figs.2,3,4 are done for one ray. The dashed line in Fig.4 shows the result of averaging over 12 rays.

The calculations have shown that there is an optimal trajectory of a wave launch into the plasma from the viewpoint of current drive efficiency. Some characteristic EC-system parameters necessary for obtaining maximal currents in ITER and in the planned experiments on T-10 and T-15 have been found. The results of calculations on the power launch optimization are given in TABLE II.

T A B L E II

OPTIMAL EC-POWER LAUNCH PARAMETERS

Tokamak	f GHz	n_{e0} $10^{20}m^{-3}$	T_{e0} keV	ξ_0	ψ_0	d_0 cm	I_0 MA	η $10^{20}A/(W*m^2)$
T-10	86	.10	5	23°	±15°	∓9.0	.022	.015
		.10	10				.044	.03
		.30	10				.019	.04
T-15	86	.30	5	15°	equatorial launch		.30	.03
		.30	10	20°			.50	.05
ITER	170	1.0	30	40°	equatorial launch		7.7	.31
	180			40°			6.3	.25
	170			40°	25°	-150	8.0	.32

The studies on the tearing mode stabilization in ITER in the vicinity of the surface q=2 with EC-waves have been done [5]. Some characteristic EC-system parameters necessary for stabilization have been found. A zone of energy release upon the magnetic surface s, dependent on the launch angle ξ_0 on the

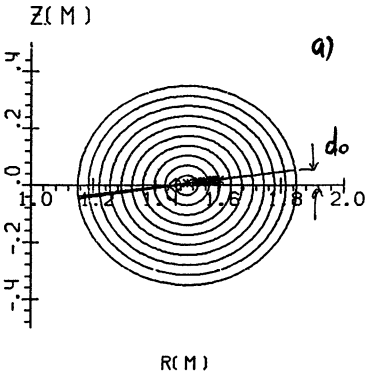

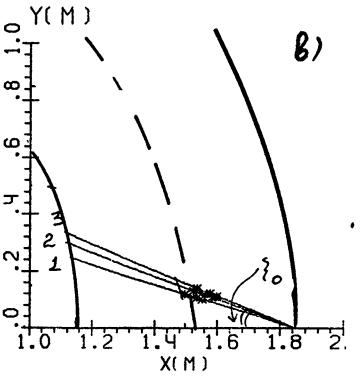

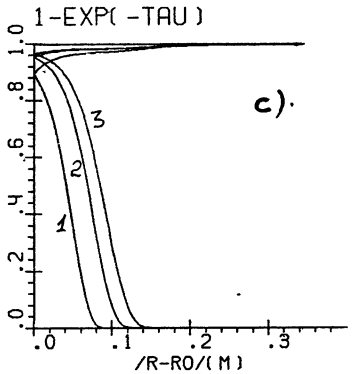

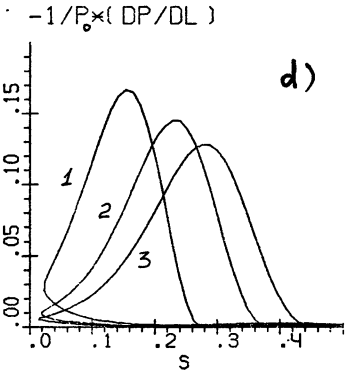

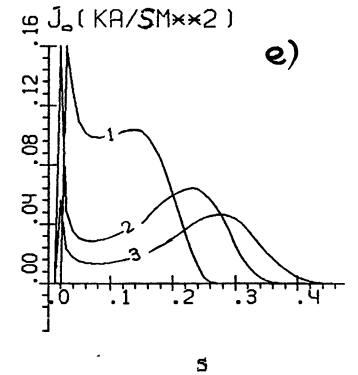

Fig.1
T-10
T_{e0}=10keV; n_{e0}=0.3 $10^{20} m^{-3}$.
1)ξ_0=20°; 2)ξ_0=23°; 3)ξ_0=25°.
a)The projection of O-wave trajectories on (ROZ) plane;
b)The projection of O-wave trajectories on (XOY) plane;
c,d)The wave damping characteristics;
e)The current profiles.

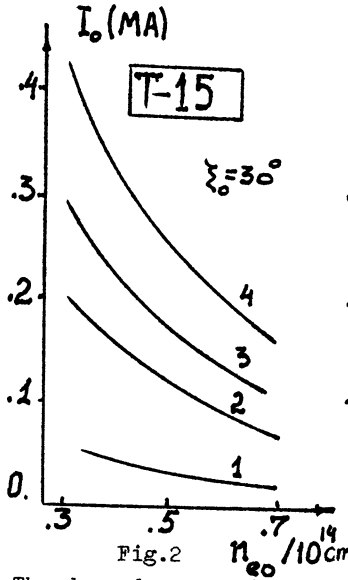

Fig.2

The dependence of the current I_0 on the plasma density.
1) T_{e0}=2keV; 2) T_{e0}=5keV;
3) T_{e0}=7keV; 4) T_{e0}=10keV;

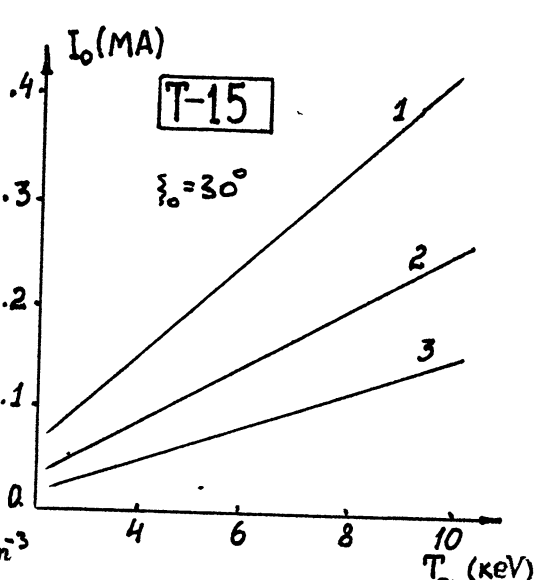

Fig.3. The dependence of the current I_0 on T_{e0}. 1) $n_{e0}=0.3*10^{20}m^{-3}$; 2) $n_{e0}=0.5*10^{20}m^{-3}$; 3) $n_{e0}=0.7*10^{20}m^{-3}$.

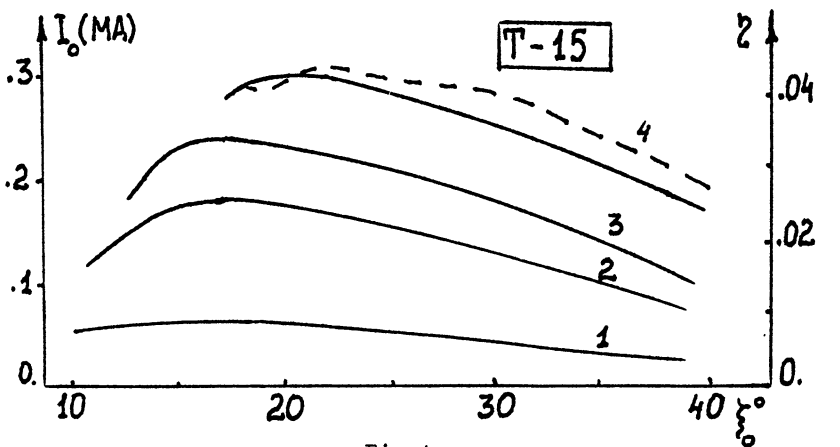

Fig.4

The dependence of the driven current I_0 and η on the angle ξ_0. $n_{e0}=0.5*10^{20}m^{-3}$.

equatorial plane, is shown in Fig.5 for T_e=30 keV. A solid line within the zone shows the magnetic surface on which the energy absorption profile has a maximum. The driven current and η for various launch angles are shown in Fig.6. The energy should be released upon the magnetic surface s=.80-.85 to stabilize the tearing mode in the vicinity of the surface q=2. For this purpose, as calculations show, the power launch should be realized at f=120 GHz at the angle ξ_0=32°-36°. The power about 10-20 MW is enough for the tearing mode stabilization.

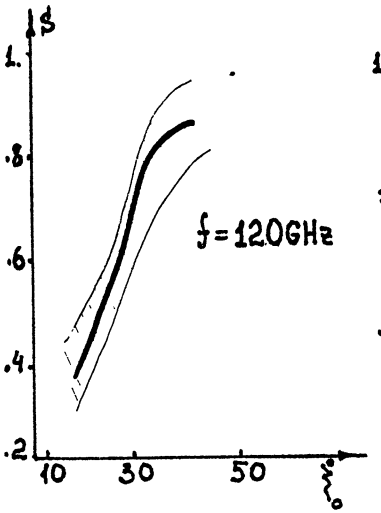

Fig.5. ITER. The area of energy absorption along magnetic flux coordinate s depending on ξ_0. T_{e0}=30keV.

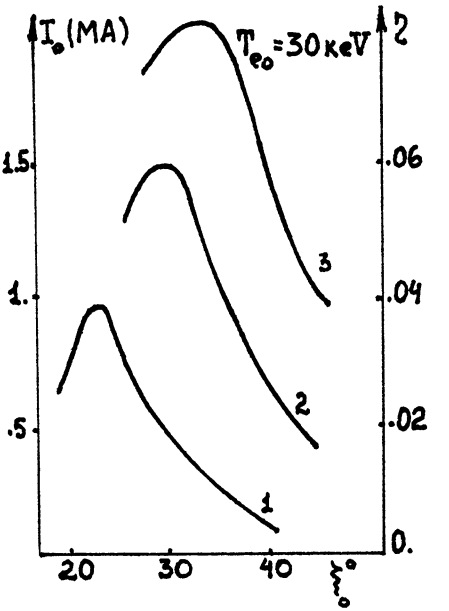

Fig.6. ITER. The dependence of the driven current and η on ξ_0. 1)f=110GHz; 2)f=115GHz; 3) f=120GHz.

[1] T.Stix "The Theory of Plasma Waves." M.Atomizdat,1965

[2] M.Bornatici et al., Nuclear Fusion, 1983, V.23, p.1153

[3] V.V.Alikaev,C.V.Bazdenkov,L.K.Kuznetsova,V.V.Parail, Preprint IAE-5152/6, M.,1990

[4] A.P.Smirnov, A.G.Shishkin - ITER-IL-PH-6-9-S-24, Garching, 1989

[5] E.Westerhof, Nuclear Fusion, V.27, (1987), p.1929

FORMATION OF ENERGY DISTRIBUTION OF ELECTRONS UNDER ELECTRON CYCLOTRON HEATING IN A TOKAMAK

M.M.Larionov
A.F.Ioffe Physical-Technical Institute, Leningrad, USSR

The maxwellian distribution of electrons in a tokamak plasma can be violated under electron cyclotron resonance heating (ECRH), and this process depends on the microwave field strength in a resonance zone. This phenomenon was observed in experiment at FT-1 Tokamak, and some data on the electron energy distribution under ECRH are presented in this report.

ECRH at the fundamental cyclotron frequency of 30 GHz was produced by a gyrotron, providing 60 - 100 kW in 0,5 - 2 ms pulses. The parameters of FT-1 are: R_0=62 cm, a=15 cm, $B_0 \leq 1,2$ T, I= 30 kA. Mean electron density was in this experiment $n_e=(0,5 - 0,7)\cdot 10^{13}$ cm^{-3} , and the electron energy life time in ohmic discharge was $\tau_e \cong 1$ms. The central electron density $n_e(0)$ equals to (0,9 - 1,1) n_{cr}, the critical density, $\omega = \omega_p$, at 30 GHz. To improve the penetration of a wave to the ECR zone in a relatively dense plasma, the extraordinary mode was launched from the stronger magnetic field side of a torus. The circular wave guide, 32 mm in diameter, turned round the plasma in a limiter shadow. The ceramic vacuum window and the radiating antenna of Vlasov type were mounted at its end. The microwave beam was entering the plasma at 42^0 to the magnetic field direction, and the wave was polarized perpendicularly to this direction, (Fig.1). The fan-shaped antenna pattern was rather broad, about 60^0 [1]. So the power flux density in a beam decreased strongly as the distance along the beam increased. ECRH process was studied depending on the position of a resonance zone in a plasma cross-section, R. This position was varied from +5 cm to -12 cm relative to the axis of a discharge chamber R_0, by proper variation of a magnetic field B_0. At the same time the strength of a microwave field in the ECR zone was changed, from 1 kW/cm^2

to 6 kW/cm^2 (Fig .2).

Some diagnostic tools were used: 1. Microwave interferometry and laser scattering were used to measure the mean density n_e and the radial profiles $T_e(r)$, $n_e(r)$. 2. The oscyllograms of a loop voltage U_l and a diamagnetic probe signal U_d were studied. The diamagnetic probe coil was placed around the discharge chamber, and correction taking into account the eddy currents in it was need to obtain the true value of a plasma energy W and its growth rate under ECRH dW/dt,[2]. 3. Soft X-ray radiation, (SXR), was registered and analyzed by the scintillation detector and the set of 5 beryllium filters, from 57μm to 912μm thick. 4. The microwave plasma emission at 2-nd EC harmonics, (ECE), was studied by the superheterodyne receiver operating at 8 frequency points, from 44 to 66 GHz. The sensitivity calibration was used, so the absolute value of a radiation temperature T_r was determined.

The results of a diamagnetic measurements are presented in Fig. 3,4 [2]. The corrected time evolutions of dW/dt during and after ECRH pulse (100 kW, 0,5 ms) are shown in Fig.3 for some positions of ECR zone. In the case of a central position maximal energy increase ΔW occurs, and the time constant of its variation is about 1 ms, so it equals to τ_e of ohmically heated plasma. Fig. 4 presents the dependence of ΔW after 0,5 ms ECRH pulse on the position of ECR zone. Central position is the best one, ΔW= 12 J, but the increase of a total plasma energy in this case is only 20%. Laser scattering measurements confirm the diamagnetic ones, [3,4]. $T_e(0)$ = 400 - 450 eV in ohmic discharge, and ΔT_e = 100 - 150 eV under ECRH. The reasons of relatively low efficiency of ECRH in FT-1 experiments are discussed in [2,3]. The shift of the ECR zone inside of the center of the discharge cross-section leads to the fast decrease of ΔW. This result is important for the experiment considered now.

The data of SXR and ECE radiation measurements are presented in Fig. 5,6,7. SXR flux in ohmic discharge and its increase under ECRH (60 kW, 2 ms) are plotted in Fig. 5 depending on the position of ECRH zone R. If the resonance zone is shifted inside, strong increase of SXR signal is observed, whilst ΔW decreases. At ΔR = -10 cm, SRX under ECRH exceeds 3 times its level in ohmic discharge. It is clear, that nonthermal SXR radiation is observed in FT-1 experiment. Attenuation measurements in beryllium filters

have shown that SXR spectrum contains mainly photons of elevated energy, E ≅ 5 keV. Probably, there is the radiation of K-lines of heavy impurities, Cr, Fe, Ni, excited by suprathermal electrons, E > 5 keV. The increased production of these electrons arises under ECRH if the resonance zone is shifted inside. Fig.6 presents the the evolution of some signals during and after the ECRH pulse (2 ms, 60 kW): loop voltage U_l, SXR radiation, ECE signals at 44 GHz, 52 GHz, 62 GHz. Resonance zone is shifted inside, ΔR =-10 cm. The decrease of loop voltage is observed under ECRH, time constants of its variations is about 1 ms. The same time constant have the variations of a diamagnetism of a plasma, Fig.3. The signals of U_l and U_d both reflect the process of electron temperature changes during ECRH. At the same time, strong increase of SXR and ECE radiations is not explained only by changes of T_e. These signals are lasting for a long time after ECRH pulse is finished. Time constants of their rise and decay are 3-4 ms and exceed considerably the energy life time τ_e= 1 ms. Evidently, SXR and ECE radiations are of nonthermal origin, they are generated by fast electrons. These electrons are produced in ECRH and their confinement time in a plasma is 3 - 4 ms.

The profiles of a radiation temperature, $T_r(R)$, are presented in Fig. 7 A,B. They are constructed using measurements of ECRH spectral distribution in the range of 44GHz - 66GHz, in assumption of plasma emission at 2-nd EC harmonics. T_r distributions on R in ohmic discharge and in the final moment of ECRH are shown, in the cases of central heating, Fig. 7A, and shifted inside ECR zone, ΔR=-10 cm, Fig. 7B. In ohmic discharges the profiles of T_r have their maximum at the discharge axis and are similar to T_e profiles measured by laser scattering. The essential difference between A and B cases arises under ECRH. Under central heating T_r radial distribution remains almost symmetrical and reflects the increase of T_e. In the case of a shifted position of ECR, T_r distibution becomes strongly asymmetric.

Sharp increase of emission appears at lower frequency points, corresponding to $R > R_o$.This distortion of T profile may depend on the radiation of fast electrons, forming the "tail" of energy distribution. Observed shift of ECE spectrum in lower frequency side can be explained as a relativistic shift of EC radiation, if the energy of fast electrons is E≅100 keV. Another explanation is also possible: Toroidally trapped electrons of

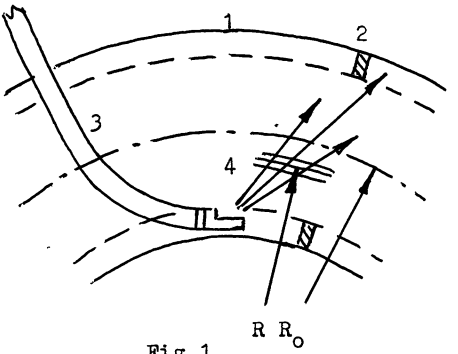

Fig.1

1- vacuum chamber
2- limiter
3- waveguide and antenna
4- ECR zone

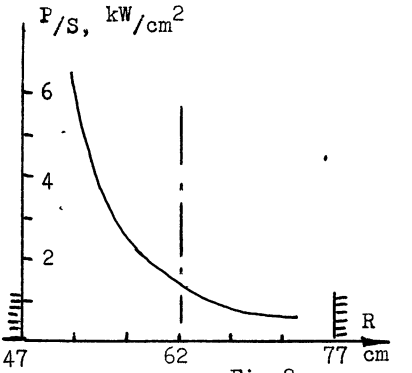

Fig.2

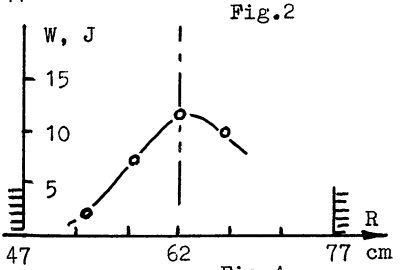

Fig.4

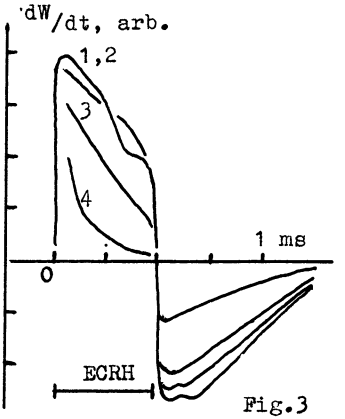

Fig.3

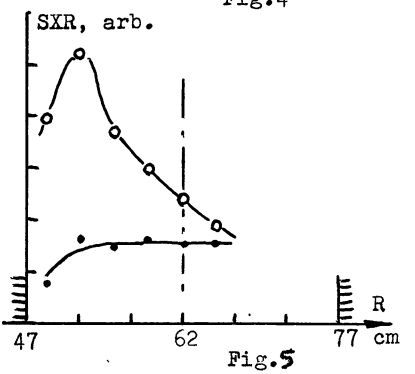

Fig.5

ECR zone positions :
R= +4,7 cm(1), 0 cm(2),
-4,7 cm(3), -9,4 cm(4)

• - ohm.discharge. o - ECRH

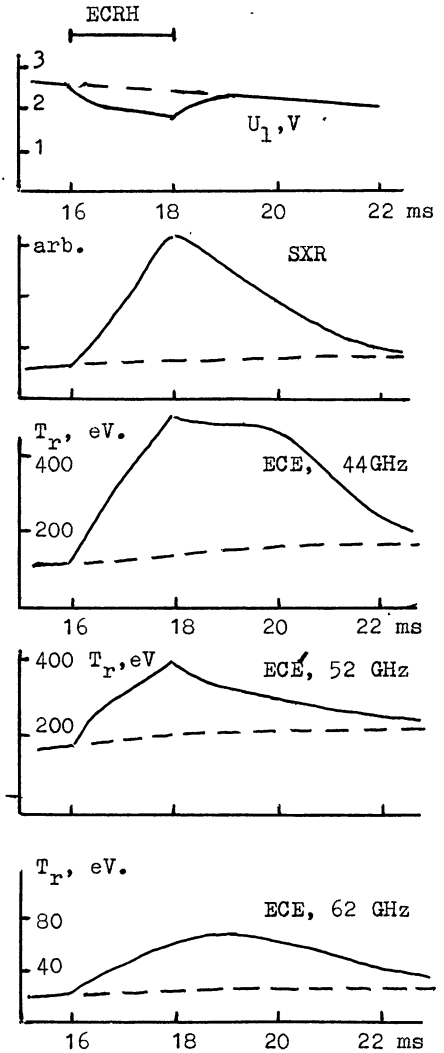

Fig. 6

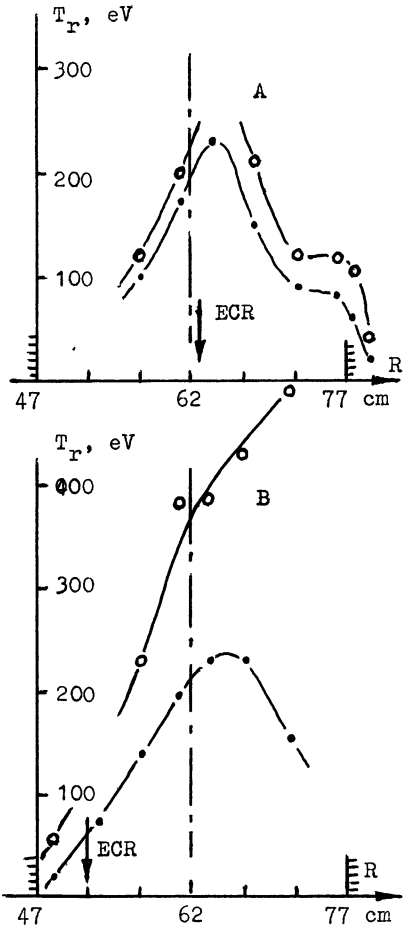

Fig. 7 A,B

• - ohm.discharge. o - ECRH

moderate energy, E≅10 keV, are produced under ECRH, and the asymmetry of T_r distribution reflects the process of their accumulation in a magnetic trap formed by the weak magnetic field in the external part of a torus, $R > R_o$.

In conclusion, some results can be mentioned:

1. In the case of a central position of ECR zone in a plasma volume the highest efficiency of a total increase of energy is found, and the disturbance of the maxwellian distribution of electrons is weak under ECRH. In this case the microwave power density in a resonance zone is about 1 kW/cm^2 , and the plasma density is $1 \cdot 10^{-13} cm^{-3}$. If the resonance zone is shifted inside, towards the radiating antenna, the power density in a resonance zone reaches 5-6 kW/cm^2 and a plasma density in it drops towards $3 \cdot 10^{12} cm^{-3}$. In this condition the maxwellian distribution is violated, and the excess of fast electrons appears in a plasma. As a result, nonthermal SXR and ECE radiations are observed.

2. The confinement time of fast electrons is 3-4 ms, and it exceeds considerably the electron energy life time in FT-1, τ_e=1 ms. If the confinement time of fast electrons is limited by electron collisions, their energy must be about 10 keV. Otherwise, their energy can exceed 10 keV, but their confinement time can be limited by the anomalous diffusion. It is interesting to note, that in similar conditions the confinement time of protons, measured by optical methods [5] , and the confinement time of carbon ions, measured in pellet injection experiment [6], are of the same value, 3 - 5 ms.

REFERENCES

1. Baranov Yu.F, Bulyginsky D.G.et al.Fizika Plasmy 1982,V.8 p.682
2. Bulyginsky D.G, Kalmykov S.G, Kantor M.Yu, Larionov M.M. et al. 15-th ECCFPH, Dubrovnik 1988,Contr.Papers Pt 2 p. 823
3. Akatova T.Yu, Bulyginsky D.G. et al. Plasma Phys. and Contr. Fusion, 1988,V.30 p. 801
4. Akatova T.Yu, Bulyginsky D.G. et al. 17-th ECCFPH, Amsterdam 1990, Contr. Papers Pt 3 p.1125
5. Larionov M.M, Levin L.S. et al. Plasma Phys. and Contr. Fusion, 1988, V.30 p. 1637
6. Kuteev B.V, Larionov M.M, Lebedev A.D. JTP letters, 1983, v.9, p.529.

NONLINEAR PLASMA HEATING AT THE ELECTRON CYCLOTRON HARMONICS

D. Farina, R. Pozzoli*

Istituto di Fisica del Plasma, Consiglio Nazionale delle Ricerche, EURATOM-ENEA-CNR Association, via Bassini 15, I-20133 Milano, Italy

**Dipartimento di Fisica, Università di Milano, via Celoria 16, I-20133 Milano, Italy*

Introduction

In electron cyclotron plasma heating experiments the electromagnetic field is localized within the plasma in form of a radiation beam, and the power absorption results from the electron energy variation due to the crossing of it. Depending on the electron flight time accross the beam, and on the intensity and space profile of the electromagnetic field, the electron trajectories can be either slightly or strongly modified, e.g., due to trapping in the e.m. field, with respect to the unperturbed orbits, corresponding to the linear and nonlinear regime, respectively. In the nonlinear case, the expressions for the absorbed power considerably differ from the linear. The present theoretical investigation deals with the problem of nonlinear power absorption for physical situations of interest when very high power radiofrequency sources are used (e.g. powerful gyrotrons or free electron lasers).

Qualitative and quantitative analyses of the of the nonlinear power absorption of a localized electron cyclotron wave have been performed e.g. in Refs. 1 - 5. Here, we consider the power absorption process in the weakly nonlinear regime, which provides the analytical computation of the absorbed power density at any cyclotron harmonics. The investigation is performed via the relativistic Hamiltonian formalism.

Formulation of the problem

The motion of an electron interacting with an EC wave propagating perpendicularly to the magnetic field $\mathbf{B}_0$, parallel to the z axis, with a frequency $\omega \approx n\Omega$, being $\Omega = eB_0/mc$ the classical cyclotron frequency, and with a z –dependent amplitude, can be characterized by a time independent Hamiltonian

$$H(z, P_z, \theta, I) = \gamma - v_n I = H_0(P_z, I) + H_1(z, P_z, \theta, I), \tag{1}$$

with

$$H_0 = \Gamma - v_n I, \quad H_1 = -\varepsilon(z)\frac{\Theta_n(I, P_z)}{\Gamma}\cos n\theta, \tag{2}$$

where γ is the relativistic factor, $\varepsilon(z) = (E(z)/B_0)\,\Omega/\omega < 1$, $v_n = \omega/n\Omega$, $\Gamma = \sqrt{1 + P_z^2 + 2I}$, P_z the canonical momentum conjugate to the variable z, and I and θ are action-angle variables. Here and in the following t, z, I, P_z, and H are normalized over Ω^{-1}, $c\Omega^{-1}$, mc^2/Ω, mc, and mc^2, respectively. In the absence of the perturbation ($\varepsilon(z) = 0$), I is the perpendicular electron energy $p_\perp^2/2$, and $P_z = p_z$. In Eq. (2), assuming the wave propagation along the x direction, the polarization term Θ_n reads

$$\Theta_n = \sqrt{2I}\,[e^- J_{n-1}(b) + e^+ J_{n+1}(b)] + P_z e_z J_n(b), \tag{3}$$

being $e^\pm = (e_x \pm e_y)/2$ the right and left components of the electric field polarization, J_n the Bessel function of argument $b = N\omega/\Omega\sqrt{2I}$, and $N = kc/\omega$ the refractive index.

We refer to physical situations where the electron flight time τ_T in the radiation beam exceeds the trapping time τ_T in the wave field, so that nonlinear effects play a major role. Moreover, during the motion the variation of the field amplitude felt by the electron is assumed sufficiently slow, so that the action integral $J = 1/(2\pi)\int I\,dn\theta$ can be considered an adiabatic invariant, experiencing abrupt variations only as the separatrix between trapped and untrapped orbits in the (θ, I) plane is crossed. The breaking of J provides the connection between two unperturbed states (before and after the crossing of the beam), characterized by the same value of the Hamiltonian and, in general, by different values of the energy. A net electron energy variation is made possible by the existence of an interval of values of the unperturbed Hamiltonian H_0 for $P_z^2 < (1/v_n^2 - 1)$, where any value of H_0 pertains to two different electron states, with the same P_z and different energies.

The absorbed power per unit area in the (x, y) plane, normalized over nmc^3, where n is the electron density, can be written as

$$W = \int d\mathbf{p}\,|v_z|\,\langle \Delta\gamma \rangle f(\mathbf{p}), \tag{4}$$

where v_z is the parallel velocity, f is the unperturbed distribution function, and $<\Delta\gamma>$ the energy variation due to the crossing of the radiation beam, averaged over the initial phases.

The value of $<\Delta\gamma>$ is obtained by means of the analysis of the electron motion in phase space, and is given by the energy variation of the single electron $\Delta\gamma$, times the probability transition $q(I, P_z)$: $<\Delta\gamma> = q\,\Delta\gamma$. By the constancy of H, the energy variation is simply proportional to the action variation: $\Delta\gamma = \nu_n \Delta I \equiv \nu_n(I_f - I_0)$. Thus, we need to determine the final action I_f as a function of the initial action I_0 [4,5]. Being the motion adiabatic, we note that $I_f \neq I_0$, only if the particle trajectory in phase space crosses the separatrix between trapped and untrapped orbits, and, at the end of the interaction, ends on a branch of the Hamiltonian different from the initial one. In this case, we obtain $\Delta I = J_s(\varepsilon_s, P_{zs})$, being J, the area of the enclosed by the separatrix, and ε_s and P_{zs} the ε and P_z values for which the crossing the separatrix occurs. These quantities are determined by means of the constancy of H and of the adiabaticity of J [5]. The transition probability q can be given in terms of the variation of the area of the phase space regions determined by the separatrix [6]. The condition for the occurence of the energy variation is $\varepsilon_s < \varepsilon_M$, where ε_M is the maximum value of ε.

Therefore, the computation of W requires the analysis of the conditions under which the separatrix crossing takes place, and the evaluation of the adiabatic integral on the separatrix, in order to determine $<\Delta\gamma>$. In the following, we perform the explicit investigation for a generic harmonic in the weakly nonlinear regime.

The weakly nonlinear regime

In the weakly nonlinear limit, the Hamiltonian function can be developed around the unperturbed resonance condition, i.e., the unperturbed stationary point $\bar{I} = 1/2\,(1/\nu_n^2 - 1 - P_z^2)$ for $\nu_n \leq 1$. Putting $I = \bar{I} + \delta I$, we obtain

$$\begin{aligned} H &\simeq H_0(P_z, \bar{I}) + \frac{1}{2}\frac{\partial^2 H_0}{\partial I^2}\Big|_{\bar{I}} (\delta I)^2 + H_1(\bar{I}, P_z, \theta, z) \\ &= \frac{1}{\nu_n} - \nu_n \bar{I} - \frac{1}{2}\nu_n^3 (\delta I)^2 - \varepsilon \nu_n \Theta_n(\bar{I}, P_z) \cos n\theta, \end{aligned} \tag{5}$$

For this Hamiltonian, the equation of the separatrix reads $\delta I = \pm 2\sqrt{\varepsilon\overline{\Theta_n}}/\nu_n \sin n\theta/2$, and the adiabatic integral on the separatrix is given by $J = \bar{I} \pm 4\sqrt{\varepsilon\overline{\Theta_n}}/(\pi\nu_n)$, being $\overline{\Theta_n} = \Theta_n(\bar{I}, P_z)$. Requiring that the adiabatic integral be constant up to the first crossing of the separatrix, the region in the space of initial momenta corresponding to electrons experiencing the energy variation reads

$$|\delta I| \leq 4\sqrt{\varepsilon_M \overline{\Theta_n}}/(\pi \nu_n), \qquad P_z^2 \leq 1/\nu_n^2 - 1,$$

where the variation of P_z during the motion has been neglected.

By the constancy of the Hamiltonian, the energy variation is simply $\Delta\gamma = -2\nu_n \delta I$. The computation of the transition probability gives $q = 1/2$ [1,3,5]. The expression for W can then be obtained from Eq. (4), developing the distribution function around the stationary point $\bar{I}$

$$W = -\frac{2^7}{3\pi^3 \nu_n} \varepsilon_M^{3/2} \int d\mathbf{P} \frac{|P_z|}{\gamma} [\Theta_n(I, P_z)]^{3/2} \frac{\partial f}{\partial I} \delta(\gamma - 1/\nu_n). \tag{6}$$

This expression for W in the weakly nonlinear limit has to be compared with the linear

$$W_l = -\frac{\pi}{2} n \nu_n \varepsilon_M^2 L_z \int \frac{d\mathbf{P}}{\gamma} [\Theta_n(I, P_z)]^2 \frac{\partial f}{\partial I} \delta(\gamma - 1/\nu_n), \tag{7}$$

where $L_z = \int dz\, \varepsilon^2(z) / \varepsilon_M^2$, and the frequency broadening due to the finiteness of the interaction has been neglected.

The two expressions exhibit the same dependence on the derivative of the distribution function with respect to the perpendicular energy and on the resonant condition, and scale differently with ε_M and with the polarization term. Moreover, W depends only on the peak ε value ($W \propto \varepsilon_M^{3/2}$), and not on its profile, while the linear expression depends on the total incident power (proportional to $\varepsilon_M^2 L_z$).

In order to obtain Eq. (6), the variation of P_z during the motion has been neglected. This variation can be estimated from the analysis of the equation $J(\varepsilon, P_z) = const.$, which, in the weakly nonlinear limit, gives $|P_{z0,f}^2 - P_{z,i}^2| \approx \varepsilon_M \Theta_n$, and $P_{zf}^2 - P_{z0}^2 \approx (\varepsilon_M \Theta_n)^{3/2}$, being P_{z0}, and P_{zf} the initial and final P_z values. Both variations are much lower than the maximum $\Delta\gamma$.

The weakly nonlinear regime can be characterized by suitable conditions for the parameter ε. First, we require that trapping in the wave field takes place. Since, for the Hamiltonian (5) the period of the motion can be estimated as $\tau_T \simeq 2\pi/(\varepsilon \overline{\Theta_n})^{1/2}$, and $\tau_F \simeq L_z/P_z$, this condition can be written as

$$\varepsilon_M > \frac{(2\pi P_z)^2}{L_z^2 \overline{\Theta_n}}. \tag{8}$$

Moreover, the Hamiltonian (5) describes the electron motion correctly, only when higher order terms in Eq.(5) can be neglected, leading to

$$\varepsilon_M^{1/2} \frac{\partial}{\partial I} \Theta_n^{1/2}(I, P_z)\Big|_{\bar{I}} \ll 1. \tag{9}$$

Note that both conditions are not uniformly met in momentum space, and tend to be violated for $P_z^2 \approx 1/v_n^2 - 1$.

Results

We present here the results for the absorbed power density W obtained for a Maxwellian distribution function with temperature T_e. The absorption profile can be computed analytically from Eq.(6) for any value of n and both ordinary (OM) and extraordinary (XM) polarization, at lowest order in Larmor radius. In this limit, the polarization term reads $\varepsilon\Theta_n \approx \alpha_n P_z^n (2I)^{n/2}$, where for the XM $p = 0$, $\alpha_n = \varepsilon e^{-}(Nv_n n)^{n-1}/[2^n (n-1)!]$, and for the OM $p = 1$, $\alpha_n = \varepsilon (Nv_n n)^n/(2^n n!)$.

We obtain for W the following expression as a function of the frequency and of the temperature

$$\begin{aligned} W &\propto \mu^{-3(n-1)/4} s_n^{(3n+7)/4} \exp(-s_n) \quad \text{for the OM} \\ W &\propto \mu^{-3(n-2)/4} s_n^{n+3/2} \exp(-s_n) \quad \text{for the XM} \end{aligned} \tag{10}$$

where $\mu = mc^2/T_e$, and $s_n = \mu(1/v_n - 1)$.

In case of OM1 and XM2, W exhibits the same T_e dependence and v_n profile as in the linear case:

$$W = C s_n^{5/2} \exp(-s_n), \tag{11}$$

where the constant C has the following expression

$$\begin{aligned} C_O &= \frac{2^9}{3\pi^{7/2}} \frac{[\Gamma(7/4)]^2}{\Gamma(7/2)} \alpha_O^{3/2} \quad \text{for OM1} \\ C_X &= \frac{2^{17/2}}{15\pi^{7/2}} \alpha_X^{3/2} \quad \text{for XM2} \end{aligned} \tag{12}$$

being $\alpha_O = 1/2\, \varepsilon_M\, kc/\Omega = 1/2\, NE/B_0$, and $\alpha_X = \varepsilon_M\, e\ kc/\Omega = 1/2N(E_x - E_y)/B_0$. In both cases it is convenient to introduce the ratio $R = W/W_l$, between the weakly non-linear and the linear absorbed power density. This ratio reads

$$R_O = 5\frac{2^6}{\pi^4}\frac{[\Gamma(7/4)]^2}{\Gamma(7/2)}\frac{1}{\alpha_O^{1/2}L_z} \simeq \frac{0.83}{\alpha_O^{1/2}L_z} \qquad \text{for OM1}$$

$$R_X = \frac{2^{9/2}}{\pi^4}\frac{1}{\alpha_X^{1/2}L_z} \simeq \frac{0.23}{\alpha_X^{1/2}L_z} \qquad \text{for XM2} \tag{13}$$

Note that the expressions for R presented here have been derived rigorously on the basis of the adiabatic invariance of J only. The expressions (11,12) for W are valid for $R < 1$, which corresponds to the lower limit of condition (8), for the whole plasma. This condition represent a lower boundary for ε_M. The upper boundary is obtained from the condition (9) for thermal particles, which yields: $\mu\alpha_{O,X} \ll 1$.

In case of OM for $n > 1$ and of XM for $n > 2$, the absorption profile turns to be more peaked than the corresponding linear profile, with a maximum shifted towards $v_n = 1$. Moreover, the temperature dependence of W is weaker than in the linear case. Referring to the validity of Eq.(10), we note that, for increasing n, the condition (9) is easily satisfied for most experimental conditions, while condition (8) becomes critical

$$\left(\frac{2\pi}{L_z}\right)^2 \mu^{(n+p-2)/2} < \alpha_n \ll \frac{4}{n^2}\mu^{(n+p-4)/2}.$$

For increasing n and finite values of L_z, the absorption process becomes linear.

In conclusion, we have computed analytically the absorbed power density in the weakly nonlinear regime, and determined the ε range of validity of the expression for W. By means of the above expressions, the optical depth can also be computed in any given configuration.

References

[1] W. M. Nevins, T. D. Rognlien and B. I. Cohen, Phys. Rev. Lett. **59**, 60 (1987).

[2] E. V. Suvorov and M. D. Tokman, Sov. J. Plasma Phys. **14**, 557 (1988).

[3] I. A. Kotelnikov and G. V. Stupakov, Phys. Fluids B, **2**, 881, 1990; Preprint 89-100, Institute of Nuclear Physics, Novosibirsk (1989).

[4] D. Farina, R. Pozzoli, D. Ronzio, Internal Report FP 89/12, Istituto di Fisica del Plasma, Milano, (1989).

[5] D. Farina, R. Pozzoli, Internal Report FP 90/4, Istituto di Fisica del Plasma, Milano, (1990); D. Farina, R. Pozzoli, Proc. 17th EPS Conf. on Controlled Fusion and Plasma Heating, Amsterdam, p. 1088, 1990.

[6] A.I. Neishtad, Sov. J. Plasma Phys., **12**, 568 (1987).

RF discharge processes in wave fields

Nonlinear dynamics of a freely localized gas discharge in microwave beams

A. Litvak

Institute of Applied Physics, USSR Academy of Science, Nizhny Novgorod, USSR

A new line of investigations connected with the study of a high-frequency discharge in the fields of electromagnetic waves has recently arisen along with renewed interest for traditional types of a gas discharge. It is freely localized plasma that can be produced and confined at a distance from the electrodes and limiting walls of the discharge chamber by wave beams of the optical or microwave bands. Development of investigations of freely localized gas-discharge plasma is due to the progress in high-power electronics [1], and interest for them is caused not only by evident practical advantages of such plasma as compared to the plasma of a usual glowing discharge widely used in plasma chemistry and gas lasers, but by specific applications discussed in literature (from plasma pre-ionization in magnetic traps and electron-cyclotron sources of multi-charged ions to creation of an artificial ionized layer in the Earth atmosphere).

1. Historical remarks. A few words of the history of investigations in the field under discussion. A widely known and most evident example of a freely localized discharge in the fields of electromagnetic waves is the laser spark. In the last few years similar phenomena were given detailed investigation in the beams of centimeter and millimeter waves. It is peculiar, however, that the concept of gas ionization by the

[1] Moreover, discharge ignition in a focused radiation beam is often used by experimentalists as a way to indicate the power obtained.

field of an electromagnetic wave was introduced by Bailey already (1937) in application to the problem of propagation of strong radio waves in the ionosphere [1].

Experimentally, plasma production in the beam of electromagnetic waves was also realized using microwave radiation sources before the laser was invented. Experiments described in [2,3] are meant, in which radiation of an oscillator with the wavelength 3cm was focused by a metal mirror or a dielectric lens and the discharge was ignited in a gas-filled bulb placed in the focus of the microwave beam. These experiments demonstrated also one of the basic instabilities of the microwave discharge, being formation of filaments stretched along the electric field of the wave (thermal ionization instability).

It is also necessary to mention interesting science fiction ideas of G.I.Babat who was one of the first investigators of an induction RF discharge. In his interview to the Tekhnika-Molodezhi popular science magazine (1957) he suggested to ignite an atmosphere discharge in the region of crossing of focused beams of microwaves over cities in order to light them. According to Babat, this discharge would also serve as a source of nytrogen fertilizers that would spill out of the discharge zone onto agricultural fields. More serious discussion of the possibilities to produce regions of artificial ionization in the Earth atmosphere by radio waves was resumed by physicists only after two decades and independently (see [5,6]).

In the middle of the 60ths primary interest was given to the study of the laser spark observed for the first time in the experiments desribed in [7]. They revealed the possibilities to produce dense high-temperature plasma. Experiments of P.L.Kapitsa ([8]) lay also in the thermonuclear line; he investigated a new object, a localized plasma column in gas under high-pressure within a microwave cavity.

Freely localized gas discharge in a focused microwave beam is a new peculiar object of nonlinear physics, since the pincipal part in formation of its structure and its dynamics is played by nonlinear electrodynamic processes being an ionization analogy of the known processes in collisionless plasma. Ionization nonlinearity has, as a rule, the threshold character:

in electric fields whose amplitude is lower than a certain threshold one, the gas remains un-ionized, but, if the excess over the threshold is even small, sufficiently dense plasma is produced that essentially influences spatial distribution of electric field. Nonlinear processes determine also spatial distribution of induced discharges ignited in pre-threshold wave fields with external initiators.

The present paper is a try to analyze general properties of the freely localized gas discharge in focused microwave beams, as well as to give a brief review of its possible applications. The discussion is mainly based on the results of the investigations performed at the Institute of Applied Physics.

Investigations of a discharge in microwave beams began to develop rapidly only in the 70ths due to introduction to the experimental practive of powerful microwave generators, mainly, due to creation of gyrotrons. It is noteworthy that so-called waveguide discharges and discharges in surface waves (surfotrons) used in many ways, particularly, in plasma chemistry (see, e.g., [9]).

2. Non-equilibrium self-sustained microwave discharge in a focused wave beam. To illustrate peculiarities of a freely localized microwave discharge as an object of nonlinear physics, let us consider in more detail investigation of a non-equilibrium gas discharge in a single focused wave beam [10,11].

2.1. The discharge was investigated experimentally using radiation of a millimeter wavelength gyrotron with sufficiently high values of pulse power and duration. It permitted us to perform detailed investigation in a wide range of gas densities.

Microwave radiation of the gyrotron was converted into a Gaussian wave beam with a linearly polarized electric field and directed into an echoless vacuum chamber. The electromagnetic wave length was $\lambda =$ 8mm, pulse duration, $\tau = 100\mu$s, and pulse power within the beam $P =$ 100kW. Transverse and longitudinal dimensions of the focal region in a nonperturbed wave beam (by the level of e-fold intensity decrease) were, respectively, $\alpha = 1.5$cm, $l = ka^2 = 20$cm ($ka = 10$, $kl = 150$, $k = 10/c = 2\pi/\lambda$). The chamber was filled with technically pure nytrogen, helium

or argon (impurities not more than 1%). The discharge was ignited in the focal region of the beam at a sufficient distance from the chamber walls under pressure $p = 0.1$—600Torr in helium and argon, and $p = 0.3$—70Torr in nytrogen. Dynamics and structure of the discharge were investigated with the help of photographs of plasma luminescence taken by a photo camera and by LVE-IB and FER-2 devices based on electron-optical converters, in the framing exposition and chronographic regimes.

Freely localized gas discharges in focused microwave beam are new peculiar objects of nonlinear physics, since the pinciple part in formation of their structure and their dynamics is played by nonlinear electrodynamic processes being an ionization analogue of the known processes in collisionless plasma. Ionization nonlinearity has, as a rule, the threshold character: in electric fields whose amplitude is lower than a certain threshold one, the gas remains un-ionized, but, if the excess over the threshold is even small, sufficiently dense plasma is produced that influences essentially spatial distribution of electric field. Nonlinear processes determine also spatial distribution of initiated discharges ignited in pre-threshold wave fields with external initiators.

The present paper is a try to analyze general properties of the freely localized gas discharge in focused microwave beams, as well as to give a brief review of its possible applications. The discussion is mainly based on the results of the investigations performed at the Institute of Applied Physics.

2.2. When we began experiments, we took as a theoretical basis some ideas that followed from a comparatively simple theoretical model. The problem can be described by the set of equations consisting of the balance equation for electron density $N(r, z, t)$, and wave equation for the quasi-monochromatic electromagnetic field.

In the simplest case the balance equation can be represented as

$$\frac{\partial N}{\partial t} = \nu_i(E)N - \nu_a N \qquad (1)$$

with the given power dependences of the ionization frequency on the field amplitude $\nu_i(E)E^\beta$, and the given effective frequency of electron losses $\nu_a = \text{const}$. The steady state is possible when the ionization rate equals

the rate of losses. If at the breakdown start ν_i is much higher that ν_a, the equilibrium state can arise only due to the decrease of the amplitude of the electric field caused by increasing density of the plasma. There are two mechanisms of such a decrease of the electric field. Under high gas pressure, when the electron collision frequency exceeds the field frequency $\nu > \omega$, the steady state can follow from the collision absorption of radiation. In sufficiently rare gas $\nu < \omega$ beam refraction in the produced plasma decrease field intensity in the focus zone and terminates further evolution of the electron avalanche. Distribution of plasma density in the steady state can be found by solving a peculiar boundary problem for electromagnetic field. This solution can, particularly, yield evaluations of maximal density N_{max} achieved in the steady state in the zone of the electromagnetic beam, [10,11]:

$$\nu/\omega \gg I \quad N_{max} = N_{cr}\theta^2(\omega/\nu)$$
$$\nu/\omega \gg I \quad N_{max} = N_{cr}\theta^2$$

Here $N_{cr} = m\left(\omega^2 + \nu^2\right)/4e^2$ is critical concentration, and θ, initial angle of beam convergence.

It is evident that in the both cases maximal electron density achieved in a weakly converging beam $\theta \ll 1$ is much lower than the critical one $N_{max} \ll N_{cr}$.

2.3. The first experiments showed that the problem is much more complicated and interesting than the previous theoretical analysis predicted.

Figure 1 shows integral structure of the discharge glow in the plane of the electric field vector $\vec{E}$ in air for three values of gas pressure. It is evident that the general character of the glow is strongly dependent on pressure. There are three types of the structure, which follow each other consecutively as the pressure grows: 1) continous (diffuse) luminescence under low pressures; 2) luminescent strips coaxial to the beam and perpendicular to the electric field vector $\vec{E}$ (in the region of moderate pressures); 3) luminescent filaments parallel to $\vec{E}$, in the region of high pressures.

Explanation of the sufficiently complicated spatial structure of the discharge in the region of moderate and high pressures required further

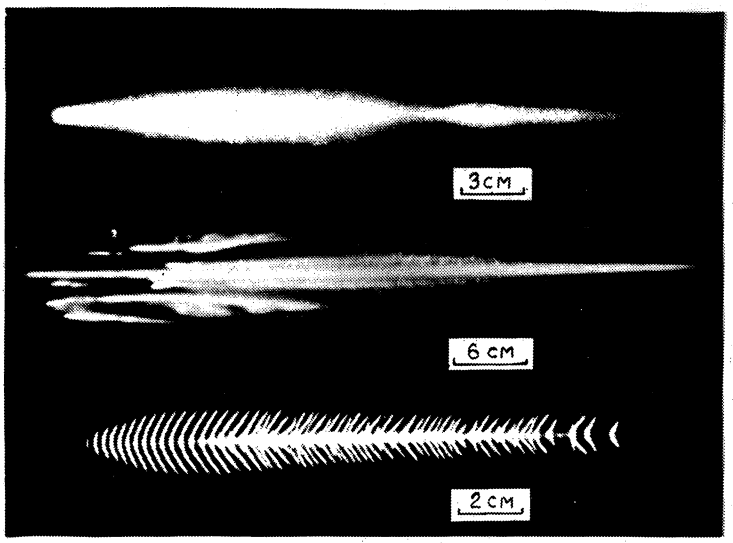

Figure 1:

coordinated experimental and theoretical investigations that permitted us to comprehend many of principle peculiarities of the observed phenomenon [10,11]. However, a number of discharge peculiarities and, in particular, its "fish-bone" structure under high pressures have not been completely explained yet.

Investigations of the discharge dynamics using the methods of rapid photography made it possible to ascertain main stages of its evolution: breakdown formation near the focus plane, movement of the ionization front (head maximum of the breakdown wave) towards the incident radiation with formation of a quasi-homogeneous plasma column, rise of secondary running waves of ionization and small-scale splitting of the produced structures (in corresponding pressure regions) in the direction that is parallel or perpendicular to the field $\vec{E}$.

Movement of the ionization front towards the incident radiation is a well-known phenomenon characteristic for discharges in the fields of various frequency bands. In self-sustained microwave discharges the main mechanism of such a movement is the breakdown wave whose kinemat-

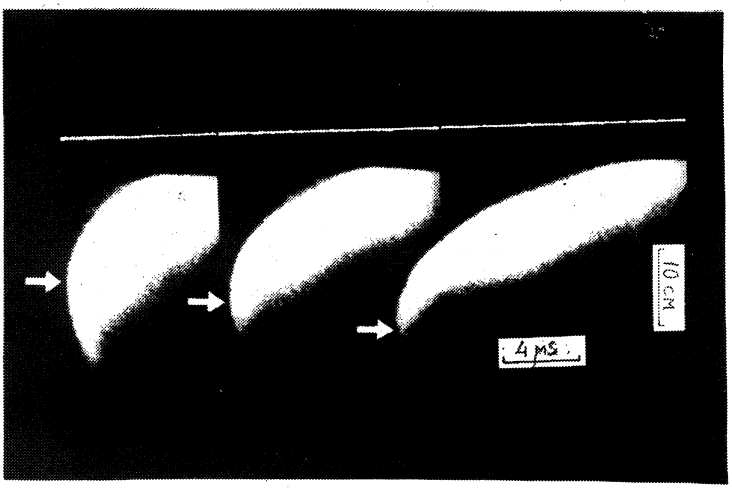

Figure 2:

ics in quasi-optic wave beam is determined by field inhomogeneity and ionization frequency depending on it.

Figure 2 shows photo chronogram of the initial stage of the discharge under three values of gas pressure $p = 1, 3, 5$Torr. Note that the point, where the first sufficiently intensive (device-detectable) luminescence appears, is shifted from the focus to some distance (increasing with pressure increase) towards the radiation. First, ionization fronts propagate to the both sides of this point (Fig.2, c). However, very quickly (that is caused, evidently, by field screening with the produced plasma) there remains on the photo evolution only one ionization front facing the incident wave; the velocity of the front movement depends on the level of radiation intensity and gas density.

A similar pattern of evolution of a continuous discharge (with no small-scale splitting present) is given by numerical calculation of a comparatively simple mathematical model, in which the discharge dynamics in a focused axially-symmetrical wave beam is described with the help of the balance equation for electron density (1) and parabolic equation for

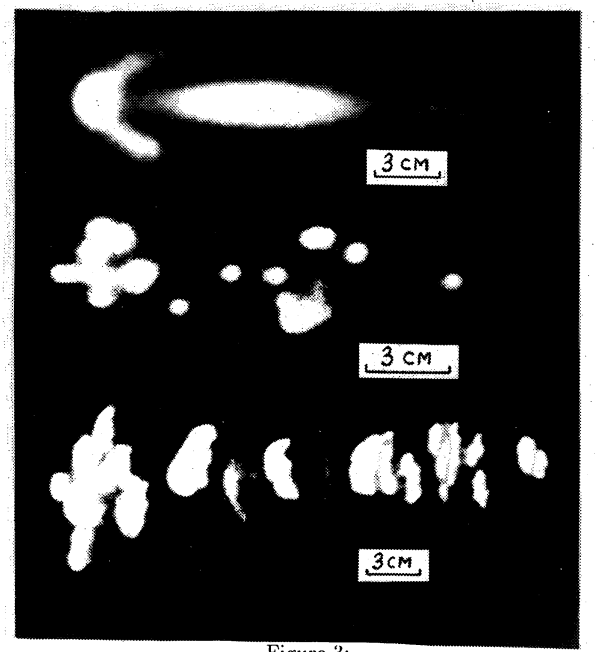

Figure 3:

the amplitude of electric field of the beam (see [10,11]).

Investigation of the discharge dynamics using framing exposition showed that until the moving front of ionization is near the boundary of the breakdown zone and is not strongly decelerated, instantaneous photoes of the discharge (exposition time $\tau = 0.2\mu$s) in all the regions of gas pressure correspond qualitatively to the evolution pattern of the "continous" discharge, described in the previous section. This is valid for the entire discharge during all its existence in the region of low pressures corresponding to formation of the type I structures (see 2.3.)

Analysis of instantaneous photoes of the discharge under higher pressures permitted us to trace the process of its small-scale splitting leading to formation of the type 2 or 3 structures.

In dependence on gas type, gas pressure, and the position in the beam, the small-scale structures observed in the integral photographs are

formed either at once as an integrity against the background of of quasi-optical luminescence (of the type showed in Fig.3 a), or as the result of fast motions or growth of smaller formations having evolved earlier. Bright longitudinal strips in the integral photograph of the discharge (Fig. 1b, 2 type structure) are the traces left by individual quasi-spherical plasmoids that appear due to splitting of ionization fronts and move towards the microwave radiation. Instantaneous photographs of the first ionization fronts under low pressures, of plasmoids under moderate ones, as well as of the filament structure formed in the case of high pressures are presented in Fig. 3.

The observed splitting of the discharge in the wave beam is naturally interpreted on the basis of the theoretical concepts of ionizational plasma instabilities in wave fields [12]. In accord with them, the main part in microwave discharges with moderate duration, which do not allow the processes of stimulated ionizational scattering, is played by quasi-static (plasma-resonance) ionization-field instability. If the frequency of electron collisions is small, $\nu \ll \omega$, this instability is the ionization analogue of the known modulational instability of the longitudinal field in plasma with electro-striction nonlinearity. It is caused by the self-amplifying effect of perturbations of the longitudinal (parallel to ΔN) field and electron density in transparent plasma ($N < N_c$) and results (at the linear stage) in formation of layers perpendicular to the field.

Theory [12] yields that in the case of $\nu/\omega \ll 1$ instability takes place if

$$\beta n_s/(1 - n_s) > 1 + 2\sqrt{\beta D k^2/\alpha N_c} \qquad (2)$$

The perturbation wave number determining the characteristic scale of stratification at the instability threshold is

$$\kappa_c = \sqrt{2\beta N_s(1 - N_s)/[n_s\beta + 1 - 1]} > k\sqrt{2(1 - N - sa)} \qquad (3)$$

Here D is coeficient of ambipolar diffusion, α, recombination coefficent, and $n_s = N_s/N_c r$ is electron density in the non-perturbed discharge.

When $n_s = N_{s\,max} \simeq 30\theta^2$, which is achieved in the "smooth" discharge, condition (4) with known dependence $D(p)$ determines some threshold pressure p (when $p < p_1$, instability is damped by diffusion). Values of p for discharge in He and N_2, evaluated in this way, lay in this

very pressure regions where transitions from the diffused discharge to the multi-plasmoid one were observed.

In the region of $\nu > \omega$ another instability is dominant in the discharge, namely, thermal-ionizational one [12]; it arises due to mutual amplification of electron density perturbations and gas temperature, resulting in discharge decay into filaments (columns) parallel to the field. In the performed experiments gas pressure $p = p_2$ determined by the condition $\nu(p_2) \simeq \omega$ is in the region of transition to the filament discharge repeatedly observed in the same region of pressures ($\nu > \omega$) earlier.

3. Induced microwave discharge. These results were obtained after investigation of a so-called microwave discharge taking place if the microwave field amplitude exceeds some threshold value. Breakdown threshold vs gas pressure is shown in Fig. 4.

Discharge formation is possible in the fields whose intensity is lower than that of the threshold one, if one uses an initial external ionization source producing "primary" plasma. Such a discharge that is generally called "induced" can take place, e.g., in gas under high pressure due to gas heating caused by radiation absorption in fore-plasma, and corresponding decrease of gas density. These processes lead to increase of gas ionization velocity and decrease of electron death velocity, i.e., they also cause avalanche increase of electron concentration that can be restrained to the back-influence of plasma on the intensity of electric field.

The induced discharge tends to propagate towards the radiation source due to the processes of the heat and density transport being nonlocal; these processes lead to ionization and heating of the gas in front of the discharge. Mechanisms of the discharge propagation in the beam of microwaves with pre-threshold intensity are invesitigated in sufficient detail in [13,14]. Typical dependence of the velocity of discharge propagation on the density of microwave energy flow is shown in Fig. 5a. The graph can be subdivided into three characteristic regions corresponding to different mechanisms of the discharge propagation. When the wave intensities are low, the main part is played by gas heating in front of the discharge due to heat conductivity from the main plasma and the following density decrease leading to the decrease of the threshold field.

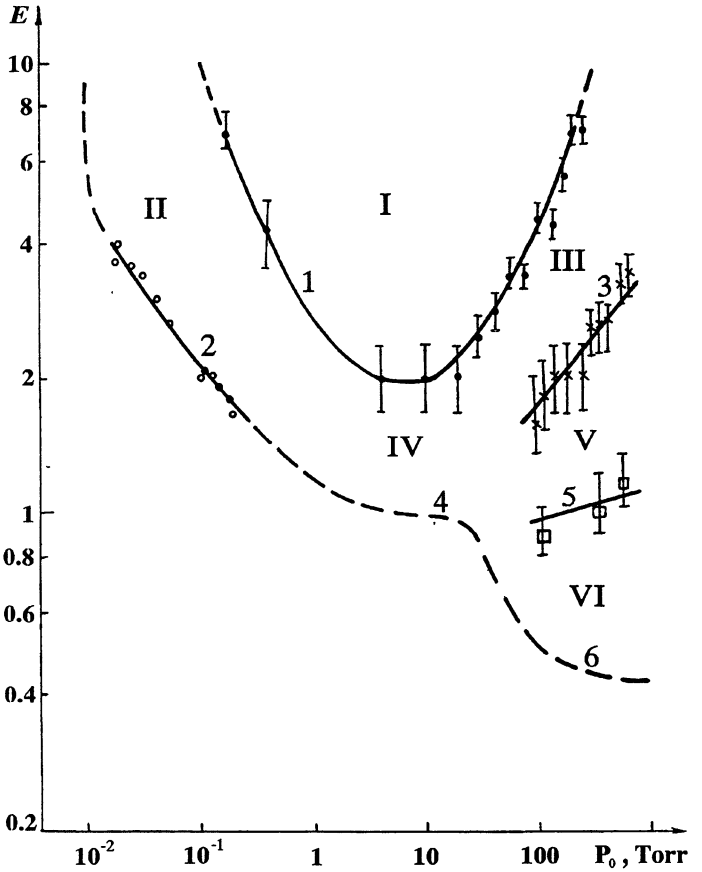
E
10
8
6
4
2
1
0.8
0.6
0.4
0.2
II
I
III
IV
V
VI
1
2
3
4
5
6
10^{-2}
10^{-1}
1
10
100
P_0, Torr

Figure 4:

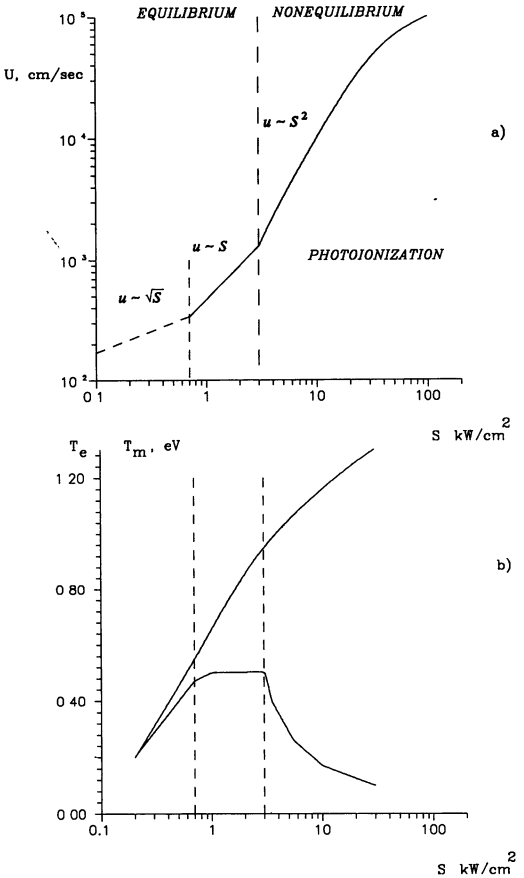

Figure 5: Dependence of discharge propagation velocity (a), electron and molecular temperatures behind the front (b) on microwave power flux density

This mechanism is similar to slow burning and typical both for microwave and optical discharges [15]. When the microwave intensites are higher, the gas becomes photo-ionized in front of the discharge by UV radiation of the discharge plasma. The newly produced fore-plasma can absorb incident microwaves; this also results in gas heating and decrease of the threshold field, and, consecutively, to discharge propagation. Molecule and electron temperatures in the induced discharge are functions of the microwave energy flux density S too, and, as S grows, T_e is detached from T_m (Fig. 5b), i.e., the degree of the discharge being non-equilibrity is changed. This fact permits us to propose a scheme of producing a non-equilibrium microwave plasmotron with controlled degree of plasma non-equilibrity. Plasma can be produced in gas flow, whose velocity equals the velocity of the discharge propagation; this permits one to fix the region of discharge formation spatially. Coordinated variations of gas velocity and density of microwave energy flow allows for required variations of the degree of plasma being non-equilibrium [14].

The induced low-pressure discharge is also noteworthy, in which the discharge can be supported if the initial plasma density is close to the critical N_{cr} due to gas ionization in the region of plasma resonance where the electric field gets considerably increased as compared to the field in vacuum [14].

New possibilities of creating ionization-wave structures arise in the presence of continuous magnetic field. One of these possibilities is related to gas ionization by plasma waves of magnetized plasma. Paper [16] gave theoretical basis for the effect of ionization self-channeling of oblique Langmuir waves. Later this interesting effect was observed and investigated in full detail in the experiments described in [17]. In these experiments low-frequency plasma wave excited by a loop antenna converges along the so-called resonance cone, and forms behind it a plasma column isolated from the bulb walls that guides plasma waves, which are, in their turn, supported by gas ionization with these waves.

4. Ionization phenomena in a superstrong microwave beam. Now let us turn to discussion of discharge phenomena in superstrong microwave fields, i.e., in the fields whose intensity is so strong that quiver energy of electrons in them essentially exceeds the ionization

potential of the gas $\epsilon_N = \frac{e^2 E_0^2}{2m^2(\omega^2+\nu^2)} \gg U_i$. These conditions can be experimentally realized by use of relativistic microwave generators; great success has been achieved in their design recently.

To make this concept clearer using numerical evaluates, let us remember that in a focused microwave beam with power $P = 8.5$GW and diameter of the focal spot equaling the radiation wavelength, quiver energy of electrons proves to be equal to their rest energy, i.e., highly nonlinear effects are possible, which are caused by relativistic dependence of the electron mass on its oscillatory energy [18]. Now such experiments use beams of microwaves with pulse power $P > 1$GW, in which quiver energy exceeds essentially ionization potential measuring tens of eV, and relativistic nonlinear effects are, in principle, possible.

The discharge in such superstrong fields differs from the case of moderate intensity in a number of interesting physical peculiarities; a part of them has been already experimentally observed, the others are theoretically predicted. For example, high rate of gas ionization in strong fields leads to the rise of discrete and independent ionization centers at individual primary electrons; to changes in kinematics of the breakdown wave in the wave beam, and, in particular, to realization of ionization fronts moving with near-light or even super-light velocity [19]; to formation of dense plasma clusters, with electron concentration exceeding the critical one by several orders of magnitude, etc. The latter is caused by the fact that ionization goes on for a sufficiently long time after the microwave pulse ends, since the quiver energy of electrons exceeds the ionization potential. The discharge in a superstrong field is also a source of accelerated ions. In the experiments described in [19] ion fluxes with energies up to 20keV were observed. All these effects as well as formation peculiarities of the function of electron distribution in superstrong fields are discussed in A. Vikharev's paper ([22]) in more detail.

Along with its kinetics, particularity of the discharge in superstrong fields must manifest itself also in some new nonlinear electrodynamic effects predicted theoretically in [20,21]. The first one is the so-called ionization self-channeling of radiation. That this effect is possible, follows from the falling down region of the dependence of ionization frequency ν_i on the field amplitude, which is characteristic for superstrong

fields and was observed in the experiment of [19]. In such a beam of electromagnetic waves plasma density increases during ionization along its axis slower than at the periphery. As a result, a profile of dielectric constant is formed, which provides further field concentration in the center of the beam due to refraction. Ionization self-channeling was numerically modeled in [21] within the simplest approximation $\nu_i(E) = \nu_0 \ E_0/E$ using the equations of nonlinear quasi optics. The authors of [21] found self-similar solutions of these equations in the form of waveguide channels adiabatically contracting in time, and performed numerical calculations of nonstationray dynamics of the channels excited by the field of the incident wave beam.

Another interesting effect of ionization self-channeling can be related to conversion of radiation frequency by fast increase of electron density. Frequency conversion was studied earlier mainly for the cases of a given external medium parameter changes. Investigations on the dynamics of the high-frequency breakdown assumed implicitly that evolution of an electron avalanche leads mainly to essential absorption of an electromagnetic wave; parametric effects of frequency conversion for damped radiation were neglected. Particularity of superstrong fields manifests itself in this case in that ionization occurs with rather insufficient power losses in the propagating wave beam, so these are parametric processes that play the main part. The theory of ionizational frequency conversion, developed in [20] predicts, particularly, that due to such up-conversion a powerful ionizing microwave pulse can penetrate to the regions with electron density greatly exceeding the critical one for the initial incident wave. The effect of ionization up-conversion of frequency of powerful microwaves was observed in [29].

Another possibility of up-conversion is connected with wave frelection from an ionization front moving with a near-light velocity. Recently this effect whose theory is discussed in much detail in [30,31] has aroused great interest and been experimentally observed ([32]). Near-light velocities of motion of ionization fronts registered in our experiments ([19]) verify the possibility of radiation self-up-conversion by reflection from the ionization front. It would be also interesting to investigate experimentally excitation of Langmuir oscillations with frequency essentially exceeding

the frequency of the incident wave by a TM-polarized electromagnetic wave obliquely incident on the moving ionization front; this was theoretically predicted in [31]. Along with beat-wave excitation, this effect can be used for creation of particle accelerator with high acceleration rate.

5. Applications. Freely-localized gas discharge in focused microwave beams has a number of advantages as compared to an ordinary electrode discharge; these advantages are important for application. They are higher stability of the discharge due to the absence of electrodes and purity of the used gas, as well as high efficiency of radiation absorption, high specific energy contribution increasing with frequency increase, the possibility to obtain extended dense plasma and control the degree of its being non-equilibrium. These properties greatly raise the interest for applications of plasma produced by radiation of the centimeter and millimeter wavebands for various ways of material processing with near-surface discharge, and, in particular for dry etching in X-ray lythography, production of film coatings, oxidation processes in high-temperature superconducting films, etc.

To exemplify the prospects of using freely localized microwave discharges in plasma chemistry let us present the data obtained by Yu.V. Bykov on production of hydrazine N_2H_4 from ammonium NH_3, hydrazine being the oxidizer for aviation fuel. In his experiments he used the gyrotrons with pulse magnetic field at the frequency 75GHz, power 50kW, and pulse duration, 0.1μs. Typical parameters of reaction productivity in an ordinary glowing discharge are as follows: reaction output 0.025 with energy consumption 25eV/molecule. In the microwave beam the output was almost 3 times increased: $\frac{p(N_2H_4)}{p(NH_3)} \leq 0.08$, and energy consumption decreased to 12eV/molecule.

Rather advantageous is use of electron-cyclotron (EC) discharge that require rather low densities of microwave flow for its ignition and support. Modern thermonuclear set-ups use EC breakdowns for preionization of plasma in tokamaks and realization of currentless regimes of plasma confinement in stellarators (see, e.g., [23,24].

Of great interest are electron-cyclotron sources of multiply charged ions, in which plasma production and heating by microwave radiation

at the EC resonance are used to obtain intensive ion flows with maximal possible charges. At present, in the world there are several tens of such ECR sources operating in the range of frequencies 2.45—18.0GHz; they are used as injectors for accelerators and for applied investigations (e.g., ion implantation). Paper [25] showed that increase of microwave frequency will permit one to make the parameters of the ion source considerably better, in particular, current of ions with charge Z must be proportional to the squared frequency $I_z \sim \omega^2$, and average charge of ions $< Z > \sim \ln \omega^{3.5}$. The investigations presently performed at IAP aim at creation of an ECR source of multiply charge ions in the range of frequencies 100GHz on the basis of the corresponding continuous gyrotron [26]. ECR sources containing plasma with highly energetic electron component can be also applied as sources of powerful coherent X-ray radiation.

Another line of application of collisionless microwave discharge appeared due to creation of UV pulse gas lasers. Up to now a series of succesful experiments has been performed, in which the gas discharge produced by powerful short-pulse focused microwave radiation was used for laser excitation at electron transitions. Of great interest is the possibility of distant pumping of an UV nytrogen laser [27] using focused microwave radiation demonstrated in these experiments. Using a relativistic microwave generator with pulse power 100MW at the frequency 10GHz the researchers obtained UV radiation power $\sim$ 100kW; the duration of laser-generated pulses practically coincided with the duration of the microwave pulse ($\sim$ 50ns).

The interest for creation of an artificial ionized region in the Earth atmosphere by focused microwave beams is supported, particularly, by some concepts proposing ot use such a discharge for atmosphere purification of hazardous minor components, like chlorides, etc. The theoretical and experimental investigations of the discharge in crossed microwave beams that have been recently performed verified the possibility of creation in the beams of TM-polarized radiation of a single plasma layer with electron density close to the critical one. This case differs principally from the case of TE-polarization since in the latter a multi-layer structure with comparatively low electron density is produced. The modern level of understanding the problem permits us to pass over to full-scale

experiments; of them, evidently the cheapest and easiest is the full-scale demonstration experiment in Arecibo proposed by American physicists [28].

I hope this brief review demonstrated that the freely localized gas discharge in microwave beams is an interesting object for physical investigations and has a number of possible practical applications.

References

1. V.A. Bailey. Nature, 1937, **139**, p.838.
2. C.W. Hamilton. Nature, 1960, **188**, p.1098.
3. S. Allison, A.L. Cullen, A. Zavody. Nature, 1963, **193**, p.156
4. G.I. Babat. Technika Molodezhi, 1957, N9, p.17.
5. A.V. Gurovich. Geomagnetizm i aeronomia, 1979, **19**, p.633.
6. V.B. Gildenburg, A.G. Litvak.–In:*Modification of Ionosphere by Powerful Radio Waves*, USSR, Apatity, 1979, p.65 (in Russian).
7. P.D. Maker, R.W. Terhune, S.M. Savage. *Quantum Electronics*, **3** / Ed. P. Grivet, N. Bloembergen, N.Y., Columbia Univ. Press, 1964.
8. P.L. Kapitsa. ZhETF, 1969, **57**, p.1801 (in Russian).
9. M. Chaker, M. Moisan, A. Zakrenski. Plasma Chemistry and Plasma Processing, 1985, **5**, N4.
10. A.L. Vikharev, V.B. Gildenburg, S.V. Golubev et al. ZhETF, 1988, **94**, p.136 (in Russian).

11. A.L. Vikharev, V.B. Gildenburg, A.V. Kim, A.G. Litvak, V.E. Semenov.– In: *High-frequency Discharge in Wave Fields*, / Ed. A.G. Litvak, IAP USSR Academy of Sciences, Gorky, 1988, p.41 (in Russian).

12. V.B. Gildenburg, A.V. Kim. ZhETF, 1978, **74**, p.141 (in Russian).

13. Yu.Ya. Brodsky, S.V. Golubev, V.G. Zorin et al. ZhETF, 1983, **84**, p.1695 (in Russian).

14. S.V. Golubev, S.I. Grishanin, V.G. Zorin, I.A. Kossiy, V.E. Semenov.– In: *High-frequency Discharge in Wave Fields*, / Ed. A.G. Litvak, IAP USSR Academy of Sciences, Gorky, 1988, p.136 (in Russian).

15. Yu.P. Raizer. *Laser Spark and Discharge Propagation*, Moscow, Nauka, 1974 (in Russian).

16. A.G. Litvak. Izv. VUZ'ov, ser. Radiofizika, 1966, **9**, p.629 (in Russian).

17. G.A. Markov, V.A. Mironov, A.M. Sergeev. Pis'ma ZhETF, 1979, **29**, p.672 (in Russian).

18. A.G. Litvak, ZhETF, 1969, **57**, p.629 (in Russian).

19. M.P. Brizhinev, A.L. Vikharev, G.Yu. Golubyatnikov et al. ZhETF, 1990, **98**, p.434 (in Russian).

20. V.B. Gildenburg, A.V. Krupnov, V.E. Semenov. Pis'ma ZhETF, 1988, **14**, p.1695 (in Russian); V.B. Gildenburg et al. Pres.Proceedings, **1**, p.324.

21. Ya.L. Bogomolov, S.F. Lirin, A.M. Sergeev, V.E. Semenov. Pis'ma ZhETF, 1987, **45**, p.532 (in Russian).

22. A.L. Vikharev. Pres. Proceedings, **1**, p.306.

23. G.M. Batanov. Pres. Proceedings, **1**, p.40.

24. S. Tanaka. Pres. Proceedings, **1**, p.73.

25. R. Geller. Proc. 1989 IEEE Particle Accel. Conf., IEEE Catalogue No.89CH2669-0, p.73.

26. S.V. Golubev, V.G. Zorin, T.N. Zorina, S.V. Razin. Pres. Proceedings, **1**, p.485.

27. A.A. Babin, A.L. Vikharev, V.A. Ginzburg et al. Pis'ma ZhETF, 1989, **15**, N5, p.31 (in Russian).

28. L.M. Duncan, G. Milikh. Proc. 2nd AIM Technical Workshop, Hanscom, MA, 1990.

29. S.P. Kuo. Phys. Rev. Lett., 1990, **65**, p.1000.

30. V.I. Semenova. Izv. VUZov, ser. Radiofizika, 1967, **10**, p.1977 (in Russian).

31. V.I. Semenova. Izv. VUZov, ser. Radiofizika, 1972, **15**, p.1793 (in Russian).

32. C. Joshi, C.E. Clayton, K. Marsh, R. Savage, IEEE Trans. on Plasma Science, 1990, v.18, p.814.

EXPERIMENTAL AND THEORETICAL INVESTIGATIONS OF BREAKDOWN PHENOMENA IN MICROWAVE TR-SWITCHES

M. Löfgren*, D. Anderson, H. Bonder, H. Hamnén, and M. Lisak**
Institute for Electromagnetic Field Theory
Chalmers University of Technology
S-412 96 Göteborg, Sweden

*Applied Electronic Physics
Chalmers University of Technology
S-412 96 Göteborg, Sweden

**Ericsson Radar Electronics AB
S-431 84 Mölndal, Sweden

Abstract
A detailed experimental and theoretical investigation is made of physical phenomena involved in the generation of a breakdown plasma in a microwave TR-switch and in the subsequent interaction between the plasma and the incident microwave. Particular emphasis is given to characteristics like breakdown and sustainment levels, turn-on time, and reflected, transmitted, and absorbed powers.

1. Introduction
Microwave breakdown in gases is a phenomenon with important consequences for microwave engineering. In particular, microwave breakdown appears as a complicating problem in many applications involving high-power microwave transmission, e.g. in microwave radar waveguide and antenna systems, space-earth communication and microwave heating of thermonuclear plasmas. However, in many applications breakdown is used for constructive purposes as,

e.g. in microwave Transmit-Receive switches, [1]. The purpose of the TR-switch is to protect the system by working as a plasma limiter which allows undisturbed microwave transmission through the TR unit for low powers, but blocks out high powers by reflection against a rapidly selfgenerated and strongly conducting plasma.

The TR-switch has recently attracted renewed interest in view of the present concern regarding the capability of conventional microwave technology to protect radar and communications receivers against high power microwave pulses with extremely short rise times [2].

The operation of a TR-switch involves many characteristic breakdown phenomena; the initial breakdown of the gas by the ionizing action of the incident wave together with the subsequent, inherently nonlinear interaction between the breakdown plasma and the microwave. This interaction also involves the propagation of a breakdown wave and leads to the strong reflection, moderate absorption, and residual power transmission which are some of the characteristic stationary properties of the switch.

Thus, apart from its technical importance, the TR-switch also offers an interesting opportunity to investigate fundamental breakdown physics, although admittedly under conditions which are not always well defined.

In the present work, we will use TR-switch operation to experimentally demonstrate and theoretically discuss, in terms of qualitative and quantitative models, a number of characteristic physical phenomena which appear in connection with microwave breakdown of a gas as well as in the subsequent interaction between the microwave and the breakdown plasma. As will be shown, good agreement between theoretical predictions and experimental results is found.

2. Breakdown thresholds

Microwave breakdown is most conveniently understood in terms of the equation of continuity for the electron density, n, viz.

$$\frac{\partial n}{\partial t} = (\nu_i - \nu_l)n \equiv \nu_{net}\, n \qquad (1)$$

where ν_i and ν_l denote the ionization frequency and the loss frequency respectively. The loss frequency contains contributions from different physical processes, the most important being diffusional losses and attachment losses. However, the main gas constituent in TR-switches is argon, which has negligible attachment frequency. The loss frequency can then be simplified as

$$\nu_l n \cong -D \frac{\partial^2 n}{\partial x^2} \cong \frac{D}{\Lambda^2} n \qquad (2)$$

where Λ approximates the characteristic length scale of the density variation and D denotes the diffusion constant of the electrons. If $\nu_{net} > 0$ in eq. (1), the electron density will exponentiate to large values. Consequently the breakdown condition is, cf [2]

$$\nu_{net} = 0 \quad \text{or} \quad \nu_i = \frac{D}{\Lambda^2} \qquad (3)$$

Since ν_i and D depend on pressure and electric field, eq. (3) corresponds to a relation between E and p. The corresponding breakdown curve for argon is illustrated in Fig. 1 for different diffusion lengths. In the TR-switch, the breakdown field is minimized with respect to pressure by working at the minimum of the characteristic Paschen curve. The optimum pressure to minimize the breakdown field is determined by the requirement that the angular frequency of the microwave equals the collision frequency of the gas. For microwave frequencies of the order of 10 GHz, this optimum pressure is $p \simeq 10$ Torr, cf Fig. 1.

In the TR-switch the breakdown threshold tends to be further decreased by the strong localized electric field enhancement created by sharp conical keep-alive contacts. On the other hand the closely spaced contacts also give rise to a much shorter diffusion length than for the undisturbed waveguide, a feature which tends to increase the breakdown field. Nevertheless

the net result of these two competing effects is a lowering of the breakdown threshold.

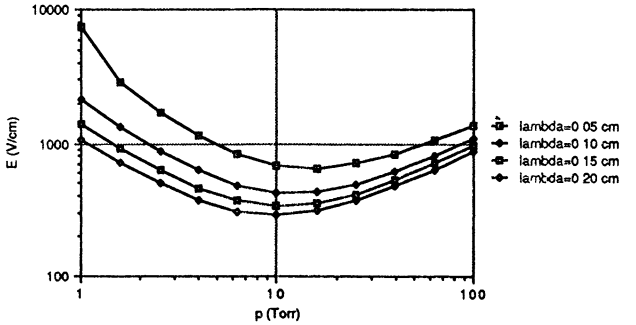

Fig. 1. Numerical calculation of breakdown field in argon as a function of pressure for different diffusion lengths, [3].

The magnitudes of the diffusion length and local electric field enhancement are difficult to estimate. The distance between the contacts is usually only a fraction of a mm. However, most of the diffusional losses should occur to the sides of the contacts, once the breakdown plasma has developed past its initial "microscopic" stage. Furthermore, the extent of the electric field enhancement region should also have importance for the proper value of Λ. As a compromise between the microscopic sub-mm distance between the contacts, the dimensions of the truncated cone contacts, and the expected extension of the field enhancement region we take $\Lambda \simeq 0.05$ cm. From Fig. 1 we then infer that the breakdown electric field is $E_b \cong 600$ V/cm.

The field enhancement factor will vary rapidly between and around the contacts. As a compromise between the very high enhancement values between and close to the contacts and the more moderate values away from the contacts, we have found that an effective enhancement factor $\beta \simeq 20$ is a reasonable estimate, [3]. Thus the microwave power needed for breakdown is (assuming the wave to propagate in the TE_{10} mode)

$$P_b = \frac{1}{4} \frac{\sqrt{1-\left(\frac{c}{2af}\right)^2}}{377} ab \frac{E_b^2}{\beta^2} \quad W \qquad (4)$$

where a and b are dimensions of the waveguide and c is the velocity of light. For $E_b \cong 600$ V/cm and β = 20, eq. (4) yields an expected power $P_b \cong 1$ W for the TR-switch under consideration.

Breakdown sustainment

It is a well-known experimental feature that the power level needed to sustain a breakdown plasma is less than that needed to cause breakdown. The physical explanation for this phenomenon in the case of the TR-switch should be that the diffusion becomes ambipolar when a significant amount of ionized electrons has diffused out of the breakdown region. The resulting diffusion coefficient, D_a, is much smaller than the free diffusion coefficient of the electrons, D_e, viz.

$$D_a \cong \left(\frac{m_e T_e}{m_i T_i}\right)^{1/2} D_e \qquad (5)$$

where T_e and T_i are the electron and ion temperatures and m_e and m_i the corresponding masses. In obtaining eq. (5) we have used the fact that $T_e >> T_i$. As a rough estimate we take $T_e \cong eU_A/2 \cong 50{,}000^\circ$K and $T_i \cong 1000^\circ$K where eU_A = 11 eV is the ionization energy of argon. This implies $D_a/D_e \sim 0.026$, i.e. the diffusion constant decreases by more than an order of magnitude when the diffusion changes from free to ambipolar.

Experimental results

The experimental arrangement for the measurements of the microwave breakdown and sustainment levels is shown schematically in Fig. 2. The signal generator, 1, delivers a 9.5 GHz signal which is amplified by a TWT amplifier capable of 35 dBm output. Incident and transmitted power were measured by two power meters at 7 and 10.

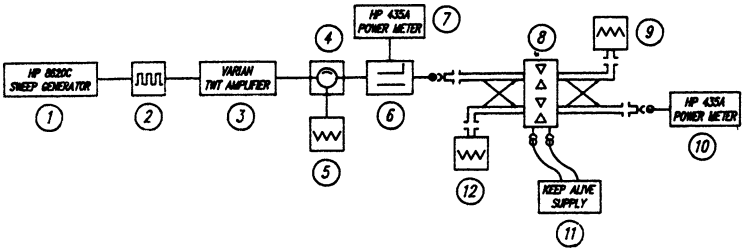

Fig. 2. Experimental set up for CW experiments.

The principal design features of a TR-switch is illustrated in Fig. 3. Two features of the TR-switch are particularly important: (i) the keep alive current which ensures that a first electron is always present to trigger the breakdown and (ii) the pairs of conical electrodes/obstacles which give rise to strong electric field enhancement and a lowering of the effective breakdown threshold for the switch. The particular TR-switch used in the experiments is a Varian BTR-216 which is a double X-band TR-switch. Although the exact composition of the filling gas of the TR-switch used in the experiments is not known we will assume argon to be the main constituent.

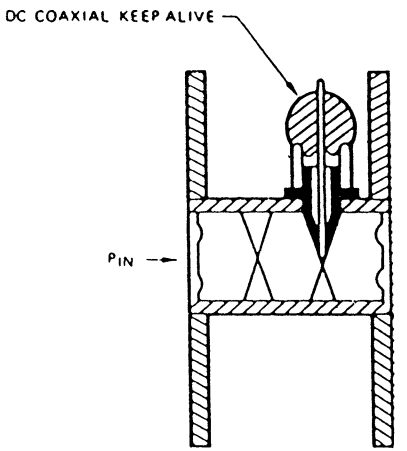

Fig. 3. Typical design of a TR-tube.

In order to determine the breakdown level of the TR-switch, the input power of the CW-wave was measured together with the transmitted power. By slowly increasing the input power, the breakdown level can be determined as the input power at which the transmitted power suddenly decreases, see Fig. 4. From Fig. 4 we infer a breakdown level of 33 dBm which corresponds to an actual power of 2W. Since the used TR-switch is a dual tube with two parallel units, the breakdown level of each unit is 1W, in good agreement with the theoretical prediction.

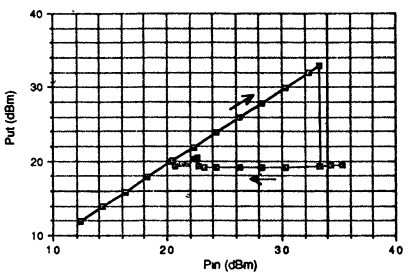

Fig. 4. Power transmitted through the TR-switch as a function of incident power. The keep-alive current is switched off.

Obviously, the uncertainties in the estimated values for the diffusion length and in particular for the field enhancement factor are considerable and could lead to a significant error in the estimate for the power breakdown value. On the other hand, we also note that smaller values of Λ lead to higher values for E_b, but also correspond to higher values of the field enhancement factor, β. This implies that the errors in Λ and β work tend to cancel in the predicted value for the breakdown power.

An interesting artifact of Fig. 4 is the hysteresis effect in the transmitted power as a function of input power. This feature is due to the fact that the microwave power needed to sustain a breakdown plasma is less than that needed to initiate breakdown. If we model the decreased ambipolar diffusion by using an effective diffusion length, Λ_a, we infer from eq. (3) and our previous estimate $D_a/D_e \cong 0.026$ that $\Lambda_a \cong 6\,\Lambda$. The corresponding breakdown field is found to decrease by approximately a factor of 4, i.e. the sustainment power should be approximately 12 dB below the breakdown power, in qualitative agreement with Fig. 4.

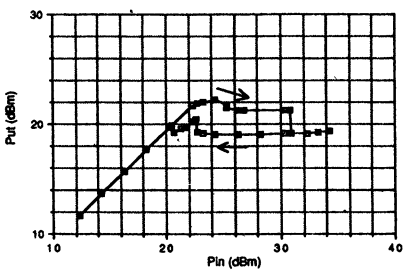

Fig. 5. Same as Fig. 4 but with the keep-alive current on.

In the experimental result presented in Fig. 4, the keep-alive current was switched off. An interesting observation, supporting our previous discussion of the importance of ambipolar effects, is shown in Fig. 5. With the keep-alive current switched on, the breakdown level decreases, but the sustainment level is constant. It seems likely that in this case a small preformed ambipolar plasma cloud is created by the keep-alive current. The breakdown process is then significantly easier to trigger when the high power microwave pulse passes through the switch. In fact, the difference

between breakdown level and sustainment level is very small, only 2 dB, and the hysteresis effect has almost disappeared.

3 Turn-on time

The breakdown condition given by eq. (3) is only valid for CW-operation or sufficiently long pulses. For short pulses and/or if the turn-on characteristics of the TR-switch are important, the finite rise time of the electron density as determined by the solution of eq. (1), must be taken into account, viz.

$$n(t) = n(0) \exp\left[\int_o^t \nu_{net}(t')dt'\right] \tag{6}$$

The turn-on, or switching time, t_s, can be estimated as the time required for the electron density to exponentiate to the value n_p at which the plasma frequency f_p equals the microwave frequency, f, i.e. $n_p \cong 1.2 \cdot 10^{-8} f^2 \quad cm^{-3}$. At this density, the dielectric properties of the plasma strongly affect the propagation properties of the wave by causing significant reflection and absorption. The interaction between the microwave and the breakdown plasma is then inherently nonlinear and the simple equation of continuity, eq. (1), must now be solved together with the equation of propagation for the microwave, viz.

$$\frac{\partial n}{\partial t} = \nu_{net}(|E|^2)n$$

$$\left[\frac{d^2}{dz^2} + k^2(n)\right]E = 0 \tag{7}$$

where z is the distance of propagation and $k^2(n)$ is given by ($k_o = \omega/c$)

$$k^2 = k_o^2\left(1 - \frac{\omega_p^2(n)}{\omega^2+\nu_c^2} - i\frac{\nu_c}{\omega}\frac{\omega_p^2(n)}{\omega^2+\nu_c^2}\right) \tag{8}$$

The wave reflection caused by the locally increasing electron density will deplete the transmitted power in the breakdown plasma and the density will eventually deviate from its first exponential increase and finally saturate when the net ionization caused by the residual transmitted power becomes zero.

However, in our estimate of the switching time, t_s, we will neglect the nonlinear character of the interaction and simply use the time variation of the incident microwave power. The turn-on time is then determined by

$$\int_o^{t_s} \nu_{net}(t')dt' = \ln \frac{n_p}{n_o} \qquad (9)$$

Before we turn to the complicated reality of the TR-switch, we will discuss the switch-on characteristics in connection with a numerical experiment, which has the advantage of providing well defined physical parameters, a situation which is seldom met in an actual experiment.

In the numerical simulation of breakdown in an S-band slot antenna radiating into air from a re-entry vehicle, studied in Ref. [5], the incident microwave power had a step variation in time and the incident power was well above the breakdown power determined by $\nu_{net} = 0$. This implies that $\nu_{net} \cong \nu_i$ and eq. (9) can be integrated directly to obtain the switching time, t_s, as

$$t_s \cong \frac{1}{\nu_i} \ln \frac{n_p}{n_o} \qquad (10)$$

For air, the ionization frequency, ν_i, can be approximated as [6] $\nu_i/p \cong 5 \cdot 10^{11} \exp(-73/\alpha^{0.44})$ where $\alpha = E/[p(1+\omega^2/\nu_c^2)^{1/2}]$ V/(cm·Torr). The physical data used for the simulation are $n_o = 2 \cdot 10^{10}$ cm^{-3}, f = 2.5 GHz, p = 10 Torr, and P = 3 kW/cm^2. This implies $t_s \cong 9$ ns in excellent agreement with simulation results.

The existence of a finite switching time implies that pulses with pulse lengths $t_p < t_s$ will pass unaffected through the breakdown region. When t_p becomes comparable with t_s, breakdown effects will become noticeable as a power dip in the trailing edge of the transmitted pulse. As the pulse length is increased further,

the dip should increase in depth and extension until it begins to limit even the rising leading part of the transmitted pulse.

An experiment has been made to illustrate this phenomenon in the TR-switch using low power microwave pulses with a pulse length, $t_p \cong 0.6\,\mu s$ and a rise time of approximately 25 ns. The experimental arrangement for pulsed operation is shown in Fig 6. The microwave generator in this case is an X-band (9.5 GHz) magnetron with pulse peak power 150 kW. Reflected and transmitted powers were measured at points 20 and 18 respectively.

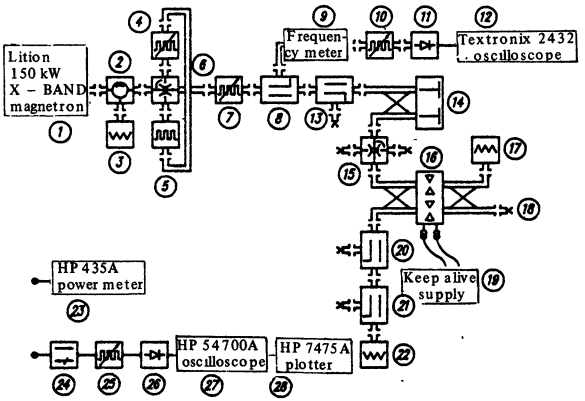

Fig. 6. Experimental set up for pulsed operation.

The transmitted pulse was measured for incident powers increasing from 0.33 W (unaffected pulse) to 2.5 W at which power level the breakdown plasma begins to limit the rising part of the pulse, i.e. the switching time is comparable with the rise time of the magnetron pulse, see Fig. 7. The transmitted pulses have been normalized with respect to the incident peak power to emphasize the successive erosion of the transmitted pulse.

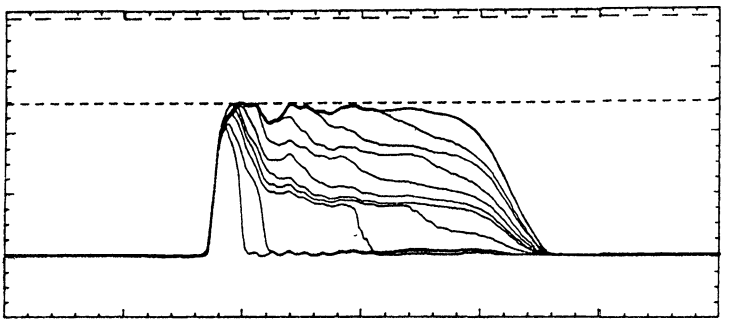

Fig. 7. Normalized transmitted pulse for increasing incident power (200 ns/div).

We note that the experimentally found breakdown threshold of the pulsed system is approximately 0.3 W which is somewhat lower than the 0.6 W observed for the (keep-alive backed) CW case, cf Fig. 5. The difference should be due to the pulse repetition frequency, f_{PRF} = 2 kHz, which is high enough to make the pulses meet a non-negligible residual plasma with partially ambipolar diffusion properties. A particular feature in the development of the pulse profiles is the appearance of a second dip in the trailing part of the pulse at "high" powers, cf Fig. 7. This should be caused by the creation of an additional breakdown plasma at the forward (unbiased) pair of field enhancement contacts, cf Fig. 3.

At low powers we can neglect the rise time of the pulse and use eq. (10) as an estimate of the characteristic time at which the intensity dip should occur. The ionization frequency for argon is approximated as, [3], $\nu_i \cong 1.7 \cdot 10^2 E^2 \equiv \bar{\nu}_i E^2$ s^{-1} where E is in V/cm. Using eq. (4) we can write for the enhanced field, E:

$$E \cong 30 \beta \sqrt{P} \quad \frac{V}{cm} \tag{11}$$

where P is half the peak power in W (because of the double parallel cell design of the TR-switch). Taking as before $\beta \cong 20$ and assuming $n_p/n_o \cong 10^2$ as an appropriate value for the residual electron density, the switching time becomes

$$t_s \cong \frac{75}{P} \quad \text{ns} \tag{12}$$

The pulse power at which the trailing part of the pulse becomes affected can be estimated as

$$P = P_c \cong \frac{75}{t_p^*} \tag{13}$$

where t_p^* is the pulse time in ns corresponding to the flat top part of the pulse. In our case $t_p^* \cong 400$ ns which implies $P_c \sim 0.19$ W, again in good agreement with the observed $P_c = 1/2 \times 0.4$ W. The switching time becomes comparable with the pulse peaking time ($t_s \sim 80$ ns) at the power level $P \sim 2 \times 1$ W also in agreement with experimental results.

The turn-on times for high incident powers in the kW-range are determined by the actual time variation of the power at the leading edge of the pulse, which can be modelled as $P(t) = P_o$ (expgt-1). The parameter γ can be characterized by the characteristic time, t_γ. needed for the power to reach its peak value $\hat{P}$ if the exponential increase had continued unimpeded, i.e. $\gamma = \ln(\hat{P}/P_o)/t_\gamma$.

Performing the integration indicated in eq. 9, the switching time, t_s can be approximated as

$$t_s \cong \frac{1}{\gamma} \ln\left(\frac{\gamma \ln \frac{n_p}{n_o}}{\overline{\nu}_i E_o^2}\right) \tag{14}$$

where E_o is the electric field strength corresponding to P_o.

Taking $P_o = 1$ W, $n_p/n_o \cong 10$, $\hat{P} = 150$ kW, and estimating $t_\gamma \cong 4$ ns, eq. (14) implies $t_s \cong 2$ ns in good agreement with the experimental switching time inferred from Fig. 7.

4. Reflected, absorbed, and transmitted power

After the initial switch-on phase, the breakdown plasma rapidly moves forward to the input window of the TR-switch.

Subsequently, a consistent, fully nonlinear, stationary state is established between the incident microwave and the breakdown plasma. The essential features of this equilibrium are: (i) The density at the input window is very high, thus reflecting the major part of the incident microwave power. (ii) The electron density profile is determined as the consistent solution of the continuity equation for the electron density coupled with the wave equation for the transmitted microwave field. (iii) As a result of this interaction, the transmitted power is strongly attenuated in the breakdown plasma where the electron density rapidly decreases towards the output window. (iv) The transmitted power at the output window, i.e. the leakage power is very small.

The refractive index of the breakdown plasma, which plays a decisive role in the plasma-wave interaction, is determined by

$$\frac{kc}{\omega} = \tilde{n} = \mu + i\kappa \tag{15}$$

where

$$\mu_2 = \frac{1}{2}\left\{\varepsilon + \left[\varepsilon^2 + \left(\frac{4\pi\sigma}{\omega}\right)^2\right]^{1/2}\right\}$$

$$\kappa^2 = \frac{1}{2}\left\{-\varepsilon + \left[\varepsilon^2 + \left(\frac{4\pi\sigma}{\omega}\right)^2\right]^{1/2}\right\} \tag{16}$$

and

$$\varepsilon = 1 - \frac{\omega_p^2}{\omega^2+\nu_c^2} = 1 - \frac{n}{n_c} \equiv 1 - N$$

$$\frac{4\pi\sigma}{\omega} = \frac{\nu_c}{\omega}\frac{\omega_p^2}{\omega^2+\nu_c^2} = \frac{\nu_c}{\omega}\frac{n}{n_c} \equiv \frac{\nu_c}{\omega} N \tag{17}$$

In simplifying eq. (17) we have used the definition $\omega_p^2(n_c) \equiv \omega^2+\nu_c^2$. In the situation presently under study we have $\omega \cong \nu_c$ and $n/n_c >> 1$ which implies $\mu^2 \cong \frac{1}{2}(\sqrt{2}-1)N >> 1$ and $\kappa^2 \cong \frac{1}{2}(\sqrt{2}+1)N >> 1$

The input window provides a sharp boundary where the incident wave is partially reflected. The reflection and transmission coefficients at the boundary are determined by

$$R \equiv \frac{E_r(0)}{E_{in}(0)} = \frac{\tilde{n}_1 - \tilde{n}_2}{\tilde{n}_1 + \tilde{n}_2}$$

$$T = \frac{E_t(0)}{E_{in}(0)} = \frac{2\tilde{n}_1}{\tilde{n}_1 + \tilde{n}_2} \qquad (18)$$

where $E_{in}(0)$, $E_r(0)$, and $E_t(0)$ denote the electric fields of the incident, reflected, and transmitted waves at the boundary. The corresponding power coefficients are

$$R_p \cong 1 - \frac{2(\sqrt{2}-1)^{1/2}}{\sqrt{N}} \cong 1 - \frac{1.3}{\sqrt{N}}$$

$$T_P = 1 - R_p \cong \frac{1.3}{\sqrt{N}} \qquad (19)$$

Thus if $N >> 1$, the incident microwave power is significantly reduced after the passage through the input window. The power transmitted through the boundary is further attenuated when passing through the breakdown plasma, leaving a small residual leakage output power.

A qualitative model giving the main features of the nonlinear wave-plasma interaction can be given as follows (for more details see [3]). In steady-state, the dominating loss

mechanism in the continuity equation is diffusional losses in the z-direction, i.e. along the direction of propagation, i.e.

$$D_a \frac{d^2 n}{dz^2} + \bar{\nu}_i |E_t(z)|^2 n \equiv 0 \tag{20}$$

Assuming that $|E_t(z)|^2$ varies much more rapidly than n(z) and using the fact that dn(0)/dz = 0, an approximate solution of eq. (20) can be obtained in the simple form

$$n(z) \equiv n(0)\left(1 - \frac{\bar{\nu}_i z}{D_a}\int_0^L |E_t(z)|^2 dz\right) \tag{21}$$

where L denotes the extent of the breakdown plasma along the direction of propagation.

The boundary condition n(L) = 0 together with a WKB-approximation to estimate the integral of $|E_t(z)|^2$ yields the relation

$$\frac{0.45\,\bar{\nu}_i L |E_t(0)|^2}{k_o D_a \sqrt{N(0)}} \equiv 1 \tag{22}$$

Eq. (22) can be used to establish some characteristic scalings. Note that $|E_t(0)|^2 \sim P_{in}/N(0)$. Eliminating $E_t(0)|^2$ we obtain $N(0) \sim P_{in}^{2/3}$ and using the fact that most of the power transmitted through the input window gets absorbed, i.e. neglecting the leakage power, the absorbed power, P_a, should scale as

$$P_a \sim \frac{P_{in}}{\sqrt{N(0)}} \sim P_{in}^{2/3} \tag{23}$$

For the reflected power, P_r, we obtain the scaling

$$\frac{P_r}{P_{in}} \equiv R_p = 1 - \frac{1.3}{\sqrt{N(0)}} \equiv 1 - \frac{\Gamma}{P_{in}^{1/3}} \tag{24}$$

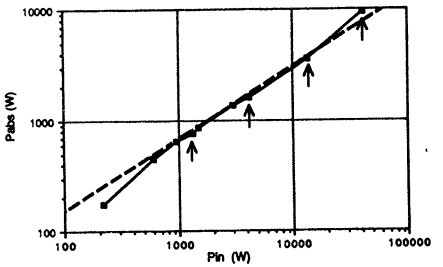

Fig. 8 Experimental result (___) and theoretically predicted scaling (---) for absorbed power as a function of incident power.

The power scalings predicted by eqs. (23) and (24) are in excellent agreement with experimental results, cf Figs. (8) and (9).

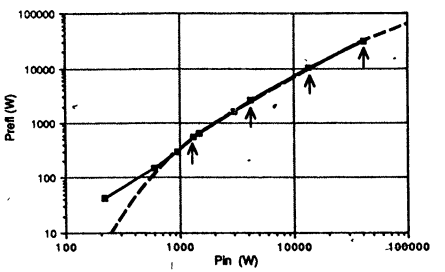

Fig. 9. Same as Fig. 8 but for reflected power.

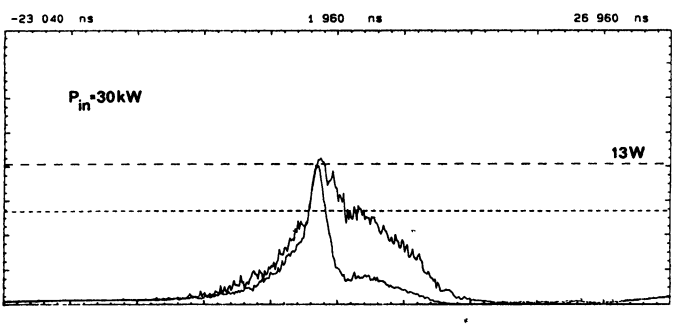

Fig. 10. Leakage power as a function of time with and without keep-alive current.

Finally, Fig. 10 illustrates the time development of the leakage power with and without the keep-alive current on. An important quantity from a technical point of view is the peak leakage power. The input power at the switching time is $P(t_s) \cong P_o \exp(\gamma t_s)$. However, most of this incoming power is spent in ionizing the gas. In fact, the microwave power going into ionization, P_i, can be estimated as $P_i \cong eU_i \partial n/\partial t\, V \cong eU_i \bar{\nu}_i E^2 n\, V$, where V denotes the volume of the breakdown region. Taking $n = n_c$ and $V \cong 10\ mm^3$, we obtain $P_i \cong P_{in}$, i.e. most of the input power is absorbed in the process of creating the plasma. Although these estimates are very qualitative, they seem to be consistent with the observation that the power input into the TR-switch at the switching time is $P(t_s) \cong 200\ W$, which is an order of magnitude above the 13 W peak leakage power observed experimentally.

6. Conclusion

The present work, which involves experimental as well as theoretical investigations, has given an extensive treatment of many physical phenomena involved in the operation of a microwave TR-switch. Very good agreement has been obtained between the predictions of the theoretical models and the experimental results. This is particularly so for important TR characteristics like breakdown level, turn-on time, and reflected and absorbed powers. The accurate modelling of the transient breakdown behaviour should make it possible to apply this analysis to similar problems, e.g. to the propagation of high power microwave pulses in the atmosphere, a problem of considerable topical interest, both for its scientific as well as for its technical importance, [7].

Acknowledgement

This work is supported by the Swedish Board for Technical Development and is performed in close collaboration with Ericsson Radar Electronics AB. We also gratefully acknowledge support, stimulating discussions, and help in performing the experiments by T. Lewin, L. Lundgren, and R. Hansson respectively.

References

[1] R.S. Smith, G.E. Thomas, D.C. Coleman, and T.J. Pappalardo, Gas-Breakdown Transmit-Receive Tube Turn-On Times, IEEE Trans. on Plasma Science PS-14 (1986), 63.

[2] A.D. MacDonald, Microwave Breakdown in Gases, Wiley (1966).

[3] M. Löfgren, D. Anderson, H. Bonder, H. Hamnén, and M. Lisak, On the Breakdown Physics in Microwave TR-switches, J. Appl. Phys. (to be published).

[4] W. Lipinski, M. Lisak, and D. Anderson, Calculation of Electric Field Enhancement in Microwave TR-Switches, CTH-IEFT/PP-1989-04.

[5] J.T. Mayhan, R.L. Fante, R. O'Keefe, R. Elkin, J. Klugerman, and J. Xos, Comparison of Various Microwave Breakdown Prediction Models, J. Appl. Phys. 42 (1971), 5362.

[6] W. Woo and J.S. De Groot, Microwave Absorption and Plasma Heating Due to Microwave Breakdown in the Atmosphere, Phys. Fluids 27 (1984), 475.

[7] S.P. Kuo and Y.S. Zhang, Propagation of High Power Microwave Pulses in Air Breakdown Environment, IEEE Int. Conf. Plasma Sci., June 6-8, 1988, Washington, USA, paper1C9.

GAS DISCHARGE IN A SUPERSTRONG MICROWAVE FIELD

A.L.Vikharev
Institute of Applied Physics, Academy of Science of the USSR
N.Novgorod, USSR

1. Introduction

The advance of microwave electronics in the development of powerful generators using intense relativistic electron beams is considerable. This is confirmed by a number of experiments [1-5], in which the atmospheric pressure air breakdown was demonstrated. In these works the air breakdown was used for the diagnostics of high-power microwave sources, namely, of the oscillation modes and the output power. Gas breakdown occurred in the focal region of a parabolic mirror placed at a short distance from the output window.

Of equal interest are ionization processes induced by high-power microwave radiation in gases with different densities. The discharge produced by intense microwave radiation in low-density gas provides the conditions when the oscillatory electron energy

$$\varepsilon = e^2 E^2 / 2 m (\omega^2 + \nu^2) \qquad (1)$$

is higher than the atomic ionization potential I_i ($\varepsilon > I_i$). Here e and m are the electron charge and mass, E is the root mean square wave field strength, ω is the wave frequency and ν is the electron collision frequency for momentum transfer.

Under these conditions the discharge development is accompanied with a number of effects which are absent in gas breakdown in moderate-intensity fields, where $\varepsilon << \bar{\varepsilon} < I_i$ ($\bar{\varepsilon}$ is the mean electron energy). Some effects are due to high ionization rate and short pulse duration [6,7]. Usually pulse durations of relativistic electron-beam oscillators range from 10 to 100 ns. Other effects are due to high electron energy [8,9]. The paper deals with analysis of these new effects. It should be noted that gas discharge in a superstrong microwave field, when $\varepsilon > I_i$,has been studied in the [6-13].

2. Experimental scheme

A discharge was produced in the focal region of a wave beam formed with a lens or a parabolic mirror in the echo-free vacuum chamber, Fig.1. The chamber was first pumped out to about $p = 10^{-5}$ Torr and then filled with the gas investigated.

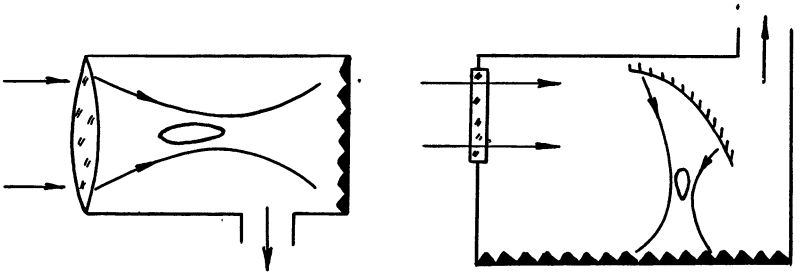

Fig.1. Schematic diagrams of experiments

A 3-cm wavelength microwave radiation was used in the experiments, the pulse duration τ_p ranged from 10 ns to 100. The microwave breakdown was investigated in different gases like helium, argon, nitrogen, oxygen, the mixture of N_2 : O_2 for a wide range of pressures: $p = 3\ 10^{-3}$ - 760 Torr. The power of the microwave beam was such that the rms electric field strength in focus E_F varied from 10 kV/cm to 120 kV/cm. The oscillatory electron energy in the fields varied within the range $\varepsilon = 1 - 3.5\ 10^3$ eV. So, at low-density gas the discharge was studied under the condition $\bar{\varepsilon} > I_i$.

3. The specific features of the discharge in a superstrong microwave ield

The peculiarity of this discharge is clearly seen when it is compared with the discharge in a weak field of the wave beam, for example, at the pulse duration $\tau_p = 10^{-6} - 10^{-5}$ s and the electric field intensity of the order of the breakdown threshold, $E = 1\text{-}3$ kV/cm.

Under a weak field, the oscillatory electron energy is $\varepsilon << \bar{\varepsilon} << I_i$. The electron energy in the weak field increases only due to their collisions with atoms. With every impact the

oscillatory energy of electrons is transformed into the translational energy. For example, when the electron collision frequency ν is independent of the velocity $\nu(v)$=const., the electron distribution function is the Maxwell's one. The gas is ionized by fast electrons (from the tail of the electron distribution function) whose energy is higher than $\bar{\varepsilon}$. The number of fast electrons is not large, therefore the ionization process has little effect on the type of the electron distribution function [14]. In the weak field the ionization frequency ν_i is much smaller than the electron collision frequency $\nu_i << \nu$.

There is another situation under the strong field. At low density gas ν is smaller than ω. In this case electrons have oscillatory motion almost escaping collisions. Since the oscillatory electron energy ε is larger than I_i, every electron - molecule impact produces an ionizing effect. It is well known that electrons can receive translational energy without collisions, if the electric field is switched-on instantaneously. This is the primary energy of oscillations. The effect of the instantaneous switch-on of the field occurs for the newly-born secondary electrons in the ionization process. As a result, the electrons immediately acquire translational motion and oscillations are imparted to it. In this way the amount of the electron translational energy in a superstrong field is determined by the phase of electron creation in the wave field. Such a process determines the type of the electron distribution function in a superstrong field at the initial stage of the microwave breakdown. In this case the ionization frequency ν_i is higher than the electron collision frequency ν .

The electron distribution function in a superstrong field was studied by Rukhadze et al.[15-18]. They showed that if only creation of new electrons is taken into account in the collision integral of the kinetic equation and if the collision-induced velocity variation of primary electron is neglected, the electron distribution function can be regarded as the function of uniform electron distribution over initial phases of their motion in the wave field :

$$f(v)= N_e(t)/ \pi \sqrt{v_o^2 -(v + v_o \cos \omega t)^2} = N_e(t)/ \sqrt{v_o^2 - u^2}, \quad (2)$$

where $v = u - v_o \cos \omega t$ is the electron velocity, u is the

translational velocity, $v_o = e E / m \omega$ and $-v_o < u < v_o$.

Validity of this approximation was confirmed by results of the numerical simulation of the discharge kinetics in a superstrong field at $\omega >> \nu$. Thus the collision integral approximation permitted to find the electron distribution function and calculate the ionization frequency.

4. Ionization rate measurements

Measurements of the ionization frequency in a wide range of microwave fields is an important problem for gas discharge physics. Many experiments were concerned with measurements of ν_i [7,9,10].The gas ionization rate in the experiments [7,9] was determined through measurements of the breakdown time τ by the cutoff of the post-focus microwave pulse. For a nanosecond gas breakdown the electron losses during the pulse are absent, therefore ν_i coincides with the avalanche constant in the expression for the electron concentration.The ionization frequency ν_i was calculated by the formula

$$\nu_i = \ln(N_{ek} / N_{ok}) / \tau , \qquad (3)$$

where N_{ek} and N_{ok} are the final and initial electron densities. At low density gas ($\nu << \omega$), ν_i can be represented in the parameter plane (ν_i / p and E / ω). This law of similarity follows from the kinetic equation. Figure 2 presents results of measurements obtained by different researchers.

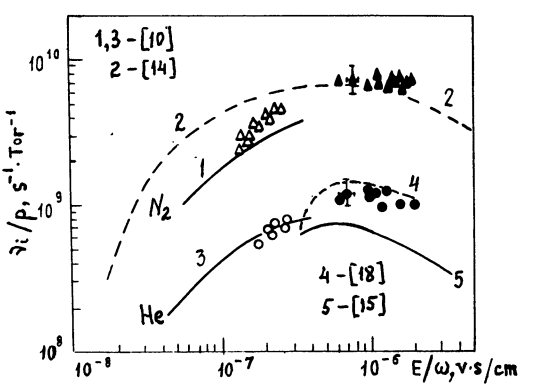

Fig.2. Reduced ionization frequecy (ν_i/p) for helium and nitrogen as a function of E / ω

It was found out that in the parameter region $5\ 10^{-7} < E/\omega < 2\ 10^{-6}$ V s / cm the ionization frequency ν_i does not change with increasing E and can be approximated by the expression $\nu_{im} = A\ 10^9 p\ s^{-1}$, where A = 1.2 for helium, A = 7 for nitrogen and gas pressure in Torr. Calculations of ν_i in this region of the parameter E/ω, taking into account the function of uniform electron distribution over the phases of electron creation [9,14,15,18], are in satisfactory agreement with the experimental data.

5. The dynamics and structure of the discharge in a wave beam

Discharge dynamics and structure in a weak field of the wave beam when $\varepsilon << \bar{\varepsilon} < I_i$ have been studied in detail [19-21]. Due to high ionization rate and short pulse duration, some new effects appear in the superstrong field [6-9].

5.1. Change of the breakdown wave kinematics

The breakdown dynamics in a wave beam was studied by examining plasma emission photographs. Figure 3 is an optical scan of the discharge in helium at the pressure p = 30 Torr and the beam focus field intensity E_F = 20 kV / cm.

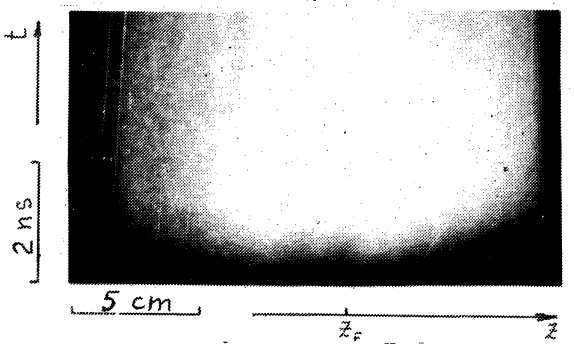

Fig.3. Optical scan of the discharge

After discharge was initiated, the ionization fronts propagated in both directions away from the point at the velocity $v = (1\text{-}5)\ 10^{10}$ cm/s. It was found out that at pressures corresponding to the minimum of the Paschen curve the point at which gas breakdown first occurred was shifted away from the

focus to 5-10 cm towards the incident radiation. This shift is due to the fact that the breakdown dynamics is affected by the fixed time of the radiation propagation through the focal region. Taking into account the propagation time of the electromagnetic wave the breakdown time τ in different cross-sections of the wave beam z is

$$\tau(z) = \ln(N_{ek} / N_{ok}) / \nu_i(z) + z/c. \qquad (4)$$

For a high ionization frequency the second term in the formula (4) is comparable with the first one and has an influence on the breakdown on the breakdown time.

One can easily derive for the Gaussian beam the relation for the shift of initial breakdown δz :

$$\delta z \left(1 + \delta z^2 / l_F^2 \right)^{(\beta/2-1)} / l_F = \tau_c / \beta \tau_F , \qquad (5)$$

where $\tau_c = l_F / c$ is the propagation time, $\tau_F = \ln(N_{ek} / N_{ok}) / \nu_{iF}$ is the breakdown time in the focus , $l_F = k a_F^2$, a_F are the longitudinal and the transverse dimensions of the focal region, $\beta = (d\nu_i / dE) E / \nu_i$. It is clear that the shift δz depends on the relation between τ_c and τ_F. For example, under the experimental condition [6] $\beta = 2$, $\tau_c = 10^{-9}$s , the estimation shows that

$$\delta z = l_F \tau_c / \beta \tau_F = 15 \text{ cm}. \qquad (6)$$

Figure 4 gives the dependence of the breakdown time on the coordinate along the beam axis.

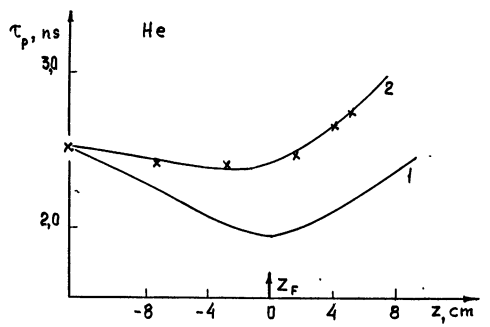

Fig.4

Curve 1 represents the calculation disregarding the electromagnatic signal delay; curve 2 is the calculation taking into account the propagation time; experimental data are plotted there, too.

5.2. Discrepancy of spatial distributions of light radiation and electron density

Figure 5 is a time-integrated photograph of the discharge in nitrogen at the pressure p = 0.5 Torr and electric field to gas density ratio $E_e/N = 2\ 10^{-13}$ V/cm^2, where $E_e = E\,\nu / \sqrt{\omega^2 + \nu^2}$ is the effective field. This figure shows that light radiation of plasma in the beam focus is much less than in the beam periphery.

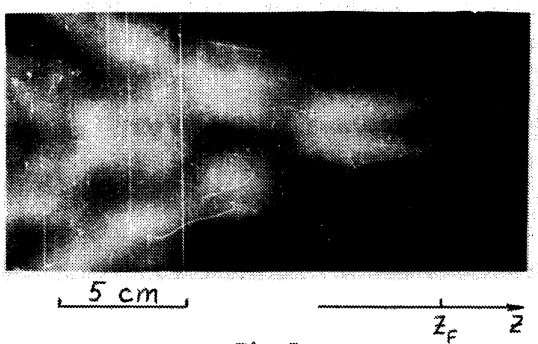

Fig.5

Spatial distribution of plasma emission is related to a different character of dependence of the ionization and the excitation cross-sections of the molecule electron levels for electron energies ranging from 10 to 100 eV. Within this region the ionization cross-section increases, while the excitation cross-section of the electron levels of the second positive system band of nitrogen decreases. We performed the calculations. Assuming that the electron concentration reaches its critical value by the end of the microwave pulse, we can construct the radial distributions of electron concentration and the density of excited nitrogen for different cross-sections of the Gaussian beam. The calculated distributions $N_e(r)$ and $N_b(r)$ are presented in Fig.6. The nitrogen pressure was p = 0,5 Torr and electric field to gas density ratio $E_e/N = 5\ 10^{-14}$ V/cm^2. It is clear, that electron density reaches its critical value at the axis in the beam focus, and the density of excited nitrogen and, consequently, plasma emission reach their maxumum values in the beam periphery.

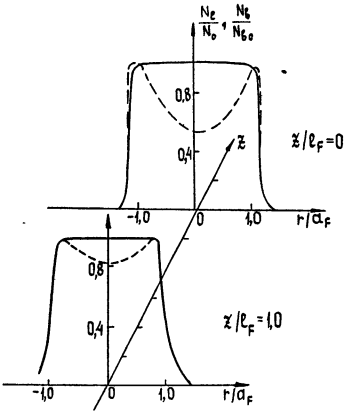

Fig.6

5.3. Additional ionization effect after low-density discharge

The discharge was studied at low pressure (p=3 10^{-3}-1 Torr) using pulse gas injection into the focal region of the wave beam. This scheme was used for the localization of the discharge in a small focal region. The electric field intensity in the focus was E_F = 70 -120 kV/cm, and the oscillatory energy in this field was ε = 1.2-3.5 keV. It was found that the electron density after the microwave pulse was 5 to 10 times larger than the critical density for the microwave radiation, $N_c = 10^{12}$ cm^{-3}. The electron density was measured using an interferometer with the wavelength λ equal to 8 mm.

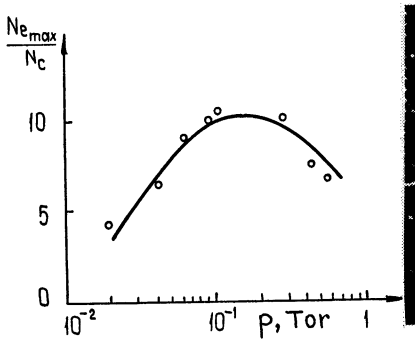

Fig.7

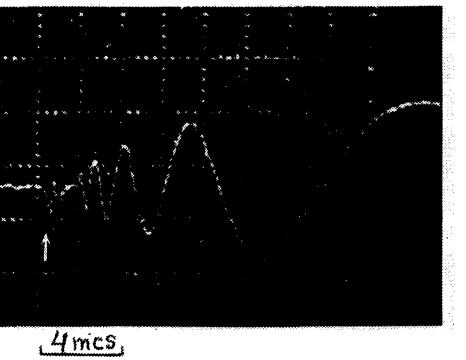

Fig.8

Figure 7 is the dependence of the maximal electron concentration after the microwave pulse on gas pressure. Figure 8 is an

interferogram of the discharge in nitrogen at the pressure p = 0.4 Torr and the initial density $N_{eo} = 10^6$ cm^{-3}. One can see a 2-ms cutoff of the probing signal, then plasma starts to decay. For the pressure p= 10^{-2}- 10^{-1} Torr no cutoff was observed, but the sign of the signal changed in 0.5 ms after the microwave pulse. It means that the electron density was increasing for about 0.5 ms.

These results can be explained in the following way. After the field switches off, the plasma contains electrons with the energy much higher than the ionization potential. These electrons lose their energy in ionizing collisions, because $\nu_i > \nu$. Therefore, N_e can increase considerably due to the continuing ionization process. Assuming that the energy loss of electrons due to the ionizing collisions is of the order of 2 I_i, we find that after the passage of the pulse the electron density increases (ε / 2 I_i) times over the electron cooling time. The electron cooling time can be approximated by the relation :

$$\tau_{di} = \int_{I_i}^{\varepsilon} d\varepsilon \,/\, 2\, I_i\, \nu_i(\varepsilon) = \varepsilon \,/\, 2\, I_i\, \nu_{im}. \qquad (7)$$

For example, in nitrogen at pressure p= 5 10^{-2} Torr and ε = 2 keV according to the fomula (7) value τ_{di} equals τ_{di}= 0.5 ms. This estimated value of electron cooling time is as in experiment.

Additional gas ionization was also observed at a higher initial density of electrons : $N_{eo} = 3\ 10^{10}$ cm^{-3}. For example, in helium we achieved N_e of the order of six times the critical density ($N_{em} = 6\ 10^{12}$ cm^{-3}) at the pressure of p = 3 10^{-2} Torr after the microwave pulse which passed through the ionized region undistorted. The fact is, that N_e increases 2 or 3 times during the microwave pulse:

$$N_k = N_{eo} \exp(\nu_{im}\, \tau_p) = e^1\, N_{eo}. \qquad (8)$$

These newly-born electrons, getting cold after the microwave pulse induce additional ionization :

$$N_{em} = N_k\, \varepsilon \,/\, 2\, I_i = 5\ 10^{12} \text{ cm}^{-3}. \qquad (9)$$

The estimation is made for ε = 2 keV. Thus, a low pressure discharge in a superstrong field is followed by considerable additional ionization process.

5.4. Effect of slow plasma decay in nitrogen - oxygen mixture

In a nanosecond microwave discharge of low pressure the stage of additional ionization is followed by plasma decay. The experiment has shown that during the first 10 mcs after the microwave pulse, plasma decay is slow. Figure 9 presents the time dependence of the inverse electron density N_e^{-1} at different nitrogen pressures. A linear dependence $N_e^{-1}(t)$ testifies to recombination plasma decay with a low effective recombination coefficient $\alpha = 2\ 10^{-8}$ cm^3/s. At longer times t > 20 mcs, the rate of decay changes and the recombination coefficient equals $\alpha = 1.6\ 10^{-7}$ cm^3/s, Fig. 10.

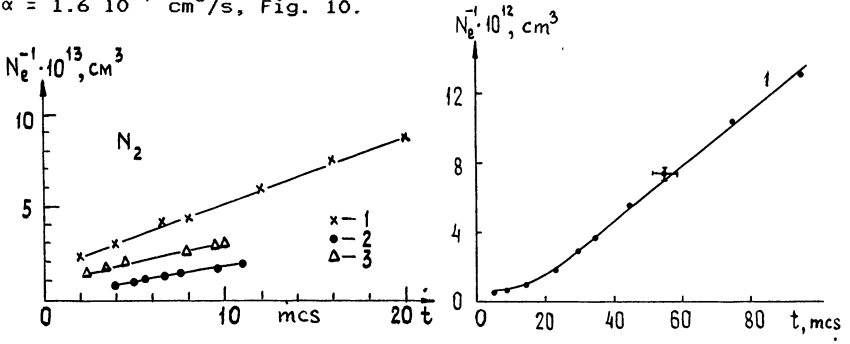

Fig.9. Dependence of the inverse electron density N_e^{-1} on time at nitrogen pressures : 1 - p = 5 10^{-2} Torr, 2 - 3 10^{-1} Torr, 3 - 6 10^{-1} Torr.

Fig.10. Dependence $N_e^{-1}(t)$ at nitrogen pressure p= 6 10^{-1} Torr: • - experiment, curve 1 -calculated data

Slow plasma decay at the time t < 20 mcs is due to slow relaxation of high electron temperature after a microwave pulse. The basic factors determining the high temperature of electrons after a microwave pulse are: 1) energy transfer to electrons in their collisions with electron - excited metastable nitrogen molecules $N_2(A^3\Sigma_u^+)$ and 2) electron - electron collisions. These processes are essential due to a large share of electron - excited nitrogen molecules and to a high level of gas ionization 10^{-4} - 10^{-3}.

This conclusion is confirmed by results of calculations. Numerical calculations of the Boltzmann equation for the electron

energy distribution function in nitrogen plasma decay for above mentioned experimental conditions were carried out in the papers [22, 23]. They showd that the electron energy distribution function has maxima at energies proportional to the excitation energy of the nitrogen electron level $A^3\Sigma_u^+$ (6.17eV). Figure 10 displays the calculated dependence $N_e^{-1}(t)$ which agrees well with the experimental results for the share of electron - excited nitrogen molecules equal to $\eta = 3\ 10^{-2}$. Thus, the rate of plasma decay after a powerful microwave pulse is influenced by a great share of fast electrons.

5.5. Delay of optical radiation of the discharge

The optical radiation of plasma in a nanosecond discharge was investigated in papers [8,24]. The experiment demonstrated that at low nitrogen pressures ($\nu < \omega$) the optical radiation of microwave discharge produced in the focal region of the beam reaches its maximum after the microwave pulse, Fig. 11.

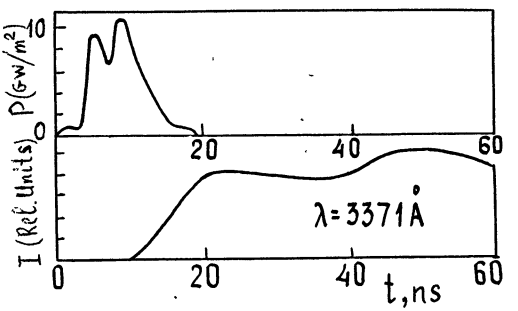

Fig.11. Oscillograms of the microwave pulse and optical radiation of the discharge at nitrogen pressure p= 0.5 Torr, as presented in paper [8]

The observed delay of the light pulse is explained by high electron energy during the microwave pulse. According to calculations this electron energy amounts to several kiloelectronvolts. Such electron energy exceeds greatly the energy corresponding to the maximum of the cross - sections for the electronic excitation of nitrogen, ε_B = 10 - 20 eV. Therefore basic excitation of nitrogen molecules takes place after the microwave pulse at a considerable decrease of electron energy.

The study of the discharge spectrum in nitrogen shows that the main contribution to optical radiation is given by the transition $C^3\Pi_u - B^3\Pi_g$ of the second positive system in the 0-0 band, 337,1 nm line, whose intensity is 2 orders greater than the radiation in the 0-1, 1-0 and 2-1 bands.

5.6. Discrete structure of discharge

Another specific feature of a nanosecond discharge, namely the breakdown at separate initial electrons, is observed due to high ionization freguency in a superstrong field. It is stated in the paper [7] that the structure of the discharge at gas pressures from 1 to 100 Torr depends greatly on the level of initial electron density. It is the type of ionizer that influences the densities of primary electrons.

In the absence of an external source of ultraviolet radiation, structures of two types are observed in the integral photograph of the discharge, Fig. 12. They are 1) separate plasma formations with the size smaller than the wavelength stretched along the external electric field E and tending to bunch along the lines like the tracks of particles in the spark chamber and 2) quasihomogeneous faint discharge plasma.

Fig.12. Integral photograph of the discharge at the helium pressure p = 50 Torr

The multiplasmoid structure observed can be explained by the discreteness of the initial electron avalanches formed around every primary electron and not merging because of short duration of the microwave pulse. Primary electrons appear in the breakdown region due to the ionization of gas by fast Compton electrons

that are generated in their turn by bremssfrahlung radiation of a relativistic electron beam in the microwave oscillator. The measurements of the γ- radiation level in the chamber showed that during the microwave pulse there exists inside it the γ- quantum flow with energy less than 300 keV. This flow can form 10^{-3} p Compton electrons per cm^3 during the pulse.

On the discharge photographs, the ionization tracks can be identified by the paths of these fast electrons through the discharge region. The interval between the plasmoids on the track can be identified by the ionization length :

$$l_i = 1/ \sigma_i N = 9\ 10^{-5}\ \varepsilon_e / p \ln(\varepsilon_e / I_i). \qquad (10)$$

Here ε_e is the Compton electron energy in eV, p is the gas pressure in Torr, l_i is the length in cm, and σ_i is the ionization cross-section. It enables us to estimate the energy of the corresponding Compton electron by the observed track parameters. For example, for the conditions given in Fig.12 in helium we find l_i= 2-10 mm and ε_e= (1-2) 10^5 eV.

According to this physical model the discrete multiplasmoid structure of the discharge must not be formed at high density of initial electrons when separate electron avalanches overlap quickly. Indeed, when the spark discharge was put into the vacuum chamber and its ultraviolet radiation increased the electron density in the breakdown region before the microwave pulse up to 10^3-10^5 cm^{-3}, then the light emission of the discharge was always homogeneous, Fig.13.

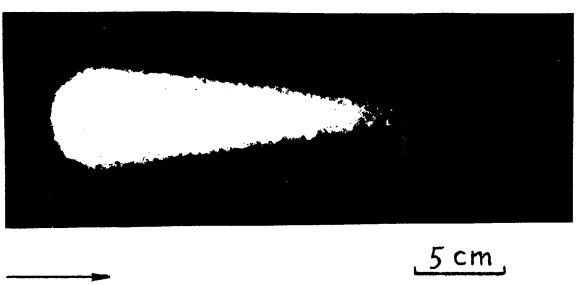

Fig.13

Development of the discharge on separate electrons can be observed only in a superstrong microwave field. This conclusion is confirmed by the following estimation. The average interval

between the initial electrons equals $r_o = N_{eo}^{-1/3}$ and the electron avalanche around every primary electron expands due to diffusion. During the breakdown time τ its dimension well be approximately equal to the characteristic diffusion length for electrons $L_e = D\tau$. Taking into account the fomula (2) for the breakdown time, one receives the expression at which the electron avalanches do not overlap and the discharge is discrete :

$$D\tau < N_{eo}^{-1/3} \qquad (11)$$

or

$$\nu_i > D N_{eo}^{2/3} \ln(N_{ek} / N_{eo}) \qquad (12)$$

Thus, there is a limitation for the ionization frequency when the discrete structure of the discharge is being observed.

5.7. The structure of a high-pressure discharge

The structure of a self-sustained nanosecond discharge was investigated in the field of linear and circular polarization at gas pressures of the atmospheric order, the field intensity was E_F = 60 - 70 kV/cm. When the primary electron density was small, the discharge retained its multiplasmoid structure. However, individual thin filaments were observed among plasmoids in the atmospheric-pressure discharge. Figure 14 is a photograph of the discharge in nitrogen under atmospheric pressure.

Fig.14

The light emission time of the filament after the microwave pulse was about 1 mcs; it was by the order of magnitude longer than the emission of the rest of the plasma.

No filaments appeared in the circular polarization field.

This filamentation in a high-pressure discharge indicates the influence of the increasing field on formation and growth of filaments. The dynamics of the plasmoid formation due to the electron avalanche development around initial electrons at high gas pressures was considered in [25]. It was stated in that work that at $\nu >> \omega$ the influence of the formed plasma on the incident field produces a field increase in the polar regions and field decrease in the equatorial region of a plasmoid. As a result, the plasmoid stretches along the external field.

6. Application of a nanosecond discharge for gas-laser pumping

At gas breakdown by nanosecond microwave pulses a strongly nonequilibrium medium is created, since the major part of the microwave energy absorbed in the plasma is spent on ionization and excitation of the molecule electron states. A number of successful experiments [26- 28] on the excitation of gas lasers at the electron transitions by means of a microvave discharge have been performed lately. The main merits of such a pump method are easy transport of microwave power and its injection into a laser installation, efficient absorption of electromagnetic energy in a plasma discharge, the absence of electrode-produced plasma instabilities in electric-discharge lasers, long purity of a laser mixture owing to the absence of electrodes and high specific pump power (10^6- 10^8 W/cm^3). Stratification of the nanosecond microwave discharge plasma is eliminated not only by a high-level preionization, but also by the circular polarization of the electric field. Therefore, a discharge produced by high-intensity microwave radiation can be successfully used for pumping of UV self-terminating and excimer lasers demanding high pumping rates.

In this paper results of the investigation of a nitrogen laser pumped by a freely localized microwave discharge in a wave beam are presented [27]. Fig.15 shows the schematic diagram of the experiment. The microwave radiation of the 3-cm wave length was focused on the quartz tube (2 cm in diameter and 80 cm long) by means of a mirror. The electric field intensity around the tube amounted to E = 15-20 kV/cm. The microwave radiation was circularly polarized and had a pulse duration τ_p = 30 ns. The gas

pressure in the tube was p = 10-100 Torr. As a result of microwave breakdown an extended plasma column was formed in a laser mixture (high-purity nitrogen and air).

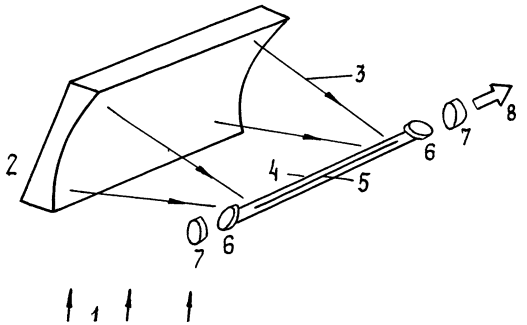

Fig.15. Schematic diagram of the experiment

The discharge tube had quartz pots making a Brewster angle with the axis. A 90-cm long optical resonator consisted of an aluminium mirror and a plane-parrallel quartz plate. Laser radiation was controlled by means of optical attenuators and a photoelectric transducer. Fig.16 shows oscillograms of the microwave and the laser pulses at a pressure p = 100 Torr. Experiments showed that the laser radiation duration weakly depended on the gas pressure in the region p = 30-100 Torr and was almost equal to the duration of microwave radiation. This result shows the difference between the excitation by a microwave discharge and the pumping by an electric discharge that is characterized by an abrupt decrease of pulse duration with increasing pressure.

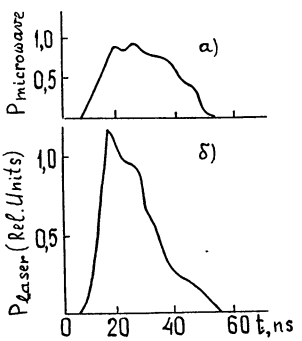

Fig.16

Laser generation is observed at the $C^3\Pi_u - B^3\Pi_g$ electron

transition of the second positive nitrogen system in the 0-0 (λ=337,1 nm), 0-1 (λ=357,7 nm), and 1-0 (λ=315,9 nm) bands. The radiation intensity in the 0-0 band was, respectively, 25 and 110 times higher than the radiation intensity in the 0-1 and 1-0 bands. The pulse power of laser generation was 60-70 kW at the pressure p =30-100 Torr. The spatial distribution of radiation intensity in the cross-section of the tube was shaped as a ring with the outer radius equal to the radius of the tube and with the thickness 3-6 mm. The laser radiation power per unit area of the ring was three times higher than the radiation energy in the center of the tube. The pump efficiency (defined as the ratio of laser power to the power of the incident microwave pulse) was 10^{-4}- 10^{-3} and the energy deposition was 0.5 -1 J/ atm. l. The generation power dropped 6-7 times when the tube was filled with air instead of nitrogen.

Experiments on the pumping of nitrogen-argon and excimer (XeCl) lasers were carried out on the analogical scheme. These experiments also confirmed the peculiarity of the microwave pumping,i.e.,the combination of high specific power (~ 10^6 W/cm^3) with a long time stability of the discharge.

References

1. S.H.Gold, W.M.Black, V.L.Granatstein et.al. - Appl.Phys.Lett., 43, 10, 922, 1983.
2. L.M.Earley, W.P.Ballard, L.D.Roose - Rer.Sci.Instrum., 57, 9, 2283, 1986.
3. S.H.Gold, A.W.Fliflet, W.M.Manheimer et.al. - Phys.Fluids, 30, 7, 2226, 1987.
4. V.L.Bratman, V.P.Gubanov, G.G.Denisov et.al. - Pis'ma v Zh.Tech.Fiz., 14, 1, 9, 1988.
5. S.P.Bugaev, V.I.Kanavets, A.I.Klimov et.al. - Dokl.Akad.Nauk SSSR, 298, 1, 92, 1988.
6. A.L.Vikharev, O.A.Ivanov, A.N.Stepanov - In : High - Frequence Discharge in Wave Fields, Gorky, Inst.Appl.Phys., 1988, p.212.
7. A.L.Vikharev, V.B.Gildenburg, O.A.Ivanov et.al. - Fizika Plazmy, 12, 12, 1503, 1986.
8. W.T.Armstrong, R.A.Roussel-Durpre, R.Karl et.al. - Proc. ICPIG-18, Swansea, 1987, p.850.
9. M.P.Brizhinev, A.L.Vikharev, G.Yu.Golubyatnikov et.al. - Zh. Eksp. Teor. Fiz., 98, 2, 434, 1990.

10.D.M.Karfidov - Fizika Plazmy, 5, 4, 929, 1979.
11.J.H.Yee, R.A.Alvarez, D.J.Mayhall et.al. - Phys.Fluids, 29, 4, 1238, 1986.
12.A.L.Vikharev, V.B.Gildenburg, O.A.Ivanov et.al. - Proc. ICPIG-18, Swansea, 1987, p.106.
13.C.A.Sullivan, W.W.Destler, J.Rodgers et.al. - J.Appl.Phys., 63, 11, 5228, 1988.
14.N.D.Borisov, A.V.Gurevich, G.M.Milikh. Artificial Ionization Region in Atmosphere. IZMIR AN SSSR, 1986, 184p.
15.S.G.Arutunyan, A.A.Rukhadze - Pizika Plasmy, 5, 3, 702, 1979.
16.S.G.Arutunyan, A.V.Ignatev, A.A.Rukhadze - Pizika Plasmy, 7, 3, 604, 1981.
17.A.V.Ignatev, A.A.Rukhadze - Pizika Plasmy, 9, 6, 1317, 1983.
18.L.G.Glasov, A.A.Rukhadze - Pizika Plasmy, 15, 12, 1484, 1989.
19.A.L.Vikharev, V.B.Gildenburg, A.V.Kim et.al. In : High - Frequence Discharge in Wave Fields, Gorky, Inst.Appl.Phys., 1988, p.41.
20.S.V.Golubev, S.I.Gritsinin, V.G.Zorin et.al. In : High - Frequence Discharge in Wave Fields, Gorky, Inst.Appl.Phys., 1988, p.136.
21.G.M.Batanov, S.I.Gritsinin, I.A.Kossyi et.al. - Trudy FIAN, 160, 174, 1985.
22.N.A.Dyatko, I.V.Kochetov, A.P.Napartovich. In : High - Frequence Discharge in Wave Fields, Gorky, Inst.Appl.Phys., 1988, p.9
23.A.L.Vikharev, G.Yu.Golybyatnicov, N.A.Dyatko et.al. - Proc. 10-European Conf. on Atomic and Molecular Physics of Ionized Gases, Orleans, France, 1990, p.266.
24.A.L.Vikharev, V.A.Gintsburg, O.A.Ivanov et.al. - Proc. 10 - European Conf. on Atomic and Molecular Physics of Ionized Gases, Orleans, France, 1990, p.268.
25.V.B.Gildenburg, I.S.Guchin, S.A.Dvinin et.al. - Zh. Eksp. Teor. Fiz., 97, 4, 1151, 1990.
26.V.N.Slinko, A.S.Sulakchin, A.A.Sulakchin et.al. - Kvantovaya Elektronika, 15, 2, 292, 1988.
27.A.A.Babin, A.L.Vikharev, V.A.Gintsburg et.al. - Pis'ma v Zh. Teh. Fiz., 15, 5, 31, 1989.
28.A.L.Vikharev, O.A.Ivanov, A.V.Kim. In : Relativistic microwave electronics, Gorky, Inst.Appl.Phys., 1990, 6, p.256.

Frequency self-upshifting of ionizing electromagnetic pulse

V.B.GILDENBURG, A.V.KIM, V.A.KRUPNOV, V.E.SEMENOV,
A.M.SERGEEV, N.A.ZHAROVA
Institute of Applied Physics of the Russian Academy of Sciences,
Nizhny Novgorod, Russia

1. Introduction

A high-frequency electromagnetic pulse propagates according to a well-known physical concept without reflection in a homogeneous or a smoothly inhomogeneous gaseous medium only if its power (at a given duration) does not exceed a threshold value for the breakdown emergence. The condition, when the electron concentration N reaches the critical value $N = N_{c0} = m\omega_0 / 4\pi e^2$ during the breakdown for the time less than the pulse duration, is usually taken as a sufficient one (at low frequencies of electron collisions $\nu << \omega_0$) for reflection (cut-off) of a powerful pulse incident on the gas at frequency ω_0. Thus the value N_{c0} is considered as an upper limit of N in the propagating pulse.

However, this criterion of the signal cut-off ($N = N_{c0}$) does not take into account a possibility of a parametric transformation (increase) of the initial signal frequency ω_0 which is caused by the plasma nonstationarity. Though the frequency conversion phenomenon has been investigated earlier both for the case of

specified variations of medium parameters [1,2] and for several problems of the wave field self-effect in nonlinear media [3,4], it remains practically unstudied in nonlinear dynamics of a high-frequency discharge, where only the role of breakdown in widening [5] and small shifting [6,7] the spectrum of powerful laser pulses has been discussed. In this paper we do not aim at a thorough analysis of frequency conversion in ionized media but following our recent short publications [8,9] we want to emphasize its role in breakdown dynamics from the viewpoint of new important possibilities, which are:

a) strong increase of the signal frequency (in the final state $\omega >> \omega_0$ *);*

b) reaching the $N >> N_{c0}$ *in the reflectionless regime;*

c) total preventing cut-off during the breakdown;

d) subsequent possibility of a strong frequency shift without pronounced energy losses.

These effects can be clearly demonstrated in the case of the so-called "superstrong" fields [10] where the energy of the electron oscillations w_- is large enough in comparison with the molecule ionization energy I and where the variation of the electron momentum due to collisions takes place over the period $1/\nu$ which is much greater than the characteristic time of the electron concentration growth $1/\nu_i$. When, on the contrary, $\nu_i << \nu$ the wave is strongly damped earlier than its frequency experiences a noticeable change. Assuming further that the condition $\omega >> \nu_i >> \nu$ is fulfilled and making a supposition on a zero value (or on isotropic distribution) of the velocity of the electrons at the moment of their birth, we will start

from the equation for the wave electric field $E(x,t)$ in the form

$$\frac{\partial^2 \vec{E}}{\partial t^2} - c^2 \frac{\partial^2 \vec{E}}{\partial x^2} = -\omega_p^2 E\,, \quad \omega_p^2 = \frac{4\pi e^2 N}{m}\,. \tag{1}$$

Two different cases of gas ionization i.e. ionization of molecules by electron impact and direct (tunneling) ionization by a wave field.

2. Ionization by electron impact

The equation for the electron concentration (or for ω_p^2 which is proportional to the concentration) has in this case the form

$$\frac{\partial(\omega_p^2)}{\partial t} = \nu_i \omega_p^2\,, \tag{2}$$

(the frequency of electron losses ν_a is considered if compared to the ionization frequency ν_i). In a locally quasiharmonic field $E(x,t) = \frac{1}{2}(Ae^{i\varphi} + c.c.)$ $(\omega(x,t) = \frac{\partial\varphi}{\partial t} >> \{\nu_i, \tau^{-1}\}$, $k(x,t) = -\frac{\partial\varphi}{\partial x} >> L^{-1}$; L and τ are spatial and temporal sizes of the pulse, respectively) the ionization frequency ν_i does not depend on the oscillation phase and can be considered as the assigned function of the relation $A/\omega = U$, $\nu_i = \nu_i(U)$ [11]. This fact enables us to treat Eq.(1) in the geometrical optics approximation and to pass to the transfer equations for the local frequency and amplitude

$$\frac{\partial \omega^2}{\partial t} + \nu_g \frac{\partial \omega^2}{\partial x} = \frac{\partial \omega_p^2}{\partial t}\,, \tag{3}$$

$$\frac{\partial (A^2\omega)}{\partial t} + \frac{\partial (\nu_g A^2 \omega)}{\partial x} = 0\,, \tag{4}$$

where $\nu_g = \frac{d\omega}{dk} = c\sqrt{1 - \frac{\omega_p^2}{\omega^2}} = c\sqrt{1 - \frac{N}{N_c}}$ is the local group velocity

of the wave and $N_c = \frac{m\omega^2}{4\pi e^2}$. The local wave number k is coupled here with ω by the usial dispersion relation

$$k = \frac{\omega}{c}\sqrt{1 - \frac{\omega_p^2}{\omega^2}} \quad . \tag{5}$$

In view of relation (2) Equation (4) can be rewritten as

$$\frac{\partial A^2}{\partial t} + \frac{\partial (v_g A^2)}{\partial x} = -\frac{\nu_i}{2}\frac{\omega_p^2}{\omega^2}A^2 \, . \tag{6}$$

Note that though Eqs.(1-6) do not contain a term with the collisions frequency, and therefore not describe the wave absorption caused by electron collisions, they take into account another source of dissipation which is much stronger at $\nu_i >> \nu$. This dissipation is due to the energy transfer to newly born electrons which acquire in the wave field the oscillating component of velocity (adiabatically varying with the field amplitude) and the constant component (which depends on the field phase at the moment of electron birth and remains after the pulse).

It follows from Eq.(3) that a change in the difference $\omega^2 - \omega_p^2$ along a group trajectory (i.e. a characteristic) $x = x(t)$, $\frac{dx}{dt} = v_g$ is described by the equation

$$\frac{d(\omega^2 - \omega_p^2)}{dt} = -v_g \frac{\partial \omega_p^2}{\partial x} \, , \tag{7}$$

It means that the plasma will always remain transparent ($\omega > \omega_p$) for the pulse during the breakdown, if $\frac{\partial \omega_p^2}{\partial x} \le 0$. Below we give some solutions of the system (2-4) which meet this condition and which

have been obtained for cases allowing certain simplifications.

Let the field at the medium boundary $x = 0$ have the form of the pulse with the duration τ_p with the given amplitude A_0 and frequency ω_0, that is switched on at the moment $t = 0$ and is propagating into the region $x > 0$. The unperturbed (startup) electron density N_0 in the medium is uniform and small as compared to the critical one ($\omega_{p0}^2 << \omega_0^2$). If the duration τ_p is shorter than the critical value τ_c for the signal cut-off at the boundary

$$\tau_p < \tau_c = \frac{1}{\nu_{i0}} \ln\left(\frac{\omega_0^2}{\omega_{p0}^2}\right), \tag{8}$$

then each group element of the pulse penetrates into the medium and, while propagating, increases its frequency up to so value that depends on the function $\nu_i(U)$. This function has in the range of superstrong fields a slowly falling-down form [11] when receding from the point of the maximum ionization rate. To simplify the analysis we make use of the approximation $\nu_i = \nu_{i_0}\,\theta(U-U_c)$ where θ denotes the unit function, i.e. $\theta = 1$ when $U \geq U_c$ and $\theta = 0$ when $U < U_c$. In this case a stationary ionization wave is produced in the medium in the range $U > U_c$. The propagation velocity of this wave coincides with the velocity of the leading front of the pulse and, by virtue of the adopted condition $\omega_0 >> \omega_{p0}$, is close to the velocity of light c :

$$\omega_p^2 = \omega_{p0}^2 \exp\left[\nu_{i0}\left(t - \frac{x}{c}\right)\right]. \tag{9}$$

Since in such a wave $\frac{\partial \omega_p^2}{\partial x} < 0$, the difference $\omega^2 - \omega_p^2$ is growing continuously along the characteristics. The resulting increase (ap-

proaching c) of the velocity v_g of each group element of the pulse and the variations of ω, ω_p and A along the characteristics are determined by the relations that are derived from the basic equations for the given $\omega_p^2(x,t)$:

$$\frac{dv_g}{dt} = \frac{c\,\nu_{i_0}}{2}\left(1+\frac{v_g}{c}\right)\left(1-\frac{v_g}{c}\right)^2, \tag{10}$$

$$\omega\left(1-\frac{v_g}{c}\right) = const, \quad \omega_p^2 \frac{\left(1-\frac{v_g}{c}\right)}{\left(1+\frac{v_g}{c}\right)} = const$$

In particular, it follows from (9) and (10) that the frequency of the group element entering the medium at the time t_1 when $\omega_p(0,t_1) = \omega_{p1} << \omega_0$ (i.e., for $v_g(0,t_1) = v_{g1} \approx c$) increases according to the linear law

$$\omega = \omega_0(t_1) + \frac{\nu_{i0}\,\omega_{p1}^2}{2\omega_0(t_1)}\,(t-t_1)\,. \tag{11}$$

Since for the impact ionization mechanism considered here the rate of the frequency increase is proportional to the plasma density ($\frac{d\omega^2}{dt} = \nu_i\,\omega_p^2$), the main frequency increase always occurs near the rear front of the pulse, i.e., a strong frequency modulation emerges inside the pulse. However, the difference between the group velocities of the leading and trailing fronts of the pulse and the consequent dispersive expansion of the pulse are pronounced only for $\omega_p \approx \omega$. Defining the relative expansion of the group element on the characteristic as $\eta = \frac{dx}{dx_1}$ (where dx and dx_1 are the lengths of the group element at a given time t and at the time t_1 immediately

on entering the medium, respectively), from Eq.(10) we find

$$\eta = \frac{v_g(t)}{v_{g1}} + \left(\frac{c}{v_{g1}}\right)^2 \left(1 - \frac{\omega_0(t_1)}{\omega(t)}\right). \tag{12}$$

We can see that for $v_g(t_1) \approx c$ the value η may increase not greater than twice (from $\eta = 1$ for $\omega = \omega_0(t_1)$ to $\eta \approx 2$ for $\omega >> \omega_0$). The decrease of the field amplitude on the characteristic in the presence of dispersive expansion is described by the integral of Eqs.(2-4)

$$A^2(t)\,\omega(t)\,\eta(t) = A_0^2(t_1)\,\omega_0(t_1) = const. \tag{13}$$

This equation under the condition $U(t) = \frac{A}{\omega} = U_c = \frac{A_c}{\omega}$ yields the limiting value for the frequency

$$\omega_{max} = \omega_0 \left(\frac{A_0^2}{A_c^2\,\eta_{max}}\right)^{\frac{1}{3}}. \tag{14}$$

When $v_{g1} \approx c$ we have $\eta_{max} \approx 2$.

The pulse evolution can relatively simply be investigated as well for varying $v_i(U)$ ($\frac{\partial v_i}{\partial U} < 0$ at $U > U_c$) and $\omega_{p0}^2(x)$, assuming $v_g = c$ ($\omega_p << \omega$), i.e., neglecting the dispersive expansion. Within this approximation equations for ω, ω_p, A have the form

$$\frac{d\omega^2}{dt} = \frac{\partial \omega_p^2}{\partial t} = v_i(U)\,\omega_p^2\,, \quad \frac{d\,A^2\omega}{dt} = 0\,, \quad \frac{d}{dt} = \frac{\partial}{\partial t} + c\frac{\partial}{\partial x}. \tag{15}$$

At constant values of A_0 and ω_0, the solutions of these equations reduce to the solution of the first-order equation

$$\frac{d\omega^2}{d\xi} = \nu_i(U)\,(\omega^2 - \omega_0^2)\ ,\ U = U_0\left(\frac{\omega_0}{\omega}\right)^{\frac{3}{2}}\ , \qquad (16)$$
$$\xi = t - \frac{x}{c} + f(x)\ ,\ \omega_p^2 = c\,\frac{df(x)}{dx}\,(\omega^2 - \omega_0^2)\ .$$

The function $f(x)$ is determined from the condition $\omega_p^2(\,t = \frac{x}{c}\,) = \omega_{p0}^2(x)$ at the leading front of the pulse. If ω_{p0}^2 is sufficiently small, so that the frequency shift at the leading front of the pulse is not large ($\Delta\omega^2 = \frac{\nu_i(U_0)}{c}\int_0^L \omega_{p0}^2(x)\,dx << \omega_0^2$) at a finite path $x \le L$, we will have

$$f(x) = \frac{1}{\nu_i(U_0)}\ \ln\int_0^x \omega_{p0}^2(x)\,dx\ . \qquad (17)$$

In the simplest case $\omega_{p0} = const << \omega_0$ ω grows explosively on the characteristic $x(t)$ for $\frac{d\nu_i}{dU} < 0$. The maximal value $\omega_{\max}$ (that coincides with (14) at $\eta_{\max} = 1$ within this approximation) is attained at a distance $x = l$ from the boundary. This distance has the order of magnitude of the length $l_0 = \frac{2\,c\,\omega_0^2}{\nu_{i0}\,\omega_{p1}^2}$, at which there occurs the doubling of frequency obeying the linear law (11) when $\nu_i = \nu_{i0} = const$. Beside ω, the plasma frequency ω_p also grows explosively on the characteristic. Being small as compared to ω, the plasma frequency becomes much higher than its input value ω_{p1} and may exceed the startup frequency of the pulse:

$$\omega_p^2(l) \approx \omega_{p1}^2\left(\frac{\omega_{\max}}{\omega_0}\right)^2\frac{l_0}{l}\ . \qquad (18)$$

For a small value of total ionizing power of the pulse $\nu_i \tau_p << 1$, the problem is also solved rather easily when ω_{p0} is not constant and is small in comparison with ω_0. The frequency modulation inside the pulse is not great for small $\nu_i \tau_p$ and the equation for the frequency of all group elements has the form

$$\frac{d\,\omega^2}{d\,t} = \nu_i(U)\,\omega_{p0}^2(x)\,. \tag{19}$$

In this case the dispersion is weak ($\omega >> \omega_p$, $v_g \approx c$) even in the region $\omega_{p0}(x) >> \omega_0$, provided the initial electron density grows in space rather smoothly: $L_N = \omega_{p0}^2 \left(\frac{d\,\omega_{p0}^2}{d\,x} \right)^{-1} >> \frac{c}{\nu_i}$. Then, the solution of Eq.(16) describing the increase of the frequency ω of a short pulse in an inhomogeneous plasma can be written as follows:

$$\int_{\omega_0}^{\omega} \frac{2\omega\,d\omega}{\nu_i(U(\omega))} = \frac{1}{c} \int_0^x \omega_{p0}^2(x)\,dx \;,\; (\omega \le \omega_{max})\,. \tag{20}$$

If we do not restrict our consideration to the case of weak dispersion, then it is sufficient to fulfil the inequalities $L_N > \frac{c}{\nu_i}$, $L_N > c\tau_p$ so as to meet the condition $\frac{\partial \omega_p^2}{\partial x} < 0$, that prevents, according to (7), the wave reflection and provides advanced growth of ω as compared to ω_p in an inhomogeneous plasma with $\omega_{p0}(x) > \omega_0$. Thus, additional ionization produced by the pulse not only blocks the signal but, paradox as it might appear at first sight, also makes the opaque ($\omega_{p0} > \omega_0$) plasma in the gas more transparent, which is due to the frequency self-conversion. Of course, the potentialities of such an "ionization transparency" are restricted by the dissipative processes

that result in the case of impact ionization in a relatively fast decrease of the field amplitude ($A^2 \sim \frac{1}{\omega}$) and in the termination of the growth of ω when $A = A_c$.

Note that the apparent restriction of $\tau_p < \tau_c$ in (8) imposed on the maximum duration of the pulse that can be injected without cutoff into a homogeneous medium with $\omega_{p0}(0) \neq 0$, is lifted if the medium boundary is spread out, i.e., if there is an extended interface where the gas density and, hence, ionization frequency $\nu_i(U,x)$ increase gradually (up to the same maximum values) with x. The scale of this interface $L = \nu_i \left(\frac{\partial \nu_i}{\partial x} \right)^{-1}$ must be larger than the pulse length ($L > c\tau_p$). Here, like in a plasma with a smoothly growing initial density $\omega_{p0}^2(x)$, we have $\frac{d(\omega^2 - \omega_p^2)}{dt} = -\nu_g \frac{\partial \omega_p^2}{\partial x} > 0$, i.e. the pulse is never reflected (even when $\tau_p >> \tau_c$).

To conclude the present section, we will give estimations exemplifying the possibilities of observing the effect of ionization frequency self-conversion for the microwave radiation. Since the pulse is strongly frequency-modulated, the important parameter characterizing the effect is, along with the maximum relative frequency shift $\frac{\Delta\omega_{max}}{\omega_0}$, the duration of the tail part Δt of the converted pulse (or the number of periods of the field $n = \frac{\omega_0 \Delta t}{2\pi}$), where $\Delta\omega \approx \Delta\omega_{max}$. Setting the values of ω_0, $\Delta\omega_{max}$, n determines ionization frequency $\nu_{i0} \approx \frac{1}{\Delta t} = \frac{\omega_0}{2\pi n}$, minimum length of the path

$L_{\min} = \lambda_0 \, n \frac{\Delta\omega_{\max}}{\omega_0}$ ($\lambda = \frac{2\pi c}{\omega_0}$), at which this shift takes place, and pulse duration $\tau_p \geq \frac{1}{\nu_{i0}} \ln\left(\frac{\omega_0}{\omega_{p0}}\right) \approx \frac{20}{\nu_{i0}}$, corresponding to the condition of reaching that minimum ($\omega_{p\max} \approx \omega_0$). Particularly, at $\lambda_0 = 3cm$ ($\omega_0 = 6 \cdot 10^{10} \frac{1}{s}$), $n = 10$, $\frac{\Delta\omega_{\max}}{\omega_0} \approx 1$ we have: $L_{\min} = 60\,cm$, $\nu_{i0} = \frac{1}{\Delta t} = 10^9\,s$, $\tau_p \geq 2 \cdot 10^{-8}\,s$. This value of ν_{i0} can be achieved in the fields of modern powerful microwave generators that produce energy flux densities $S \approx 10^7 \frac{W}{cm^2}$ ($w_{\sim} \approx 1KeV$) under gas (air) pressure $p \approx 0.2\,Torr$.

3. Direct ionization by wave field

In the fields of high-intensive laser pulses, which are not small as compared to the interatomic values the probability of the subbarrier electron tunneling from external atomic shells increases sharply so that direct separation of electrons from atoms by the wave field can be the dominating ionization mechanism. In the parameter range $\hbar\omega << I << w_{\sim}$ the ionization rate W at each moment can be determined on the basis of the known expression for the ionization probability in a static field [12,13]:

$$\frac{\partial\omega_p^2}{\partial t} = W = \gamma\,\omega_{pm}^2 \exp\left(-\frac{E_a}{|E(x,t)|}\right). \qquad (21)$$

Here $|E(x,t)|$ is the instantaneous absolute value of the electric field strength; $\omega_{pm}^2 = \frac{4\pi e^2 N_m}{m}$, N_m is the neutral particle density in gas,

$E_a = \frac{4\sqrt{2m}\, I^{3/2}}{3\hbar e}$ is a characteristic interatomic field, I is the ionization energy. The preexponential factor $\gamma \approx \frac{I}{\hbar}$ and the term ω_{pm} will be considered as given constants assuming that the conditions

$$N_m >> N \ , \ \gamma >> \omega \ , \ E_a >> A \qquad (22)$$

are satisfied. The last condition agrees with the initial assumption of slow variation of $<\omega_p^2>$ (at $A > E_a$ the gas is fully ionized over a time $\frac{1}{\omega}$) and makes it reasonable (from the qualitative point of view, at least) to neglect the dependence of the preexponent on the field E in (21). The impact-induced ionization in (21) can be neglected provided $\frac{\gamma}{\omega} >> \ln\left(\frac{\gamma N_m}{\nu_i N}\right)$.

For a wave with circular polarization we have $|E| = A$ and W does not depend on the field phase, which is similar to the impact ionization case. The difference is observed only in the law of the electron density growth in the discharge: W depends solely on the field amplitude A and does not increase with N, thus influencing, of course, the form of the functions $\omega(x,t)$ and $A(x,t)$.

In particular, in the case of homogeneous ionization, in the field of an infinite plane wave ($k = const$, $A^2\omega = const$) the equation for frequency and its solution (that governs the dependence $t\left(\frac{\omega}{\omega_0}\right)$) are given by

$$\frac{d\omega}{dt} = \frac{\gamma}{2\omega}\omega_{pm}^2 \exp\left(-\frac{E_a}{A_0}\sqrt{\frac{\omega}{\omega_0}}\right), \qquad (23)$$

$$t = \frac{4\omega_0^2}{\gamma\omega_{pm}^2 a}\left(q^{3/2}\, e^{a\sqrt{q}} - e^{a}\right), \qquad (24)$$

where $a = \frac{E_a}{A_0}$, $q = \frac{\omega}{\omega_0}$.

Below, primary attention is paid to the case of linearly polarized wave ($E = A\cos\varphi$), which presents an interesting possibility of decreasing appreciably the dissipation rate because of the nonuniform electron production over the field period.

In this case the density N that enters the set of equations (1),(21) contains rapidly oscillating components, owing to which the simplest (geometrical optics) approximation used above becomes incorrect and needs significant modification. Deriving the equation for the fundamental harmonic of the electric field we must take into account contribution of the product NE made by zero (average over φ) and by the second ($\sim \sin 2\varphi$) harmonics of density N.

Assuming

$$\frac{\partial\, \omega_p^2}{\partial t} = W = \langle W\rangle + W_2 \cos 2\varphi + \ldots , \qquad (25)$$

we find

$$\omega_p^2 = \langle\omega_p^2\rangle + \frac{W_2}{2\omega}\sin 2\varphi + \ldots , \qquad (26)$$

$$W_2 = \frac{1}{\pi}\int_0^{2\pi} W \cos 2\varphi \, d\varphi ,$$

which yields the following expression for the fundamental harmonic of the product $\omega_p^2 E$:

$$\langle\omega_p^2 E\rangle = A\left(\langle\omega_p^2\rangle\cos\varphi + \frac{W_2}{4\omega}\sin\varphi\right). \qquad (27)$$

The contribution of higher harmonics of N and E to this term can be neglected due to "nonresonant" character of their excitation.

Further simplifying Eq.(1) with the right-hand side (27) in a usual fashion (by omitting the second derivatives of the amplitude A), we arrive at the following equations for frequency and amplitude that generalize the set (3) - (5) :

$$\frac{\partial \omega^2}{\partial t} + v_g \frac{\partial \omega^2}{\partial x} = \frac{\partial < \omega_p^2 >}{\partial t} , \tag{28}$$

$$\frac{\partial (A^2\omega)}{\partial t} + \frac{\partial (v_g A^2\omega)}{\partial x} = \left(\frac{W_2}{4\omega}\right) A^2 , \tag{29}$$

$$\omega^2 = < \omega_p^2 > + k^2 c^2 . \tag{30}$$

Equations (28)-(30) can readily yield the transfer equation directly for the wave intensity A^2

$$\frac{\partial (A^2)}{\partial t} + \frac{\partial (v_g A^2)}{\partial x} = -\left(\frac{1}{2} <W> - \frac{1}{4} W_2\right) \frac{A^2}{\omega^2} . \tag{31}$$

Note that this equation may also be obtained by direct averaging of the relation for the energy conservation law in electrodynamics (Pointing theorem) for a quasi-harmonic field. Within this approach, we can also easily find the above neglected energy losses on the separation of an electron from an atom. When these losses are taken into account in the case of field ionization of atoms by radiation an additional term $-\frac{2m}{e^2} <W> I$ appears in the right-hand side of (31). Obviously this term is negligible in the region of superstrong fields where $w_{\sim} = \frac{e^2 A^2}{m \omega^2} >> I$;

Defining the Fourier expansion coefficients $<W>$, W_2 of the

function $W(\varphi)$, given by (21) at $|E| = A\,|\cos\varphi|$ we obtain the equations for $\langle\omega_p^2\rangle$, ω^2 and A:

$$\frac{\partial \langle\omega_p^2\rangle}{\partial t} = \langle W\rangle, \quad \frac{\partial \omega^2}{\partial t} + v_g \frac{\partial \omega^2}{\partial x} = \frac{\partial \langle\omega_p^2\rangle}{\partial t}, \tag{32}$$

$$\frac{\partial (A^2)}{\partial t} + \frac{\partial (v_g A^2)}{\partial x} = -F = -\langle W\rangle \frac{A^3}{E_a \omega^2} \tag{33}$$

$$\langle W\rangle = \gamma\, \omega_{pm}^2 \sqrt{\frac{2A}{\pi E_a}} \exp\left(-\frac{E_a}{A}\right). \tag{34}$$

In this case $A << E_a$ the ionization occurs mainly in the phases of field maximum ($\cos\varphi = \pm 1$), where the constant drift component of the electron velocity $v_0 = \frac{eA}{m\omega} \sin\varphi = 0$. That is why the right-hand side ($-F$) of the intensity transfer equation (33), which defines the wave energy dissipation rate, is strongly decreased ($F = F_0 \frac{A}{E_a}$) as compared to its "geometrooptical" value $F_0 = \langle W\rangle \frac{A^2}{\omega^2}$ corresponding to the uniform distribution of electron production over the field period.

We now analyze the solutions of Eqs.(32)-(34) for the case of laser pulse penetration into the medium.

We restrict ourselves to the small pulse duration τ_p assuming that in an unperturbed medium the ionization is absent and the velocity of the pulse leading front is c, while the pulse-produced perturbations are small ($\langle W\rangle \tau_p << \omega^2$), so that the rear front velocity $v_g \approx c$ ($0 < c - v_g << c$). The weak frequency modulation inside the pulse, which occurs in the transition through the medium boundary ($x = 0$), can be fully neglected bearing in mind that variations in

ω and A are accumulated only on a sufficiently long path. In variables t, $\tau = t - \frac{x}{c}$ Eqs. (32), (33) can be written as

$$\frac{\partial <\omega_p^2>}{\partial \tau} = <W> \quad , \quad \frac{\partial \omega^2}{\partial t} + \frac{1}{2}\frac{<\omega_p^2>}{\omega^2}\frac{\partial \omega^2}{\partial \tau} = <W> \ , \tag{35}$$

$$\frac{\partial (A^2)}{\partial t} + \frac{\partial}{\partial \tau}\left(\frac{1}{2}\frac{<\omega_p^2>}{\omega^2}A^2\right) = - <W> \frac{A^3}{E_a \omega^2} \ . \tag{36}$$

We have adopted $1 - \frac{v_g}{c} = \frac{<\omega_p^2>}{2\omega^2}$ and discarded the small term $\frac{\partial <\omega_p^2>}{\partial t}$ in the equation for $<\omega_p^2>$.

An important solution of Eqs.(35), (36) is the rectangular pulse with varied duration $\tau_p(t)$, homogeneous carrier frequency $\omega(t)$ and amplitude $A(\tau,t)$, assigned as

$$\begin{cases} A = A(\tau) \ ; \ 0 \le \tau \le \tau_p(t) \ , \\ A = 0 \quad ; \ \tau < 0 \ , \ \tau > \tau_p(t) \end{cases} ,$$

$$A(0) = A_0 \ , \ \tau_p(0) = \tau_{p0} \ .$$

The quantity $<\omega_p^2>$ inside the pulse increases when receding from the leading front according to the linear law $<\omega_p^2> = <W> \tau$ and reaches its maximum on the rear front:

$$<\omega_p^2>(x) = <W> \tau_p(t_2) \ , \tag{37}$$

where $t_2(x) = \frac{x}{c}$ is the time when the rear front passes through the point x. The function $\omega_p^2(x)$ defines, evidently, the structure of the plasma wake produced by the pulse in the gas. The functions $\omega^2(t)$, $A^2(t)$ are described by the equations in full derivatives

$$\frac{d\omega^2}{dt} = <W> \ , \tag{38}$$

$$\frac{dA^2}{dt} = -A^2 \frac{<W>}{2\omega^2} - A^3 \frac{<W>}{E_a \omega^2} \ . \tag{39}$$

Since $A << E_a$, the second term in the right-hand side of the equation for A^2, responsible for the wave absorption, is negligible as compared to the first term taking into account the dispersion spreading, which, unlike the impact ionization case, is the main factor governing the amplitude variation. Equations (38), (39) have the integral $A^2\omega = const$, i.e., the relationship between A and ω for this short pulse is the same as in the case of spatially homogeneous ionization (in the initial problem with $k = const$) with a rate independent of the field phase ($W_2 = 0$).

The variation of pulse duration $\tau_p(t)$ and the dispersion spreading of group elements $\eta = \frac{\tau_p}{\tau_{p0}}$ are defined by the group velocity difference on the leading and the rear fronts

$$\frac{d\tau_p}{dt} = \frac{\omega_p^2(t_2)}{2\omega^2} = \frac{1}{2} \frac{\tau_p}{\omega^2} \frac{d\omega^2}{dt} \ . \tag{40}$$

Therefore, we have $\frac{\tau_p}{\omega} = const$, $\eta = \frac{\omega}{\omega_0}$, and the pulse length $l = c\,\tau_p = l_0 \frac{\omega}{\omega_0}$ grows in proportion to the pulse frequency, which leads to a constant value $A^2\omega$ provided the total pulse energy is retained ($\varepsilon = \frac{A^2 l}{8\pi} \approx const$).

The relative change in the total energy, which was neglected by the omitting dissipative term in Eq.(39), can be directly determined

from Eq.(36) by

$$\frac{|\Delta\varepsilon|}{\varepsilon_0} = -2\frac{A_0}{E_a}\left(1-\sqrt{\frac{\omega}{\omega_0}}\right) << 1 \qquad (40)$$

and is small at any arbitrary $\frac{\omega}{\omega_0}$.

Integrating equation (38) taking into account Eq.(34) and the condition $A^2\omega = const$ we find the time t for the frequency rise to a given level $\omega = q\omega_0$:

$$t = \frac{\sqrt{8\pi}\,\omega_0^2}{\gamma\omega_{pm}^2\sqrt{a}}\left(q^{1/4}\,e^{a\sqrt{q}} - e^{a}\right), \qquad (42)$$

$$a = \frac{E_a}{A_0} << 1 .$$

This expression is slightly different (since the expression for $<W>$ was changed) from that obtained above for an infinite wave with circular polarization (24). Meanwhile, a common feature in these two cases is the sharp slowdown of the frequency conversion even at a rather small relative shift $\Delta q = \frac{\Delta\omega}{\omega_0} \approx \frac{A_0}{E_a}$ and the exponential growth of the path length $x = ct$ needed for large q to be achieved. The frequency conversion coefficient $q = \frac{\omega}{\omega_0}$ cannot exceed some limiting values because of adopted constraints $w_- > I$ and $A < E_a$. Owing to the strong decrease of energy, imparted by the wave to electrons, the losses for separating electrons from atoms become comparable. Including this factor leads to replacing the value $A^2\omega$ by the sum $A^2\omega + \frac{4m\omega^3 I}{3e^2}$ as the integral of the problem. As a result, the constraint reduces to the following requirement at $A \to 0$

$$q < q_{\max} \approx \left(\frac{w_0}{I}\right)^{\frac{1}{2}},$$

where $w_0 = \dfrac{e^2 A_0^2}{m\omega_0^2}$.

It is interesting to note that while the main spectral line of the short pulse under consideration is shifted up the frequency scale, the local width (measured at each given x) of this line $\delta\omega(x)$ decreases. Actually, estimating $\delta\omega(x)$ as a sum of two terms $\delta\omega = \delta\omega_1 + \delta\omega_2$, the first of which is defined by the finite pulse duration ($\delta\omega_1 \approx \dfrac{1}{\tau_p}(x) = \dfrac{\omega_0}{\omega\tau_{p0}}$) and the second, by the frequency shift over a time τ_p ($\delta\omega_2 \approx \dfrac{\tau_{p0} <W>}{2\omega_0}$), we find that with an increase in x we have $\delta\omega_{1,2} \to 0$, and $\delta\omega_2 << \delta\omega_1$ at large distances x, so that

$$\delta\omega \approx \delta\omega_1 = \frac{\omega_0}{\omega(x)\,\tau_{p0}}. \qquad (43)$$

In conclusion, we give estimates for the frequency conversion efficiency of laser pulses for two cases of interest at the present time, approximately within the framework of the above idealizations:

1) the pulse of a CO_2 - laser of $\tau_{p0} < 1\,ps$, energy flux density $S = 4 \cdot 10^{14}\,W/cm^2$ in atomic gas with $I \approx 15\,eV$ at pressure $p = 300\,Torr$;

2) the pulse of a KrF - laser $\tau_{p0} < 0.3\,ps$, $S = 3 \cdot 10^{15}\,W/cm^2$ at $I \approx 25\,eV$ (helium) and $p = 30 atm$.

In both cases the pulses undergo frequency doubling over a time $\tau \approx 30\,ps$, i.e., on a rather short path $L \approx 1\,cm$.

References

[1] N.S. Stepanov, *Izv. VUZ-ov - Radiofizika*, 1976, vol.19, p.960.

[2] Yu.A. Kravtsov, Yu.I. Orlov, *Geometrical optics of nonhomogenous media*. Nauka, Moscow, 1980.

[3] E. Yablonovitch, N. Blombergen, *Phys. Rev. Lett.*, 1972, vol.29, p.907.

[4] S.A. Akhmanov, V.A. Vysloukh, A.S. Chirkin, *Optics of femtosecond laser pulses*, Nauka, Moskow, 1988.

[5] P.B. Gorkum, C. Rolland, T. Srinivasan-Rao, *Phys. Rev. Lett.*, 1986, vol.57, p.2268.

[6] W.M. Wood, G. Focht, M.C. Downer, *Opt.Lett.*, vol. 13, p.984, 1988.

[7] S.P. Kuo, *Phys.Rev.Lett.*, vol.65,p.1000, 1990.

[8] V. B. Gildenburg, V. A. Krupnov, V. E. Semenov, *Sov. Tech. Phys. Lett.*, vol. 14, p. 738, 1988.

[9] V.B. Gildenburg, A.V. Kim, A.M. Sergeev, *JETP Lett.*, vol. 51, p. 104, 1990.

[10] S.G. Arutyunyan, A.A. Rukhadze, *Sov. J. Plasma Phys.*, vol. 5, p. 395, 1979.

[11] L.G. Glazov, A.A. Rukhadze, *Sov. J. Plasma Phys.*, vol. 15, p.863, 1989.

[12] L.V.Keldysh, *JETP*, vol.20, p.1307, 1965.

[13] L.D. Landau, E.M. Livshitz, *Quantum Mechanics*, 3rd ed., Pergamon, London, 1978.

The Breakdown of Rarefied Gas in Inhomogeneous Superstrong Electromagnetic Fields

S.F.Lirin, V.E.Semenov
Institute of Applied Physics
Academy of Sciences of the USSR, Nizhny Novgorod, USSR

This paper is devoted to the problem attracting much research interest at present: microwave discharge in so-called superstrong electromagnetic fields (EMF) [1-9], where the energy of electron oscillations exceeds considerably the ionization potenial of neutral particles ($\varepsilon \gg I$). Theoretical study of high-frequency (HF) gas breakdown in such fields has been limited up to the present by investigations of electron kinetics in the frames of a homogeneous space model [1,3], in which the electron avalanche growth rate γ is reduced actually to averaging the frequency of the impact ionization ν_1 for one electron over the period of its oscillation in a HF field [2,9]. The main attention in our paper is paid to breakdown kinetics in the case when field spatial nonuniformity scale Λ is less than or of the order of the electron free path length ℓ. The reason for this is that when we deal with localized field and gas is sufficiently rarefied then the process of electron expansion out of the strong field region is of vital importance for the breakdown dynamics. Simple estimates and experiments carried out recently show that this process may decelerate considerably and even suppress entirely the development of electron avalanche. Nevertheless in all previous researches concerning breakdown kinetics in superstrong EMF the electron expansion out of the field region has not been taken into account. In this paper we propose several methods of the the analysis of kinetics of the rarefied gas HF breakdown in inhomogeneous superstrong fields; the main results of this analysis for the cases of linear and circular polarization of the electric field are given.

One of the most important task in describing of HF discharge

dynamics is to determine the effective frequency of electron losses because of electrons going away out of field region (ν_e). In the fields of moderate intensity the electron thermal speed is much greater then effective velocity of oscillations, and the value of ν_e is determined by the average intensity of microwave radiation and the correlation between spatial scales ℓ and Λ. On the contrary in the superstrong fields, when ionization collisions play a main role in breakdown kinetics, the average electron velocity is of the order of oscillation one. Therefore, in this case the type of field polarization and spatial structure of field nonuniformity can essentially influence development of gas breakdown. A rough estimate of ν_e is as follows usually [9]:

$$\nu_e \approx \upsilon_\sim / \Lambda , \qquad (1)$$

where $\upsilon_\sim$ is the characteristic electron oscillatory velocity in the region of strong field. However,a characteristic peculiarity of the gas breakdown in HF fields is a strong influence of the processes of the ionization balance on the electron distribution function (EDF). Therefore, to estimate the effective frequency of the electron losses correctly, one should, generally speaking, solve the corresponding kinetic equation. To set the problem we have neglected all electronmolecule collision effects except ionization ones.For simplicity we assume also that electrons in the processes of impact ionization appear uniformly in all field phases [1,3]. In the frames of these approximations the kinetic equation for electrons averaged over high frequency $\omega \gg \nu_i$ can be represented in a form:

$$\frac{\partial f}{\partial t} + \mathbf{v}\,\nabla f - \nabla\Phi\,\frac{\partial f}{\partial \mathbf{v}} = f_0\,\nu_i\,N , \qquad (2)$$

where $f(\mathbf{v},\mathbf{r},t)$ is the function of electron distribution in velocities $\mathbf{v}$ of "the guiding centers" (i.e. in velocities averaged over the field frequency), $N(\mathbf{r},t) = \int f(\mathbf{v},\mathbf{r},t)d^3\mathbf{v}$ is the electron density in plasma, the function $f_0(\mathbf{v},\mathbf{r})$ corresponds to the field phase equipartition of nascent electrons, $\nu_i(\mathbf{r})$ is the frequency of ionization by the electron impact averaged over the field frequency ($\nu_i(\mathbf{r})$ is assumed to be locally associated with the electric field amplitude because the impact ionization as it was men-

tioned is defined by the oscillatory motion of electrons[1], $\Phi(\mathbf{r})$ is the potential of the HF ponderomotive action on electrons. To define the relation between the temporal growth rate of the electron avalanche γ and the space distribution $\nu_i(\mathbf{r})$, it is more convenient to solve the inverse problem: assigning the value γ (i.e. assuming $f(\mathbf{v},\mathbf{r},t) \sim exp\{\gamma t\}$) and the space distribution of ionization intensity $J(\mathbf{r}) \equiv \nu_i(\mathbf{r})\, N(\mathbf{r},t)\, exp\{-\gamma t\}$ we find EDF and the electron concentration solving the kinetic equation with the assigned source, than we restore the corresponding distribution of the ionization frequency in space: $\nu_i(\mathbf{r}) = J(\mathbf{r})\, exp\{\gamma t\} / N(\mathbf{r},t)$. The most simple case for solving this problem is $\nabla\Phi=0$, corresponding to the HF field homogeneous in the bounded breakdown region and to free electron expansion. In particular, in the field of circular polarization all the electrons born in the process of ionization acquire uniform speed equal to the velocity of the electron stimulated rotation in the field $v_0=eE/m\omega$ (E is the electric field intensity, e,m are the electron charge and mass). Therefore $f_0(\mathbf{v},\mathbf{r}) = \delta(v - v_0)$, where $v = |\mathbf{v}|$, $\mathbf{v},\mathbf{r}$ are the vectors in the polarization plane of the rotating electric field and from (2) we have:

$$N(\mathbf{r},t) = exp\{\gamma t\} \int \frac{J(\mathbf{r}')}{2\pi v_0 |\mathbf{r} - \mathbf{r}'|}\, exp\left\{-\gamma |\mathbf{r} - \mathbf{r}'| / v_0\right\} d^2\mathbf{r}'. \quad (3)$$

If the field space distribution has axis symmetry we find from here that

$$\nu_i = N(0,t)\, v_0 \left[\int_0^{\Lambda} N(\mathbf{r},t)\, exp\{-\gamma r / v_0\}\, d\mathbf{r}\right]^{-1} \approx \frac{\gamma}{1 - exp\{-\gamma\Lambda / v_0\}}, \quad (4)$$

because $N(\mathbf{r},t) \approx const$ in the breakdown region: $r \equiv |\mathbf{r}| < \Lambda$. The result obtained shows (see Fig.1), that according to estimate (1) the breakdown in strong circularly polarized field may occur only at $\nu_i > v_0/\Lambda$, i.e. there is a breakdown threshold of gas pressure. pressure. The case is somewhat different with the field linear polarization. In this case the constant component of the electron velocity depends on the field phase at the moment of their birth. The electrons appearing at the moment when the intensity of the

---

[1] Outside the strong field, impact ionization is defined by the time independent electron velocity component, however, the electrons born here can not get the energy from the field and, consequently, do not influence the breakdown evolution.

electric field is almost maximal leave the breakdown region very slowly. That is why the estimate (1) generally speaking is not true, and the breakdown can develop principally at the smallest value of the relation $\nu_i \Lambda/v_0$. The solution of the inverse problem in the frames of a one-dimensional problem has the following form:

$$N(x,t) = exp\{\gamma t\}\int dv\, f_0(v)\int dx' \frac{J(x')}{2|v|}\, exp\{-\gamma|x-x'|/|v|\}\ , \qquad (5)$$

where $f_0(v)=\left(\pi\sqrt{v_0^2 - v^2}\right)^{-1}$ correspond to the field phase equipartition of electrons at the moment of their birth, $v_0=eE_0/m\omega$, E_0 is the electric field amplitude in the breakdown region, Assuming as earlier that $N(x,t) \approx const$ in the breakdown region $|x|< \Lambda$, we find that at small ν_i ($\nu_i \ll v_0/\Lambda$) γ is exponentially small:

$$\gamma\Lambda/v_0 \approx exp\{-\pi v_0/\ 2\Lambda\nu_i\}. \qquad (6)$$

Figs.1,2 give some results of the numerical solution of this problem which illustrate the absence of the breakdown threshold of the gas pressure and the deprivation EDF of quick particles in the field of linear polarization. The processes associated with ponderomotive action of HF field on electrons (unlike the fields with moderate intensity) might influence greatly the development of the breakdown in superstrong inhomogeneous fields.For example, when the field intensity is almost minimal, owing to the formation of trapping electrons the losses of charged particles might vanish almost completely and the electron avalanche development

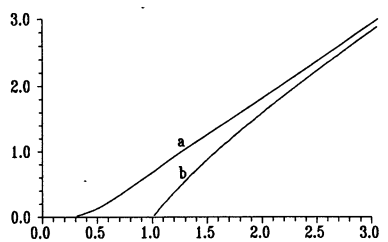

Fig.1

The electron avalanche growth rate $\gamma = \mu v_0/\Lambda$ as a function of relation $\eta = \nu_i\Lambda/v_0$ for circular - a and linear - b field polarization.

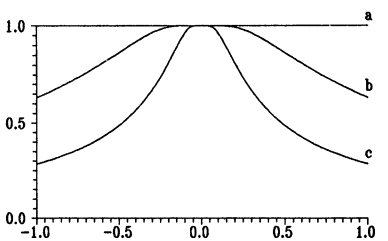

Fig.2

Normalize to $f_0 = \frac{1}{\pi}(v_0^2 - v^2)^{-1/2}$ the EDF i velocities of guiding centers $F=f(v,x=0,t)/f_0$, $u=v/v_0$ if the fieldp olarization is linear for varios values of parameter $\mu=\gamma\Lambda/v_0$: a $\mu=10$; b- $\mu=1$; c- $\mu=.333$

is possible even if gas is highly rarefied. On the other hand, when the field intensity is almost maximal,owing to the electrons throwing out from the region of the strong field the particle losses increase and, consequently, hinder the breakdown. If the field polarization is circular, the increase of electron losses due to this process is not very essential, but if the field polarization is linear, the electron losses because of their throwing out from the region of strong field might be determining. Indeed, solving the kinetic equation (2) with respect to N at the assigned source of ionization J (when the field intensity is almost maximal) we can readily obtain for the axisymmetric distribution of the circularly polarized field:

$$N(0,t) = exp\{\gamma t\} \int_0^R \frac{J(r)}{\omega_\sim(r)} exp\{-\gamma\tau(r)\}dr \qquad (7)$$

Here radius R corresponds to the boundary of the region from which the electrons born with a constant velocity component equal to $\omega_\sim(r)$ can reach the origin of coordinates, i.e. $\omega_\sim^2(0)=2\omega_\sim^2(R)$; $\tau(r)$ is the time during which the electrons born at the distance r from the origin of coordinates reach it. This suggests, in particular, that the value $\nu_1 \approx 1 / \int_0^R \frac{1}{\omega_\sim(r)} dr \approx \omega_\sim(0)/\Lambda$ corresponds to the breakdown threshold ($\gamma = 0$). For the case of linear polarization solving the kinetic equation for the field intensity almost maximal ($\Phi(x) \le \Phi(0) = 0$) we obtain:

$$N(0,t) = exp\{\gamma t\} \int \frac{J(x)\, \ell_0(\omega,x)}{2\sqrt{\omega^2 + 2\Phi(x)}} exp\{-\gamma\tau(\omega,x)\}\, d\omega\, dx , \qquad (8)$$

where $\ell_0(\omega,x) = \left(\pi \sqrt{\omega_\sim^2(x) - \omega^2}\right)^{-1}$, $\tau(\omega,x)$ is defined analogous to $\tau(r)$ in (7), and the integration is performed for the whole parameter range, where the under-the-integral expression is valid.The analysis of the expression obtained (8) shows that the estimate γ (6) is valid only for a very high degree of the field homogeneity in the breakdown region when $4\Phi(x) \equiv \omega_\sim^2(0) - \omega_\sim^2(x) \ll exp\{-\pi\omega_\sim(0)/\Lambda\nu_1\} \ll 1$. If the field inhomogeneity is greater then the mentioned one, in the case of linear polarization the breakdown is also of the threshold character and to estimate the corresponding threshold value of the ionization frequency one may use the following formula:

$$\nu_1 \approx (\omega_0/\Lambda) \left[1 + ln(\omega_0/u) \right]^{-1} \qquad (9)$$

where $v_0 = v_\sim(0)$, $u = \sqrt{2\,\Phi(\Lambda)}$ is the velocity acquired by an electron, which was initially motionless, when it reaches the boundary of quasi homogeneous field.

REFERENCES

1. Arutyunyan S.G., Rukhadze A.A.//Fizika plazmy,1979,Vol.5, vyp.3,p.702.

2. Shveigert V.A.//Fizika plazmy,1989,Vol.15,vyp.10, p.1224.

3. Glazov L.G., Rukhadze A.A. //Fizika plazmy, 1989, Vol.15, vyp.12,p.1484.

4. L.C.Pitchford, Y.M.Li, G.N.Hays et.al.//XVIII ICPIG, Contr. Papers /Swansea,1987,Vol.1,p.80.

5. Sullivan C.A., Destler W.W., Rodgers J. et. al.//J. Appl. Phys.1988,Vol.63,No.11,p.5228.

6. Vikharev A.L., Golubyatnikov G.Yu., Eremin B.G. et. al. //ESCAMPIG 90. Abstracts of invited Talks & Contr. Papers. /Orleans, 1990.Vol.14E,p.140.

7. Bogomolov Ya.L., Lirin S.F, Semenov V.E., Sergeev A.M. //Pis'ma v ZhETF,1987,Vol.45,vyp.11,p.532.

8. Gil'denburg V.B., Krupnov V.A., Semenov V.E. //XIX ICPIG, Contr. Papers Part 4 /Belgrad,1989,p.826.

9. Brizhinev M.P., Vikharev A.L., Golubyatnikov G.Yu. et.al. //ZhETF,1990,Vol.98,vyp.2(8),p.434.

Microwave Frequency Upshift Using Plasmas*

Mark Rader, Fred Dyer, and Igor Alexeff

University of Tennessee, Department of Electrical Engineering
Ferris Hall, Knoxville, Tennessee 37996-2100

Abstract

We have theoretically predicted and experimentally proven that it is possible to use a plasma-microwave interaction to shift the frequency of a fixed oscillator in free space.

Introduction

One interesting aspect of plasmas, is that they interact readily and in a nonlinear fashion with ambient R.F. radiation. We have been studying these interactions to see if it is possible to modify the frequency of the ambient radiation, in a controlled fashion, in free space. To begin this study, we first need to look at the interaction of the R.F. with the vacuum-plasma interface. From this interaction we need to solve Maxwell's equations and get an interaction of the interface with incident R.F. radiation's frequency. Next we will look at experimental evidence of this effect.

Interactions with the Vacuum-Plasma Interface

It is possible to derive a relative dielectric constant, ε_r, for the plasma, where

$$\varepsilon_r(\omega) = \left(1-\frac{\omega_{pe}^2}{\omega^2}\right).$$

This gives us a frequency dependent permittivity that in turn leads to a greater than light phase velocity of the form

$$V_p = \frac{c}{\sqrt{\varepsilon_r(\omega)}}$$

where c is the speed of light. We can also establish the fact that below the plasma frequency, and slightly above it, the plasma reflects all of the incident radiation.

* Work Supported by the Air Force Office of Scientific Research AF-AFOSR-89-0348

Frequency Modification Using The Vacuum-Plasma Interface

This modification of the wave velocity to hyper-light velocities and the reflection now lead us to two methods of frequency shifting. In the first, and simplest method, we take the interface and accelerate it to a high velocity "10^6 meters//sec". This gives us a frequency shift due to compression of the wave front. This compression gives us a frequency shift of the form

$$\omega_1 = \omega_o \left(1 + 2\frac{V}{c} + \ldots\right)$$

where ω_1 is the new frequency, ω_o is the original frequency and V is the velocity of the interface.

We have tried this experimentally and found good agreement between theory and experiment. Figure 1 shows a typical shifted spectrum using a Hewlet-Packard Spectrum Analyzer. The frequency of the incident wave was 2.6 GHZ and the span was 2 MHz/div. The source of the moving front was a Bostick gun that produced a jet of plasma flowing along a 1 meter cylindrical glass vacuum system. It can be noted that there are several peaks on the upshifted side of the spectrum. We believe that these peaks correspond to species of different velocity. It can also be noted that there is a down shift not predicted by the theory. We believe that this is produced by the plasma column as it collapses and retreats back towards the source. This is born out by the fact that this down shift is pressure dependent while the upshift is not. The base pressure was 1 X 10^{-6} torr.[1]

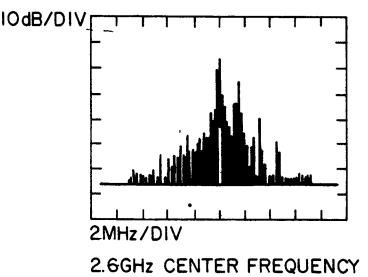

Figure 1

Frequency Modification by Velocity Shifting

The next method of frequency modification utilizes the speed of light shift in the plasma to change the wave frequency. Imagine a system with a wave traveling through it. If you suddenly create a plasma in the system, space is isotropic and the wavelength is constant. So the frequency must shift to satisfy the relationship

$$f = \frac{V}{\lambda}$$

where V is the wave velocity. At the end of the plasma region there is a discontinuity in space so the frequency is constant. It can be shown that for this case the upshift is

$$\omega_2 = \sqrt{\omega_1^2 + \omega_{pe}^2}$$

where ω_1 is the original frequency, ω_{pe} is the plasma frequency and ω_2 is the new frequency.

We have seen this effect in the laboratory, as shown in figure 2. There is also very good agreement between theory and experiment in this device and we continue to study it further.[2]

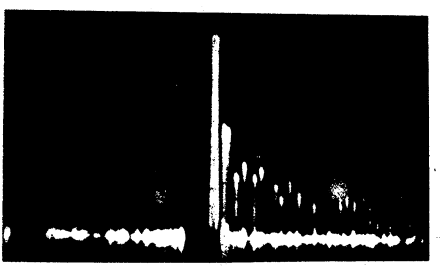

10 MHz/Div 2.6 GHz Center Frequency

Figure 2

Conclusion

We have been experimentally and theoretically studying methods of frequency modification using plasmas. We have found that this can easily be accomplished by the use of reflections from moving interfaces or hyper-light velocity shifts. There is a good agreement between theory and experiment.

References

[1]. Mark Rader, Fred Dyer, Igor Alexeff, Aaron Matas, and Adnan Basrai, Bull. Am. Phys. Soc. 34, 2004, (1989)

[2]. Mark Rader, Fred Dyer, Aaran Matas, and Igor Alexeff, IEEE International Confreence on Plasma Science, 90CH2857-1, 171, (1990)

IONIZING COLLAPSE OF HIGH FREQUENCY PLASMA FILAMENT IN DENSE GAS

Gritsinin S.I., Kim A.V.*, Kossyi I.A., Tarasova N.M.
General Physics Institute,USSR Academy of Science, Moscow, USSR,
* Institute of Applied Physics, USSR Academy of Science, Gorky, USSR

A new form of gas discharge has been added during the last years to numerous ones described in the scientific literature viz. the high pressure microwave discharge initiated in the subthreshold fields [1,2]. Discharge dynamics, its structure and parameters of the produced plasma are rather specific and do not have analogies among the gas discharges studied before. As a rule, the discharge is excited according to the such a scheme : pulse microwave radiation is formed by the dielectric lens into a beam focused on the axis of the vacuum chamber. Special characteristics of the discharge appear when the following relation holds:

$$\nu_{eff} >> \omega \qquad (1)$$

and

$$\frac{E_{eff}}{n_m} < \left[\frac{E_{eff}}{n_m}\right]_{thr} \qquad (2)$$

where ν_{eff} is effective electron-neutral collision frequency; ω is the angular frequency of the microwave radiation; n_m is the concentration of the gas molecules; $E_{eff}=\frac{E_o}{\sqrt{2}\sqrt{1+(\omega^2/\nu_{eff}^2)}}$; E_o is the amplitude of the microwave electrical field; $[E_{eff}/n_m]_{thr}$ is the threshold value for excitation of self-sustained discharge in free space.

Evidently if relation (2) is valid gas discharge is not able to appear without any stimulator. As the least ones in the majority of experiments metal-dielectric plates, systems of metallic edges, laser flames etc. are used [1]. The presence of the stimulator results in the local increase of the parameter

E_{eff}/n_m up to the threshold value. Discharge arising near the stimulator begins to spread from the initiation point towards the radiation.

The following parameters are usual for the experiments: wavelength of the microwave radiation $\lambda_f \simeq 0.8 \div 10$ cm; the duration of the microwave pulse $\tau_f \simeq 1 \div 1000$ μs; the parameter $[E_{eff}/n_m] \simeq 2 \div 8 \cdot 10^{-16}$ V·cm^2; the range of the pressure investigated 50 ≤p≤ 750 Torr; the working gases are N_2, He, Ar, Xe, air et al.

Characteristic photographs of the discharge are given in Fig.1 (integrated over the microwave pulse time). One of the main features of the discharge, namely strong spatial inhomogeneity of the glow, can be distinctly recognized on the photographs. The discharge in general looks like "thread clew" with transversal dimensions of elementary threads constituting shares of millimeter. Transversal dimensions of the "clew" coincide with the borders of the microwave beam. Longitudinal dimensions grow simultaneously with the increase of the microwave pulse duration as far as space occupied by the discharge enlarges consequent on its spreading towards the radiation from the point of initiation.

The experiments by the use of photoelectron recorder show that with the duration of time initial filament glow is dying away while new ones appear between the stimulator and source of microwave radiation more and more distant from the stimulator. Characteristic lifetime of a filament is about 2÷10 μs.

Phenomena of contraction is rather common for gas-discharge devices. But among the numerous structures described in literature it is difficult to find out analog to such unusually branched system of channels as in high pressure microwave discharge. It is natural that the interest to construct physical model of the processes resulting in visible in experiments inhomogeneities arises for this reason. Attempts to explain the features of the microwave discharges analogous to the ones shown in Fig.1 have been done recently in a series of theoretical investigation (see [3]-[7]). Analyzing them we can first of all indicate two hypotheses: 1) characteristic form of the discharge results from the development of thermal-ionizational instability; 2) discharge structure and dynamics can be

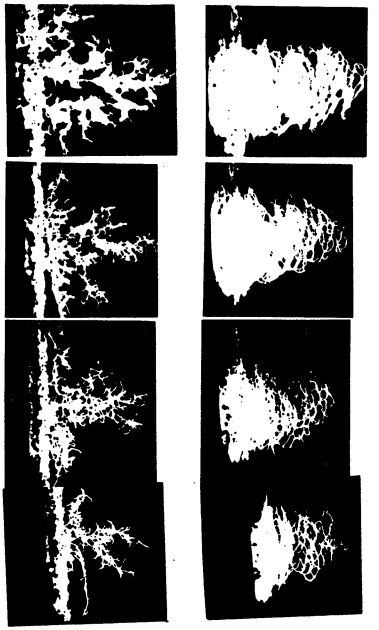

Fig.1

Microwave stimulated dicharge image taken simultaneously along the vector (left column) and normal to the vector of line polarized electric field. I=35 kW/cm^2 ,λ_f=2.5cm,τ_f=30μs.

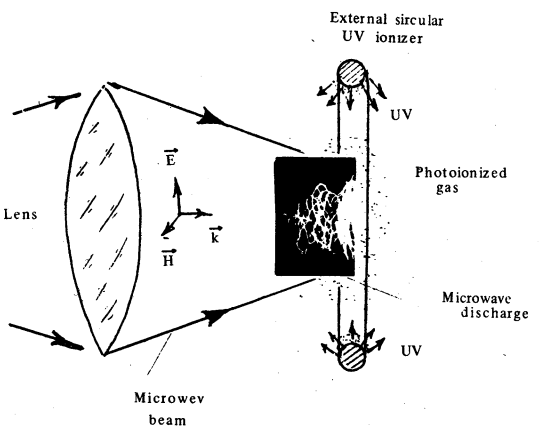

Fig.2

Principle setup.

explained by the processes lying in the foundation of the well known "streamer" model [8].

Let's start our analysis from contraction which may be a result of a development of thermal-ionizational instability in high pressure gas. Physical nature of the instability often commented by the following locked sequence of the processes:

$$n_e \uparrow \Rightarrow \sigma \uparrow \Rightarrow \sigma \tilde{E}_0^2 \uparrow \Rightarrow T_g \uparrow \Rightarrow n_m \downarrow \Rightarrow \frac{E_{eff}}{n_m} \uparrow \Rightarrow T_e \uparrow \Rightarrow \nu_i \uparrow \Rightarrow n_e \uparrow \quad . \quad (3)$$

The arrows indicate the character of parameter variation (increase or decrease). Here $\sigma = \frac{e^2 n_e}{m \nu_{eff}}$ is plasma conductivity; T_g is gas temperature; ν_i is electron impact ionization frequency. Fluctuating growth of electron concentration in local volume as it comes from (3) results in consecutive variation of the medium parameters accompanied by the increase of initial perturbance. Linear theory of the instability in microwave fields investigated for the first time by V.B.Gildenburg & A.V.Kim in Ref.[9] predicts the threshold value and increments of instability resulting in dropping initially homogeneous discharge into the filaments "distended" along electric field vector E. An enrichment of the paper [9] and an important new step forward was done in the investigation of A.V.Kim & G.M.Fraiman (Ref.[3]) studying non-linear stage of the instability. As principal initial assumptions (their validity is analyzed specially in the paper) the authors take for granted the following:

a) it is supposed that plasma concentration in spite of its increase in the process of developing instability has always such small magnitude that electric field amplitude variations can be neglected in comparison with "vacuum" one (i.e. transversal size of tread always is smaller than depth of e.m. wave penetration) ;

b) it is considered that isobaric approximation holds true; gas pressure is constant in the developing filament i.e. time of acoustic wave transit across the filament is small in comparison with the characteristic time of the problem involved.

On these assumptions the following system of equations is solved:

$$\frac{\partial n_e}{\partial t} - D_a \cdot \Delta n_e = (\nu_i - \nu_a) \cdot n_e - \alpha_r \cdot n_e^2 \quad (4)$$

$$\frac{\gamma}{\gamma-1}\cdot n_m\cdot\frac{\partial T_g}{\partial t}=\frac{1}{2}\cdot\sigma\cdot|E|^2 \qquad (5)$$

$$n_m\cdot T_g = p = \text{const}, \qquad (6)$$

where D_a is coefficient of ambipolar diffusion; ν_a is attachment frequency of electrons to molecules: α_r is recombination coefficient; γ is politropic index; p is gas pressure; E is microwave electric field vector.

The solution of the system (4)-(6) allows to describe the latest non-linear stage of thermal-ionizational instability. As it was shown by the authors of the Ref.[3] amplitudes of localized perturbations amplify up to infinity during the finite time interval t_o in initially homogeneous plasma while characteristic dimension (diameter of the filament ϕ_c) tends to zero. In physical sense it means that after the development of the thermal-ionozational instability within the filament regions such parameters as electron and gas temperature, electron density amplify in explosive manner faster than exponent. It is supposed that explosive evolution continues until gas density is not lowered to the values under which microwave field frequency ω and electron-neutral collision frequency ν_{eff} become equal. The growth of plasma parameters transforms from explosive to exponential manner in a narrow region near the filament axis. Afterwards the discharge can go over to stationary regime. In the framework of the theory developed in [3] it is possible to estimate quasi-steady parameters of the filament:

$$T_g \approx \frac{\nu_{eff_\circ}}{\omega}T_{g_\circ} \qquad (7)$$

$$T_e \approx \frac{\nu^2_{eff_\circ}}{\omega^2}T_{e_\circ} \qquad (8)$$

$$n_e \approx \left(\frac{\nu_{eff_\circ}}{\omega}\right)^{\beta+1}\frac{\nu_a}{\nu_T}n_{ef} \qquad (9)$$

$$\phi_c \approx \frac{L}{(\nu_{eff_\circ}/\omega)^{\beta+2}} \qquad (10)$$

Here $L=\sqrt{D_a/\nu_a}$ is diffusional attachment path; symbol "$\circ$" marks parameters of initial spatially homogeneous medium with concentration of primary plasma n_{ef}. Ionization frequency ν_i is considered as well-known rapidly increasing function of electron

temperature $\nu_i \simeq T_e^{\beta/2}$ ($\beta \approx 5 \div 6$ for air [8]); ν_T is determined by the relation:

$$\nu_T \simeq \frac{\gamma-1}{\gamma} \frac{\sigma \tilde{E}_o^2}{2p} \qquad (11)$$

Substituting numerical values of ν_{eff_o}, T_{e_o}, ν_T and ν_a which are characteristic for the experiments [1,2] we come to a conclusion that final state of plasma in the channels is total ionization ($n_e \simeq 10^{18} \div 10^{19} cm^{-3}$), the temperature of electrons achieving several hundreds eV. In practice increase of concentration, decrease of channels dimensions and growth of electron temperature can be limited by a series of processes not taken into consideration in (3). For example it is very important that according to the solution obtained in [3] transversal dimension of the filament decreases so rapidly that all the time remains less than skin-depth in spite of the growth of the electron concentration n_e in the filament. It approves the initial assumptions that the difference between electric field within the filament and initial "vacuum" one is not essential. However it can not be excepted that at the latest stages of the process the perturbance of the microwave radiation can not be neglected and reflection of electromagnetic wave from the conducting breakdown channel can limit the growth of plasma parameters.

Numerical solution of the system describing non-linear stage and saturation phase of instability in microwave non-self-sustained discharge in air is obtained later by E.V.Kogan & B.Y.Kuzin [4] . They show that quasi-steady parameters of the filament are $T_e \simeq 5$ eV and $n_e \simeq 10^{16} \div 10^{17}$ cm^{-3}. Solving the problem the authors of [4] rejected the assumption on a total penetration of the microwave electric field into the breakdown channel, additionally taking into account a series of elementary processes e.g. a dissociation of nitrogen molecules.

Summarizing the results of the theory it is possible to propose that visible in experiments brightly glowing filaments are a result of a development of thermal-ionizational instability which achieves and passes through the non-linear phase proceeding as a peculiar "explosion". There occurs an abrupt transformation from primarily cold rarefied plasma to hot

($T_e \geq$ 5 eV) plasma with extremely high concentration $n_e >> n_{ecrit}$, where n_{ecrit} is critical concentration for the incident microwave radiation. In general the phenomenon can be classified as ionizational collapse coming into being in rather specific conditions i.e. in high pressure gas discharge.

Strictly saying "streamer" model doesn't answer on the cause of the appearance of the contractible structures. If, however, they have already been arose (e.g. as in the case they are being predicted by thermal-ionizational theory) further "germination" of the channels and rise of branched configurations can be connected exactly with physics of "streamer" phenomenon. It should be pointed out that plasma channel develops as a streamer only in the case when electric field is dislodged by plasma from the channel "body" and reinforced on its "head". Consequently, there can be an opportunity for such order of the processes: channel appearance, resulting from the development of thermal-ionizational instability including passing through the non-linear phase, and the following transition to the "streamer" model, the conditions of total penetration of the electric field into the channel stopping to work at the final stage.

Let's consider now in what degree the results of the experimental investigation reply on the above given description of the formation and development of the breakdown channels in microwave discharge of high pressure. First of all let's attract attention to the experiments concerning excitation of non-self-sustained microwave discharge according to the scheme illustrated in Fig.2 (see [10,11]. The microwave beam is introduced into the gas medium which is previously ionized by the ring source of ultraviolet radiation. Initial value of the parameter E_{eff}/n_m is less than threshold one for self-sustained discharges. Nevertheless, after definite period from introduction of the microwave radiation into the chamber spatially homogeneous energy release is replaced by abruptly contracted one. Brightly glowing filament, stretched along the vector of electric field of microwave radiation, appears in the plane of the ring source near the axis of the beam. The duration of the microwave pulse increasing, new filaments arise and the discharge "runs away" from the plane of the ring towards the

microwave radiation. Appearance of the discharge in a plane of a ring-shape UV source may occur exactly as a result of a development of thermal-ionizational instability in a non-self-sustained discharge. Probably this is the nature of arising of every new filament in the ionization wave "running away" from the focal plane towards microwave radiation. If it is so, the following question appears: does the discharge achieve the "explosive" stage of the instability predicted by the theory or "explosion" is unattainable.

Realization of extremely high electron concentrations ($n_e >> n_{ecrit}$) differs ionization collapse from regions of contraction in steady electric fields in particular and is one of its main features. That is why it appears reasonable to carry out experiments for determination of n_e concentration in filaments. Measurements of electron concentration in contraction regions is considerably difficult due to the small spatial scales, randomness of the place and unpredictability of time appearance. First attempts to determine the parameters of breakdown channels in such difficult conditions with the help of probe method have been done in [10,12]. Two floating electrodes have been introduced into the microwave discharge in such a way, that is shown in Fig.3. Shorting of the electrodes by a discharge filament, an electric pulse arises on the load resistance connecting the electrodes without applying any external voltage. If one analyses pulse magnitude depending on load resistance, distance between the two electrodes and on gas pressure it is possible to estimate the concentration and the temperature of electrons in the channel: $n_e \simeq 10^{16} \div 10^{17}$ cm^{-3}, $T_e \simeq$ 3÷5 eV. Characteristic oscillograms of the probe current (Fig.4) show that the filament is formed during the time less or about several decimal shares of microsecond and exists during several microseconds.

Summing up the probe measurements there should be mentioned two obvious reasons not allowing to limit oneself to the utilization of this simple method only:

- the drawback connected with the "contactness" of the method and principal opportunity to disturb discharge conditions;
- uncertainty in estimation of magnitudes of n_e and T_e connected with relatively low accuracy of measurement of the transversal

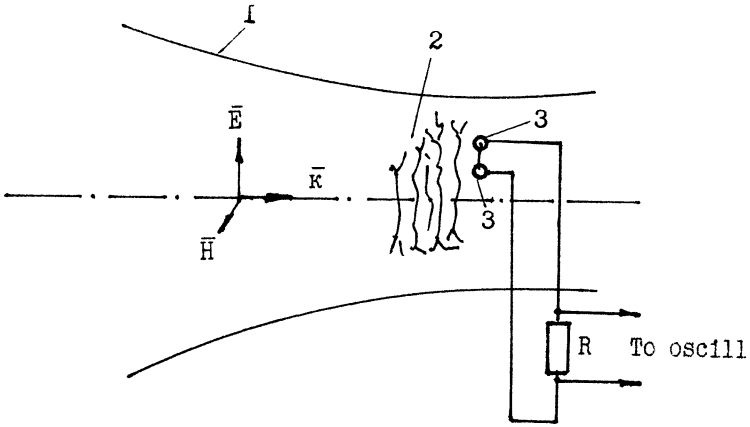

Fig.3. Experimental setup.1- microwave beam; 2- microwave discharge; 3- probs.

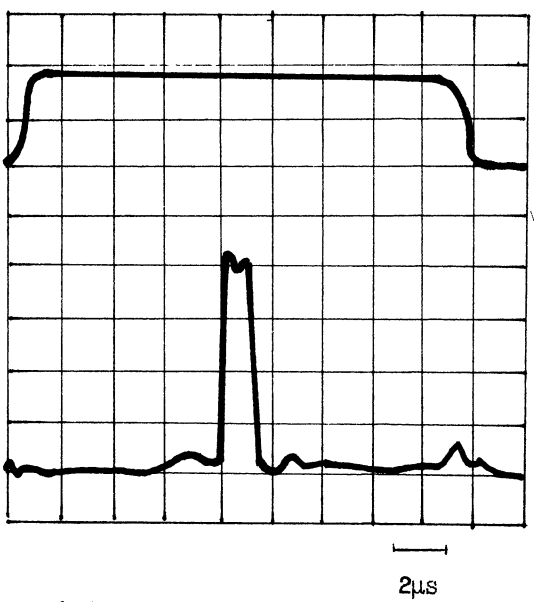

Fig.4. Oscillograph image of prob signal, p=500 Tor, I=27 kW/cm^2. a)- microwave pulse; b)- probe signal.

dimensions of the channel.

The transition to contactless technique of n_e measurements which do not have above mentioned drawbacks is done at the expense of utilizing of two spectroscopic methods [13,14]:

- passive one, connected with measurement of the discharge radiation in the visible spectrum;
- active one, based on testing of the discharge by the infrared tunable laser radiation.

Both the first and the second measurements are intended to obtain electron concentration by Stark broadening of spectral lines [15] determined in the radiation and absorption spectra.

The investigation of the discharge radiation is done according to the scheme presented in Fig.5. Spectrum line is picked out by MDR-3 monochromator and registered by photoelectric multiplier. Characteristic shapes of spectral lines obtained in discharges excited in Ar and Xe are given in Fig.6,7 (ArI(7030 Å), XeI(4671Å)). One can see that the spectral lines are considerably broadened asymmetrical ones. The half-widths of Ar and Xe spectral lines are $\lambda_{Ar} \simeq 1.6$ Å and $\lambda_{Xe} \simeq 0.65$ Å respectively. The broadening and asymmetry can be interpreted as a result of the case when regions with high and inhomogeneous concentration of electrons are the source of radiation. Really, considering the channels as axisymmetric cylindrical formations we obtain for the optically thin plasma the following expression:

$$I(\lambda) = \int d\lambda' \int 2\pi r \, f(r,\lambda') \, F(\lambda-\lambda') \, N_a(r) dr \qquad (12)$$

where $F(\lambda)$ is the apparatus function . It is valid to take the shape of spectral line $f(r,\lambda)$ as Lorentz one with parameters depending on r. For example, considering electron $n_e(r)$ and excited atoms $N_a(r)$ distributions as Gaussian ones for plasma with characteristic radial dimensions ρ_e and ρ_a we can represent the expression (12) in the following form:

$$I(\lambda) = \int d\lambda' F(\lambda-\lambda') \frac{N_{ao} \rho_e^2}{\omega n_{eo}} \int_0^1 x^{(\rho_e/\rho_a)^2-1} \frac{\delta_1 + x}{(\delta_1+x)^2 + (\Delta\lambda_1 + S_1)} dx \qquad (13)$$

where ω and S are Stark broadening and shift constants consequently; $\delta_1 = \frac{\delta_o}{\omega n_{eo}}$; δ_o is an inherent width of line; $S_1 = S/\omega$; $\Delta\lambda_1 = (\lambda-\lambda_o-S\, n_{eo})/\omega\, n_{eo}$; λ_o is non-shifted wavelength; N_{ao} and n_{eo} are the values of the corresponding concentrations on

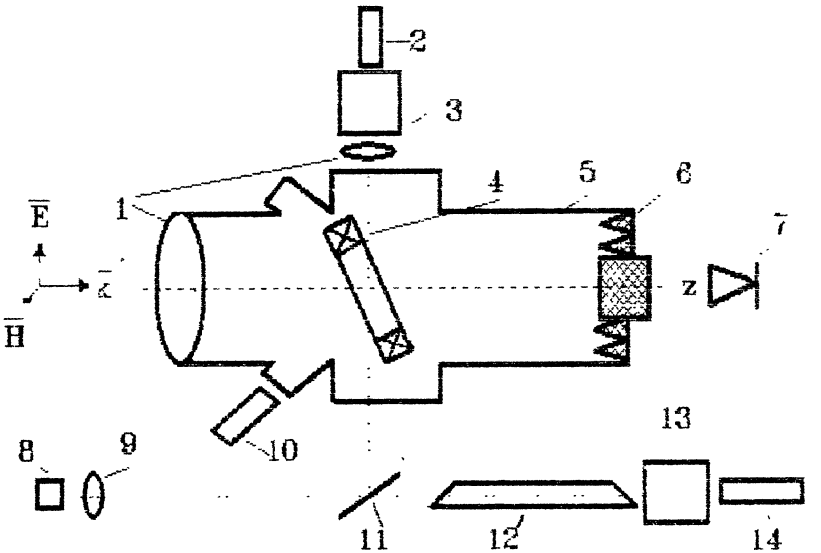

Fig.5

Scheme of experiment.

1,9- lenses; **3,13**- monochromators; **2,14,10**- photomultipliers; **4**- external ionizer; **5**- vacuum chamber; **6**- microwave beam absorber; **7**- microwave detector; **8**- diode laser; **11**- laser beam divider; **12**- glow discharge tube.

the axis of the channel. As contribution into the $I(\lambda)$ is made both by the near axis atoms (the radiation suffering greatest shifts and broadenings and contributing mostly to the wings of the line measured) and by peripheral atoms (slightly perturbed radiation influencing mostly on the $\lambda \approx \lambda_o$ region) the shape of the registered line essentially depends on ρ_e/ρ_a and absolute value of electron concentration n_{eo} on the axis.

In Fig.6 experimentally obtained dots are shown in comparison with calculated curve (solid curve) for $n_{eo}=6\cdot10^{16}$ cm^{-3} and $\rho_e/\rho_a=1$. As far as experimental points lay rather well on the calculated curve we may conclude that quasi-steady electron concentration achieves values of $n_e \geqslant 6\cdot10^{16}$ cm^{-3} within the filaments. The magnitude obtained is close both to the calculated one [4] and to the values measured by probe methods [10].

As far as diagnostic opportunities are concerned the second (active) technique is of great interest. In this method absorption spectroscopy is based on utilization of tunable injection laser ("diode laser") [16]. Working band of the lasers used in the experiments includes argon metastable level ArI(8663Å) (the transition $^3P_0(4S_3)-^3D_1(^4P_7)$). Extremely high spectral resolution along with suitable time and spatial ones are among indisputable advantages of the method as well as high sensibility. So in variant realized in the experiment was determined by an instability of laser radiation frequency from pulse to pulse because of the absence of thermostabilization. Spatial and time resolutions were $\delta z \approx 5 \div 8$ mm (dimension of the diagnostic beam) and $\delta t \leqslant 0.1$ μs consequently.

The scheme of the experiment is illustrated in Fig.5. Probing beam generated by the laser is divided into two ones. One of them is directed into vacuum chamber and passes through the microwave discharge under study while the second one is passed through the continuous glow discharge which is induced in a tube filled with Ar or Xe. The second beam is "basic" one conforming to the non-shifted ("zero") position of absorption line. Attributing broadening and shift of the spectral line to Stark phenomenon it is possible to estimate electron concentration in the filament.

Typical of the absorption spectral line is given in Fig.8.

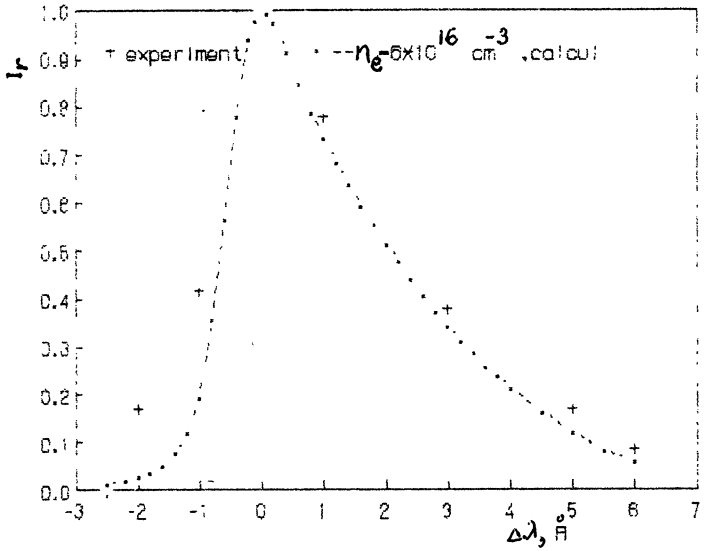

Fig.6. The radiation of ArI(7030.3 Å) line .

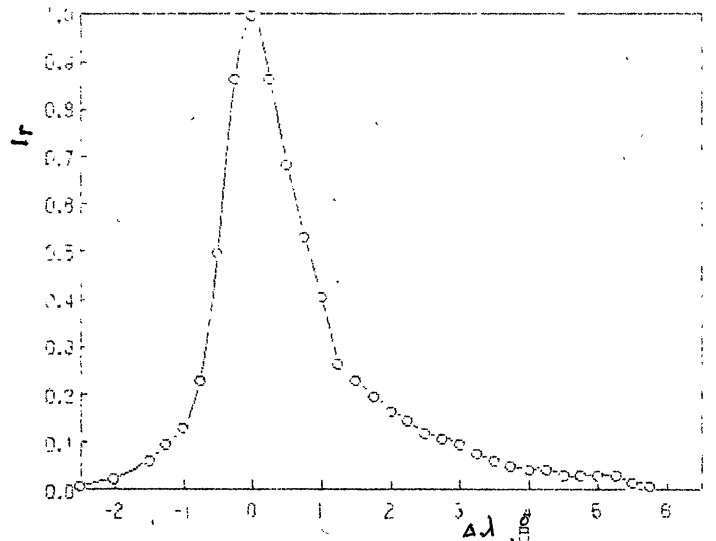

Fig.7. The radiation of XeI(4671 Å) line.

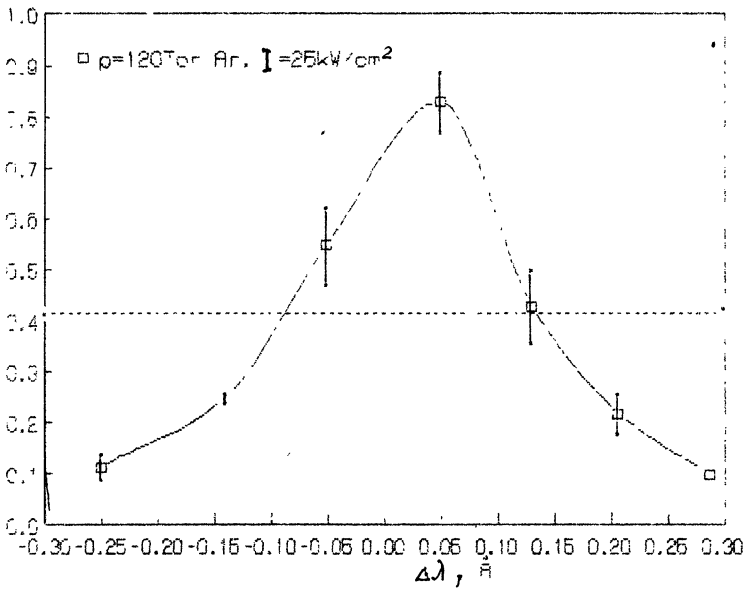

Fig.8
The shape of the line ArI (λ_o=8667.9 Å) in the absorption spectrum.

An integral analogous to (12) for the radiation absorption in inhomogeneous plasma has the following form:

$$I(\lambda) = I_o \int \exp(- \int k_o \, f(x,y,\lambda) \, N_a(x,y) \, dy) \, dx \qquad (14)$$

where k_o is an absorption coefficient in the center of the line. We neglect the width of the diagnostic radiation spectrum.

As in the case described by the relation **(13)** the inner integral **(14)** includes the parameters ρ_e/ρ_a and n_e whose values determine the shape of the absorption line. The estimation of the electron concentration in accord with the broadening of the absorption line and its shift also gives us the magnitude $n_{eo} \geq 1 \cdot 10^{16}$ cm^{-3}.

It should be emphasized that used spectral techniques determine n_e magnitude averaged both in filaments quantity and in their lifetime. In reality true value of electron concentration exceeds the measured one several times at least.

Relatively broad dynamic range provided by active method allows to obtain electron concentration as a function of initial gas pressure P (Fig.9) and of incident power of microwave radiation (I) (Fig.10). How it comes from the figures n_e value firstly grows with the increase of the pressure almost in linear way and than with a tendency to saturation in the interval of maximum pressures in accord with the law near to $n_e \simeq P^{1/2}$. The concentration slightly changes with the increase of the microwave radiation intensity.

In summary our measurements show that the electron density in a filament increases from an initial level $n_{eo} \simeq 10^{12} cm^{-3}$ to values $n_e \geq 1 \cdot 10^{16} cm^{-3}$ (when the displacement of the gas is taken into account , the degree of ionization could approach unity), which are substantially higher than n_{ecr} ($n_{ecr} \leq 10^{15} cm^{-3}$) in a time $\tau \leq 0.5$ μs.

Such high as $n_e \simeq 10^{16} \div 10^{17}$ cm^{-3} values of plasma concentration are an argument in favour of the assumption on the realization of the "explosive" phase of thermal-ionizational instability. This concentration considerably exceeds the "critical" one for the microwave radiation wavelength under the experimental conditions. The fact of its existence proves that collapse really takes place and that contraction region has small final scales. So, if we use for the estimation the relation (17), we have:

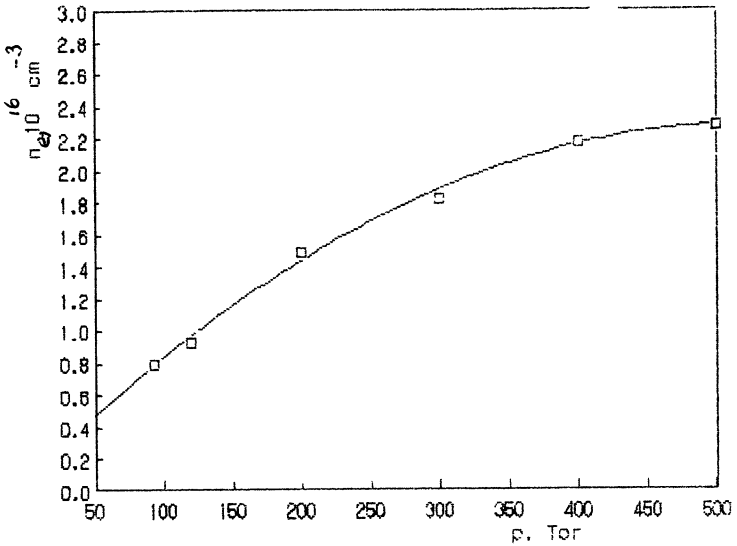

Fig.9. The density of electrons in a "thread" as a function of an initial pressure.

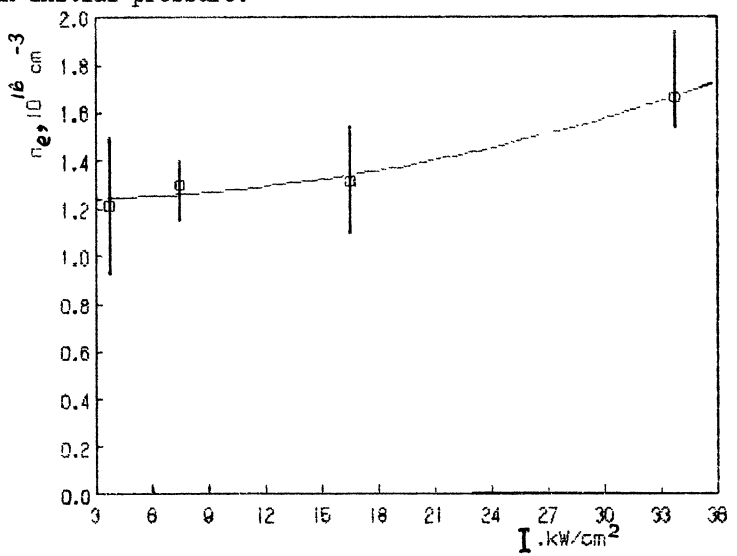

Fig 10. The density of electrons in a "thread" as a fuction of the microwave radiation intensity.

$$\phi_c \leqslant \frac{c\, n_{e\ crit}}{\omega^2\ n_e} \nu_{eff} \qquad (15)$$

Substituting the values $n_e \simeq 10^{16}$ cm^{-3}, $n_{ecrit} \simeq 10^{13}$ cm^{-3}, $\omega \simeq 2 \cdot 10^{11}$ s^{-1} and $\nu_{eff} \simeq 10^{12}$ s^{-1} into the relation (15) we obtain: $\phi_c \leqslant 10^{-3}$ cm

(The relation (15) is obtained on the condition of unhampered penetration of microwave field into the breakdown region).

Extremely high electron concentration and small transversal dimension of contraction regions must indicate an achievement of extraordinary high densities of energy input into every elementary filament. As a consequence an intensive gas heating followed by a formation of quasi-cylindrical shock waves moving from the discharge channels must take place. The characteristic shadow photographs and holograms approve this assumption.

The energy deposition can be estimated proceeding from the simple relation:

$$\bar{w}_o \simeq \sigma \bar{E}_o^2 \tau_c \qquad (16)$$

where τ_c is lifetime of the filament. For $n_e \simeq 2 \cdot 10^{16}$ cm^{-3}, $\nu_{eff} \simeq 2 \cdot 10^{11}$ s^{-1}, $\bar{E}_o \simeq 2 \cdot 10^3$ V/cm and $\tau_c \simeq 2 \cdot 10^{-6}$ s we obtain that $\bar{w}_c \simeq 200$ J/cm^3.

Special experiments by means of laser interferometer were conducted by us for investigation of gas-dynamic phenomena accompanying the single filamentary breakdown. It was discovered that the filament is the source of cylindrical shock wave which is satisfactory described by the theory of point explosion in the infinitesimally thin channel [18]. Comparing the experimental velocity of the shock wave with the theory it is possible to estimate the magnitude of energy release per distance in the discharge region. An estimation for $\bar{w}_o$ can be done by comparing the diameter of glowing filament ϕ_c (the diameter of energy release region) with the diameter of expanded and achieved the quasi-steady dimension ϕ_r, region of rarefied gas medium in the neighborhood of the axis:

$$\bar{w}_o \simeq \frac{\gamma}{\gamma - 1} \left(\frac{\phi_r}{\phi_c} \right)^2 P_o \,, \qquad (17)$$

where P_o is initial gas pressure. According to the experimental data we have $\bar{w}_c \simeq 140$ J/cm^3, what is near enough to the calculated with the help of (16) value. Elementary quasi-cylindrical shock waves spreading from the filaments

approve in such a way the assumption on the discharge development as a sequence of microexplosions in gas medium.

It is worth to emphasize the following circumstance which should be taken into consideration. A high density and high electron temperature make plasma filaments a source of intensive ultraviolet radiation. It results in the formation of characteristic plasma "halo" in its neighborhood and has influence on the discharge dynamics, an efficiency of a transference of the microwave radiation into gas medium etc.[1,2].

There is one more interesting feature of the filamentary structures.Namely plasma density achieved within them is so high that there appears an opportunity of resonant conditions for ion plasma (or ion-acoustic) waves and, consequently, an opportunity for parametric model of microwave energy dissipation.

In conclusion it must be emphasized that none of the above mentioned theoretical papers has analysis of what frequency interval ionization collapse phenomenon may occur in. It shouldn't be excepted that predicted by the theory and discovered in the experiment phenomenon is inherent for ultrahigh-frequency band only. In particular the experimental data testify that in the regions of the fields with constant sign the phenomenon of explosion is excluded because of rapidly forcing out external electric field from the contracted filament (already at the level $n_e \simeq 10^{11} \div 10^{12}$ cm^{-3}) while the temperature in the filament decreases in comparison with the initial one [3]. As regards optical band it is possible that analogous with microwave discharge structure of "exploding filaments" occurs in the experiment under the condition $\nu_{eff} \gg \omega$. However, there may be limits in connection with screening of the energy release region by light-detonated waves [8].

Finally, let's direct our attention to the fact that the described experiment can be considered as one of numerousless demonstrations of non-linear regime with abruptness [19], where a development of the instability in dissipative system leads to a decrease of spatial and time scales of parameters distribution. Really, the authors of the papers [3,4] pointed out that in the case of strong non-linearity the equations describing ionization-heating instability are reduced to the

equation describing the dynamics of so called "T- layer" [19]. Having at our disposal such an analogy we classify observed in the experiment inhomogeneities as "T-filaments".

REFERENCES

[1] G.M.Batanov, S.I.Gritsinin, I.A.Kossyi, A.N.Magunov, V.P.Silakov, N.M.Tarasova. M.: Nauka, Trudi FIAN (in russian), v.160, 1985, p.174-203.

[2] S.V.Golubev, S.I.Gritsinin, V.G.Zorin, I.A.Kossyi, V.E.Semenov.In "VCh razryad v volnovykh polyakh " (in russian), Gorki, 1988, p.136-197.

[3] A.V.Kim, G.M.Fraiman- " Fizika Plazmy " (in russian), 1983, v.9, p.613-617

[4] E.Ya.Kogan, B.Yu.Kuzin-" Zh. PM i TF "(in russian), № 3 , 1988, p. 28-34.

[5] O.A.Sinkevich- " Zh T F" (in russian), v.56, 1986, № 4 , p.752-754.

[6] S.A.Dvinin- " Vestnik MGU", ser.3, Fizika, astronomiya (in russian) , v.26, № 6, 1985, p.30-33

[7] V.G.Brovkin, Yu.F.Kolesnichenko- " Pis'ma v Zh T F "(in russian), 1990, v.16, № 3, p.55-58.

[8] Yu.P.Raizer." Fizika gazovogo razryada"(in russian), 1987.

[9] V.B.Gildenburg, A.V.Kim- " Fizika Plazmy "(in russian), 1980, v.6, № 4, p.904-910.

[10] S.I.Gritsinin, A.A.Dorofeyuk, I.A.Kossyi, A.N.Magunov - "Teplofizika Visokich Temperatur " (in russian), 1987, V.25, № 6, p.1068-1072.

[11] S.I.Gritsinin, I.A.Kossyi, V.P.Silakov, N.M.Tarasova, V.E.Terekhin- " Zh. T F " (in russian), 1987, v.57, № 4 , p.681-686.

[12] P.S.Bulkin, S.A.Dvinin, G.S.Solntsev, I.E.Shkradyuk - "Vestnik MGU " (in russian), 1986, v.27, № 5, p.15-17.

[13] S.I.Gritsinin, I.A.Kossyi, V.P.Silakov, N.M.Tarasova-XIII IGPIG, Invited Papers, 1987, Swansea.

[14] V.G.Avetisov, S.I.Gritsinin, A.V.Kim, I.A.Kossyi, A.Yu.Kostinskii, M.A.Misakyan, A.I.Nadezhdinskii, N.M.Tarasova, A.N.Khusnutdinov- " Pis'ma v Zh. E T F " (in russian), 1990, v.51, № 6, p.306-309

[15] G.Grim " Broadening of spectral lines in a plasma " (ir

russian), M.:Mir,1978
[16] V.G.Avetisov, Yu.V.Kosichkin, V.I.Malakhov, A.V.Merkulov, A.I.Nadezhdinskii, S.L.Palei, A.N.Khusnutdinov, S.D.Yakubovitch - " Kvantovaiya electronika " (in russian), 1989, v.16, № 4, p.853-858.
[17] V.E.Golant " SVCh Metody issledovaniya plasmy "(in russian) M.: Nauka, 1968
[18] V.P.Korobeinikov- " Zadachi Teorii Tochechnogo Vzriva " (in russian), M.: Nauka, 1985.
[19] A.A.Samarskii, N.V.Zmitrienko, S.P.Kurdyumov, A.P.Michailov- "Dokladi AN SSSR "(in russian), 1976, v.227, № 2, p.321-324.

THE FREE LOCALIZED MICROWAVE DISCHARGE IN AIR IN THE FOCUSED ELECTROMAGNETIC BEAM

Devyatov A.M., Kuzovnikov A.A., Lodinev V.V., Shibkov V.M., Shibkova L.V., Zlobin V.V.
Department of Physics, Moscow State University, USSR

A nonequilibrium plasma of molecular gases mixtures is widely used as an active media of gas lasers. This fact as well as the development of plasma chemistry and various methods of plasma technology provide intensive investigations of these objects. The most important tasks the nonequilibrium plasma solve are: searching for ways to create it, investigation of micro- and macro-processes taking place in the nonequilibrium discharges, improvement of effectiveness of devices wich use a nonequilibrium plasma as a working body and on the basis of data obtained the creation of new devices.

In many discharge plasma applications on have to use energy supply systems without electrodes. One of possible ways to supply energy without electrodes is to use the free localized microwave discharge in the focused beam of electromagnetic energy [1]. The electrodeless microwave plasma behavior far from both discharge chamber walls and radiation supplies seems interesting from the point of view of the following problems: the energy of powerfull electromagnetic radiation transportation from space to Earth throgh the atmosphere [2], the creation of radioreflecting fields by the artifitial ionization of the atmosphere upper layers [3], the pumping of powerfull gas lasers [4], problems of plasma chemistry [5], using the source of energy far from an accelarated object to produce the jet traction [6]. The successfull use of the microwave discharge in these applications make it necessary to research the physics of a new kind of discharge - the electrodeless microwave discharge in the focused beam in the free space and search for ways to optimize this discharge parameters.

The experimental equipment is sketched in fig.1.

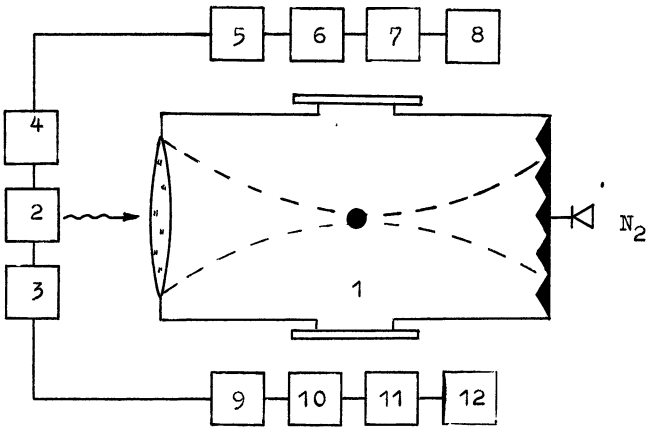

Fig.1

The experimental equipment. 1 - the discharge chamber; 2 - microwave generator; 3 - block of sinchronization; 4 - block of control and registration; 5 - plant of spectral measurement; 6 - microwave interferometer; 7 - schlieren photography; 8 - interferometric holography; 9 - infrared receiver; 10 - plant of high velocity registration; 11 - microwave receiver; 12- TV.

To exclude the walls influence experiments were made in approximately free space conditions $R/\lambda \gg 1$ (where R is the discharge chamber dimension, λ is the wavelength of the centimeter range microwave radiation). The electric field amplitude in the beam focuse was about $E \lesssim 5$ kV/cm, the wave having been linearily polarized. The microwave pulse duration could be changed from 1 μs to 1 s. The gas pressure (nitrogen, air) varied from 1 to 760 torr.

One of the most important parameter of the nonequilibrium plasma is the translational temperature. Therefore, intensive theoretical and experimental investigations are being performed now of the molecular gas heating and mechanisms, responsible for the "anomalously" quick gas heating at the pulsed field switching. It this work the gas temperature was determined with the resolution in time from the distribution of relative intensities of lines rotational structure of the band (0;2) λ =

3805 Å the second positive system of nitrogen. To measure T_g after the microwave pulse action, the second diagnostic pulse of small amplitude and duration was used which induced gas lightning but did not change it's temperature because of low energy input. The gas temperature was determined also from the gas density distribution in the discharge zone, at different times after the microwave pulse ending, obtained by the interferential-holographical method. The vibrational temperature was measured using the relative intensities of the bands second positive system of nitrogen. The electrons concentration was registered with the help of the 8-mm microwave interferometer, their temperature having been determined from absolute intensities of the 2^+ and 1^- bands of nitrogen systems.

When the electric field in the focused beam exceeds a threshould value, in the focal zone of the chamber the gas breakdown takes place. After the breakdown, the plasma appeared in the beam focuse starts to absorb intensively the applied energy. The plasmoid doesn't stay at one place, but moves to a focused antenna with the rate of about 10^5 cm/s.

The measurements of the concentration and temperature of electrons in the running microwave discharge have shown (see Figs. 2 and 3) that the concentration reaches the critical

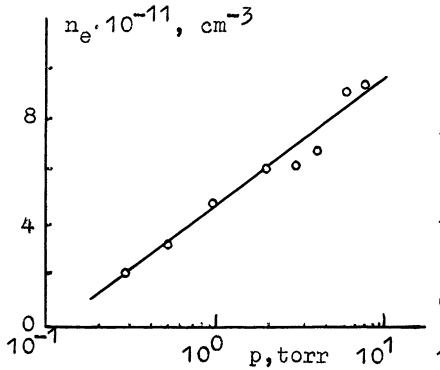

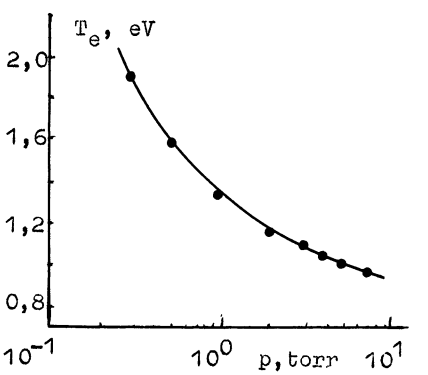

Fig.2. The electron concentration dependence upon the nitrogen pressure in the running microwave discharge.

Fig.3. The electron temperature dependence upon the nitrogen pressure in the running microwave discharge.

value n_{ec} for the investigated band of wavelengths and increases with the increase of the gas pressure and energy input, while electron temperature decreases monotonously with the increase of the gas pressure. The investigation of the molecular gas heating kinetics in the region where the running microwave discharge exists, has shown (see Fig.4) that, if the field is switched on by pulse, quick heating takes place. In our experimental conditions (pressure p = 35 torr, the density of energy flow S = 10^4 Watt/cm^2, the pulse duration τ_{im} = 100 μs) the heating rate was up to 40 K/μs in the first 10 - 15 μs, at 20 μs the temperature reached the value of 850 K and then during the pulse it was practically stable. This

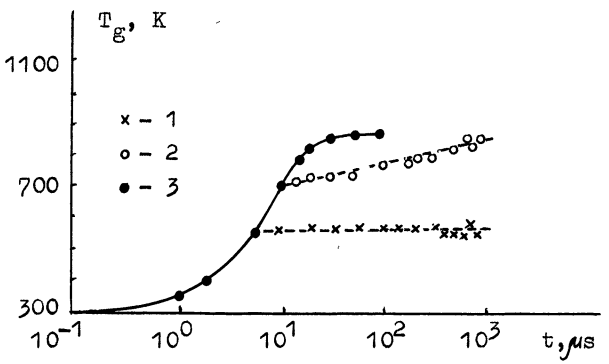

Fig.4. The time dependence of gas tempetature in the running microwave discharge in air. p = 35 torr, S = 10^4 W/cm^2, τ_{im}, μs: 1 - 5; 2 - 10; 3 - 100.

indicates that the use of long microwave pulses to heat gas up to high temperatures within a fixed region of space is not effective. This fact can be explained by that due to the skin-effect the energy is absorbed mostly in the relatively narrow layer of the front of the moving discharge, and dissipates in a large mass of gas involved in the region of the running microwave discharge existance. The obtained heating rate in the active phase of discharge can be explained by neither elastic heating, nor the energy output due to the unharmonism in settling the molecules' distribution function on vibrational

levels, nor VT-relaxation processes. Thus, according to data of the work [7] , the characteristic time for the vibrational relaxation of nitrogen molecules at our conditions is ~2 ms, this value being greater by two orders than that we have in experiment.

To make clear the influence of energy stored in vibrationally excited molecules on the kinetics of gas heating, we have measured the dependence on time of the vibrational temperature in the plasma of the microwave discharge in air. The energy stored in the vibrational reservoir of molecules happend to increase with the microwave discharge duration rising up to 20 μs and to be practically constant during 1 ms after microwave action (Fig.5), which fact indicates that the relaxation time in the experiment is approximately equal or greater than one millisecond. This result is in good correspondence with data obtained on the heat kinetics of air after the microwave discharge action.

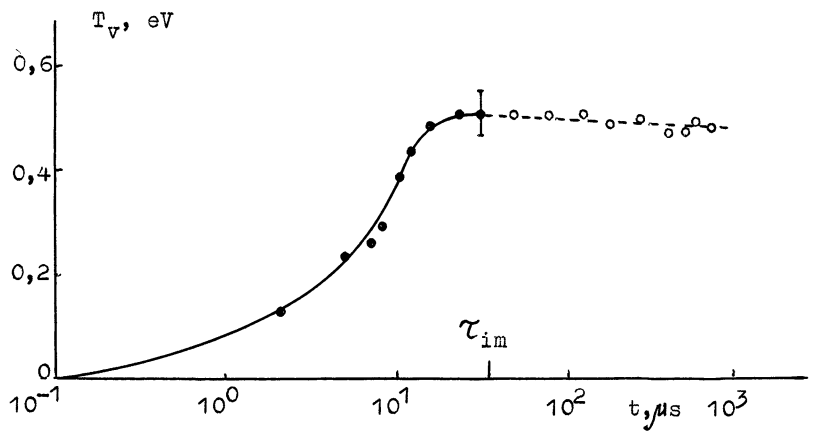

Fig.5. The time dependence of the vibrational temperature in the plasma of the microwave discharge in air. p = 35 torr, $S = 10^4$ W/cm^2, τ_{im} = 30 μs.

For example, after the 5 μs pulse the gas temperature is approximately constant within 1 ms (Fig.4, curve 1), while for τ_{im} = 10 μs, that corresponds to greater energy input to vibrational degrees of freedom, the further heating of gas is going

on with the rate of 0,1 K/μs (Fig.4, curve 2). Data obtained by the interferencial-holographic method have also show that the gas heating is going on during few milliseconds after the end of the microwave discharge (Fig.6). It follows from estimations

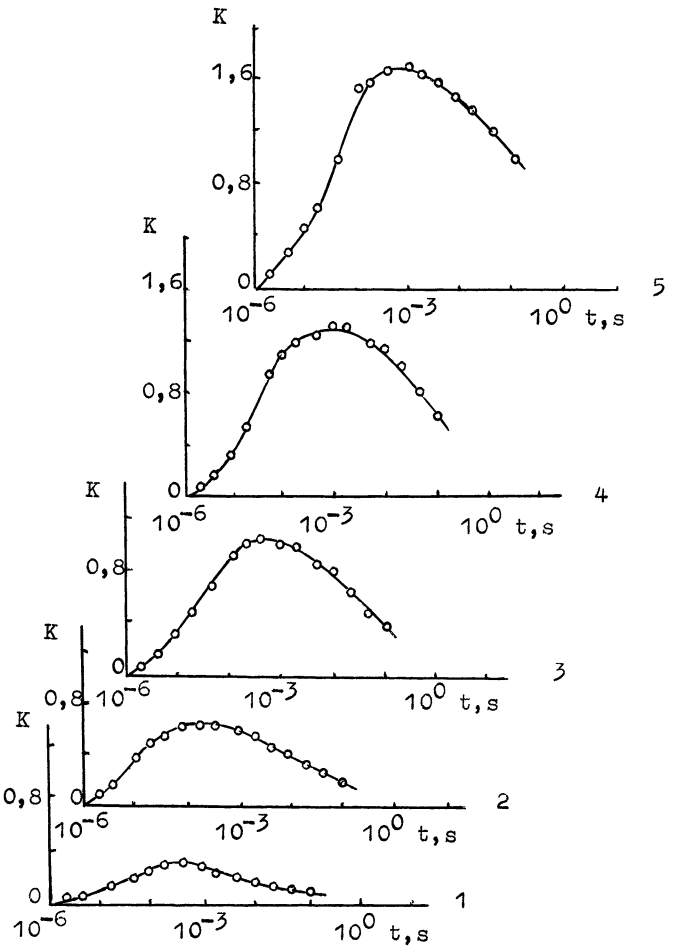

Fig.6. The time dependence of the displacement of interferencial band obtained by the holographic method. p = 70 torr, τ_{im}, μs: 1 - 5; 2 - 10; 3 - 20; 4 - 50; 5 - 100.

that the vibrational-translational relaxation is quite enough to provide with the gas heating rate on the stage of plasma deionization.

To explain the molecular gas heating in the active phase of discharge a mechanism is invoked in works [8 - 10] dealt with the energy transport to the translational degrees of freedom of nitrogen in self-quenching the metastable nitrogen states. With the aim to determine the importance of electron-excited states of nitrogen we have carried out a numerical calculation of the behavior in time of the nitrogen molecules concentrations in the $A^3\Sigma_u^+$ and $B^3\pi_g$ states and the gas temperature. According to estemations, at the experiment conditions the main channel of occupying the $A^3\Sigma_u^+$ and $B^3\pi_g$ states is the excitation from the ground state of nitrogen (the dependence of exitation constants on the value of electric field is given in [5]). The extinction of the $n_2(A^3\Sigma_u^+)$ molecules goes through the following main channels: their self-quencher at the interaction with each other (values of this constant giving in literature are from 10^{-12} to $1{,}5\cdot10^{-9}$ cm^3s^{-1}; we have used in our calculations $k_q = 5\cdot10^{-10}$ cm^3s^{-1}); the quencher by the vibrationally excited molecules of nitrogen $k_{N_2} = 3\cdot10^{-10} cm^3s^{-1}$ [11] and by oxygen molecules $k_{O_2} = 3\cdot10^{-12}$ cm^3s^{-1} [12]. Molecules of nitrogen in the state $B^3\pi_g$ are quenched effectively with the transmission of the excitation to the $A^3\Sigma_u^+$ level due to collisions with havy particles and self-induced transitions ($\tau = 5\cdot10^{-6}$ s). We have also taken into considerations the deexcitation by an electron strike and the diffusion of the molecules $n_2(A^3\Sigma_u^+)$ from the discharge zone ($D\cdot N = 5{,}9\cdot10^{18}$ $cm^{-1}s^{-1}$ [13]). Because the calculation has only considered initial parts of the pulsed discharge, so we have neglected the influence of atomic nitrogen. When calculating the gas temperature we have taken into account the energy transmission into the translational degrees of freedom at the self-quencher of the electronically excited states of nitrogen (the part of energy transmissed in this process $\eta_1 = 0{,}4$) and their quencher in interacting with the vibrationally excited molecules of nitrogen ($\eta_2 = 0{,}3$), as well as energy loses from the discharge zone to outer space. The influence of the skin-effect and the motion of the discharge has been modeled in the calculation by a correcting

coefficient introduced into the balance equation. The transmission of energy from vibrational levels to translational degrees of freedom has been neglected for conditions of the pulsed discharge. The calculation has been made for various reduced electric field ranging from 50 to 500 Td. It should be noted, that according to results of the numerical calculation, the constants' k_q and k_{N_2} values effect strongly on calculated concentrations of nitrogen molecules in the $A^3\Sigma_u^+$ and $B^3\Pi_g$ states but they practically don't on the gas heating rate. Thus, for example, increase of the constants results in the concentration decreasing, the product $k_q \cdot n_m$, however, remains unchanged.

The calculation has shown (Fig.7) that the dependence of the concentration of metastable molecules on time is not monotonous, a maximum value of the $n_m(A^3\Sigma_u^+)$ concentration reached in the beginning of action exceeding the stationary value $n_m^{st} = (1 - 5)\cdot 10^{14}$ cm^{-3} for one order of magnitude, while the occupation of the $B^3\Pi_g$ states being approximately two times lower.

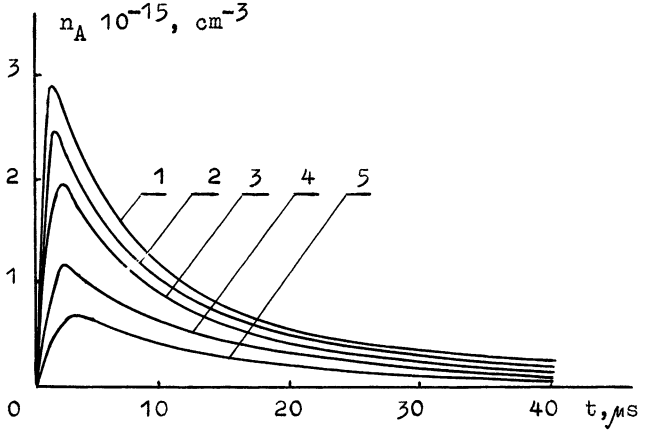

Fig.7. The time dependence of the concentration of metastable $A^3\Sigma_u^+$ molecules calculated by numerical method. p = 35 torr, $n_e = 10^{12}$ cm^{-3}, E/N, Td: 1 - 500; 2 - 375; 3 - 255; 4 - 175; 5 - 135.

Moreover, the growth of the reduced electric field results in the metastable molecules concentration rising up and

quick increase of the gas heating rate (see Figs. 8 and 9).

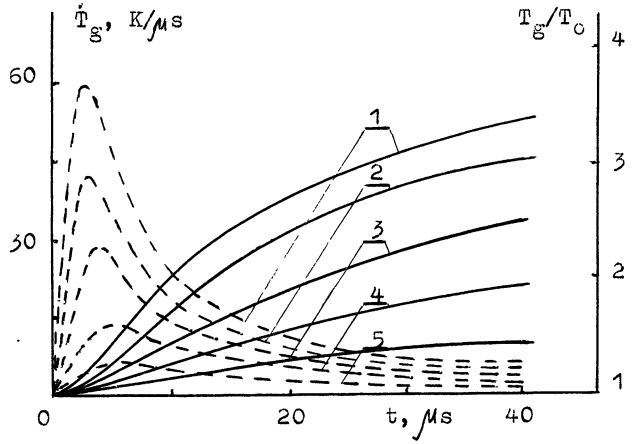

Fig.8. The dependence on time of the gas temperature (full curves) and of the gas heating rate (broken curves) at different values of the reduced electric field E/N, Td: 1 - 500; 2 - 375; 3 - 255; 4 - 175; 5-135. (p = 35 torr, $n_e = 10^{12}$ cm^{-3}).

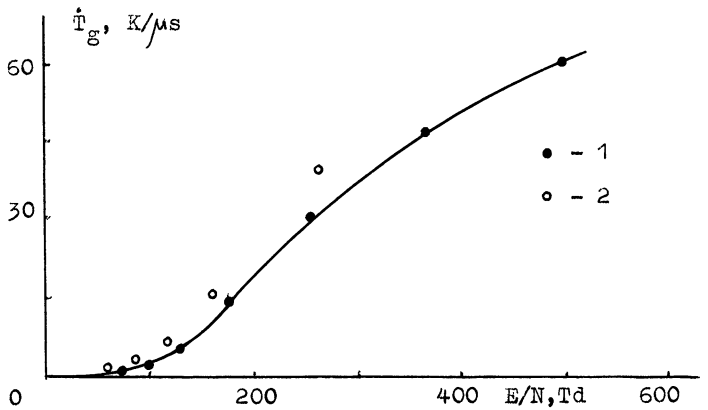

Fig.9. Calculated (1) and experimental (2) dependence on the reduced electric field of the gas heating rate, p = 35torr, $n_e = 10^{12}$ cm^{-3}.

In a microwave discharge with a small convergent angle, a wave of breakdown as well as a zone of promoted energy output

escape a focus quickly backward the energy flow. There are various methods to localize microwave discharge within a fixed region of free space. In this work we used a so-called programable action regime, the essence of which was as follows: the gas breakdown was resulted by a short powerfull pulse during which the discharge had no time for living the focal region, while a second pulse of small amplitude was used to support the discharge. This second pulse can not induce the breakdown of gas by itself but, wether the breakdown is realized, the microwave power of the pulse is enough to support the discharge for a long time. At the same time, it is possible to control parameters of the localized microwave discharge (e.g., size, velocity of discharge moving, electrons density and temperature, gas heating) in a wide range by changing the amplitude of the second pulse.

It follows from optical measurements that the temperature of electrons in plasma of the localized microwave discharge in air is of the order of 1 eV, and changes little during the pumping pulse and if the air pressure is changed, while the electron density in plasma during that pulse is one order of magnitude and more less than the critical value for an pumping generator. Such a low value of the electron concentration in plasma of the localized microwave discharge is due to kinetics of the charged particles balance with negative ions considered. There is experimentally shown also that the electron concentration in plasma of the localized discharge depends on the power level of the pumping generator, an effective coefficient of recombination being of the order of 10^{-7} $cm^3 s^{-1}$ at the experimental conditions described above, which fact is in good agreement with data of other authors [14].

To make it clear what's the role of electronically excited nitrogen molecules, the measurements have been carried out of the gas heating rate in plasma of the localized microwave discharge. The heating rates obtained in the experiment for various densities of energy flow in the pumping pulse is given in Fig.9. One can see that the values obtained by experiment are in satisfactory agreement with the calculated dependence.

There has been also measured the rate of the gas heating, during the pumping pulse for various its delays (t_{del}= 0-1 ms)

in relation to the back front of the first pulse. Fig.10 shows the obtained results.

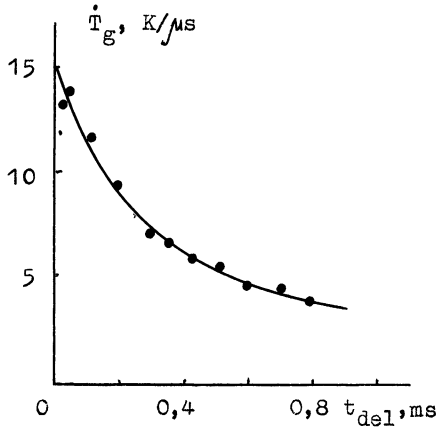

Fig.10. The rate of the gas heating during the pumping impulse for various its delays.

As one can see, the rate of the gas heating lowers from 15 K/μs to 4 K/μs for t_{del}= 1 ms. The vibrational temperature in the localized discharge remains constant for any delays, i.e., the contribution of the vibrational reservoir doesn't change at that. Because the electric field of the pumping pulse is less than that of the first pulse $E_2 < E_1$ and, respectively, the electron density in plasma of the localized microwave discharge is less than that in plasma of the running discharge, so, as it follows from the calculation, the gas heating rate in the pumping pulse at its zero delay with respect to the breakdown pulse, must be less than the rate T_g in the first pulse, what has been observed in the experiment. As t_{del} increases, the concentration of metastable molecules of nitrogen which remain in the discharge zone in the while between the end of the first pulse and the beginning of the second one, decreases. Accordingly, the rate of the gas heating decreases (Fig.10).

So, these experimental and theoretical results let us conclude that for high values of the redused electric field quenching of metastable electronically excited states of nitrogen molecules is one of the main mechanisms resulting in gas hea-

ting in the free localized microwave discharge in a focused beam.

Investigations with the help of a schlieren photography of dinamics of formation and disappearance of a cavern (i.e., zone with the reduced gas density) in a region where the localized discharge exists have shown that the cavern is in fact a field with sharp borders, no sharp gradients of molecules of a gas concentration, however, is observed inside (Fig.11). Time of formation of the density pit lowers with the air pressure rises up (Fig.12). The speed of the distribution of a cavern border which is less that the sound speed in cold, unexcited air, shows a maximum value in the beginning of the programed pulse and decreases by the end of the pumping pulse (Fig.13).

Power microwave generators used in experiments possess is not enough for a breakdown in gas at pressures greater than 100 torr. It's known, though, [1] stimulated by one or another way discharge can be supported for a long time at conditions of weaker field (of less than a threshold value for unexcited gas). Our experiments showed a common condition of a microwave discharge and plasma parameters do not depend on a method of the stimulation. Moreover, at pressure $p < 100$ torr they don't, depend on is there an stimulator or not, as well. With the use, of the stimulation by spark, there has been obtained a homogeneously shinning plasma formation at the atmospheric pressure of air in the regime of single pulse of the microwave radiation 1 ms long. In the beginning of influence a brightly shining channel appeares which transforms some time later into a homogeneously shining ball, and futher on it expands anywhere with the rate of 10^3 cm/s. The gas temperature within such a discharge approaches 6000 K. After the microwave discharge ends this plasma formation is shining for a few millisecond in the visual range of spectrum and for 100 ms in the infrared range. This fact points that the ionisation has a thermal nature and the discharge represents a quasiequilibrium plasma formation. With rising up gas pressure, the electron density in plasma of the localized discharge increases and approaches at $p = 760$torr the value of $7 \cdot 10^{14}$ cm^{-3} (Fig.14). The calculation of the ionization temperature from the Saha equation with the use of measured values of n_e (Fig.15) gives $T = 6500$ K, which correlates with

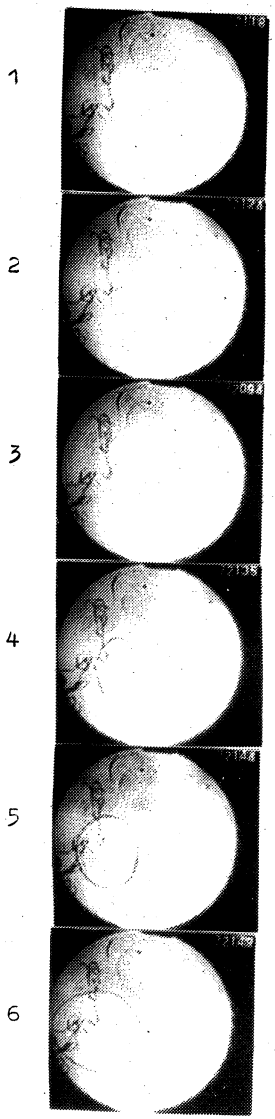

Fig.11. The dinamics of a cavern formation in a region of existence localized discharge. p = 70 torr, t, μs: 1 - 20; 2 - 50; 3 - 100; 4 - 200; 5 - 500; 6 - 1000.

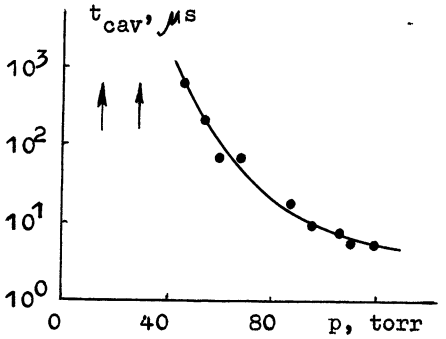

Fig.12. The time of formation of the density pit dependence upon the air pressure.

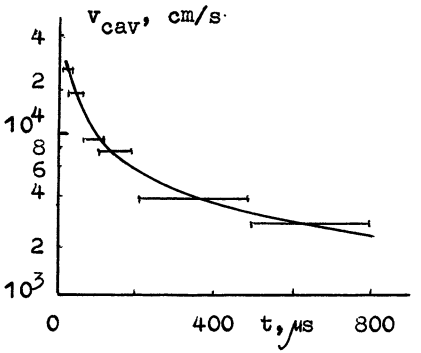

Fig.13. The dependence on time the speed of the distribution of a cavern border in the localized discharge.

the determined by spectroscopic methods plasma temperature T = 6000 K quite well (Fig.16). As the flux density of applied energy rises up, a time constant of the electron concentration increase lowers (Fig.15), while the electron concentration at the end of the microwave pulse increases (Fig.17), that is,the mic-

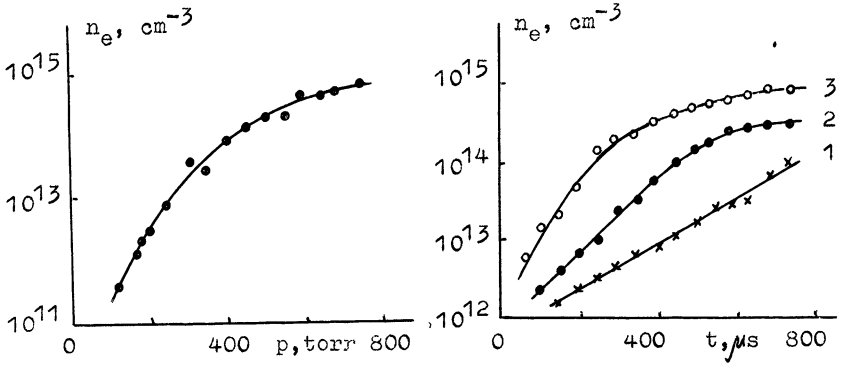

Fig.14. The electron density dependence upon the gas pressure in the localized discharge.

Fig.15. The time dependence of the electron density in the localized discharge. p = 760 torr, S,kW/cm^2: 1 - 5; 2 - 8; 3 - 10.

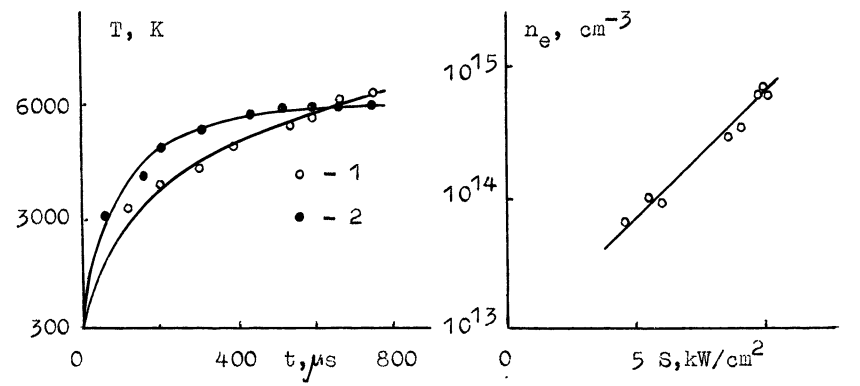

Fig.16. Calculated (1) and determined (2) by spectroscopic method the time dependence of the plasma temperature, p = 760 torr.

Fig.17. The electron density dependence upon the flux density of applied energy, p = 760 torr.

rowave energy applied to the discharge let us control plasma parameters of a quasiequilibrium microwave discharge in air in a focused beam.

Electrons are distributed along the axis of the discharge chamber in a table-like fashion with quite sharp borders (Fig.18), which is characteristic for a slow burning regime of the microwave discharge expantion. On the stage of the plasma recombination of the atmospheric pressure, as a gas is cooling, a slow descent of the electron concentration is taking place up to the level 10^{12} cm^{-3}, at low air pressure, though, n_e descends sharply on the microwave field switching off, which is characteristic for unequilibrium plasma.

In the quasiequilibrium discharge at p = 760 torr, the rate of the gas heating approaches the value of 50 K/μs in the beginning of the microwave pulse, the temperature of gas increasing up to 6000 K by the end of the pulse and, after switching off field, the slow cooling takes place with the characteristic time 1 ms defined by the thermoconductivity (see Fig.19). At low pressures of air, a strong vibrationally -

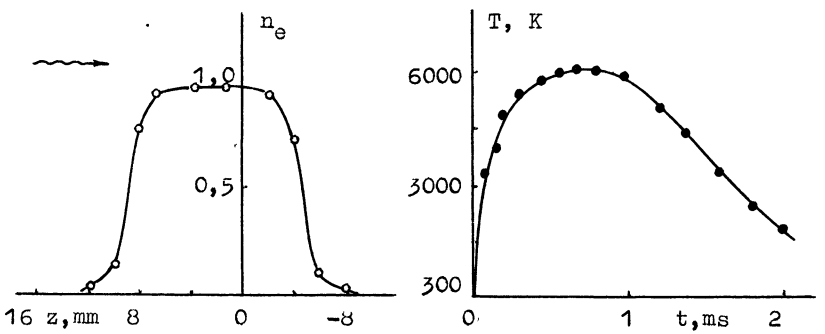

Fig.18. The distribution of electrons along the axis of the discharge chamber. p = 760 torr.

Fig.19. The time dependence of the plasma temperature in the afterglow stage of the microwave discharge in air.

translational nonequilibrium of the order of $T_v/T_g \sim 10$ is observed (Fig.20). With pressure rising up, the vibrational temperature lowers and the that of gas increases, so at the air pressure of about p = 400 torr, the vibrationally-translational

nonequilibrium disappears.

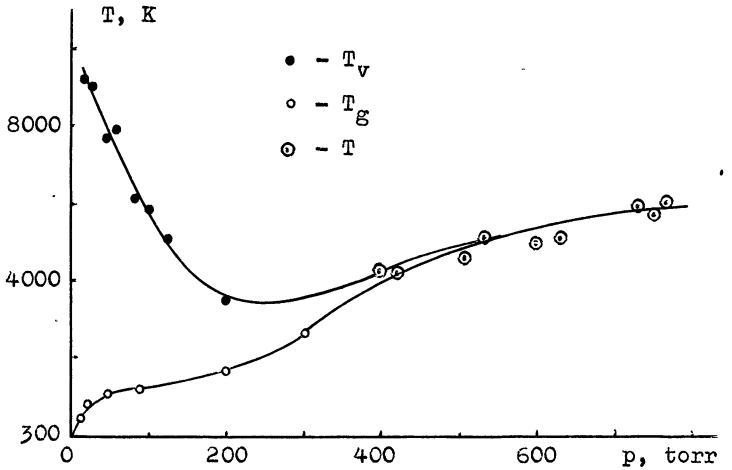

Fig.20. The temperature dependence upon the air pressure in the localized microwave discharge.

It follows from the interferencial-holographic method that the temperature distribution along the chamber axis displays sharp gradients at the plasma's boundary (Figs.21, 22), which fact is typical for discharges expanding in the slow burning

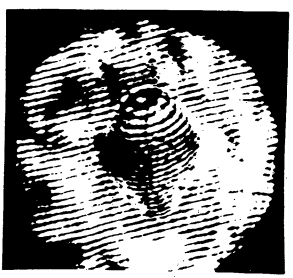

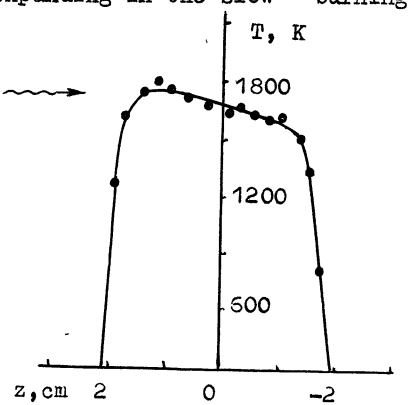

Fig.21. Interferogramma localized microwave discharge in air, p = 200 torr, τ_{im} = 1 ms, t_{del} = 1 ms.

Fig.22. The distribution of temperature along the axis of the discharge chamber. p = 200 torr, τ_{im} = 1 ms, t_{del} = 1 ms.

regime, and on last stages of the deionization of plasma the convective flow of the gas is transformed into mushroom-like structures.

A problem has arised: if it's possible to support in a definite place of free space the microwave discharge in air produced by a focused beam of electromagnetic waves. Experiments showed that at the power flux density $S \sim 10^3$ W/cm^2 the discharge represents a more or less homogeneoudly shining object stretched in the direction of the focusing aerial (Fig.23). The

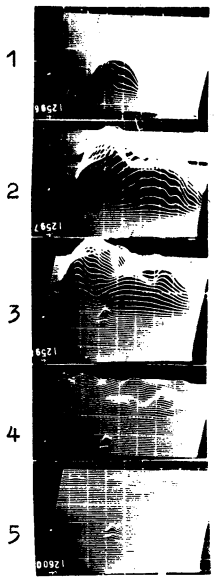

Fig.23. Cinematogramma of the thermal profile microwave discharge in air. p = 760 torr, S = 10^3 W/cm^2, τ_{im} = 100 ms, t_{del},ms: 1 - 0; 2 - 100; 3 - 200; 4 - 300; 5 - 400.

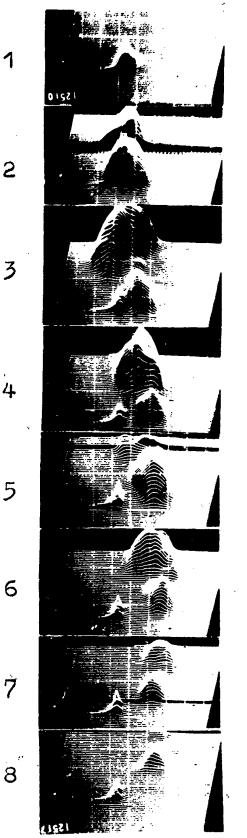

Fig.24. Cinematogramma of the thermal profile microwave discharge in air. p = 760 torr, S = 200 W/cm^2, τ_{im} = 600 ms, t_{del},ms: 1 - 0; 2 - 100; 3 - 200; 4 - 300; 5 - 400; 6 - 500; 7 - 600; 8 - 700.

The velocity of the discharge's front is of the value of $5 \cdot 10^2$ cm/s. Heated up to high temperature, strongly excited and shining, the volume of air goes up because of the Archimed's law and, colling down, leaves the focal region. Since the gas in the volume of discharge has high temperature (T = 6000-7000 K) and ionizing and exciting air is due to the thermal process, so the region of space where the discharge existed, continues to light brightly for 300 ms after the microwave pulse has finished.

At the less microwave energy flux density ($S < 10^3 W/cm^2$) one could obtain a discharge looking like a separated plasma formation of the size of centimeters, moving through the free space to the focusing aerial in the slow burning regime (see Fig.24). The velocity of the discharge's motion is controlled by the change of the energy flux applied (Fig.25). A threshould exists at which this regime appears equaled to 200 Watt/cm^2, the movement velocity at this point decreases up to 5 cm/s, and the time of arising the slow burning regime increases (Fig.26). Since the process is going with rates much less that the sound speed, it is possible in the framework of the adiabatic approach on the basis of data of the thermal profile cinematogramma in the inverse mode (see Figs. 23, 24), to investigate the dinamics of the appearance, the existance and the decomposition of the cavern in the focal region of the discharge chamber.

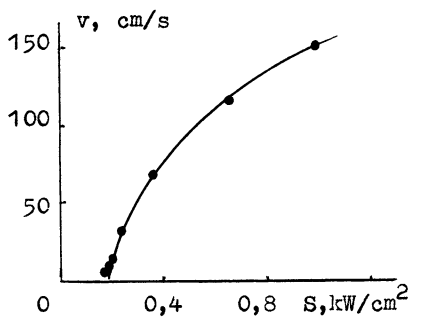

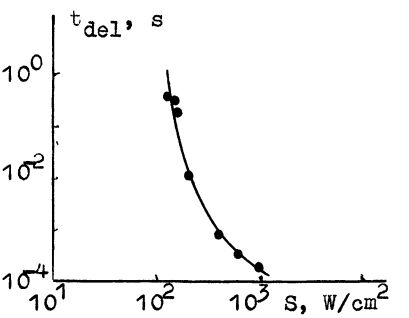

Fig.25. The velocity of the discharge's motion dependence upon the energy flux density. p = 760 torr.

Fig.26. Dependence on the energy flux density of the time of arising the slow burning regime. p = 760 torr.

If the microwave energy is applied in the horisontal plane, two destinguished directions exist, namely, the horisontal one of the discharge expantion and the vertical one of the most effective thermal evaluation from the discharge because of convective motions. The discharge at this starts to move as a hole back in relation to the flow of energy applied and simultaneously rising up, it leaves a threshould zone where its support is possible. To make the full stop of the discharge and provide it with energy for a long time in a fixed place of the free space, i.e., realize the stationary microwave discharge in the focused beam, we introduced in this work and experimentally arranged a method of the vertically applience of the microwave energy to a discharge from below, as it was in the experiment in the laser range [15]. In this case, moving down back to the energy flow, the discharge reaches boundaries of the threshold zone where it had to die out. However, due to the convective flow of the heat up, a field above the discharge happens to be hot, the gas density in there being lower than the density of the unexcited gas in front of the discharge. Moreover, the electric field in the focal region is greater that at the boundary of the threshold zone due to the beam focusing. In other words, in the focal region promoted conditions are present for the discharge support. Under these conditions the discharge can be supported stationary in a fixed place of the free space.

By using this method, a microwave discharge has been realized in the focused beam, burning in a fixed place of the free space for 10 s. And what's more, different regimes of the microwave discharge have been observed depending on the level of the energy applied flux density: the motion down with different speeds, the localization in the beam's focus or the motion of a plasma ball with the diameter 10 - 30 cm vertically up with the speed of about 10^2 cm/s.

REFERENCES

1. G.M. Batanov, S.I. Gritsinin, I.A. Kossiy et al. Proc. of Phys. Inst. Acad. Sci. USSR, 1985, **160**, 174-203. (in Russian)
2. V.A. Vanke, V.M. Lopukhin, V.L. Savvin. Usp.Fiz.Nauk, **123**, 633-654, 1977 (in Russian).
3. A.V. Gurevich. Usp.Fiz.Nauk, **132**, 4, 685-805. 1980 (in Russian).
4. G.M. Batanov, I.A. Kossiy, G.S. Luk'anchikov. Zh.Teor.Fiz. **50**, 2, 346-349. 1980 (in Russian).
5. V.D. Rusanov, A.A. Fridman. Physics of Chemically Active Plasma. Nauka, Moscow. 1984, 415 p. (in Russian)
6. G.M. Batanov, I.A. Kossiy, M.I. Rabinovich. Pis'ma Zh.Teor.Fiz. **5**, 7, 432-435, 1979 (in Russian).
7. A.Kh. Mnatsakanyan, G.V. Naidis. Teplofiz.Vys.Temp. **23**, 4, 640-648. 1985(in Russian).
8. J.P. Boeuf, E.E. Kunhardt. J.Appl.Phys. **60**(3), 915-923, 1986.
9. A.V. Berdyshev, A.L. Vikharev, M.S. Gitlin et al. Teplofiz.Vys.Temp. **26**, 4, 661-666. 1988 (in Russian).
10. A.A. Kuzovnikov, V.V. Lodinev, V.M. Shibkov. In: Proc. 1st All-Union Conference on Interaction of Acoustic Waves with Plasma. Erevan, 1989, p. 39-40. (in Russian)
11. N.A. Bogatov, M.S. Gitlin, S.V. Golubev, S.V. Razin. Preprint N 219. IAP, USSR Academy of Science. Gorky. 1988, 38 p. (in Russian).
12. B.M. Slovetsky. Mechanisms of Chemical Reactions in Nonequilibrium Plasma. Nauka, Moscow, 1980, 310 p. (in Russian).
13. B.M. Smirnov. Ions and Excited Atoms. Atomizdat, Moscow, 1974, 415 p. (in Russian).
14. A.L. Vikharev, O.A. Ivanov, A.N. Stepanov. Plasma Phys., **10**, 4, 792-800, 1984.
15. N.A. Generalov, V.P. Zimakov, G.I. Kozlov et al. Pis'ma Zh.Eksp.Teor.Fiz. **11**, 447. 1970 (in Russian).

MECHANISMS OF FREELY-LOCALIZED SHF-DISCHARGE STRUCTURE FORMATION IN A HIGH PRESSURE GAS

E.Ya.Kogan, B.U.Kusin.

Pedagogical Institute, 443043 Kuibyshev, USSR

The dynamics and spatial structure of a discharge in under threshold SHF-fields have a number of peculiarities related to the mechanism of non-self-maintained to self-maintained dicharge transition. Generally, it is based on ionization-superheating instability in one of its manifistations. In a molecular gas it manifests through the ionization frequency dependence $\nu_i(E/N)$ on the electric field intensity E in the radiation falling on gas and the density N of the gas.

In atomic (inert) gases the ionization, characterising the transition to a self-maintained discharge develops from metastable states more rapidly.

The characteristic temporal scale of superheating instability is connected with the gasdynamics of gas locally heated by plasma $\tau \sim P/\sigma E^2$ where σ, P is the conductivity and the pressure of the gas, respectively . Therefore the temporal and spatial dynamics of the discharge through molecular gases is defined by the gas parameter evolution. The plasma parameters come to a dynamic equilibrium on the characteristic scales of the evolution. It allows to reduce the combined equations for gas, plasma and field to the relations describing the temperature of the gas, T, and the density of plasma, n_e.

$$\frac{\partial n_e}{\partial t} = \tilde{D}_a \frac{\partial}{\partial x}\left(T^{\varphi} \frac{\partial n_e}{\partial x}\right) + LT\, n_e - FTn_e^2 \qquad (1)$$

$$\frac{\partial T}{\partial t} = \frac{\gamma-1}{\gamma} Fn_e T^2 \qquad (2)$$

This couple of equations is true at an adiabatic gasdynamics, P=const, and a dissociative recombination. Contrary to Ref [1], it considers the plasma transfer during the gas motion on the account of

friction between them.

This circumstance brings a number of features into the evolution of a discharge, they can be seen in the automodel solutions (3).

Itroducing an automodel variable $\xi = x / (t_0 - t)^{\frac{\beta-\varphi}{2\beta}}$, we have

$$n_e = (t_0 - t)^{\frac{-(\beta-1)}{\beta}} \vartheta(\xi); \quad T = (t_0 - t)^{1/\beta} \cdot f(\xi) \qquad (3)$$

The asymptote of $\xi \to \infty$ of the introduced funtions is $\vartheta(\xi) \sim \xi^{-\frac{2(\beta-1)}{\beta-\varphi}}$; $f(\xi) \sim \xi^{-2/\beta-\varphi}$. The characteristic dimension of the discharge is $\Lambda (t) \sim (t_0 - t)^{\frac{\beta-\varphi}{2\beta}}$, it defines the possibility of the three different regimes : $\beta < \varphi$, $\Lambda(t_0) \to \infty$; $\beta = \varphi$, $\Lambda(t_0) = \text{const}$, $\beta > \varphi$, $\Lambda(t_0) \to 0$ - the discharge collapses. $\beta = 5$, $\varphi = 3$ for the discharge through the air and the last condition is realized. An explosive instability, described by that regim is characterized by a slower variation of plasma density and Λ, than in the model in Ref [1].

The dimension of the SHF- power absorption $\Lambda (t \to t_0) \to \lambda$, is the maximum scale of a collapsing discharge. If a superheating-ionization instability defines the regime of the discharge evolution, its threshold is defined not by the local processes of the particle death, but by their transfer from the region of heating by expanding gas

Note here, that in a molecular gas along with the ionization-superheating instability the development of the dissociation-ionization instability may occur. The latter is connected with the decrease of the accomodation ratio of the electron in the process of dissociation of gas and growth of electron-atom collisions. $\tau_d \sim \frac{N \mathcal{E} d}{\sigma E^2}$, is the characteristic time of dissotiation, the time of gas heating is defined by one of the two mechanisms either VT-relaxation, or elastic scattering with a characteristic time $\tau_{vT} \sim \frac{1}{p} \cdot \exp (-\text{const} \cdot T^{-1/3})$, $\tau_y \approx \frac{M}{m} \cdot (\eta \cdot \nu_{em}^{y})^{-1}$. At $\tau_d \ll \tau_{vT}$, τ_y dissociation-ionization instability defines the regime of the discharge evolution. The gasdynamic processes do not control the plasma parameters in the discharge.

In atomic (inert) gases the growth of plasma density is caused by the development of instability related to a stepwise ionization. The occupation of the excited states by an electron shock results in the increase of the rate of the electron level excitation. The numerical

analysis of the SHF-discharge dynamics and kinetics in Ar [Ref.2] allows to assert that in a wide range of parameters (p ~ 100-760 tor, E/N ~ $5\cdot 10^{-17}$ w·sm^2 - $2\cdot 10^{-15}$ w·sm^2) the instability cansed by a stepwise ionization is the only mechanism controlling the discharge evolution.

Fig.1 presents a temporal variation of FSH-dischange parameters in Ar at one set of guantities - p = 760 tor, E_o = 2600 w/sm, $\omega = 7{,}85\cdot 10^{10}$ s^{-1} (T, T_e are the temperatures of gas and electron, respectively; n_e, N^+_m, N^*_{4s}, N^*_{4p}, N are the concentrations of electrons, molecular ions, excited 4S and 4P states, neutral particles of gas, respectively; E is the electric field intensity in plasma; λ is the skin-layer). Ionization-superheating instability is of no sufficient importance in the discharge dynamics, so far as the electric field intensity E decreases more rapidly, than the gas density N at its heating and expansion.

In this case the initial stage of the discharge evolution can be discribed by a set of equations

$$\frac{\partial n_e}{\partial t} = D_a \Delta n_e + (k_i N + k_i^* N^*) n_e - \beta_r n_e^2 \qquad (4)$$

$$\frac{\partial N^*}{\partial t} = k_v N n_e \qquad (5)$$

Here k_i, k_i^*, k_v are the constants of the ionization from the ground and excited states, excitation of electron states, respectively, N^* is the concentration of the excited states. At $k_i^* N^* >> k_i N$, $\beta_r n_e$ Eqs. (4-5) are assumed to have an automotel solution $N^* = (t_o - t)^{-1/2}\theta(\xi)$, $\xi = X/(t_o - t)^{1/2}$, describing N^*, n_e and thecollapse of the characteristic dimension of the discharge at $t \to t_o$. When the loss of electrons is related to local processes the exact solution of Eqs.(4-5) at $\beta_r N_o^*/k_v N << 1$ is

$$\tilde{N}^* = \frac{1 + \frac{2c-b}{\sqrt{-A}} \operatorname{tg} \frac{\sqrt{-A}}{2} t}{1 + \frac{b-2a}{\sqrt{-A}} \operatorname{tg} \frac{\sqrt{-A}}{2} t} \qquad (6)$$

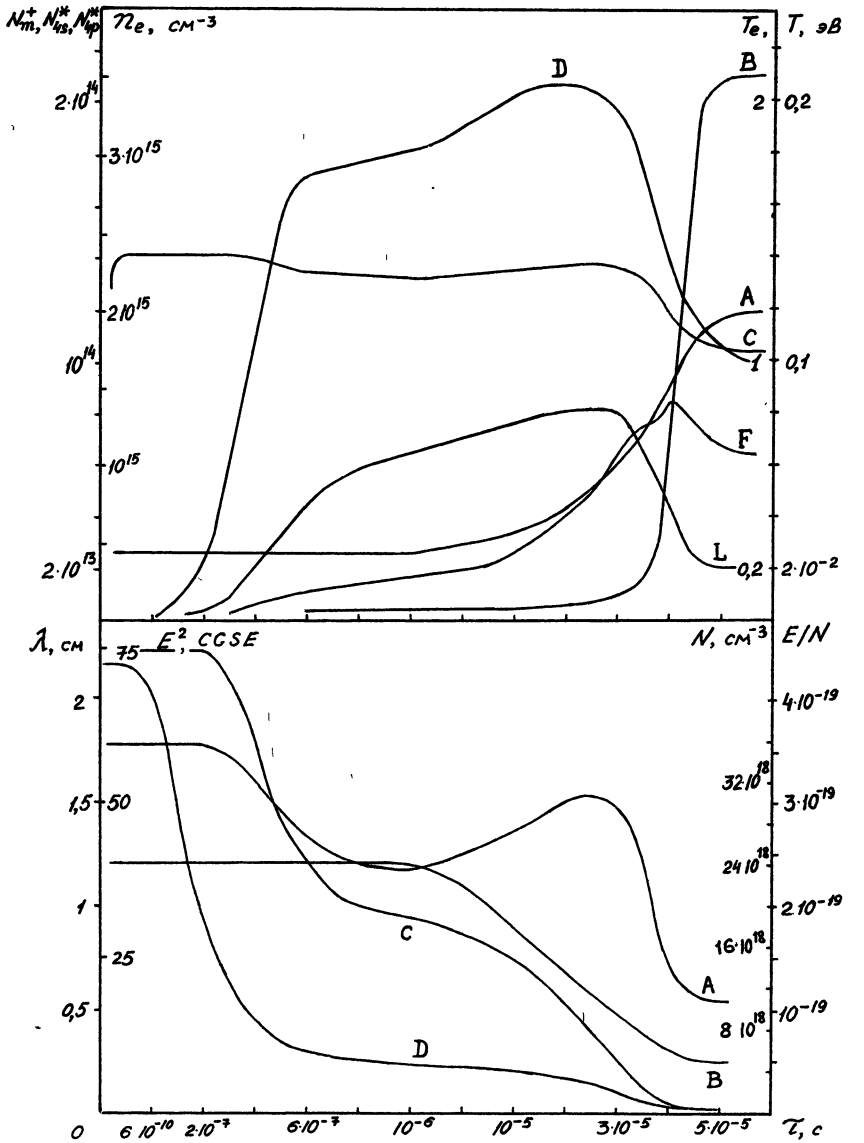

Fig.I Evolutionary variation of SHF discharge parameters in Ar P=760 Torr, E^2=75 CGSE
a) A-T, B-n_e, C-T_e, D-N_{4s}^*, F-N_{4p}^*, L-N_m^+;
b) A-E/N, B-N, C-E^2, D-λ

$$A = (k_i N)^2 + 2\frac{k_v N}{\beta_r N_o^*}(k_i^* N_o^*)^2 - 2k_v N k_i^* n_{eo} - (\beta_r n_{eo})^2 < 0 ,$$

$$a = -\frac{1}{2}[k_i^* N_o^* + \frac{\beta_r N_o^*}{k_v N}(\beta_r n_{eo} - k_i^* N_o^* - k_i N)], \quad b = [\beta_r n_{eo} - k_i^* N_o^* - k_i N],$$

$$C = \frac{k_v N}{\beta_r N_o^*}(\beta_r n_{eo} - k_i^* N_o^*), \quad \tilde{N}^* = N^*/N_o^* .$$

If follows from the eguation that the explosive charaeter of the solution in realized at $\beta_r n_{eo} < 2k_i^* N_o^* + k_i N$, $A<0$. On the base of the above mentioned one may come to a conclusion: since the filamentary structure of SHF-discharge was observed both in molecular and inert gases,(Ref [3]),and the development of the ionization - superheating instability in inert gases is impossible in scales of parameters of Ref [3], the formation of its stationary structure does not depend on a concrete type of instability.

The discharge structure in SHF-fields is formedby not only the processes of kinetics, bound and free states of electrons and by the transfer of particles and heat. The transfer of the discnarge radiation with a sufficient ionizing part in the spectrum turns to be important. The significance of the radiation is in the formation of the regions of a non-self-maintained discharge with the parameters near the instability threshold. If the radiation transfer occurs on the length L, and the time of instability development is $\sim\tau_i$, then L/τ_i is the velocity of the transfer. The time of the instability development is characterized by a slower process of gas expansion $\tau_i \sim l/C_s$ (l is the discharge dimension, C_s is the acoustic velocity). The velocity of the discharge transfer $U \approx C_s L/l$. At $L/l > 1$ the wave becomes supersonie.

The analysis shows, that a supersonic wave of abreakdown may appear in the under thershold field only under the condition of the photostimulated ionization of the region L in plasma before the breakdown.

The analysis shows that (if the photoprocesses and radiation transfer are taken into considiration) the consideration of the photoprocesses and radiation transfer results in the construction of the three types of structures - a soliton like, periodic nonlinear wave and a stationary periodic structure. The first and the second are realized depending on the level of an incident field, i.e. the periodic structure

changes into a soliton like wave of ionization with the increase of the field intensity. The velocities of the structure propagation are equal.

$$U = 2\beta \frac{\gamma-1}{\gamma} \frac{\sigma|E|^2}{P} \frac{\nu^j}{\beta_r n_o k_o} \approx 2\beta \frac{C_s}{k_o l} \qquad (7)$$

where is difined by $\nu_i \sim (\frac{E}{N})^{2\beta}$, ν^j is the eleectron excitation frequency of particles; $\beta_r n_o$ is the frequency of the dissociative recombination; k_o is the absorption ratio of ionizing radiation in the centre of the line.

The set of equations describing a one-dimensional model of a breakdown in the approximation of isobaric gasdynamics [4] includes

$$\frac{\partial N}{\partial t} + \frac{\partial}{\partial x} (N\upsilon) = 0 \qquad (8)$$

$$\frac{\partial n_e}{\partial t} + \frac{\partial}{\partial x} (n_e\upsilon) - D_a \frac{\partial^2 n_e}{\partial x^2} = \nu_i n_e - \beta_r n_e^2 + \alpha JN \qquad (9)$$

$$\frac{\gamma}{\gamma-1} P \frac{\partial \upsilon}{\partial x} = \frac{1}{2}\sigma|E|^2 + \frac{\partial}{\partial x} (\varkappa_e n_e \frac{dT_e}{dx}) - \nu^j \varepsilon n_e \qquad (10)$$

$$C \frac{\partial J}{\partial x} = \nu^j n_e - \alpha JN \; ; \qquad (11)$$

$$\frac{\partial |E|^2}{\partial x} = -\mathcal{M}|E|^2 \; , \qquad (12)$$

where υ is the velocity of the gas motion, C is the velocity of light, is the everage excitation power of the electron states, P=const., γ is the adiabatic gradient, α is the absorption ratio of radiation, J is the quantum density.

This set of equations gives the equation for a breakdown stationary wave for $\chi=N_o/N$, where N_o is the undisturbed gas density.

$$a_1 \frac{\partial}{\partial y} (\chi^{2\beta+1} \frac{\partial \chi}{\partial y}) + a_4 \chi^{2\beta+1} - a_5 \chi^{\beta-1} + a_6 = 0$$

y=x-ut; u is defined by relation (7). Without presenting the values of the coefficients a_1 in the text, note, that this equation allows the periodic structure and solitonlike solutions. The former has form $X = \frac{\Gamma}{(\gamma_1 - \gamma_2 \sin^2 \delta(y-y_0)}$ the latter has form $X = X_0 + \gamma_3[1-\mathrm{th}^2(\delta(y-y_0))]$.

The stationary structure is the alternation of regions of hot gas of lower density and a high degree of ionization, and of cold gas of low degree of ionization. These stationary regions can co-exist, if there is no energy stream between them:

$$(\chi \frac{\partial T}{\partial x})^2 \Big|_{T_1}^{T_2} = 0 .$$

$\frac{\partial}{\partial x}(\chi \frac{\partial T}{\partial x}) + F(N,T) = 0$ is a stationary equation of energy trans fer; T_1, T_2 are the gas temperatures in cold and hot regions, respectively. The given condition allows to find P values for which a steady stationary structure may be realized.

1. A.V.Kim, J.M.Friman. Physika plasmy. 1983. V.9.N3.P.613.

2. E.Ya.Kogan, B.U.Kusin. J.prikladnoy mehaniki i Tehnicheskoy Physiki 1988. N3. P.28.

3. S.V.Golubev, S.I.Gritzinin, V.J.Zorin, I.A.Kossui, V.E.Semenov. Sbornik naychnyh trudov vysokochastotnui razryad v volnovyh polyah 1988.Gorky.P.136.

4. T.I.Demidova, E.Ya.kogan, B.U.Kusin. J.prikladnoy mehaniki i Tehnicheskoy Physiki. 1989. N1. P.3.

STRUCTURIZATION IN STIMULATED MICROWAVE DISCHARGE

V.G. Brovkin and Y.F. Kolesnichenko
Moscow Radio Engineering Institute of USSR Academy of Sciences
Warsaw Highway, 132, Moscow

At the present time the formation of structures in the open nonequilibrium systems in one of the most intensively developing trends. In the respect the gaseous discharge is a very promising material. The discussion is specific to the microwave discharge in free space which demonstrates a great variety of structural forms [1-3]. This report discusses the formation of only some structures observed in the stimulated microwave discharge with the linear polarization of radiation.

Experiment Results. The time-space dynamics of formation of the discharge glow picture has been studied with the use of the integral and high-speed methods of photoregistration in the visible radiation range. It has been found out that the base of the discharge structure is formed by the longitudinal, relative to wave vector $\vec{k}$, branches, a significant number of elements of which lies in the plane of vectors $\vec{E}$ and $\vec{k}$. At the initial stage a discharge channel oriented in opposition to the microwave radiation is started from the initiator region. During about one microsecond (at $E > 2$ *kV/cm*) it assumes the size close to $\lambda/4$, and, bending at an angle varying within 55 to 70°, it resumes the same size. A new channel oriented along $\vec{E}$ and also having the size about $\lambda/4$ is formed near the break point of the main channel. As a result of it, a branch presenting a sinusoidal channel (with the axis along $\vec{k}$) is formed in plane $(\vec{E},\vec{k})$. This channel branches with the orientation along vector $\vec{E}$ before every extremum point (in the direction of propagation). The wavelength of the sinusoid is approximately equal to $\lambda/4$. Thus, the motion of the discharge at large is continuous.

Structural Zones. The analysis of the results of the experiments made both at the Moscow Radio Engineering Institute and other organizations makes it possible to divide the region of the stimulated discharge into several structural zones (SZ). The SZ are present in all the tested gases (air, pure nitrogen, helium, hydrogen and carbon dioxide). Every structural zone has its specific base element which serves as a basis for forming the structure of the discharge at large in a casual or determined way. At the variation of the external parameters the formation of the structure as well as the discharge propagation within SZ are determined by one mechanism that is not liable to the qualitative changes. There is a narrow transient region between the neighbouring structural zones. The transition from one SZ to another is accompanied with the qualitative changes in the structure and nature of the discharge propagation and with the appearance (pending the neglecting of the width of the transition region) of a fracture in the logarithmic graph illustrating the discharge propagation speed as function of the wave field intensity or gas pressure Let us consider two structural zones in detail

The wave structural zone (WSZ). This zone is determined by conditions $E > E*$ and $E/P < (E/P)*$, where E is the wave field intensity and P is the gas pressure. Here the discharge propagates in a streamer way that is as a result of continuous elongation of the channels in space which forms the discharge structure [4]. The sinusoidal element of structure with the branches described above is the basic in the formation of the discharge structure at large [3]. At the fixed external conditions that is pulse field intensity, pulse duration, gas pressure, the realization of the discharge structure varies from pulse to pulse. This is indicative of stochasticity in the formation of the discharge structure which is specific of the system formed in the streamer way. In the tested gases $E*$ amounts to *(1.2 - 1.8) kV/cm* (the first value is true for helium and the second - for carbon dioxide) at the frequency of the external field equal to $F = 7$ *GHz*. Hence there is critical pressure $P*$ for every gas below which the given structure cannot be realized. The

experiment has yielded the following approximate values of the critical pressure: air, N_2 - *70 torrs*, CO_2 - *50 torrs*, H_2 - *150 torrs*, *He - 500 torrs*.

The dipole structural zone (DSZ). This structural zone is determined by the condition $(E/P)_* < E/P < (E/P)_{brk}$, where $(E/P)_{brk}$ corresponds to breakdown value E/P of the gas in the microwave beam (without the initiator). Here the discharge propagates by jumps. The base element of this SZ is a half-wave dipole oriented along vector $\vec{E}$. The distance between the dipoles successively formed in the space is about $\lambda/4$. The dipoles are formed with the aid of the streamer mechanism. At first the avalanche of self-sustained breakdown originates at the beam axis at a distance of $\lambda/4$ from the previous dipole. Then the avalanche grows quickly into a streamer amounting to a half wave of the incident radiation. Then the process is repeated. Value $(E/P)_*$ amounts to *0.6* of value $(E/P)_{brk}$. The structure is steadily reproduced from pulse to pulse which is evidently connected with the appearance of the regions of self-sustained breakdown in the summary field of the incident wave and the wave reflected from the dipole.

Other structural zones. At $E < E_*$ but above the discharge initiation threshold there are at least two structural zones, one of which is a well-known thermic discharge [5,6].

Models of structural zones. The basis for forming a structure in the wave structural zone is the development of the streamer in the subthreshold microwave field. We have divided a very complicated problem of describing the formation of the structure into two parts: 1) considering the straight-line motion of the streamer in the quasi-static field with due account for the kinetics of the elementary processes and 2) the description of the curvilinear motion of the streamer tip involving the dependence of its motion on the parameters obtained in 1) and with the introduction of the wave effects 1). In [7] an expression has been obtained for the speed of the streamer straight-line motion in the form of an oblong ellipsoid of revolution in the subthreshold field: $V_s = gE_{oa}\lambda$, where g is the gas constant depending on the type of the gas, E_{oa} is in the

projection of the wave field intensity vector on the longer axis of the ellipsoid. It has been assumed that the active length of streamer 2a is of the order of a half wave of the incident radiation. By the assumption that the propagation of the discharge in opposition to the microwave radiation flux is effected due to the fractures and branching-off of the streamers taking place periodically in time and casually in space we have obtained a linear relation between the speed of discharge V_d and that of a streamer: $V_d = (2/\pi^2)V_s^{max}$, where V_s^{max} is the streamer maximum speed reached during its motion along wave vector $\vec{E}$. The maximum speed of discharge propagation in opposition to radiation is reached during the "sawtooth" motion of the streamer in plane $(\vec{k}, \vec{E})$ at an angle equal $\pi/4$. It amounts to a half of value V_s^{max}. Thus the structure resembling the base element of the wave structural zone appears in the simplest model 2). In making the equations of the curvilinear motion of the streamer tip we have assumed that the trajectory of motion is determined by the ratio of the amplitudes of the longitudinal (amplified) and transverse fields near the streamer tip (comp. [8]). The amplitude of the transverse field is taken at the moment when the amplified field is maximum. Phase incursion between the amplified and transverse components has been assumed in a first approximation proportional to the streamer elongation. For the plane problem we have obtained the original equations with variables (φ, ψ): $d\varphi/dt = V_s/\rho$, $d\psi/dt = kV_s$, where φ is the angle between vectors $\vec{E}_o$ and $\vec{V}_s$, $\rho = 0.5aE_{\parallel}/E_{\perp}$ is the radius of the streamer trajectory curve near its tip, $E_{\parallel}(\varphi)$ is the projection of vector $\vec{E}_o$ onto $\vec{V}_s$, $E_{\perp}(\varphi, \psi)$ is projection of vector $\vec{E}_o$ onto perpendicular direction $\vec{V}_s$ taken in phase ψ, k is wave number. The solution of the system of equations is a space-periodic function with a period close to a that is in the assumption of the first model to a quarter of the radiation wavelength. More realistic model of forming the structure discharge at large probably should combine both simplest models with the actual wave electrodynamics of the structure considered as a reception antenna. The antenna approach makes it possible to estimate the minimum value of electron concentration N_e in a channel. Considering that the maximum

impedance of the matched absorbing plasma medium (channel) does not exceed a half of the impedance Z of free space (i.e. $Z_p < 190$ ohms) [10], let us determine σ from equation $R = 4l/\sigma\pi d^2$ (where $l = 1$ cm, $d = 0.1$ cm are the experimental values of the channel length and diameter). Using formula $N_e = \sigma\nu_m/2.82\ 10^{-4}$ [5] keeping in mind that at the pressure close to atmospheric $\nu_m \gg \omega$, (where ω is the circulating frequency of the incident wave), let us determine $N_e \simeq 10^{18} cm^{-3}$ in a separate channel.

The base of the model describing the structure and propagation in the dipole structural zone consists in the fact that the scattering of the electromagnetic wave on the high-conductivity dipole leads to the appearance of the regions where the field intensity is higher than the intensity of the incident field. At not very small electrical dimensions of the dipole the first field maximum is located at a distance about $\lambda/4$ from it. The wave scattering at the half-wave dipole gives the maximum excess of the summary field of the incident and reflected waves over the incident field 1.583 times. Thus, if avalanche formation time τ_i in summary (breakdown) field exceed the time of the next growth of the streamer (the process considered in [9], the discharge propagation speed $V_d \approx \lambda/4\tau_i$, or $V_d \sim P\lambda\exp(-BP/1.58E_0)$, where B is included into the expression for ionization constant $K_i \sim \exp(-BP/E)$ [5]. The mechanism considered above ensures faster propagation of the discharge at $1.58E/P \geq (E/P)_{brk}$, that is $(E/P)_* \approx 0.6(E/P)_{brk}$ in accordance with the experiment results.

Universality of structural zones. The structural zones described above may be presented as universal, in other words, independent of the type of gas. Let us determine critical pressure P_*. It should be noted that $(E/P)_{brk} = kB$ where k is a coefficient which is but slightly dependent on the type of gas and other parameters (for estimates $k \approx 0.1$). Then it is easy to obtain $P_* \approx 1.58E_*/kB$ which well agrees with the experimental values of the critical pressure of the tested gases In dimensionless coordinates E/kBP and P/P_* the picture of breaking the region of stimulated discharge into the SZ is universal.

The obtained results prove the electrodynamic basis of

forming the structure of the stimulated, that is subthreshold discharge In this aspect the stimulated discharge, as it appeared, has but minor difference with the self-sustained discharge, that is overthreshold discharge. The main difference consists in that in the wave structural zone of the stimulated discharge the structure reproducibility from pulse to pulse is typologic but not absolute. Besides, the obtained set of data proves that the structure realized under the given conditions provides maximum speed of discharge propagation in opposition to the microwave flux and probably, performing the function of an adaptive antenna, its optimum reception.

The existence of the universal structural zones of the stimulated microwave discharge makes it possible to hope for creating a universal dynamic model of the microwave discharge in free space.

References

1. High-Frequency Discharge in Wave Fields. Gorky Institute of Applied Physics, USSR Academy of Sciences, 1988.
2. L.P.Grachev, I.I.Ishakov, and others. ZhTF, V 50, No 10, 1989, p. 149-154.
3. V.G.Brovkin, Y.F.Kolesnichenko. Letters to ZhTF, V 16, No 3, 1990, p. 55-58.
4. V.V.Baranov, V.G.Brovkin. Letters to ZhTF, V 16, No 15, 1990, p. 39-43.
5. Y.P.Raiser. Physics of Gas Discharge. M.: Nauka, 1987.
6. T.V.Borodacheva, V.E.Semenov. ZhTF, V 55, No 9, 1985, p. 1743-1747.
7. Y.F.Kolesnichenko. In book: Radiation and Plasmachemical Methods in Ecology. M. Moscow Radio Engineering Institute of USSR Academy of Sciences, 1989.
8. P.Uhlig, J.C.Maan, P.Wyder. Phys. Rev. Lett., V 63, No 18, 1989, p.1968-1971.
9. V.B.Gildenburg, I.S.Gushchin, A.V.Kim. Theses of Reports at the IInd All-Union Conference "High-Frequency Discharge in Wave Fields", Kuybychev: Kuybychev State Polytechnical Institute, 1989, p.33-34.
10. F.Grawford. Waves. M.: Nauka, 1974, p.527.

MODELING OF IMPULSE DISCHARGE IN MICROWAVE FIELDS IN NITROGEN

N.Yu.Babaeva, A.Kh.Mnatsakanyan, G.V.Naidis
Institute of High Temperatures, Moscow, USSR

The microwave discharge initiated in the beams of electromagnetic fields in millimetre and centimetre wavelength range tends to propagate towards the source of electromagnetic radiation. Experimental studies of discharge dynamics in air and nitrogen at pressures ~ 0.1-1 bar [1] show that at low values of electromagnetic energy flow density S the discharge front motion is continuous while at high (but still underthreshold) values of S the discharge propagates by jumps. In this case it has a form of separate plasmoids elongated in the direction of the electric field.

Earlier a model [2] describing continuous propagation of discharge front in nitrogen has been presented. The main ionization process in the model was the associative ionization in collisions of two metastable molecules $N_2(a'^1\Sigma)$ born in binary collisions of $N_2(x^1\Sigma)$ molecules in high vibrational states:

$$2\ N_2(x^1\Sigma, v \geq 16) \longrightarrow N_2(a'^1\Sigma) + N_2(x^1\Sigma), \qquad (1)$$

$$2\ N_2(a'^1\Sigma) \longrightarrow N_4^+ + e. \qquad (2)$$

The discharge motion in this case was due to gas photoionization ahead of the discharge front in the process of absorption of radiation from Birge-Hopfield bands of nitrogen by trace amounts of oxygen (0.1-1%). Excitation of these bands in discharge was supposed to occur in reaction analogous to (1)

$$2\ N_2(x^1\Sigma, v \geq 25) \longrightarrow N_2(b^1\Pi, b'^1\Sigma) + N_2(x^1\Sigma). \qquad (3)$$

(Essential role of traces of oxygen in the formation of the photoionization precursor ahead of the discharge in nitrogen and in its propagation was established experimentally in [3]).

For the excitation mechanism of electronic states (1),(3) to take place the energy input into the discharge should be slow enough since the quasistationary distribution of molecules at high

vibrational levels is to be formed. This distribution contains a region with slowly changing densities (a plateau).The rate of energy input increases with the growth of S, and at S high enough the validity of quasistationary model is violated. On the other hand when S grows the mean electron energy increases and the excitation of levels $N_2(a'^1\Sigma, b^1\Pi, b'^1\Sigma)$ by electron impact becomes effective as well as stepwise and direct ionization. Due to the strong dependence of excitation and ionization rates upon the mean electron energy the ionization takes place preferably in regions of maximum E/n values (E is the amplitude of microwave field and n is the gas number density). In the case of noticeable reflection of incident microwave radiation from discharge front it causes a transition to discontinuous regime of discharge propagation. In this work the model for this type of discharge in nitrogen is given[1].

The onedimensional motion of the discharge along the direction of linearly-polarized microwave radiation propagation is considered. The mean square root value of microwave field E is described by the following equation

$$\frac{d^2E}{dx^2} + \frac{\omega^2}{c^2}\varepsilon(x)\,E = 0, \qquad \varepsilon = 1 - \frac{4\pi e^2 n_e}{m\omega(\omega - i\nu)}, \qquad (4)$$

where n_e is the electron number density, ω and ν are the frequencies of microwave field and of electron-molecule collisions. The solution of eq.(4) is expressed as a superposition of incident and reflected waves, the value of the field E in incident wave is given at $X \longrightarrow -\infty$,and there is no reflected wave at $X \longrightarrow +\infty$. Kinetic scheme includes the processes of excitation and quenching by electron impact of the excited states $N_2(A^3\Sigma)$, $N_2(a'^1\Sigma)$, $N_2(b^1\Pi, b'^1\Sigma)$, the ionization of molecules in these states and in ground state by electron impact, their quenching by heavy particles, associative ionization and electron-ion recombination. The equation for the number densities of excited molecules can be written as

$$\frac{\partial n_i(x,t)}{\partial t} = F_i(x,t), \qquad (5)$$

where the right parts F_i are responsible for local processes of formation and annihilation of particles, the equation for n_e

---

[1] The analogous model for the discharge development in inert gas (krypton) was presented in [4].

contains the photoionization term

$$\frac{\partial n_e(x,t)}{\partial t} = F_e(x,t) + \int \frac{n_b(x')}{\tau} K(x-x')\, dx' \qquad (6)$$

(where n_b and τ are the number density and mean radiation life time of molecules at levels $N_2(b,b')$; $K(z)$ is the kernel describing the propagation and absorption of ionizing radiation [5]). Convective and diffusive terms can be neglected as compared with collision processes.

The experimental data [1] show that in conditions under discussion the noticeable heating of gas in plasmoids and the corresponding decrease of gas number density n as well as the essential increase of vibrational energy of molecules ε_v take place. Due to strong dependence of electron-impact ionization and excitation rate coefficients on E/n and ε_v the discharge model should include the equations for n and ε_v.

Two ways of account for the density and vibrational energy changes are used in this paper. The first model includes the full system of gas dynamics equations

$$\frac{d\rho}{dt} + \rho \frac{\partial v}{\partial x} = 0, \qquad (7)$$

$$\rho \frac{dv}{dt} + \frac{\partial p}{\partial x} = 0, \qquad (8)$$

$$\frac{d\varepsilon_v}{dt} = \frac{Q_v}{n\,\omega_v} - \frac{\varepsilon_v - \varepsilon_v^\circ}{\tau_{VT}}, \qquad (9)$$

$$\frac{\gamma}{\gamma-1} n \frac{d}{dt}\left[\frac{p}{n}\right] - \frac{dp}{dt} = Q_T + n\,\omega_v \frac{\varepsilon_v - \varepsilon_v^\circ}{\tau_{VT}}, \qquad (10)$$

where $\frac{d}{dt} = \frac{\partial}{\partial t} + v\frac{\partial}{\partial x}$, ρ is the gas density, v is the gas velocity, p is the pressure, ω_v is vibrational quantum, τ_{VT} is the vibrational relaxation time, γ is specific heat ratio, ε_v° is equilibrium value of ε_v at gas temperature T, Q_v and Q_T are densities of energy input in vibrational and translational degrees of freedom. The values of Q_T and Q_v take into account the direct heating and vibrational excitation as well as the transfer of energy to vibrational and translational degrees of freedom in quenching of electronically excited states of N_2 by heavy particles:

$$Q_v = \eta_v \frac{e^2 E_e^2 n_e}{m\,\nu} + \zeta_v \sum_i I_i n_i / \tau_i, \qquad (11)$$

$$Q_T = \eta_T \frac{e^2 E_e^2 n_e}{m \nu} + (1-\zeta_v) \sum_i I_i n_i / \tau_i . \qquad (12)$$

Here $E_e^2 = E^2/(1 + \omega^2/\nu^2)$, η_v and η_T are the parts of Joule dissipation transferred to vibrations and to gas heating, I_i and τ_i are the values of energy defect in quenching of i^{th} excited state and the quenching time, ζ_v is the part of energy transferred to vibrations in the quenching collision.

The second model corresponds to isobaric approximation with convective terms neglected:

$$p \sim n T = \text{const} , \qquad (13)$$

$$\frac{\partial \varepsilon_v}{\partial t} = \frac{Q_v}{n \omega_v} - \frac{\varepsilon_v - \varepsilon_v^\circ}{\tau_{VT}} , \qquad (14)$$

$$\frac{\gamma}{\gamma - 1} \frac{p}{n} \frac{\partial n}{\partial t} = -Q_T - n \omega_v \frac{\varepsilon_v - \varepsilon_v^\circ}{\tau_{VT}} , \qquad (15)$$

The initial Gaussian profile of n_e is set at the right part of numerical region (the incident wave comes from the left).

The results of calculation of discharge dynamics in isobaric approximation are presented in Fig. 1 for $E_o/n_o = 6.10^{-16}$ V.cm^2, $n_o = 5.10^{18}$ cm^{-3}, $\lambda = 2\pi c/\omega = 2$ cm. The spatial distributions of n_e, T, ε_v and E_e/n are given for various time moments. The discharge propagates as a successively formed set of plasma layers separated by the distance $\sim \lambda/4$. The values of maximum concentration ($\sim 10^{14}$ cm^{-3}) and of the thickness are in accordance with the experiment [6]. Gas heating occurs mainly after the layer is formed. The velocity of propagation of discharge front towards the microwave source ($\sim 10^5$cm/s) is close to the measured one [1]. Note that in this conditions vibrational- translational relaxation is not essential and the vibrational distribution is not quasistationary.

The solution of the full gas dynamics system is considerably more cumbersome. Due to the computational difficulties connected with sharp inhomogeneities of plasma parameters the solution was obtained only for the initial stage of discharge dynamics. Fig. 2 shows the n_e profiles for the same conditions as in Fig.1. It is seen that the type of distributions as well as the velocity of discharge movement are analogous to the isobaric case. The account of convective movement leads to the displacement of plasmoids towards the microwave source with velocity being ~ 0.1 of that of front movement. This effect was also observed experimentally [1].

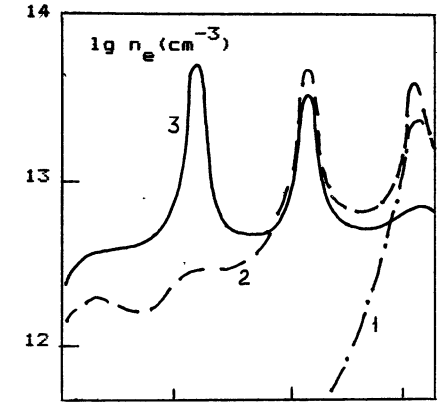

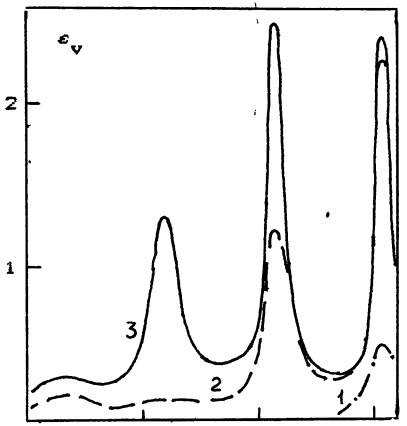

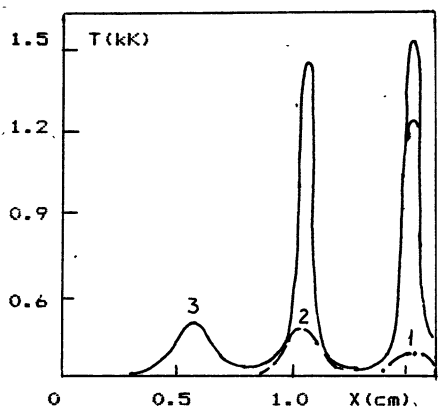

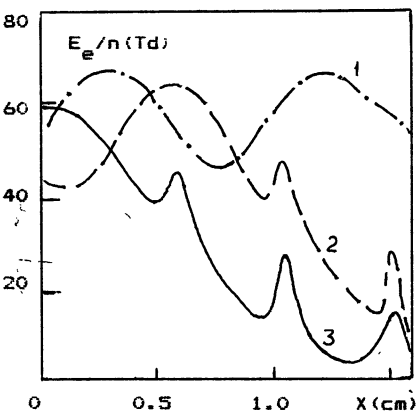

Fig.1
t(μs): 1-3.0; 2-9.0; 3-15.0

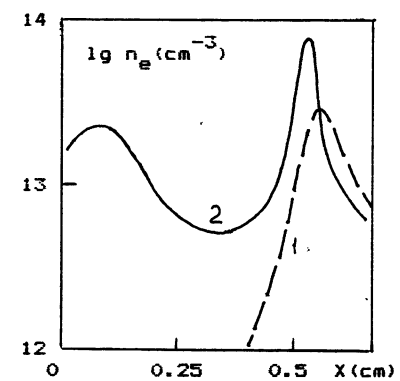

Fig.2
t(μs): 1-3.0; 2-9.0

References

1. Golubev S.V., Gritsinin S.I., Zorin V.G., Kossyi I.A., Semyonov V.E. "High-frequency discharge in wave fields". 1988, Gorky, Institute of Applied Physics, p.136-197 (in Russian).
2. Babaeva N.Yu., Mnatsakanyan A.Kh., Naidis G.V. Proc. XIX Intern. Conf. on Phenomena Ioniz. Gases. 1989, Belgrade, p.432-433.
3. Bogatov N.A., Golubev S.V., Zorin V.G. Proc. All-Union Conf. "High-frequency discharge in wave fields". 1987, Gorky, Institute of Applied Physics, p.40 (in Russian).
4. Mnatsakanyan A.Kh., Naidis G.V., 1990, Fiz. Plazmy, 16, p.481-486.
5. Zheleznyak M.B., Mnatsakanyan A.Kh., Sizykh S.V., 1982, Teplofiz. Vys. Temp., 20, p.423-428.
6. Zlobin V.V., Kuzovnikov A.A., Shibkov V.M., 1988, Vestn. MGU, fiz., 29, p.89-90.

INVESTIGATION OF INSTABILITY AND NONLINEARITY MECHANISMS OF A NON-SELF-SUSTAINED DISCHARGE IN A MICROWAVE BEAM

N.A. Bogatov, M.S. Gitlin, S.V. Golubev, V.G. Zorin, S.V. Razin

Institute of Applied Physics, USSR Academy of Science,
Nizhny Novgorod, USSR

A non-self-sustained microwave discharge (NSMD) is the process of electromagnetic microwave field effect on a weakly ionized plasma sustained by an external ionizer. NSMD takes place in plasma halos surrounding self-sustained microwave discharge and can essentially influence the dynamics of these discharges [1]. In NSMD, strong nonequilibrium excitation of the vibrational and electron levels of molecules can be achieved (nonequilibrium state means that the electron or vibrational excitation temperature differs from the temperature of the gas)[1]; this fact is of interest for gas laser application and plasma chemistry. NSMD plasma also shows promise as a nonlinear medium for phase conjugation of microwaves. The nonlinearity mechanism is related to the dependence of the electron concentration and the transport collision frequency of electrons on the amplitude of the electric field in a plasma.

One of the most important characteristics of NSMD is its stability as related to the transition into a self-sustained discharge, when the discharge is no longer homogeneous and its useful for application properties are lost. The problem of NSMD stability in nitrogen was studied earlier in [2, 3] where it was shown that in the instability mechanism an important part is played by electron-excited nitrogen molecules; however, the specific instability mechanism was not ascertained. The present paper aims at further experimental investigation of the instability mechanism of NSMD in nitrogen, and measurement of dependence of electron density in NSMD on microwave radiation intensity; from this measurement, efficiency of phase-conjugated wave generation by four-wave mixing in this medium can be evaluated.

NSMD occurred in the focal region of a microwave beam focused

within a vacuum chamber filled with nitrogen. The gas was ionized by the UV radiation of a bare spark placed at the distance of 2-3 cm from the beam focus. The microwave wavelength was 6.7 mm, pulse duration, 40 and 100 μs, power, 0.1-100 kW, and the beam diameter in the focal region, 1 cm.

Fig. 1 shows time behavior of electron density n_e, NSMD radiation intensities in the visible (I_v) and ultraviolet (I_{uv}) regions, and intensity of the radiation passing through the microwave discharge S_t with various intensities of the incident radiation S_0. With rather high S_0, NSMD after some time τ_s less than microwave pulse duration becomes self-sustained. By this, n_e increases and nonhomogeneous structure arises. It is completely similar to the structure of a self-sustained discharge in the over- breakdown field [1]. Duration of stable NSMD burning τ_s and specific energy deposition in gas W at that stage of the discharge decrease sharply when S_0 increases (Fig. 2). Since a major part of the energy absorbed by NSMD goes into vibrational excitation of nitrogen molecules, the degree of the gas vibrational excitation to the moment τ_s varies greatly with comparatively small variations of the microwave field. Hence, the following conclusion can be made (a similar conclusion was made in [2,3]): NSMD instability cannot be explained by vibrational excitation only, as well as by gas heating caused by relaxation of vibrational excitation. An important part in NSMD must be played by electron-excited molecules whose excitation rate in the discharge depends strongly on the value of the electron field. Spectrum measurements showed that NSMD radiation in the visible range is produced generally by the 1^+-system of N_2 (upper level $B^3\Pi_g$, 7.3 eV), and in the UV range, by the 4^+system of N_2 (upper level $D^3\Sigma_u^+$, 12.9 eV). I_v is stable during NSMD and proportional to n_e; after the microwave pulse it sharply (≈ 1 μs) drops. From these facts it follows: 1) the level $B^3\Pi_g$ is excited from the ground state by an electron impact; 2) $B^3\Pi_g$ excitation rate constant does not vary during NSMD . The latter yields that the electron energy distribution function remains unchanged in NSMD; it means that the excitation rate constants for all electron levels by an electron impact must not vary. At the same time, I_{uv} increases nonlinearly during NSMD. Since the level $D^3\Sigma_u^+$ has a short life-time ($1.4 \cdot 10^{-8}$s), I_{uv} is proportional to the excitation rate for this level. Nonlinear increase of the excitation rate means that the level $D^3\Sigma_u^+$ is excited by collisions of metastable

molecules whose concentration in NSMD can increase.

$$N_2(Y)+\left[\frac{N_2(Z)}{N_2(Y)}\right]=N_2(D)+N_2(X) \qquad (1)$$

where Y is an electron metastable level, and Z, an electron or vibrational metastable level. The excitation mechanism acts also after the microwave pulse has gone off, providing the observed slow ($\approx$ 20 μs) relaxation of I_{uv} (see Fig.1d). One can suppose that reactions of type (1) dominate in excitation of other high electron levels including metastable ones $E^3\Sigma_u^+$ and $a''^1\Sigma_u^-$. The value of I_{uv} to the moment τ_s practically does not depend on τ_e, i.e., one can state that NSMD becomes a self-sustained discharge when some degree of population of high electron levels is achieved Hence, it is quite natural to suppose that ionization of high exited metastable molecules provides transition of NSMD into a self-sustained discharge

Estimations of efficiency of various high level excitation channels using gas-kinetic cross-sections as the upper limit of reaction cross-sections show that only $A^3\Sigma_u^+$ can play the part of Y; other low levels have the life-time too short in relation to quenching by molecules in the ground state [4-6]. The estimations also yield that with small energy deposition into gas W < 0.2 J/cm^{3}atm, population of the high vibrational levels is small and their contribution to the reactions of type (1) is of no importance. In this case, the instability mechanism is as follows:

$$e + N_2(X) \rightarrow N_2(A)$$
$$N_2(A) + N_2(A) \rightarrow N_2(E,a'')$$
$$N_2(E,a'') + N_2(A) \rightarrow \left[\begin{array}{l} N_4^+ + e \\ N_2^+ + e + N_2(X) \end{array}\right]$$

This instability mechanism provides highly nonlinear increase of the ionization frequency in time

$$n_e \sim t^{\alpha} \qquad \alpha = 3\text{-}4,$$

explaining the observed sharp transition of electron density from a quasistationary value to rapid increase (fig. 1b).

With increase of the energy deposition to gas, population of high vibrational levels of the ground state rapidly increases and with W > 0.2 J/cm^{3}atm quenching of the A by N_2 (X,v $\geq$ 7) must become significant [7]. At the same time, with such energy deposition, on the one hand, the density of molecules of N_2 (X,v $\geq$ 13-14) able of taking part in the associative ionization reaction becomes sufficiently great; on the other hand, the rate of electron

level excitation from the ground state by an electron impact increases (increase of the energy deposition is achieved by increase of the electron density). Estimations show that if the energy deposition is great, the following mechanism is most possible:

$$e + N_2(X) \rightarrow \begin{bmatrix} N_2(a'') \\ N_2(X,v) \end{bmatrix}$$

$$N_2(a'') + N_2(X,v) \rightarrow \begin{bmatrix} N_2^+ + e + N_2(X) \\ N_4^+ + e \end{bmatrix}$$

(It was proposed to explain ionization in glow discharges under low [8] and average [9] pressures). In this case, nonlinearity of increase of the ionization frequency is caused by nonlinear time-increase of the population of high vibrational levels.

Electron density in NSMD depends on the intensity of microwave radiation (see Fig. 1b). It is caused by the dependence of the recombination and attachment coeffitients on the electron temperature determined by the microwave field amplitude. Plasma polarization is proportional to electron density, therefore it nonlinearly depends on the field strength. Nonlinearity of NSMD plasma can be used for the phase-conjugation of microwaves using the four-wave mixing (FWM) method. Advantages of NSMD as a nonlinear medium for FWM of microwaves are related to the possibility of producing a homogeneously ionized gas with high-electron density (up to 10^{13} cm^{-3}) in a large volume (~$10^3 cm^3$) and of using pump waves with relatively low intensities (≤ 10 W/cm^2). To conjugate the phase of the microwave by the FWM one must send two counter-propagating plane beams at an angle to the signal wave on the layer of a nonlinear medium [10]. Scattering of each pump beam on the plasma susceptibility variations caused by interference of the signal wave and the other pump beam results in the generation of a wave phase-conjugated to the signal one.

Fig. 3 shows one of the experimental dependences of n_e on the parameter E_e/N where $E_e=E_{amp}/[2(1 + \omega^2/\nu^2)]^{1/2}$ is effective field, N_e - molecule density, ν - electron transport collision frequency, ω - circular field frequency. The initial part of the dependence of n_e on E_e/N can be approximated by the power law:

$$n_e(E_e/N) = n_e^0 \left[\frac{E_e/N}{(E_e/N)_0}\right]^p \qquad 0.1 \le E_e/N \le 5 \text{ Td}$$

where n_e^0 is the electron density produced by an UV source with no microwave field present, and $(E_e/N)_0$ = 0.1 Td, p = 0.2-0.25. Then

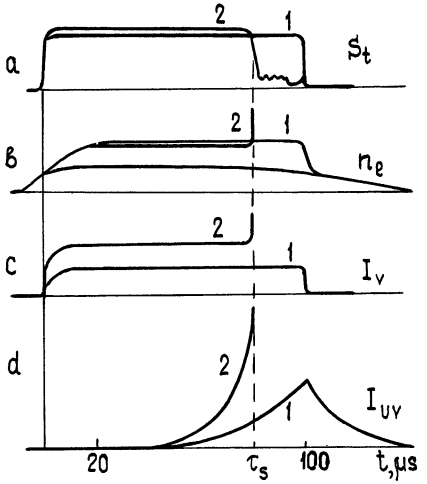

Fig. 1

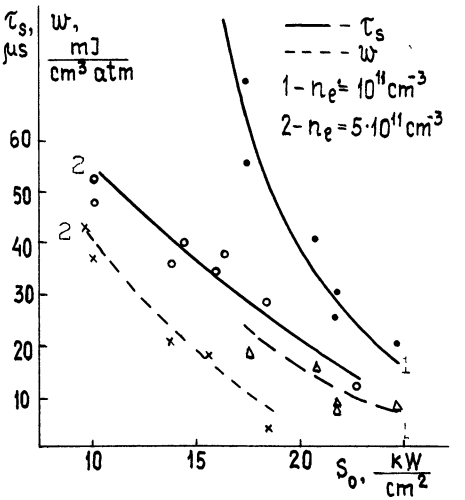

Fig 2

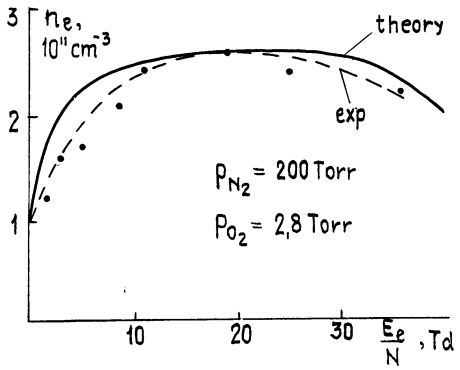

Fig 3

the plasma polarization amplitude is $\mathcal{P} = \chi(|E|)E = \chi^{NL}|E|^pE$ where χ^{NL} is nonlinear plasma susceptibility equal to

$$\chi^{NL} = \frac{n_e^0(1+\frac{\nu}{\omega})}{4\pi\, n_c(1+\nu^2/\omega^2)} \left[\frac{(E_e/N)_0\, N}{\sqrt{2(1+\omega^2/\nu^2)}}\right]^{-p},$$

where n_c - critical density. To determine the reflection coefficient of microwave into a phase-conjugated wave in NSMD plasma, the problem of a stationary degenerate FWM in a nonlinear medium with susceptibility depending on the electric field amplitude modulus by the power law, was considered theoretically. In the approximation of pump waves which are constant and equal in intensity ($I_f=I_b=I$ = const), and if $\omega \gg \nu_m$, the coefficient of reflection from a plasma layer with length L is

$$R = tg^2\beta L, \qquad \beta = \frac{\omega}{c}\, p\, \frac{\Gamma(\frac{p+1}{2})}{\Gamma(\frac{p}{2}+1)}\, \chi^{NL}(4I)^{-p/2}$$

here $\Gamma(x)$ is the gamma function. For the initial electron density $n_e^0=10^{11}cm^{-3}$ nonlinear susceptibility of the NSMD plasma at the frequancy 40 GHz is equal $3\cdot10^{-4}$esu. For the interaction length L $\simeq$ 50 cm, and intensity of the pump beams I $\simeq$ 15 W/cm^2, the reflection coefficient may be as high as 10%. Response time of phase-conjugating devices based on the nonlinear medium considered above, is determined by the electron recombination time which for these experimental conditions is about 30 μs.

REFERENCES

1 Golubev S.V. et al. In: High-Frequency Discharge in Wave Fields, Gorky, 1988, p. 136-198. (in Russian).
2. Gritsinin S.I. et al., ZhTF, v.57, 1987, 4, p.681. (in Russian).
3. Bogatov N.A. et al. ZhTF, v. 57, 1987, 1, p. 194. (in Russian).
4. Piper L.G., J.Chem.Phys., v. 87, 1987, 3. p. 1625.
5. Marinelli W.J. et al., J.Chem.Phys., v. 92, 1988, 12, p. 3429.
6. Rotem A., et al. Chem.Phys.Lett., v. 83, 1981, 2.
7. Bogatov N.A. et al. Preprint IAP, N 219, 1988. (in Russian).
8. Slovetsky D.I. Mechanisms of Chemical Reaction in Plasma. Moscow, Nauka, 1980. (in Russian).
9 Golubovsky Yu.B., Telezhko V.M. Teplofiz.Vys.Temp., v. 22, 3. (in Russian).
10. Zel'dovich B Ya. et al., Principles of Phase Conjugation. New York: Springer, 1985.

DETECTION OF SUPERPOWER MICROWAVE RADIATION

G.A.Ascaryan, G.M.Batanov, N.K.Bereznetskaya, A.A.Dorofeuk
V.A.Ivanov and I.A.Kossyi

Institute of General Physics, Moscow, USSR.

The new generation of high-power microwave energy sources [1,2], recently introduced into modern technology and physical research, makes it possible to generate freely sustained microwave beams with an intensity exceeding 10^3 W/cm^2 and sometimes even reaching 10^6W/cm^2 [3-5]. Detection of beams of this high power level is rather difficult because exposure of any solid-state device to such a strong beam of electromagnetic wave leads either to breakdown of surrounding gaseous medium (with formation of a flare [3]) or to formation of a plasma "corona" in vacuum [6]. The emergence of plasma in the medium immediately surrounding the device drastically and unpredictably affects its detecting properties. Yet it is precisely plasma formation, which is usually regarded as a source of interference when all known types of solid-state microwave sensors are employed, that underlies the radically new principle of detecting beams described here.

The detector is shown schematically in Fig.1. Its basic components are a plasma-inducing solid dielectric target (1) placed in an evacuated space (residual pressure $P_0 \leq 10^{-4}$ Torr), a metal electrode surrounding the plasma-inducing target (it can be a vacuum chamber made of metal (2)), and finally, a central measuring pin-type electrode (3).

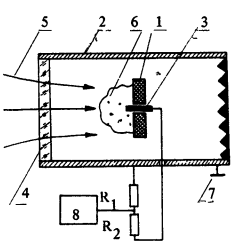

Fig.1 The scheme of power detector: 1-dielectric target; 2-metallic vacuum chamber; 3-probing electrode; 4-radio-transparent window; 5-microwave radiation; 6-microwave flare; 7-matched load; 8-oscilograph; R_1, R_2-resistances.

As high-power microwave pulses hit the surface of the dielectric, the latter undergoes partial sublimation followed by ionization of the sublimed substance and formation of a plasma corona near the surface. The properties of the resulting corona have been carefully studied [7] in the wavelength range $\lambda=(0.8-15)$cm at powers $P \leq 1$ MW, intensities $I \leq 10^5 W/cm^2$ and microwave pulse duration $\tau \leq 100$ ms. The experimental date indicate that:

(1) The corona is a complex entity consisting of a gaseous cloud of the target substance, preceded by plasma as the sublimed substance scatters in the surrounding vacuum (Fig.2). In essence, we are dealing with transition from a highly collisional region deep inside the corona to a highly ionized non-collisional peripheral region.

(2) The electron concentration in the corona reaches the critical value $n_{cr}= m\omega^2/4\pi e^2$ within relatively short time intervals, and even goes beyond it (ω being the angular frequency of the external field).

(3) Attainment of the critical concentration is accompanied by an intermittent increase in the corona potential as well as emergence of ultrafast epithermal electrons (with energy $\varepsilon_f \simeq 10^2 - 10^4$ eV) in the spectrum of the electronic component and also a burst of ultraviolet radiation and soft X-rays from target surface.

The potential acquired by the plasma after it attains the critical concentration ranges from hundreds of volts to several kilovolts.

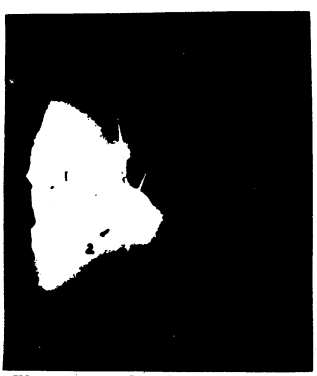

Fig.2 Photograph of microwave flare: 1-the glowing of microwave flare; 2-the glowing on probing electrode.

The predominant physical process determining the corona characteristics after the critical concentration is reached is nonlinear absorption of the beamed microwave energy in the plasma "resonance" region (region where the Langmuir frequency ω_p equals the

angular frequency of the microwave beam: $\omega_p = \omega$).

The plasma potential ϕ_p (with respect to the external electrode) can be roughly estimated assuming that $e\phi_p \simeq \varepsilon_e$, where ε_e is the average amount of energy acquired by electrons in the "resonance" region. Simple calculation show that:

$$e\phi_p \simeq (A_s I/n_{cr})^{2/3} ,$$

where A_s is the coefficient of absorption of the microwave beam incident upon the target by the corona.

If the load impedance R_1+R_2 of the sensing electrode (3) in Fig.1 is high ($R_1+R_2 \gg R_p$ where R_p is the corona resistance), the electrode will be able to measure the corona potential. But when R_1+R_2 is low ($R_1+R_2 \ll R_p$), a unique property comes to the fore - it was observed earlier [9] and resides in generation of extremely high (from 10^2 to 10^4A) quasi-stationary currents I_s in the follow circuit: central electrode - plasma - external electrode - load impedance - central electrode. Such currents occur without any external emf source. This phenomenon is based both on the already mention of nonlinear interaction between the microwave beam and the plasma induced thereby and on "burst" emission at the central electrode [6].

Fig.3 presents characteristic corona potential and quasi-stationary current I_s versus microwave beam intensity curves. Such curves may be regarded as calibration tools for the superpower microwave energy detector.

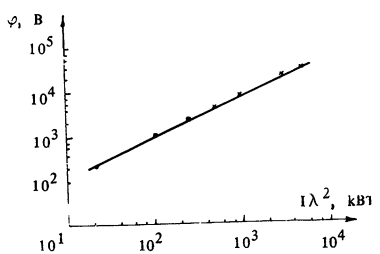

Fig.3 The potential of microwave flare versus $I\lambda^2$: -λ=0.8cm; -λ=2.5cm; -λ=16cm.

Specially conducted experiments have shown that the proposed detection technique is almost independent of the microwave beam mode, material of the plasma-inducing dielectric, as well as material and configuration of the electrodes. Nor is there any limitation on the measure beam intensity level.

The proposed method has been tried on superpower microwave generators producing relativistic electron beams ($I \geq 10^6$ W/cm^2). The experimental results are encouraging enough to hope that the new detection method will be useful in modern physical laboratories even at such extremely high beam intensities.

Reference

1. N.I.Zaitsev, M.I.Petelin Radiotekhnica i electronica, 1974, vol.19, 5, 1056-1058.
2. Microwave and Particle Beam Sources and Propagation, Proceedings of SPIE,1988.
3. S.I.Gritsinin, I.A.Kossyi, V.P.Silakov, N.M.Tarasova. XVIII ICPIG Invited Papers, 1987, Swansea, pp. 232-240.
4. G.M.Batanov, S.I.Gritsinin, I.A.Kossyi, et al., Trudy FIAN, 1985, vol. 160, 174-203.
5. W.T.Armstrong, R.A.Russell-Dupre, R.Karl, M.I.Buchwald, G.Graham, XVIII ICPIG, contributed paper, 1987, Swansea, vol.4, pp.850-852.
6. V.N.Aldokhin, G.M.Batanov, N.K.Berezhetskaya et al., Fhyzika plazmy, 1982, vol.1, pp. 189-195.
7. .Generatsiya nelineynykh voln i kvazistatsionarnykh tokov v plazme (Generation of Nonlinear Waves and Quasi-Stationary Currents in plasma), Trudy IOFAN, vol.16, 1988.
8. G.A.Askaryan, G.M.Batanov, N.K.Berezhetskaya et al., Pisma v ZhETF 1979, vol.29, 11, pp. 706-709.

NONLINEAR DYNAMICS OF A SPACE LOCALIZED DISCHARGE IN THE FIELD OF A TRAVELLING ELECTROMAGNETIC WAVE IN THE ATMOSPHERE

I.N.Inovenkov, A.V.Kim, V.E.Semenov, A.E.Chukhin
Institute of Applied Physics
USSR Academy of Sciences, Nizhny Novgorod, USSR

An important feature of a discharge produced by the field of an electromagnetic wave in the atmosphere [1,5] is its space localization that influences significantly the properties of the discharge such as its evolution and the parameters of appearing discharge structures. Such a free space localization of a discharge is, actually, a consequence of two factors: space boundedness of the wave field (e.g.,wave beam) and/or atmospheric inhomogeneity. A freely localized discharge is usually investigated within a multi-dimensional and, consequently, a rather complicated problem [1,2,6]. In this paper, the dynamics of a freely localized discharge produced by the field of a travelling e.m.wave is studied within a one-dimensional approach.

We take the following basic equations for the complex amplitude of electric field $E(x,t)\exp(i\omega t)$

$$\frac{\partial^2 E}{\partial x^2} + k^2 \varepsilon E = 0, \quad \varepsilon = 1 - (1+i\cdot\frac{\nu}{\omega})\frac{N}{N_c}, \tag{1}$$

and electron density $N(x,t)$

$$\frac{\partial N}{\partial t} = D\,\frac{\partial^2 N}{\partial x^2} + \nu_i N - \nu_a N + J, \tag{2}$$

where $k = \omega/c$ is the wave number in a vacuum, ε is the complex permittivity of a discharge plasma, ν is the effective collision frequency of electrons, $N_c = m(\omega^2+\nu^2)/4\pi e^2$ is the critical density, D is the coefficient of ambipolar diffusion, ν_i is the frequency of ionization by electron impact, ν_a is the frequency of attachment of electrons to molecules(to oxygen molecules in the

atmosphere), and J denotes the intensity of an extraneous source of gas ionization. The kinetic coefficients D, ν_a, ν are assumed to be constant and the dependence of ν_i on the field amplitude $|E|$ and on the x-coodinate is approximated as

$$\nu_i = \nu_a\left[|E|\cdot f(x)\right]^{\beta}, \tag{3}$$

where the function $f(x)$ describes the space inhomogeneity of ionization frequency in an unperturbed electromagnetic field. This inhomogeneity may be caused, for example, by gas inhomogeneity. Such a formulation of the problem allows also for the description of the discharge dynamics in a wave e.m. beam, provided that the ray tubes are specified [1]. Actually, within such an approximation, the equation for the complex field amplitude $\mathcal{E}$ can be represented in the form

$$\frac{1}{S(x)}\frac{\partial}{\partial x}\left(S(x)\frac{\partial \mathcal{E}}{\partial x}\right) + k^2\varepsilon\mathcal{E} = 0 \tag{4}$$

Substituting the variable $\mathcal{E} = E\cdot[S(0)/S(x)]^{1/2}$ we transform the dependence $\nu_i(|\mathcal{E}|) = \nu_a\cdot\left(|\mathcal{E}|/E_c\right)^{\beta}$ into (3) and reduce Eq.(4) to the form (1) to an accuracy of the term $-\mathcal{E}\cdot\left[d^2\sqrt{S(x)}/dx^2\right]\Big/\sqrt{S(x)}$ that is not significant in the case of interest, i.e. when the cross sectional area $S(x)$ of the beam varies slowly along the wavelength k^{-1}. The function $f(x) = E_c^{-1}[S(0)/S(x)]^{1/2}$, where E_c is a characteristic breakdown field.

In dimensionless variables $t \to \nu_a t$, $x \to kx$, $E \to E/E_c$, and $n = N/N_c$, the basic system (1)-(3) has the form

$$\frac{\partial^2 E}{\partial x^2} + \varepsilon E = 0, \quad \varepsilon = 1 - (1+i\cdot\nu)n, \tag{5}$$

$$\frac{\partial n}{\partial t} = L^2\cdot\frac{\partial^2 n}{\partial x^2} + \left\{\left[|E|F(x)\right]^{\beta} - 1\right\}\cdot n + I, \tag{6}$$

where $L = \left(Dk^2/\nu_a\right)^{1/2}$ is the dimensionless diffusion length of attachment and $\nu \to \nu/\omega$, $I=J/\nu_a$. The function in the form $F(x)=[1+(x/\ell)]^{-1}$ was taken as $F(x)=E_c f(x)$ and the parameter β was equal to 4.

Numerical calculation of the joint system of equation

(5)-(6) was performed on the section $-x_0 \le x \le x_1$, with the boundary conditions for the field

$$\left(\frac{\partial E}{\partial x} - iE\right)\Big|_{x=-x_0} = iA_0 \; ; \quad \left(\frac{\partial E}{\partial x} + iE\right)\Big|_{x=-x_1} = 0 \qquad (7)$$

and for the electron density

$$\frac{\partial n}{\partial x}\Big|_{x=-x_0,\, x_1} = 0 \; , \qquad (8)$$

that corresponded to the absence of diffusional plasma fluxes, to the absence of an incident e.m.wave at the right boundary $x=x_1$ and to the given amplitude A_0 of the incident wave at the left boundary $x=x_0$. The boundaries of the integration region were chosen such that it included the entire discharge region where $n(x, t)>0$.

We took the folowing range of parameters: A_0= 1.3, 2; I=0, 0.01; L=0-1; ℓ=5-80; ν=0-10. Some results of calculations are presented in Figs.1-3, where the density distribution and the field modulus $A = |E|$ are plotted at different moments of time t. The general analysis of results shows the following qualitative regularities of breakdown dynamics.

Four different scenarios of discharge development can be distinguished in a homogeneous primary plasma ($n(x, 0)$=const=0.01) in the absence of extraneous source of ionization (I=0). In all cases, at its initial stages the breakdown is qualitatively the same (Fig.1a) : plasma density increases fastest in the neighbourhood of the maximum of the function $F(x)$ (x=0), after that the ionization wave shifts towards the incident radiation (to the region $x<0$). The maximum electron density n_{max} in the first ionization wave is determined in conformity with the consideration presented in [1]. For $\nu\ell \gg 5$, the product n_{max} is taken to be $n_{max} \sim (2\div3)/\nu\ell$; for $\nu\ell \le 5$, $n_{max} \ge 1$ and, consequently, the coefficient of e.m.wave reflection at a discharge plasma and, correspondingly, the velocity of the discharge propagation increase.

Further dynamics of the discharge depends qualitatively on ℓ, ν and L. For small values of ν and L ($\nu, L^2 \le 0.1$) and sufficiently great ℓ ($\ell \ge 15$), the ionization waves successively

appearing in the region x=0 give birth to multisoliton plasma structures (Fig.1b) having narrow ($\leq \lambda/4$ thick, where $\lambda=2\pi/k$ is the wavelength of incident radiation) density distributions (peaks) slowly moving in the $-x$ direction.

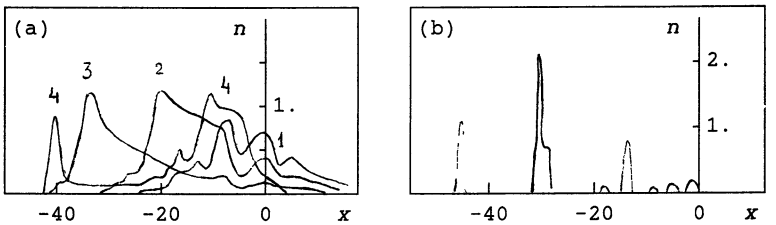

Fig.1. Density distributions for A_0=1.3, ℓ=50, n=0, L=0 at different moments t: a) t=1.71(1), 2.1(2), 3.6(3), 8.95(4); b) t=80.3

The reflection of the e.m.wave from these peaks is rather strong. For ν=0, L=0 and ℓ=50 we even observed the amplification of the field between two plasma density peaks that formed a specific Fabri-Perot resonator. Ionization solitons appear to be "tied" to the electric antinodes caused by the reflection of the incident wave from subsequent density peaks. However, this "rule" is violated time and again when subsequent peaks are relatively fast to come $\lambda/2$ closer to the previous peaks, after which quasi-equilibrium is established again. Eventually, the ionization waves successively escape the breakdown region and the plasma in them decays, while the multisoliton structure of the discharge is retained at very long time (we counted up to $t\sim$90). As ℓ decreased down to 15, only the distance between the peaks and the amount of simultaneously existing peaks decreased, while the qualitative picture described above was retained.

Quasiperiodic generation of ionization waves occurred in the region of rare collisions ($\nu\ell \leq 5$) and of relatively strong diffusion ($L \geq 1$). Strong diffusion does not allow the ionization waves to significantly decrease their thickness which always remains greater than λ. Consequently, each subsequent ionization wave is formed only after a nearly complete relaxation of the previous one, and the resulting development of the first ionization wave is almost completely repeated in subsequent waves.

For $\nu\ell \gg 5$ and small L ($L^2 \leq 0.1$), there also occurs the

secondary generation of ionization waves but in this case it is completed by the onset of a stationary state. Because of small values of n_{max} in ionization waves, the e.m.wave reflection here is insignificant and subsequent ionization waves do not affect the previous ones.

A "fast" onset of a stationary state (in the development of the first ionization wave) was observed only at large ν and L, for example, when ℓ=50, this occurred only for $\nu \geq 1$ and $L \geq 1$. It should be noted, however, that for small ℓ (in dimensional variables $\ell \leq \lambda$), there were no secondary ionization waves at any values of ν and L.

The picture of discharge development is essentially different in sufficiently extended discharges (great ℓ). On passage of the first ionization wave in the plasma wake (Fig.2) the instability of stimulated ionization scattering is developed (I=0.01, an extraneous source stimulated the development of instability but was not its necessary condition), which greatly influences further dynamics and, in particular, leads to the formation of a sufficiently stable density lattice with the period $\lambda/4$ [1].

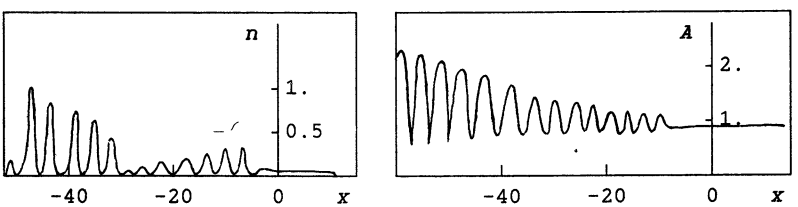

Fig.2. Density distribution and field modulus at t=38.49 under the condition of stimulated ionization scattering (A_0=1.3, ℓ=50, ν=0)

In all considered cases of homogeneous startup density, there were no ionization front jump over, that were considered in [3,4], in spite of strong reflection of the e.m.wave from the generated plasma (for small ν and L). So as to find out possible realization of jump over, we investigated the breakdown dynamics for different inhomogeneous initial distributions $n(x, 0)$ specified in the form

$$n(x, 0)=n_1 \exp(-x^2/b^2) + n_2 \qquad (9)$$

Calculations show that stepwise transitions of ionization front at a distance of $\lambda/4$ actually occur in the absence of background plasma (n_2=0), with weak diffussion ($L^2 \leq 0.1$), narrow primary plasma ($b \leq 0.1$) and only with a sufficiently great amplitude of incident wave ($A_0 \geq 2$). However, only a few jumps are formed (Fig.3), after which the ionization front propagates continuously and the discharge dynamics after the first, partially stepwise ionization wave, only slightly differs from the one observed for $n(x, 0)$=const.

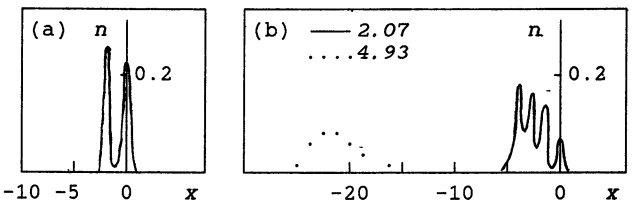

Fig.3. Density distributions at t=0.85(a); 2.07, 4.93(b) in the nonhomogeneous primary plasma (I=0, ℓ=50, ν=10, L=0.1, A_0=2, n_1=0.1, b=0.1)

In the case of a stronger diffusion, smaller amplitude A_0 or broader primary plasma b, as compared to the ones considered above, the ionization wave is propogating continuously from the very beginning. But unlike in the case $n(x, 0)$=const, where an independent breakdown took place at each point of the space and the propagation of the ionization front was specified by the delay of this breakdown, in this case the motion of the discharge is related to plasma diffusion and its velocity expressed in dimensional variables is close to the known value $2\sqrt{\nu_i D}$.

References

1. A.L.Vikharev et al. In: High-Frequency Discharge in Wave Fields. Inst.Appl.Phys., Ac.Sci.USSR, Gorky,1988,p.41-135.
2. Y.B.Gil'denburg et al. J.Phys.**40**,215,1979.
3. W.M.Bollen et al. J.Appl.Phys.**54**,101,1983.
4. C.L.Yee, A.M.Ali, W.M.Bollen, J.Appl.Phys.**54**,1278,1983.
5. W.Woo, J.S.De Groot, Phys.Fluids **27**,475,1984.
6. A.L.Vikharev et al. Zh.Eksp.Teor.Fiz.**94**,136,1988.

ON THE STATIONARY MICROWAVE DISCHARGE INDUCED BY THE INFINITE COPHASED CURRENT

Higer L. Ya. and Valiev Kh. V.
Physics Department, Tashkent State University,
Tashkent 700095, USSR

To study a nonlinear problem of the interaction between radiation and intrinsic-discharge plasma without resorting to approximations whose validity is hard to estimate, we choose a one-dimensional model - the cophased current on the surface of an infinite cylinder, for which a numerical solution has been obtained. Setting of the problem and a method for its solution was outlined in Ref.(1). It has been pointed out there that in the range of currents of 6.5 ÷ 9 A the solution is unstable. Further investigations showed that this instability is a numerical artifact of the chosen scheme of the solution of the equation for electron density, that is due to the infiniteness of the trial function basis in the Galerkin method. The correction of the basis in this range of currents as well allowed us to obtain a stable solution.

We investigated the influence of various values of the kinetic plasma coefficients on parameters of the microwave discharge plasma and radiation characteristics of the infinite current. For pressure p = 1 Torr we chose the following values: for the ambipolar diffusion coefficient $D = 5\cdot10^3$, 10^4, $5\cdot10^4$ cm^2s^{-1}; sticking frequency $\nu_a = 10^4$, $5\cdot10^4$, $10^5 s^{-1}$ and recombination coefficient $\alpha = 5\cdot10^{-8}$, 10^{-7}, $5\cdot10^{-7} cm^3s^{-1}$. All the calculation results for radiation frequency f = 300 MHz are plotted in figures.

Fig.1 shows I-dependences (I is the value of the applied current) of the maximal electron concentration n_{max} (1), the coefficient K of far-field weakening (2) and the value W (3) that is proportional to radiation power, for different values of the sticking coefficient; a minimal value of ν_a is indicated by a

solid line, its average value by a dashed line and a maximal value of ν_a is drawn by a dashed-dotted line. Here $D=10^4 cm^2 s^{-1}$ and $\alpha = 10^{-7} cm^3 s^{-1}$.

Fig.2 shows the dependence of n_{max}, K and W on various values of the diffusion coefficient for $\nu_a = 5 \cdot 10^4 s^{-1}$ and $\alpha = 10^{-7} cm^3 s^{-1}$. Finally, Fig.3 presents the dependence of the same magnitudes on the recombination coefficient for $D=10^4 cm^2 s^{-1}$ and $\nu_a = 5 \cdot 10^4 s^{-1}$. Note that this figure lacks the curves for n_{max} and K for the average values of $\alpha = 10^{-7} cm^3 s^{-1}$, since they are practically coincided with the ones for minimal α.

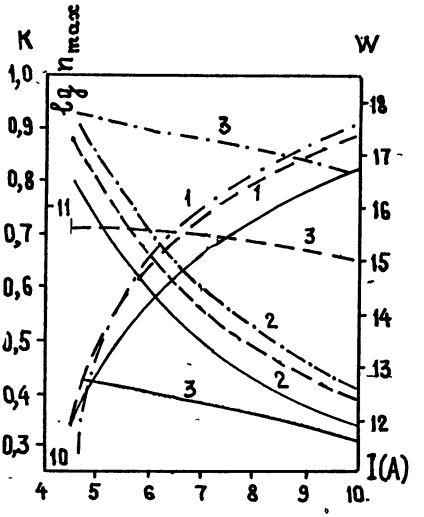

Fig.1

The analysis of the data obtained allows us to make the following conclusions: 1) The influence of diffusion and sticking on the value of the striking discharge current I_{crit} is essential and almost the same. For instance, for a maximal diffusion coefficient $D=5 \cdot 10^4 cm^2 s^{-1}$ (maximal sticking frequency $\nu_a = 10^5 s^{-1}$) the critical striking discharge current increases from 4.0 A up to 4.4 A with ν_a varying from $5 \cdot 10^4 s^{-1}$ to $10^5 s^{-1}$ (D varying from $10^4 cm^2 s^{-1}$ to $5 \cdot 10^4 cm^2 s^{-1}$); for the average diffusion coefficient $D=10^4 cm^2 s^{-1}$ the variation of the sticking frequency from $10^4 s^{-1}$ to $10^5 s^{-1}$ alters I_{crit} from 3.5 A to 4.0 A, whereas for the average sticking frequency $\nu_a = 5 \cdot 10^4 s^{-1}$, I_{crit} grows from 3.6 A up to 4.0 A with the diffusion coefficient varying from $5 \cdot 10^3 cm^2 s^{-1}$ to $5 \cdot 10^4 cm^2 s^{-1}$. Note that recombination for the values of α we have chosen in contrast to dif-

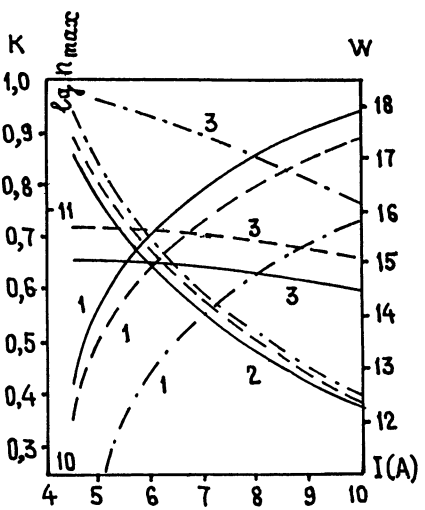

Fig.2

fusion and sticking does not affect the value of the striking discharge current.

2) The maximal electron concentration n_{max} is largely defined by diffusion, in a less greater extent by sticking and is nearly independent of the recombination coefficient.

3) The coefficient K of the far-field weakening and radiation power W depend mostly on sticking, less on diffusion and quite slightly on recombination.

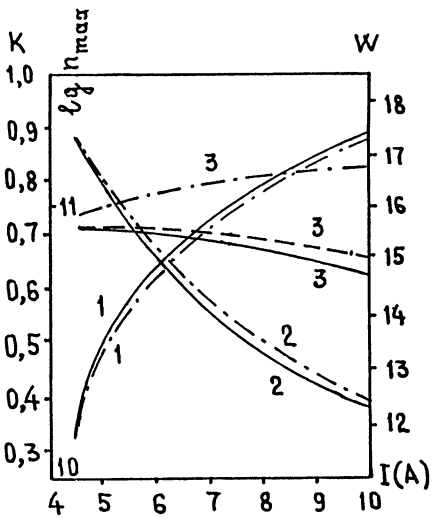

Fig.3

The results of calculations of the electron concentration n (1) and modulus of the electric field |E| (2) for f=3 GHz with I = 50A ($D=10^4 cm^2 s^{-1}$, $\nu_a = 5 \cdot 10^4 s^{-1}$, $\alpha = 5 \cdot 10^{-8} cm^3 s^{-1}$) plotted in Fig.4, seem to serve the manifestation of the effect of nonlinear plasma transparency. The width of a "supercritical" plasma layer is ~1.2 cm having the average concentration $\sim 10^{12} cm^{-3}$ for which the dimension of the skin layer is ~1 cm. At the plasma boundary given by the condition $\varepsilon = 1 \pm 0.01$ that is placed ~6 cm from the cylinder surface the coefficient K of field weakening is equal to o.0286. In a similar calculation with the same values of the initial parameters except for the recombination coefficient which was put to be $5 \cdot 10^{-7}$ $cm^3 s^{-1}$, K turned out to be 0.0718 that is consistent with the behaviour of radiation power W for the highest recombination coefficient (see Fig.3) it indicates a positive role of the latter in plasma bleaching. Note that in our calculations the condition for modulation instability to occur (2) has been not fulfilled,

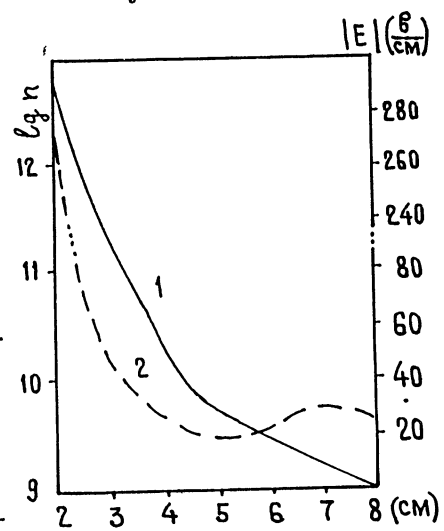

Fig.4

though it is on the way to be fulfilled. However, our method fails to study this instability.

REFERENCES

1. Valiev Kh.V. et al.// Izvestiya VUZov. Radiofizika. 1987. V.30. P.801.
2. Litvak A.G., Mironov V.A. and Fraiman G.M.// Pisma v Zh. Eksp. Teor. Fiz. 1975. V.22. P.368.

THE EFFECT OF DYNAMIC CHANNELING OF MICROWAVE RADIATION BY EXTENDED PLASMA FORMATIONS

V.I.Kolpakov, L.V.Norinskii, V.S.Rogov
Moscow Radio Technical Institute, Academy of Sciences of the USSR
113519 Moscow, USSR

1. Introduction

Much attention has been paid in literature to the use of plasma formations induced by laser radiation for the control of the direction of radio wave propagation [1,2] as well as elements of the antennas in receiving and transmitting devices [3].

The potentialities of axisymmetric extended plasma formations (EPF) as channeling surface wave lines are studied in this paper.

In our experiments EPF were formed by focusing neodium glass laser radiation (the wavelength 1055 nm), which resulted in air induced optical breakdown. Plasma channels of two types were used in the experiments. In the first case, the radiation was focused by means of a spherical long-focus lens with a focal length of 7 m to produce a quasi-continuous channel that consisted of separate merging breakdown points. In the second case, a regular longitudinally uniform structure of EPF was produced with the help of a conical lens (axicon) [4].

2. Experimental Setup

The experimental setup is shown schematically in Fig.1. A plasma channel was produced as a result of the optical air breakdown by laser radiation directed by the focusing element (2) to the region between the quasi-mirror (3) and the receiving antenna (6). The quasi-mirror (3) was transparent to the laser beam and directed the radio wave from the transmitting antenna (5) along the channel (4). The antennas were of a circular horn type and had the width of the directivity diagram 30°. The receiving antenna was mounted on the laser axis at a distance R from the quasi-mirror (3), while $R/\lambda \gg 1$, where λ is the wavelength. The microwave generator (7) was used as a source of continuous

electromagnetic radiation. The signal from the detector of the receiving antenna propagated along the matched cable to the input oscillograph (8).

The experimental procedure was as follows. In the absence of a plasma channel, the experimental equipment was installed for the optimal reception of the initial signal U_o coming from the detector. Starting from the moment of breakdown the variation of the amplitude of the detector signal ΔU was recorded on the oscillograph.

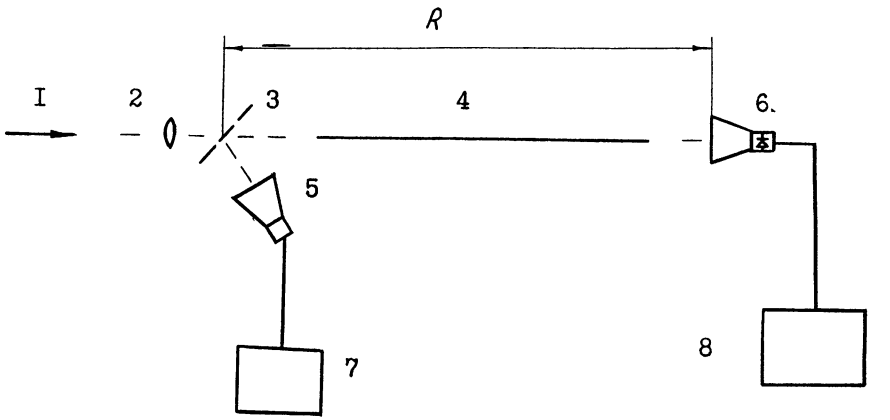

Fig.1. Schematic of microwave propagation experiment.

3. Experimental Results

1. In the channel produced by an axicon, the signal from the receiving antenna had an increased amplitude when the radiation propagated along the channel with the wavelengths λ=10cm, λ=7.5cm and λ=3cm. A typical oscillogram of the detector signal with the linear density of breakdown energy is presented in Fig.2a for λ=7.5cm. It follows from Fig.2a that in 120 μs after the breakdown the amplitude increased by ΔU. The maximal increase as compared to the initial signal U_o is equal to $(\Delta U/U_o)$=0.4. Figure 3a shows the maximal relative increase of the amplitude versus the energy consumed on the production of the channel. Typical durations of the amplitude increase T_a above the initial level during the propagation of radiation along the channel are given in Table I.

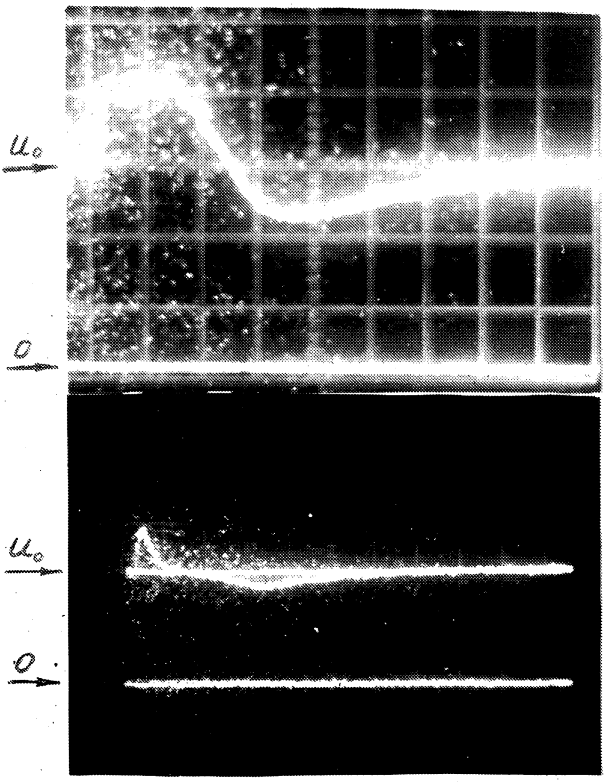

Fig.2. Oscillogram of the detector signal of the receiving antenna:a) axicon-produced channel; EPF energy consumption is ε=1.8 J/cm, λ=7.5cm; b) lens-produced channel;effective length of the channel is L=0.9, λ=10cm. The "0"-line is the zero level signal, U_o is the signal level in the absence of a plasma; one scale division equals 50 μs.

One can conclude from Fig.3a that the maximum of the relative increase of the signal amplitude depends significantly on the linear density of the breakdown energy, while the duration of the effect decreases strongly with the wavelength shortening (see Table I).

Table I

λ (cm)	10	7.5	3
T_a (μs)	250	120	3
T_y (μs)	80	80	2

2. In the channel produced by a lens, an increase of the signal amplitude was registered on the detector of the receiving antenna for the propagation of radiation with the wavelengths 10 cm, 7.5 cm and 3 cm. Because of the quasi-continuity of this type of channel, we have introduced the parameter L (the effective length of the plasma channel) which is equal to the sum of the lengths of individual breakdown points divided by the parameter R.

The oscillogram of the signal from the receiving antenna detector for the channel (L=0.9) is presented in Fig.2b (λ=10 cm). It follows from Fig.2b that in 70 μs after the breakdown the amplitude increases by ΔU. The maximal increase above the level of the initial signal U_o is equal to $\Delta U_{max} / U_o = 0.4$. In Fig.3b this quantity is plotted versus the effective length L for the propagation of radiation with the wavelengths mentioned above. Typical durations of the effect of the amplitude increase T_a above the initial level in the propagation of radiation along the channel with the same wavelengths are given in Table I. One can conclude from Fig.3b and Table I that in the case of a quasi-continuous channel, the quantity $\Delta U_{max} / U_o$ grows in proportion to the increase of the parameter L for all radiation wavelengths, while the duration of the effect decreases strongly with the wavelength shortening in the range λ=7.5-3 cm.

3. In the channel produced by an axicon, the decrease of the signal amplitude relative to the initial level was registered during the propagation of radiation along the channel with the wavelength λ=7.5 cm (Fig.2a) and λ=3 cm. It follows from Fig.2a that the signal amplitude decreases below the initial level when the effect of the signal amplitude increase disappears. The effect of the signal amplitude decrease was recorded when the linear energy consumed on the production of the channel was (ε>1J/cm).

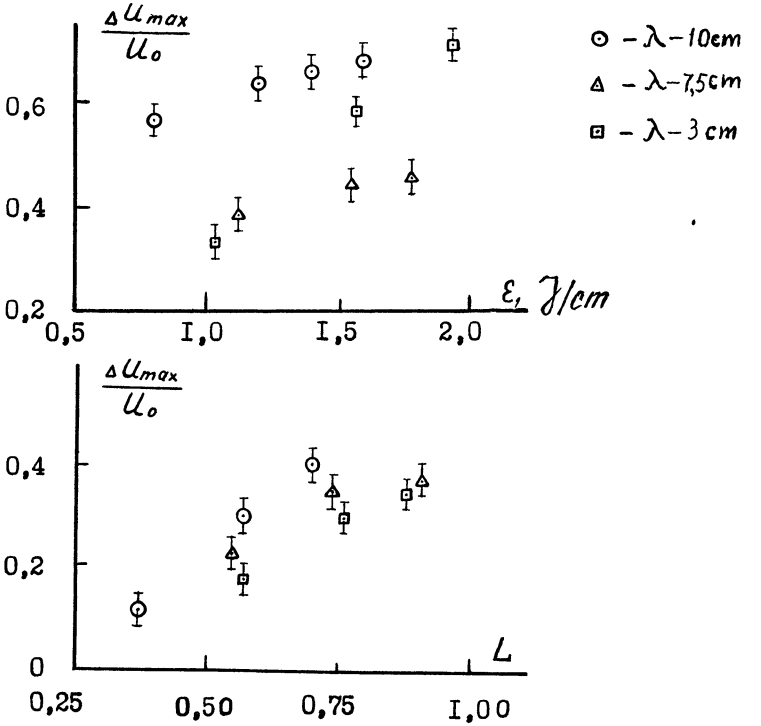

Fig.3. a)The maximal relative increase of the signal amplitude $\Delta U_{max} / U_o$ versus the EPF energy breakdown ε for λ=10, 7.5, and 3 cm.
b)The maximal relative increase of the signal amplitude versus effective length for λ=10, 7.5 and 3 cm in the lens-produced channel.

The duration of the effect of the signal amplitude decrease was T_y=400 μs for ε=2 J/cm, the radiation wavelength being λ=7.5cm and λ=3 cm. This effect is apparently related to radiation in the plasma channel.

4. In the lens-produced channel the decrease of the signal amplitude relative to the initial level was recorded during the propagation of radiation along the channel with the wavelengths λ=10 cm (Fig.2b), λ=7.5 cm and λ=3 cm. The effect of the signal amplitude decrease for the linear energy consumption on the production of the channel was ε>1 J/cm, the duration of the effect amounted to T_y=250 μs for the mentioned wavelengths.

4.Conclusion

The main results of our paper are the following:

-the effect of channeling of microwave radiation along the extended plasma formations with diffuse boundaries that is manifested as the increase of the signal amplitude from the detector of the receiving antenna during channel formation. Apparently, this phenomenon is caused by the propagation of the E-type surface wave along EPF;
-the effect occurs in continuous as well as in quasi-continuous channels; moreover in the latter case its duration is shorter, which correlates with the characteristic lifetimes of such channels;
-in the case of a continuous channel, the effect increases monotonically with the increase of the energy consumption on the formation of the channel in the wavelength range of interest;
-the duration of the effect depends significantly on the radiation wavelength for channels of both types, which is, apparently, caused by the absorption of the surface wave in EPF;
-in the case of a continuous channel, there exists a direct connection between the increase in the continuity of the channel and the growth of the magnitude of the effect;
-the signal from the receiving antenna is attenuated below the initial level in channels of both types, which, apparently, is caused by the resonance absorption of the surface wave in the plasma channel.

References

1.G.A.Askarjan, M.S.Rabinovich. Sov.Journ.Exp.Theor.Phys.**48**, 290 (1965).
2.G.A.Askarjan, I.M.Raevskii. Sov.Tech.Phys.Lett.**8**, 1131 (1982).
3.T.Dwyer, J.Greig, D.Murphy. IEEE **AP-32**, 141 (1984).
4.M.Y.Marin, L.Y.Polonskii, L.N.Pjatnitskii. Sov. Phys. Teach. Lett. **12**, 146 (1986).

RF OR MICROWAVE PLASMA REACTORS? FACTORS DETERMINING THE OPTIMUM FREQUENCY OF OPERATION

M. Moisan, C. Barbeau, R. Claude, C.M. Ferreira[a], J. Margot-Chaker, J. Paraszczak[b], A.B. Sá[a], G. Sauvé and M.R. Wertheimer[c]
Département de physique, Université de Montréal, B.P. 6128, Succursale A, Montréal, Québec, H3C 3J7
a) Centro de Electrodinâmica da Universidade Técnica de Lisboa (INIC), Instituto Superior Técnico, 1096 Lisboa Codex, Portugal.
b) IBM T.J. Watson Research Center, P.O. Box 218, Yorktown Heights, New York, 10598.
c) Groupe des Couches Minces and department of Engineering Physics, Ecole Polytechnique, B.P. 6079, Succursale A, Montréal, Québec H3C 3A7

1. Introduction

It is now generally accepted that the frequency $\omega/2\pi$ at which a high frequency (HF) discharge is sustained has considerable influence on the properties of the plasma. For example, the electron density obtained for a given HF power density deposited into the plasma is usually higher at microwave than at radio frequencies (RF) [1]. Along the same line, it has been shown that the plasma stimulating frequency can be varied to improve the efficiency of plasma processing, for example, in etching of polyimide [2] and in the deposition of polymer [3] or amorphous silicon [4]. The analysis developed for such results calls on the dependence of the electron energy distribution function (EEDF) upon ω. In this communication, we review the theoretical work on this subject and then we draw general conclusions concerning the frequency optimization of plasma processes.

1.1. Physical conditions corresponding to the analysis developed for the influence of the plasma stimulating frequency. It is important to make sure that the model presented will be applied to the adequate physical context. Such a question arises, for example, when one attempts to determine the effects, on a given plasma process, of converting from a RF capacitive discharge reactor at 13.56 MHz to a reactor derived from a microwave induced plasma (MIP) at 2.45 GHz. A few remarks are in order since such a situation generally implies making other changes in the setup besides frequency.

(i) Most MIP can be generated using a microwave field applicator located outside the discharge vessel, the latter usually consisting of a low loss dielectric material such as fused silica. This method of field application allows a substrate exposed to the MIP to be biased independently of the microwave power, which is rarely possible for RF capacitive discharges where the parallel plates are in direct contact with the discharge. In the latter case, the powered electrode holding the substrate is said to be self-biased. The corresponding potential drop across the sheath, before the substrate, depends on the RF power applied to the discharge and it cannot be adjusted independently of the bulk plasma parameters (e.g. electron density). An independent biasing is advantageous in providing the means for adjusting the flux and energy of ions bombarding the substrate during reactive ion etching (RIE) or deposition processes. The model that we present ignores any biasing effect and thus, when using it to compare results from RF and microwave plasma reactors, one implicitly assumes that the substrate is at the same potential in both cases.

(ii) The coupling scheme of the RF power to the discharge is different from that employing microwaves, preventing the use of the same reactor in both situations. This is the case not only with the RF capacitive discharge but, in general, when comparing RF and microwave plasmas. To our knowledge, the only case where the RF and microwave fields are applied in the same way to the discharge is that of surface wave produced plasmas. The model elaborated in this communication does not take into account differences in the HF field configuration when changing frequency. It must also be borne in mind that modifications to the reactor dimensions not only affect the charged particles' characteristic diffusion lengths but also influence the hydrodynamics of the gas flow which often plays a significant rôle in plasma processing.

(iii) The power density absorbed into the plasma is an operator-dependent parameter. *A priori*, one would think that in order to observe the influence of the plasma stimulating frequency upon plasma parameters it should be kept constant. This is certainly not the case when, under constant power density, the electron density varies with frequency [1]. In such a situation, frequent in reduced gas pressure discharges, two effects can result: 1) a variation of the EEDF when the latter is electron density sensitive. This situation may occur with discharges where the charged particles' losses are dominated by volume recombination. With diffusion controlled plasmas, as will be discussed later, changes in the degree of ionization (past a certain critical value) can also affect the EEDF; 2) a change in $\dot{n}_j$, the density of species produced per second for a given process (e.g. atom excitation, molecule dissociation). This is the case, for example, for processes that

result from electron impacts: $\dot{n}_j$ then increases with the electron density (see Sec. 4). Thus, when varying frequency under constant power density (a condition which is experimentally more easily achieved than working at a constant electron density), one must take into account the above two effects when interpreting the results. Our analysis will consider both situations: constant electron density and constant power density operation.

1.2. Requirements for the EEDF to be time independent with respect to the HF field amplitude variation. The EEDF describes the probability of finding electrons in a given interval of energies. In plasmas dominated by binary collisions, it is the solution of the Boltzmann equation. Assuming the plasma to be homogeneous and the anisotropy induced in the direction of the electric field to be weak, the EEDF can be expressed as a two-term expansion of the form $F(u) \simeq F_0(u) + F_1(u)$, where u is the particle energy and F_0 is the isotropic and main part of the EEDF; F_1, which is much smaller than F_0, accounts for the anisotropy of the EEDF resulting from the electric field action. In what follows, we only consider the rôle of F_0.

The relaxation of the electron energy through electron-neutral collisions is described by the characteristic frequencies for energy transfer and for momentum transfer, ν_u and ν_p , respectively. These are defined, for a given particle energy u, by [5]

$$\nu_u = (2m/M)\nu_c + \sum_j \nu_j \,, \quad \nu_p = \nu_c + \sum_j \nu_j \,, \tag{1}$$

where ν_c and ν_j are the corresponding electron-neutral collision frequencies for momentum transfer and for atom or molecule excitation (including ionization) to energy level j, respectively. The temporal evolution of the isotropic distribution F_0 is determined by the value of the field angular frequency ω relative to the characteristic frequency for energy transfer ν_u while that of the anisotropic distribution F_1 is governed by the frequency ν_p. When the frequency of the field is such that $\omega << \nu_u$, the distribution F_0 is modulated over all its energy range at twice the frequency ω. The amplitude of this modulation decreases as ω increases. When ω becomes larger than $\nu_u(u)$, the electrons in the distribution F_0 for which the inequality $\omega > \nu_u(u)$ is verified cease to oscillate. This condition implies that it is the bulk rather than the tail of F_0 that first stops oscillating when ω increases, because $\nu_u(u)$ is smaller there than in the tail where the inelastic collisions contribute to increase the value of $\nu_u(u)$ (see eqn. (1))[2].

When applied to the case of atomic gases like neon, the calculations [6] show that the modulation of F_o has almost completely stopped for $\omega/p \geq p \times 10^8\ s^{-1}\ Torr^{-1}$ (p is the pressure reduced to a gas temperature of 300 K). This means that at 200 mTorr, for example, the EEDF should not be oscillating with the HF field at all for frequencies above 10 MHz. A very similar situation is expected with argon since our calculated values for $\nu_u \simeq \sum_1 \nu_j$ are comparable to those reported [6] for neon. With molecular gases, the EEDF modulation is predicted to persist to higher frequencies, typically up to 40 MHz in H_2 and CO at 200 mTorr [5], [7]. This means that the modulation is likely to influence most of the EEDF energy range at 13.56 MHz, with some modulation in the tail possibly remaining up to 40 MHz.

2. Changes in the EEDF shape and average energy as a function of the plasma stimulating frequency

2.1. The physical mechanism responsible for the frequency effect on the EEDF. When the EEDF is time independent, the Boltzmann equation for the electrons yields [8]

$$\frac{2}{3}\frac{d}{du}\left[u^{3/2}\,\nu_c(u)\,u_c\frac{dF_o}{du}\right] = S_o(u) \quad . \tag{2}$$

where the electron energy $u = m\omega^2/(2e)$ is in eV (e is the electron charge); the variable

$$u_c = \frac{e}{m}\,\frac{1}{\nu_c^2(u)+\omega^2}\,\frac{E_o^2}{2} \tag{3}$$

represents the **energy** transferred on the average per collision over one period, from the HF field to electrons initially having a random energy u: thus, $\nu_c\,u_c$ is the **power** transferred per electron. The important point to note in relation (2) is that the power transfer $\nu_c\,u_c$ is maximum for $\nu_c(u) = \omega$: this equality defines the value of u at which occurs the optimum power transfer at frequency $\omega/2\pi$. This latter dependence is the basic physical mechanism that makes the shape of the time independent EEDF vary with frequency. Such a dependence can however be overwhelmed when the number of electron-electron collisions in the term $S_o(u)$ becomes large enough. For argon, this occurs when the degree of ionization of the discharge approximately exceeds 10^{-4}. Then, as a result, the EEDF is nearly Maxwellian, whatever the frequency of the field.

When the contribution of electron-electron collisions in the term S_o and the step-wise ionization can be neglected, and provided that the charged particles' loss occurs through diffusion, the shape of the EEDF is not influenced by the value of the electron density but it depends on E_o/N and ω/N (N is the neutral atom density), or on any other combination of these parameters. To see this dependence of the EEDF on E_o/N and ω/N, consider the parameter u_c appearing in eqn. (2), as defined in eqn. (3) and recall that $\nu_c^2(u) = N^2(\sigma_c^2\, 2eu/m)$ where σ_c is the electron-neutral collision cross-section for momentum transfer. The general dependence of the Boltzmann equation on the two parameters E_o/N and ω/N reduces to only one parameter in two limiting cases: for $\omega/N \to 0$ (DC case), it is E_o/N whereas for $\omega/N \to \infty$ (designated as the microwave case), it comes to E_o/ω. As $\omega/N \to 0$, the model assumes that the EEDF is time independent i.e. it is not valid for too small values of ω/N except $\omega/N = 0$.

2.2. Balance of charged particles. The solution of the Boltzmann equation (2) i.e. the EEDF, can be obtained for any given set of E_o/N and ω/N values. To correlate precise discharge conditions to values of E_o/N, the continuity and momentum transfer equations coupling electrons and ions need to be involved. Clearly, the shape of the EEDF will also have some influence on the value of E_o/N. When such a problem of simultaneously determining E_o/N and the EEDF can be solved i.e. the set of equations is closed, the solution is said to be self-consistent. In what follows, we examine one of the plasma equations involved in such a formulation.

Under steady-state and ambipolar diffusion conditions, the balance between the production and loss rates for charged particles (continuity equation) can be expressed by

$$\langle \nu_i(u) \rangle = D_a/\Lambda^2, \qquad (4)$$

where $\langle \nu_i(u) \rangle = NC_i$ is the average ionization frequency, C_i denoting the electron rate coefficient for ionization (note that $C_i = \langle \sigma_i w \rangle$, where σ_i is the cross-section for ionization by electron impact and the symbol $\langle\ \rangle$ denotes averaging on the EEDF), D_a is the ambipolar diffusion coefficient, and Λ is the characteristic diffusion length for the discharge vessel. When the field intensity E_o is independent of position, we get $\Lambda = a/2.405$ for a long, cylindrical discharge tube of inner radius a. Note that with surface wave discharges, E_o varies radially and spatial averaging is thus further required in eqn. (4) which however only slightly affects the value of D_a [9]. As a rule, the EEDF obtained from eqn. (2) is such that $\langle \nu_i \rangle$ and D_a (in fact u_k, see further) can only be calculated numerically.

As it is well known, for reduced gas pressure discharges, the average energy of the electrons is much larger than that of the ions and we can write [10] $D_a \simeq \mu_i u_k$, where μ_i is the ion mobility and $u_k = D_e/\mu_e$ is the electron characteristic energy, i.e. the ratio of the electron diffusion coefficient to the electron mobility. We further note that $\mu_i N = \mu_{io} N_L$, where μ_{io} is the ion reduced mobility for a given ion in a given gas and for $N_L = 2.687 \times 10^{19}$ cm^{-3}, the Loschmidt number. Therefore, we can write eqn. (4) in the form

$$\frac{C_i(F_o)}{u_k(F_o)} = \frac{\mu_{io} N_L}{(N\Lambda)^2} \quad . \tag{5}$$

Though the quantities u_k and C_i depend on the EEDF, the rearrangement of eqn. (4) shows that the ratio C_i/u_k can be expressed as a unique function of the $N\Lambda$-product or equivalently of the pa-product.

This result is fundamental. It means that, for a discharge in a given vessel (setting Λ) at a given pressure p (setting N), the parameters on which the EEDF depends necessarily adjust themselves so that C_i/u_k = constant, whatever the frequency of the sustaining field. Two cases are then to be considered: 1) when the effects of electron-electron collisions are negligible, the EEDF, hence C_i and u_k, are functions of E_o/N and ω/N as stated earlier. Clearly, for a given frequency of operation, eqn. (5) sets the discharge maintenance field E_o, *independently of the intensity of the externally applied electromagnetic field*; 2) at sufficiently high degrees of ionization, when the EEDF is a Maxwellian, C_i and u_k depend only on the electron temperature $T_e = 2/3 \langle u \rangle$ and the latter adjusts itself so as to satisfy eqn. (5). Then, for a given ω/N, T_e determines the value of E_o/N.

Figures 1a and 1b show the EEDF obtained from a self-consistent calculation for an argon discharge in a long, cylindrical tube for a given pa-product of 0.15 Torr-cm and 1 Torr-cm, respectively. In each figure, three limiting situations are considered: A - no electron-electron collisions and $\omega \rightarrow 0$ (DC case), H - no electron-electron collisions and $\omega \rightarrow \infty$ (microwave case), and M - dominating electron-electron collisions and any ω value (Maxwellian distribution). As can be seen, the shape of the distributions are quite different in these three cases. In particular, the relative number of electrons in the body and in the tail of the EEDF differs considerably for all three cases (the tail corresponds to the energy range above the lowest energy threshold for excitation; in argon, it is 11.55 eV).

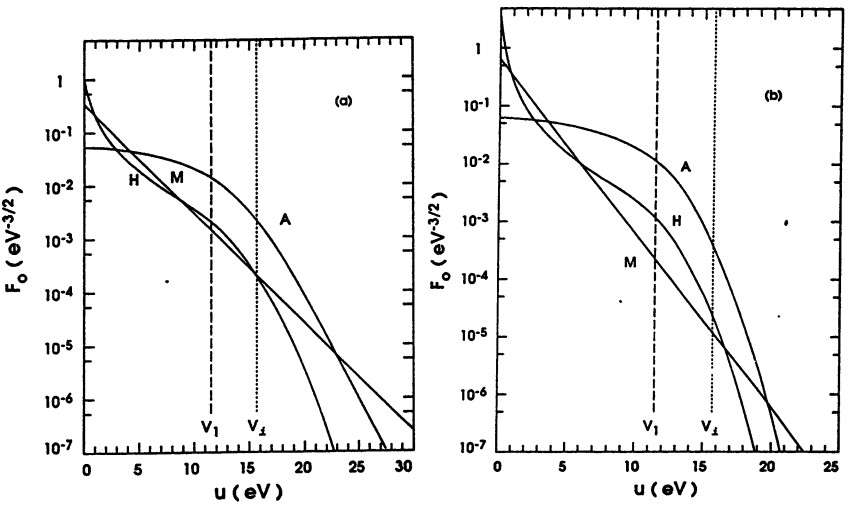

FIG. 1. Electron energy (u) distribution functions calculated from a self-consistent model for an argon discharge in a long, cylindrical tube, under ambipolar diffusion conditions, in three limiting cases. Curve A: no electron-electron collisions and $\omega \rightarrow 0$ (DC case); curve H: no electron-electron collisions and $\omega \rightarrow \infty$ (microwave case); curve M: dominating electron-electron collisions, any ω value (Maxwellian distribution). The vertical dashed and dotted lines correspond to the first excitation level and ionization level threshold energies, respectively. (a) pa = 0.15 Torr-cm and (b) pa = 1 Torr-cm. The distributions are normalized such that

$$\int_0^\infty F_0\,(u)\,\sqrt{u}\,du = 1.$$

We have seen from Fig. 1 that the EEDF changes markedly as frequency is increased from zero (DC) to microwaves. At the same time, as we are going to show, the average electron energy decreases significantly. To see this point in general terms, one must be aware that u_k only weakly depends on the EEDF [11] and thus C_i in expression (5) is to a first approximation only a function of the product $N\Lambda$. The validity of this approximation, as far as determining the average electron energy is concerned, can be appreciated by referring to Table 1. Figure 2 shows the value of C_i calculated for argon, as a function of the average electron energy <u>, for the three limiting cases considered in Fig. 1. Considering that C_i is a constant for a given pa-product, one sees from Fig. 2 that <u> is larger at $\omega \rightarrow 0$ (curve A) than at microwave frequencies (curve H). Also noteworthy is the fact that the microwave EEDF (H) and the Maxwellian one (M) have nearly the same average energy for any C_i value, although their respective shape can be quite different as can be seen in Figs. 1a and 1b. The excitation rates for levels with a

TABLE I Average electron energy (eV) obtained from the approximation C_i = const., as compared to the exact value given by the set of Eqs. (2) and (5)

Exact	C_i = const. approximation	
Given Maxwellian (M), $\langle u \rangle = 3.15$[a]		
DC case (A)	6.8	6.4
Microwave case (H)	2.35	3.05
Given Maxwellian (M), $\langle u \rangle = 2.15$[b]		
DC case (A)	6.0	5.7
Microwave case (H)	1.87	2.15

a) Corresponds to pa = 0.15 Torr-cm.

b) Corresponds to pa = 1 Torr-cm.

threshold energy lower than that for ionization are such that a higher excitation rate is obtained for $\omega \rightarrow 0$ than at microwaves or than under dominating electron-electron collisions. This result is documented with exact calculations further in Sec. 4. However, it is possible to use the approximation C_i = const. as a handy means to illustrate this point. Consider in Fig. 2 the excitation rate $C(^3P_2)$ of the argon $^3P_2$ metastable level from the ground level. Given the value C_i, the value of $C(^3P_2)$ for each limiting situation is that corresponding to the average electron energy set by the value of C_i for that particular situation. Clearly, the value of $C(^3P_2)$ is larger in the DC case.

The above changes of the EEDF with frequency have a strong effect upon the power which is transferred from the HF field to the electrons. They also determine how this power is shared between ionization and excitation processes. These points are discussed in the following section.

3. Variation of the average power absorbed per electron (parameter θ) as a function of the plasma stimulating frequency

The power balance between the HF field and the discharge can be expressed by the key parameter θ[12], a quantity which is readily accessible experimentally. It is defined as

$$P_a = \theta n_t, \qquad (6)$$

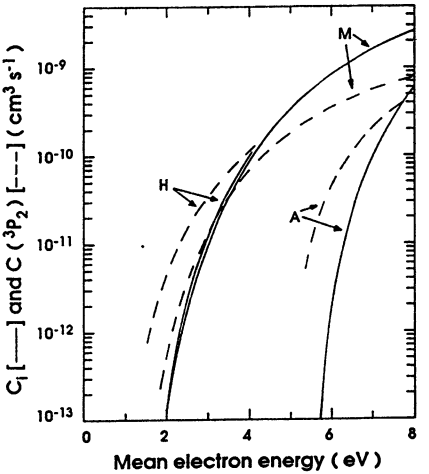

FIG. 2: Argon atom $^3P_2$ metastable level excitation rate 2. C($^3P_2$), and ionization rate by electron impact on the atom in the ground state C_i, calculated as a function of the average electron energy < u > , in the three limiting situations given in Fig. 1.

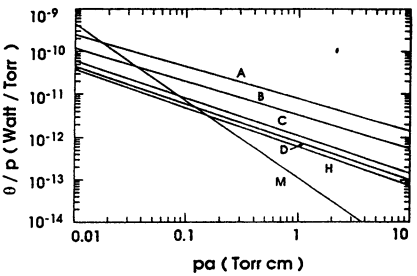

FIG. 3. Plot of θ/p vs. pa calculated for different values of ν_{ce}/ω : (A) ∞, (B) 6.67, (C) 1.25, (D) 0.67, (H) 0.0. Curve M is for a Maxwellian EEDF corresponding to dominant electron-electron collisions.

where P_a is the HF power absorbed in a plasma of volume V containing a total number of electrons n_t. In this relation, θ represents the average power absorbed per electron from the HF field and can also be considered as the power required to sustain an electron-ion pair in the discharge. Under steady-state conditions, the value of θ adjusts to compensate for the power expenditure of the electrons by elastic and inelastic collisions with the gas molecules. This power expenditure is influenced by the EEDF and, to a first approximation, is given by

$$\theta = (2m/M) \langle \overline{\nu_c(u)\, u} \rangle + \sum_j \langle \overline{\nu_j(u)} \rangle \, eV_j + \langle \overline{\nu_i(u)} \rangle \, eV_i \quad . \tag{7}$$

Recall that $\langle \nu_j(u) \rangle$ is the EEDF averaged electron-neutral collision frequency for excitation to the j^{th} level of the atom, assumed to be initially in the ground state, and eV_j is the corresponding energy threshold. The horizontal bar indicates a spatial averaging (which is required when the field intensity E_o is not uniform).

The value of θ has been calculated by Ferreira and Loureiro [11] for argon at reduced gas pressures (typically pa ≤ 1 Torr-cm). They obtained the curves θ/p vs. pa labelled A to H in Fig. 3 using the EEDF calculated from the Boltzmann equation

and eqn. (5), with the assumption that electron-electron collisions can be neglected. These curves correspond to different values of the ratio ν_{ce}/ω or, equivalently, N/ω, since ν_{ce} is essentially the value of N expressed in the same frequency unit as ω. For the case of argon [13], $\nu_{ce} = 2.0 \times 10^{-7} N\ s^{-1}$ where the neutral atom density N is in cm^{-3}. For each value of ν_{ce}/ω, the representation θ/p vs. pa emphasizes the existence of a similarity law in terms of the product pa (or equivalently $N\Lambda$ as in eqn. (5)). The model shows that for a fixed gas pressure, the value of θ decreases when the frequency is increased from zero to microwave frequencies. The curve M shows the value of θ when the EEDF is Maxwellian. In the latter case, the value of θ can be smaller or larger than that given by the curves A to H depending on the product-pa. The fact that θ decreases when keeping constant the HF power density deposited into the plasma means a greater efficiency in producing electron-ion pairs.

The physical reason for the different θ values at a given value of pa can be readily understood from the considerations expressed in the preceding paragraph and the shape of the EEDF shown in Figs. 1a and 1b. The situation is particularly simple in the range pa $\leq$ 0:5 Torr-cm, where the electron energy losses by elastic collisions with the gas atoms are negligibly small as compared to the inelastic terms (see also Fig. 4): eqn. (7) then reduces to

$$\theta/N \simeq \sum_j \overline{C_j}\, eV_j + \overline{C_i}\, eV_i \qquad (8)$$

where

$$C_j = (2e/m)^{1/2} \int_{V_j}^{\infty} \sigma_j(u)\, F_o(u)\, u\, du \qquad (9)$$

is the rate coefficient for atom excitation to the j-th atomic level by electron impact, $\sigma_j(u)$ denoting the corresponding excitation (or more generally any process) cross-section. As seen from Figs. 1a and 1b, the EEDF (in argon) has a much larger relative number of electrons in the tail in case A ($\omega \rightarrow 0$) than in case H ($\omega \rightarrow \infty$), which means that C_j (for all j), thus θ/p, are larger in the former limiting case. Since $F_o(u)$ gradually evolves from curve A to curve H (Fig. 1) as ω is increased, θ/p correspondingly decreases for a given value of pa, as shown in Fig. 3. In the same figure, it can be seen that the θ/p curve for a Maxwellian EEDF crosses the non-Maxwellian curves. This leads to smaller values of θ than with non-Maxwellian

EEDF for large enough pa values. Indeed, at pa = 1 Torr-cm (Fig. 1b), the number of electrons in the energy range that contributes significantly to the excitation rates C_j is much larger in the microwave case than for the Maxwellian distribution, which results in θ/p being larger in case H than in case M, as indicated in Fig. 3. However, as the gas pressure is decreased, the respective contributions from the EEDF of the H and M cases to the excitation rates, as can be inferred from Fig. 2a, tend to reverse. For pa $\leq$ 0.15 Torr-cm, θ/p is the smallest in the microwave domain (Fig. 3).

One important conclusion which can be drawn from the θ/p curves presented in Fig. 3 is that, for a given pa value and a given absorbed power per unit volume, the electron (and ion) density is higher in the microwave range than at lower frequencies. The reason for this is that, on the average, less energy is spent per electron in atomic excitation. Recall that these theoretical results are obtained assuming ambipolar diffusion conditions, typically for pa $\leq$ 1 Torr-cm. Calculations for a discharge dominated by charged particles losses through volume recombination would yield larger θ/p values.

Another important aspect of the electron power transfer stems from the way that this input power is divided into the various types of electron-atom collisions (eqn. (7)). Figure 4 shows the calculated percentage of the electron power losses in argon for each type of processes (excitation, ionization and elastic collisions) as a function of the pa-product, for the limiting cases A, H and M already mentioned. One can see that the various percentage losses are very much the same in the cases A and H as compared to the Maxwellian case. This is because, for a given pa value, as shown in Figs. 1a and 1b, the tail of the EEDF in cases A and H nearly has the same shape, differing only by a scale factor. The latter affects the absolute value of θ but not the percentage losses. Compared to cases A and H, the Maxwellian distribution possesses a much richer tail well beyond the ionization threshold ($\simeq$ 15.76 eV for argon). This fact leads to a larger fractional power transfer into ionization and, consequently, less goes into excitation, as shown in Fig. 4

4. Density of excited atoms created per second as a function of the plasma stimulating frequency

When varying the operating frequency with the idea of optimizing the efficiency of a given process, it is natural to keep the density of the HF power absorbed into the plasma constant. This method provides the correct answer as far as power efficiency is concerned. However, drawing conclusions about the influence of the frequency change on the process is not as simple as it would be if the electron density had been kept constant: the fact that, under constant absorbed power

density, n generally varies with frequency (the only well exception being for helium gas) introduces additional effects which act on the process considered. These are listed below: 1) in many instances, the EEDF, besides being frequency dependent, also varies with the electron density; 2) the density $\dot{n}_j$ of species (e.g., excited atoms or molecules, radicals) produced per second in the discharge through electron impact depends on the electron density n. More specifically, in the case of atoms or molecules initially in their ground state, we have $\dot{n}_j = (C_jN)n$.

In the following, we shall examine the calculations which show the effects of frequency upon C_j (constant electron density operation) and C_jn (constant power density operation). Both these parameters in their respective operating conditions are proportional to the number of species produced per second, $\dot{n}_j = (C_jN)n$. The higher the density of species produced, the more efficient is the corresponding process. This study is developed as a function of the process threshold energy eV_j, for the three limiting cases A, H and M previously described. We have performed these calculations in argon using the EEDF given in Fig. 1.

In order to estimate to what extent the value of C_j and C_jn obtained depend on the specific shape of the process cross-section, we considered two really distinct types of cross-sections. These are shown in Fig. 5 and are both given by the same analytical expression [14]

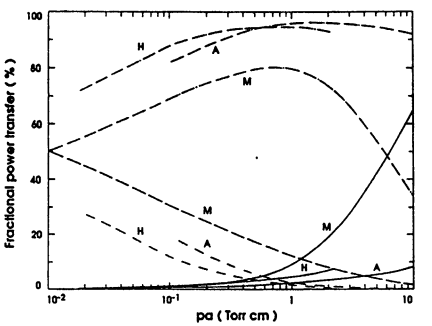

FIG. 4. Calculated fraction of the power per electron (θ) transferred to the atoms resulting from elastic collisions (——), excitation (-···) and ionization (- - -), as a function of the product-pa.. Curves A, H and M refer to three limiting cases: DC, microwave and Maxwellian EEDF, respectively.

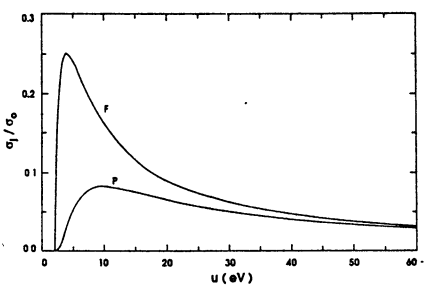

FIG. 5. The two different types of cross-sections assumed in our calculations of process rates resulting from electron impact. The cross-section F simulates the case of an optically forbidden transition whereas curve P corresponds to an optically permitted transition. The process threshold energy here is $eV_j = 2$ eV.

$$\sigma_j(u) = \sigma_o(V_j/u)^{\alpha}(1 - V_j/u)^{\beta} \qquad (10)$$

for different values of α and β. Note that the cross-section maximum is attained for energy $u_{max} = [(\alpha + \beta)/\alpha]V_j$. Curve F($\alpha = \beta = 1$) typically represents optically forbidden transitions which usually have their maximum at about twice the threshold energy, while curve P($\alpha = 1, \beta = 4$) corresponds to allowed transitions whose cross-section maximum is generally located at 5 to 10 times the threshold energy [14].

4.1. Process rate coefficient C_j as a function of the threshold energy eV_j in the three limiting cases A, H and M (constant electron density operation). Experimental results on plasma polymer deposition with a monomer molecule in an argon-based HF discharge have been obtained as a function of ω [1]. To interpret these and similar results, we complete our study for a pure argon discharge by looking at the excitation rate coefficients of atoms or molecules with lower excitation energy thresholds than for argon, in an argon controlled discharge. Such an approach, using the EEDF calculations from the model for an argon discharge, is strictly speaking only valid if the molecular additives can be assumed to be at the trace level.

Figures 6 and 7 present the excitation coefficient $C_j(V_j)$ as calculated for an argon controlled discharge with cross-sections for optically allowed and optically forbidden transitions, respectively. Figure 6a shows, for the three limiting cases A, H and M, the ratios of the corresponding coefficients $C_j(V_j)$, at pa = 0.15 Torr-cm. Comparing the DC and the microwave situations, it can be seen that the value of C_j in the DC case is always larger, whatever the threshold energy of the process. When the discharge evolves from the microwave case (H) to a situation where electron-electron collisions dominate (M), the latter rate coefficient is the larger, except for a limited energy interval (extending approximately from 4 to 8 eV) over which the microwave rate coefficient is only very slightly larger than that from the Maxwellian EEDF. Finally, when considering the three limiting cases in Fig. 6a together, it can be seen that it is the EEDF of the DC limit that leads to the largest coefficient for all energies from zero to approximately 17 eV (the argon ionization threshold is 15.76 eV), above which the largest of the three coefficients is then that for the Maxwellian distribution. Figure 6b refers to the same allowed transition as in Fig. 6a but at pa = 1 Torr-cm. The results are qualitatively similar to those for pa = 0.15 Torr-cm, but the larger the pa-product, the larger the $C_j(A)/C_j(M)$ ratio at a given energy below the ionization threshold. The calculations for the forbidden transition are shown in Figs. 7a and 7b (pa = 0.15 and 1 Torr-cm, respectively). They do not significantly differ from those for the allowed transition at the same pa value, showing that the exact

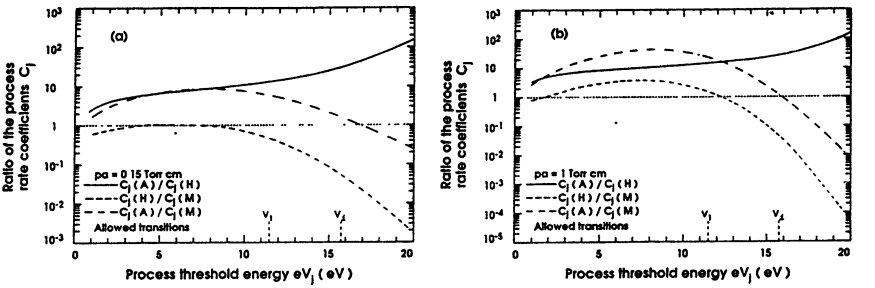

FIG. 6. Ratio of the process rate coefficients C_j calculated with the EEDF corresponding to the three limiting situations A(DC), H(microwave) and M(Maxwellian EEDF), as a function of the process threshold energy eV_j. The assumed process cross-section (Fig. 5) simulates an optically allowed transition. (a) pa = 0.15 Torr-cm and (b) pa = 1 Torr-cm.

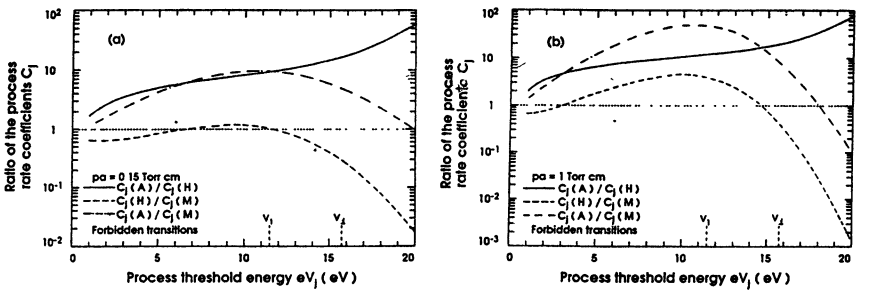

FIG. 7. Ratio of the process rate coefficients C_j calculated with the EEDF corresponding to the three limiting situations A(DC), H(microwave) and M(Maxwellian EEDF), as a function of the process threshold energy eV_j. The assumed process cross-section (Fig. 5) simulates an optically forbidden transition. (a) pa = 0.15 Torr-cm and (b) pa = 1 Torr-cm.

shape of the process cross-section in contrast with the value of the process threshold energy does not really matter in such a comparative study.

4.2. Density of species produced per second $\dot{n}_j$ as a function of the process threshold energy in the three limiting cases A, H and M (constant absorbed power density operation). Figures 8 and 9 compare $\dot{n}_j = (C_j N)n$, the density of species produced per second by direct electron impact on the atom (or molecule) in the ground state, as a function of the threshold energy eV_j under constant absorbed power density conditions, for the three limiting cases A, H and M. Figures 8 and 9 correspond to optically allowed and optically forbidden energy transitions, respectively. The value of the electron density n appearing in these calculations is adjusted so that the power density (equal to θn) remains constant as θ varies. The values of θ used in these three limiting cases are those shown in Fig. 3.

Figures 8a and 8b show the results obtained for an allowed transition at pa = 0.15 and 1 Torr-cm, respectively. Determining the most efficient limiting case in Fig. 8a requires a division of the energy range into three distinct intervals: 1) from zero to about 3 eV, where the best situation is that for the Maxwellian EEDF; 2) from 3 eV to about 9 eV, where it is the microwave case; 3) above 9 eV, where the Maxwellian distribution is once again the most efficient one. In Fig. 8b, except for a very narrow threshold energy range around 7.5 eV, the Maxwellian case is the most efficient one everywhere. The results for a forbidden transition, presented in Figs. 9a and 9b, are

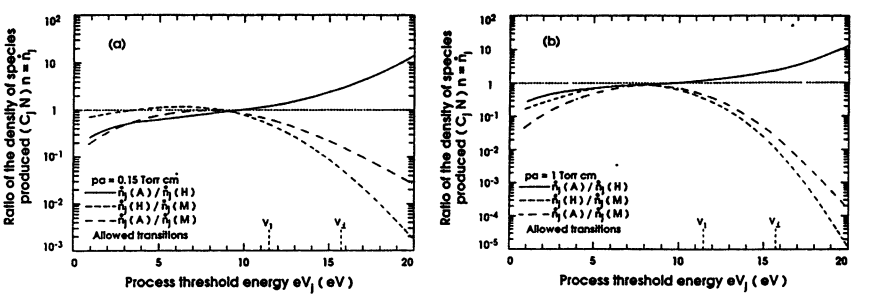

FIG. 8. Ratio of the densities of species produced per second $(C_j N)n$ calculated with the EEDF corresponding to the three limiting situations A(DC), H(microwaves) and M(Maxwellian EEDF), as a function of the process threshold energy eV_j, under constant power density conditions. The process is assumed to result from electron impact on the atom (molecule) in the ground state and the cross-section (Fig. 5) used simulates an optically allowed transition (a) pa = 0.15 Torr-cm and (b) pa = 1 Torr-cm.

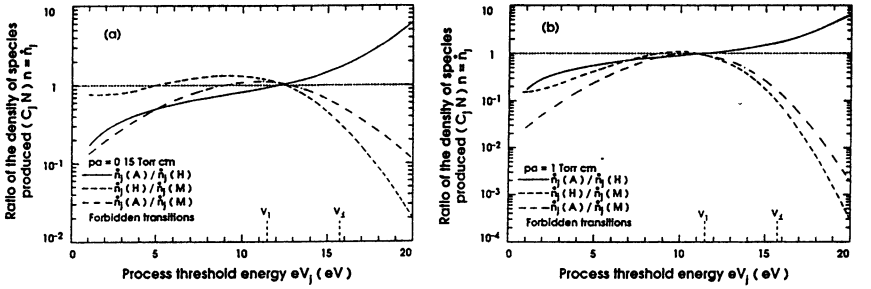

FIG. 9 Ratio of the densities of species produced per second (C_j N)n calculated with the EEDF corresponding to the three limiting situations A(DC), H(microwaves) and M(Maxwellian EEDF), as a function of the process threshold energy eV_j, under constant power density conditions The process is assumed to result from electron impact on the atom (molecule) in the ground state and the cross-section (Fig. 5) used simulates an optically forbidden transition (a) pa = 0.15 Torr-cm and (b) pa = 1 Torr-cm

qualitatively the same as those for the allowed transition at the same pa value, indicating that the exact shape of the process cross-section considered does not play a significant rôle in our comparative study.

In conclusion, when operating under constant power density conditions, the efficiency of a given process depends not only on the applied field frequency but as well on the process threshold energy with respect to the ionization energy of the gas controlling the discharge.

5. Guidelines about frequency optimization of plasma processing

From our theoretical analysis, we can set out general conclusions about the frequency optimization of plasma processing. We need to distinguish two operating conditions: constant electron density and constant power density. We also have to consider three possible scenarios for the evolution of the discharge characteristics as frequency is raised from DC to microwaves. These scenarios are defined schematically according to three limiting situations: case A or DC case ($\nu_{ce}/\omega \rightarrow \infty$), case H or microwave case ($\nu_{ce}/\omega \rightarrow 0$), and case M, whatever the field frequency, when the EEDF is Maxwellian. The possible scenarios for $0.15 \leq pa \leq 1$ Torr-cm, as f varies typically from 13.56 to 2450 MHz, are: 1) A → H: this situation is governed by the evolution of the parameter ν_{ce}/ω; 2) A → M: it means that the ionization degree increases with frequency to such an extent that it reaches a level above which the electron-electron collisions are dominating, yielding then a Maxwellian EEDF. In

such a case, the parameter ν_{ce}/ω is meaningless; 3) $A \rightarrow H \rightarrow M$: it corresponds to a degree of ionization becoming large enough to yield a Maxwellian EEDF only once ν_{ce}/ω has become close to or smaller than unity.

Considering operation at **constant electron density**, the theoretical analysis in argon indicated that, for a process energy threshold below ionization, the rate coefficient for plasma processing is always the largest in the DC case i.e. $C_j(A)/C_j(H)$ or $C_j(A)/C_j(M)$ is always larger than unity. For the $A \rightarrow H$ scenario, $C_j(A)/C_j(H)$ increases continuously with the process threshold energy whereas, for the $A \rightarrow M$ scenario, $C_j(A)/C_j(M)$ goes through a maximum at about half the ionization energy threshold.

Regarding the **constant power density** operation, the results are markedly different. In the $A \rightarrow H$ scenario, $\dot{n}_j$, the density of species produced per second, is lower in the DC case for processes with a threshold energy below about half the ionization energy, whereas it is the opposite for larger process energy thresholds. For $A \rightarrow M$ scenarios, the value of $\dot{n}_j$ is almost always the largest when the EEDF is Maxwellian, whatever the process energy threshold. Finally, for $A \rightarrow H \rightarrow M$ scenarios i.e. for cases such that the H situation is reached at an intermediate frequency, the results depend critically on the process energy threshold: for low energy thresholds ($\leq V_i/2$), one gets a maximum of species production per Watt at large enough frequencies; for large energy thresholds, there is a minimum of efficiency at the frequency for which the H case is reached.

6. Conclusion

The analysis presented in this chapter is a first step toward the understanding of the rôle of the plasma stimulating frequency upon discharge parameters and plasma processing. It assumes the EEDF to be time independent, corresponding to frequencies $\omega/2\pi$ typically above 13.56 MHz, and it is valid for argon gas in discharges with pa-values below approximately 1 Torr-cm. The respective influence of electron-electron collisions and electron-neutral collisions with ω still needs to be accounted for. The model also neglects any variation with ω of the ion sheath potential drop, a factor of importance in materials processing where the ion bombardment is often a key parameter. Some work has very recently been achieved in the modeling of molecular (O_2, N_2[15]) and other atomic gas (He[16]) HF discharges: the behaviour of the EEDF in these gases, with the exception of helium show a significant dependence on ω.

As far as experimental results are concerned, there are only few available reports in which a true frequency dependence investigation is performed i.e. experiments where the only external parameter varied is ω. For the time being, such experiments in the domain 13.56 - 2450 MHz seem to be restricted to surface wave derived plasmas. The results obtained in such a setup can be summarized as follows:

(i) With respect to charged particle production, in argon gas at reduced pressure, depending on discharge conditions, 2 to 7 times less power per ion-electron pair was required at 2450 MHz than at radio-frequencies.

(ii) As far as the rate of plasma processes is concerned, the plasma polymer deposition from hydrocarbon and fluorocarbon monomers, the growth of amorphous silicon and the etching of polyimide indicate a possible frequency optimization that leads to typically a factor of 5 to 10 in increased efficiency.

(iii) These experiments point out that the optimum process efficiency is not necessarily attained at either 13.56 or 2450 MHz: under the operating conditions of the above experiments, the polymer deposition is more efficient at frequencies above typically 100 MHz and its quality satisfactory below 400 MHz; the amorphous silicon deposition in a RF capacitive discharge is the most efficient around 70 MHz; the etching of polyimide in an O_2 - CF_4 discharge is optimum close to 50 MHz. These various results imply that some flexibility in choosing the operating frequency of the plasma reactor is desirable to achieve the optimum process efficiency.

Depending on the situation considered, a higher process efficiency may translate into more rapid processing and lower cost. On the other hand, the technological problems associated with plasma processing at other than authorized frequencies (in the USA, 13.56, 27.12, 40.68, 915 and 2450 MHz) and, for the time being, the related scarcity and high cost of equipment, are obviously factors which should not be overlooked.

References

[1] M. Moisan, C. Barbeau, R. Claude, C.M. Ferreira, J. Margot-Chaker, J. Paraszczak, A.B. Sá, G. Sauvé, and M.R. Wertheimer, J. Vac. Sci. Technol. B (submitted August 1990).

[2] G. Sauvé, M. Moisan, J. Paraszczak, and J. Heidenreich, Appl. Phys. Lett. 53, 470.

[3] R. Claude, M. Moisan, M.R. Wertheimer, and Z. Zakrzewski, Plasma Chem. Plasma Process. 7, 451 (1987).

[4] H. Curtins, N. Wyrsch, and A.V. Shah, Electronics Lett. 23, 228 (1987).

[5] R. Winkler, J. Wilhelm, and A. Hess, Ann. Physik 42, 537 (1985).

[6] R. Winkler, H. Deutsch, J. Wilhelm, and Ch. Wilke, Beitr. Plasmaphysik 24, 285 (1984).

[7] R. Winkler, M. Capitelli, M. Dilonardo, C. Gorse, and J. Wilhelm, Plasma Chem. Plasma Process. 6, 437 (1986).

[8] C.M. Ferreira and J. Loureiro, J. Phys. D: Appl. Phys. 16, 2471 (1983)pp

[9] C.M. Ferreira, J. Phys. D: Appl. Phys. 22, 705 (1989).

[10]J.L. Delcroix, *Physique des Plasmas* (Dunod, Paris, 1966), Vol. 2, Chap. 16.

[11] C.M. Ferreira and J. Loureiro, J. Phys. D 17, 1175 (1984).

[12] C.M. Ferreira and M. Moisan, Physica Scripta 38, 382 (1988).

[13] The relation between ν_{ce} and ω is *a priori* arbitrary. However, it can be set so as to yield an effective electric field representation as a function of frequency ω in cases where ν_c varies with the energy u. This is why ν_{ce} depends on the nature of the gas.

[14] L.R. Peterson and J.E. Allen Jr., J. Chem. Phys. 56, 6068 (1972).

[15] C.M. Ferreira and J. Loureiro, J. Phys. D. 22, 76 (1989).

[16] L. Alves, Pedagogical aptitude diploma, Institute Superior Técnico, Universidade Técnica de Lisboa (1989).

EFFECT OF ELECTROMAGNETIC WAVE ON THE UPPER ATMOSPHERE PLASMAS WITH HALOCARBONS

Aleksandrov N.L., Konchakov A.M.,
Moscow Physicotechnical Institute, 141700 Dolgoprudny, USSR

Kochetov I.V., Napartovich A.P.,
Branch of Kurchatov Atomic Energy Institute,
142092 Troitsk, Moscow region, USSR

The increase of the halocarbon molecules density in the upper atmosphere is the main cause for the ozone layer destruction. Wong and co-authors [1] have proposed to remove the harmful chlorine atoms, making use of the electromagnetic wave effect on the lower ionosphere plasmas. In accordance with Wong the plasma electrons are heated by the electromagnetic wave being radiated by the high power ground based transmitter. The electron density increases with the electron temperature growth due to the diminishing of the recombination coefficient. This results in the speeding up of the electron attachment to the halocarbon molecules and the conversion of the chlorine atoms into the chlorine negative ions.

The chlorine negative ions don't take part in the ozone destruction processes. These ions may be removed from the site due to the drift upward in the atmosphere in the naturally occurring vertical electric field components. Another way of the negative ions destruction is the associative detachment in the collisions with hydrogen atoms, resulting in the free electron and the stable molecule HCl

$$Cl^- + H \rightarrow e + HCl. \qquad (1)$$

The aim of the present paper is to make analysis of the proposed by Wong et al. [1] effect taking into account the strong electron nonequilibrium in the ionosphere plasmas.

The main process to form negative ions is the

dissociative electron attachment to the halocarbon molecules:

$$\begin{aligned} e + CCl_4 &\rightarrow Cl^- + CCl_3, \\ e + CFCl_3 &\rightarrow Cl^- + CFCl_2, \\ e + CF_2Cl_2 &\rightarrow Cl^- + CF_2Cl, \\ e + CH_3Cl &\rightarrow Cl^- + CH_3. \end{aligned} \qquad (2)$$

The attachment coefficient is equal to

$$k_a = \left(\frac{2}{m}\right)^{1/2} \int_0^\infty \sigma_a(\varepsilon) f(\varepsilon) \varepsilon \, d\varepsilon , \qquad (3)$$

where m and ε are electron mass and energy, σ_a is the attachment collisional cross section, $f(\varepsilon)$ is the electron energy distribution function (EEDF).

Wong and co-authors [1] have neglected the difference of the attachment coefficient k_a on the electron temperature T_e. As will be seen later, the inclusion of this dependence may be of importance in the case under consideration.

The effect of the strong electromagnetic wave on the ionospheric weakly ionized plasmas results in the electron heating and the nonequilibrium of EEDF. We have solved numerically the Boltzmann equation and have obtained the EEDF in the two-term approximation. The elastic collisions, the excitation of the rotational, vibrational, electronic levels of nitrogen and oxygen molecules have been included. The set of the electron-molecule collisional cross sections has been taken from our previous work [2]. The results of the calculation of the electron transport coefficients in the direct electric field in nitrogen, oxygen, and air are in agreement with the available experimental data.

The coefficients of the electron attachment to the halocarbon molecules have been calculated using the attachment cross section data from the swarm experiments [3-5]. The calculations making use of the Maxwellian EEDF have been carried out, too.

The attachment coefficients obtained in the case of the Maxwellian EEDF are shown in fig. 1. The difference between these data and ones with the nonequilibrium EEDF is not more than 30%. The higher rate of the electron attachment to the

molecules CCl_4 and $CFCl_3$ is observed. Here, the attachment coefficients decrease with the electron temperature growth. This results in the diminishing of the effect proposed by Wong et al. [1].

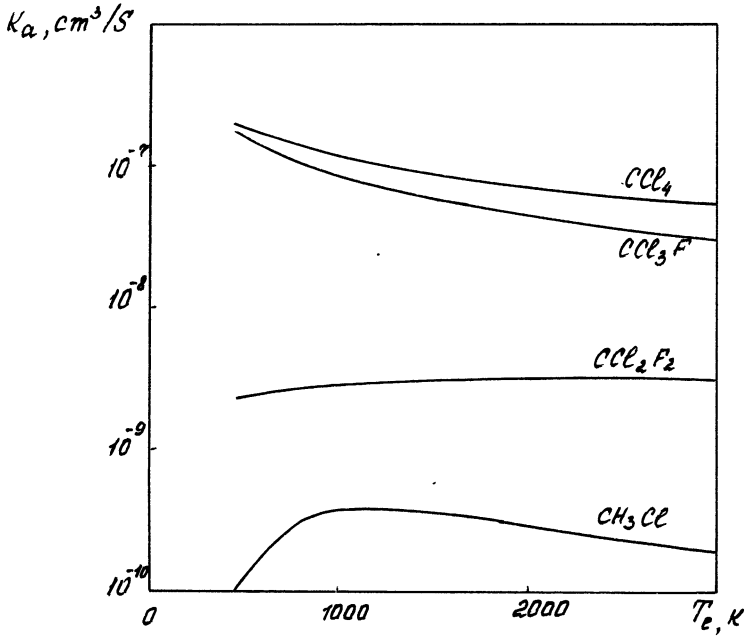

Fig. 1.

The electromagnetic wave effect on the halocarbon molecules balance is characterized by the value $\varphi = k_a n_e/\nu_p$ as a function of electron temperature T_e. Here, n_e is the electron density, ν_p is the halocarbon molecules loss frequency resulted from the photodissociation, diffusion and convection transport upwards. The value $\varphi(T_e)$ overestimates the effect of halocarbon molecules removal because of the neglecting the production of the chlorine atoms from the

negative ions and molecules HCl. For example, this may be the result of photodetachment and photodissociation processes.

In the present paper the value φ as a function of T_e and of height h has been obtained. The ν_p data have been taken from [6]. We have used the functions $n_e(T_e)$ resulted from the calculation [7] of the charged particles density in the daytime upper atmosphere.

The curves obtained are shown in fig. 2 a ($CFCl_3$) and 2 b (CF_2Cl_2).

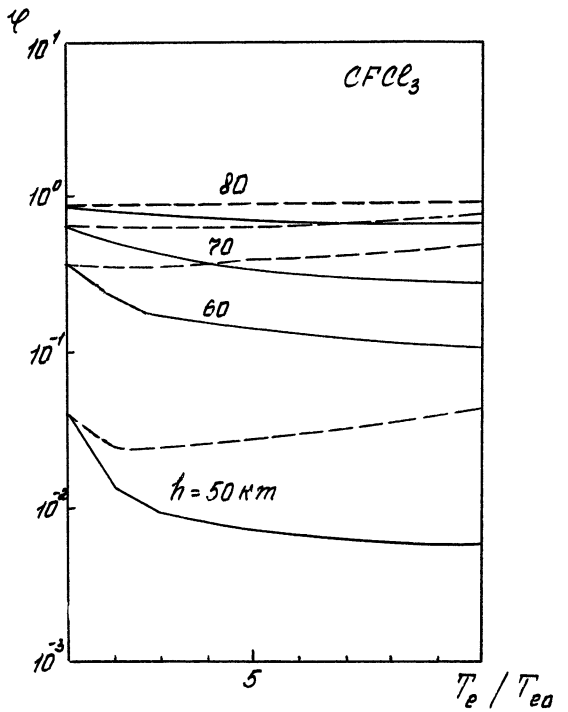

Fig. 2 a.

(The solid curves are obtained with dependence of k_a on T_e and the dotted curves without dependence.) The effect under consideration has positive sign only for the

molecule CCl_2F_2, but its magnitude is small in this case. The effect has negative sign for other halocarbon molecules. Although above 75 km the increase of T_e causes the growth of n_e but the attachment coefficient diminution results in the disappearance of the positive dependence of the attachment frequency $k_a n_e$ on T_e. In addition, below 75 km no electron density growth in the plasmas in the electromagnetic wave is observed because the electron loss is controlled by the three-body attachment to the molecule O_2.

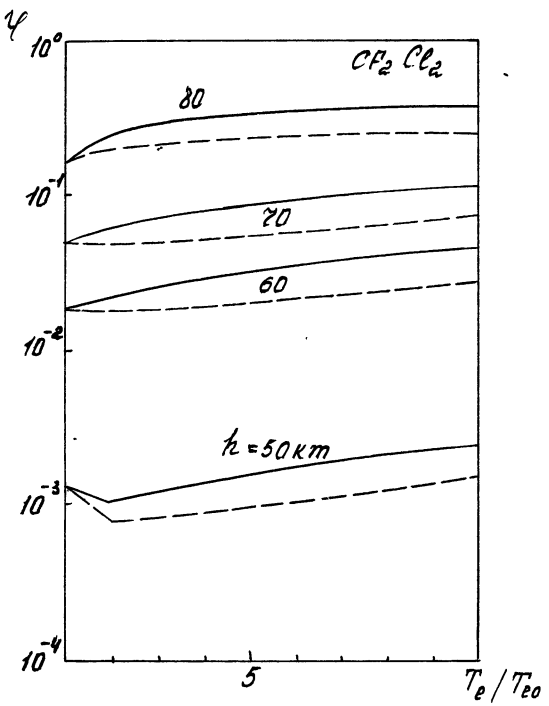

Fig. 2 b.

In summary, the dependence of attachment coefficient on the electron temperature essentially decreases the effect, proposed by Wong et al. [1]. It should be noted that the problem considered is complicated and our results are preliminary. These may be changed if the plasma layer in the atmosphere would be created by the external ionizator.

References

1. Wong A.Y., Steinhauer J., Close R. et al. Comments Plasma Phys. Controlled Fusion 1989, v.12, p.223.

2. Aleksandrov N.L., Vycikailo F.I., Islamov R.Sh. et al. Teplofiz. Vys. Temp. 1981, v.19, p.22 (High Temp.(USSR)).

3. Christodoulides A.A., Christophorou L.G. J. Chem. Phys. 1971, v.54, p.4691.

4. Blaunstein R.P., Christophorou L.G. ibid. 1968, v.49, p.1526.

5. Petrovic L.Lj., Wang W.C., Lee L.C. ibid. 1989, v.90, p.3145.

6. Brasseur G., Solomon S. Aeronomy of the Middle Atmosphere. Dordrecht, Holland: D. Reidel Publishing Company, 1984.

7. Tomko A.A., Ferraro A.J., Lee H.S. et al. J.Atm. Terr. Phys. 1980, v.42, p.275.

THE MEASUREMENT OF OZONE CONCENTRATION PRODUCED BY THE PULSED MICROWAVE DISCHARGE

A.N.Stepanov, V.V.Yazenkov
Institute of Applied Physics, Academy of Science of the USSR
N.Novgorod,USSR

The problem of creating artificial ionized region (AIR) in the Earth atmosphere [1] which is now discussed in literature has given rise to the lively discussion on ecological aftereffects of such an influence on the atmosphere [2,3]. A microwave discharge proposed for creating AIR initiates essential dissociation of molecules of oxygen and nitrogen which is the beginning of a long chain of chemical conversions. Some fears were expressed in paper [2] that the formation (due to the microwave discharge effect on the atmosphere) nitrogen oxides might lead to the destruction of the ozone layer in the Earth atmosphere.

In the present paper a somewhat another aspect of the problem is experimentally studied, namely, the possibility of the effective ozone formation under the action of powerful microwave radiation on the upper atmosphere.The experiment was performed as follows.The radiation of a microwave generator (a magnetron, power P_{max}=100 kw, the wavelength λ=3 cm, the pulse duration τ_p=1-10 mcs)was focused by a spherical mirror into a vacuum chamber. The microwave discharge was ignitedλin the focus of the electromagnetic radiation beam and had the form of the ellipsoid of rotation a little bit stretched along the electric field vector. The major part of the experiments was performed in a technical oxygen at pressure p=30 Torr, although some results referred to the discharge in the air.

The measurement of the ozone concentration was performed by the absorption in Hartley band of the fourth harmonic radiation of a YAG laser (λ=2650A). The method of the multiple transition of the laser radiation through the discharge region was used to increase the sensitivity. The sensitivity achieved in the

experiment was $n_{O_3}=10^{14}cm^{-3}$ at the dimension of the discharge along the laser beam l=2cm. The time dependence of the behavior of the ozone concentration for the oxygen pressure p=30 Torr and the duration of the microwave pulse τ_p=6mcs is given in Fig.1. It can be seen from the figure that the ozone concentration attains its maximum after the microwave pulse ceases and then begins to decrease slowly. The dependence of the maximally attainable ozone concentration $n_{O_3}^{max}$ on the pulse duration given in Fig.2 indicates that there exists an optimal (from the viewpoint of ozone formation) duration of the microwave pulse. The values $n_{O_3}^{max}$ obtained in the discharge in the air are approximately three times less.The electron concentration necessary for estimates was measured by the resonator method [5] and was equal to $n_e=(1-2)10^{12}cm^{-3}$.

The analyses of possible reactions defining the time dependence of the ozone concentration has shown that for the discharge in oxygen during the microwave pulse the dissociation of oxygen molecules is determining, but after the discharge is over the following reactions dominate

$$O + O_2 + O_2 \xrightarrow{k_1} O_3 + O_2$$

$$O + O_3 \xrightarrow{k_2} 2O_2$$

The corresponding set of equations describing the dynamics of the behavior of the concentrations of monatomic oxygen n_o and ozone n_{o_3} has the form

$$\begin{aligned} \dot{n}_o &= -k_2 n_o (k_1 n^2/k_2 + n_{o_3}) \\ \dot{n}_{o_3} &= k_2 n_o (k_1 n^2/k_2 - n_{o_3}) \end{aligned} \qquad (1)$$

Here n is the concentration of the molecular oxygen, $k_1=1.1\cdot10^{-34}\cdot e^{510/T}$ cm^6/s, $k_2=1.9\cdot10^{-11}\cdot e^{-2300/T}$ cm^3/s [4]. As it follows from the second equation of system (1), the ozone concentration does not exceed the value $\xi=k_1n^2/k_2$, therefore we neglect n_{o_3} in the first equation in comparison with ξ. Then for the ozone concentration the following solution may be obtained:

$$n_{o_3}=\xi(1-\exp(n_{oo}/\xi\cdot(1-\exp(-k_2\xi t)))) \qquad (2)$$

Here n_{oo} is the concentration of monatomic oxygen at the end of the microwave pulse. Exact (numerical)solution of the system of

equation (1) shows that the result obtained practically does not differ from the one obtained by formula (2). According to (2) the ozone concentration increases up to a certain stationary level $n_{o_3}^{st}$ defined by the relation of the values n_{oo} and ξ : if $n_{oo} < \xi$ then $n_{o_3}^{st} = n_{oo}$ and the entire monatomic oxygen converts to ozone, if $n_{oo} > \xi$, then $n_{o_3}^{st} = \xi$. Fig.1 shows the theoretical dependence of the dynamics of the ozone concentration according to formula (2), the diffusion spread during long time period was taken into account.

The maximum in the dependence of the ozone concentration on the duration of the microwave pulse (Fig.2) is caused, in our opinion, by the gas neating due to the microwave discharge. If at first with the increase of τ_p the concentration of monatomic oxygen n_{oo} grows, and, consequently, $n_{o_3}^{st}$ does, then n_{oo} becomes of the order of ξ, which begins to define the stationary ozone concentration. Since $\xi = k_1 n^2 / k_2$ is a sharply decreasing function of the temperature (see, for definition k_1 and k_2), the further increase of τ_p, leading to the grow of gas temperature, decreases ξ.

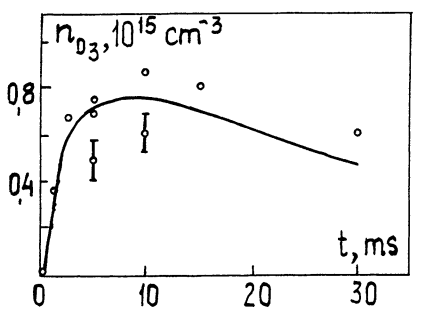

Fig. 1

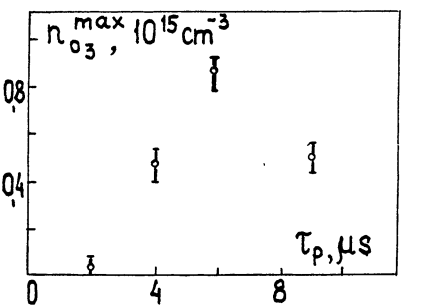

Fig. 2

References

1.Borisov N.D., Gurevich A.V., Milikh G.M. Artificial Ionized Region in Atmosphere. M.: IZMIRAN, 1986, p.184.

2.Askaryan G.S., Batanov G.M., Kossyi I.A. Dokl. Akad. Nauk SSSR, 1988, v.302, N3,p.566-570.

3.Larin V.F., Rumyantsev S.A. Optika atmosfery, v.2, N12,p.1273-1279.

4.Mc Evan M., Phillips L. Chemistry of the Atmosphere. M.: MIR, 1978,p.375.

5.Vikharev A.L., Ivanov O.A., Stepanov A.N. Fizika plazmy, v.10,vyp.4,p.792-800.

Ultraviolet Radiation of Artificial Ionized Layer in the Upper Atmosphere

A.L.Vikharev.,O.A.Ivanov.,A.V.Kim,A.G.Litvak

Institute of Applied Physics,USSR Academy of Sciences.

Nizhny Novgorod, USSR

The possibility of an artificial ionized layer (ALL) formation in the Earth's atmosphere is widely discussed nowadays. A microwave nanosecond discharge is supposed to be used for this purpose [1].A large portion of the energy absorbed in this disharge is spent on the excitation of the molecules electron levels .The population inversion that may occur under these conditions will result in the regime of the spontaneous amplification of radiation in the direction of the AIL maximum size.In the air atmosphere such a regime can be realized at the $C^3\Pi_u - B^3\Pi_g$ transition of the second positive nitrogen system (0-0 band,λ_0=337,1nm). UV radiation can be used to determine and control the AIL parameters.

The possibility of creating the induced UV radiation for one of the proposed regime of AIL formation [1] can be estimated. AIL is expected to be formed at the height H=30km (p=10 Torr,$\nu=\omega$) by a microwave discharge (λ=3cm) in the intersection region of the beams formed by antennas with diameter d=60m located at the distance D=30km. The radius of the focal spot R is 9 m,the angle between the beam axes $\varphi=30^o$,and the size of AIL L=40m. The microwave pulse duration is chosen to be equal to the radiation lifetime of the upper laser level τ_u=40ns. The intensity of the electric field E in the pulse is assumed to be

close to the breakdown one, therefore the electron concentration N_e in the discharge reaches the critical value at the end of the pulse. The ionization frequency ν_1 required for this regime should be equal to:

$$\nu_1(Ee/p)=\ln(Nc/No)/\tau_c \sim 5\ 10^8 s^{-1} \qquad (1)$$

(where $Ee=Eo\ \nu/(\omega^2+\nu^2)^{1/2}$ -is the effective field). This can be achieved wiht the parameters Ee/p=120 V/cm Torr [2].Under theseconditions the electron levels of nitrogen are excited effeciently. Figure.1 shows the constants of the excitation of the level $C^3\Pi_u(v=0)$ and $B^3\Pi_g(v=0)$ which are the operating levels of a nitrogen laser. The calculation was made for a Maxwellian distribution function.To provide this regime the power of microwave radiation in each beam should exceed the level $P=4\ 10^9$W

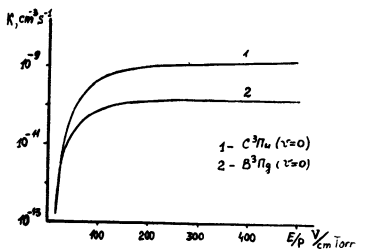

Fig.1

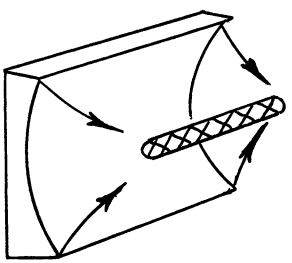

Fig.2

The condition required for the amplification of spontaneous radiation is as follows. The photon born at the one end of the discharge will provoke the birth of the photon at the other end: $\eta L>1$, where

$$\eta=(\lambda_o^3/8\pi c)(\lambda_o/\Delta\lambda_o)A_{21}Nc^* \qquad (2)$$

is the amplification factor ,λ_o is the wavelength, $\Delta\lambda_o$ is the

width of the spectral line, A_{21} is the Einstein coefficient, and Nc^* is the population of the operating level. From Eq.(2) one can estimate the threshold population Nc^* which gives rise to amplification

$$Nc^* > \frac{8\pi}{\lambda^2\delta} \cdot \frac{\Delta\lambda_o}{\lambda_o} \cdot \frac{1}{A_{21}\tau_u} = 1{,}2\ 10^{12}\ Cm^{-3} \qquad (3)$$

The electron concentration at which the value N_c^* is achieved was estimated from the equation

$$dNC/dt = Ne\ N\ K_c - Nc/\tau_c \qquad (4)$$

It follows from (4) that the necessary population of the operating level is achieved if the electron concentration at the end of the microwave pulse exceeds the value:

$$Ne(\tau_u) = 2\ 10^{13}/p(Torr)\ \ Cm^{-3} \qquad (5)$$

For p=10Torr this value is $Ne(\tau_u) = N_{ec} = 2\ 10^{12} cm^{-3}$ and thus it can be realized in the discharge. It should be noted that in contrast to the case of the TE wave intersection where the density $Ne = N_{ec}\sin^2\varphi$ is achieved, here preference is given to the TM beams are where the discharge homogeneity is higher and the critical density is easy to achieve [3].

The possibility to obtain the induced UV radiation from the microwave discharge plasma was studied experimentaly [4]. Figure.2 shows the scheme of the experiment. A relativistic microwave generator (λ =3cm, τ =40ns) serves as the radiation source. The discharge is ignited in the focus of the wave beam formed by a metal mirror and is shaped as a cylinder 1-1,5 cm in diameter and 20-30cm long. Figure 3 and 4 show the oscillograms of the microwave pulse (a) and the pulse of the discharge UV radiation (b) (λ_c=337.1nm). The radiation power, without the laser mirrors, reaches 1-3 kW, the specific power output is approximately 50-150 W/cm^3.

A simplified set of equations discribing the operation of a nitrogen laser is given below

$$dNc/dt=K_c N\ Ne - (K_{tc}N+1/\tau_c)N_c - P$$
$$dNb/dt=K_b N\ N_e - K_{tb}N\ N_b + N_c/\tau_c+P \qquad (6)$$

where K_{tc} and K_{tb} are the constants of the quenching of levels B and C , P is the power of the induced radiation. Assuming that P is the saturation power, one can estimate from (6) the radiation power corresponding to the regime of maintaining AIL. The estimates show that at the end of the microwave pulse the specific power of radiationin this regime reaches the values $\rho\sim150$ W/cm^3 and the total power of the UV radiation is $P\sim500$ MW.

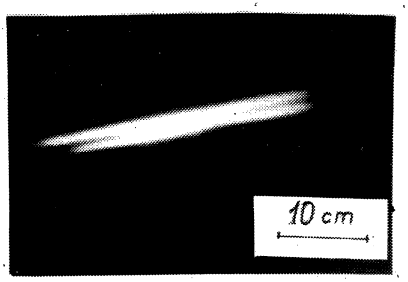

Fig.3

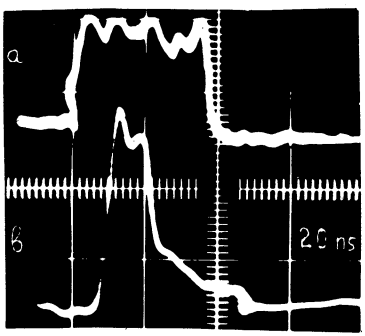

Fig.4

Measuring the power of UV radiation one can find the discharge parameters. Thus in our experiment it was possible to determine the ionization frequency by the time of the light signal delay with respect to the onset of the microwave pulse (1). From the relation $\nu_i(Ee/p)$ [2], $Ee/p=60$ V/cm Torr is determined in the discharge regime , which corresponds to the electric field intensity in the beam E=45 kV/cm.Having defined the coefficients Kc and Kb corresponding to this value ofEe/p ,from Eq.(6) we

obtain the value of Ne corresponding to the power of the OV radiation generated by the discharge $N_e \sim 10^{12} cm^{-3}$.

REFERENCES

1.N.D. Borisov, A.V.Gurevch, G.M. Milikh . An Artificial Ionized Region in the Atmosphere. M:IZMIRAN, 1986

2. A.L.Vikharev , V.B.Gil'denburg ,O.A.Ivanov . et al. Fizika Plasmy, 1986 ,v.12 ,p. 1503.4

3. A.L.Vikharev ,V.B.Gil'denburg , A.V.Kim . et al. In: High-Frequency Discharge in Wave Fields.Inst. Appl. Phys., USSR,Acad. Sci. ,Gorky,1988.

4. A.L.Vikharev ., O.A.Ivanov ., A.V.Kim . In: Relativistic Hihg-Frequency Electronics.Issue 6.,(Ed.by A.V.Gaponov-Grekhov) Inst. Appl. Phys., USSR,Acad. Sci. ,Gorky, 1990.

A NEW APPROACH TO THE DEVELOPMENT OF ECR PLASMA SOURCES

J. Margot-Chaker, M. Moisan and J. Teichmann
Département de physique, Université de Montréal, C.P. 6128, succursale A, Montréal, Québec H3C 3J7

1. Introduction

Microwave produced plasmas operated at electron cyclotron resonance (ECR) are nowadays attracting most of the efforts in plasma processing developments for the semiconductor industry and for materials treatment in general. The advantages attributed to these plasmas basically amount to four features: (i) a higher electron density as compared to RF capacitive discharges, (ii) the possibility of operating at extremely reduced gas pressures (below a few mTorr), thus optimum conditions for plasma homogeneity, (iii) the low energy of the ions striking the substrate and (iv) a possible independent biasing of the substrate.

Despite all these positive features and a strong demand from high technology industries, the modelling of ECR plasmas is far from being complete. To contribute remedying this situation, we are extending our current theoretical and experimental expertise on surface wave produced plasmas (SWP) to the case where the discharge is submitted to an axial, static magnetic field B_0.

The advantages of using SWP concern both theory and experiment. With respect to theory, in short, these come from the possibility of fully writing down and solving the equations describing the whole wave-discharge system: in fact, this is one of the reasons why SWP are at the present time the best modelled high frequency (HF) discharges and why they have led to a better understanding of HF discharges ($B_0 = 0$) in general. One thus strives to achieve the same for HF discharges submitted to B_0. As concerns experiments, the main advantages of SWP are their excellent stability and reproducibility (monomode operation), and the existence of a complete set of HF field applicators to efficiently launch and select these guided waves at frequencies covering both the RF and microwave frequency domain (1MHz - 10 GHz demonstrated).

2. Equation of guided waves along a magnetoplasma

2.1. Description of a plasma submitted to an axial magnetic field. We have used a hydrodynamic, cold plasma description, assuming collisional damping through electron-neutral

collisions as characterized by ν, the effective collision frequency for momentum transfer (The kinetic theory aspect needed to consider the resonant absorption at $\omega_c = \omega$, where $\omega_c/2\pi$ is the electron-cyclotron frequency, will be the object of future publications). The system configuration is that of a cylindrical plasma column represented by the permittivity tensor $\underset{\sim}{\varepsilon}$ (relative to ε_0, the vacuum permittivity); the plasma column is contained within a dielectric tube (permittivity ε_g) of inner and outer radius R_1 and R_2, respectively, the latter being surrounded by vacuum. The plasma permittivity is

$$\underset{\sim}{\varepsilon} = \begin{pmatrix} \varepsilon_1 & -\varepsilon_2 & 0 \\ \varepsilon_2 & \varepsilon_1 & 0 \\ 0 & 0 & \varepsilon_3 \end{pmatrix} \qquad (1)$$

where $\varepsilon_1 = 1 - x^2(1-i\delta)/[(1-i\delta)^2 - \tau^2]$, $\varepsilon_2 = i\,\tau\, x^2/[(1+i\delta)^2 + \tau^2]$, and $\varepsilon_3 = 1 - x^2(1-i\delta)$, with $i = \sqrt{-1}$, $x^2 = \omega_p^2/\omega^2$, $\delta = \nu/\omega$ and $\tau = \omega_c/\omega$; $\omega_c = eB_0/m$ where e/m is the electron charge to mass ratio and ω_p is the electron plasma angular frequency. Clearly, ε_1 and ε_2 diverge at ECR if $\nu = 0$.

2.2. Guided wave equations and field solutions. Using Maxwell equations and the dielectric tensor from (1), assuming field intensities varying as $\exp(i\omega t - \gamma z)$ where $\gamma = i(\beta + i\alpha)$, β being the wavenumber along the plasma column axis and α, the corresponding wave attenuation coefficient, we find that the axial electric and magnetic field of the wave obey the equations

$$\nabla_T^2 E_z + aE_z = bH_z \quad \text{and} \quad \nabla_T^2 H_z + cH_z = dE_z, \qquad (2)$$

where ∇_T is the Laplacian in the direction transversal to the column axis, and $a = (\gamma^2 + \beta_0^2\,\varepsilon_1)\,\varepsilon_3/\varepsilon_1$, $b = i\omega\mu_0\gamma\varepsilon_2/\varepsilon_1$, $c = \gamma^2 + \beta_0^2\,\varepsilon_r\varepsilon_l/\varepsilon_1$, $d = -i\omega\varepsilon_0\gamma\varepsilon_3\varepsilon_2/\varepsilon_1$; $\varepsilon_r = \varepsilon_1 - i\varepsilon_2$, $\varepsilon_l = \varepsilon_1 + i\varepsilon_2$; μ_0 is the free space magnetic permeability and $\beta_0 = \omega/c^*$ where c^* is the speed of light in free space. The E_z and H_z equations are coupled unless $\varepsilon_2 = 0$ or $\gamma = 0$. After some manipulations on eqns. (2), we get in the plasma

$$(\nabla_T^2 + p_1^2)\,(\nabla_T^2 + p_2^2)\,E_z = 0, \qquad (3)$$

where $(a+c) = p_1^2 + p_2^2$ and $(ac-bd) = p_1^2 p_2^2$. Thus, as a rule, the E_z field is a linear combination of two solutions and, in cylindrical coordinates, it is expressed as

$$E_z = [A_1\,J_m(p_1 r) + A_2\,J_m(p_2 r)]\,\exp(im\phi), \qquad (4)$$

where J_m is the Bessel function of order m with complex argument, m is an integer (positive, zero or negative) defining the azimuthal configuration of the electromagnetic field; p_1 and p_2 are the transversal wavenumbers, which are related to the complex wavenumber γ. Solutions in the dielectric tube and in vacuum are as with surface waves ($B_0 = 0$).

3. Wave solutions

Requiring the continuity of the tangential components of the E and H fields at the various interfaces, we get the dispersion equation, namely γ vs. ω. Various solutions to this equation are obtained but we only retain those such that $\alpha \to 0$ when $\nu \to 0$.

3.1. Transversal wavenumber at ECR. For $\omega_c = \omega$ (and $\nu = 0$ for simplicity), we find

$$2\,p^2_{1,2} = \gamma^2 - \beta^2_0 \pm [(\gamma^2 - \beta^2_0)^2 - 4\beta^2_0\varepsilon_3\{2\gamma^2 - \beta^2_0(1+\varepsilon_3)\}]^{1/2}, \qquad (5)$$

showing that the wavenumbers within our model do not diverge at ECR since they do not involve ε_1 and ε_2.

3.2. Wave phase and attenuation diagrams. For each given azimuthal configuration m, we find m propagation modes that converge toward the surface wave solution for $B_0 = 0$. These are designated as the fundamental hybrid (E and H combinations) modes and identified by HE_{m1}. Their phase diagram (ω constant, ω_p varying in the ratio ω/ω_p) and corresponding attenuation coefficient are shown in Fig. 1, for $\omega_c/\omega = 1$, and for m=0, ±1. As a rule, the wave propagates for larger ω/ω_p values (i.e. for smaller electron densities) than for $B_0 = 0$. Besides the fundamental modes, we found that other modes could appear for $\omega_c/\omega \gtrsim 1$: these tend toward TM_{mn} mode ($n \geq 1$, integer) when $B_0 = \infty$, and are named magnetic hybrid modes and designated by HE^*_{mn}. From Fig. 2, one sees that the HE_{01} (m=0) and HE_{11} (m=1) fundamental modes transform continuously into HE^*_{01} and HE^*_{11} magnetic modes. The HE_{-11} mode is asymptotic at β_0 for $\omega_c/\omega > 1$ and its coefficient α drops considerably. Figure 3 examines, as an example, magnetic hybrid waves for given m and three different values of n. For $n \geq 2$, these modes do not exist for $\omega_c/\omega < 1$, as they are resonant ($\beta \to \infty$) at $\omega_c = \omega$.

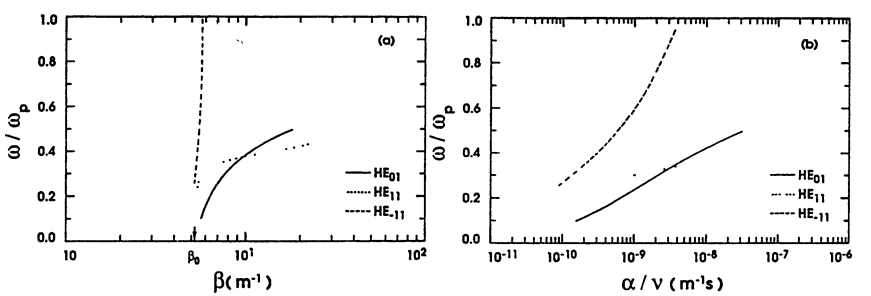

Fig. 1. Calculated phase (a) and attenuation coefficient (b) diagrams for the fundamental hybrid modes of azimuthal configuration m=0, ± 1 at $\omega_c = \omega$. Calculation parameters: $\omega/2\pi$ = 2.45 GHz, R_1 = 13 mm, R_2 = 15 mm, ε_g = 4.52, $\nu/\omega = 10^{-3}$.

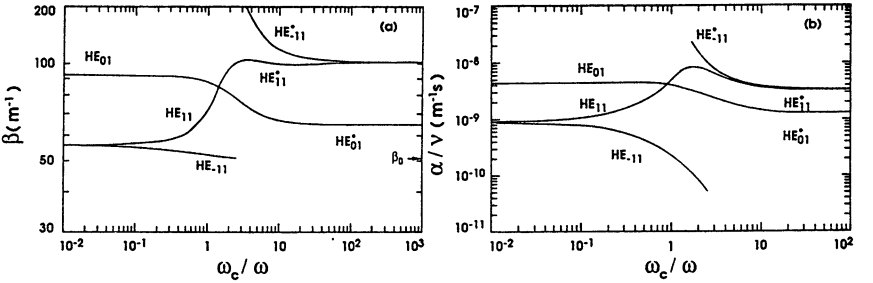

Fig. 2. Calculated axial wavenumber (a) and attenuation coefficient (b) vs. $\omega_c = \omega$ for the fundamental hybrid modes of azimuthal configuration m=0, ± 1 and corresponding magnetic hybrid modes with m = 1. Other conditions as in Fig. 1 with $\omega/\omega_p = 0.35$.

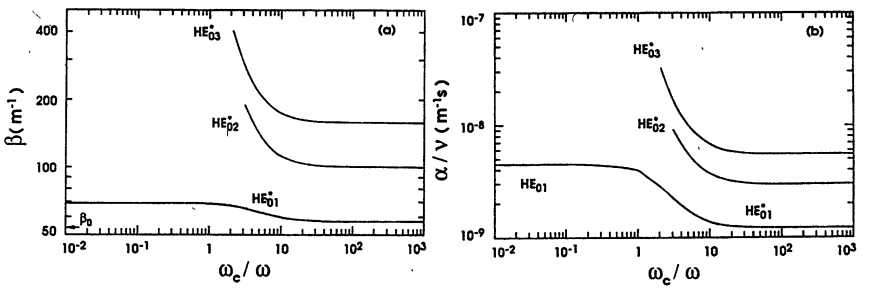

Fig. 3. Calculated axial wavenumber (a) and attenuation coefficient (b) vs. $\omega_c = \omega$ for the magnetic hybrid modes of azimuthal configuration m = 0 and radial configuration n = 1, 2, 3. Other conditions as in Fig. 1 with $\omega/\omega_p = 0.30$.

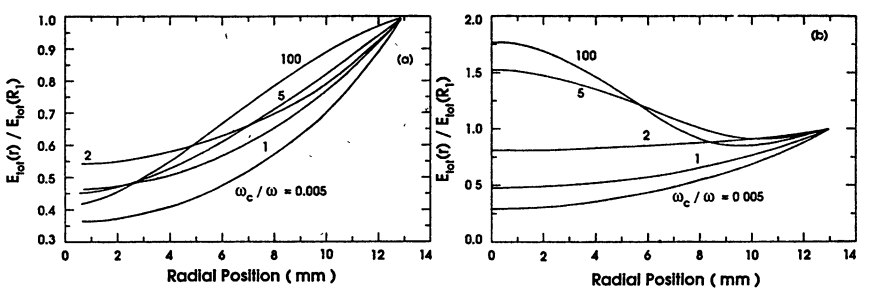

Fig. 4. Calculated total electric field intensity as a function of radial position within the plasma column at various values of ω_c/ω, for the m = 0 (a) and m = 1 (b) fundamental hybrid modes. Other conditions as in Fig. 1 with $\omega/\omega_p = 0.35$.

Because of lack of space, we end with Figs. 4a and 4b showing the total electric field variation as a function of radial position r within the plasma (the fields intensities are normalized at unity at the tube wall) for the fundamental HE_{01} and HE_{11} modes, respectively. In the present case (depending on tube radius and frequency), the HE_{01} mode field intensity grows with r, whatever ω_c/ω. In contrast, the field intensity of the HE_{11} mode decreases with the radial position beyond some ω_c/ω value.

4. Conclusion

We have presented a theoretical analysis of the influence of an axial, static magnetic field B_0 on travelling waves assumed to sustain a plasma column contained within a cylindrical dielectric tube surrounded by vacuum. The problem is based on guided waves that reduce to the well known electromagnetic surface waves for $B_0 = 0$. This communication is the first stage of a general study intended to model ECR plasmas. The knowledge of the equations of the present wave-plasma system is an essential feature of our approach to ECR plasmas. At this point, we only considered a collisional absorption and we assumed the plasma to be homogeneous. Our results can be summarized as follows.

- *Wave dispersion and attenuation properties*: 1) for each given azimuthal configuration m of the wave field and for $B_0 \neq 0$, there exist m propagation modes that converge toward the surface wave solution for $B_0 = 0$. These are called fundamental hybrid modes and are designated by HE_{m1}; 2) for these fundamental modes, there is no singularity in the wavenumber β and in the attenuation coefficient α at $\omega_c = \omega$, though two out of three of the basic components of the plasma dielectric tensor diverge at ECR; 3) providing the value of B_0 is typically such that $\omega_c/\omega \gtrsim 1$, for any given azimuthal wavenumber m, one finds an infinity of waves, each identified by the positive integer n. Each such wave is characterized by the number of zeroes (n-1) in the radial variation of the E_z field intensity. These are named magnetic hybrid modes and are designated by HE^*_{mn}. Except for $HE_{01}{}^*$ and HE^*_{11} that transform continuously into the fundamental modes HE_{01} and HE_{11} when B_0 decreases from infinity toward zero, all other magnetic hybrid modes are resonant ($\beta \rightarrow \infty$) at $\omega_c = \omega$.

- *Plasma density*. The plasma density increases with the HF power deposited into the plasma per unit axial length. To ensure that, under given discharge conditions, the wave transfers the largest amount of its power flow to the plasma implies obtaining the largest value of α by adequately selecting the wave mode. As far as the fundamental hybrid modes are concerned, the largest value of α at $\omega_c/\omega < 1$ is obtained from the HE_{01} mode whereas for $\omega_c/\omega \gtrsim 1$, it comes from the HE_{11} mode. In contrast, the value of α for the HE_{-11} mode α value starts decreasing with increasing ω_c/ω when the attenuation coefficient of the HE_{11} mode begins increasing; as a matter of fact, for $\omega_c/\omega \gtrsim 1$, the HE_{-11} mode reaches values of α that are so low that it is not clear that a plasma column could be sustained, since a minimum density n_{min} (see further) must be reached for the discharge to hold. As for the magnetic hybrid

modes, for n = 1 (no zero in the field intensity along the plasma radius), the modes with an azimuthal configuration m=±1 have a larger attenuation coefficient than for the m = 0 (HE^*_{01}) configuration. Concerning HE^*_{mn} modes with $n \geq 2$, the results are more complex and the real question is the possibility of exciting and selecting these modes; for example, starting from zero magnetic field value and increasing B_0, only the HE_{01} and HE_{11} modes can be continously excited.

- *Minimum electron density n_{min} for sustaining a plasma column.* This minimum value corresponds to the largest ω/ω_p value on the phase diagram: beyond, the wave does not propagate. It is found that n_{min} decreases with increasing B_0, typically up to a factor 2 to 5 for ω_c/ω varying from zero to unity. Clearly, the lower the minimum density, the easier the starting of the HF discharge for a given HF power incident on the plasma.

- *Radial variation of the electric field total intensity and homogeneous plasma processing.* Our calculations showed that the value of B_0 affects the radial distribution of the wave total electric field intensity $E_{tot}(r)$. In particular, for fundamental modes, at low B_0 values, $E_{tot}(r)$ generally increases from the axis to the tube wall. With increasing ω_c/ω values, this radial increase tends to flatten. An interesting exception to this behaviour occurs with the HE_{11} mode, where above a certain ω_c/ω value, $E_{tot}(r)$ starts decreasing with radial position. Such a flexibility in the setting of $E_{tot}(r)$ permits to adjust B_0 so as to obtain an almost radially constant distribution of excited atom density [1]. This shows how the homogeneous plasma processing of a substrate could be achieved at gas pressures where the particle mean free path is lower than the vessel radius (i.e. large gas pressures), in contrast with ECR plasma processing which requires a large mean free path regime (typically pressures below a few mTorr).

- *Polarization of the wave electric field.* Strict ECR conditions call for a circular polarization with the electric field rotating in the same direction as the electrons in their cyclotron motion around the B_0 field lines. From the above we know that *only fundamental hybrid modes can be excited in a continuous way* starting from $B_0 = 0$ up to $\omega_c = \omega$: 1) the HE_{11} mode always shows the adequate ECR polarization; 2) for the HE_{01} mode, polarization depends on the setup conditions: at 2.45 GHz and in a 30 mm o.d. tube, it shows the required ECR polarization whereas this is not always the case at lower plasma stimulating frequencies; 3) the polarization of the HE_{11} mode is a function of radial position and the right ECR condition can be met at some radial positions only.

The above results strongly emphasize the fact that extending the surface wave modelling to HF sustained magnetoplasmas leads to a deeper understanding of such discharges.

[1] M. Moisan, C.M. Ferreira, Y. Hajlaoui, D. Henry, J. Hubert, R. Pantel, A. Ricard and Z. Zakrzewski, Rev. Phys. Appl., 17, 707 (1982).

LONG-LIVING RELATIVISTIC ELECTRON PLASMA PRODUCED AT GYROMAGNETIC AUTORESONANCE IN PLASMA SYNCHROTRON-ACCUMULATOR GYRAC-D

Andreev V.V.*, Golovanivsky K.S.*, Colunga S.**

*Patrice Lumumba Univ. Plasma Phys.Lab.,Moscow, **National Institute of Nuclear Researches, Mexico

In this work a new plasma-physical installation is described,which is intended for creation,accumulation and confinement of plasma with the electron temperature of hundreds keV. The physical mechanism,that forms the basis of functioning of the installation (named GYRAC-D) is Synchrotron Gyromagnetic Autoresonance (SGA) presented by Electron Cyclotron Resonance (ECR) in the conditions of the magnetic field growing in time or in space[1,2,3].

First SGA was displayed on the plasma synchrotron GYRAC-O[4] where plasma was got with density 2 $10^{8}cm^{-3}$,average energy of electron componenta (called lower electron temperature) up to 300keV and the confinement time of particles estimated in dozen milliseconds.GYRAC-O was a compact mirror trap,where in the single pulse operation mode SGA was realised in the pulse magnetic field.Confinement of obtained plasma was carried out in static magnetic field corresponded to the non-relativistic ECR.This scheme was in full accordance with the main aim of the installation GYRAC-O that was to demonstrate SGA effect.But it (scheme) is not optimum for getting plasma with maximum density and electron temperature since at the back front of magnetic field pulse decompression of plasma take place,caused by the fact that induction electric field decreases the electrons density and temperature.Besides,the single pulse regime ruled out the possibility of accumulating electron-hot plasma.But,it turned out to be possible owning to the fact that generation time of such plasma is in dozen and hundreds time shorter than their confinement time in the magnetic field.

The new installation GYRAC-D,described in this work,had the following main aims to encrease the density of such plasma: 1) division of the generation area of plasma with the relativistic electron vortex (e-vortex) and the area of its confinement,2) confinement of such plasma in the magnetic field,corresponded to the relativistic (not to classical as in GYRAC-0) ECR, 3)simultaneous generation of two e-vortex and their confinement in one and the same volume,localized beyond the area of their generation, 4)accumulation of e-vortexes,generated in regime of series of pulses,5)realization of the regime of external ingection.

The installation GYRAC-D (fig.1a) consist of a vacuum cylindrical resonator-1 with two pulsed magnetic coils,placed symmetrically as to the main area of the resonator-2,put in the static magnetic field created by three couples of coils-3.The vacuum TE_{118} resonator exited by magnetron generator in the pulse at friequency 2.35 GHz, power-150 W.The coils of the static magnetic field form the mirror trap magnetic field with the mirror ratio 1.2 (figlb). The pulsed (τ - 1 ms) magnetic field is realized by the capacitor discharge (C=100 cF, U=400 V) through two coils-2.The thickness of the resonator walls is several times smaller than that of the skin.The installation (except the ingection and static magnetic field) works in the pulsed regime.The forplasma (ECR-injector ,Lysitano type) is a cord in 6mm diameter.It's parameters can vary in the following limits : n_e =1 10^9 - 1 10^{10} cm^{-3},T_e = 20 - 80 eV in the woking pressures range from 1.5 10^{-5} to 7 10^{-5}Torr.

The trapping of electrons in the SGA regime was realized in two equally placed as to the main area of the resonator zones, in which pulsed magnetic coils were situated.In these zones the second maximums of the HF electric field of the resonator were localized (counting out of the end walls of the resonator,fig.1a). The pulsed magnetic field (decay time 500 μs) locally lowers the value of static magnetic field (B_{max}=1150 G) to the value, corresponding to the ECR for the rest mass (B_o=840 G).The profile of superpositional magnetic field in time is presented at fig.1b.

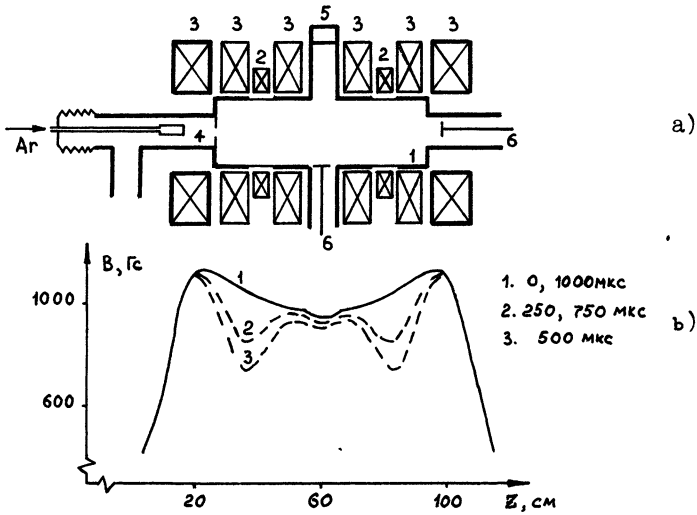

FIG.1. a)the scheme of the experimental installation, b)the longitudional profile of the superpositional magnetic field in time.

400 μs after the beginning of the pulse of the magnetic field the pulse of the HF field with the duration 600 μs comes into action. Then,when the quantity of induction of the riverse magnetic field begins to fall down at the expense of current reducing in the pulsed coils at the back front of current pulse, the quantity of induction of superpositional magnetic field increases in time,achieving it's maximum value,equal to the initial value of the static magnetic field B_{max} in the areas of the second (from the end walls) maximums of standing wave.Then,the interaction of electrons with the field of standing wave in the increasing in time magnetic field (SGA) results in the creation of plasma with relativistic electron componenta,which is confined in the mirror trap.Installation makes it possible to realize the accumulation of such plasma by repeating of the described process in the regime of tandem pulses during one working cycle (fig.2).

As the means of registration of relativistic plasma we used X-ray radiation,imitated by plasma,which was detected in the cross and longitudional directions as to the magnetic field by the scintillatory detectors ,registed only radiation from the gas.The radiati-

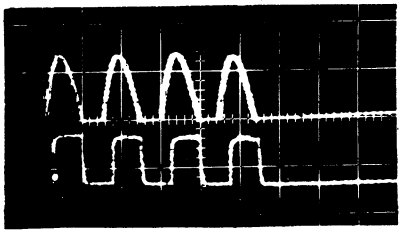

FIG.2. a)the time dependence of the pulsed magnetic field and b) HF electric field in resonator in the tandem pulse regime.

on quanta were registered during the first 5 - 10 ms and allowed to define the electron energy,which turned to be close to the calculated one (200keV).With the aim to determine the areas of plasma localization we used the X-ray radiation,imitated under the interaction of relativistic electrons with the target,put into the central part of the resonator.The experiments showed that the integral intensity of the registered radiation significantly depends on the orientation of the target's plate and the number of heating zones and pulses in use.Thus,if the target's plate is perpendicular to the cross-section of the chamber the registered intensity is maximum,when the 90°turn of the targed leads to the quick decrease of the signal.The use of one or two pulsed coils doesn't quantatively change the picture of observing processes,but in the second case the intensity of X-ray radiation grows.Obtained results showed that the relativistic plasma is concentrated in the central area of the resonator and has configuration of a cylinder with 2.5 cm radius and 3.6 cm height.The relativistic Larmore radius of the electron with the energy 200 keV in the central area is $\simeq$1.6 and the radius of forplasma$\simeq$ 0.3 cm. If we imagine that plasma looks like a e-vortex rotating around the axis of the trap,then the radius of such plasma should be about 2cm that correlates with the experimentally achieved value.

The registration of loss current was carried out by two flat collectors,both beyond the area of localization of hot electron plasma.Both collectors were kept under the negutive potential enough for the measuring of the saturation ion current (proportional to the plasma density) under different discharge conditions.The obtained

results made it possible to define the density and the number of relativistic electrons,trapped in SGA regime.After HF pulse and pulse of magnetic field the growing of the ion saturation current is conditioned by the ionization of background gas by relativistic electrons.The mesuring of full losses of particles,considering the ionization time rate we defined relativistic electron's density equals~2 $10^{8}cm^{-3}$,noting that they concentrated in the volume~70 cm^{-3} their number is~2 10^{10}.These results are in agreement with the ones,obtained in[4,5]where the measurements were carried out by analysing synchrotron radiations.It's worth mentioning, that~2 10^{10}electrons are contained in the forplasma cord 6.4cm length.It means that in each SGA zone all the electrons from the 3.2cm length of cord are trapped in the acceleration regime.The length of the cord coincides with the width of the hole,formed by the riversed pulsed magnetic field in the SGA zone (fig1b).The experiments also showed that the accumulation of plasma really took place. The oscillogram (fig.3b) of ion saturation current in tandem pulse regime clearly shows it.For comparison the oscillogram in single pulse regime is taken (fig.3a).It'sseen that the amplitude in the packet of pulses is in 4 times higher than that in single pulse regime.The obtained density~1 $10^{9}cm^{-3}$,and the number of relativistic electrons reached ~7 10^{10}.The study of plasma decay process showed that there were 2 stages after SGA cycle.The first one is rather quick particles losses at time 40-70 ms,which depends on the pressure,not pulses of heating (fig.3).At the second stage the plasma decay is much slo-

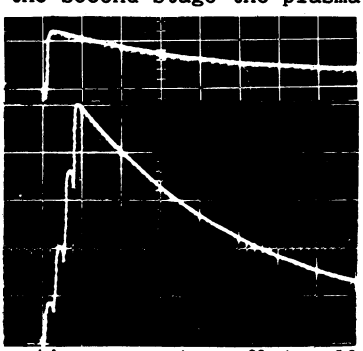

FIG.3, Ion saturation current on flat collector in single pulse regime-a),and tandem pulses regime-b) (5ms/div,5 10^{-5}Torr).

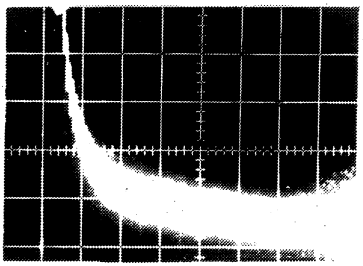

FIG.4 Decay of ion saturation current in tandem pulses regime (0.5s/div,1.5 10^{-5}Torr), continues ingection is presented.

wer with time constant 200 ms- 1 s (fig.4) at gas pressure in interval 5 10^{-5} ~ 1.5 10^{-5}Torr.These results lead to the conclusion that accumulation of plasma isn't complicated by any unstabilities.Plasma decay time correspondes to binar e-n collisions of relativistic particles.

The main results of the work are:a)the reproduction of SGA-effect on another installation in much more complicated physical conditions,b)using of riverse magnetic field,allows to eliminate decompression and cooling of produced plasma,c)e-vortexes throwing from two SGA zones flow together without any instabilities and confined in the trap during rather long time,d)life-time is limited by the collisions (binar,e-n),e)The accumulation of plasma in tandem SGA cycles regime is possible,the density of plasma is proportional to the number of SGA cycles,f)it's realistic for GYRAC-D to put as an aim the achieving of plasma with following parameters - $n_e \sim 10^{11} cm^{-3}$ $T_e \sim 500$ keV;$\tau \sim 10s$;$p_o \sim 10^{-7}$Torr.Such plasma can serve as a pulse or quazistatic source of multicharged ions,such as Kr^{36+},Xe^{52+},U^{82+} [6].

Referenses

1.K.S.Golovanivsky//Physica Scripta,1980, 20,p.126

2.K.S.Golovanivsky//Physics Letters,1973, 44A, N3, p.190

3.A.I.Neishtad,A.V.Timofeev//JTF, 1987,v.93, N5(11),p.1706

4.V.V.Andreev,K.S.Golovanivsky//Physics Letters,1984,100A,p.357

5.V.V.Andreev,K.S.Golovanivsky et al//VII Int.Con on Pl Sci,Kiev USSR,1987,v.2,p.228

6.K.S.Golovanivsky//Sov.Inst.andExp.Technics,1985.v.5,p.7

ECR Sources of Multiply Charged Ions, Involving Millimeter-Wave Gyrotron

S.V.Golubev, V.G.Zorin, T.N.Zorina, S.V.Razin

Institute of Applied Physics, USSR Academy of Science, Nizhny Novgorod, USSR

The sources involving microwave discharge plasma produced in a simple magnetic mirror under the electron-cyclotron resonance (ECR) seem to be most promising in terms of generating intensive beams of multiply charged ions. Such sources are primarily employed for the ion injection into cyclotron accelerators whose efficiency largely depends on the efficiency of an ion source [1]. Besides, an ECR discharge is regarded as a source of non coherent soft X-ray radiation for lithography needs [2]. The possibility of fabricating exotic semiconductors by the multiply-charged ion irradiation of their surface was discussed elsewhere [3].

ECR sources of multiply-charged ions have traditionally been upgraded by improving the conditions of plasma confinement in a magnetic mirror. Yet, another way was discovered recently which is connected with the increase of plasma concentration in a discharge.

This is usually achieved using higher-frequency electromagnetic waves.[+)] The tendency to increase plasma concentration in ECR sources is accounted for by the possibility to obtain an ion flux of higher intensity and higher charged ions.

The charge state distribution is determined by the electron

[+)] Efficiency of microwave radiation frequency enhancement in ECR sources of multiply-charged ions was first demonstrated experimentally in [4]. It was shown that frequency enhancement from 10 to 16,6 GHz led to 100 times increase of the flux of neon ions with charge plus 10.

temperature maintained at the optimal level 1-10 keV, and by the product $N_e\tau$ which has to be as large as possible. In recent papers [5,6] one finds descriptions of the first experiments involving millimeter-wave radiation. The electron concentration in the experiments amounts to $N_e \approx 10^{13}$-$10^{14} sm^{-3}$.

Possibilities of increasing the frequency of microwave radiation in ECR sources were analyzed in [8,9], but no account was taken in them of how the plasma confinement regime changed with higher concentration of plasma. Therefore, in this work we have attempted to analyze the operation regime of a source with a high electron concentration and to estimate possible parameters of the ECR-sources of multiply charged ions, in which plasma is sustained by the radiation of powerful millimeter-wave gyrotrons.

As plasma concentration increases in ECR-sources of multiply charged ions, the condition of "collisionless" confinement of cold ions (T_i=1 eV) in the magnetic mirror is violated in the first place (the length of a mean free path for ions becomes comparable with the characteristic size of a mirror $\lambda_i \leq L$). Yet, for electrons (T_e=1-10 keV) the confinement remains "collisionless" ($\lambda \gg L$). The plasma boundary value obtained from the condition $\lambda_i = L$ is determined by the relation

$$N_{ep} = 2\ 10^{12} T_i^2 / z^3 L$$

(here z is the ion charge). At z=1, L=10 sm, T_i=1eV we have $N_{ep} = 2\ 10^{11} cM^{-3}$. Thus, for plasma densities of our interest $N_e \geq 10^{13}$ cM^{-3} (which largely exceeds N_{ep}) the confinement regime is more like a gas-dynamic than a collisionless one. There is no reliable theory of plasma confinement in such a regime (it can be called quasi-gas-dynamic) at present, therefore, for estimation of the ion life-time we have used the experimental results in [7]. There, investigation of plasma relaxation after a pulsed ECR-discharge in a simple mirror at $N_e = 10^{13}$ cM^{-3} yielded an equation

$$\tau_i = L\ \kappa / V_i \quad , \qquad (1)$$

where V_i is the ion thermal velocity, κ is the mirror ratio. Validity of this formula is verified by the analysis of a plasma life-time in the mirror using the measurements of ambipolar

potential distribution along the mirror axis [2].

Calculations of the plasma parameters for a stationary ECR-discharge in a magnetic mirror are given below. We used the following assumptions. Neutral gas is fed into a mirror, ionized in it completely, and the produced plasma flows out of the magnetic mirror.

It should be noted, that the plasma life-time in the mirror is determined by expression (1). The electron and ion temperatures were found from the energy balance equations

$$2m\upsilon_{ei}T_e/M = T_i/\tau_i \qquad (2)$$

$$N_e(T_e/\tau_i + 2m\upsilon_{ei}T_e/M) = kW/V. \qquad (3)$$

Here: m, M, υ_{ei}, V, W are the masses of electrons and ions, collision rate of electrons and ions, plasma volume, power of microwave radiation, respectively, k is the absorption coefficient of microwave radiation by plasma, which can be close to 1 if the radiation injection into the mirror is optimal.

The charge state distribution was determined using a system of ionization balance equations for ions with the ion charge i (i=1...n, where n is the nucleus charge).

$$dN_i/dt = k_{i-1,i}N_eN_{i-1} - k_{i,i+1}N_eN_i + C_{i+1,0}N_{i+1}N_0 - C_{i,0}N_iN_0 - N_i/\tau_i. \qquad (4)$$

The equations for the neutral gas is as follows:

$$dN_0/dt = I - k_{o,1}N_0N_e - C_{2,0}N_2N_0 - \ldots - C_{n,0}N_nN_0. \qquad (5)$$

N_i is the concentration of ions with the ion charge i, $k_{i,i+1}$ is the ionization constant for the ions N_i, $C_{i,0}$ is the charge exchange constant for the ions N_i and neutral atoms [10].

Figures 1,2 give the values of T_e, $N_e\tau_i$ obtained in solution of the set of equations 1,2,3 for different densities of the microwave radiation flux S (curve 1 corresponds to S=10kW/cm^{-2}, 2 -to 30 kW/cm^{-2}, 3 -to 100 kW/cm^{-2}, 4 -to 300 kW/cm^{-2}) and different electron concentrations (N_e is supposed to be changed by controlling a gas supply to the mirror, calculations were done for the oxygen ions).

At S = 30 kW/cm^2 and N_e= 2 10^{14}cm (present-day millimeter-wave gyrotron allows for experimenting with these parameters [12,6]) the electron temperature T_e=10 keV (fig.1)

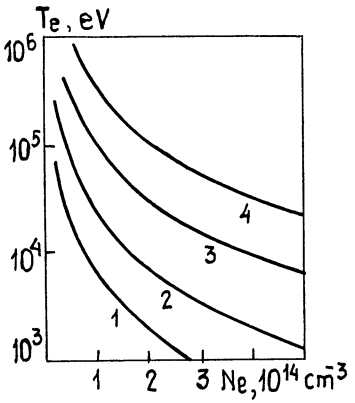

Fig.1

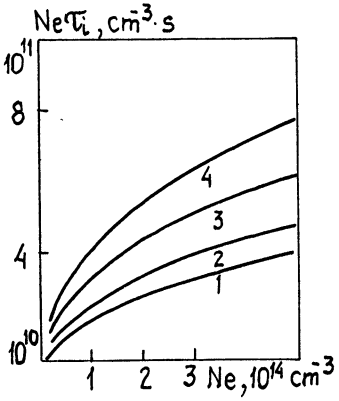

Fig.2

which is approximately equal to the optimal level of ionization for high charge ions. For these parameters the value of $N_e\tau_i$ is more than 2 10^{10} $cm^{-3}s$. This value can facilitate effective generation of ions with very high charge.

Figure 3 show the charge state distribution of ions, which was obtained by solving equations 4,5 (curve 1 is calculated for $N_e\tau_i$=5 10^9 $cm^{-3}s$, 2 for $N_e\tau_i$=2 10^{10} $cm^{-3}s$). At $N_e\tau_i$=2 $10^{10}cm^{-3}s$ one obtains a maximum distribution of oxygen ions for the nucleus charge 8.

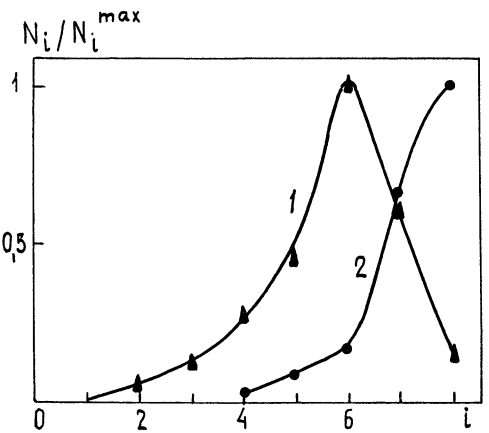

Fig.3

Our estimates show promise for utilization of powerful short-wave radiation in ECR sources of multiply charged ions.

The authors are thankful to V.E.Semenov, M.D.Tokman for valuable discussions.

REFERENCES

1.R.Geller, Journal de Physique, v.50, p.C1-887, 1989.

2.J.H.Booske, F.A.Aldabe, R.F.Ellis, W.D.Getty. J.Appl.Phys., v.64, n.3, p.1055.

3.A.M.Howald et al. Phys.Rev., A33, p.3779, 1986.

4.R.Geller, B.Jacquot, P.Sortis. Nuclear Instruments and Methods in Physics Research, A243, p.224, 1986.

5.Y.Arata et al. Japanese Journal of Applied Physics, v.27, n.7, p.1281, 1988.

6.Yu.V.Bykov, S.V.Golubev, A.G.Eremeev, V.G.Zorin. Physics of plasma (in Russian), v.16, N4, 1990.

7. A. G. Demekhov, B. G. Eremin, A. V. Kostrov, E. V. Suvorov, A.A.Fraiman, A.L.Chekanov, Yu.M.Shagiev. Preprint IAP (in Russian), N146, 1986.

8.W.Halverson et al. Journal de Physique, v.50, p.C1-751, 1989.

9. K.S. Golovanivsky. Instruments and technology of experiments (in Russian), N5, p.7, 1985.

10. W.Lotz. Zeit. fur Phys. v.216, p.241,1968.

11.A.Muller et al. Atom.Molec.Phys, v.13, p.1877,1980.

12.A.Sh.Fix et al. Int. Jour.Elect. v.57, p.821,1984.

ГИПП «Нижполиграф». Заказ 3744. Тираж 1000 экз.